Summer 2022

Inclusive and Inelastic Scattering in Neutrino-Nucleus Interactions

Amy Filkins
William & Mary - Arts & Sciences

Inclusive and Inelastic Scattering in Neutrino-Nucleus Interactions

Amy Filkins

Clifton Park, New York

Master of Science, College of William & Mary, 2018
Bachelor of Arts, State University of New York College at Geneseo, 2016

A Dissertation presented to the Graduate Faculty of
The College of William & Mary in Candidacy for the Degree of
Doctor of Philosophy

Department of Physics

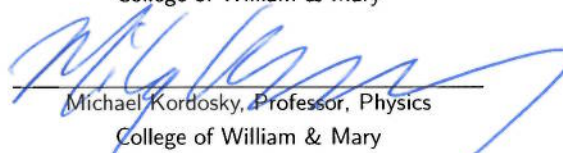College of William & Mary
August 2022

APPROVAL PAGE

This Dissertation is submitted in partial fulfillment of
the requirements for the degree of

Doctor of Philosophy

_____
Amy Filkins

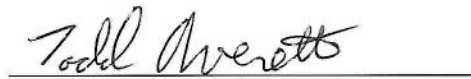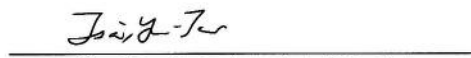Approved by the Committee July 2022

_____
Committee Chair
Jeffrey Nelson, Professor, Physics
College of William & Mary

_____
Michael Kordosky, Professor, Physics
College of William & Mary

_____
Justin Stevens, Assistant Professor , Physics
College of William & Mary

_____
Todd Averett, Professor, Physics
College of William & Mary

_____
Yun-Tse Tsai, Associate Scientist
SLAC National Accelerator Laboratory

ABSTRACT

Neutrino-nucleus cross section measurements can provide both insights into nuclear physics and important data that can be used to improve model predictions used for neutrino oscillation physics. Two measurements of neutrino-nucleus cross sections were performed using data from the MINERvA experiment, each probing different classes of neutrino interactions. Double and single-differential flux-integrated measurements of inclusive charged current neutrino-nucleus cross sections at a peak neutrino energy of 3.5 GeV are presented as a function of the longitudinal and transverse momentum of the muon produced in the interaction. Additionally, an analysis of charged-current deep inelastic scattering (DIS) of muon neutrinos was performed in carbon, iron, lead and hydrocarbon in a neutrino beam with a peak energy of 6 GeV. Cross sections were measured in each material, and ratios were also taken between the cross sections of each of the materials and hydrocarbon, allowing for examination of nuclear dependencies of the neutrino cross section. Absolute DIS cross sections as a function of neutrino energy and flux integrated differential cross sections as a function of the Bjorken-x scaling variable were both measured.

TABLE OF CONTENTS

ACKNOWLEDGMENTS

LIST OF TABLES

LIST OF FIGURES

INCLUSIVE AND INELASTIC SCATTERING IN NEUTRINO-NUCLEUS INTERACTIONS

CHAPTER 1

Introduction

The Standard Model has been exceptionally successful at predicting many of the observations in particle physics. It has a lot of power in its ability to describe the weak, strong and electromagnetic forces. However, it does still leave some phenomena unexplained. One such case is in the field of neutrino physics. According to Standard Model predictions, neutrinos should be massless. The discovery of neutrino oscillations, where neutrinos change type over time, upended that assumption, since this observation requires neutrinos to have a mass. Further measurements in the field of neutrino physics will allow for further testing of possible extensions to the Standard Model and opportunity to enhance our understanding of the universe at both its largest and smallest scales.

There remains many unanswered questions in neutrino physics. The study of neutrino oscillations is an incredibility active field with multiple experiments currently studying them, and large scale experiments planned for the future. Open questions include what is the amount of CP violation (divergent properties of matter and antimatter) in the neutrino sector, which of the neutrinos is the heaviest, are neutrinos Dirac or Majorana particles (are neutrinos their own antiparticles?), are there sterile neutrinos, and many more.

1.1 Standard Model

There are seventeen fundamental particles in the Standard Model, plus anti-matter partners of all of those particles. The particles of the Standard Model are divided based on particle spin into groups called fermions and bosons, as shown in Fig. 1.1. Bosons have integer spins and are force carriers for the electromagnetic, weak, and strong forces. The last boson, the Higgs boson, gives particles mass through electroweak symmetry breaking. The photon is the force carrier for the electromagnetic force, the gluon for the strong force, and the W and Z bosons for the weak force.

The fermions are spin 1/2 particles and are further divided into quarks and leptons. Quarks are the building blocks of protons and neutrons, and are also the constituent parts of all particles called hadrons, which include protons, neutrons, pions, and many more particles. The quarks are the only fundamental particles that interact with gluons through the strong force, which holds nucleons together. Quarks each have a color charge but only exist in colorless combinations of multiple quarks, thus are not observable on their own. The energy required to separate quarks within a nucleus is enough to create another quark. There are three generations of fermions, for each generation there are a pair of quarks with +2/3 and -1/3 electromagnetic charge, and an additional pair of anti-quarks with opposite charges.

There are also three generations of leptons. Leptons include the electron and its heavier cousins the muon and tau. These particles are charged, and thus interact through the both the weak and the electromagnetic force, while not interacting with the strong force. For each generation of charged leptons there is also an extremely light neutral partner, the neutrino.

The three generations of neutrinos are referred to as different neutrino "flavors", and are named after their charged particle counterparts as the electron-neutrino, muon-

Standard Model of Elementary Particles

three generations of matter
(fermions)

interactions / force carriers
(bosons)

I   II   III

QUARKS

mass
charge
spin

≈2.2 MeV/c²	≈1.28 GeV/c²	≈173.1 GeV/c²	0	≈124.97 GeV/c²
⅔	⅔	⅔	0	0
½ u	½ c	½ t	1 g	0 H
up	charm	top	gluon	higgs

≈4.7 MeV/c²	≈96 MeV/c²	≈4.18 GeV/c²	0	
−⅓	−⅓	−⅓	0	
½ d	½ s	½ b	1 γ	
down	strange	bottom	photon	

LEPTONS

≈0.511 MeV/c²	≈105.66 MeV/c²	≈1.7768 GeV/c²	≈91.19 GeV/c²	
−1	−1	−1	0	
½ e	½ μ	½ τ	1 Z	
electron	muon	tau	Z boson	

<1.0 eV/c²	<0.17 MeV/c²	<18.2 MeV/c²	≈80.39 GeV/c²	
0	0	0	±1	
½ νe	½ νμ	½ ντ	1 W	
electron neutrino	muon neutrino	tau neutrino	W boson	

GAUGE BOSONS
VECTOR BOSONS

SCALAR BOSONS

FIG. 1.1: Diagram of Standard Model particles. [1]

neutrino, and tau-neutrino. As neutrinos are neutral, they do not interact electromagnetically, they only interact through the weak force (and gravitationally, which is not within the scope of the Standard Model). Neutrinos were not predicted to have mass by the Standard Model, but have been experimentally shown to do so. Lepton number is conserved within the Standard Model, where matter leptons have a number of +1, while anti-matter leptons have a lepton number of -1. For example, the electron and neutrino have +1 lepton numbers, while the positron and antineutrinos have -1 lepton numbers. Within weak interactions the lepton flavor number is also conserved. A weak interaction with an electron as the sole initial state lepton could have a final state in which an electron-neutrino is the only lepton, but could not result in a final state in which the only lepton is a tau or a muon-neutrino, for instance.

1.2   Overview

The work of this thesis concentrates on neutrinos, and their interactions through the weak force with nuclei. Two sets of measurements from the neutrino-nucleus scattering

experiment, MINERvA are presented. The remainder of this chapter will discuss the historical and theoretical background motivating these measurements, as well as discuss the simulations of neutrino interactions. In Ch.2 I will discuss the MINERvA detector. The neutrino beam that MINERvA utilized is described in Ch.3. The process of transforming the detector read outs into physics variables, called reconstruction, is discussed in Ch.4. The common steps involved in measurements of a cross section that are used on MINERvA are discussed in Ch.5; this chapter also includes a discussion of the systematic uncertainties incorporated into the analyses. My work performing cross section measurements is detailed in Ch. 6 and 7. Measurements of inclusive charged current ν_μ cross sections as a function of the longitudinal and transverse components of the muon momentum are presented in Ch.6. Cross section measurements of deep inelastic scattering are shown in Ch.7.

1.3   Neutrinos

Neutrinos were proposed by Wolfgang Pauli in 1930 as a solution to the observed continuous distribution of electron energies in beta decay ($n \rightarrow p + e^- + \bar{\nu}_e$). The first detection of the neutrino occurred 26 years later at the Savannah river detector by Cowan and Reins, which used inverse beta decay ($\nu + p \rightarrow n + e^+$) to detect scintillation light from both the positron annihilation and neutron capture [14]. The first evidence for the neutrino mass came along years later via the Homestake experiment, which was designed to detect electron neutrinos produced as a result of solar fusion. The processes through which solar neutrinos were produced were thought to be well understood, however they did not observe a neutrino flux consistent with expectation. Instead they observed a neutrino flux with a significant deficit of the neutrinos they had expected [15]. Their experiment was designed to specifically detect electron neutrinos, the reason that they

were seeing so many fewer neutrinos than anticipated was later understood to be not due to an incorrect modeling of the solar neutrino flux but was instead caused by the process of neutrino oscillations. Neutrino oscillations only occur if the neutrinos have mass, so direct detection of oscillations has allowed us to determine that the previously thought of as massless neutrino, was in fact massive.

The three flavor states of neutrinos (electron, muon, and tau neutrinos) do not directly align with the mass states of the neutrinos. When traveling neutrinos are in a mass state, which is a superposition of a combination of different flavor states. When participating in weak interactions the wave function collapses to a single flavor state. This means that an electron neutrino produced in the Sun, may oscillate into a muon or tau neutrino by the time it is detected on earth. For the Homestake experiment, which expected the neutrino signal to be a pure signal of electron neutrinos, these oscillations were the cause of their observed flux deficit.

Neutrino oscillations have since become a topic of interest, which is being heavily studied. Through measurements of neutrino oscillations many different properties of the neutrino can be determined.

The mass state of the neutrino ν_i are given by:

$$|\nu_i\rangle = \sum_\alpha U_{i\alpha}|\nu_\alpha\rangle \tag{1.1}$$

where i is the index indicating the mass state, and α indexes the different flavor states. The U is the unitary PMNS matrix which describes the mixing of the neutrino flavors and masses. This is akin to the CKM matrix, which describes the mixing of quark mass and flavor. However while the CKM matrix is largely diagonal, meaning there is relatively small amounts of quark mixing, the PMNS matrix is not. It is typically parameterized as:

$$U_{i\alpha} = \begin{pmatrix} 1 & 0 & 0 \\ 0 & c_{23} & s_{23} \\ 0 & -s_{23} & c_{23} \end{pmatrix} \begin{pmatrix} c_{13} & 0 & s_{13}e^{-i\delta_{cp}} \\ 0 & 1 & 0 \\ -s_{13}e^{-i\delta_{cp}} & 0 & c_{13} \end{pmatrix} \begin{pmatrix} c_{12} & s_{12} & 0 \\ -s_{12} & c_{12} & 0 \\ 0 & 0 & 1 \end{pmatrix} \qquad (1.2)$$

$$= \begin{pmatrix} c_{12}c_{13} & s_{12}c_{13} & s_{13}e^{-i\delta_{cp}} \\ -s_{12}c_{23} - c_{12}s_{23}s_{13}e^{i\delta_{cp}} & c_{12}c_{23} - s_{12}s_{23}s_{13}e^{i\delta_{cp}} & s_{23}c_{13} \\ s_{12}s_{23} - c_{12}c_{23}c_{13}e^{i\delta_{cp}} & -c_{12}s_{23} - s_{12}c_{23}s_{13}e^{i\delta_{cp}} & c_{23}c_{13} \end{pmatrix} \qquad (1.3)$$

where $c_{ij} = \cos\theta_{ij}$ and $s_{ij} = \sin\theta_{ij}$ represent the mixing angles and δ_{cp} is the CP violating phase.

The two flavor oscillation disappearance probability can be given by:

$$P_{\nu_\alpha \to \nu_\beta} = \sin^2(2\theta_{\alpha\beta})\sin^2\left(\frac{\Delta m^2 L}{4E}\right). \qquad (1.4)$$

As can be seen in this two flavor example, the rate at which neutrino oscillate is dependent on the ratio of the oscillation distance to neutrino energy (L/E) [16]. This can be controlled for accelerator based neutrino experiments, allowing for focus their efforts in studying particular neutrino oscillation parameters. The oscillation probability is also dependent on the mixing angles θ_{ij} and δ_{cp} parameters in the PMNS matrix, and difference between the squares of the mass states $\Delta m_{ij}^2 = m_i^2 - m_j^2$. The neutrino masses have not been directly measured, however measurements of oscillations are able to tell us about the mass splittings.

The mixing angles θ_{12} and θ_{13} are both fairly well constrained. A global data fit by NuFIT produces values of $33.44^{+0.77}_{-0.74}$ deg and $8.57^{+0.13}_{-0.12}$ deg for these parameters, respectively [17, 18]. Determining value of θ_{23} is still an active focus of neutrino oscillation experiments. The global best fit point has a near maximal mixing angle of $49.2^{+1.0}_{-1.3}$ deg,
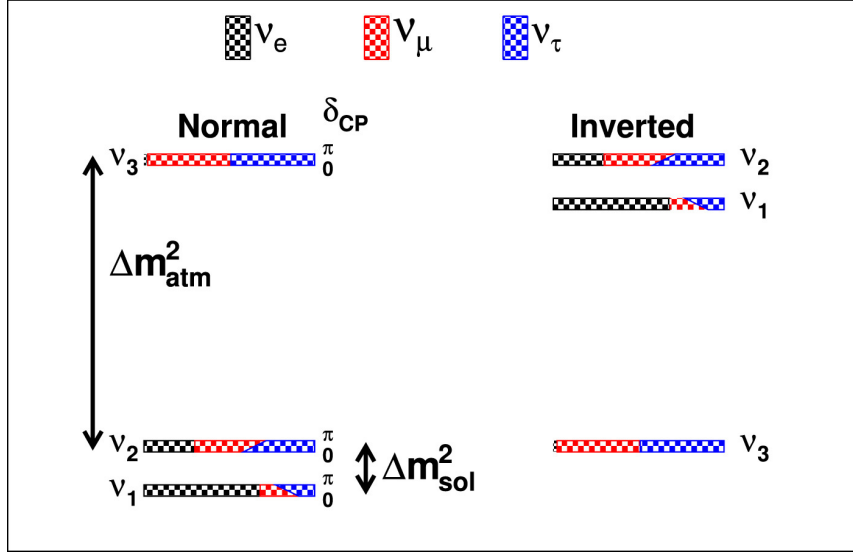
FIG. 1.2: The normal (left) and inverted (right) neutrino mass hierarchies [19].

however, it is not yet known if θ_{23} is in the upper octant (greater than 45deg) or lower octant (less than 45deg). The CP violating phase, δ_{cp} is the least constrained of the mixing parameters, with most values still allowed.

The order of the neutrino masses is also still currently unknown, with either a normal order $\nu_1 < \nu_2 < \nu_3$ or an inverted ordering $\nu_3 < \nu_1 < \nu_2$ both possible. A diagram of these different mass orderings or hierarchies are shown in Fig. 1.2. Measurements from NOvA [2] and T2K [3] show 1σ and 89% posterior probability preferences for the normal mass ordering, respectively as shown in Fig. 1.3. However, each experiment prefers different values of δ_{cp} in the normal ordering, and it has been suggested that a joint fit between the two would produce a preference for the inverted mass ordering [20]. Oscillation measurements also will be able to measure the charge-parity (CP) violating phase in the neutrino sector. Large amounts of CP violation could hold the key to understanding the matter-antimatter asymmetry generated in the earliest moments of the universe. As these measurements can only detect oscillations through studying the products of neutrino
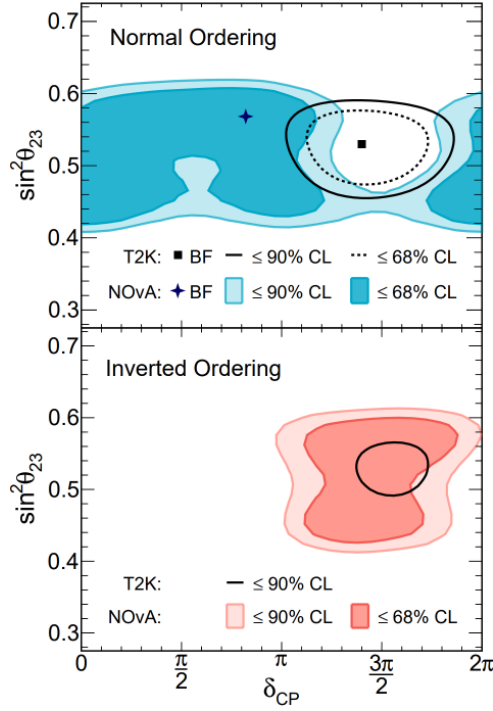
FIG. 1.3: Constraints on values of δ_{cp} and $\sin^2(\theta_{23})$ from NOvA [2] and T2K [3] for the normal and inverted mass hierarchies. The best fit points occur in the normal ordering for both experiments. From Ref. [2].

interactions, neutrino interaction models are an important input parameter when conducting oscillation measurements. The measurements of oscillation probabilities are affected by the neutrino cross section, efficiencies and ability to estimate neutrino energies; all of which are dependent on the neutrino interaction model.

1.4   Neutrino interactions

As neutrinos have neutral electric charge, they can only be detected through their interactions via the weak force. Neutrino interactions can be separated into two categories, neutral current (NC) and charged current (CC) interactions. Feynman diagrams of these two processes are shown in Fig. 1.4.

Neutral current interactions are mediated by a Z^0 boson. A neutrino scatters off of a
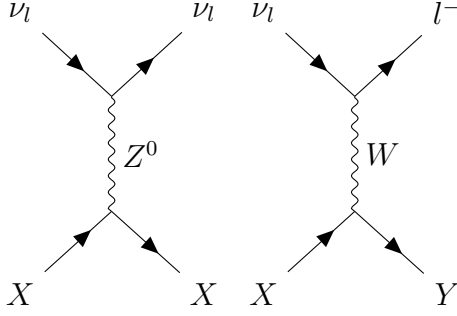
FIG. 1.4: Feynman diagram of neutral (left) and charged (right) current neutrino interactions.

target (such as a nucleon or atomic electron) and transfers some momentum through the exchange of the Z boson, but the same flavor state of neutrino both enters and exits the interaction. A NC interaction channel where the incoming and outgoing neutrino are of the same flavor state is denoted by

$$\nu_l + X \rightarrow \nu_l + X. \tag{1.5}$$

The other category of neutrino interactions are charged-current interactions, which are the focus of the measurements presented in this dissertation. In a charged-current interaction, a $W^\pm$ boson is exchanged between the neutrino and the target, resulting in an outgoing charged lepton matching the flavor of the incoming neutrino. Charged current interactions of neutrino and antineutrinos, respectively, are given by:

$$\nu_l + X \rightarrow l^- + Y \tag{1.6}$$

$$\bar{\nu}_l + X \rightarrow l^+ + Y \tag{1.7}$$

where l indicates the flavor of the charged lepton and neutrino.

Charged current interactions can further be broken down into quasielastic interactions, resonant pion production, two-particle two-hole, non-resonant pion production and deep
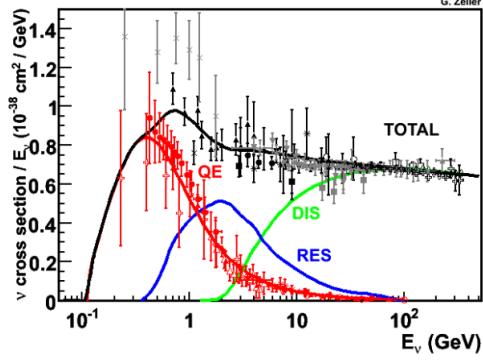
FIG. 1.5: Neutrino cross section as a function of energy [4]. Model predictions come from NUANCE [5] showing the inclusive cross section and components from quasi-elastic (QE), resonant (RES) and deep inelastic scattering (DIS). Global neutrino data of inclusive and quasieleastic scattering is also shown.

inelastic scattering and other categories. The energy of the incoming neutrino determines the relative contribution of the total cross section of each of these interaction channels, with quasi-elastic occurring at the lowest neutrino energies and deep inelastic scattering occurring at higher energies. All of these processes have significant contributions at the few GeV energy ranges in which MINERvA operated, as can be seen in Fig. 1.5. This figure shows a models predicted contributions from the quasi-elastic, resonant and deep inelastic scattering interaction channels as a function of neutrino energy and compared with world data measurements of theses channels. The following sections further describe these processes.

1.4.1 Quasi-elastic

Quasi-elastic (QE) interactions occur predominately at the lower momentum transfers. In QE interactions, the incoming neutrino scatters off of a nucleon exchanging a W boson, producing a charged lepton and leaving the nucleus mostly in tact. Quasi-elastic channels are among the most heavily studied and utilized by neutrino experiments as they have a clean detector signature, and are abundant in the lower beam energies used by

11
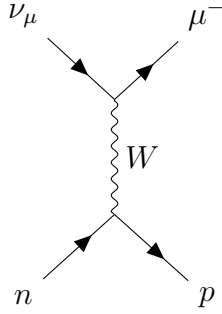
FIG. 1.6: Feynman diagram of quasi-elastic interaction.

contemporary oscillation experiments. The energy transfer of QE events is relatively low, so the outgoing muon often carries the majority of the neutrino energy, allowing for the neutrino energy to be fairly easily estimated.

In a similar energy regime, there are also interactions from meson exchange currents, where a pair of correlated nucleons are interacted with and knocked out of the nucleus. These interactions are referred to as two particle–two hole interactions, or "2p2h". Understanding and correctly modeling 2p2h interactions is an ongoing area of interest by oscillation experiments and those trying to measure and model neutrino interactions, as it was not included in many early models but has been experimentally shown to have a large effect in the few GeV energy regime.

1.4.2 Resonance production

Peaking at a slightly higher momentum transfer than QE interactions are baryonic-resonance interactions. In these interactions the nucleon goes into an unstable excited state, which decays generally producing pions. The resonant state that is the least massive and is the most common is the Δ resonance state. CC Resonant pion production is given by:

$$\nu_\mu + N \rightarrow \mu^- + \Delta \rightarrow \mu^- + N + \pi \tag{1.8}$$
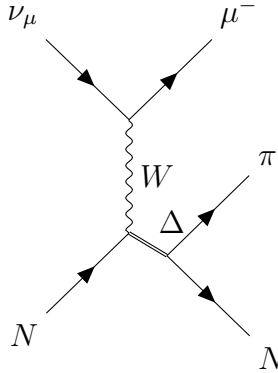
FIG. 1.7: Feynman diagram of a resonant neutrino interaction.

where N is a nucleon, and π is any type of pion. A Feynman diagram for single pion production with is given in Fig. 1.7. Single pion production is often a primary focus when studying resonances. Higher mass resonance states may decay producing multiple pions. The resonant states are never directly observed due to their short life times, instead the decay products (pions and a nucleon) are the observable signature that can be used in exclusive analyses to study resonance rich samples.

1.4.3 Non-resonant and inelastic transition

Pions are not exclusively produced through resonance production however, they may also be produced through non-resonant interactions. These interactions are indistinguishable from resonant interactions as they produce the same final state particles.

Non-resonant pion production occurs within a regime called shallow ineleastic scattering where the four momentum transfer is within the range of $M_\Delta < W < 2$ GeV (see Eq.1.10 for W definition). Mutli-pion resonant events also populate this kinematic regime. At increased energy transfers the interactions start producing more particles, with sufficient energy to produce multiple final state hadrons. In this energy regime perturbative quantum chromodynamics (QCD) breaks down. However, the energy is not large enough
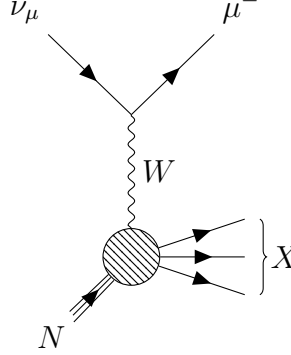
FIG. 1.8: Feynman diagram of DIS ν_μ CC interaction.

to enter the deep inelastic scattering regime where the quark structure of the nucleon can be directly probed.

1.4.4 Deep inelastic scattering

At even higher four momentum transfer and hadronic invariant mass are high enough that the cross sections are dominated by deep inelastic scattering (DIS). In DIS interactions, the neutrino interacts with a quark, transferring enough energy to break the nucleon structure and create a shower of hadronic particles, shown in Fig. 1.8. DIS is defined kinematically, with a four momentum transfer, $Q^2 \geq 1.0\,\text{GeV}^2$ as the commonly used threshold to indicate the onset of DIS interactions. An additional kinematic threshold is used to define the phase space in order to further differentiate from resonance interactions, this requirement is based on the invariant mass of the hadronic system $W \geq 2.0\,\text{GeV}$. The process of charged current deep inelastic neutrino scattering is mediated by a virtual W boson with the four momentum q.

These two variables which define the kinematic region are given by:

$$Q^2 = -(P_\nu - P_\mu)^2 = 2E_\nu(E_\mu - p_\mu \cos\theta_\mu) - m_\mu^2 \tag{1.9}$$

$$W^2 = P_X^2 = (P_\nu + P_N - P_\mu)^2 = -Q^2 + 2(E_\nu - E_\mu)m_N + m_N^2 \tag{1.10}$$

where P_ν, P_μ, P_X, P_N are the four momenta of the incoming neutrino, outgoing muon, outgoing hadronic system, and incoming nucleon respectively. E_ν and E_μ are the energies of the neutrino and muon, p_μ is the muon momentum, m_μ is the muon mass, and θ_μ is the scattering angle of the muon with respect to the incoming neutrino direction.

The Lorentz invariant Bjorken scaling variable x_{bj}, and inelasticity y are helpful for discussing DIS cross sections, where they are defined as

$$x_{bj} = \frac{-q^2}{2P_N \cdot q} \tag{1.11}$$

$$y = \frac{P_N \cdot q}{P_N \cdot P_\nu}. \tag{1.12}$$

In the lab frame where the nucleon momentum can be assumed to be zero, and the hadronic energy $E_{had} = E_\nu - E_\mu$ these variables can be written as

$$x_{bj} = \frac{Q^2}{2m_N E_{had}} \tag{1.13}$$

$$y = \frac{E_{had}}{E_\nu}. \tag{1.14}$$

The Bjorken-x scaling variable represents the fraction of the nucleon momentum carried by the struck quark, and the inelasticity y is a measurement of the fraction of the neutrino energy transferred to the hadronic system.

The differential DIS cross section is given by

$$\frac{d\sigma_N}{d\Omega dE_l} = \frac{G_F}{(2\pi)^2} \frac{|\boldsymbol{k'}|}{|\boldsymbol{k}|} \left(\frac{M_W^2}{q^2 - M_W^2} \right) L_{\mu\nu} W^{\mu\nu} \tag{1.15}$$

for a nucleon target in its rest frame, where the incoming neutrino has momentum $\boldsymbol{k}$, the outgoing charged lepton momentum is $\boldsymbol{k'}$, G_F is the Fermi coupling constant, M_W is the W boson mass, and $L_{\mu\nu}, W^{\mu\nu}$ are the lepton and hadronic tensors. See [8] for further details.

15

This cross section can also be rewritten as a function of x_{bj}, y, and structure functions that describe the nucleon structure. These structure functions are different for free nucleons and nucleons bound in a nucleus. The neutrino DIS cross section is specifically dependent on xF_1, F_2, and xF_3, where the F_3 is only accessible through studying neutrino interactions.

Nuclear effects

A charged current ν_μ DIS interaction needs to scatter off of a down quark (or other -2/3 charge quark) in order to obey charge conservation ($\nu_\mu + d^{-1/3} \rightarrow \mu^- + u^{+2/3}$). The parton distribution function (PDF) can describe a nucleon's quark makeup. Nucleons contain both valence quarks (e.g. two up and one down quark for a proton) and sea quarks which carry a smaller momentum fraction. The charge conservation means that the cross section for neutrons is larger than that of the proton as there are twice as many valence down quarks in the neutron. When studying interactions with nuclei, the ratio of protons to neutrons within the nucleus will affect the per nucleon cross section. Light nuclei are more likely to have the same number of protons and neutrons (isoscalar), while heavier nuclei generally have more neutrons per proton. Therefore, it is expected that the lead cross section per nucleon would be larger than that of an isoscalar element like carbon. However, interactions do not always take place on the valence quarks, sometimes instead interacting with sea quarks. The regions in which scattering is primarily off of valence quarks such as at high x_{bj}, are then expected to see the largest differences from non-isoscalarity.

There are four different nuclear effects that can be seen in DIS cross sections when comparing different nuclei, dependent on x_{bj}. These can be most easily studied by looking at ratios of heavy to light nucleus cross sections. At the lowest range, $x_{bj} < 0.1$, is a region of nuclear shadowing where the heavier nucleus cross section is suppressed. Slightly above that from $0.1 < x_{bj} < 0.3$ is a region of anti-shadowing where the the heavy nucleus cross
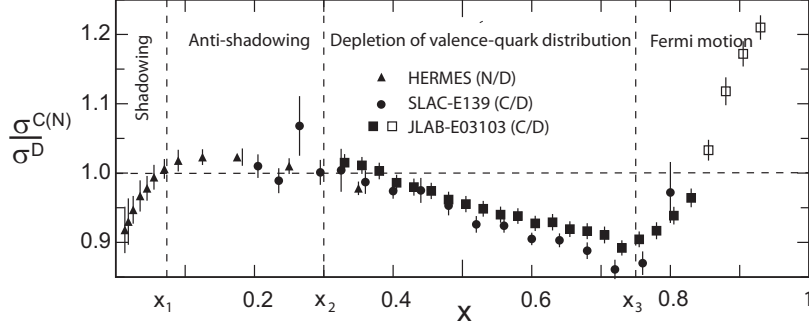
FIG. 1.9: Charged lepton measurements of carbon and nitrogen to deuterium cross section ratios, with data from HERMES, SLAC-E139 and JLAB-E03103 as a function of x_{bj}. Figure from [6].

section is enhanced. The EMC effect (named after the European Muon Collaboration which first measured it) in the range of $0.3 < x_{bj} < 0.75$ where the heavy nuclei are again depleted. Above this range the heavy nucleus cross section again increases. Charged lepton cross sections measured as a function of the Bjorken-x scaling are shown in Fig. 1.9, and labeled with regions for each of these nuclear effects.

1.5 Motivation for Neutrino Cross Section Measurements

The neutrino fluxes used by various modern and future neutrino experiments are shown in Fig. 1.10. Note that there are two different flux distributions for MINERvA which took data both with a flux of $\langle E_\nu \rangle \sim 3$ GeV and 6 GeV (called "low" and "medium" energy)

Both NOvA and T2K (currently operational long baseline neutrino oscillation experiments) operate in significantly lower energy regimes than MINERvA, while DUNE will operate in a very similar energy regime to MINERvA. Cross section uncertainties are among leading systematic uncertainties for neutrino oscillation experiments, and DUNE will be made of liquid argon, which means nuclear effects for heavy nuclei will be relevant.
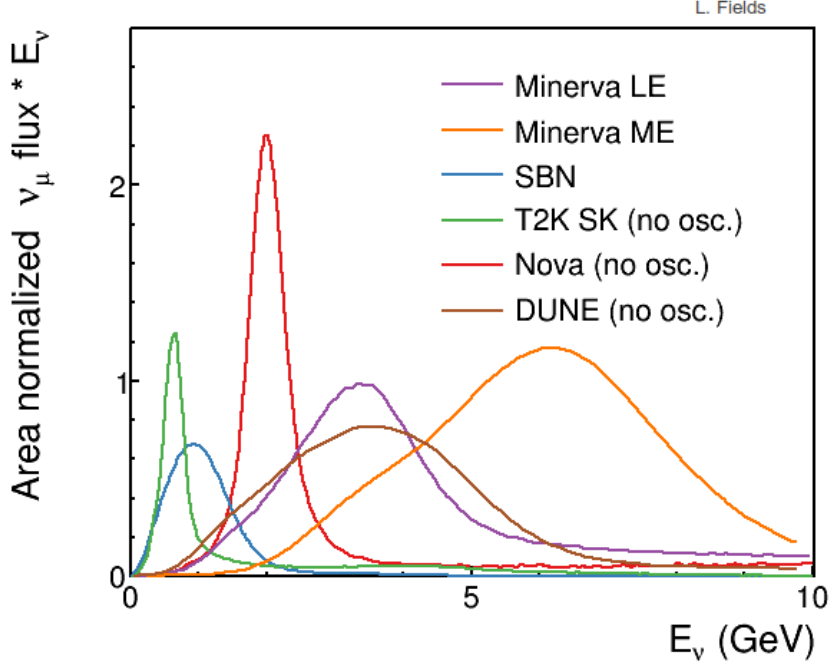
FIG. 1.10: Flux energy distributions for various neutrino experiments. The MINERvA LE beam maps quite closely to the DUNE flux, while the ME flux is at a slightly higher energy regime not probed by other experiments.

Liquid argon detectors are a relatively new technology that is currently being utilized by SBN, a short baseline neutrino oscillation program, comprised of three experiments in the same beam μBooNE, SBND, and ICARUS. The energy regimes that T2K, NOvA and SBN operate in are dominated by quasi-elastic interactions with some resonance production but little deep inelastic scattering. While at MINERvA and on DUNE deep inelastic scattering accounts for a significant portion of interactions.

Its expected that over 30% of the events DUNE will come from DIS interactions, and that more than 50% will come from the regions with $W \geq M_\Delta$ [8]. This is a large motivation for the results presented in the this dissertation. The inclusive cross section measurements, performed in the low energy beam, include a very similar mix in interaction type as will be seen by DUNE. In order to understand which interaction channels are playing major roles in any discrepancies with the total simulated cross section in the

CP Violation Sensitivity
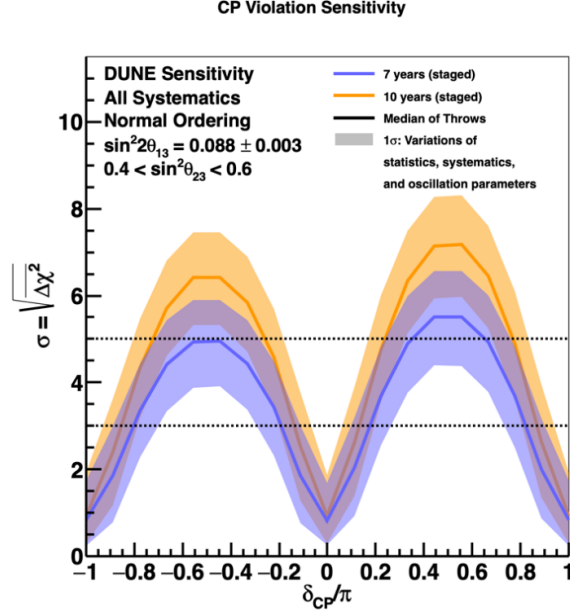
FIG. 1.11: Significance at which DUNE can observe CP violation for a range of true δ_{cp} values, for exposures of 7 and 10 years. The bands represent fluctuations in systematic uncertainties and in other oscillation parameters. Taken from Ref. [7].

inclusive results, it is useful to separate out different processes into measurements of specific kinematic regions. Therefore, a measurement of deep inelastic scattering is of import as MINERvA has a unique ability to measure it on multiple nuclear media with few GeV neutrino energies where the W and Q^2 regions are the same as those that will be populated in DUNE. With measurements on carbon (Z=6), iron (Z=26), and lead (Z=82), we span a wide range of nuclei with measurements both above and below the atomic number of argon (Z=18), allowing for extrapolation of nuclear effects.

The sensitivity at which DUNE is predicted to be able to measure CP-violation for a range of δ_{cp} is shown in Fig. 1.11. The bands represent variations in systematic uncertainty and oscillation parameters, thus reductions in cross section uncertainties can results in discovery threshold measurements in shorter time periods and a larger range of δ_{cp} values [7].

19

1.6 Models of Neutrino Interactions

In order to predict effects in the data when making cross section measurements we make use of simulated data samples that undergo a parallel data analysis process as applied to the experimental data. This need is met through the usage of neutrino event generators, which simulate neutrino interactions through to providing a simulated set of final-state particles and their four-vectors. In particle physics it is not unusual to refer to this simulated data as the "Monte Carlo" or just as the "MC".

There are a variety of different generators that are used by the neutrino physics communities, each based on different variations of theoretical predictions. GENIE [21] is a generator widely used in US based neutrino experiments, while NEUT [22] is commonly used elsewhere including by modern neutrino oscillation experiment T2K. Other neutrino generators include NuWro [23] and GiBUU [24] which will be discussed later in this section.

Neutrino interaction events are individually simulated by the generator. A single neutrino interaction is referred to as an "event". On MINERvA, we use GENIE, Generates Events for Neutrino Interaction Experiment, to predict aspects of interactions needed in order to make measurements, such as the efficiency and number of background interactions which take place. The particles produced in the neutrino interaction are propagated through the detector using GEANT4 v4.9.4p6, which simulates the secondary particles paths through the detector and any re-interactions that occur [25].

While GENIE is used as the base model used to extract the cross section measurements presented, other event generators such as NuWro and GiBUU are used for the purpose of model comparisons.

1.6.1 GENIE

In this thesis two slightly different versions of GENIE are used. GENIE 2.8.4 is used for the low energy inclusive analysis, while GENIE 2.12.6 is used for the medium energy DIS analysis. Different versions are used because the low energy simulation was produced prior to the later GENIE versions release. One of the most significant differences in these two versions of the simulation is that unmodified GENIE 2.8.4, which is used for model comparisons, did not include any predicted 2p2h interactions, while GENIE version 2.12.6 does include them by default.

One feature of the GENIE generator is that all non-resonant pion, resonant multi-pion, shallow inelastic scattering processes are classified as "DIS" by the generator. This classification does not align with the definitions that we generally use on MINERvA, so I will refer to the category of all events classified by GENIE as DIS as "GENIE DIS". GENIE DIS can be further broken down into subcategories based on kinematic properties of the interaction.

Nuclear effects are modeled using the relativistic Fermi gas model [26] with a maximum momentum for a struck nucleon of $0.221\,\mathrm{GeV/c}$ and the Bodek-Ritchie short range correlation model for the inclusion of higher momentum struck nucleons [27]. The Llewellyn-Smith formalism [28] with electromagnetic form factors from BBBA2005 [29] is used for modeling quasielastic interactions. The axial form factor is assumed to have a dipole form and an axial vector mass of $M_A = 0.99\ \mathrm{GeV/c^2}$. Resonance production in GENIE is simulated using the Rein-Seghal model [30]. The Bodek-Yang model [31] is used to leading order for simulation of DIS. GENIE models hadron rescattering (final-state interactions) using the GENIE INTRANUKE-hA package [32]. In place of a full intranuclear cascade, final state interactions (FSI) are modeled using an effective particle cascade. At most one particle rescatter is allowed before absorption or exiting the nucleus, with pion-nucleus

scattering data used to determine the relative scattering probabilities[33]. Initial-state nuclear effects for all GENIE-DIS processes are modeled in GENIE using an iron measurement. Historically, this was because the simulation was initially modeled based on CCFR data and was developed in the context of the Soudan 2 and MINOS experiments. All three experiments used steel plates as their target materials.

1.6.2 MINERvA tune v1

We take GENIE and apply alterations to it that have been shown to be better supported by data in other cross section measurements, or are theoretically driven. We refer to these alterations as "tunes" as we are tuning the simulation to look more like data from prior measurements. There are many combinations of different alterations which can be applied to GENIE, but the primary tune used throughout this dissertation in order to produce cross section measurements is called MINERvA tune v1. This is a combination of 3 different effects, a suppression of non-resonant pion production, a suppression of quasi-elastic interactions at low four momentum transfer, and an enhancement of 2p2h interactions.

These tunes are implemented by "reweighting" events. Reweighting is a technique we use in order to alter the relative strength of a given simulated process, by assigning a weight to every event produced by the neutrino generator. If, for instance, we wanted to uniformly reduce the generated cross section across all interaction channels by 20%, we would assign all of the MC events a weight of 0.8, and that would result in a 20% reduction in the sum of predicted MC events. We generally wish to do a more refined tune than that however, so we generally tune one interaction channel at a time, and the applied weights are often a function of kinematics such as momentum transfer, rather than a uniform scaling.

22

Non-resonant pion suppression

The first modification made is based on deuterium bubble chamber data from Argonne and Brookhaven National Labs that has been reanalyzed [34]. These reanalyzed measurements of pion production were compared to GENIE predictions, and found that the GENIE prediction for non-resonant pion production needed to be substantially decreased in order to reproduce the bubble chamber data [35]. As result of these studies MINERvA tune v1 reduces the non-resonant pion production predicted by GENIE to 43% of its value, and also reduces the data-driven systematic uncertainty on that process accordingly.

Quasielastic RPA

The second modification we make is to the quasielastic channel in order to account for nuclear effects. At low four momentum transfer the quasielastic cross section gets suppressed due to long range nuclear correlations. These correlations affect the electroweak couplings, resulting in a screening effect analogous to an electric charge screening in a dielectric. This suppression is calculated by the Valencia group using the Random Phase Approximation, and thus referred to as "RPA" [36]. It is implemented by reweighting the quasielastic events predicted by GENIE [37].

Enhancement of 2p2h

We simulate 2p2h using the Valencia model [38, 39, 40]. The strength of the 2p2h predicted by this model did not provide sufficient strength to reproduce a prior MINERvA measurement of ν_μ inclusive CC scattering at low momentum transfer in our $\langle E_\nu \rangle \sim 3$ GeV data [41]. In order to account for these differences the 2p2h model was enhanced using an empirical fit to the observed hadronic energy spectrum, causing the modified simulation

to better match these results by construction. However, when this same fit was applied in a parallel $\bar{\nu}_\mu$ analysis, good agreement was also seen in this independent data set [42]. These modifications also improve the description of muon kinematics of CC events where there are no pions in the final state ("quasi-elastic like" interactions) for both neutrino and antineutrino measurements our low energy beam[43, 44].

1.6.3 Other tunes applied to GENIE

Low Q^2 resonant suppression

MINERvA measurements of pion production for ν_μ $\pi^\pm$ [45], $\bar{\nu}_\mu$ $\pi^\pm$ [46] and ν_μ π^0 [47] interaction channels all showed a common trend, in which the GENIE simulation was overpredicting the resonant cross section at low Q^2. In order to account for this we apply a suppression to resonance events at low Q^2, based on fits to these measurements [48]. When we apply this suppression in addition to all of the modifications that are a part of MINERvA tune v1, we refer to it as MINERvA tune v2.

MINERvA was not the only experiment to notice this effect. MINOS also measured a similar effect, and developed their own empirical tune, which is quantitatively similar to the one based on MINERvA data [49]. Another variation of this type of suppression can come from using the Valencia RPA suppression used on the quasielastic channel, and also applying it to the resonance channel.

DIS models

Different models of DIS are also used for comparisons. The first two true DIS models are nCTEQ15 [50] and nCTEQν [51], which are global analyses of nuclear parton distributions based on charged lepton-nucleus and neutrino-nucleus scattering, respectively. The third is a beyond-leading-order microscopic model developed at Aligarh Muslim University
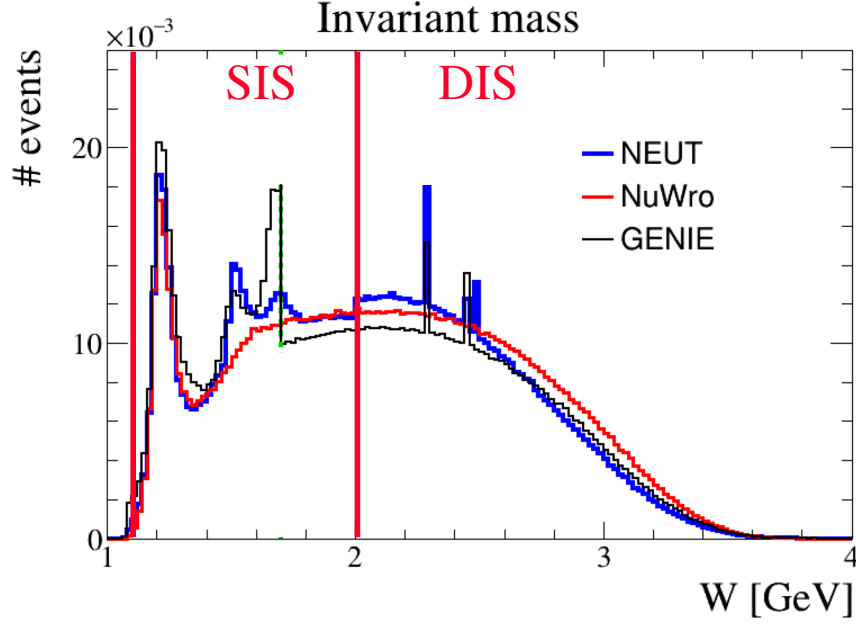
FIG. 1.12: Comparisons of NEUT, GENIE and NuWro for a 6 GeV neutrino on iron, from Ref. [8] .

(AMU) referred to in plots as AMU DIS [52].

1.6.4   Other neutrino generators

NuWro is another event generator which is used for comparisons, it has two variations, one which is based on spectral functions and one which uses a Local Fermi Gas model[23]. The 2019 version of GiBUU is referenced [24].A comparison NuWro, NEUT and GENIE predictions as a function of W is shown in Fig. 1.12. Some of the modeling differences highlighted in this figure are that GENIE transitions from using KNO scaling [53] at low W to using PYTHIA [54] at high W by using the AGKY model [55], which gradually transitions to PYTHIA from KNO for 2.3 < W < 3.0 GeV; while NuWro uses a linear transition to DIS simulations based on modified PYTHIA [8].

CHAPTER 2

MINERvA Detector

MINERvA is a neutrino cross section measuring experiment that measures neutrino interactions on different nuclei, with results which can be used by neutrino oscillation experiments. The MINERvA detector sits approximately 100 meters underground on site at Fermilab in the NuMI beamline (discussed in detail in Ch.3). The detector is composed of hexagonal planes of both active scintillating materials and passive materials used as interaction targets. A diagram of the detector is shown in Fig. 2.1, with the neutrino beam entering the detector from the left. More in depth details can be found in Ref. [10]. MINERvA took data from March 2010 until the end of its run in February of 2019.

At the front of the detector where the neutrino beam first hits (or the upstream end) we have a scintillator based veto wall that is used to detect any charged particles entering the detector. The majority of these particles are muons, which were the result of neutrino beam interactions in the rock upstream of our detector. Downstream of the veto wall there is a cryogenic helium tank, which took data in both empty and full configurations, but is not used for any analyses in this dissertation. Then begins the main detector, which is comprised of inner and outer detector regions in the shape of a regular hexagon. The
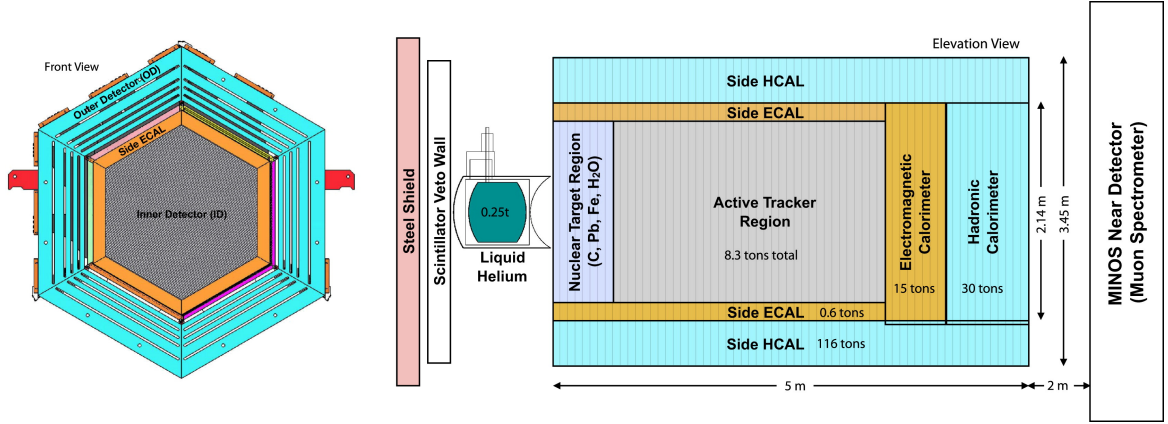
FIG. 2.1: Diagram of the MINERvA detector [10].

detector is comprised of vertical planes, approximately perpendicular to the beam direction. The MINERvA coordinate system is defined with the x direction as horizontal across the hexagonal front face of the detector, the y direction is vertical, and the z direction is horizontal along the detector axis, starting at the front of the detector and going towards MINOS. There is a 58 mrad offset between the direction of the beam, and the z direction of the detector due to the beam's downward slope. At the front of the main detector is the nuclear target region. In this region there are planes of active tracking material interspersed with planes of passive target materials. After that there is the central region of the detector, which consists of exclusively material that is able to actively track charged particles as they travel through the detector. These active tracking planes are made up of a scintillating hydrocarbon (scintillator), which collect the light emitted by the charged particles. Charged particles excite atoms nearby, which will return to their ground state emitting photons. Different particles can have distinct energy depositions, for instance muons are minimum ionizing particles, while electrons go through more Bremsstrahlung due to their lighter mass. The active tracker region is followed by an electromagnetic calorimeter (ECAL) consisting of alternating planes of lead and the same scintillator used
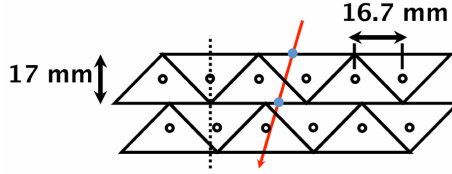
FIG. 2.2: Scintillator strips are arranged side by side to form a plane.

in the central portion of the detector. After this there is a hadronic calorimeter (HCAL), which has alternating planes of steel and scintillator. Surrounding the inner detector is an outer detector region, comprised of steel and scintillator (side HCAL).

2.1 Scintillator planes

The central region of the detector is made of active tracking planes that allow for particle detection. These hexagonal tracking planes are composed of 127 triangular prism strips of scintillator, with a wavelength shifting fiber at the center. The strips are made of extruded polystyrene scintillator, which emits near UV light that is then picked up by a wavelength shifting fiber in the center that converts to green and carries light to photomultiplier tubes. The triangular strips are arranged into planes as shown in Fig.2.2. The wavelength shifting fibers are connected to multichannel photomultiplier tubes, further discussed in Sec. 2.8. The scintillator planes have elemental compositions of 7.42% H, 87.6% C, 3.18% O, 0.26% Al, 0.27% Si, 0.55% Cl, and 0.69% Ti.

The detector uses three different scintillating strip orientations in order to facilitate three dimensional tracking. The three different orientations are called the X, U, and V views, where the X orientation has the strips of scintillator oriented vertically–giving horizontal position information, while the U and V views have them oriented 60°clockwise and counterclockwise from the vertical, respectively. The detector is divided into planes of scintillator and grouped into modules. A hexagonal steel frame is used to support up
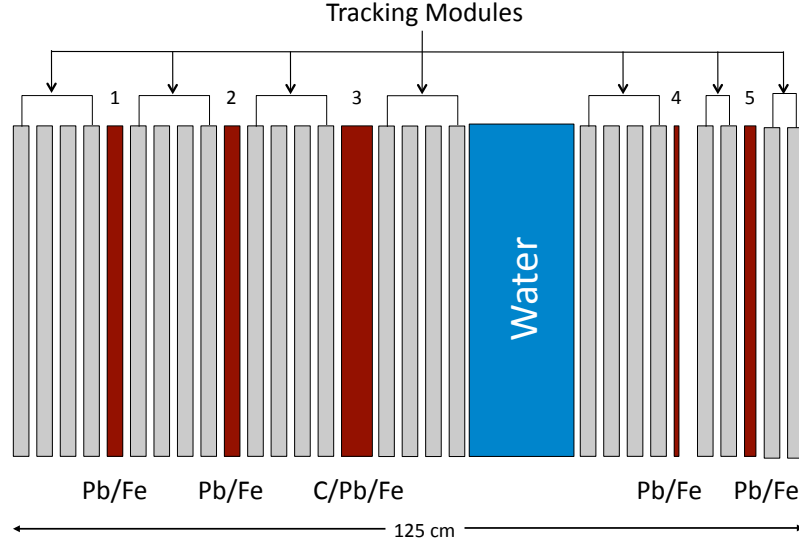
FIG. 2.3: The nuclear target region of the MINERvA detector with the beam direction coming in from the left.[10]

to two planes of scintillator, forming a single "module". In the active tracking region a plane is a single sheet of stacked scintillating strips, and modules are composed of two planes in either the UX or VX configuration. Planes are assembled in an alternated UX VX pattern. The active tracking area is composed of 62 tracking modules.

2.2 Nuclear target region

MINERvA does not have a single uniform material composition throughout the detector. Instead there is both an active tracking region, and a nuclear target region at the upstream end of the detector which is used to study neutrino interactions on different nuclei.

The nuclear target region consists of 5 passive hexagonal targets made of iron, lead and carbon, and a liquid water target, as show in Fig. 2.3. There are 8 scintillator
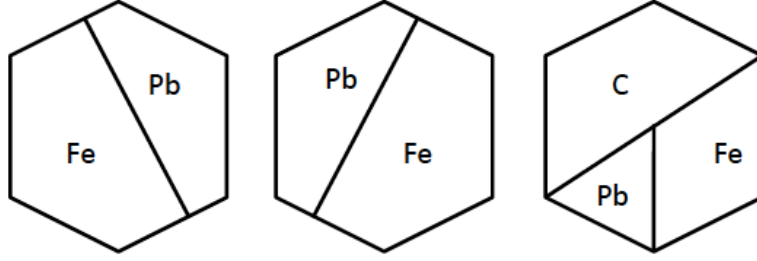
FIG. 2.4: The target material schematics looking downstream. The left most orientation corresponds to target 1 and 5, the middle target 2, and target 3 has the right most orientation.[10]

planes in between each passive nuclear target in order to be able to precisely determine the interaction vertex, as well as planes ahead of the first nuclear target, for a total of 22 modules of scintillator in the region. Each passive target is divided into sections of different materials to allow for the ability to account for differences in acceptance due to detector position. This also helps us to account for the differences in the neutrino flux as a function of position in the detector.

Targets 1, 2, and 5 have both iron and lead sections, while target 3 has iron, lead and carbon, and target 4 is a pure lead target. A schematic of the different material distributions is shown in Fig. 2.4. The positions of each nuclear target material, mass and thickness is shown in Table 2.1

2.3   Veto Wall

A veto wall at the front of the main detector is used to detect muons which originated from interactions with the bedrock the neutrino beam traveled through before reaching our detector (rock muons). Two steel planes, each with a plane of scintillator downstream of it, make up the veto wall. The upstream steel plane has a thickness of $5\,\mathrm{cm}$ and the second steel plane is $2.5\,\mathrm{cm}$ thick. The ability to filter out rock muons from signal interactions that the veto wall provides is especially vital for analyses in the liquid helium cryotank,

30

Target	z-Location (cm)	Thickness (cm)	Fiducial area (cm^2)	Fiducial mass (kg)	Total mass (kg)
1-Fe	452.5	2.567 ±0.006	15999	322	492
1-Pb	452.5	2.578 ±0.012	9029	263	437
2-Fe	470.2	2.563 ±0.006	15999	321	492
2-Pb	470.2	2.581 ±0.016	9029	263	437
3-Fe	492.3	2.573 ±0.004	7858	158	238
3-Pb	492.3	2.563 ±0.004	3694	107	170
3-C	492.3	7.620 ±0.005	12027	160	258
Water	528.4	17-24	25028	452	627
4-Pb	564.5	0.795 ±0.005	25028	225	340
5-Fe	577.8	1.289 ±0.006	15999	162	227
5-Pb	577.8	1.317 ±0.007	9029	134	204

TABLE 2.1: Positions and masses of each nuclear target.[10]

which sits upstream of the main detector, but the veto wall is not used in either of the measurements presented in this dissertation.

2.4 Electromagnetic calorimeter

The electromagnetic calorimeter (ECAL) region of the detector begins just downstream of the active tracking region. The area is made of 10 modules of scintillator, which are assembled in the same manor as described in Sec. 2.1, but are covered with an additional 0.2cm sheet of lead over the entire plane of scintillator. The purpose of this region is to help contain electromagnetic showers inside of the detector, and are additionally used for calorimetry.

Similarly, on the scintillator planes of the active tracking and nuclear target regions, there is a 0.2cm lead collar around the perimeter of the scintillator plane, which acts as a side ECAL. This helps contain electromagnetic showers that would escape the sides of the detector.

2.5   Hadronic calorimeter

The hadronic calorimeter is the most downstream region of the detector, and is comprised of 20 modules, which each are made of one plane of scintillator followed by one plane of 2.54 cm thick steel. Like the ECAL region does for electromagnetic showers, the HCAL region is designed to help contain energy from hadronic particle showers.

2.6   Outer detector

On the outer edge of the hexagonal planes that make up the detector is an outer detector (OD) region (or side HCAL), made of steel and scintillator. The outer detector region in a single module is also the frame that supports the inner detector region of the module. This acts as a hadronic calorimetry on the sides of the detector.

The scintillator strips used in the outer detector are rectangular prisms instead of being made of triangular prisms. In the majority of the detector the strips have a cross section of 19±0.5 mm by 16.6±0.5 mm. However in the area of the detector with the hadronic calorimeter, the outer detector has a slightly different structure with thicker steel so the scintillator strips in that region are also thicker.

2.7   MINOS ND as muon spectrometer

The near detector for the oscillation experiment MINOS sits 2.1 m downstream of the MINERvA detector in the NuMI beam. The MINOS near detector (ND) has a 1 kTon mass which is comprised of plastic scintillator and magnetized iron.

The MINOS ND acts as a muon spectrometer for MINERvA, where muons which exit out of the back of MINERvA can be tracked to determine their charge and momentum by using range and/or curvature data from their tracks in the magnetized MINOS ND. It has
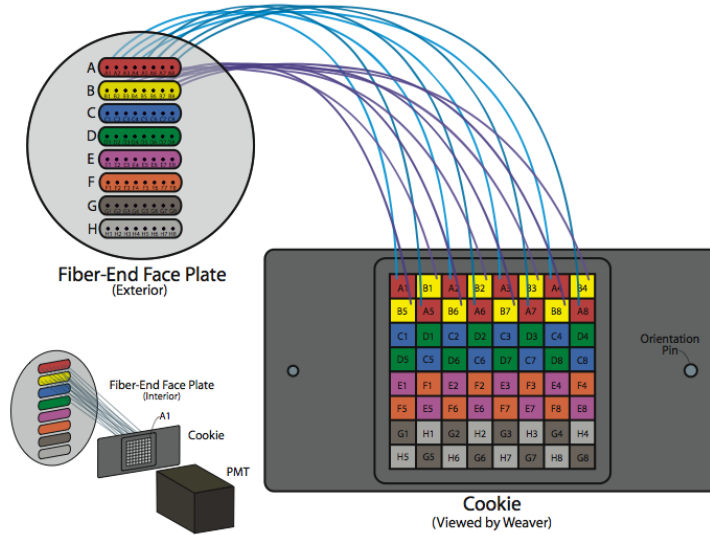
FIG. 2.5: Diagram of PMT fiber weave.

a current-carrying coil that expends for the length of the detector and produces a toroidal magnetic field with an average strength of 1.3 T.

There are acceptance restrictions that arise from requiring muons detected in MIN-ERvA to enter MINOS, but MINERvA does not have a magnetized detector or a large enough size to contain most muons, so use of the MINOS ND is vital.

2.8 Photomultiplier tubes and front end boards

The wavelength shifting fibers, which are embedded in the scintillator strips, are connected with clear optical fibers to multichannel photomultiplier tubes (PMTs), each with 64 channels. Using 64-channel Hamamatsu H8804MOD-2 photomultiplier tubes, light signals are converted into analog electrical signals via the photoelectric effect. With 127 scintillator strips in each plane, and each strip getting read out by an individual channel, two PMTs are used to read out each plane. The PMTs are each housed in a steel cylinder which provides shielding from magnetic fields due to the nearby MINOS magnetic

coil. The PMTs are mounted to Cockroft-Walton high voltage generators that provide the signal, which can then be read out by front end boards.

A method of interweaving channels so that strips of scintillator which neighbor each other are not read out into adjacent PMT channels (shown in Fig. 2.5) is used in order to minimize effects from light contamination called cross talk. Cross talk occurs when the neighboring PMT channel causes some light to be detected by the adjacent channel which did not have any light signal. By interweaving we are able to separate these instances that appear as isolated pixels reading a small number of photo-electrons without any activity in physically nearby strips within the detector and account for that effect in reconstruction processes. If there was no weave, cross talk would be harder to distinguish as a neighboring pixel would also correspond to a neighboring scintillator strip which could have reasonably detected a true signal from a particle. Cross talk is dependent on the energy deposition of the strip which was hit, for almost all of the PMTs the fractional cross talk energy is less than 4%.

The PMT gain, or output charge signal, is able to be optimized for different amounts of charge. There are three different PMT gains which are used for each channel in order to allow for a greater range of resolution: low, medium and high gain. If the signal is small the high gain channel is used, while the low gain channel is used for larger signals.

2.9   Data read out

Each PMT is read out by a front-end board (FEB) using TriP-T circuit chips which amplify and digitize the signal [56]. The FEBs are connected to each other by Ethernet cables in a daisy chain configuration that is read out by a Chain Readout Controller - Ethernet board (CROC-E). When the signal threshold to record the data of approximately 0.8 photoelectrons is met, the Trip-T must be reset, a process which takes 188 ns to

complete. For this time all the 32 channels for that Trip-T and associated PMT experience "deadtime" in which they cannot take any new data. The data acquisition system (DAQ) reads out the entire detector for every beam spill [57]. Further details on the data readout process are provided in Ref. [10].

The time at which the first signal is measured on the FEB is associated with the hit as the uncalibrated time. This time then needs to be adjusted in order to account for effects such as the time it took the light to travel the length of the fiber. The timing resolution is approximately 3 ns, with some energy dependence, allowing for sufficient resolution in order to distinguish one neutrino interaction from another.

2.10   Detector Simulation

Simulating the detector starts with the input of the neutrino interaction information from GENIE, described in Ch. 1.6.1. The particles produced from neutrino interactions and nuclear reinteractions which come from GENIE are then propagated through the detector using GEANT4 v4.9.4p6 [25].GEANT handles the simulation of particle interactions with the matter of the detector through processes of ionization, radiation and nuclear reactions in order to produce particle track trajectories using a simulated MINERvA detector geometry. GEANT uses discrete steps, determining if the particle interacted within each step, and calculating the four momenta of all of the particles. The particle tracks are then converted into a photon signal in each simulated scintillator strip using Birks' law [58]. The attenuation effects from the fibers which carry the photon signal to the PMTs, the number of photo-electrons produced by the PMT and the electronic readout system are all simulated.

CHAPTER 3

NuMI Beam

The MINERvA experiment is designed to measure the cross sections of accelerator produced neutrinos. These accelerator neutrinos are produced by the Neutrinos at the Main Injector(NuMI) beam [59], located at Fermi National Accelerator Laboratory in Batavia, IL. MINERvA sits on axis (with the beam centered in the detector) approximately 1 km downstream of the target hall. Further details on the MINERvA detector are discussed in Ch.2.

The neutrino beam is produced by first taking a supply of hydrogen, and accelerating them through a series of accelerators to the Main Injector proton synchrotron to an energy of 120 GeV. The proton beam is directed to a graphite target, which it collides with producing a variety of particles, largely hadrons. The target is able to be positioned either in front of or inside of the first of two magnetic horns. The horns act like a lens that focuses certain particles. This capability to change the target position allows for the beam to be tuned to produce a range of different neutrino fluxes and peak energies.

The pions and kaons produced from the interactions of the proton beam with the graphite target go through the magnetic field of the horns, focusing them into a beam of

mostly positive (negative) mesons in order to produce a neutrino (antineutrino) rich beam. These beams are often referred to as the forward horn current (FHC) and reverse horn current (RHC) configurations, which correspond to neutrino and antineutrino enriched modes, respectively. These charged mesons then enter a helium filled decay pipe in which they decay into muons and neutrinos. The beam then goes through approximately 200 m of rock, which is used to absorb the muons produced by these decays as well as working to stop any further hadrons that had not decayed. A schematic drawing of the beam is shown in Fig. 3.1.
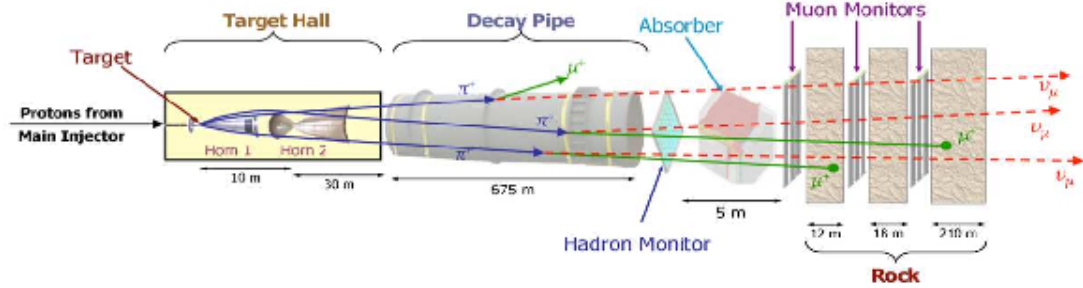
FIG. 3.1: A schematic drawing of the NuMI beam.

The beam can be set to different energy ranges. MINERvA took data in both the low energy (LE) range, which had an peak energy of approximately 3.5 GeV, and the medium energy (ME) beam configuration, which has a peak energy of approximately 6 GeV, with FHC and RHC data in both of these energy regimes. The LE neutrino mode beam is used for the inclusive analysis presented here, while the ME neutrino mode beam is used for the deep inelastic scattering analysis. The neutrino beam produced is not monochromatic, since only the charged particles which decay to produce the neutrinos can be focused and energy selected, the resulting neutrino energies have a wide spread to them.

The number of protons that are used to produce the neutrino beam, or protons on target (POT) can be a useful way to gauge the intensity of a neutrino beam since neutrinos

are hard to characterize. For instance, MINERvA took approximately 3.3×10^{20} protons on target of data in the LE neutrino mode beam, and 10.6×10^{20} in the medium energy neutrino mode. Inclusive charged current analyses in these two beam modes had approximately 300,000 and 6 million events, respectively. The beam energy and meson yield is also a factor in this, which is why ME had 3 times the POT, but 20 times the events.

3.1   Proton beam

The proton beam, which the NuMI beam originates from is produced by using a series of consecutive accelerators that each increase the energy of the beam. The accelerator complex is shown in Fig. 3.2. The process begins with a H^- source which are accelerated up to 400 MeV in a linear accelerator, before being sent through a carbon foil which removes the electrons from the H^- ions, leaving a pure proton beam. The proton beam then travels to the Booster ring, where they are accelerated to 8 GeV, separated into batches and sent to the Recycler.

At this stage a process called "slip-stacking" is sometimes used to increase the beam intensity. In this process six batches get injected in to the Main Injector Ring, while six more batches are readied in the Recycler before also being sent to the Main Injector. The RF system is controlled in such a way that the two sets of batches are combined into a single set of six batches which each have roughly twice the number of protons in them.

As described above, this process is sometimes used, because it was only first implemented for the medium energy beam. The low energy beam does not use any slip stacking, and since the slip stacking process was just turning on for the ME run there are some portions of the ME run which only have the first two of the set of six batches slip stacked, some that only have four slip stacked batches, and the data from the end of our ME run has all six batches slip stacked. The intensity of the beam therefore changes in these dif-
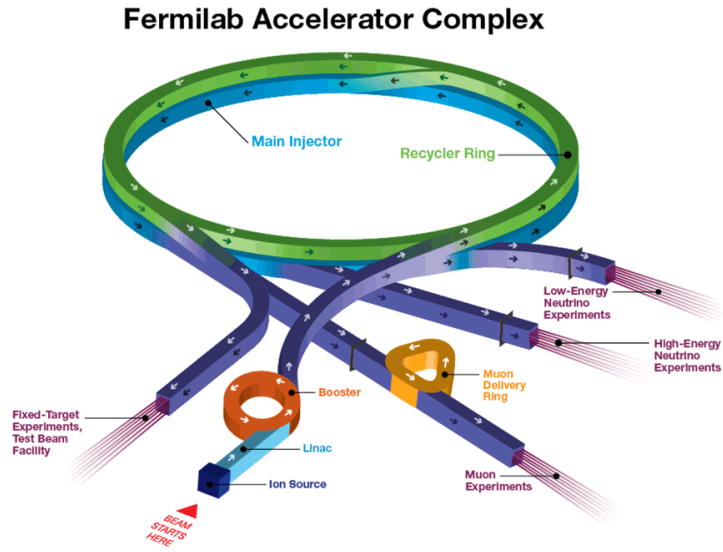
FIG. 3.2: The Fermilab accelerator complex used to produce the 120 GeV proton beam that the NuMI beam uses, taken from Ref. [60]. The NuMI beam is labeled "High-Energy Neutrino Experiments".

ferent periods. These intensity effects were included within the MC simulation, studied by comparing data and MC events/POT, and determined to be modeled within 2% [11].

3.2   Target

Interactions of the proton beam inside of the target are what produces the particles used to make the neutrino beam. The target is a 1.2 m long rod made of graphite with water cooling fins. It is divided into 48 regular segments each 24 mm long. The target position is able to be moved with respect to the horn position which results in changes the energy focused mesons used to make the beam. There is a balancing act to optimizing the design of the target, longer targets result in more difficulty focusing pions, but shorter targets are more likely to have the protons from the beam escape out of the side of the target without interacting. Narrower targets allow more mesons to escape without rescattering but are weaker mechanically. It also needs to be constructed in such a way that it can withstand significant radiation damage, heating and corrosion that comes with interacting with a high powered proton bean.

3.3   Horns

Two magnetic horns in the target hall are used to filter the particles produced by the target interactions. The aluminum horns have a parabolic shaped inner conducting surface and a cylindrical outer surface and are 3 m long. A toroidal magnetic field is generated in between the inner and outer conducting surfaces of the horn. A 200 kA current is run over the surface of the horn, generating a magnetic field perpendicular to the direction of the beam. A schematic of the cross section of the horns is shown in Fig. 3.3.

The magnetic field can be set to either a forward or reverse horn current (FHC, RHC).
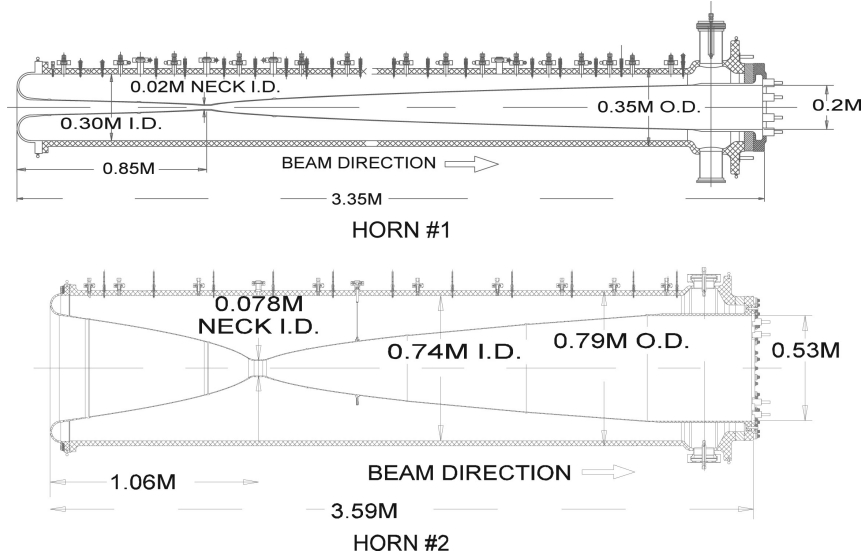
FIG. 3.3: A schematic of the cross section of the magnetic horns in the beam direction. Horn 1 is shown on the top, with horn 2 on the bottom.

In the forward horn current mode negatively charged mesons are defocused, and positively charged mesons are focused to produce a neutrino rich beam. The opposite configuration for the reverse horn current produces a anti-neutrino rich beam. In this dissertation only forward horn current data is used.

3.4 Decay pipe and absorber

Downstream of the target and magnetic horns there is a 675 m long pipe filled with low-density helium. This decay pipe allows for the mesons produced in the target inter-actions to decay and produce muons. The majority of the mesons in the beam are π^+ for a FHC beam, which produce muon neutrinos through the decay $\pi^+ \to \mu^+ \nu_\mu$ which occurs over 99% of the time.

On the downstream end of the decay pipe is a hadronic absorber comprised of steel, aluminum and concrete which functions to catch hadronic particles which haven't decayed. The beam then enters a region of 200 m of rock that is used to absorb any muons produced
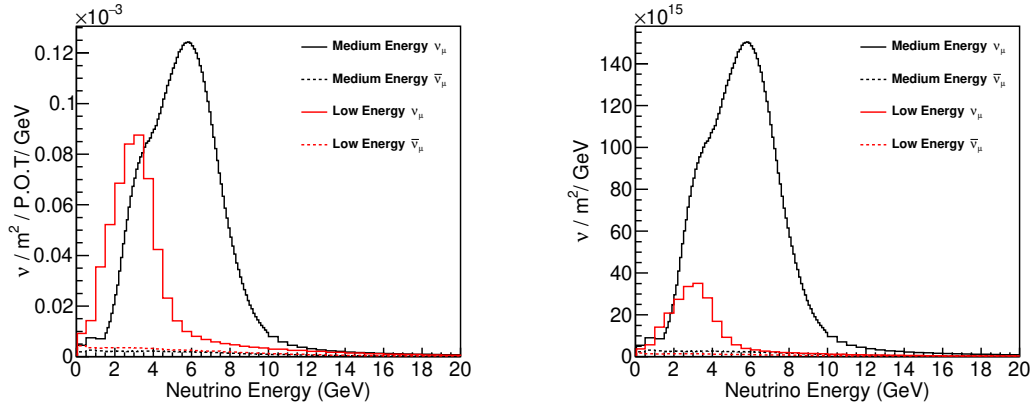
FIG. 3.4: The FHC fluxes for the low and medium energy beams as well as their anti-neutrino contamination. The plot on the right has the flux scaled per POT, while the one on the right is scaled with the accumulated POT for each run.

in the pion decay. There are various muon monitoring sites within the rock which can be used as a method of beam monitoring. Muons created through decays will be stopped by the amount of rock that it has to traverse before arriving at MINERvA. However, the neutrinos may interact within the rock and produce muons, which may enter our detector (especially the far front end). These are the same "rock muons" referred to in Ch. 2, which are monitored by the veto wall.

3.5 Beam modes

As mentioned earlier, the beam energy can be adjusted by moving the target and horns. There are two different configurations, resulting in different beam energies that were used for MINERvAs data taking. There are a few relevant differences between the low energy and medium energy beams in addition to the different flux profiles. In the LE beam we had an exposure of 3.3×10^{20} protons on target (POT), while in the medium energy beam there was a significantly larger exposure of 10.6×10^{20} POT. The fluxes for the LE and ME are shown in Fig. 3.4. The plot on the right shows the comparative intensities

of the two beam modes, while the plot on the right shows the number of neutrinos scaled to the relevant POT exposure. The LE flux more closely maps to the expected DUNE flux, however the ME data has the benefit of substantially increased statistics while still probing the kinematic of interest. The ME beam is especially beneficial for studying DIS, as the higher beam energy results in a larger portion of DIS interactions.

3.6 Flux simulation

Simulations and predictions of the flux are an important element of our cross section measurements. We simulate the NuMI beam first using G4NuMI, a package based on GEANT4 that models the geometry of the beam, propagating an initial proton beam through the interactions and decays which produce neutrinos [25]. This beam simulation is reliant on modeling of the hadron production that occurs when the proton beam interacts with the graphite target, as well as any additional interactions the particles undergo. It uses the FTFP_BERT hadron shower model [61], with Bertini intranuclear cascade model [62] and Fritiof with precompound (FTFP) [63] . However, we also make use of experimental data to help account for discrepancies between these predictions and measurements of hadron production data. Specifically, experimental measurements by NA49 at CERN[64] and Main Inject Particle Production (MIPP)[65] are used in order to constrain the hadron production. NA49 measured hadron production of 158 GeV protons at CERN on NuMI thin target replica [64]. The 158 GeV data is translated to 120 GeV (as used by the NuMI beam) using the FLUKA simulation [66]. MIPP used 120 GeV protons on a spare target, which was later used in the NuMI beam [65].

We use the Package to Predict the Flux (PPFX) which generates flux predictions and associated uncertainties. It incorporates the external data on hadron production measurements into these predictions [67].

3.6.1 Constraining the flux

In both the LE and ME beams a similar technique was used in order to better determine the flux by looking at the process of neutrinos scattering of atomic electrons. This is a well understood process that is not complicated by any nuclear effects since it takes place outside of the nuclear environment. It can be computed to high precision, and produces an electromagnetic shower which can be distinguished from ν_μ CC interactions, thus making it an ideal standard candle measurement that can be used to help better understand our flux.

In the LE mode the neutrino-electron scattering constraint is done independently using only the forward horn current beam, while in medium energy, measurements of ν-e scattering in the FHC and RHC are combined with each other and with a further constraint from inverse muon decay to produce a joint fit with greater precision. The process of inverse muon decay ($\nu_\mu e^- \rightarrow \mu^- \nu_e$), is similarly a process which can be calculated to high precision and used as a standard candle in order to constrain the high-energy tail of our flux [68]. The fluxes resulting from these constraints are show in Fig. 3.5, which show the flux before and after constraints are applied.

There is a significant reduction in uncertainties that results from these constraints. In the low energy beam uncertainties in the flux are reduced from 9% to 6% [69]; the medium energy uncertainties are reduced from 7.6% to 3.3% [70]. The effect of the constraint on the uncertainties is shown in Fig. 3.6. The flux uncertainty is one of the largest uncertainty contributors in the LE inclusive cross section measurement. It is also one of the larger uncertainties in the absolute neutrino energy cross sections in the ME DIS measurements.
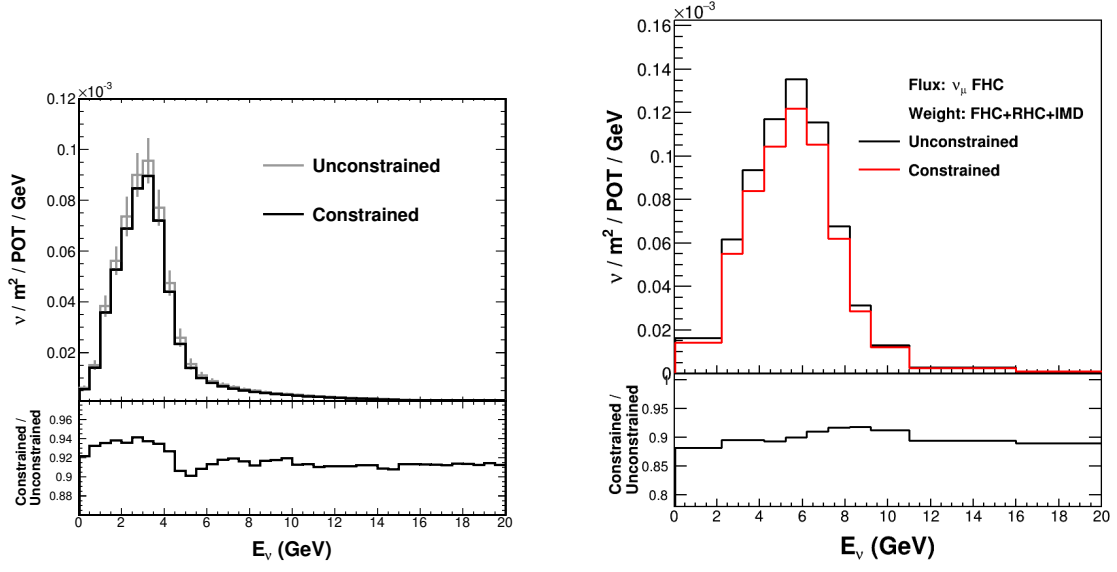
FIG. 3.5: The flux before and after constraint for the FHC beams for LE [69] (left) and ME [70] (right).
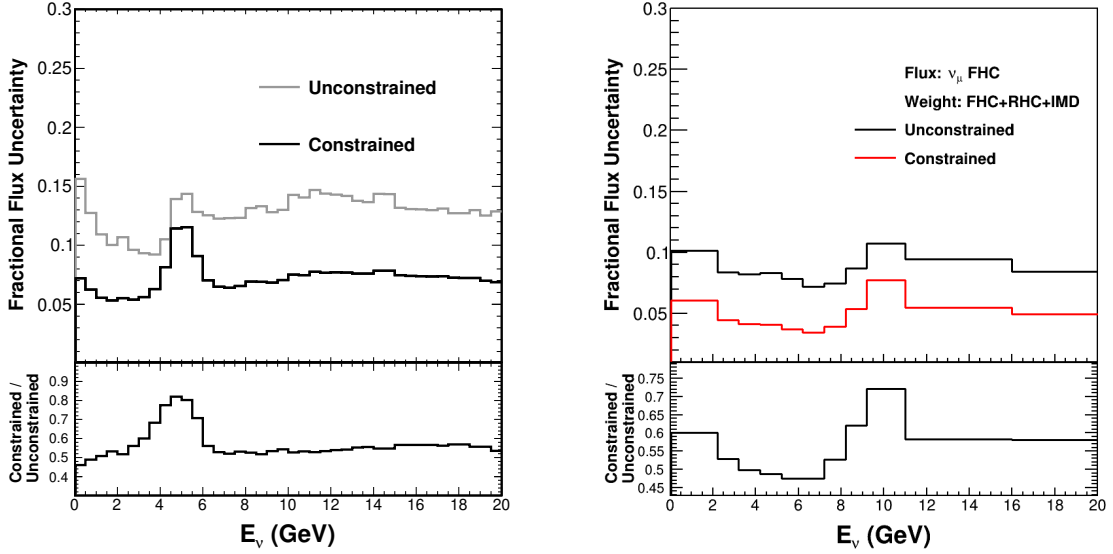
FIG. 3.6: Uncertainties on the flux before and after constraint for the FHC beams for LE [69] (left) and ME [70] (right).
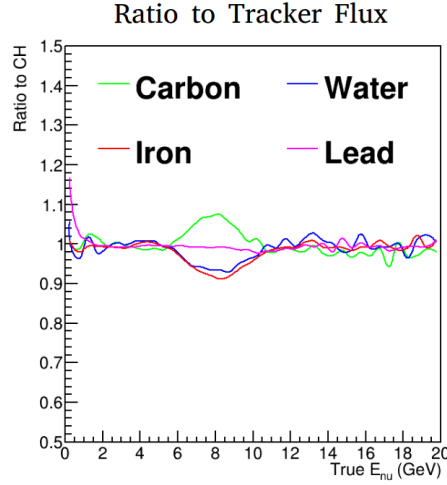
FIG. 3.7: Fluxes for each nuclear target material and water as a ratio to the tracker flux [9].

3.6.2 Nuclear target fluxes

The flux is not uniform as a function of x and y detector position. All of the flux constraints discussed previously constrain the average flux for the tracker region. This is not an issue when looking at the tracker since it's entire volume is averaged over, but the nuclear targets are irregularly shaped and populate different transverse positions in the detector.

Spacial flux dependence is handled by PPFX to account for the differences in neutrino interaction rates as a function of position. However, in order to directly compare the cross sections in the tracker region and nuclear target regions, as we wish to do in the DIS analysis, further corrections have to be made. The objective of this process is to attempt to limit the effect of these flux differences when taking ratios of the nuclear targets and tracker. We also need to use the correct fluxes for each nuclear target when measuring their absolute and differential cross sections, as the last step of cross section measurements is to normalize the measured event rate by the neutrino flux (detailed in Ch. 5).

In order to handle the latter situation of cross section measurements in the nuclear targets, we calculate the flux for each of the summed nuclear target materials (i.e. all
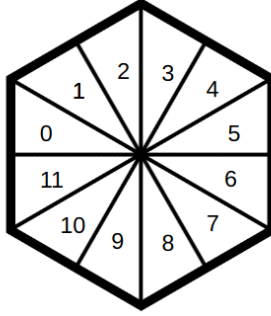
FIG. 3.8: A diagram of a plane divided into "daisy petals" which can be used to account for flux differences.

of the iron targets), and normalize by those fluxes when measuring the nuclear target cross sections. To calculate these target fluxes we could run PPFX for each of the target materials but that process is computationally expensive. So instead we look at the true generated CC event rates in each of the nuclear targets, and divide that by the GENIE cross section and normalization factors to get the flux for each target material. The ratio of the flux in each material summed across targets to the flux in the tracker is shown in Fig. 3.7.

However, the flux does not only enter our cross section measurements at the final stage of normalization. It is also used by the simulation to populate neutrino interaction events. When looking at the cross section ratios this second element is an important difference between the nuclear targets and tracker. To account for the differences in the flux that is used to generate the simulated events in the different detector regions we apply weights to events from different segments of the tracker. We divide the tracker planes up into a variety of slices that we call "daisy petals", which are 12 radial segments, as shown in Fig. 3.8. Every petal has its own associated flux, so we perform a fit which creates a linear combination of the petal fluxes such that the weighted sum of the petal fluxes approximates the summed target material flux. The weight for each petal produced from this fit then gets applied to the efficiency corrected event rate in each daisy petal of the tracker for

both data and MC. The petals are summed over to produce a different reweighted tracker event rate for each target material, and those event rates are then used in the cross section ratio measurements.

CHAPTER 4

Reconstruction

In order to be able to perform an analysis we have to first take the PMT readings of energy deposits or "hits" in each of the scintillator scripts and convert them into physical quantities, through a process called reconstruction. The variables that are determined by looking at the detector signatures are referred to as reconstructed variables, while values which come straight from the event generator without any simulation of the detector effects are the true variables. However, before the hits can be reconstructed into physical quantities, the detector must first be calibrated.

4.1   Calibration

The signal which the DAQ reads out undergoes a series of calibrations based on measurements of the detector response. Effects which need to be accounted for include variations in the responses of different PMTs and pixels, accounting for degradation of scintillator strip responses over the years of operations, and correcting for offsets in the measured time of light pulses from different scintillator strips due to varying distances from the PMTs. The quality of the optical fibers, scintillator and their optical couplings

are also calibrated for. Some noteworthy calibration steps are discussed here, however further detail on calibration processes can be found in [10].

The readout of the PMTs is vital to our measurements of energy deposits within the detector, so we perform several calibration steps to test that all of the channels are operational, what noise they are seeing, and how many photoelectrons are detected for a given light signal. The first way to achieve this is through pedestal data, which was taken twice daily during the times in between beam spills. This is used to measure the background activity in the detector when there should not be any present accelerator neutrinos, so any noise measured in the electronics during this pedestal runs can be used as a baseline for defining what an absence of signal looks like. The PMTs can further be calibrated using data from a process called light injection. In this process a LED with a consistent light produced is flashed directly in front of the PMT sensors. The number of photoelectrons detected in each of the channels for the PMT is determined from a fit to the collected charge distribution.

Differences coming from the light attenuation of the scintillator strips throughout the detector is also calibrated by looking at the energy deposits of through-going muons which were produced in the rock upstream of the detector. As these muons should have consistent energy deposits as they travel through the detector, the differences in the recorded energy in the scintillator strips in which they travel through can be used to calculate a strip-by-strip correction factor, and identify any strips which are dead.

The timing information is also calibrated and has three primary methods of calibration. First, the travel time for the light travel from the detector to the PMT along the optical fibers is accounted for using the length and speed of light in the fiber. Identified rock muons are used to measure time slewing and channel-to-channel timing differences. Time slewing originates from scintillator decay times, and is energy dependent. Differences in the channel-to-channel timing come from cable delays and timing offsets between FEBs

and FEB daisy chains. By using rock muon activity, the time slewing and channel-to-channel differences are iteratively calibrated, with a single time offset measured for each set of channels read out by a single Trip-t.

4.1.1   Time slices

Data is taken in "gates" of 16 μs, which coincide with the NuMI beam spills. However, over that period of time there can be many different neutrino interactions that take place, each within a much smaller portion of time. In order to account for this we split the 16 μs gate into different "slices", which represent smaller fractions of time where there was ideally a single interaction in the detector.

Fig. 4.1 shows all of the detector activity over the span of an entire gate, as well as a single time slice in which there is a single neutrino interaction. Slicing into a finer time segments allowed for detector activity associated with things like rock muons to be separated from the physics interactions we are interested in studying. The smaller time slice contains all of the hits associated with the neutrino interaction.

A time slice is created when there are at least 10 photoelectrons worth of charge detected within a 25 ns time window of calibrated time (which takes into account the time for the light to propagate from the center of the strip to the PMT and Trip-t). The relative time information of the hits within each slice is also retained and used in later reconstruction steps.

4.2   Reconstruction

In order to reconstruct the paths of individual particles (in these analyses we only look for the muon) and the total hadronic energy which is deposited in the detector, we use the calibrated light signal within a single time slice, and single plane, and sort the activity
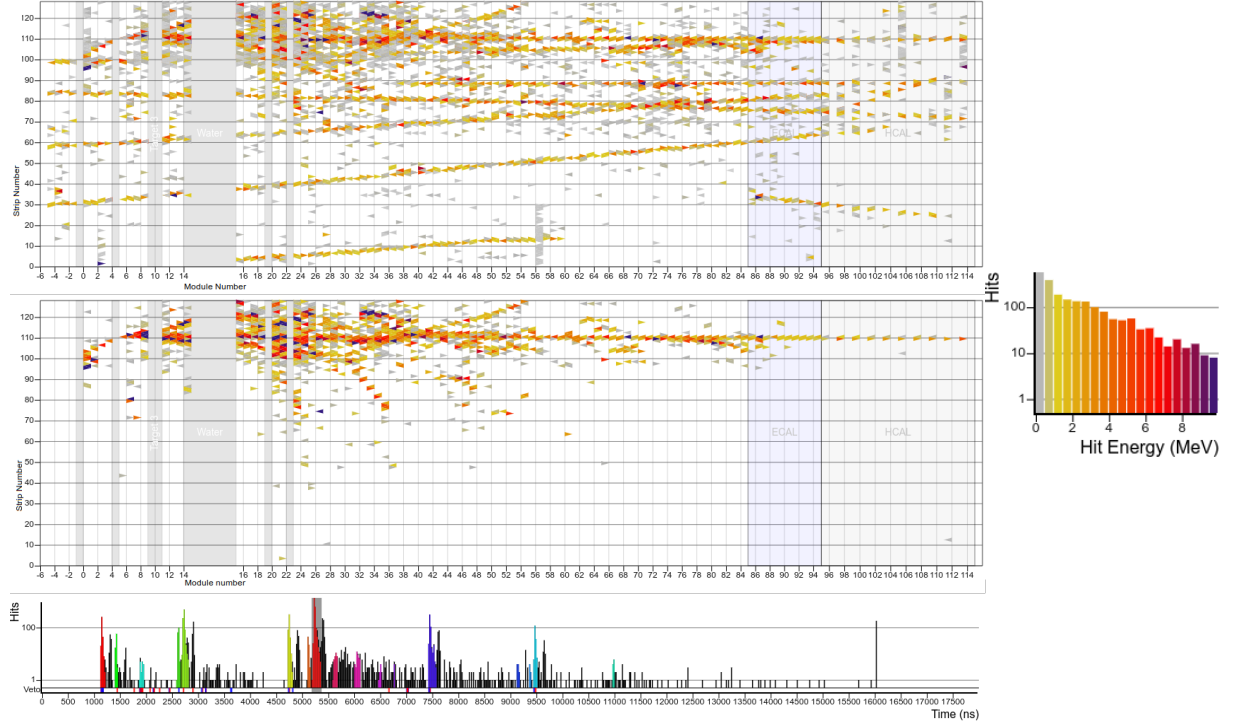
FIG. 4.1: A data DIS candidate event with the entire 16 μs gate (top), and a smaller time window slice (approximately 300 ns) in which neutrino interaction occurs (middle). This XZ view of the detector shows the z position in the detector by indexing the module number with the beam entering from the left, while the vertical plot axis is a function of the detector's horizontal x position. The colored triangles are the scintillator strips where there were energy deposits. Darker colors represent larger energy deposits, the color scale is shown on the right. The hits seen as a function of time in the 16 μs gate are shown on the bottom.

52

into groups called "clusters". These clusters can then be used to reconstruct the path of the muon through the detector ("muon track"), and the hadronic energy. At this point we also filter out cross talk, detector activity where there is light signal contamination from one strip to another which occupy adjacent PMT channels (see Sec. 2.8). The cross talk is identified by low activity without other activity in strips which physically neighbor it, but with activity in a strip which is read out by a neighboring PMT channel. The clusters are classified as either low activity (less then 1 MeV of summed energy), trackable (consistent with the energy deposits of a minimum ionizing particle such as a muon), heavy ionizing (extremely energetic deposits onto a single scintillator strip), or super-clusters (broad energy deposits spanning multiple scintillator strips, consistent with an electromagnetic or hadronic shower).

Reconstructing further particle tracks is possible depending on the topology of the interactions being studied. In the inclusive analysis presented in this thesis, additional particle track reconstruction is not needed as only the muon properties are used for the signal definition, selection criteria and measured cross sections. In the case of the DIS analysis, the DIS interactions produce showers of many hadrons, such that their tracks overlap one another and cannot be individually distinguished or reconstructed, therefore the total hadronic energy is summed instead.

4.2.1 Muon reconstruction

The next process in the reconstruction is to find the tracks left by minimum ionizing particles and group them together. This is how the muon track is identified. A similar process could also be used to track other particles that may be of interest such as pions or protons, but tracks of particles other than the muon are not used for either of the analyses presented here, and is thus outside the scope of this thesis.

When looking for particle tracks, only the "trackable" and "heavy-ionizing" types of clusters are used. We require that the tracks are seen in each of the different plane orientations (X, U, and V) so that we are able to reconstruct the (x, y) detector position of the track. The track must be present in three planes of each view, thus the track must have hits in at least 11 total planes to meet these requirements due to the alternating plane arrangement. For example, if the track began in a U view plane, it could form a track with the minimum number of traversed planes with hits in the following plane orientations UXVXUXVXUXV. If a track candidate was found, additional clusters consistent with it in each view are added, allowing for gaps where there may be dead detector regions.

Candidate tracks are found in each of the two dimensional single detector views by looking for clusters with consistent slope and intercepts and requiring at least one cluster in each plane. The candidate tracks from each detector view are then merged together by looking for candidates that have consistent lengths and produce a consistent three dimensional line. The tracks are fit using a Kalman fitter to account for altering track direction from multiple scattering. The resulting three dimensional tracks are then projected up and downstream, and any clusters in their projected paths are added to the track (including the low activity and super-clusters not previously included). Super-clusters, which get included in the muon track, are divided into smaller clusters based on position to ensure that cluster energy is consistent with a minimum ionizing particle. The remaining energy left over after dividing the super-cluster is considered to be part of the recoil system.

4.2.2   MINOS matching

Reconstruction information is used from both MINERvA and the MINOS detector. We then look for tracks in the MINOS ND in a similar method and see if the trajectory of the track in MINERvA matches the trajectory of the track in MINOS. In order for

tracks to be matched between the detectors they must occur within 200 ns of each other. Additional requirements are made that the track visible in MINERvA ends within the 5 most downstream modules of the detector, and that the track in MINOS begins within its four most upstream planes. The tracks in each detector are extrapolated to their position in the other. If the end position in MINERvA extrapolated from the track seen in MINOS, and the start position in MINOS as extrapolated from the MINERvA track are within 30cm of the track reconstructed in that detector, then there is considered to be a matched track. The MINOS track reconstruction process is very similar to that used in MINERvA, with hits classified by time and detector position, and using a Kalman fitter.

The energy of the muon can be measured in MINOS by using the distance traveled in MINOS (range), and the curvature of the track within MINOS's magnetic field. While the beam is running in forward horn current mode (neutrino enriched) negatively charge muons are focused towards the MINOS coil, which causes there to be the longest possible MINOS track. The range is the highest precision method of estimating the muon energy. Some muons have tracks which stop within MINOS as it is largely composed as steel which has significant stopping power, however higher energy muons are less likely to do so. If a muon is contained inside MINOS the momentum can be calculated from the range by using the total energy loss within the detector.

Muons with energies about 10 GeV have high enough energy to travel the length of the MINOS detector, while some muons with lower energies may escape out the side of the MINOS ND. If the muon does not range out in the detector, it's energy is calculated by using its curvature by relating the radius of curvature, R, via

$$\frac{1}{R} = \frac{0.3BQ}{p_\mu} \tag{4.1}$$

where B is the magnetic field in kGauss, Q is the charge of the muon in units of electron
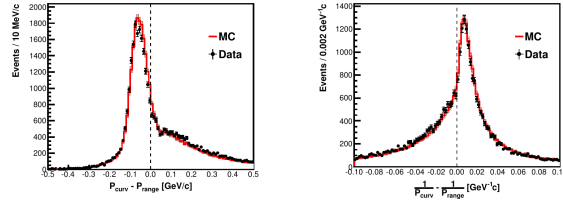
FIG. 4.2: Comparisons of range and curvature reconstructed muon momentum [10].

charge, and p_μ is the muon momentum in MeV/c. If the muon momentum is calculated with the range (curvature) it has a 2% (2.6%) systematic uncertainty associated with it. The energy deposited while the muon traverses the MINERvA detector is also accounted for. Comparisons of muons in which the momentum was able to be reconstructed through both range and curvature, were consistent to within 0.6% [71]. Residuals comparing the curvature and range reconstructed momenta are shown in Fig. 4.2.

4.2.3 Muon angle

The muon angle can be calculated using the 3D muon momentum vector and the slope information from the track. This angle is between the direction of the muon track, and the beam direction (not MINERvAs coordinate system which is slightly shifted).

4.2.4 Longitudinal and transverse muon momentum

The longitudinal and transverse components of the muon momentum can be calculated using the muon momentum vector, and are directly related with the muon angle. However, as the z direction of the detector has a 58 mrad angle with respect to the beam direction the muon momentum must first be transformed into a coordinate system based on the beam direction. This difference in the z direction of MINERvA, and the direction of the beam comes about because the detector is level, but the beam has a slight downward slope so that it can be seen hundreds of kilometers away at far detectors for oscillation

56

experiments.

The three dimensional muon momentum vector in the detector coordinate system is given by (p_x, p_y, p_z). Accounting for the additional angle θ_{beam}, the momentum components can be shifted into a primed coordinate system aligns the beam direction with the z' axis.

$$p_x' = p_x \tag{4.2}$$

$$p_y' = \cos(\theta_{beam})p_y - \sin(\theta_{beam})p_z \tag{4.3}$$

$$p_z' = \sin(\theta_{beam})p_y + \cos(\theta_{beam})p_z \tag{4.4}$$

With each of these shifted momenta, the longitudinal component $p_{||}$, with direction parallel to the beam, and transverse momentum p_T which is perpendicular to the beam direction are given by:

$$p_{||} = p_z' \tag{4.5}$$

$$p_T = \sqrt{p_x^2 + p_y'^2} \tag{4.6}$$

4.2.5 Hadronic energy reconstruction

The hadronic energy, or recoil energy of the interaction, is an important quantity that is heavily utilized in the DIS analysis in this dissertation. This is all of the energy that is produced in the neutrino interaction which does not go to the muon, and is instead involved in part of the hadronic recoil system. We find the sum of the hadronic energy in the detector by using calorimetric corrections. The reconstructed hadronic energy is found by summing all of the energy in the detector which is not associated with the muon track or coming from low activity clusters.

In order to determine the total hadronic energy including that lost to passive material

and not directly observed, we use calorimetry. Calorimetry uses the energy that is visible within the detector to predict the how much energy was lost, and what the total energy of the hadronic system originating from the neutrino interaction was. In addition to accounting for passive materials like the iron and steel that is a part of our ECAL and HCAL regions, and the passive nuclear targets, calorimetry also uses a simulation to correct for the energy of unobservable neutral particles and energy that escapes out of the sides of the detector. Energy may not be directly visible due to a few different effects: e.g. there can be neutral particles produced which do not leave an electromagnetic signal, energy can be lost to final state interactions or the binding energy of the nucleon, and energy may leak out of the sides of the detector. The true hadronic or recoil energy is defined as the difference between the energy of the incoming neutrino and the energy of the outgoing muon. The reconstructed hadronic energy, $E_{had,reco}$, has a more involved calculation which accounts for these energy losses, as the energy of the neutrino is not directly observable. The first step to determining $E_{had,reco}$ is to sum the detected energy in each of the different regions of the detector and apply a correction factor based on the fraction of passive material in that region. An additional scale factor α is found by performing a fit which compares the sum of the passive material corrected reconstructed energy of each detector region to the true recoil energy. The reconstructed calorimetric hadronic energy $E_{had,reco}$ is then given by

$$E_{had,reco} \equiv \alpha \times \sum_i c_i E_i \tag{4.7}$$

where i indexes the different detector components (the active tracking volume, ECAL, HCAL, OD, side ECAL), E_i is the sum of the energy from all of the hits in a given detector section, and c_i is the calorimetric constant used for in a given detector component.

The calorimetric constant c_i for each region of the detector is determined based on
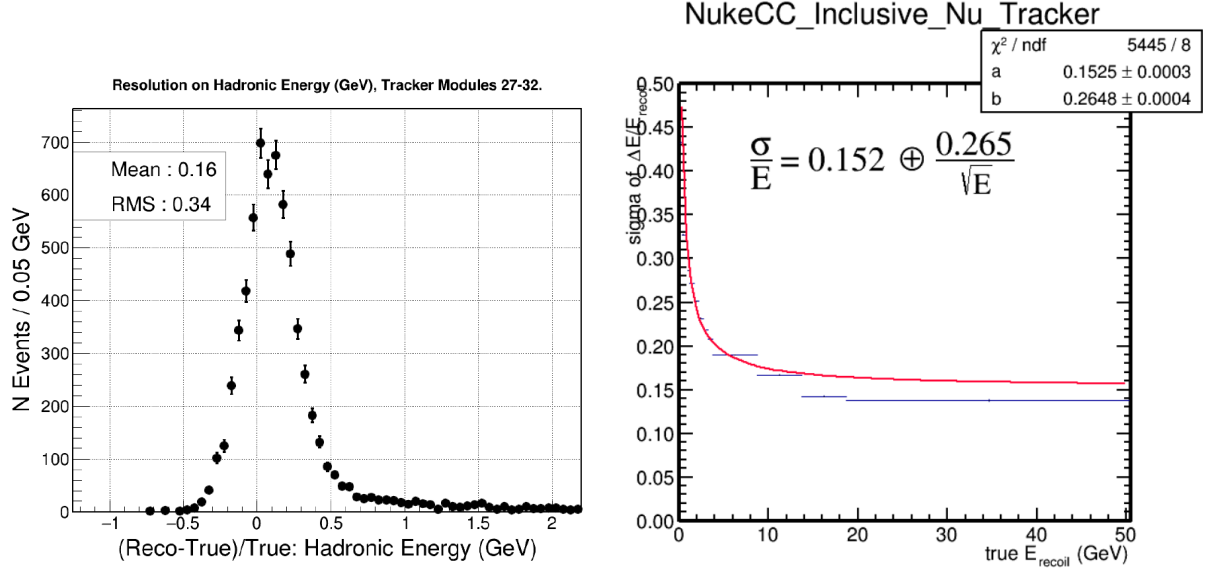
FIG. 4.3: The calorimetric energy resolution for the active tracker region of the detector [11].

the fraction of the sub-detector which is comprised of active scintillator, and the amount of energy lost to the lead and steel passive materials in the calorimeters. Calorimetric resolution is shown in Fig. 4.3. The correction factors are calculated by summing together weights of the passive material in each sub-detector and dividing them by the fraction of active material in each tracker plane. So for tracker $c_i = 1/f$, where f is the fraction of a scintillator plane which is made of active materials. The ECAL, HCAL and outer detector regions have has an additional factor which accounts for the energy lost to the lead and iron passive materials in those regions. Similar corrections are applied for interactions taking place in the nuclear target region of the detector to account for the target passive materials.

After the hadronic energy is calculated according to Eq. 4.7, an additional bin-by-bin energy correction is applied. This correction accounts for any differences in the initial reconstruction of hadronic energy and the true hadronic energy. This would include effects such as any energy which escaped the detector, however, our downstream and side
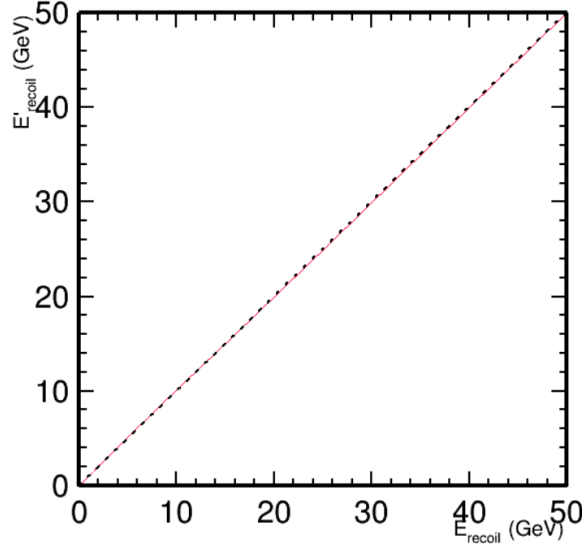
FIG. 4.4: The polyline fit for the recoil energy in the active tracking region of the detector [11].

calorimetry is allows for us to contain most hadronic energy. The fractional difference between the calorimetric and true energy recoil energy:

$$\frac{\Delta E}{E_{had,true}} = \frac{(calorimetric - true)}{true} \tag{4.8}$$

is fit with a polyline such that there is an average difference of 0 between the calorimetric and true recoil energy. The polyline has fixed points at (0,0) and (50,50) where the coordinates represent the ($E_{had,calorimentric}$, $E_{had,true}$) values given in GeV. This polyline function (shown in Fig. 4.4) is then applied to the previously calculated calorimetric energy.

A test beam program which used a scaled down version of the MINERvA detector in a charged particle beam was used to validate the calibration of the calorimetric response to single particles. It showed agreement between the data and simulation of particle interactions to within 4% [72].

4.2.6 Vertex Reconstruction

We have to know where in the detector an interaction takes place, or the "vertex" of the interaction. In order to determine this, there are two different types of vertex reconstruction methods which are used in this dissertation. The first type of reconstruction involves finding the starting point of the muon track. This is sufficient when trying to study the large active tracking volume of the detector, but is imprecise when interactions are in the nuclear target region, where a small difference in position changes the material which we reconstruct the interaction to take place within.

When reconstructing the interaction vertex using track based methods, the reconstructed muon track is used to find the vertex by tracing it to its most upstream position in the detector. The inclusive analysis presented here exclusively uses track based vertex reconstruction methods.

In order to increase precision in the vertex reconstruction in the nuclear target region we also use a vertex reconstruction algorithm which utilizes machine learning (ML). As MINERvA has tools to view interactions in the detector as images, a machine learning image classification technique can be used to identify the plane in which the interaction took place. A deep convolutional neural network was used with images from each of the X, U and V detector views to classify the event as having a particular vertex. Events that have muon tracks which match a MINOS track and a track based vertex is within the MINERvA detector are passed to a machine learning algorithm which had been trained using a distinct set of simulated interaction images, which assigns a plane number for the interaction vertex. In this process the network also assigns a probability associated with the neural network's confidence that the vertex has been correctly identified, when using the ML vertex only events which have probabilities greater than 20% are included. This number was chosen as the ML is able to reconstruct a comparable portion of simulated
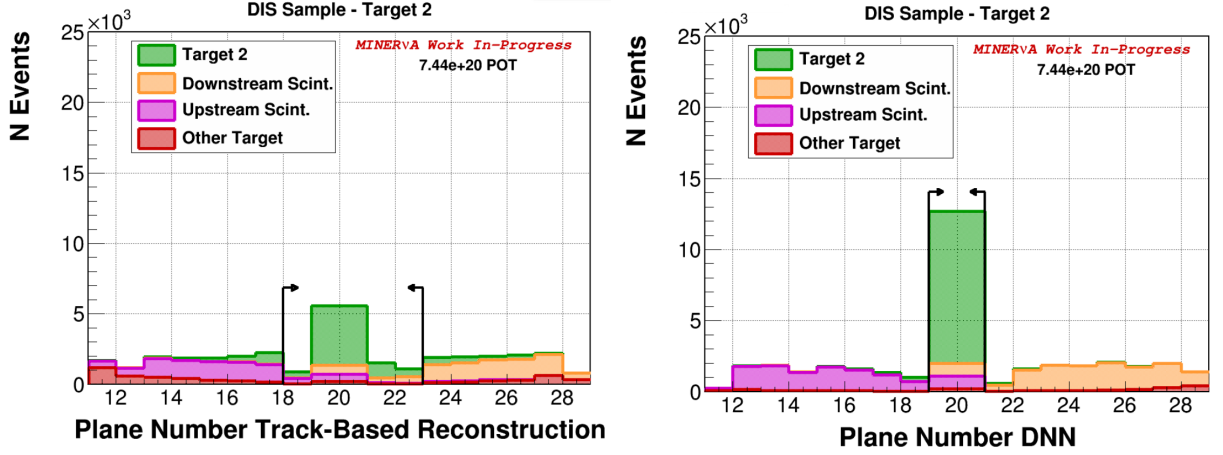
FIG. 4.5: The vertex position reconstructed using the muon track (left) and using machine learning (right) for target 2. The color indicates the true position of the vertex. The true target 2 events in green are correctly reconstructed if they are within areas denoted with the black arrows. A wider range of reconstructed vertex positions were accepted for the targets in the track-based reconstruction than ML due to the difference in precision. Taken from Ref. [12].

and data events with that confidence level. All of the reconstructed quantities that are associated with the vertex position are then recalculated based on the most probable ML vertex plane. The full details of this technique can be found in Refs. [73, 12]. The improvement in the vertex identification in the nuclear target region while using machine learning techniques is shown in Fig. 4.5. Scanning studies were done to further validate the ML vertex predictions, where individual event displays from both data and simulation were examined by eye and the human predicted vertices could be compared with the ML vertices. These studies showed consistent behavior between data and MC [**?**]. The machine learning vertex is used for the deep inelastic scattering analysis in this thesis.

CHAPTER 5

Cross Section Extraction Process

5.1   Cross Section Measurement Methodology

In this section I describe the process for measuring a cross section on MINERvA. The steps detailed here are almost all the same the inclusive and DIS analyses presented in this dissertation. The only step which is unique to the DIS analysis is the data driven background constraint process. Due to the extremely small backgrounds of the inclusive analysis such an estimation was not necessary.

For each of the variables we want to measure the differential cross section, there is a continuous distribution of possible values that quantity could have (e.g. neutrino energy). In order to examine these distributions in a meaningful way with statistical significance, we discretize the distributions into a finite number of bins that span some range of possible values. For instance when looking at a distribution in E_ν we collect all events whose neutrinos energies lie between 5.0 and 7.5 GeV and place them in a single bin. The width of these bins is determined by the population in that region of the distribution, our ability to reconstruct the measured quantity, and physics-motivated boundaries.

I measure three different types of cross sections in this dissertation. An absolute cross section measured as a function of neutrino energy, differential cross sections as functions of bjorken-x and longitudinal and transverse muon momentum, and a double differential cross section which is given as a function of both the longitudinal and transverse muon momentum. The cross section as a function of neutrino energy is normalized by the flux, $\Phi(E_\nu)$ averaged over the neutrino energies in each bin, while the differential cross sections measured in all other variables are normalized by the integrated neutrino flux from $0{\leq}E_\nu{<}120\,\text{GeV}$.

The total cross section as a function of neutrino energy, $\sigma(E_\nu)$, in a given true energy bin, α, is given by

$$\sigma_\alpha(E_\nu) = \frac{\sum_i U_{i\alpha}\ (N_{data,i} - N_i^{bckgd})}{\epsilon_\alpha\ \Phi_\alpha(E_\nu)\ T\ \Delta E_{\nu_\alpha}} \tag{5.1}$$

where $U_{i\alpha}$ is the smearing matrix, which accounts for detector effects resulting in misreconstructing the energy (i indexes the reconstructed bin number). $N_{data,i}$ are data events that we select as potential signal, and that we measure to be in reconstructed bin i. Some of these selected events will actually be backgrounds to the signal we want to measure, so we subtract an estimate of the background, N_i^{bckgd}.

For every interaction produce in the MINERvA detector, we only are able to measure a fraction of them. This can be for a variety of reasons, for example perhaps the detector was experiencing "deadtime" (described in Sec. 2.9) when the interaction occurred, or a cut that was made to select the sample removed the event (such as the muon produced did not travel through the MINOS ND). In order to account for this we divide by the efficiency ϵ_α (percent of signal events which we selected out of all signal events) in each bin α. We do not have data driven means to predict the efficiency and must rely on the simulation.

In order to measure a per nucleon cross section we have to normalize by the total number of target nucleons, T, in the detector volume. We also normalize by the width of

the bin ΔE_ν.

For a differential cross section in a variable other than E_ν, the cross section formula is very similar, with the main difference being that the normalization is by the integrated flux. For a given variable, x, it is given by

$$\left(\frac{d\sigma}{dx}\right)_\alpha = \frac{\sum_i U_{i\alpha}\left(N_{data,i} - N_i^{bckgd}\right)}{\epsilon_\alpha\ \Phi\ T\ \Delta x_\alpha},\tag{5.2}$$

where each of the quantities are defined in the same manner as in Eq. 5.1, except for Φ, which is instead the total flux integrated over all neutrino energies.

The formula used to measure a double differential cross section $d^2\sigma/dxdy$, which is a cross section measured as a function of two variables (x, y), is given by

$$\left(\frac{d\sigma}{dxdy}\right)_{\alpha\beta} = \frac{\sum_{ij} U_{ij\alpha\beta}\left(N_{data,ij} - N_{ij}^{bckgd}\right)}{\epsilon_{\alpha\beta}\Phi T\ \Delta x_\alpha \Delta y_\beta}.\tag{5.3}$$

Here there are additional bin indexes to represent the second variable. The true x bin is indexed by α and true y bin by β, while i and j index the reconstructed x and y bins, respectively.

5.1.1 Event Selection

The first stage in the analysis process is to select a sample of events. We use a series of selection criteria (cuts) that allow us to balance between having a high selection efficiency with a large fraction of the total signal events and high purity sample where only a small fraction of events are non-signal backgrounds.

Examples of cuts we use to select the data and simulated event samples are:

- Requiring the reconstructed muon energy to be greater than a threshold,

- A maximum reconstructed muon angle requirement,

- Selecting for interactions that originated in certain regions of the detector,

- Requiring the events to meet a reconstructed Q^2 threshold.

The specific cuts used in each analysis are detailed in Ch. 6 and 7. After removing events that do not meet the various requirements, we are left with a reconstructed distribution that can be background subtracted, unfolded and efficiency corrected to measure the cross section.

5.1.2 Background subtraction

A portion of the selected events will inevitably be interactions that are not signal events, because our detector is imperfect, and there is some finite resolution on the reconstructed values used to made our selection. In order to account for this we take the prediction of how many simulated background events are in the selected sample, and subtract that prediction from the data and Monte Carlo events in order to predict backgrounds and estimate the signal in the data. Subtracting MC events instead of doing an extra truth based cut in the MC event selection is done because it is helpful to treat the MC and data with exactly the same processing, as this allows for cross checks to be done at various stages using the MC. In the inclusive analysis, this is the entirety of the process.

However, in the DIS analysis were there are more significant background contributions, we use a procedure called "sideband fitting" in order to use the data to constrain the simulated background prediction.

Data based background constraints

We know that our simulation is imperfect at predicting neutrino interactions, that is why we need cross section measurements, so we would like to minimize dependence on the model in our measurement. One of the ways that model dependence can enter the analysis is at the background subtraction stage since we are not able to directly measure the data backgrounds, and have to rely on model predictions.

In order to get a better handle on a prediction of the true data background, we look at regions called "sidebands" which lie just outside of the signal selected region and have properties similar to that of the backgrounds in the signal region. These regions have many events with the same truth properties like the true W, or the true interaction material and vertex position, as the background events that are reconstructed in the signal region.

An example of this for the DIS analysis are sidebands that look at the scintillator around the nuclear targets in order to get a handle on contamination coming from events interacting in the scintillator but making their way into our selected nuclear target sample due to a misreconstructed vertex position. Another is a region of reconstructed W, just below the selected W interval which has a high fraction of true low W events like those entering the selected sample, allowing us to constrain the true low W behavior in the simulation.

These sideband regions are defined with reconstructed quantities, so we are able to select both a data and MC sideband and perform a fit to the MC to better match the data distribution. The results of the fit are the scale factors that are applied to create a constrained MC. These scale factors help better describe the sideband which should have physical properties similar to the background contributions in the signal selected region. The scale factors are then applied to the MC predicted backgrounds ("tuning" the background) before they are subtracted from the data. Tuning is not applied when doing
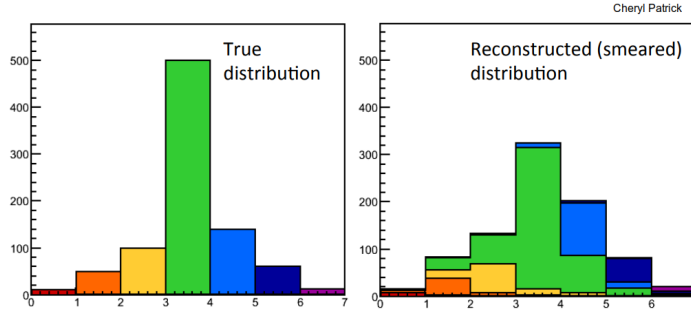
FIG. 5.1: A cartoon showing the effect of detector smearing. A underlying true distribution like the one on the left, might get reconstructed like something on the distribution on the right. Here the color is indicating the true bin in both distributions [74]

the MC background subtraction, because the MC is already self consistent.

5.1.3 Unfolding

When data events are reconstructed, the reconstructed values we are making measurements in are smeared away from their true values due to detector resolution effects. For example, for a batch events all with exactly the same momentum muon there will be a spread of reconstructed values of momentum. A cartoon of this effect is shown in Fig. 5.1. An example from the DIS analysis showing the reconstructed and true neutrino energy distributions is shown in Fig. 5.2.

The process of removing these smearing detector effects and converting the selected events into an estimated true variable distribution that can be used more directly when comparing to models and other experimental results is called "unfolding".

The unfolding process makes use of a migration matrix that shows which reconstructed MC events belong in which true bin (see Fig. 5.3 for an example in x_{bj} from the DIS analysis). We do not directly invert the migration matrix in order to unfold our distributions, as many migration matrices are not invertable and that process has significant associated uncertainties.

Instead we use a process of iterative Baysean unfolding, called the D'Agostini method
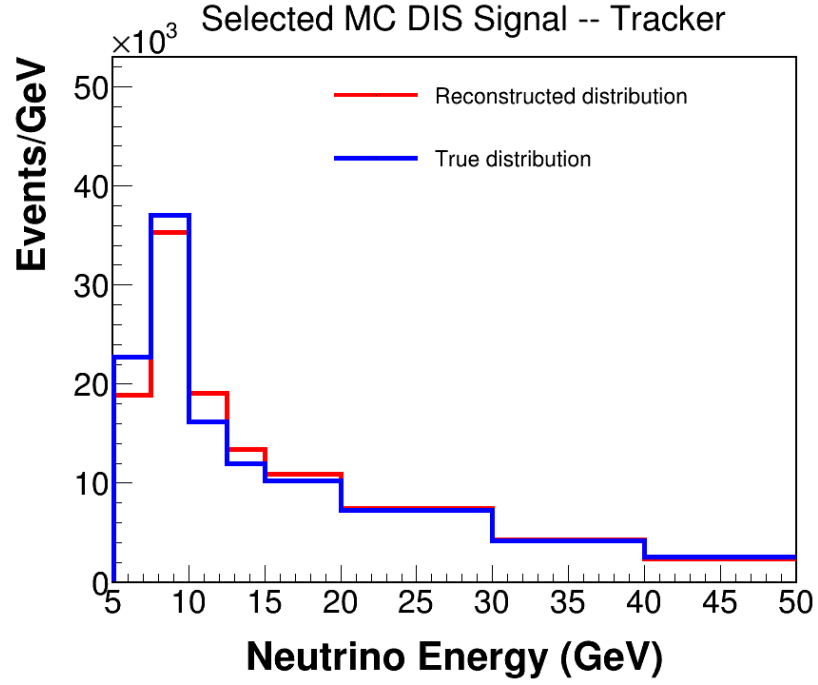
FIG. 5.2: The reconstructed smeared (red) and true (blue) neutrino energy distributions for MC signal DIS events in the tracker.
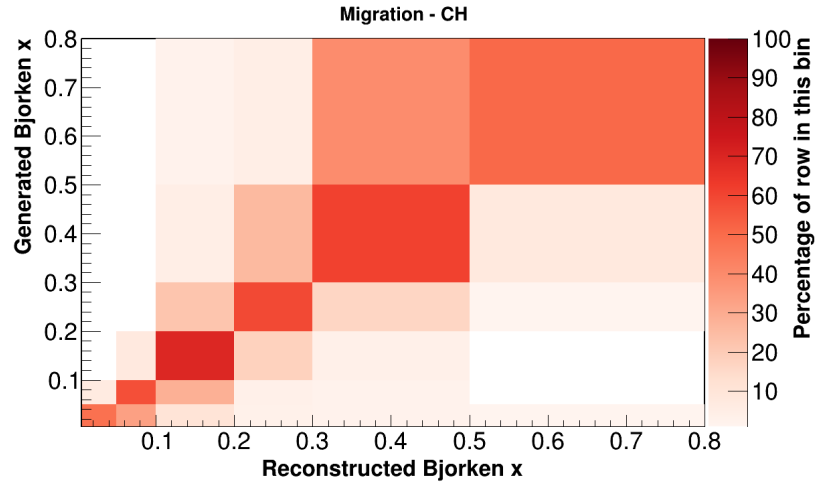
FIG. 5.3: The migration matrix for the DIS analysis in tracker for x_{bj}.

69

detailed in Refs. [75][76]. MINERvA makes use of the implementation of this technique in ROOT [77] called RooUnfold [78].

Unfolding tests

We want to be confident that the unfolding process is working as expected for a given distribution, so we perform a series of "pseudo-data" tests. These are also used to determine the optimal number of iterations to use when unfolding each variable.

Here we use a different simulation as "pseudo-data" which we try and unfold with the central value MINERvA tune v1 migration matrix. We do this test because unfolding a model with its own migration is easier to do then unfolding a different distribution. Forms of pseudo-data that we use for these studies are different tunes to GENIE (for instance turning off the RPA effect or 2p2h weight, or using a different model for DIS interactions), and "warped" MC which has had a variable dependent weight applied that is designed to make the MC closer mimic the features of the data distribution. These warpings can either be done in the variable we are trying to unfold or some other variable which it is dependent on. Generally speaking the warps in the unfolded variable are the most stringent test on the unfolding process.

We try to unfold each type of pseudo-data using a wide variety of iterations for 100 different varied "universes". The universes each have statistical fluctuations applied to the best guess model prediction or "central value" based on a Gaussian distribution. Then we calculate the χ^2 between the unfolded and the true pseudo-data distribution and look to see what number of iterations produces a minimum χ^2 with the smallest stable number of iterations. The other feature we look for is if the unfolding process diverges when going out to a large number of iterations. If the χ^2 reaches a minimum quickly but then experiences a step increase at higher iterations, that is a sign that the unfolding process is unstable and we may not be accurately reproducing the true data distribution.
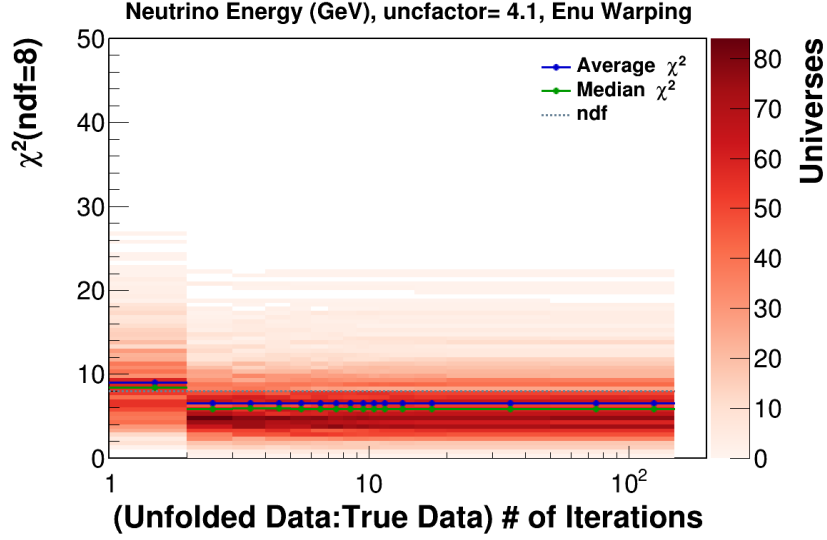
FIG. 5.4: χ^2 per iteration for a warping test in neutrino energy for the DIS analysis.

An example of what these tests look like is shown in Fig.5.4, which shows the χ^2 per iteration when unfolding a warped distribution of neutrino energy in the DIS analysis. The red shading indicates the number of universes in each bin of χ^2, for a given number of unfolding iterations. The mean and median χ^2 across all of the universes is also shown. The metric we look for is a χ^2 that converges to approximately the number of degrees of freedom of the analysis. The number of degrees of freedom for these analyses is equal to the number of measured bins.

5.1.4 Efficiency Correction

One of the last components needed for cross sections measurements is determining how efficiently we were able to select the true signal events in the analysis, and correct for that effect. The efficiency of the analysis is found by finding the quotient of the simulated true signal events that were selected, and all of the true signal events in the generated MC sample.

Since the unfolding process takes place before the efficiency correction, and we are

not able to reconstruct all of the true signal events that are generated by the MC, the efficiency is measured in bins of the true variable value. Dividing the unfolded distribution by the efficiency produces the distribution of events that the event generator produced in MC, and gives a distribution in data that is just a normalization factor away from a cross section measurement.

5.1.5   Normalization and flux

The last step in the cross section process is to calculate the total number of targets, and the flux and normalize by them. As mentioned earlier in this chapter, when doing measurements in neutrino energy we calculate the average flux in each bin of neutrino energy and divide the efficiency corrected distribution by that. In all other variables we integrate the flux from 0 to 120 GeV and normalize by the integrated flux. Further details on the flux prediction are given in Sec. 3.6.

5.2   Systematics

Systematic uncertainties are evaluating using the "multi-universe method", in which the simulation has many different universes with small variations made to them. A universe is a varied simulation in which the underlying model has had one or more of its input parameters shifted according to the uncertainty associated with that parameter. Each universe gets propagated through every stage of the analysis to determine the effect that changing a given quantity has on result.

Most of the uncertainties are calculated using two universes, however the flux uncertainty uses 100 universes. The two universe method, takes the predicted uncertainty in the quantity we are interested in and shifts it by $+(-)1\sigma$ in first (second) universe. We then create distributions using that shifted universe. Each of the shifted universes are used

along with the average of all of the universes in order to calculate a covaraince matrix and the associated uncertainty. All of the shifted universes are carried throughout the entire analysis process so effect of the shifts at each stage is properly accounted for.

We can calculate the covariance matrix (cov) using these shifted universes with

$$cov_{ij} = \frac{1}{N} \sum_{n=1}^{N} (U_{ni} - \overline{U}_i)(U_{nj} - \overline{U}_j),\qquad(5.4)$$

where N is the total number of universes, i and j index the bin number, U_n is the universe histogram, and $\overline{U}$ is the mean of all of the universes. The uncertainty in a given bin i is then given by $\delta x_i = \sqrt{cov_{ii}}$. All correlation information is retained and used when calculating χ^2s.

5.2.1   GENIE uncertainties

Underlying model uncertainties in GENIE are a portion of the systematic uncertainties we account for. GENIE has an available framework to shift a variety of parameters that go into its predictions. The uncertainties in GENIE's parameter values come from prior experimental measurements. All of these uncertainties are found by using the method of performing a $\pm 1\sigma$ Gaussian shift to them in two universes. One category of uncertainties is those related to the interaction model which shift the initial neutrino interaction probabilities. The other category of uncertainties in GENIE, are uncertainties on the final state interaction model or FSI. These are related to re-interactions that take place in the nucleus after the initial interaction.

MFP_pi and MFP_N are examples of uncertainties in the final state interaction model, they shift the mean free path of pions and nucleons in the nuclear medium. Another FSI uncertainty that appears in these analyses is the FrAbs_pi, which alters the nuclear pion absorption rate, where a pion is produced in the initial interaction but does not escape the

nucleus. Some of the relevant interaction model uncertainties are the MaRES and MvRES uncertainties which affect the resonant pion production and use the Rein Seghal model [30]. The Rvn1pi, Rvp1pi, Rvn2pi, and Rvp2pi uncertainties affect non resonant pion production and use the Bodek-Yang model [31]. There is also a normalization uncertainty on DIS interactions, NormDISCC, which is a 3% uncertainty on GENIE DIS interactions.

5.2.2 Flux Uncertainties

The uncertainty on the flux is computed using the multi-universe method. 100 flux universes were used in the low energy analysis, and 500 universes were used for the medium energy DIS analysis. This method is used instead of using a two universe shift by $\pm 1\sigma$ for the flux because there are a large number of different uncertainty parameters which contribute to the overall flux uncertainty. Many of these parameters are interdependent and have correlated effects on the flux. The way we account for these dependencies is to simultaneously perform random shifts within a $\pm 1\sigma$ Gaussian on these different parameters over a large number of universes.

All of the constraints that are discussed in Sec. 3.6, involving the neutrino-electron scattering constraint in both the LE and ME beams, the ME inverse muon decay constraint, constraints from hadron production measurements all have their uncertainties combined into a single flux uncertainty. Uncertainties arising from other sources such as the beam focusing and hadron production within the target are included in this error as well, shown in Fig. 5.5.

5.2.3 Normalization-like uncertainties

There are uncertainties in the measured cross sections that coming from the number of protons on target, the detector and target masses, and the MINOS and MINERvA tracking

74
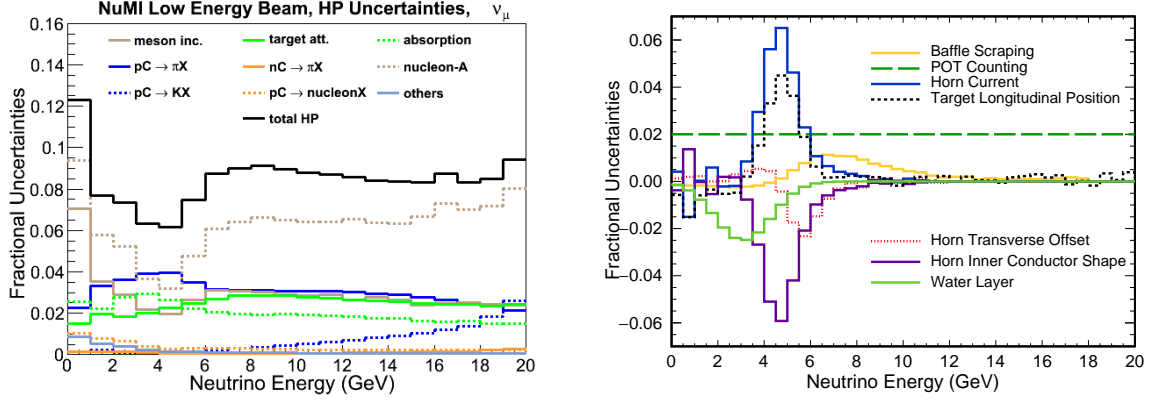
FIG. 5.5: Hadron production flux uncertainties for the LE beam [13].

Target material	Mass uncertainty
CH	$\pm 1.4\%$
Fe	$\pm 1.0\%$
Pb	$\pm 0.5\%$
C	$\pm 0.5\%$

TABLE 5.1: Uncertainties in the target mass for each material.

efficiency. The uncertainty in the POT is $\sim 1\%$ coming from the precision at which the primary protons are counted when producing the NuMI beam [10].

We also have an uncertainty associated with the efficiency at which we can track muons between the MINOS and MINERvA detectors. MC events have a weight applied to them to account for any tracking inefficiencies, which is derived from the rate of detected MINOS muons which are seen in MINERvA and was validated using data. The uncertainty associated with this efficiency comes from the statistics on measurements of the efficiency, and are a function of muon energy and beam intensity.

The uncertainties in the target and detector mass come from density uncertainties, and are shown in Tab. 5.1 [10].

5.2.4   Muon and hadronic reconstruction uncertainties

Uncertainties coming from detector resolution effects (eg. the muon energy, muon angle and hadronic energy) have a direct effect on both the event selections and the distributions in all measured variables. Reconstruction based uncertainties are among the larger systematic uncertainties in both analyses.

Shifts in muon energy result in the movement of events from one bin to another, as well as affecting whether or not events pass event selection cuts. Most of the cuts and measured variables are dependent on muon energy, so this shift can have far-reaching effects. A shift to the muon angle, will change the muon $p_{||}$, and p_T in the inclusive analysis. The kinematic quantities Q^2 and all of the quantities derived from it will also be shifted, which is especially relevant in the DIS analysis. In the inclusive analysis the hadronic energy is not especially important, since we do not try to measure nor make any selection cuts that are dependent on it. However, as Q^2, W, x_{bj}, and E_ν are all calculated with the hadronic energy, the DIS analysis is more affected by shifts to the hadronic energy.

For all of these uncertainties a two-universe shift method is used, where one universe shifts all of the values of the given quantity to a higher value by 1 sigma, while the other downshifts all of the values by 1 sigma. We determine what effect the shift has on each of its derived quantities, for instance $p_{||}$ and p_T are recalculated in the inclusive analysis when there are shifts in either muon energy or angle. Variations to all three of the reconstruction quantities will result in changes to the E_ν, x_{bj}, Q^2, and W which are recalculated. We then test to see whether events in the shifted universes would have passed an event selection cut with this complete set of shifted quantities; thus accounting for events that would pass say a DIS event selection to still be accounted for in the event uncertainties.

We also have an uncertainty associated with our ability to correctly resolve the vertex position when using ML vertex algorithms. A 0.5% uncertainty is assigned for events in

the nuclear target region of the detector, and a 0.25% uncertainty is assigned for events in the active tracking region.

5.2.5   Unfolding uncertainty

An additional statistical uncertainty is added to account for MC statistical limitations of the unfolding processes [78]. This uncertainty was recently added to our standard suite of uncertainties after the low energy analyses were completed, so they are only included in the DIS analysis and not the inclusive measurement presented in this thesis. The first step in adding this uncertainty is to determine the "uncertainty factor", which will later be used to determine scaling applied to the statistical covariance matrix. The uncertainty factor is found using the warping study described in Sec. 5.1.3, in which the same model is given as the pseudo-data and migration matrix with which we unfold. An additional uncertainty factor is added in order to achieve a χ^2/dof of 1 when using the full MC statistics. The statistical covariance matrix of the unfolded distributions is ultimately multiplied by $1 + \frac{1}{uncertainty\ factor}$, increasing a bins statistical uncertainty by a factor of $\sqrt{1 + \frac{1}{uncertainty\ factor}}$, and affecting all bin correlations. A total of four uncertainty factors are determined for the DIS analysis, as the factors are dependent on variable (x_{bj}, E_ν) and detector region (nuclear targets, tracker). The determined values are given in Table 5.2.

The active scintillator region has larger statistics than the nuclear target region, therefore it does not require as much additional uncertainty and has a smaller uncertainty factor. These additional statistical uncertainties are included in all distributions which have gone through unfolding.

	Targets	Scintillator
E_ν	4.1	4.85
x_{bj}	3.4	3.5

TABLE 5.2: Uncertainty factors for the statistical uncertainty associated with the unfolding process for the different regions and variables used in the DIS analysis.

5.2.6 Total uncertainty

The total uncertainty that is derived out of all of these individual components is found by taking the sum in quadrature of all of the different individual uncertainties found through the multi-universe method, detailed at the beginning of this section. Statistical uncertainties are included in this sum, but are also often shown as an inner tick mark on the data error bars.

CHAPTER 6

Double Differential Inclusive Charged Current ν_μ Cross Section Measurement

6.1   Introduction

In this chapter I will discuss the measurement of inclusive charge current cross sections on hydrocarbon at MINERvA with a peak neutrino energy of $3.5\,\mathrm{GeV}$ (in the low energy beam configuration)[79]. This analysis is looking for neutrino interactions in which a muon neutrino interacts in the active tracking region of the detector, described in Ch.2, exchanges a W boson, and produces a negatively charged muon. The data used for the results in this chapter correspond to a neutrino beam exposure of 3.34×10^{20} protons on target in the NuMI beam at Fermilab. The low energy neutrino mode data used in this inclusive analysis is from March 2010 until April 2012.

In order to a cross section, there are five main steps: event selection, background

subtraction, unfolding, efficiency correction and normalization. An overview of this process is provided in Ch.5.

For this analysis the goal is to measure an inclusive cross section in the active scintillator of the detector. Studying a cross section with an expansive signal with few cuts allows for the results to be directly compared between experiments. Many other experiments have also measured inclusive cross sections as a function of muon kinematic variables, similar to this analysis. T2K [80] first made one such measurement in 2018, μBooNE [81] in 2019, my work on the MINERvA measurement presented here was published in 2020 [79], and subsequently an equivalent measurement has also been performed on NOvA [82]. The measurement is performed in variables of muon momenta, which can be measured to a high precision that is not possible in some other variables that require greater understanding of the hadrons produced in the interaction. The high precision of our muon momentum measurements means that we are subsequently less reliant on models, and introduce less model dependence into our measurement. This makes this result advantageous for comparing a variety of models of neutrino interactions. The cross section presented here is measured as a double differential function of the longitudinal and transverse muon momentum. The momentum of the muon is broken into two components, the portion that is parallel to the direction of the beam $p_{||}$ or the longitudinal momentum, and the portion of the momentum which is perpendicular to the beam direction: the transverse momentum p_T.

The longitudinal muon momentum roughly correlates with the neutrino energy, while the square of the transverse momentum correlates strongly with the four momentum transfer. GENIE predictions of the average Q^2, E_ν, and W in each of the bins measured in this analysis are shown in Fig. 6.1.
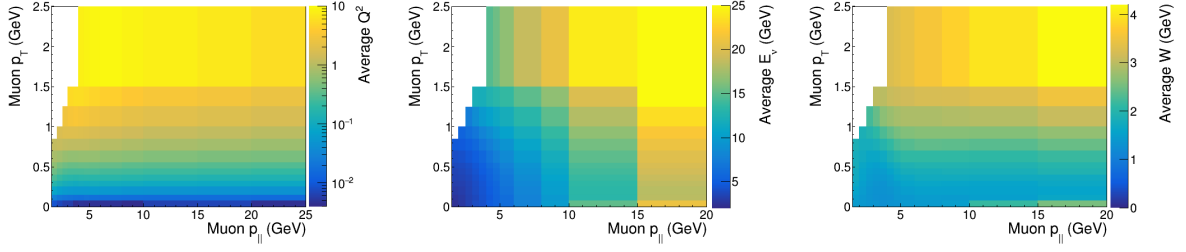
FIG. 6.1: Average Q^2, E_ν, and W simulated by GENIE 2.8.4 for each bin of p_T and $p_{||}$ in which cross sections are measured.

6.2 Event selection

Since the interaction channel of interest is ν_μ charged current interactions, which produce a μ^-, exactly one muon is required for the event to be included in the analysis. In order to be able to sign select μ^- from μ^+ (and thus distinguish between ν_μ and $\bar{\nu}_\mu$ interactions), the muon must enter the magnetized MINOS near detector downstream of MINERvA, thus having a muon matched to a muon in the MINOS near detector is the second event selection requirement. The MINOS match also allows for greater precision in momentum reconstruction as you can measure the range and curvature in that detector as well as the energy loss in MINERvA.

Since MINOS sits 2.1 m downstream of MINERvA only forward going muons are also detected by MINOS. Due to this geometric effect there is also a constraint placed on the angle of the muon track with respect to the direction of the beamline of less than 20 degrees.Without this angle cut there would be highly model dependent bins with low acceptance.

A cut is also placed on the position of the event vertex. The vertex must be within the fiducial volume of the active tracker area of the detector, defined as the scintillator volume between modules 27 and 79 and within a 850 mm apothem of the hexagonal planes.

The event sample after these cuts are applied is comprised of 325,588 events, a sample with unusually rich statistics for the neutrino community. As there are few background

processes for inclusive channels the selected event sample is also of high purity, with 99.4% of selected Monte Carlo events truly belonging to the ν_μ CC interaction channel.

A distribution of the selected events is shown in Fig. 6.2 in muon p_T and $p_\parallel$. A breakdown of the interaction channels contributing to the Monte Carlo event rates are shown alongside the selected data. The total predicted interaction rate is broken down into these interaction channels:

- QE+2p2h – events coming from quasielastic interactions and events coming from multi nucleon scattering,

- RES – events coming from baryonic resonance production that results in the production of a single pion,

- Soft DIS – events coming from non-resonant pion production, multi-pion resonant production, soft inelastic scattering, and deep inelastic scattering, where $W<2.0\,\mathrm{GeV}$ or $Q^2<1.0\,\mathrm{GeV}^2$,

- True DIS – events with $W>2.0\,\mathrm{GeV}$ and $Q^2>1.0\,\mathrm{GeV}^2$, coming from non-resonant pion production, multi-pion resonant production, soft inelastic scattering, and deep inelastic scattering. The majority of these events come from DIS interactions as defined within the neutrino physics community,

- Background – neutral current interactions and charged current events which originated from a different neutrino type (mostly muon antineutrinos, with some electron neutrino events).

A version of Fig. 6.2 in which multipliers are applied to all of the contents of panels with fewer events in them is shown in Fig. 6.3 in order to better see the contents in these bins.
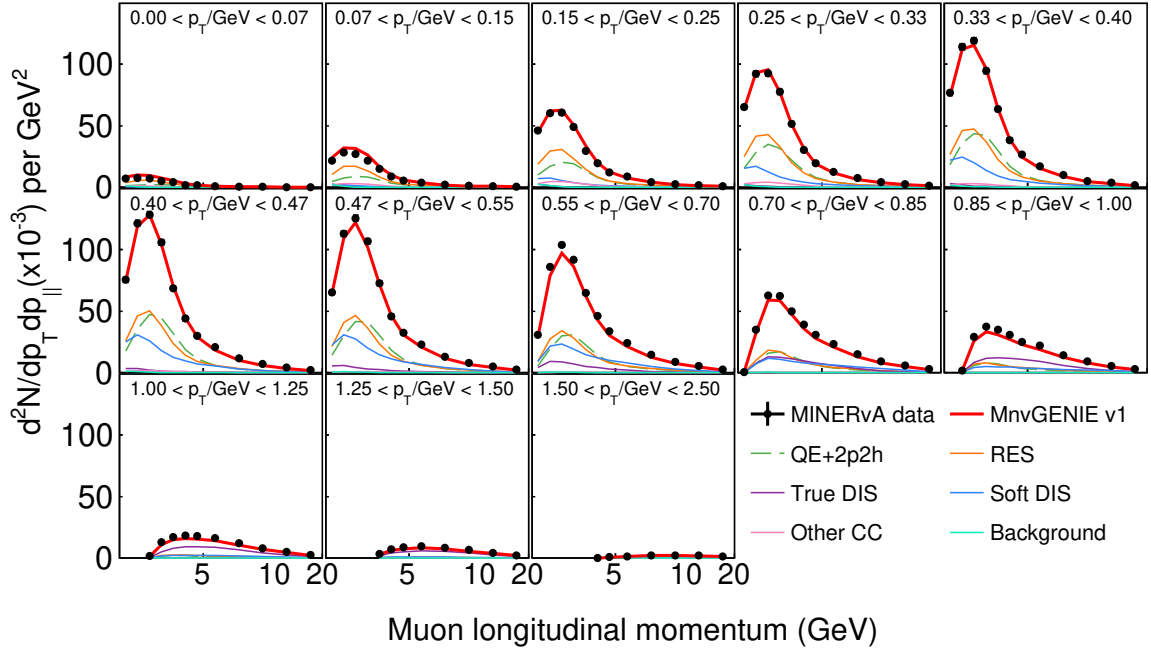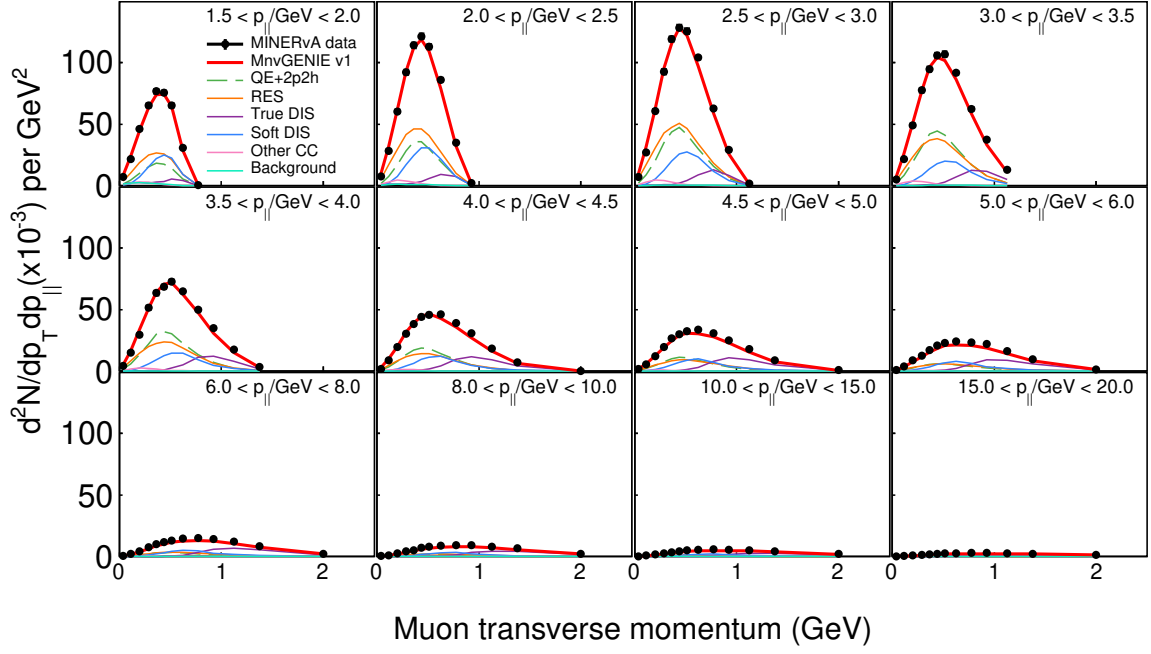
FIG. 6.2: The double differential distribution of events inclusive selected events. In the top plot each panel is a bin of longitudinal muon momentum and transverse muon momentum is on the x axis. The bottom plot shows the same data and simulation projected in the other direction; each transverse momentum bin is a panel, and the longitudinal momentum is on the x axis. Data points are shown in black with statistical error bars. The total Monte Carlo prediction is shown in red, with the predicted component interaction channels each shown unstacked.
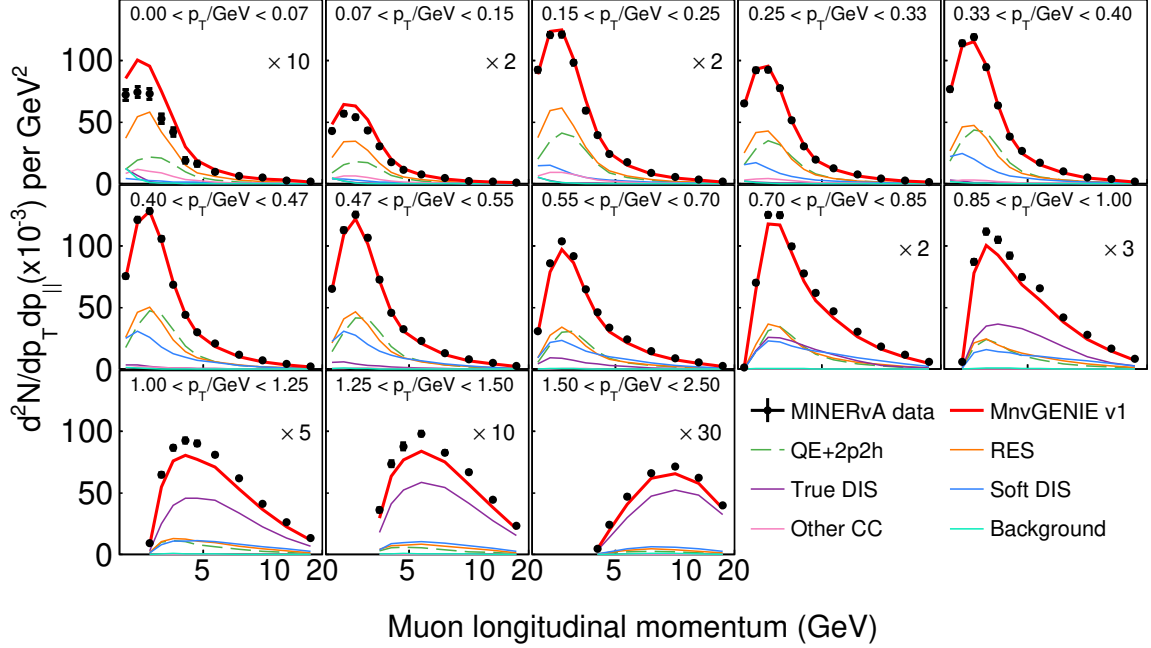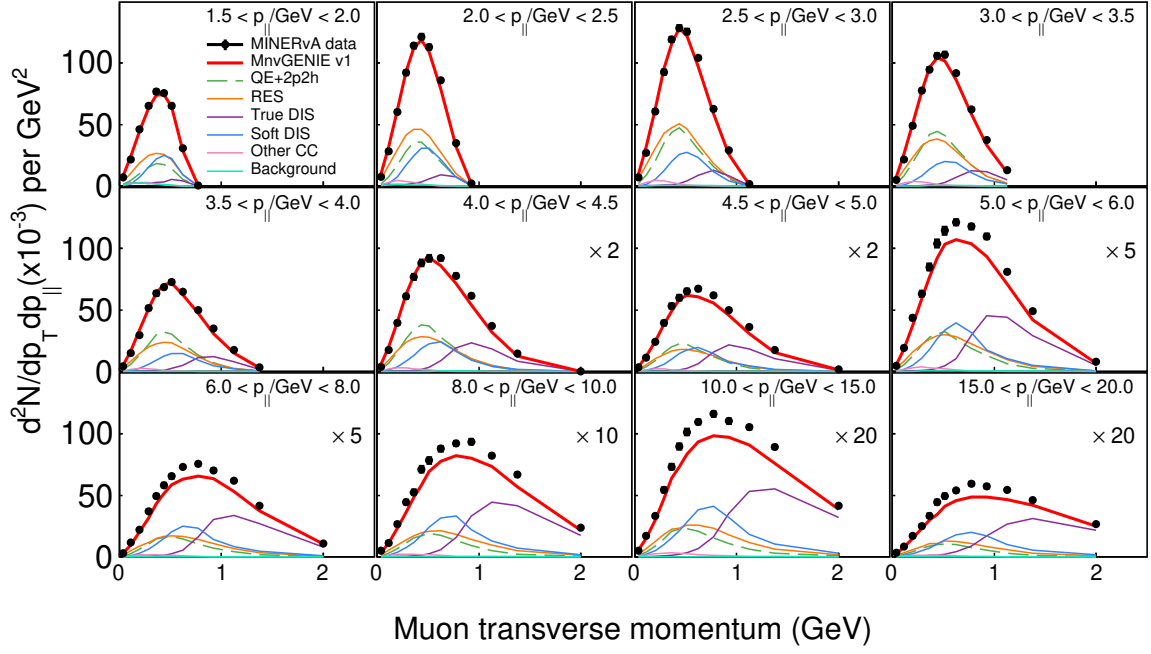
FIG. 6.3: The double differential distribution of inclusive selected events. Data points are shown in black with statistical error bars. The total Monte Carlo prediction is shown in red, with the predicted component interaction channels each shown unstacked. Multipliers are added to all of the content in certain panels for better visibility.
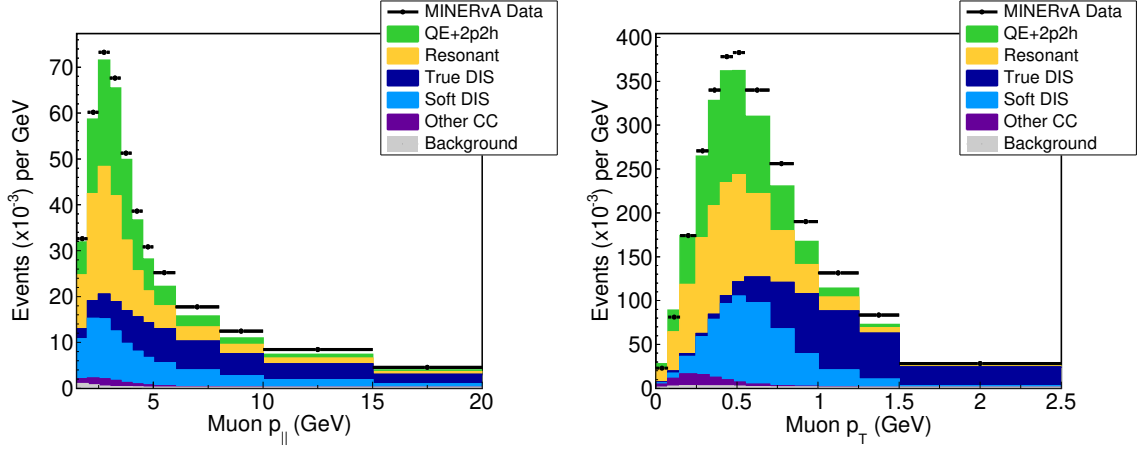
FIG. 6.4: The single differential distribution of inclusive selected events. Data points are shown in black with statistical error bars. The Monte Carlo interaction channels are stacked on top of another, showing the total Monte Carlo prediction.

A single differential distributions of the event selection are shown in Fig. 6.4. Here the various interaction components, the same as shown in the prior figures, are shown stacked on top of one another.

6.3   Background Subtraction

As this is an analysis based on an inclusive sample in the large fiducial volume scintillator of the detector (thus not limited by vertex resolution), backgrounds only make up of 0.75% of events. Due to this, what can be a complicated procedure of fitting background events and subtracting them is drastically simplified. A direct subtraction of Monte Carlo background is done instead; since the number of background events is small, it does not introduce significant model dependence to do so.

Neutral current events make up 0.50% of selected events, while the other background contribution comes from charged-current interactions originating from a neutrino other than a ν_μ. Over 99% of the other neutrino flavor events come from $\bar{\nu}_\mu$ interactions, where the charge of the produced muon is misreconstructed; with a small remaining fraction

originating from electron neutrino interactions.

Fig 6.5, shows the distribution of background events using the same multipliers as Fig. 6.3, where the projection into cells of $p_{||}$ has a scale approximately 50 times smaller than that of the selected event sample. The ratio of background to the total number of MC selected events is shown in Fig. 6.6.

The majority of selected neutral current events are in the lowest muon energy bins. These events pass selection cuts largely due to pions produced in the interaction punching through the downstream end of the MINERvA detector and into MINOS, mimicking the signal of a muon. Contamination from other neutrino flavor charged current events is more evenly distributed throughout phase space.

6.4 Unfolding

As detailed in Sec. 5.1.3, detector smearing is accounted for using migration matrices to unfold reconstructed quantities and map them to their true values. Since this is a double differential analysis the migration matrix is shown by global bin number (indexing both longitudinal and transverse bins) in Fig. 6.7. Underflow and overflow bins which are designed to catch events that lie outside of the binned values are also included in this binning scheme. In this case the underflow bin for p_T, which would correspond to events with a traverse momentum of less than 0 GeV, is non-physical and empty. However, the underflow for $p_{||}$ ($p_{||}$<1.5 GeV), and overflow bins in both p_T and $p_{||}$ (p_T>2.5 GeV, and $p_{||}$>20.0 GeV) are physical and populated.

In this figure, the bin numbers 0-13 all correspond to the (empty) underflow bin of p_T, with bin 1 also being the first bin of $p_{||}$, bin 12 corresponding to the last measured $p_{||}$ bin which ranges from 15 to 20 GeV, and bin 13 being the p_T overflow for events with longitudinal muon momenta greater than 20 GeV. This same pattern continues with bins
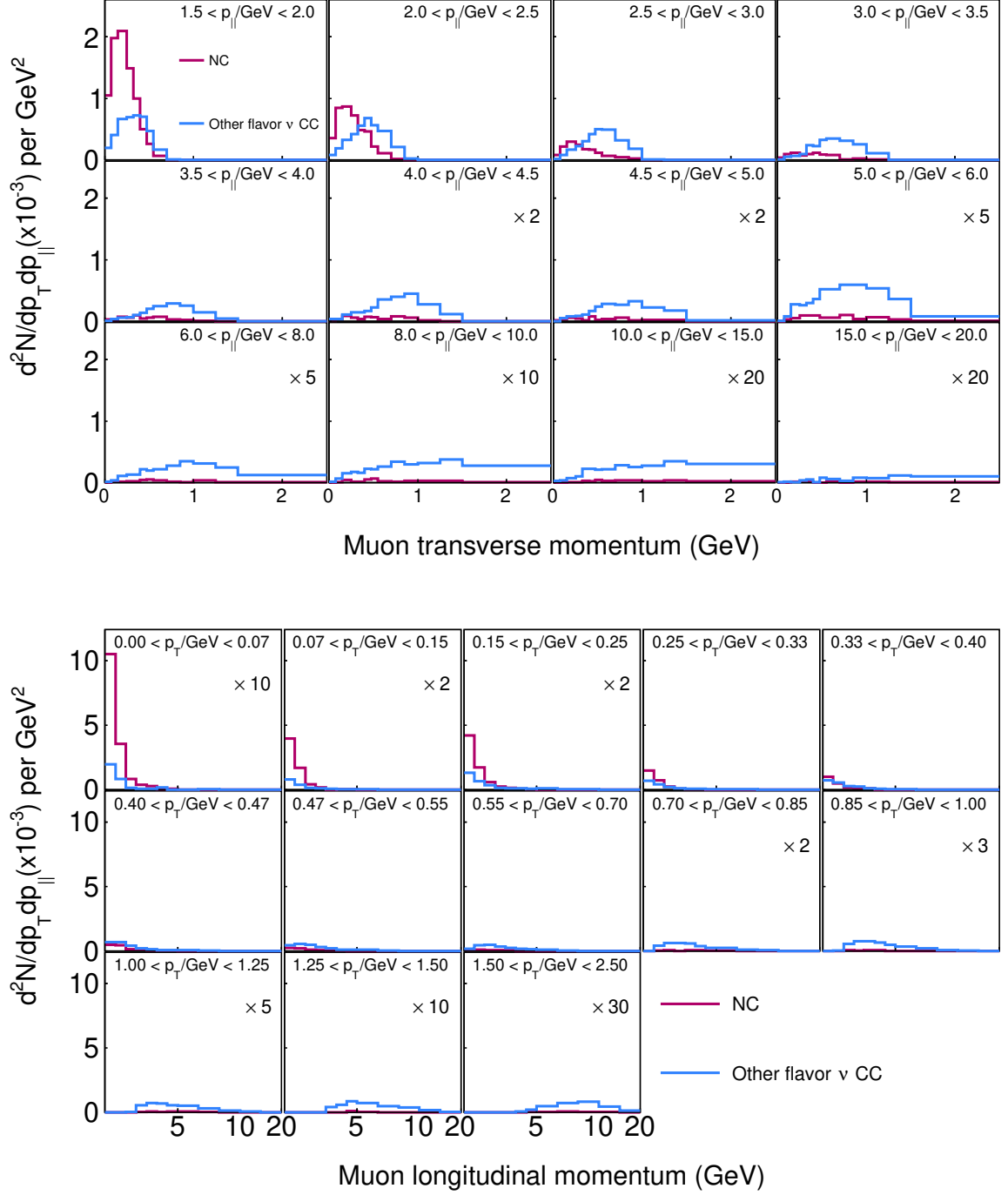
FIG. 6.5: The double differential distribution of background events, coming from neutral current interactions (NC) and CC interactions with another neutrino flavor (mostly $\bar{\nu}_\mu$).
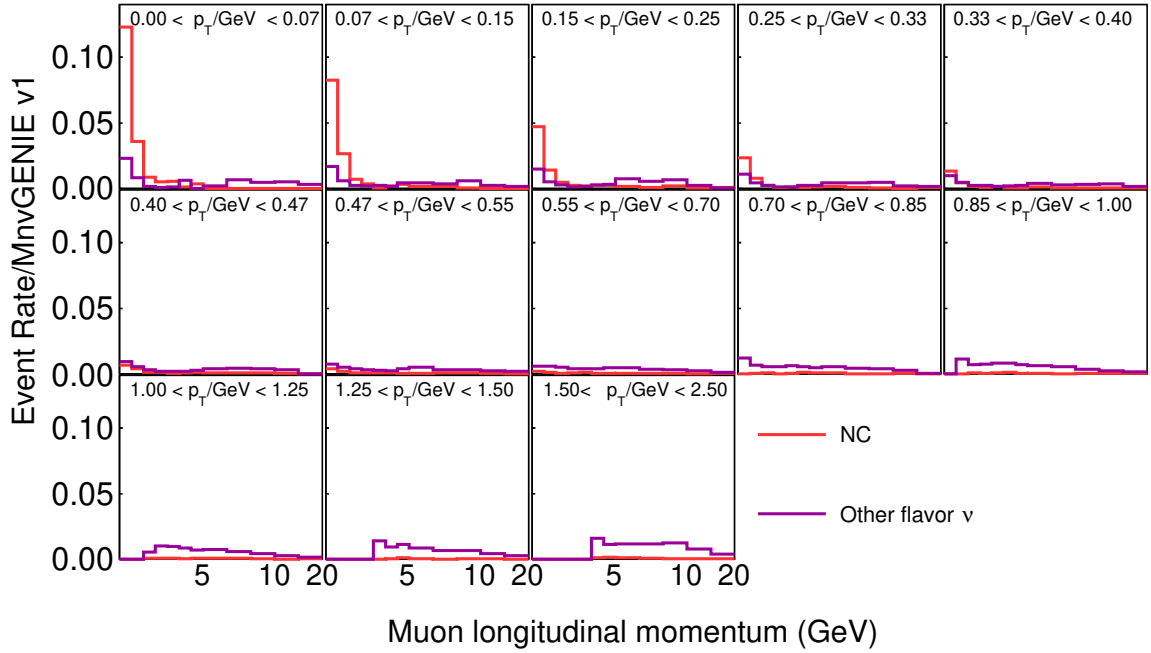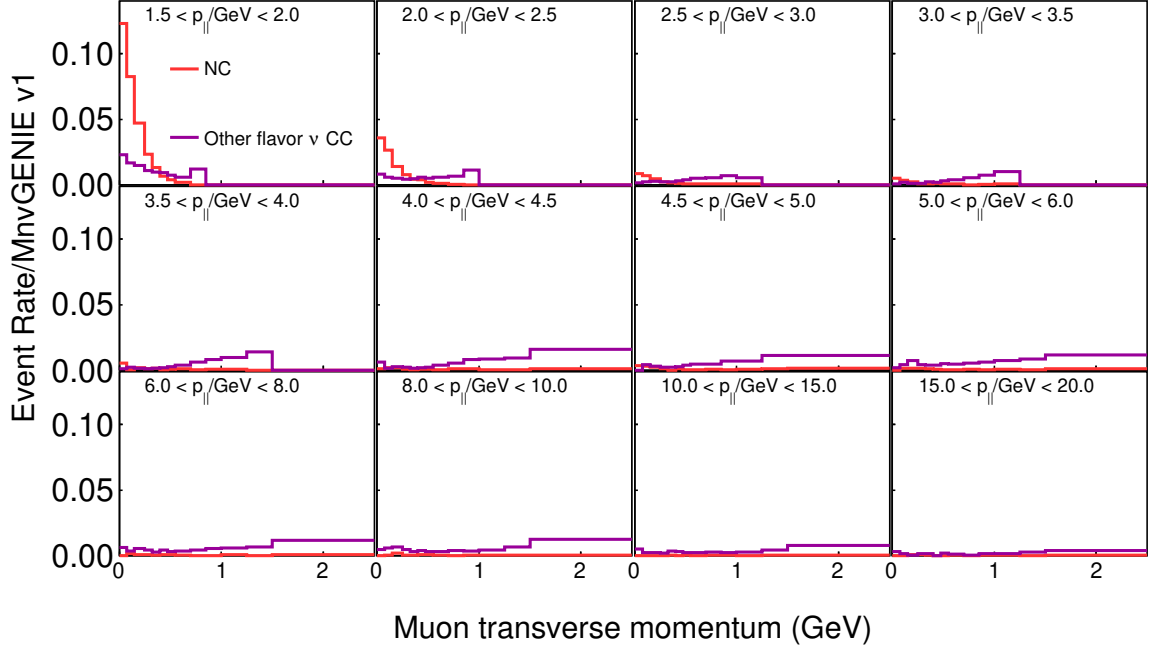
FIG. 6.6: Ratio of background events to total selected MC.

13-24 spanning the full $p_{||}$ range with a p_T between 1.5 and 2.0 GeV (the first measured p_T bin), and bins 25-48 corresponding to transverse momenta between 2.0 and 2.5 GeV. While the two dimensional migration matrix is the one used in the unfolding procedure, the one dimensional projections are more intuitive and can be found in Fig. 6.8. These projections are the migration matrices for single differential measurements in $p_{||}$ and p_T. All of these migration matrices are normalized to the number of entries in that row (true bin) to show the fraction of events that are reconstructed in the correct bin.

6.4.1   Migration Matrices

The migration matrix is filled using the simulated events that passed the above event selection, as well as passing constraints on the true signal definition. Only true ν_μ CC events are included, however, events with a reconstructed muon angle less than 20° are included regardless of the true muon angle, to properly account for movement in and out of the phase space around this 20 degree edge.

6.4.2   Warping study

In order to test the validity of the unfolding method, we did a series of different tests using 100 statistically varied universes to confirm that the smeared distribution of events were able to be accurately placed in truth bins. Additionally, we use these studies to determine the number of iterations required in order for the data to converge to a best fit when comparing the unfolded distribution to the true one.

The first series of tests that we did involved taking different neutrino interaction model versions and trying to unfold them using the migration matrix from MINERvA tune v1, the model variation used for the central value. These versions had various alterations, such as different models of DIS interactions, the removal of 2p2h interactions, and an
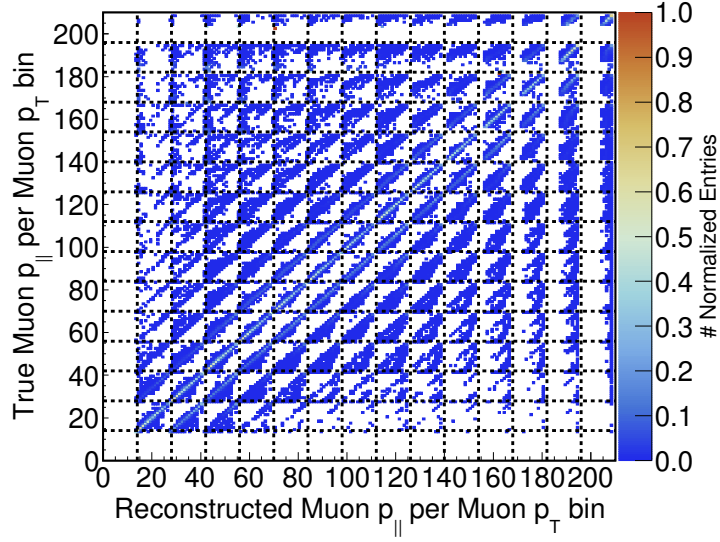
FIG. 6.7: Two dimensional inclusive migration matrix by bin number. Each large cell represents a single bin of transverse momentum, with the longitudinal momentum bins as the smallest cells.
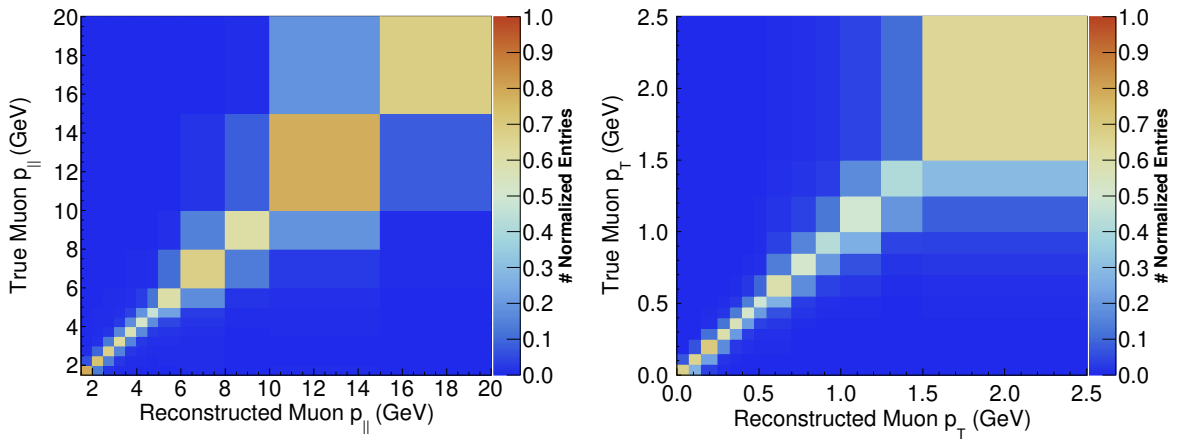
FIG. 6.8: One dimensional projections of the two-dimensional migration matrix into $p_{||}$ and p_T.

increased rate of quasielastic interactions, to name a few. Each of these model variations were treated in the same manner that we use to treat the data, and unfolded using the MINERvA tune v1 migration matrix using a varying number of iterations. Then the unfolded pseudo-data is compared to the true distribution, and we calculate a goodness of fit for each number of iterations. The unfolding study using GENIE 2.8.4 without any of MINERvA's standard tunes as pseudo-data is shown in Fig.6.9, which converged to its minimum χ^2 at 8 iterations.
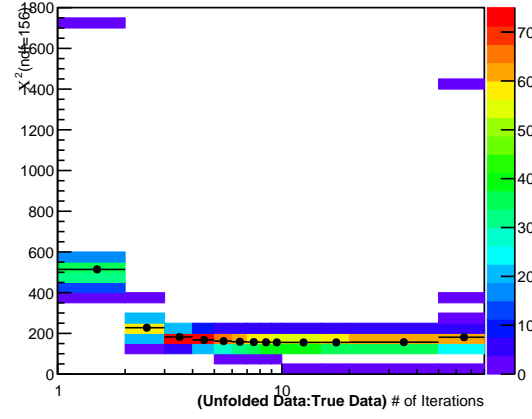
FIG. 6.9: The χ^2 for the unfolding studies performed when using GENIE 2.8.4 as pseudo-data.

For the second test, we used the ratio of data to simulation, and fit that distribution with a Gaussian function. Fig. 6.10 shows the data/MC ratio, and the resulting fitted function, the form of which was chosen in order to mimic general trends seen in the data/MC ratio shape. The function is given by

$$f(p_z, p_T) = 0.5 + 0.7e^{-0.002(0.8(p_z+15p_T-30)^2+.2(p_z-15p_T+6)^2)}. \tag{6.1}$$

Then I warped the reconstructed Monte Carlo distribution using that function, such that the Monte Carlo behavior could be used as an approximation of the data. We then tried unfolding the warped MC distribution with the standard unwarped migration matrix in

91

order to simulate how well the unfolding procedure will work in the data distributions and the optimum number of iterations. The results of the study with the warped distribution was that a minimum χ^2 of 151 was reached after 10 iterations. For an analysis with 144 bins (144 degrees of freedom), which was considered to be an acceptable χ^2 to validate the unfolding procedure. The optimal number of iterations ia 10 for this analysis.
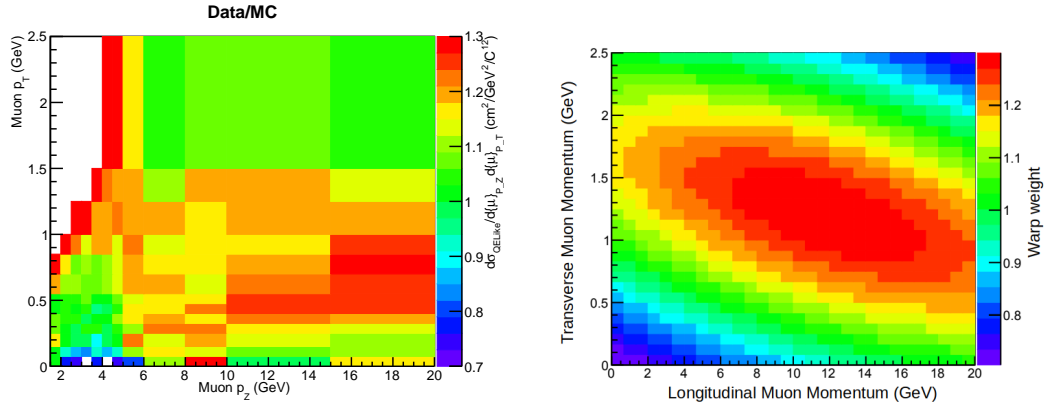
FIG. 6.10: Data/MC event rate ratio(left) was used to determine a warping function (right) for unfolding studies.

6.5 Efficiency Correction and Normalization

The next step in the cross section extraction is the efficiency calculation and correction. Sec. 5.1.4 describes this process in further detail. In this analysis, the efficiency is a function of the longitudinal and transverse muon momentum and is shown in Fig. 6.12. The region in the top left of the plot, which corresponds to regions that have muon angles greater than 20 degrees, and are not included in our signal definition. The efficiency is highest (>85%) for high $p_{||}$ and low p_T, as this region has good muon acceptance in the MINOS near detector. The region around the 20 degree cut has the lowest efficiency due to the larger angle muons to miss the MINOS detector more often.
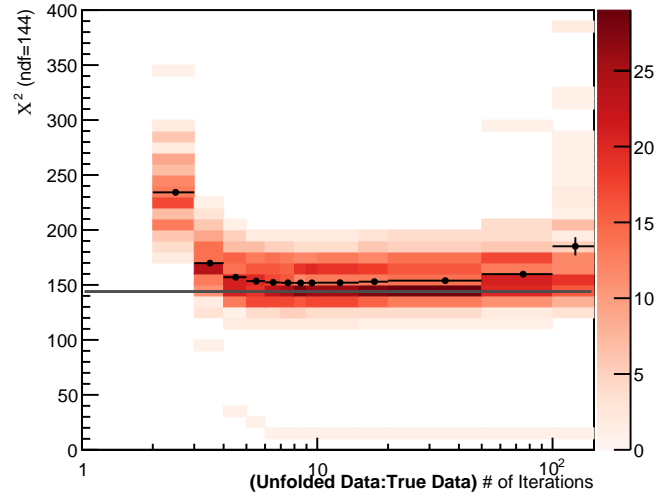
FIG. 6.11: The χ^2 for 100 unfolded universes of the warped MC distribution plotted verses number of iterations.
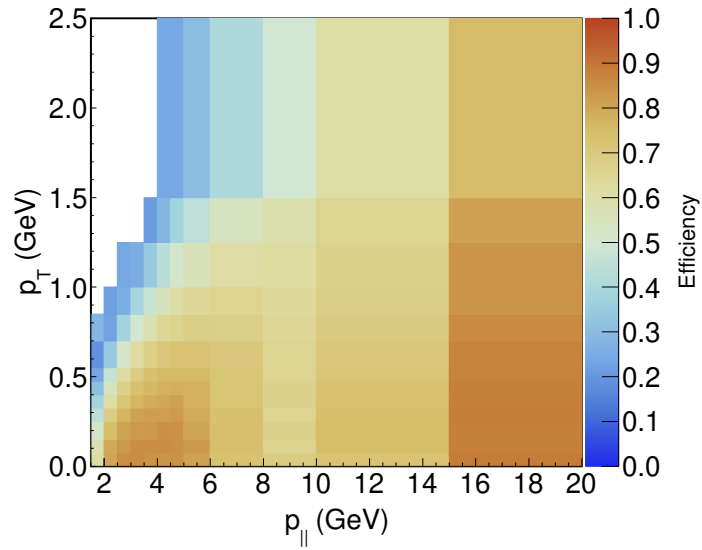
FIG. 6.12: Efficiency for the ν_μ CC inclusive signal in bins of muon longitudinal and transverse momentum.

93
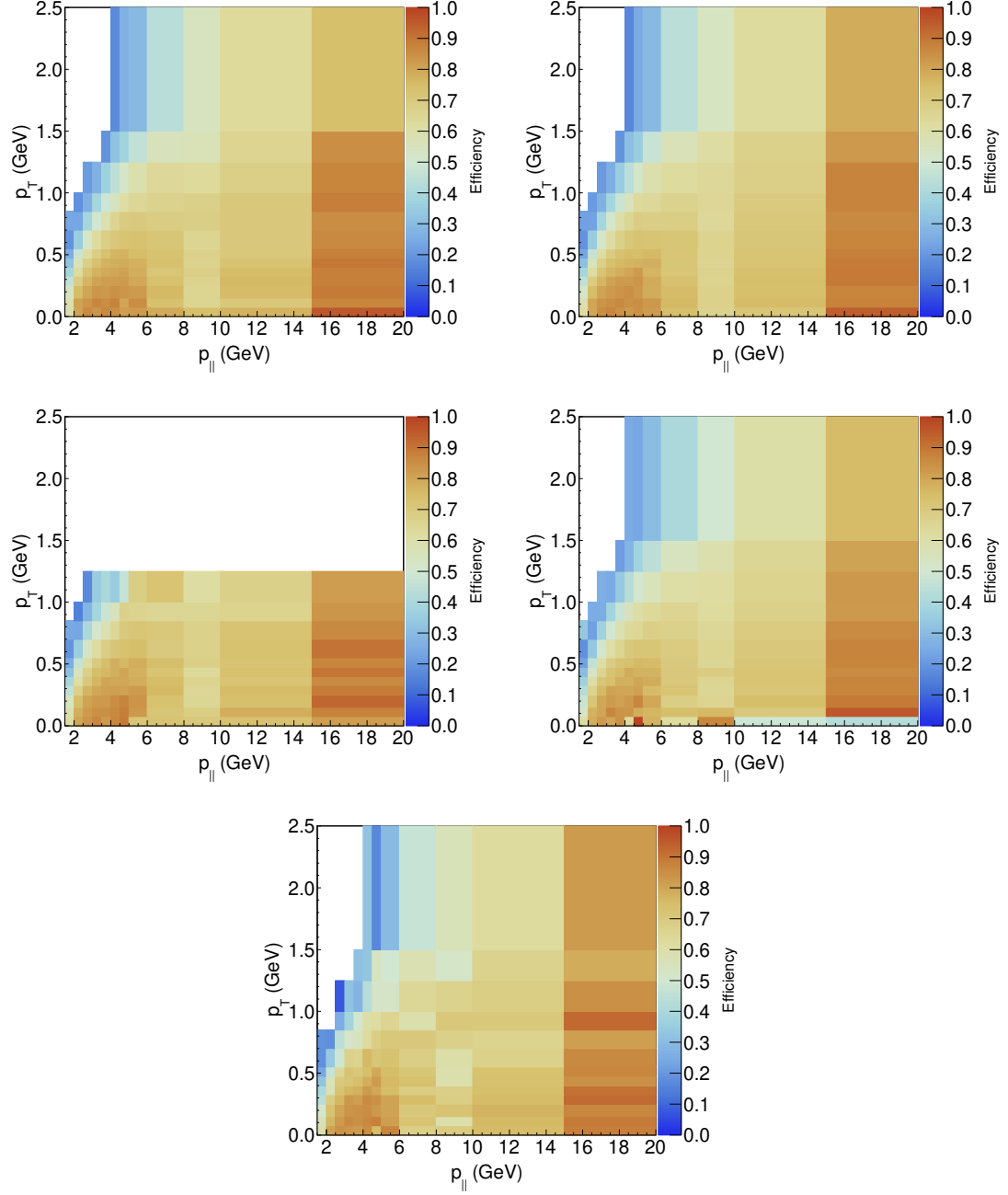
FIG. 6.13: Efficiencies for the quasielastic (top left), resonant (top right), 2p2h (middle left), DIS (middle right), and other CC (bottom) interaction channels in bins of muon longitudinal and transverse momentum.

Fig. 6.13 shows the efficiencies for each different interaction channel. These efficiencies are not used for the cross section extraction process, but were used as a method of verifying that there were not large discrepancies in the efficiencies of different types of interactions. All show very similar patterns. The 2p2h uncertainty has the sharp cut off at $1.25\,\mathrm{GeV}$ p_T due to a phase space restriction in its definition.

6.6   Systematic Uncertainties

The systematic error summaries for the data at each stage of the analysis are shown in this section, see Sec. 5.2 for descriptions of the included systematics and methods. Fig. 6.14 shows the measured background subtracted event rate (before unfolding), and Fig. 6.15 shows the corresponding uncertainty on the data. The systematic uncertainties on the data at this stage are exclusively originating from the MC systematic uncertainties on the predicted background which was subtracted. As such they are extremely small due to the minimal background contamination, with the largest contributions in the lowest bin of longitudinal and transverse momentum of approximately 2% coming predominantly from the flux uncertainty. The majority of the systematic uncertainty in this analysis instead comes from the unfolding, efficiency correction, and flux normalization stages which rely on simulation.

The unfolded event rate and corresponding systematics are shown in Figs. 6.16 and 6.17 respectively, and Fig. 6.18 and 6.19 show the efficiency corrected event rates and uncertainties. The bins at the lowest momenta and around the angle cut have the largest increases from efficiency correction, as the efficiency is lowest in these regions due to MINOS acceptance effects. The muon reconstruction uncertainties enter predominantly as a result of the unfolding procedure, and are the dominant systematic uncertainty in the low p_T bins.

95
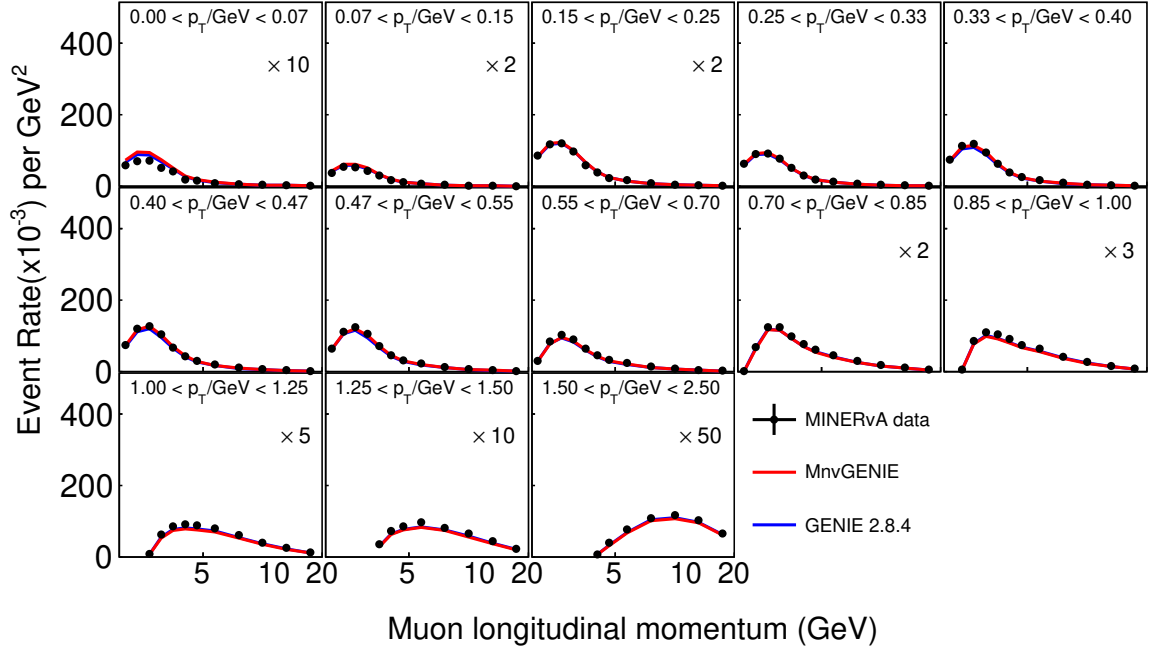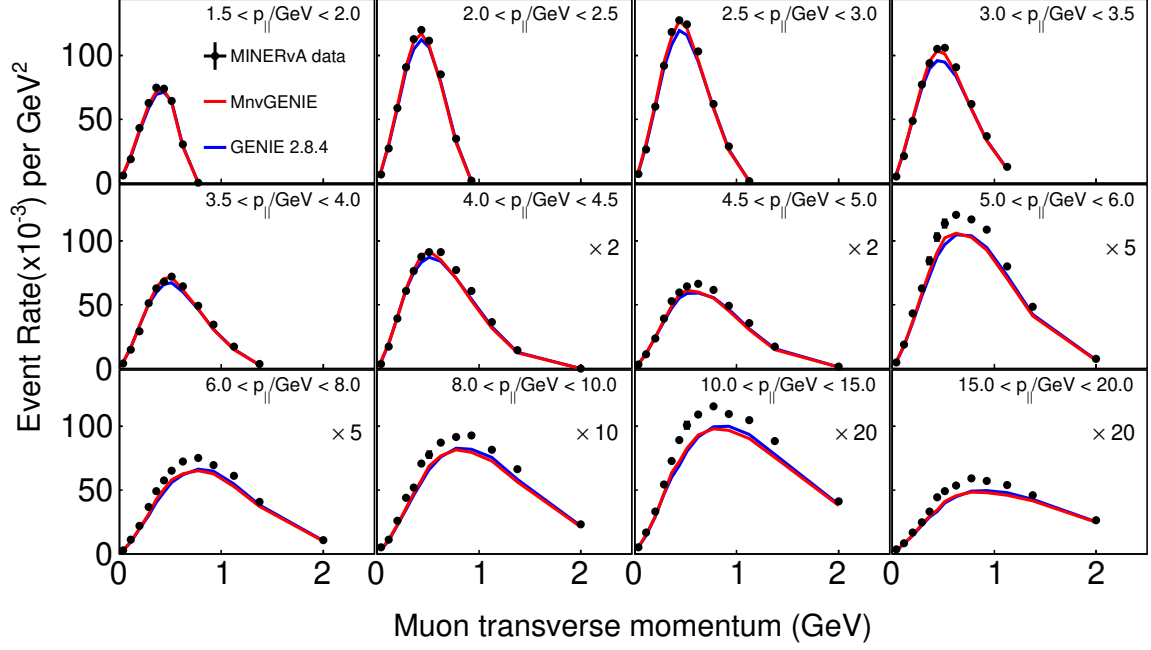
FIG. 6.14: Background subtracted double differential event rate with MINERvA tune v1 and GENIE 2.8.4 predictions.
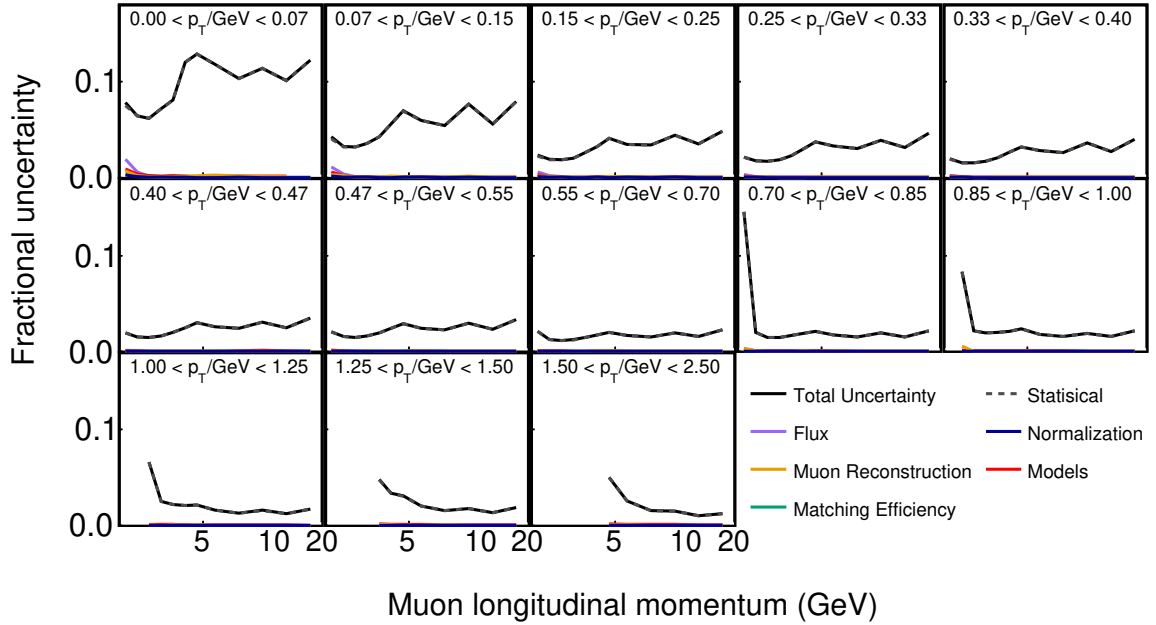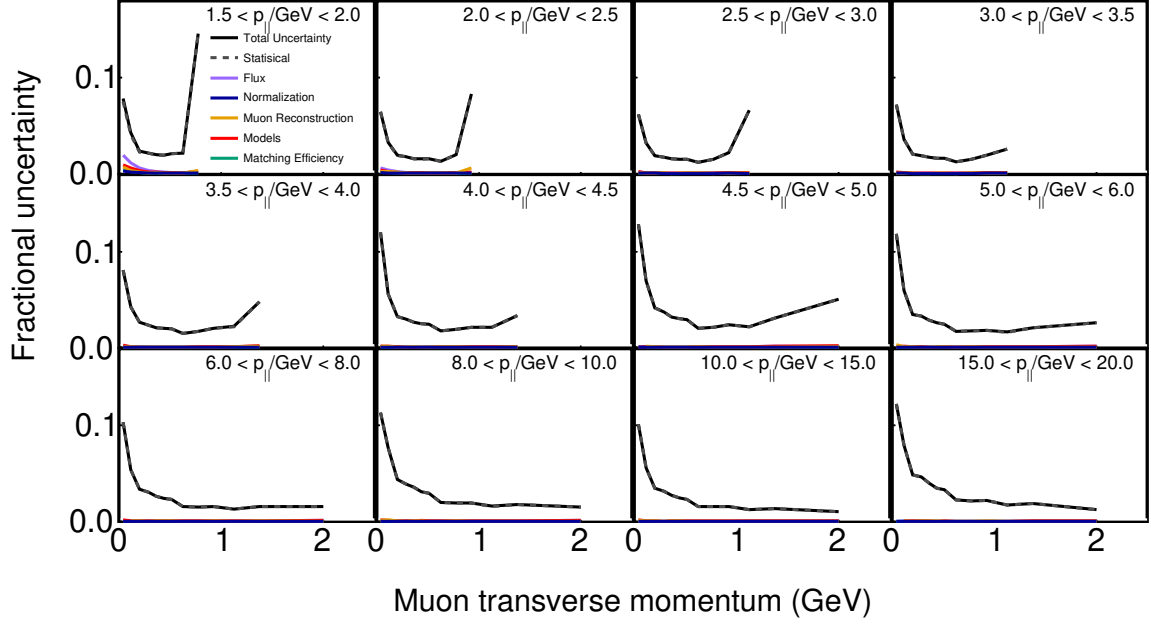
FIG. 6.15: Uncertainties on the background subtracted data double differential event sample. At this stage the majority of the total uncertainty comes from statistics, causing the statistical and total uncertainty curves to overlap in most bins.

97
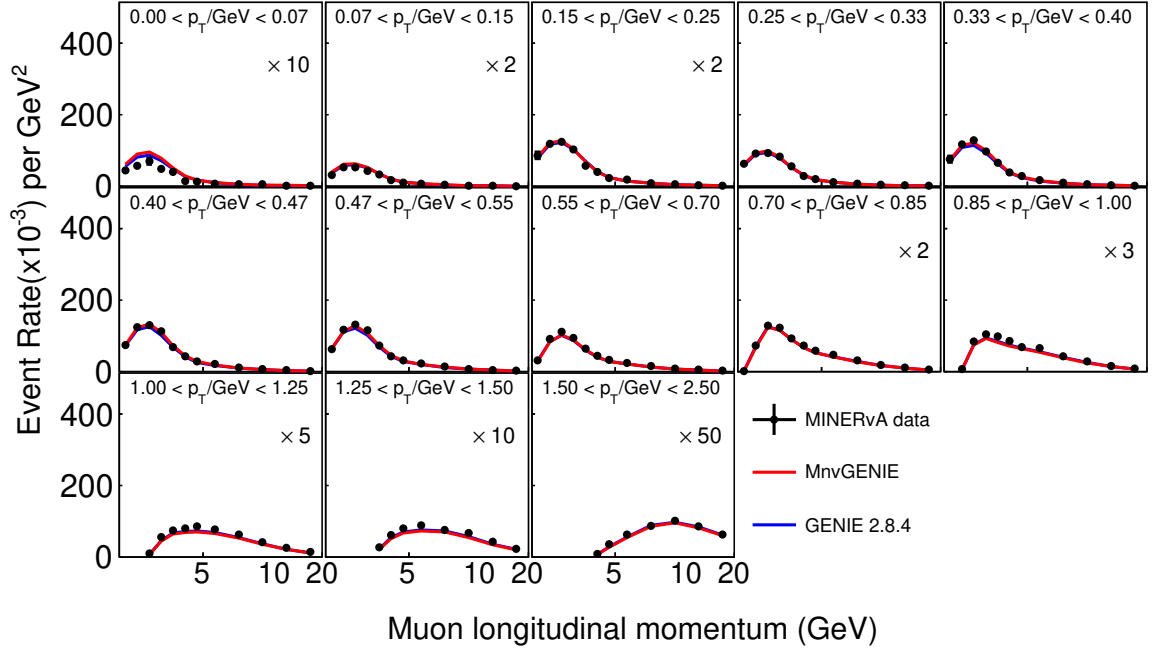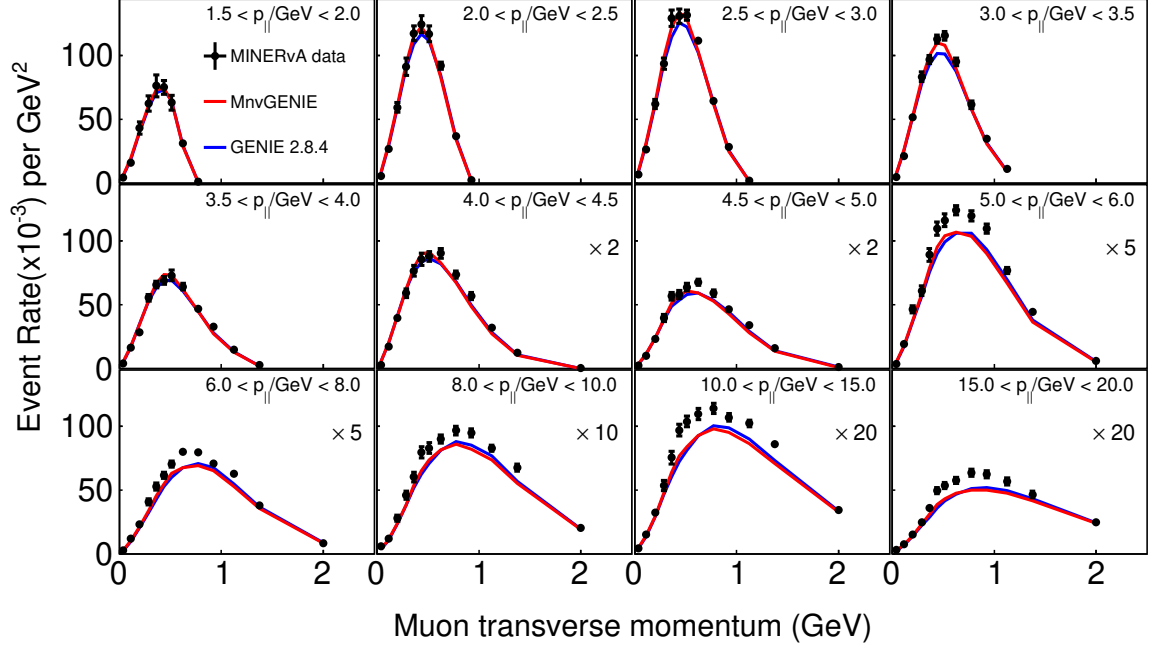
FIG. 6.16: Unfolded double differential event rate with MINERvA tune v1 and GENIE 2.8.4 predictions.
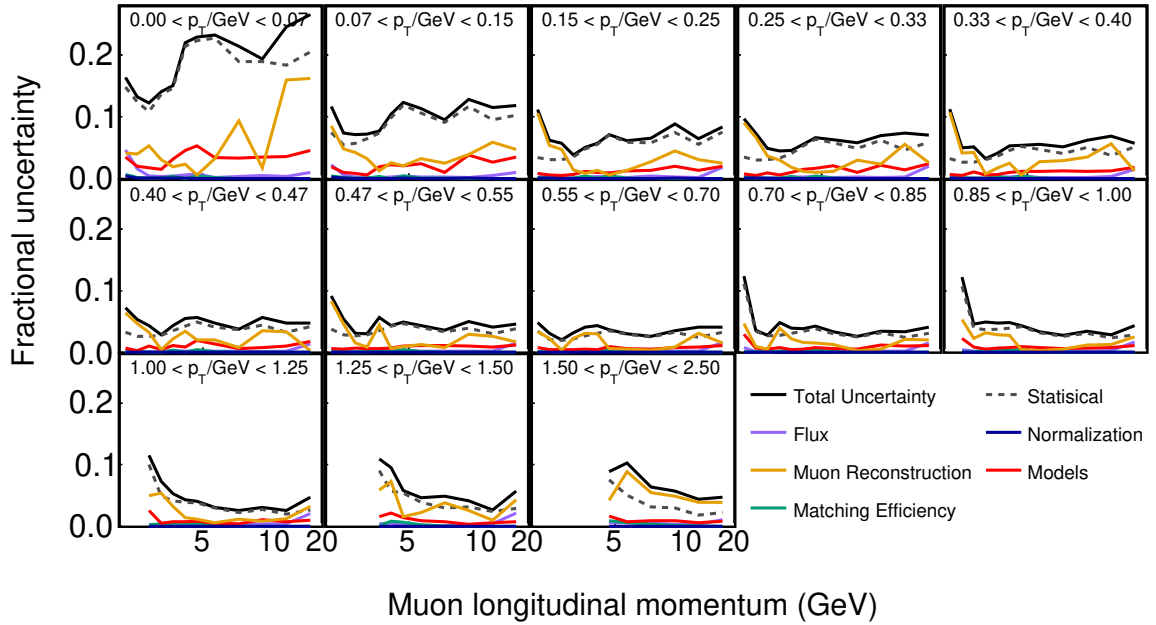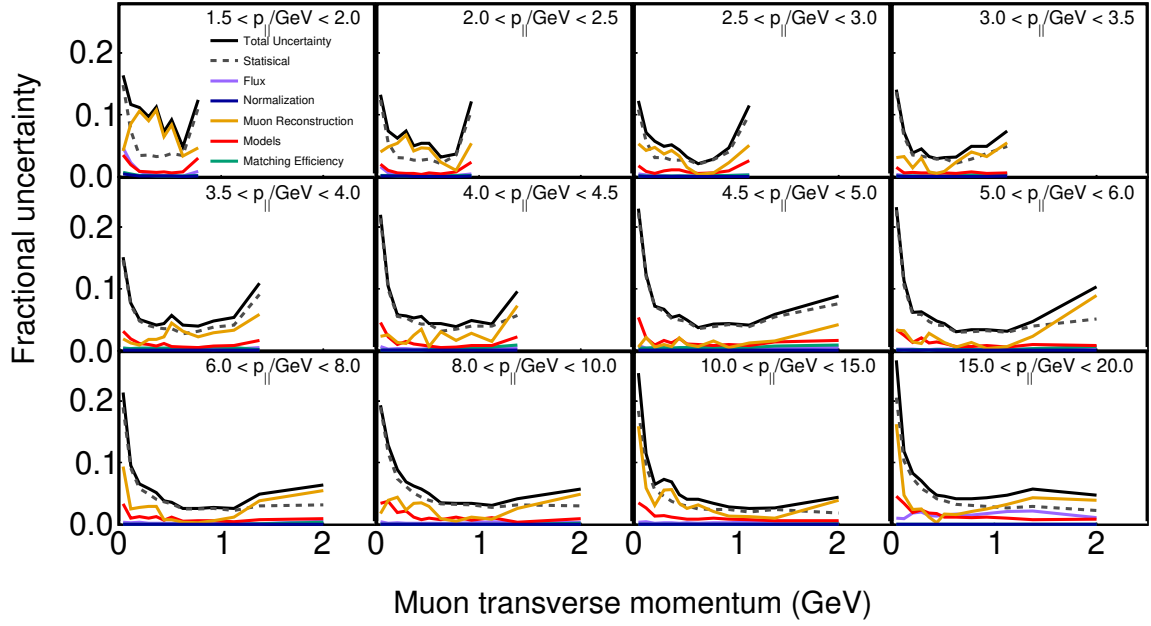
FIG. 6.17: Uncertainties on the unfolded data double differential event sample.
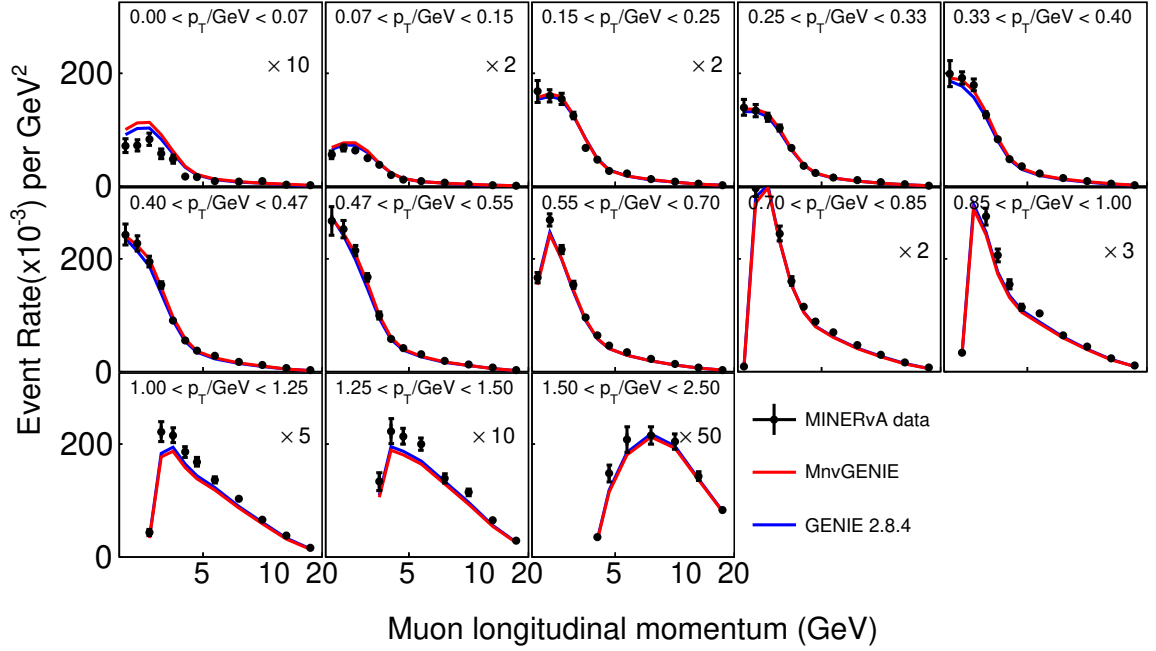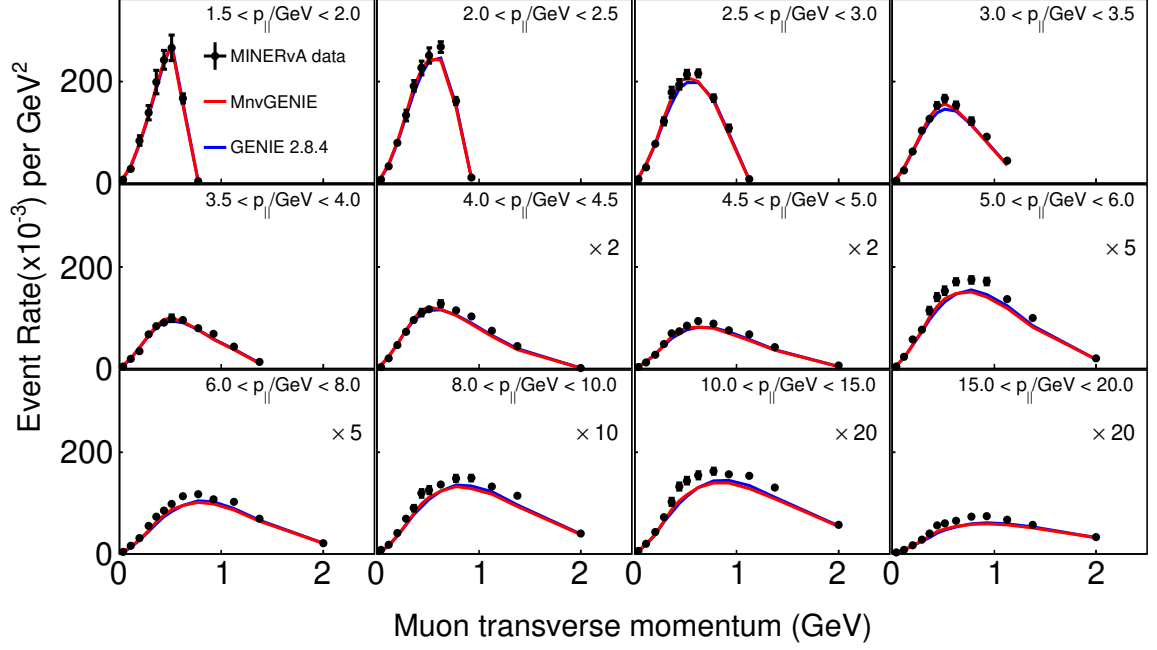
FIG. 6.18: Efficiency corrected double differential event rate with MINERvA tune v1 and GENIE 2.8.4 predictions. Note the axis scale changes in both projections.

100
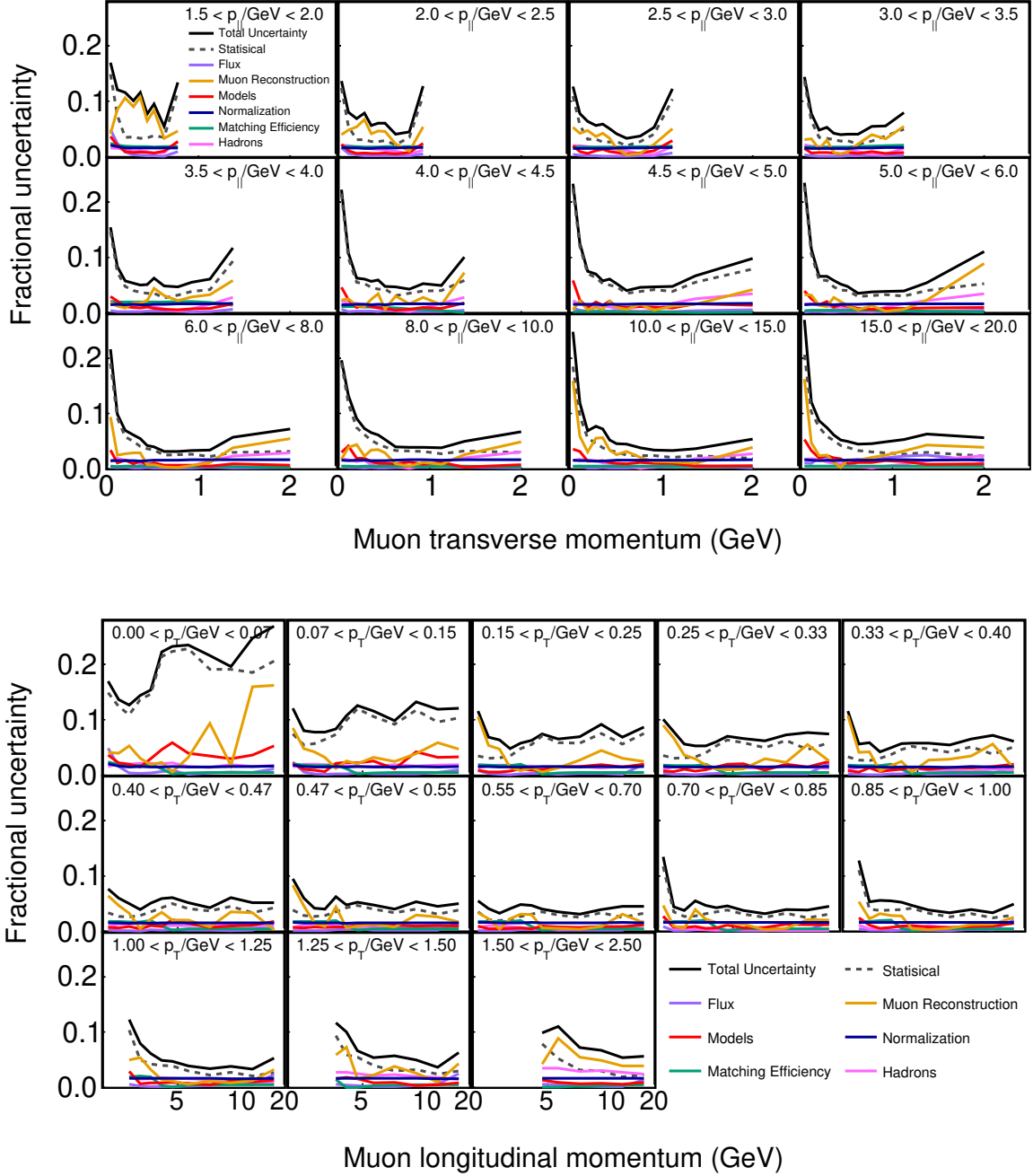
FIG. 6.19: Uncertainties on the unfolded and efficiency corrected data double differential event sample.

6.6.1 Cross section uncertainties

The dominant systematic uncertainty is the integrated flux, which is at the 7% level throughout the two dimensional phase space. The uncertainty in the muon energy scale which is the dominant component of the muon reconstruction uncertainty is comparable to the flux uncertainty at low longitudinal momentum. A breakdown of the muon reconstruction uncertainties is shown in Fig. 6.20. The flux is the dominant uncertainty in most of the two dimensional bins, with a handful of bins at the edges of the phase space dominated by statistics and muon reconstruction uncertainties. The equivalent cross section systematic uncertainty summaries for the single differential projections are shown in Fig. 6.21.

The muon reconstruction systematic is the other leading uncertainty that enters the analysis at the unfolding stage and is present through to the cross section. The muon reconstruction uncertainty can be broken down into individual uncertainties on the muon energy and muon angle, both of which shift the p_T and $p_{||}$ values. In the $1.5 < p_{||} < 2.0$ GeV bin, there is a noticeable up and down saw-tooth structure present in the muon energy uncertainty, as shown in Fig. 6.23. There are strongly anti-correlated bins in the muon energy systematic, which are causing this shape as a result of the unfolding procedure using a large number of iterations. These anticorrelations can be seen for the first $p_{||}$ bin in Fig. 6.22. The weighted average fractional uncertainty, defined as the summed uncertainty across all bins divided by summed cross section across all bins (a quantity that NOvA quotes for their inclusive cross section measurements [82]), is 2.8% for the muon reconstruction systematics in this measurement as the bins with larger fractional uncertainties also have smaller cross section contributions.
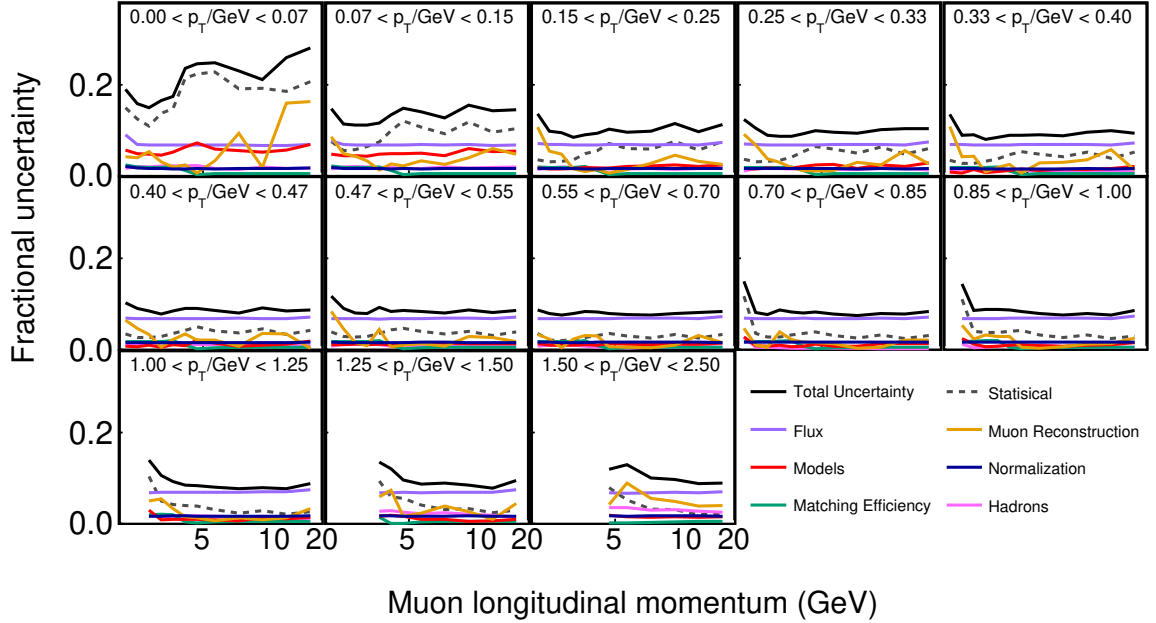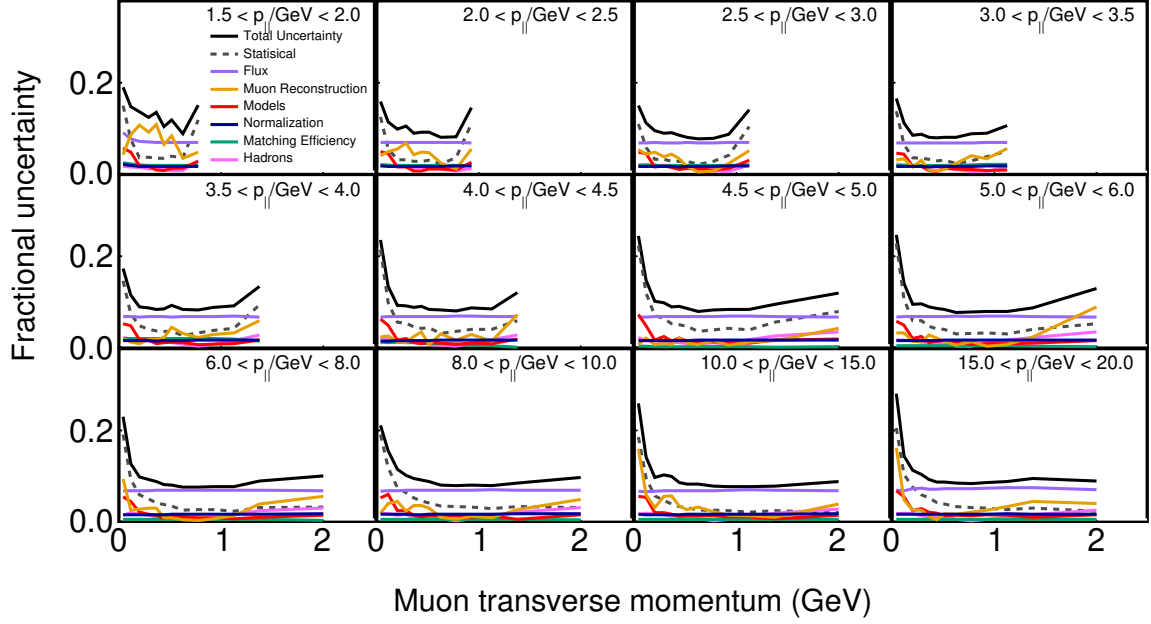
FIG. 6.20: Error summary for the double differential inclusive cross section. Systematic uncertainties are broken into 6 different error groups. The total statistical plus systematic uncertainty is shown by the solid black line.
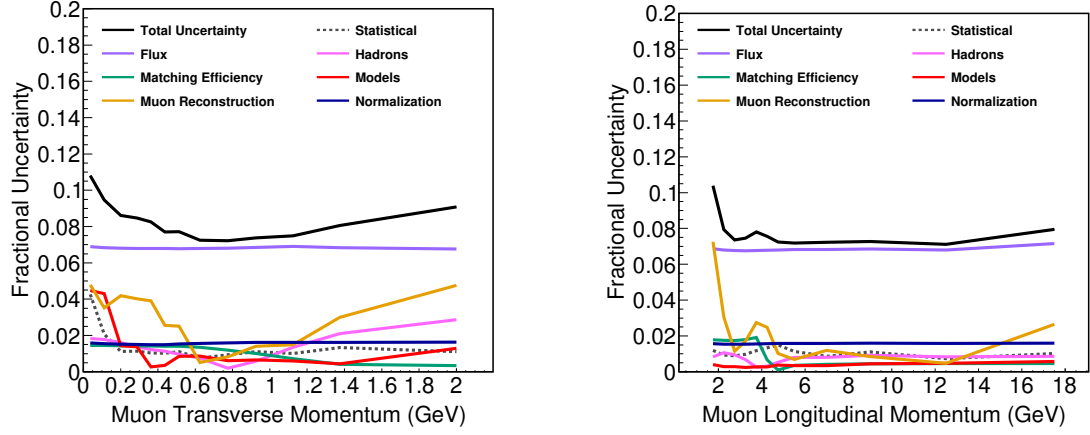
FIG. 6.21: Error summaries for the single differential inclusive cross section projections in p_T (left) and $p_{||}$ (right) Systematic uncertainties are broken into 6 different error groups. The total statistical plus systematic uncertainty is shown by the solid black line.
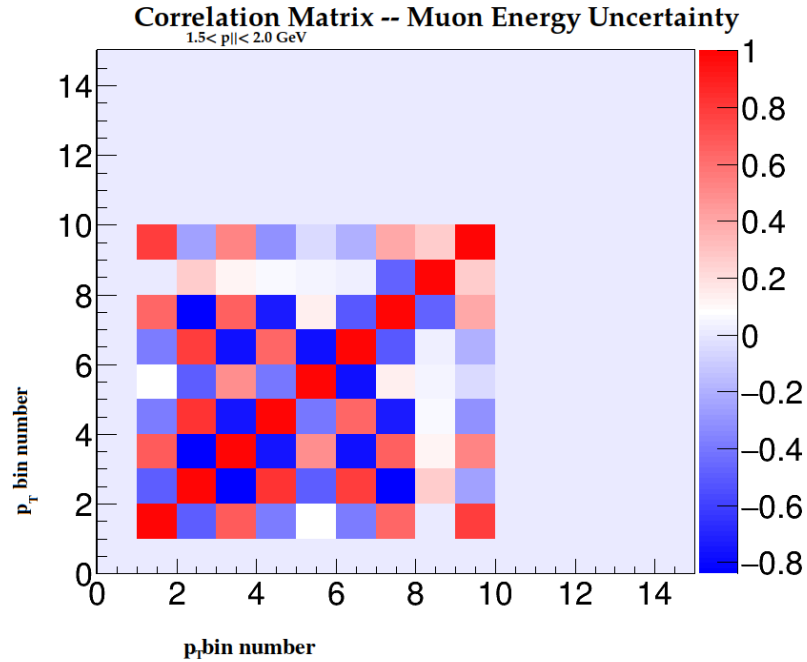
FIG. 6.22: Correlation matrix for the muon energy uncertainty in the lowest longitudinal momentum bin as a function of the p_T bin number.
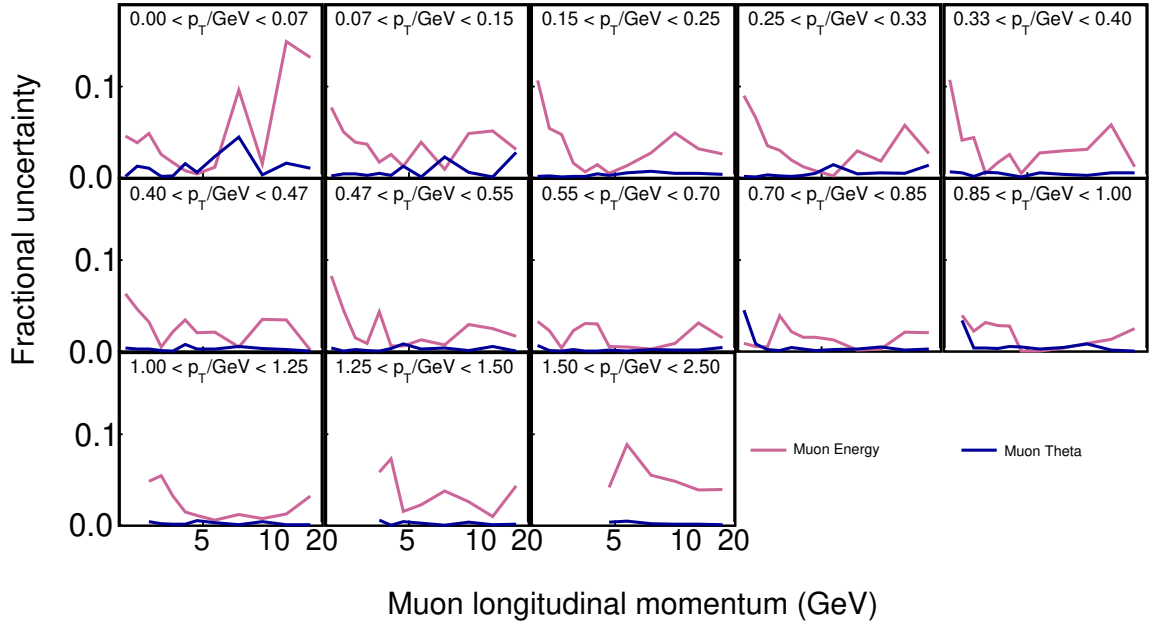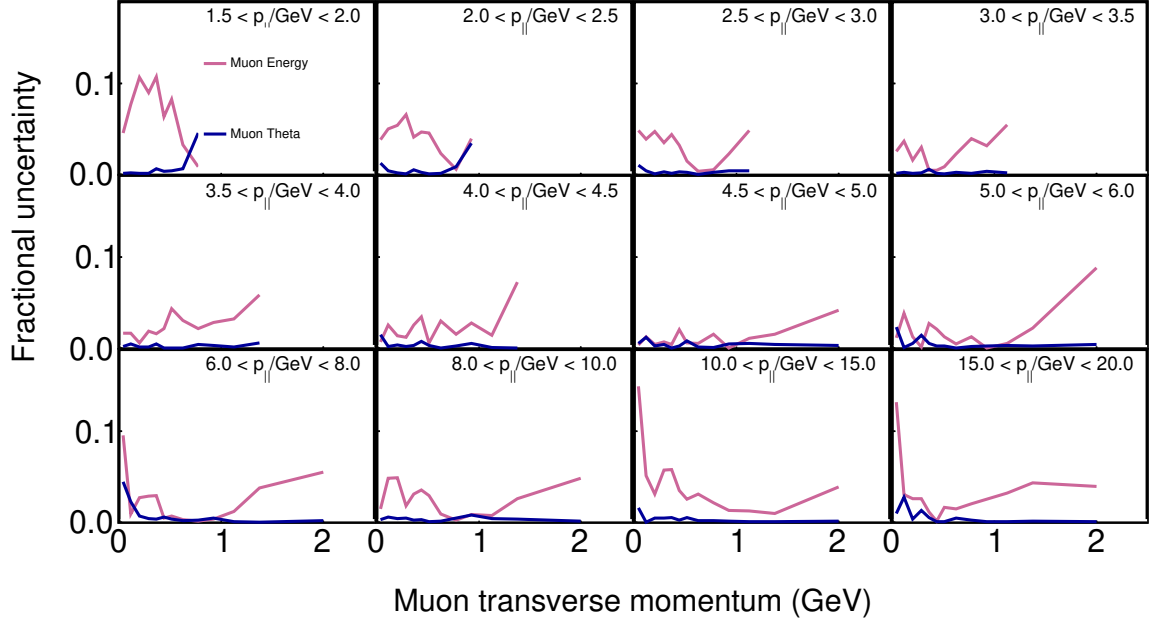
FIG. 6.23: The uncertainties in the muon reconstruction error group for the double differential data cross section in cells of $p_{||}$ (top) and p_T (bottom).

6.7 Cross sections

The efficiency corrected event rate is scaled by the integrated flux, the number of nucleons in the fiducial region (3.2348×10^{30}), and the number of protons on target (3.33×10^{20}) in order to calculate the cross section. The flux given in [67] is integrated from 0 to $120 \, \mathrm{GeV}$ resulting in a normalization factor of $2.877 \times 10^{-8} \nu/\mathrm{cm}^2/\mathrm{POT}$.

6.7.1 Single differential cross section

The one dimensional cross sections are projections of the full two dimensional cross sections. As such they have the same phase space constraints, such as a muon angle of less than 20 degrees. The projections do not include under/overflow bins so the cross sections presented are for $p_T \leq 2.5 \, \mathrm{GeV}$, and $1.5 \leq p_{\parallel} \leq 20 \, \mathrm{GeV}$. They are flux integrated cross sections.
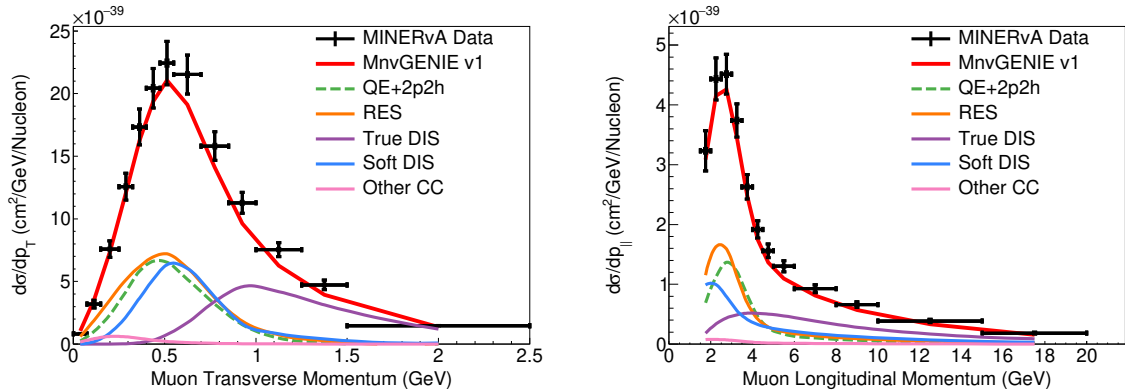
FIG. 6.24: Single differential cross sections as a function of muon transverse (left) and longitudinal (right) momentum with statistical (inner) and total (outer) uncertainties on data. MINERvA tune v1 is shown with its unstacked interaction channel components.

Fig. 6.24 shows the measured single differential cross sections, compared to MINERvA tune v1, along with the unstacked interaction channel components of MINERvA tune v1. In the transverse momentum projection, the true DIS events separate at higher end of the momentum range, however the QE+2p2h, RES, and soft DIS MC contributions all
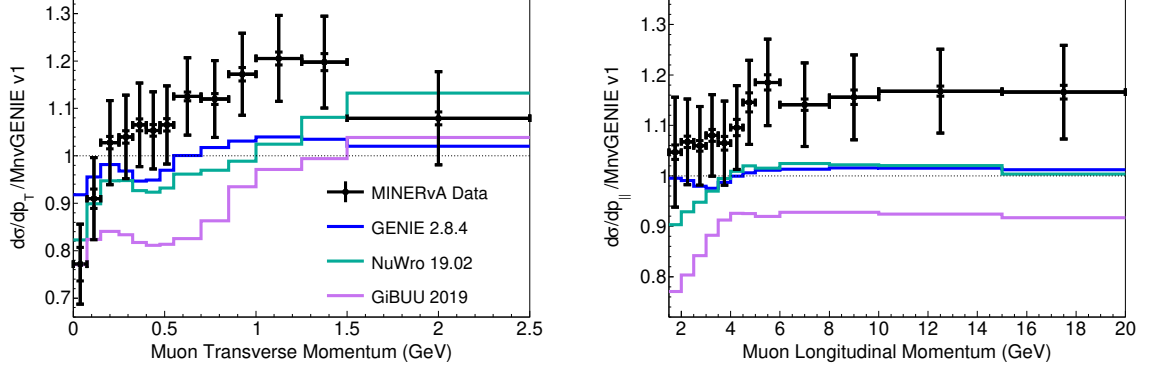
FIG. 6.25: Ratio of measured cross section to MnvGENIE v1 in transverse (left) and longitudinal (right) muon momentum. GENIE 2.8.4, NuWro 19.02 and GiBUU 2019 are also shown as ratios to MINERvA tune v1 for comparison purposes.
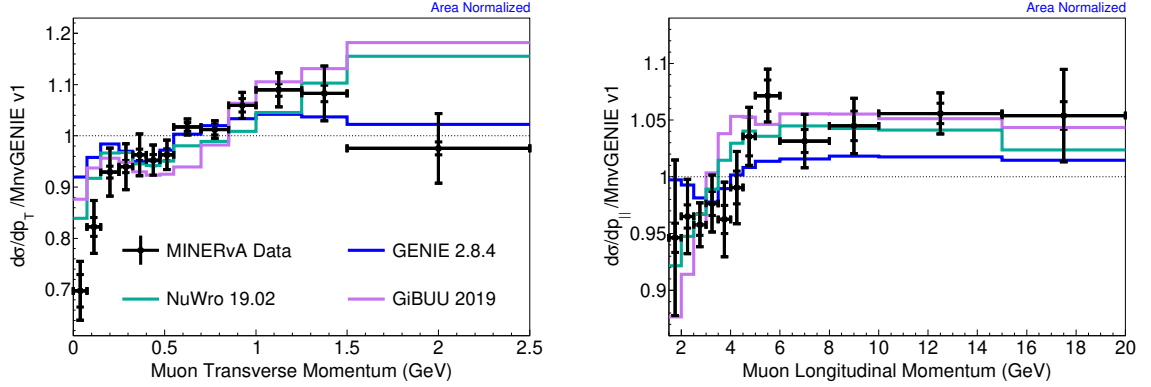
FIG. 6.26: Area-normalized ratio of measured cross section to MnvGENIE v1 in transverse (left) and longitudinal (right) muon momentum. GENIE 2.8.4, NuWro 19.02 and GiBUU 2019 are also shown as ratios to MINERvA tune v1 for comparison purposes.

occupy the same region of p_T, with similar shapes and strengths. MINERvA tune v1 underpredicts our measured cross section from $0.55 < p_T < 1.5$ GeV, with agreement within 1σ in the highest p_T bin and in the mid range p_T. Fig. 6.25 shows this with the ratio of the measured cross section to MINERvA tune v1. The longitudinal momentum projection does not provide much separation of different interaction channels. The data-MC ratio is flatter in $p_{||}$, with less shape dependence than seen in p_T.

Area normalized single differential ratios of data and model predictions are shown in Fig. 6.26. These models are discussed further in Sec. 6.7.3.

6.7.2 Double differential cross section

The double differential cross section is shown in Fig. 6.27, along with the same interaction channel breakdowns, and compared to MINERvA tune v1. A version of the cross section and components taken as a ratio to MINERvA tune v1 is shown in Fig. 6.28. One notable feature in the double differential result is the overpredictions of the cross section in the majority of the lowest p_T bin, a region with primarily resonant, quasi-elastic and 2p2h interactions. Additionally we see underpredictions for bins with high $p_{||}$ and p_T values in the mid range of our bins, where soft DIS is the dominant process but there are also substantial contributions from the resonant, QE and 2p2h channels.

The differences between the measured and predicted cross sections do not track with any single interaction channel and occur in regions with different dominant processes. There are consistent underpredictions in all of the regions where the soft DIS interaction channel is dominant. Bins that have an average W >3.5 GeV all show good agreement with the data and have true DIS contributions of greater than 80%. This region includes the 5 highest $p_{||}$ bins with $p_T > 1.50$ GeV and the highest $p_{||}$ bin with 1.25 GeV $< p_T < 1.50$ GeV. Plots showing the average W and Q^2 in simulation in each bin are available in Appendix A.2.
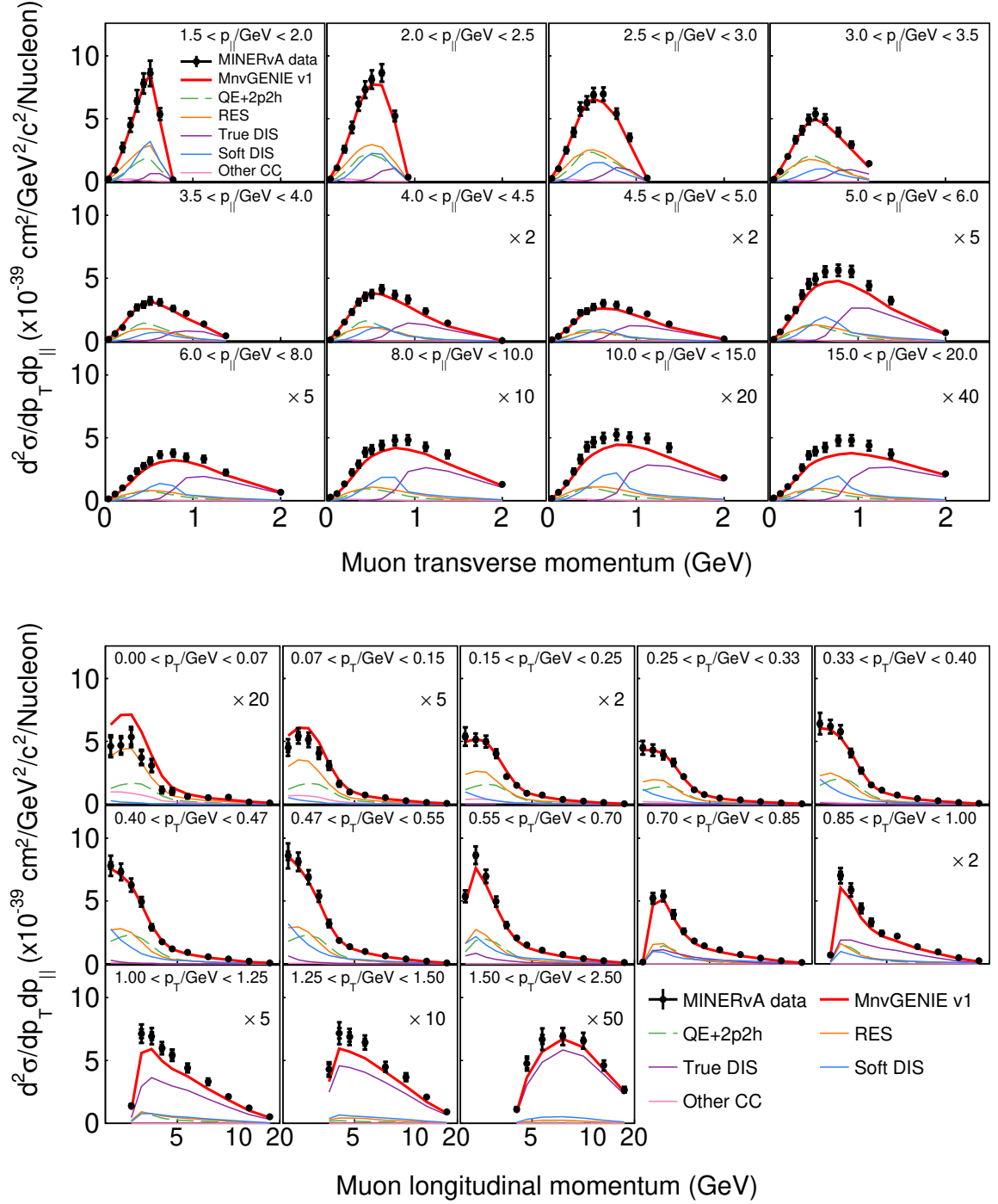
FIG. 6.27: Measured double differential cross sections with breakdowns by interaction channel. Multipliers are applied to some panels to improve readability.
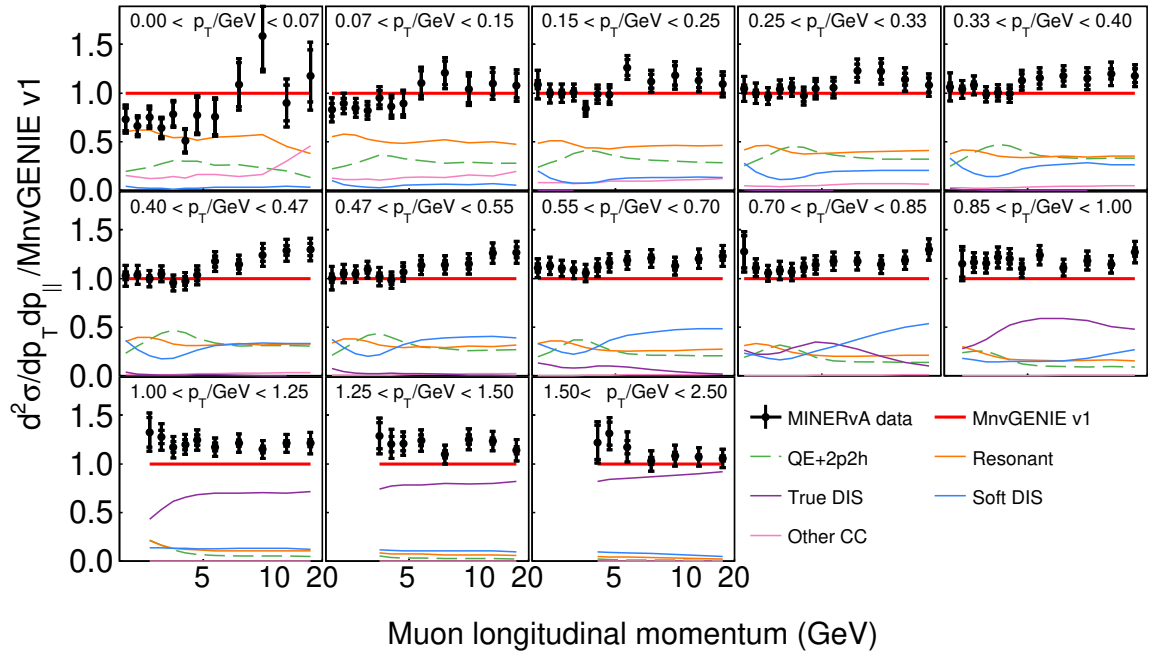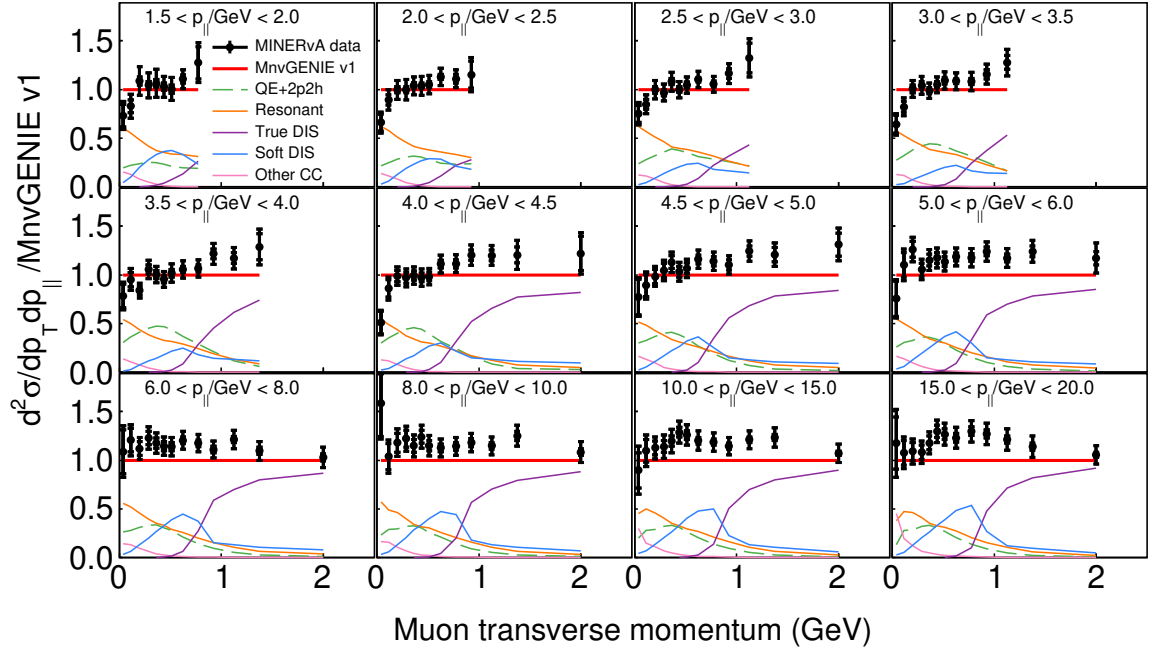
FIG. 6.28: Double differential cross section shown as a ratio to MINERvA tune v1.

110

Process Variant	Standard χ^2	Log-normal χ^2
MINERvA tune v1	495	547
GENIE 2.8.4	422	491
MINERvA tune v2	475	665
GENIE + piontune	477	580
GENIE + RPA	327	459
GENIE + RPA + 2p2h	402	464
GENIE + 2p2h	690	725
MINERvA tune v1 + MINOS π low Q^2 sup.	381	526
MINERvA tune v1+ nCTEQ15 DIS	503	551
MINERvA tune v1+ nCTEQν DIS	506	565
MINERvA tune v1+ AMU DIS	549	636
NuWro	820	587
GiBUU	767	815

TABLE 6.1: The χ^2 calculated via standard and log normal calculations for each model and model variant used in this analysis. There are 144 degrees of freedom.

6.7.3 Model comparisons

Comparisons are made to the neutrino generators GENIE 2.8.4 (without MINERvA's standard modifications), NuWro, and GiBUU; as well as 3 different models for DIS interactions nCTEQ15, nCTEQν, and AMU; and various tunes and reweights applied to GENIE. Further details about each of these models are discussed in Ch. 1.6. Versions of the single differential projections of these comparisons can be found in Sec. 6.7.1.

Model goodness of fit

The double differential χ^2 values, calculated bin-by-bin, are shown in Table 6.1 for each model and variant. The χ^2s are calculated with full systematic correlations accounted for in both a standard and log-normal calculation. The log normal χ^2 can be an advantageous method to use when there are highly correlated uncertainties that affect the overall normalization such as is the case with the flux uncertainty.

Of the tested models and tunes, GENIE with the addition of the non-resonant pion

tune and Valencia model's quasielastic random phase approximation (GENIE+RPA) had the best performance in both the standard and log-normal χ^2s. High χ^2/DOF have been seen in prior double differential cross sections as well, such as a quasielastic-like measurement by MINERvA [43], and inclusive measurements made by T2K [80] and μBooNE [81].

Event generator comparisons

Three neutrino generator predictions are shown in Fig. 6.29 and Fig. 6.25. Fig. 6.25 shows GENIE 2.8.4 (without MINERvA's standard modifications), NuWro, and GiBUU as ratios to MINERvA tune v1 as single-differential projections. In the longitudinal momentum projection, all of the neutrino generators used tend to underpredict the cross sections at high longitudinal momentum. All of the generators, with the exception of GiBUU, underpredict the data in this area by approximately 10% to 15%. GiBUU shows the largest discrepancy, with a 10 to 20% normalization difference with respect to the other models, resulting in a 20% to 40% absolute normalization difference with the data. In the transverse momentum projection, the highest bin, ranging from $1.5 < p_T < 2.5\,\text{GeV}$, is the best-modeled, with all 4 models in agreement with the data. GENIE 2.8.4 and NuWro both agree with the majority of the data bins for $p_T < 0.33\,\text{GeV}$. MINERvA tune v1 has the best agreement in the range of $0.15 < p_T < 0.55\,\text{GeV}$, and GiBUU has the worst agreement with only three bins being consistent with data.

Fig. 6.26 shows an area normalized version of this plot in order to study shape comparisons. In terms of shape, GENIE 2.8.4 has the best agreement with the data in the transverse momentum projection, having a majority of bins within 1σ. GENIE 2.8.4, NuWro and GiBUU all match the shape of the data in the $0.25 < p_T < 0.55\,\text{GeV}$ bins. MINERvA tune v1 performs the worst in the transverse momentum shape comparison, with only three bins in agreement with the data. For the shape-only longitudinal momentum model comparisons, NuWro and GENIE 2.8.4 have the best agreement, each with only a

few scattered bins not in agreement. In neither projection does MINERvA tune v1 stand out as being a particularly good fit to the inclusive data.

The full double-differential cross-section ratios for these three event generators are shown in Fig. 6.29 Again, none of these models have good agreement with the data throughout the full phase space. The mid-range p_T shows the same GiBUU normalization difference seen in the longitudinal momentum projection. NuWro has the best agreement at high p_T, with all but one of the highest p_T bins in agreement, and the most bins in agreement in the second highest p_T bin. The bins with $p_{||} < 5.0\,\text{GeV}$ and $0.15 < p_T < 0.55\,\text{GeV}$ are among the best modeled, with MINERvA tune v1 in agreement with data within 1σ for 33 of these 35 bins and GENIE 2.8.4 with 83% of bins in agreement. NuWro also has fairly good agreement in this region, especially for the sub-range of $3.5 < p_{||} < 5.0\,\text{GeV}$, where 80% of the bins are in agreement. All of the models consistently underpredict the data in the region with a longitudinal momentum greater than $5\,\text{GeV}$ and $0.33 < p_T < 1.25\,\text{GeV}$, similarly seen in Fig. 6.28.

An area normalized version of Fig. 6.29 is shown in Fig. 6.30. The area normalization is applied as a single factor to all panels simultaneously for all of the double-differential results. The 7% flux uncertainty is largely uniform, so the χ^2 calculated using the covariance matrix partially accounts for such overall normalization effects. The area normalized MINERvA tune v1, NuWro and GiBUU curves are scaled by normalization factors of 1.11, 1.13, and 1.26, respectively. The shape agreement is also poor for these models. NuWro and GiBUU model the shape at high p_T with $p_{||} < 5.0\,\text{GeV}$ better than MINERvA tune v1, with 81% and 94% of the four highest p_T bins in this range in agreement with data, respectively.
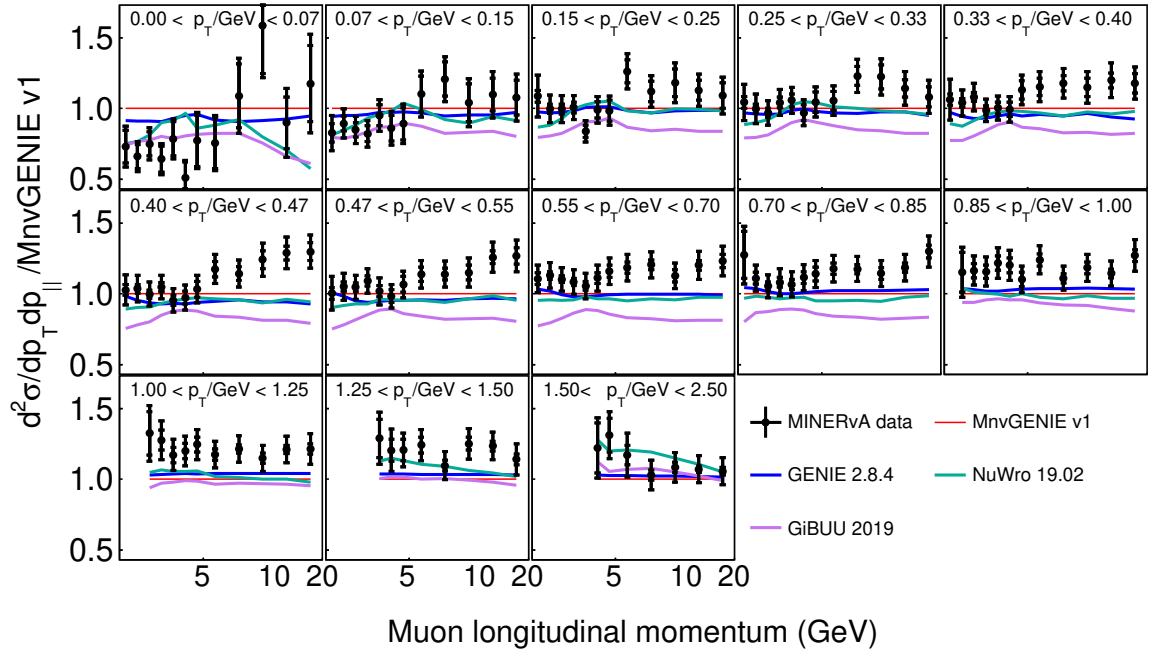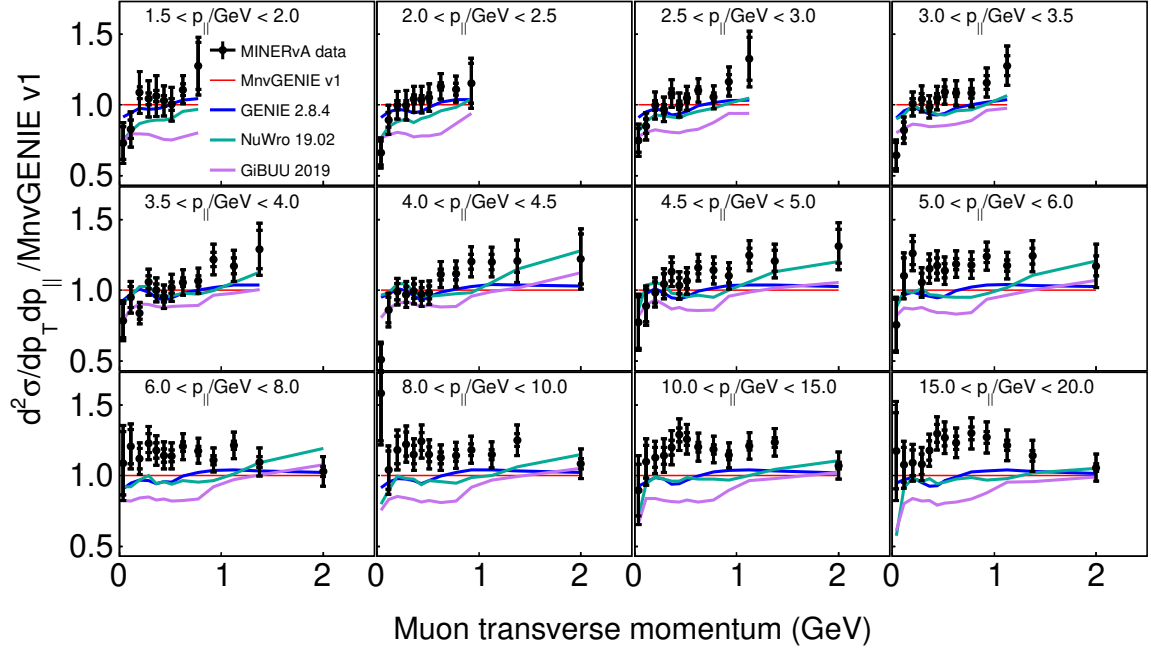
FIG. 6.29: Model comparisons to other neutrino generators as a ratio to MINERvA tune v1.

114
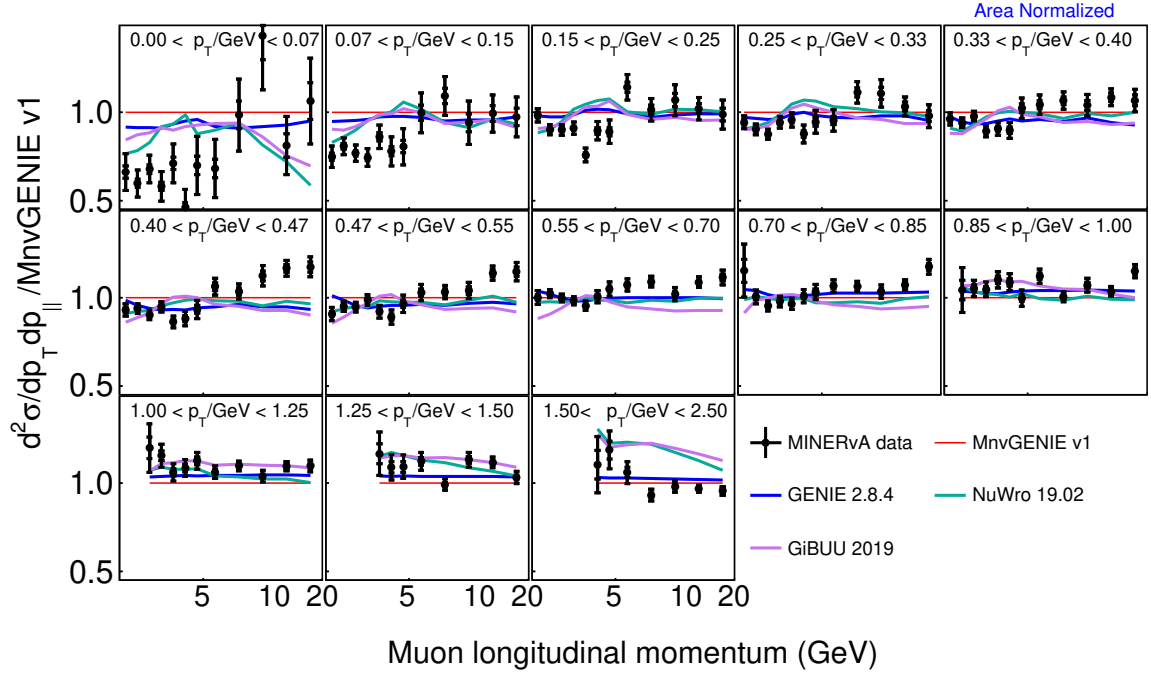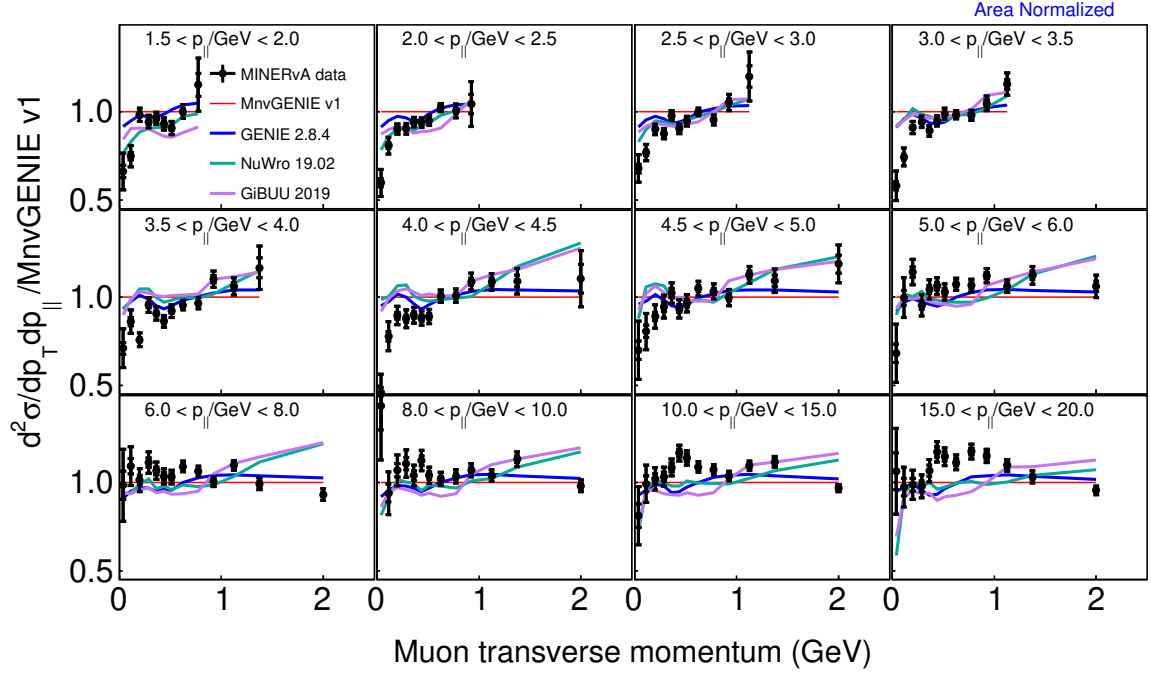
FIG. 6.30: Area normalized model comparisons to other neutrino generators as a ratio to MINERvA tune v1.
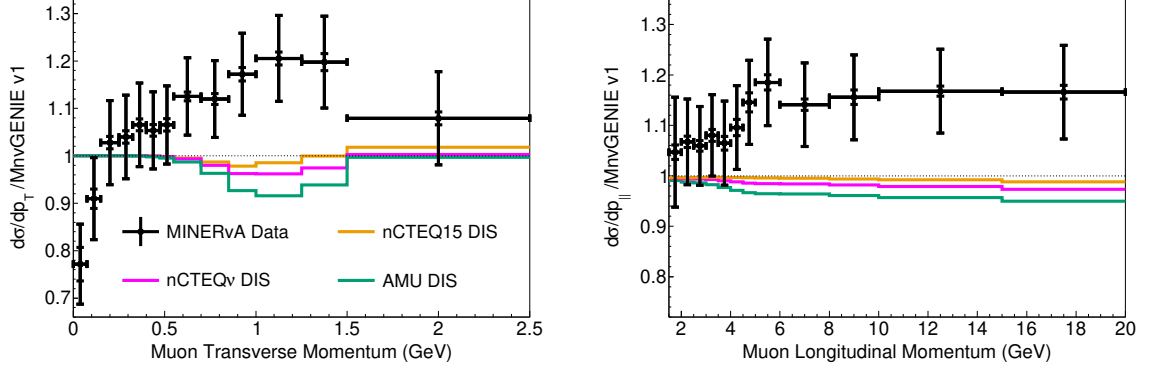
FIG. 6.31: Ratio of measured cross section to MnvGENIE v1 in transverse (left) and longitudinal (right) muon momentum. Three models of DIS: nCTEQ15, nCTEQν, and the AMU DIS model, are applied on top of the other components of MINERvA tune v1, and shown as ratios to MINERvA tune v1.

Examination of DIS models

Single-differential DIS model comparisons to nCTEQ15, nCTEQν and AMU are shown in Fig. 6.31. These comparisons use MINERvA tune v1 with weights derived from the DIS models, introduced in Sec. 1.6.3, applied to only the true DIS ($W > 2.0\,\mathrm{GeV}$, $Q^2 > 1.0\,\mathrm{GeV}$) component, as explained in Sec. 6.7.3. All of the resulting curves tend to underpredict the cross section in the areas with significant DIS contributions, except in the highest bin of transverse momentum. A shape-only version of this DIS model comparison is shown in Fig. 6.32. All of these DIS models, when added to MINERvA tune v1, show poor shape agreement with the data.

The full double-differential comparisons to these models are show in Fig. 6.33, with the area normalized version in Fig. 6.34. These show similar trends as the single differential projections, with areas with significant contributions of true DIS events showing underpredictions across all three of these models, while there is better agreement in the highest p_T bin.

116
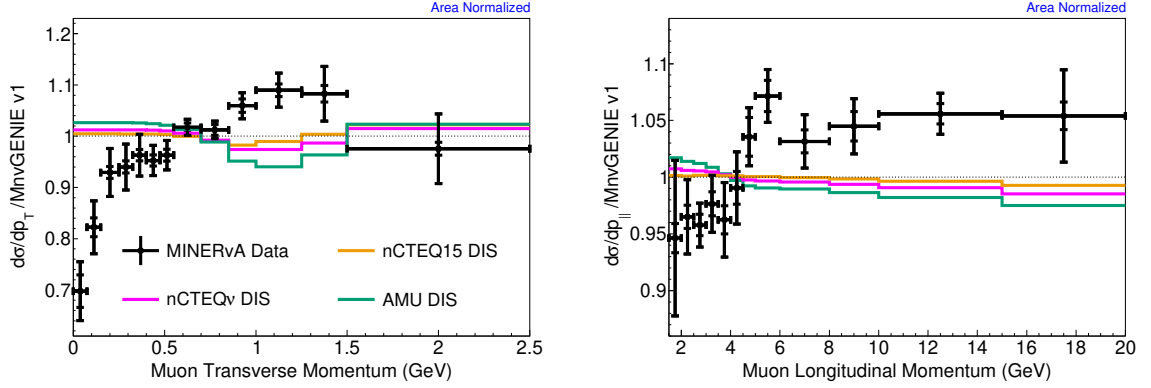
FIG. 6.32: Area-normalized ratio of measured cross section to MnvGENIE v1 in transverse (left) and longitudinal (right) muon momentum. Three models of DIS: nCTEQ15, nCTEQν, and the AMU DIS model, are applied on top of the other components of MINERvA tune v1, and shown as ratios to MINERvA tune v1.

Comparisons of Modeling Options with GENIE

Various GENIE model variants are included in Table 6.1. The addition of RPA, 2p2h and its tune to MINERvA data, and the suppression of low Q^2 resonances, are supported by comparisons using the measured hadronic system in MINERvA. Fig. 6.35 shows three model variants that have some of the lower χ^2 values.

The first of these models is MINERvA tune v2, which includes addition of MINERvA's low momentum transfer resonance suppression described in Sec. 6.7.3. This tune is identical to MINERvA tune v1 at higher transverse momenta, with all of the differences occurring with $p_T < 1\,\text{GeV}$. The addition of low momentum transfer resonance suppression to MnvGENIE v2 does a reasonable job of reproducing the data in the first half of the $p_{||}$ bins, but maintains the large underprediction at higher longitudinal momentum, starting at approximately $5.0\,\text{GeV}$. The shape of the suppression differs from the data trends; its addition generates decent agreement in the first transverse momentum bin, but is too strong in the second through fourth bins of transverse momentum. When the MINOS version of this suppression is added to MnvGENIE v1, it produces better χ^2 fits than MnvGENIE v2 [49]. A comparison to MINERvA tune v1 with the MINOS low Q^2 resonant
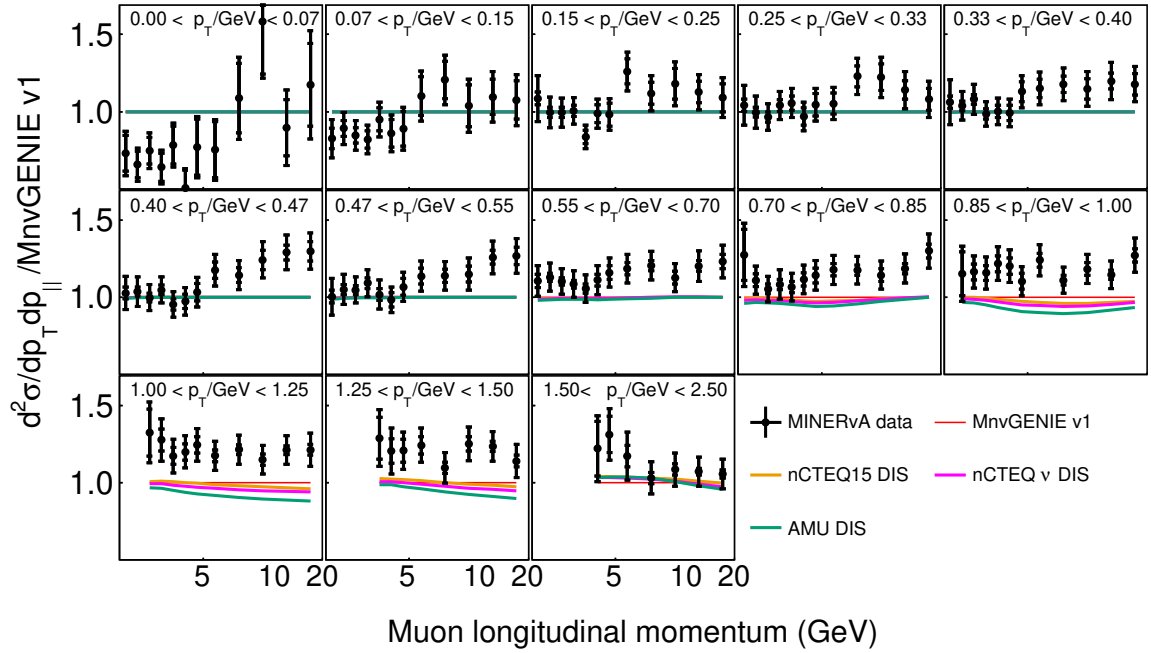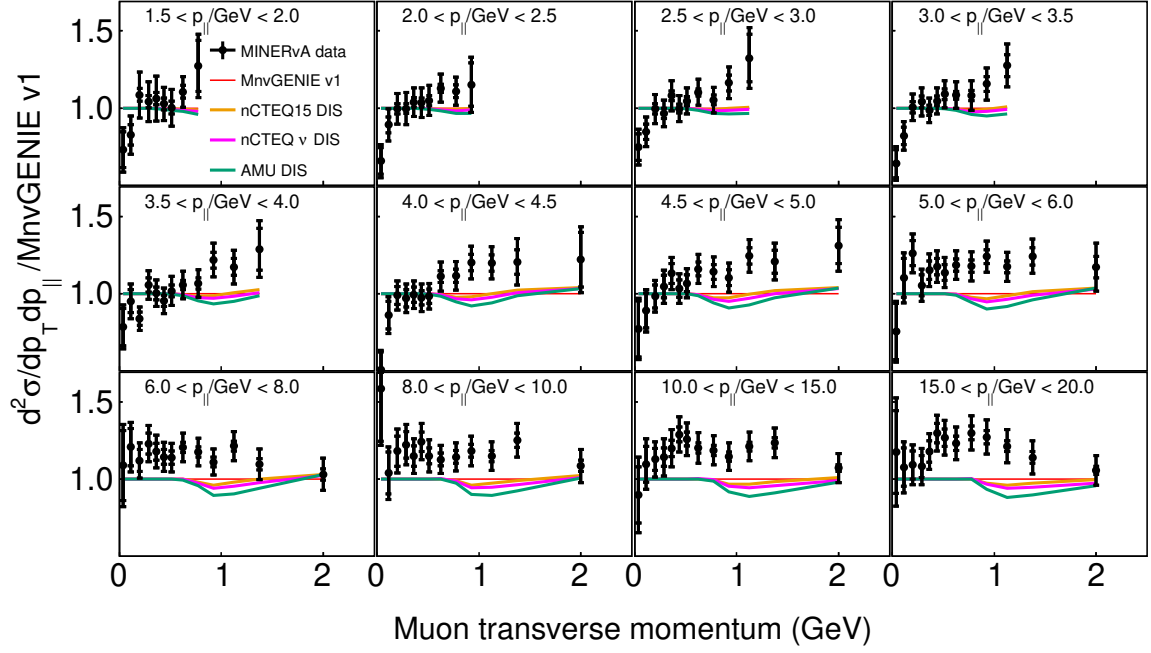
FIG. 6.33: Model comparisons to DIS model variations as a ratio to MINERvA tune v1.
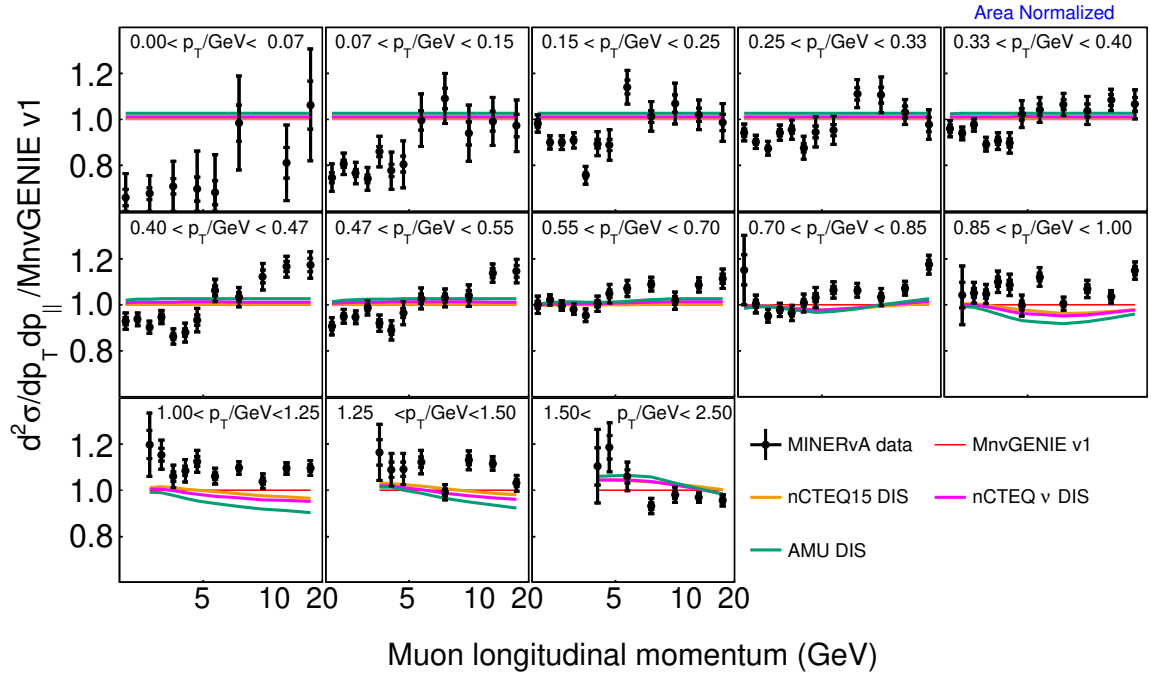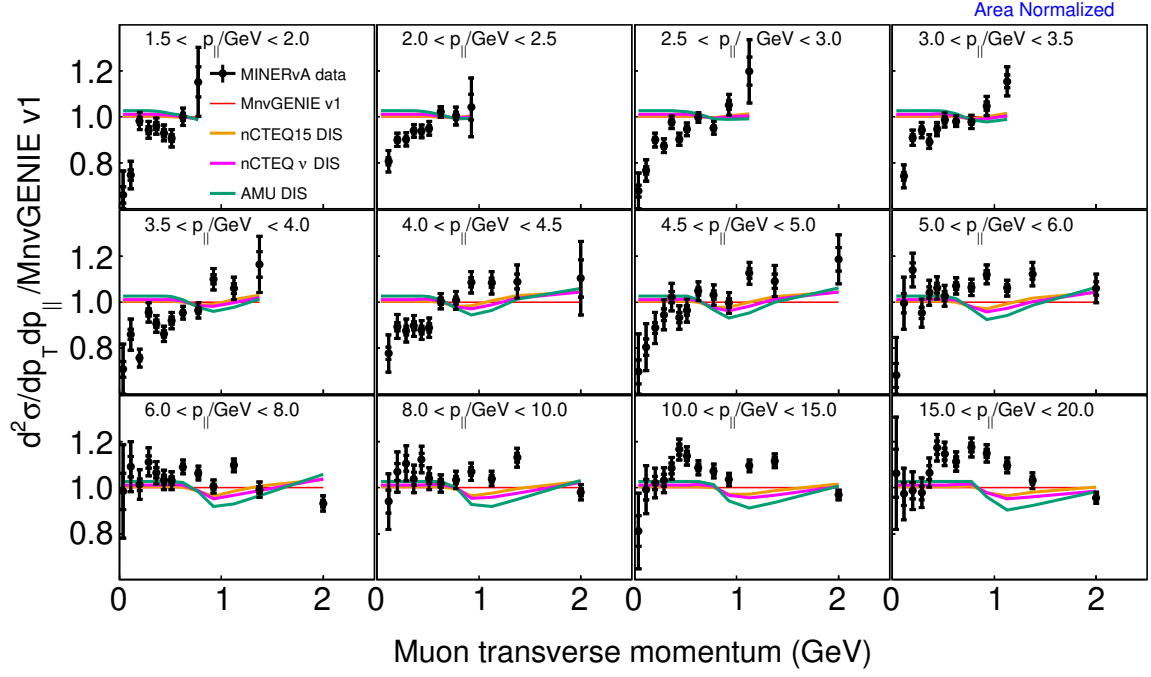
FIG. 6.34: Area normalized model comparisons to DIS model variations as a ratio to MINERvA tune v1.
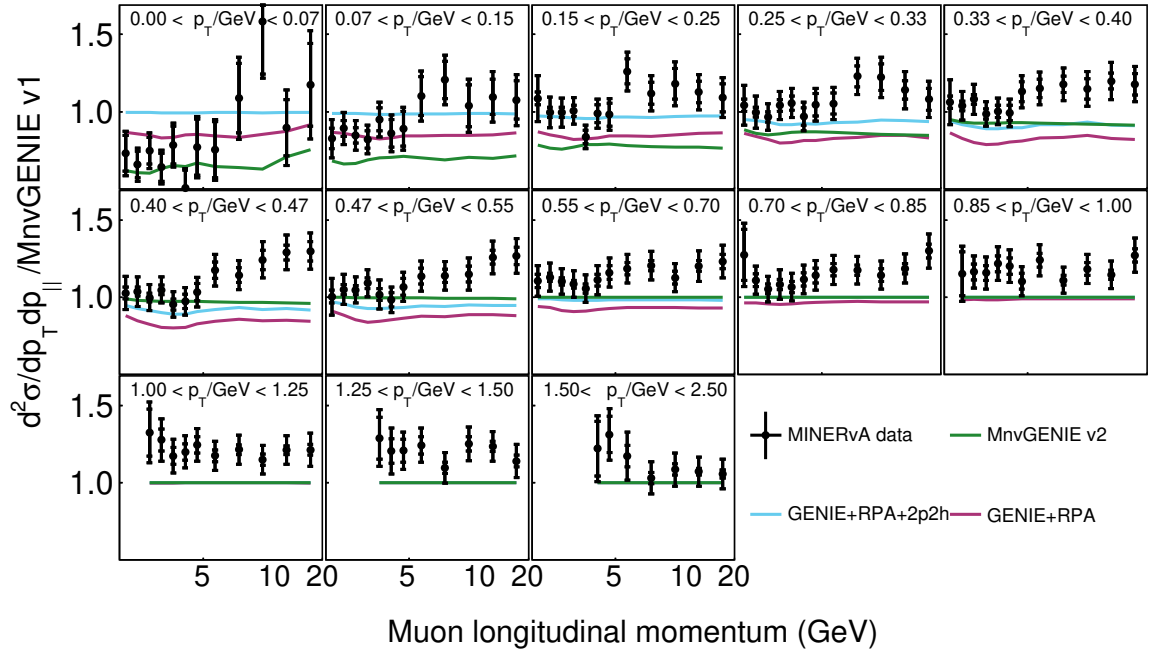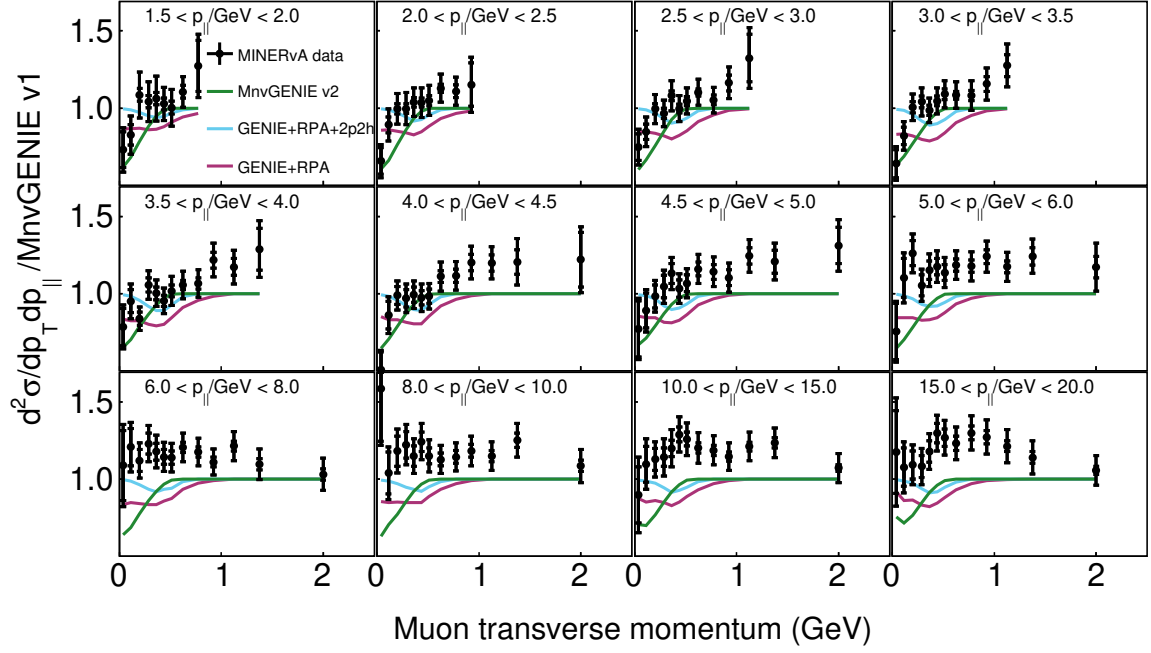
FIG. 6.35: Model comparisons to GENIE variations as a ratio to MINERvA tune v1.
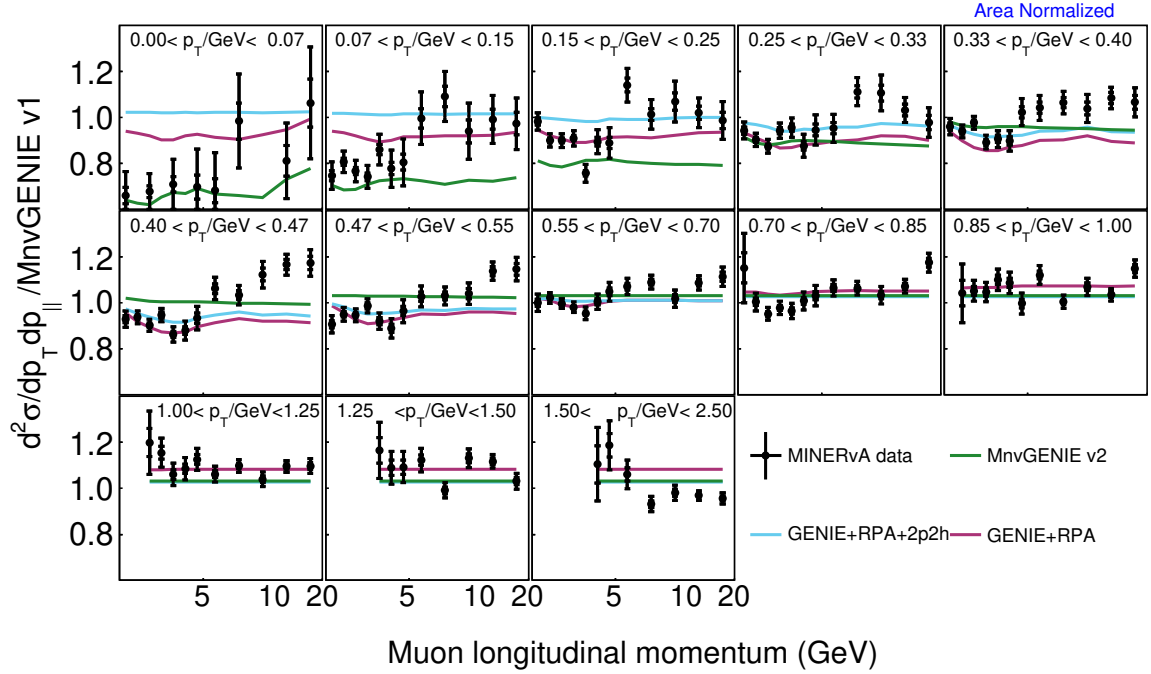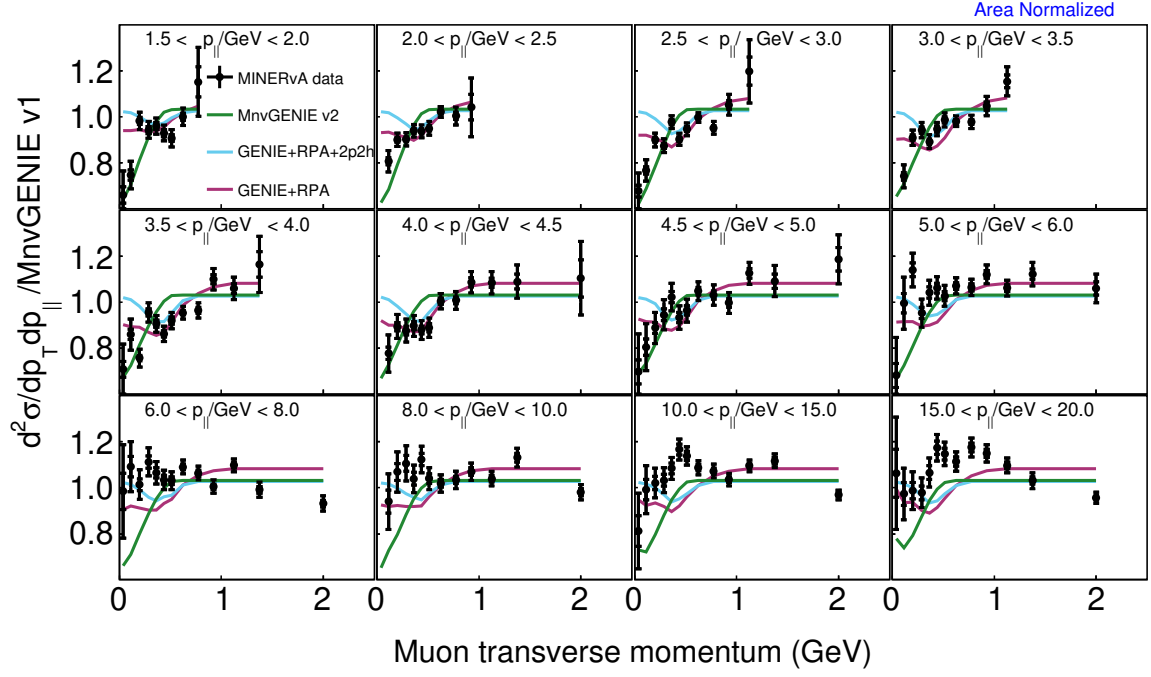
FIG. 6.36: Area normalized model comparisons to GENIE variations as a ratio to MIN-ERvA tune v1.

suppression is shown in Fig. 6.37. The MINOS suppression is similar to the MINERvA version in the lowest two p_T bins, with a weaker suppression in higher p_T bins. The latter difference produces better data agreement in those regions.

The second-best log-normal χ^2 fit (third-best standard χ^2) is GENIE with the addition of quasielastic Valencia model RPA suppression and 2p2h, GENIE+RPA+2p2h. This differs from MINERvA tune v1 only in the 2p2h component, which is enhanced in MINERvA tune v1, but not in GENIE+RPA+2p2h. For this reason, the region of interest for comparing these tunes is within the transverse momentum range of $0.15\,\mathrm{GeV}$ to $0.70\,\mathrm{GeV}$, where all differences of significance occur. There is a slight dip in the data from $2.5 < p_{||} < 5\,\mathrm{GeV}$ for $0.25 < p_T < 0.40\,\mathrm{GeV}$, which appears to slightly prefer the untuned 2p2h to the enhanced 2p2h used in MINERvA tune v1. This effect is slightly more emphasized in the shape-only model comparisons in Fig. 6.36.

Surprisingly, GENIE+RPA, which contains no 2p2h, is the model with the best χ^2. It shows a larger dip in the same area as GENIE+RPA+2p2h does, with a much larger effect at low longitudinal momentum, and extending further into low transverse momentum as well. In the absolutely normalized versions of these plots, the removal of 2p2h causes the model to dip substantially below the data in most areas of phase space (especially at higher longitudinal momenta). The shape agreement improves drastically with the removal of 2p2h in some regions; GENIE+RPA has data agreement in the range from $2.0\,\mathrm{GeV} < p_{||} < 4.5\,\mathrm{GeV}$ with $p_T > 0.15\,\mathrm{GeV}$, while MINERvA tune v1 has poorer agreement in area normalized plots. As a best fit though, this model still fails to accurately produce the cross section shapes seen in the data across the full range of p_T and $p_{||}$ and does a worse job at predicting the overall normalization than other models and tunes.

Compared to MINERvA tune v1, the description of the lowest p_T bins improves with the removal of some event rate from at least one process. MINERvA tune v2 removes low Q^2 resonances, while GENIE+RPA instead removes all the 2p2h component. These
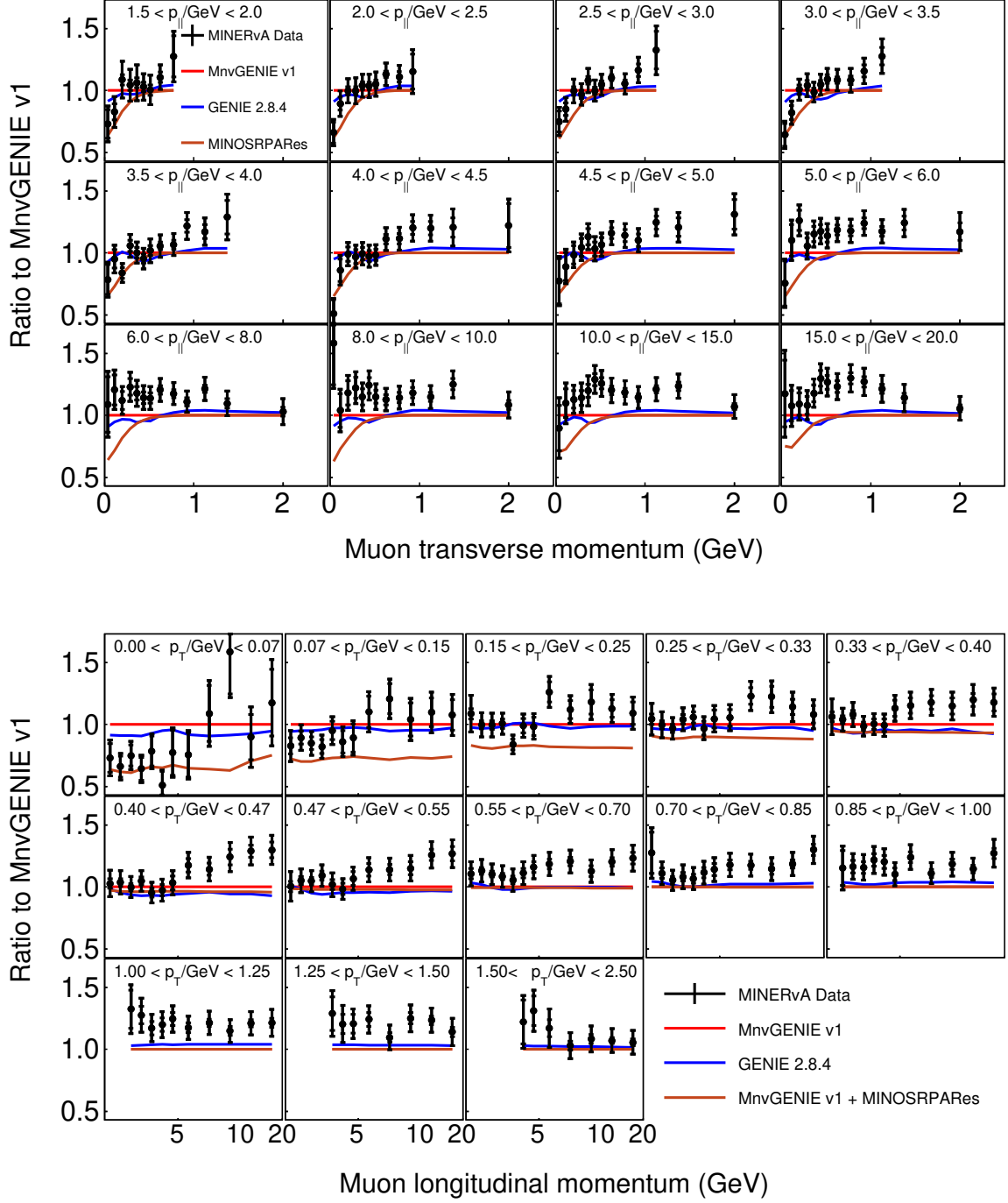
FIG. 6.37: Model comparisons to MINERvA tune v1 with the addition of a low Q^2 suppression based on MINOS data.

defining characteristics of the two MINERvA tunes operate in overlapping regions of muon kinematics. The data may prefer future models with a modification of resonances more sophisticated than just a low Q^2 suppression. Plots with all of the different model tunes are included in Appendix A.3.

The modifications of QE RPA suppression, 2p2h, enhanced 2p2h, and suppressing the low Q^2 resonance pion production are primarily motivated by MINERvA data for the observed hadronic systems. This includes direct calorimetric measurements in [41, 42], and the separation of samples with only protons and neutrons [43, 44, 83, 84] and with at least one pion [48, 85, 47, 46, 45]. Using the hadronic information in these ways provides relatively good separation of the QE, 2p2h, Delta resonance, and higher-W processes. The result is still an imperfect description of the muon kinematics in this new inclusive cross section, suggesting future focus on the detailed correlations between lepton kinematics and hadronic system.

6.8 Interpretations

Models such as MINERvA tune v1 and MnvGENIE v2 were optimized to agree with previous MINERvA measurements in exclusive channels and limited kinematic regions [41][43]. They have been shown to see good agreement across different exclusive interaction channels [44] and low-recoil samples [42]. However, the results presented here show that when all of these modifications are applied inclusively, having to contend with a large phase space with many contributing interaction channels, their predictive power is substantially diminished.

Similarly, the suite of true DIS models used as partial model comparisons in this analysis were developed as theoretical and data-driven alternatives to other true DIS models such as those implemented in GENIE. However, these true DIS models do not result in better agreement than the GENIE DIS model. In fact, the addition of these true DIS models results in larger discrepancies with the data suggesting future investigating of exclusive channels and model development is required.

This measurement indicates that some form of a low Q^2 RES suppression helps to achieve better agreement in low p_T regions, particularly for $p_{||}$,< 5.0 GeV. It also suggests that an enhancement of GENIE DIS may be called for in lower-W regions, because bins with an average $W < 3.5$ GeV, in which GENIE DIS is the dominant interaction channel, show consistent underpredictions.

The beam energies used for this analysis are comparable to what will be used for DUNE, so the inability to accurately predict the cross sections in this energy regime could have direct effects on the uncertainties and intrinsic model dependencies in measurements made by DUNE.

6.9   Medium Energy Results

We also performed a parallel analysis done using the medium energy beam[86]. This version of the analysis had increased statistics with 4 million events in the sample. It uses all of the same techniques and signal definition as the low energy beam results presented in this chapter. In this analysis $\langle E_\nu \rangle \sim 6.0\,\text{GeV}$, instead of the $\langle E_\nu \rangle \sim 3.5\,\text{GeV}$ flux in the low energy beam. This higher energy and increased in intensity in the ME beam allowed for the phase space of the ME result to be expanded to include two additional $p_{||}$ bins from 20-40 and 40-60 GeV/c and one additional p_T bin from 2.5-4.5 GeV/c. The increased statistics also allowed for finer binning in the region from 6.0-10.0 GeV/c. The areas where new bins were added can be visualized in Fig. 6.38. The double differential cross sections are shown in Fig. 6.39, with ratios to MINERvA tune v1 in Fig. 6.40. MINERvA tune v1 is broken down into the same interaction channel categories discussed in Sec. 6.2.

Most of the low energy conclusions are supported by the medium energy analysis. It also shows a preference for a low Q^2 suppression, with large overpredictions in many low p_T bins, and shows similar model underpredictions in regions where there is predicted to be a large soft DIS contribution. The LE observation that bins with higher average W, and large true DIS contributions have good agreement with MINERvA tune v1 is seen to large extent in the medium energy results as well; with a notable exception being the cross sections at especially high energies with $40<p_{||}<60\,\text{GeV/c}$. This is a region that that medium energy analysis was able to probe that was inaccessible to the low energy analysis due to statistical limitations.
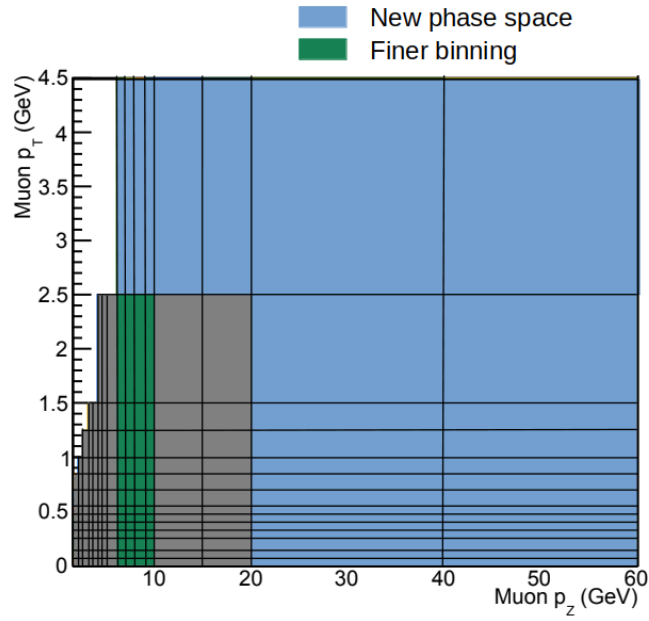
FIG. 6.38: The binning used for the medium energy version of the inclusive analysis, with the grey bins representing the bins used in the low energy analysis, green being regions where the binning became finner, and blue showing regions of expanded phase space.
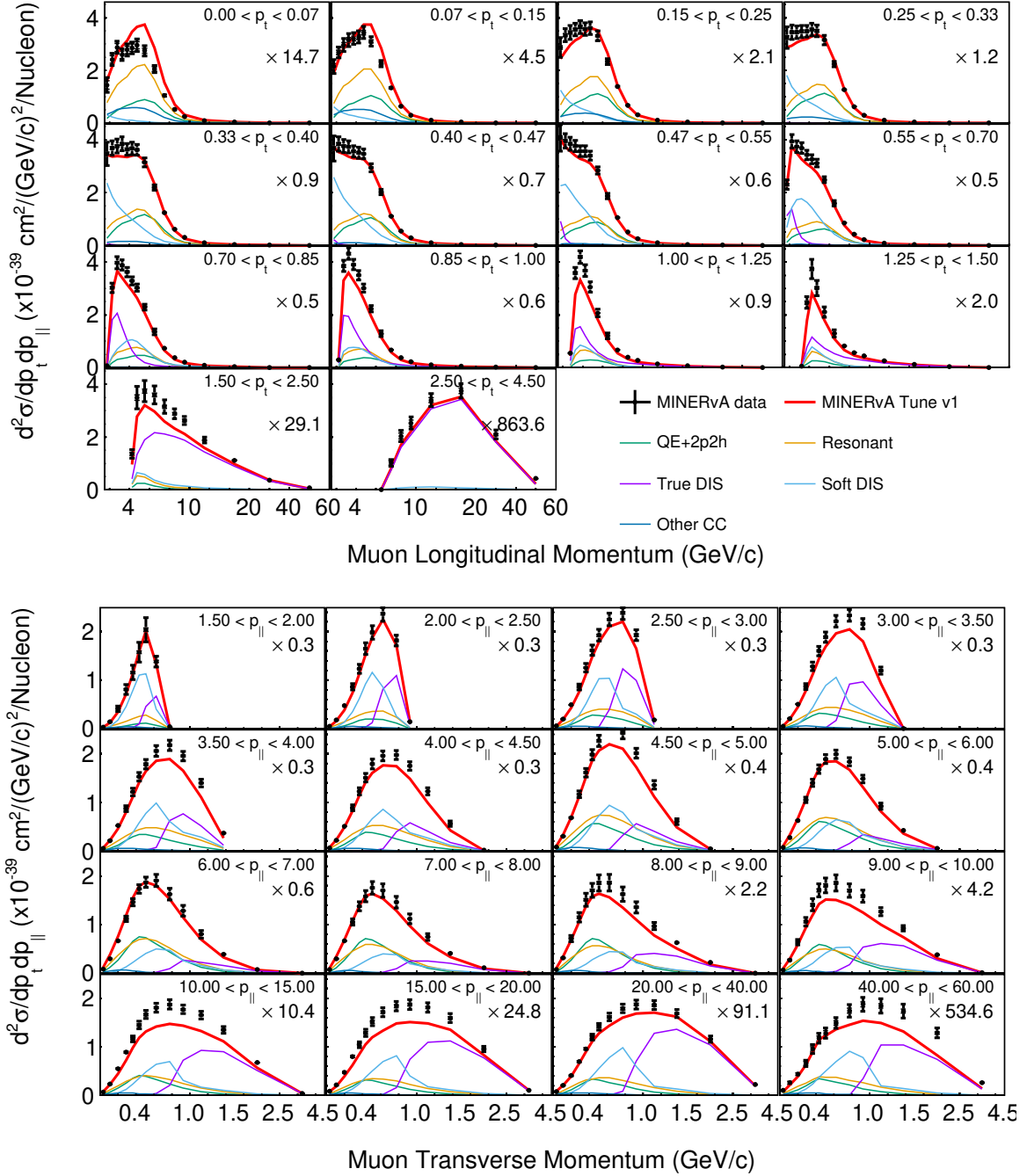
FIG. 6.39: The measured medium energy double-differential inclusive cross section as a function of longitudinal and transverse momentum, shown with MINERvA tune v1 and its unstacked interaction channel components. Inner error bar ticks represent statistical uncertainty, and the outer are statistical+systematic uncertainty.

128
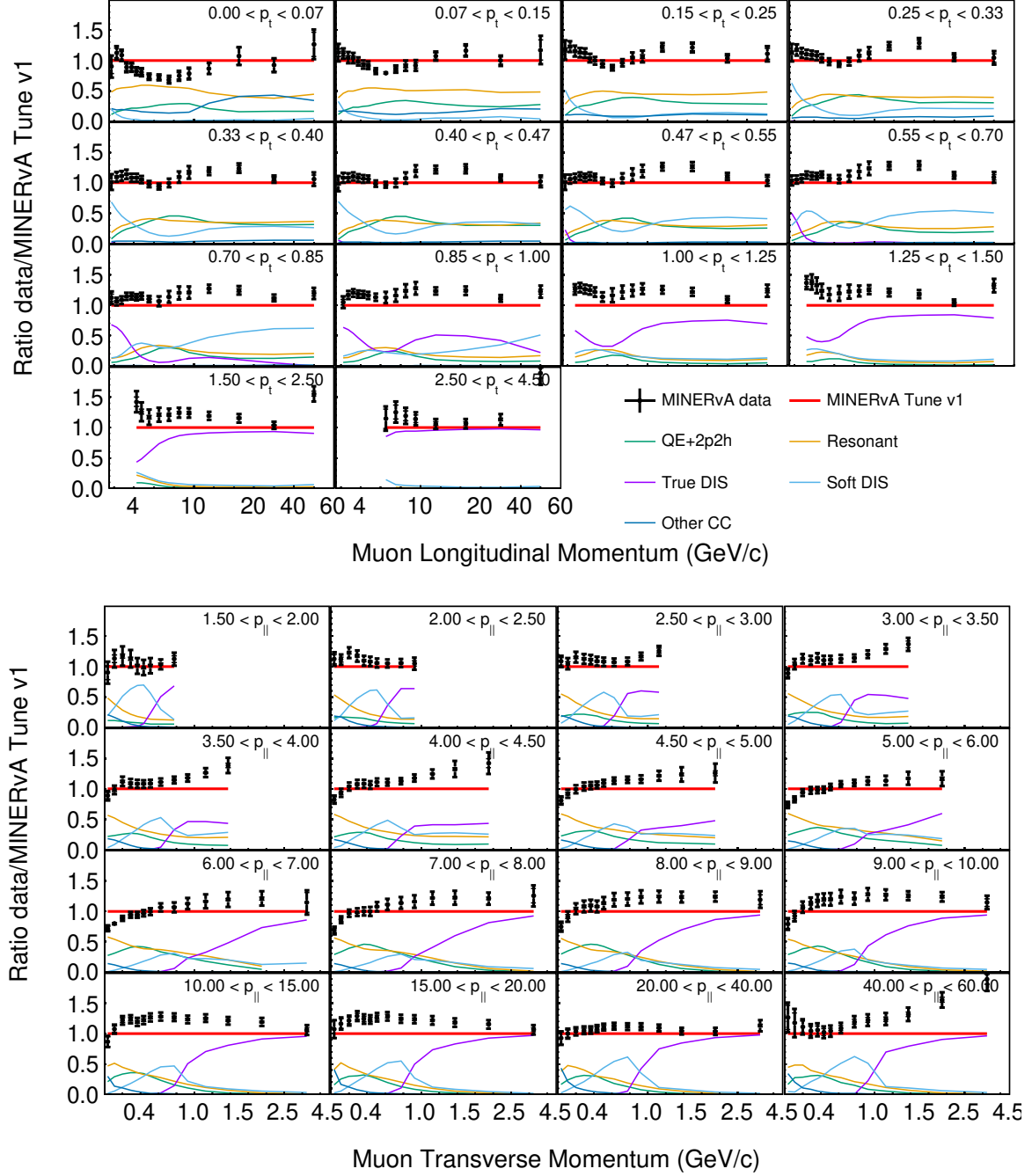
FIG. 6.40: The measured medium energy double-differential inclusive cross section as a ratio to MINERvA tune v1 and its unstacked interaction channel components. Inner error bar ticks represent statistical uncertainty, and the outer are statistical+systematic uncertainty.

CHAPTER 7

Deep Inelastic Scattering Measurement

7.1   Introduction

The analysis presented in this chapter measures deep inelastic scattering in the nuclear targets and active tracking volume of MINERvA. Cross sections on carbon, lead, iron and the active tracking scintillator (sometimes referred to as "tracker") are measured as functions of neutrino energy and Bjorken-x. Additionally, we measure cross section ratios of each of nuclear target to the scintillator cross sections in each variable. This analysis uses the medium energy neutrino mode data which was collected between September 2013 to February 2017.

The deep inelastic scattering region is defined as occupying a restricted kinematic region of the four-momentum transfer squared, Q^2, and the invariant mass W, defined as

$$Q^2 = 2E_\nu(E_\mu - p_\mu \cos(\theta_\mu)) - m_\mu^2, \tag{7.1}$$

for a charged current ν_μ interaction, where E_ν is the energy of the incident neutrino, E_μ is the energy of the muon produced in the interaction, θ_μ is the angle between the muon and the beam direction, and m_μ is the muon mass, and W defined as

$$W = \sqrt{m_{nucleon}^2 + 2m_{nucleon}(E_\nu - E_\mu) - Q^2} \qquad (7.2)$$

where $m_{nucleon}$ is the mass of the incident nucleon. When reconstructing this value, we take the average of the proton and neutron mass as we are not able to reconstruct which nucleon was struck and use the associated mass. When we determine the true W in simulations we use the mass of the nucleon that was truly struck.

Neutrino energy was chosen as a measurement variable in this analysis because the absolute cross sections, which can be found are then able to be used in direct comparisons to other experiments that are exposed to different neutrino fluxes. The kinematics of the interactions are also highly dependent on the neutrino energy. Since the neutrino energy is not directly observable, it is reconstructed from the the energy of the outgoing muon and the total hadronic energy,. Measurements in Bjorken-x are a useful way to study different nuclear effects. The Bjorken-x scaling is defined as:

$$x_{bj} = \frac{Q^2}{2m_{nucleon}(E_\nu - E_\mu)} \qquad (7.3)$$

Bjorken-x is used to probe the structure functions of deep inelastic scattering on nucleons, where x_{bj} is the fraction of the nucleon momentum carried by the quark struck by the neutrino. Further discussion around the Bjorken scaling variables is included in Ch. 1.

7.2   Signal definition

In this analysis, the requirements for an interaction to be included within our signal definition are as follows:

- ν_μ CC interaction,

- $Q^2 >1.0$ GeV^2,

- $W>2.0$ GeV,

- Muon angle less than 17 °,

- Muon energy between 2 and 50 GeV,

- Interaction vertex in the specified target and material.

The first three requirements are based on the types of physics we wish to study, while the next two signal definition requirements are in place as to avoid regions in that we have drastically changing acceptance. As with the double-differential inclusive analysis, attempting to measure cross sections in these regions where the acceptance is rapidly decreasing would introduce significant model bias, which we wish to avoid.

7.3   Event selection

Though we are measuring a single cross section for each nuclear target material, this analysis is done on a target by target basis for the event selection through to the efficiency correction stages. Only after efficiency correction are all of the targets of a single nuclear material summed together. Thus we perform 11 parallel event selections, one for the active tracking region, one for each of the 4 iron target regions, one for each of the 5 lead targets,

and one for the sole passive carbon target. These are the requirements for an interaction to be selected for a given target event selection:

- There is a muon track reconstructed in MINERvA, which is matched with a muon track in the MINOS ND.

- A negative muon curvature measured in MINOS with 5σ significance.

- The reconstructed muon angle is less than 17 °.

- The reconstructed muon energy between 2 and 50 GeV.

- Reconstructed Q^2 >1.0 GeV^2.

- Reconstructed W >2.0 GeV.

- The reconstructed vertex is within the specified target fiducial region (ie. in the iron wedge of target 1, lead wedge in target 3, the tracker fiducial volume, etc.).

- The plane probability confidence given by the machine learning vertexing algorithm is greater than 0.2 for the nuclear targets. This requirement removes events in which the machine learning vertexing was unable to confidently place the vertex position.

- The vertex must be within the 850 mm apothem of the plane.

- Vertex (x, y) position must be further than 25 mm away from the region where different materials meet up (in targets 1, 2, 3, 5).

- No more than one TriP-t (and associated PMT) are experiencing deadtime in the planes upstream of the muon track. This helps avoid contamination from rock muons.

- There are no average energy deposits from 1.5 to 6.5 MeV for 7 or more planes upstream of the interaction vertex. This protects against having a misreconstructed ML-predicted vertex downstream of the true vertex.
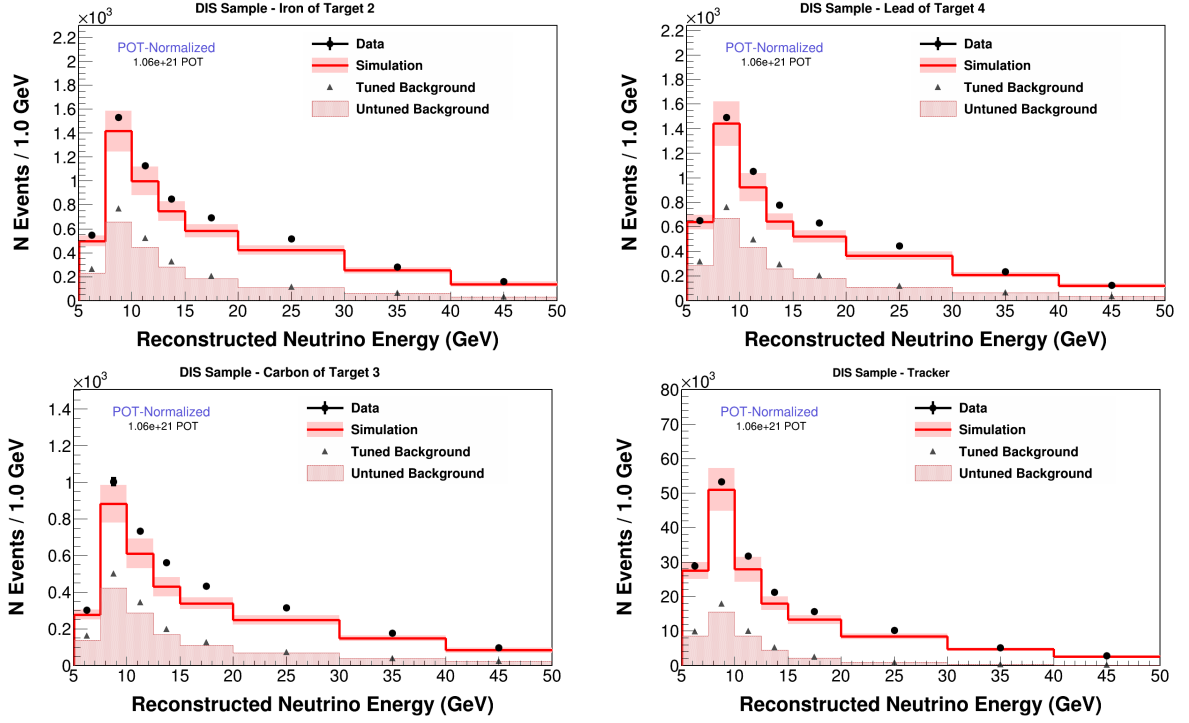
FIG. 7.1: Data (black) and MC (red) event selection distributions in E_ν for iron of target 2 (top left), lead of target 4 (top right), carbon of target 3 (bottom left), and tracker (bottom right). Data has statistical error bars only, and MC shows statistical+systematic uncertainties. Also shown are the untuned MC predicted backgrounds and simulated backgrounds with scale factors applied.

As there are a large number of different targets which this analysis is performed in, I will only be showing a selected subset of those targets throughout this chapter. A full suite of plots for all of the targets is always available in Appendix B. The selected events as a function of neutrino energy are shown in Fig. 7.1. The data only has statistical errors at this point in the analysis, so the statistical+systematic uncertainties are shown as a error band on the simulation. These figures also include the predicted background events for the data (tuned background) and MC (untuned background). These backgrounds are discussed in detail in Sec. 7.4. The companion set of these plots as a function of Bjorken-x are shown in 7.2.
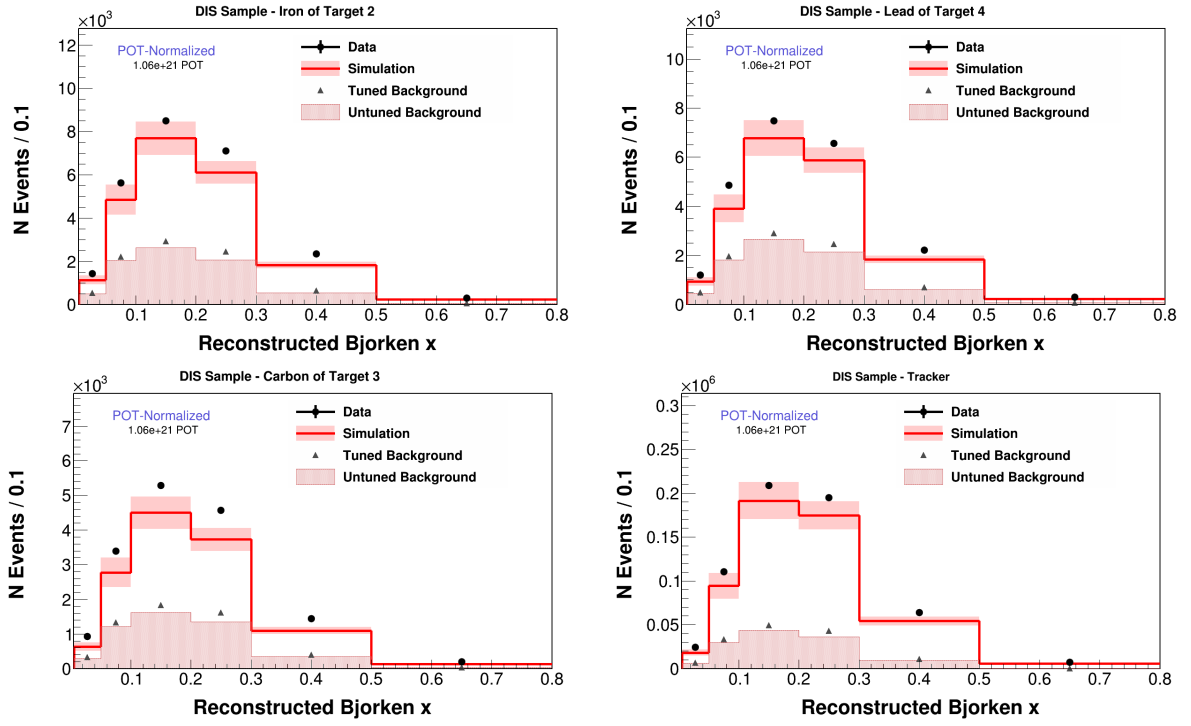
FIG. 7.2: Data (black) and MC (red) event selection distributions in x_{bj} for iron of target 2 (top left), lead of target 4 (top right), carbon of target 3 (bottom left), and tracker (bottom right). Data has statistical error bars only, and MC shows statistical+systematic uncertainties. Also shown are the untuned MC predicted backgrounds and simulated backgrounds with scale factors applied.

7.4 Background constraints and subtraction

There are two major types of background that contaminate the selected event distribution in this analysis; interactions that took place in a different material and non-DIS events that do not pass the true W and Q^2 thresholds in the signal definition due to detector resolution. We refer to the latter set of background contamination as "physics background", since it consists of interactions with different physical kinematics then those we are interested in studying in this analysis.

In order to minimize the dependence on an imperfect cross section model when removing background events from our selected sample, we perform data based constraints on the predictions using sideband regions, as introduced in Ch. 5.1.2. This analysis uses a total of four different sidebands regions, two that help constrain the wrong target background, and two that help constrain the physics background.

The selected DIS events in each of the lead targets are shown in Fig. 7.3, with stacked histogram showing the true interaction material of the simulated events. The wrong material events are primarily originating from interactions in the plastic scintillator upstream and downstream of the target, with a smaller contribution coming from interactions in the neighboring target materials.

7.4.1 Wrong target material sidebands

When studying the wrong target material events we look at an inclusive event distribution which does not have the reconstructed W and Q^2 selection cuts applied to it. The reason for doing this is that the subtraction of wrong target backgrounds is smaller and precedes the subtraction of physics backgrounds. Therefore the wrong target contamination comes from a range of events with different true kinematic properties, not exclusively true DIS interactions.
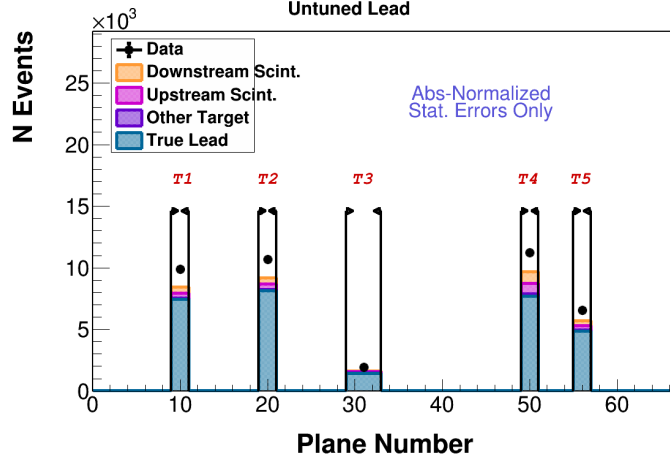
FIG. 7.3: Selected simulated and data DIS events reconstructed in the lead targets, with a breakdown of the true interaction material of the corresponding simulated events.

Otherwise, the selection that we perform in the wrong target sideband regions is very similar the signal region event selection. All of the same cuts, based on the muon track and kinematics, as well as the requirements on interaction vertices within a 850 mm apothem, maximum upstream deadtime, and the maximum amount of upstream detector activity are used. The primary difference in this sample (aside from the inclusive vs DIS kinematic selection), is the positions of the selected interaction vertices.

There are two different sidebands used for each nuclear target material that select regions which shadow the (x, y) shape of the targets in the planes upstream and downstream of the targets. We select a region of 6 planes upstream (downstream) of the nuclear target, where there is a single plane downstream (upstream) of the sideband region and upstream (downstream) of the target that is used as a buffer region between the target and the sideband planes.

The sideband regions for all of the targets of each material are combined into a single upstream sideband (i.e., targets 1, 2, 3, 4 and 5 for lead), and a single downstream sideband. This is done to allow for sufficient statistics. A χ^2 minimizing fit is then performed to determine the scale factor for each sideband. The scale factors are then used
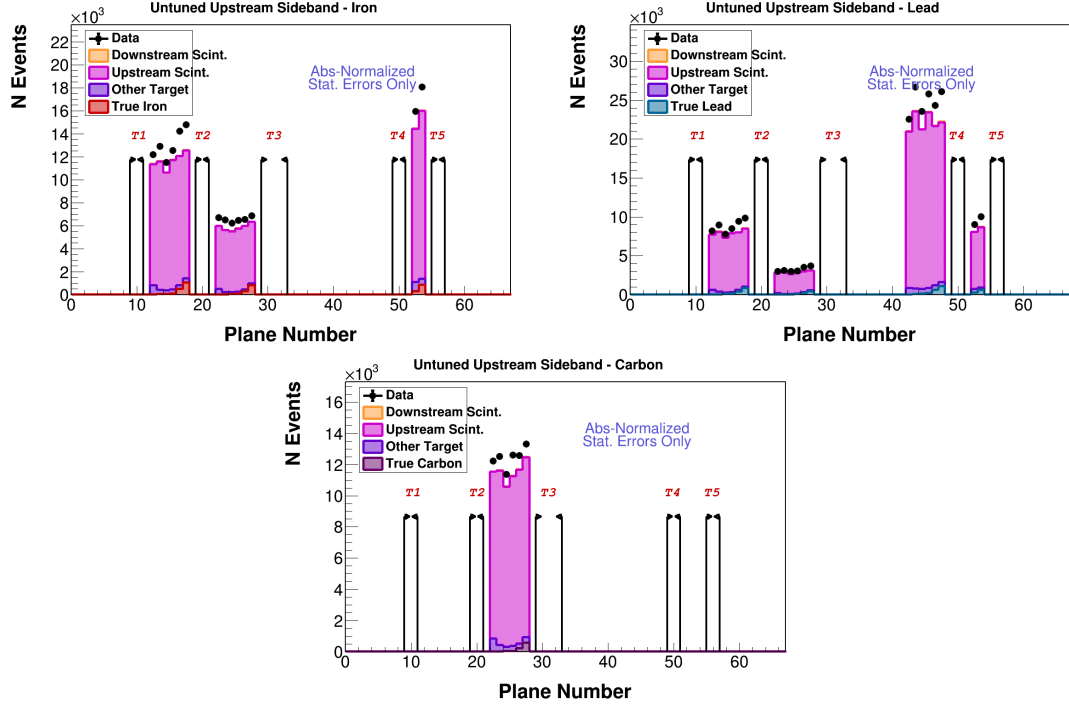
FIG. 7.4: The upstream scintillator sidebands before tuning for all of the iron targets (top left), all of the lead (top right), and the carbon (bottom).

to tune the MC predictions for the data background subtraction process.

The upstream sideband region as a function of the plane number is shown in Fig. 7.6 before any fits are applied. The corresponding untuned downstream sideband distributions in each target material are shown in Fig. 7.7.

The tuned upstream sideband region as a function of the plane number is shown in Fig. 7.6 for all nuclear target materials, with the tuned downstream sideband shown in Fig. 7.7.
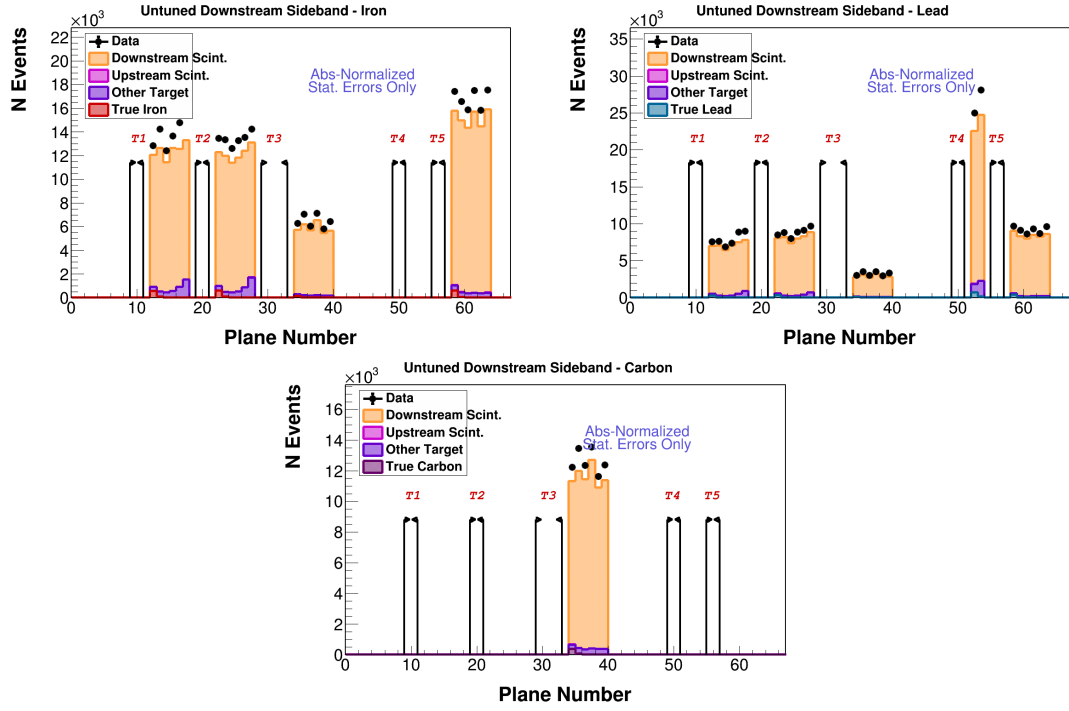
FIG. 7.5: The downstream scintillator sidebands before the tuning for all of the iron targets (top left), all of the lead (top right), and the carbon (bottom).
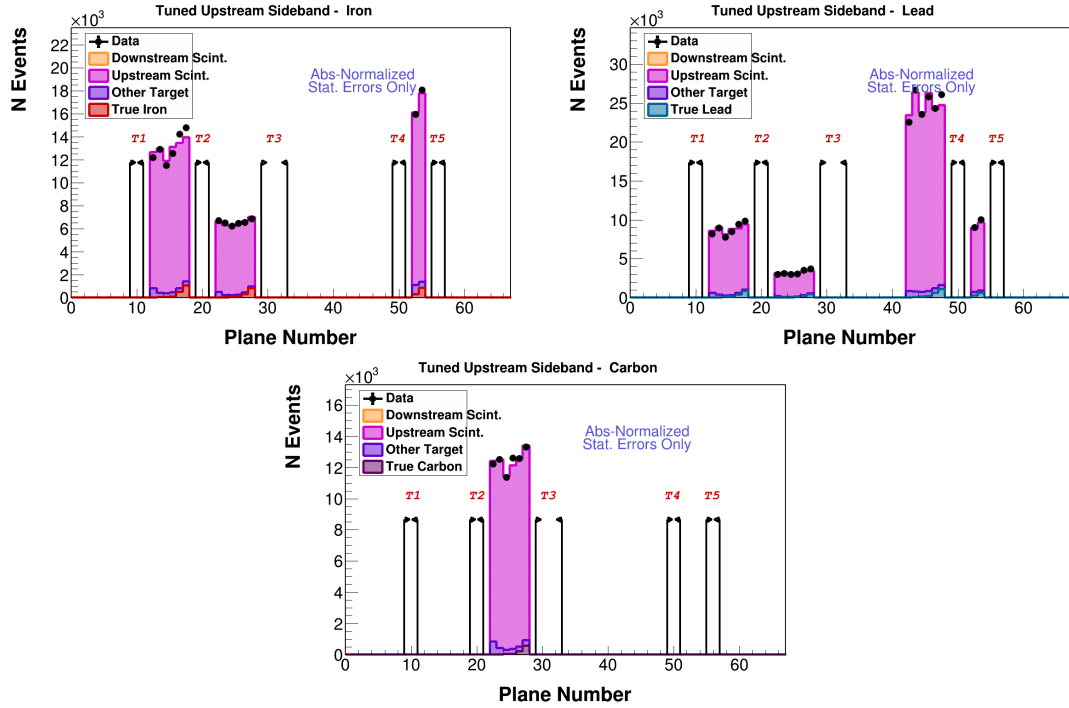
FIG. 7.6: The upstream scintillator sidebands after the tuning was applied for all of the iron targets (top left), all of the lead (top right), and the carbon (bottom).
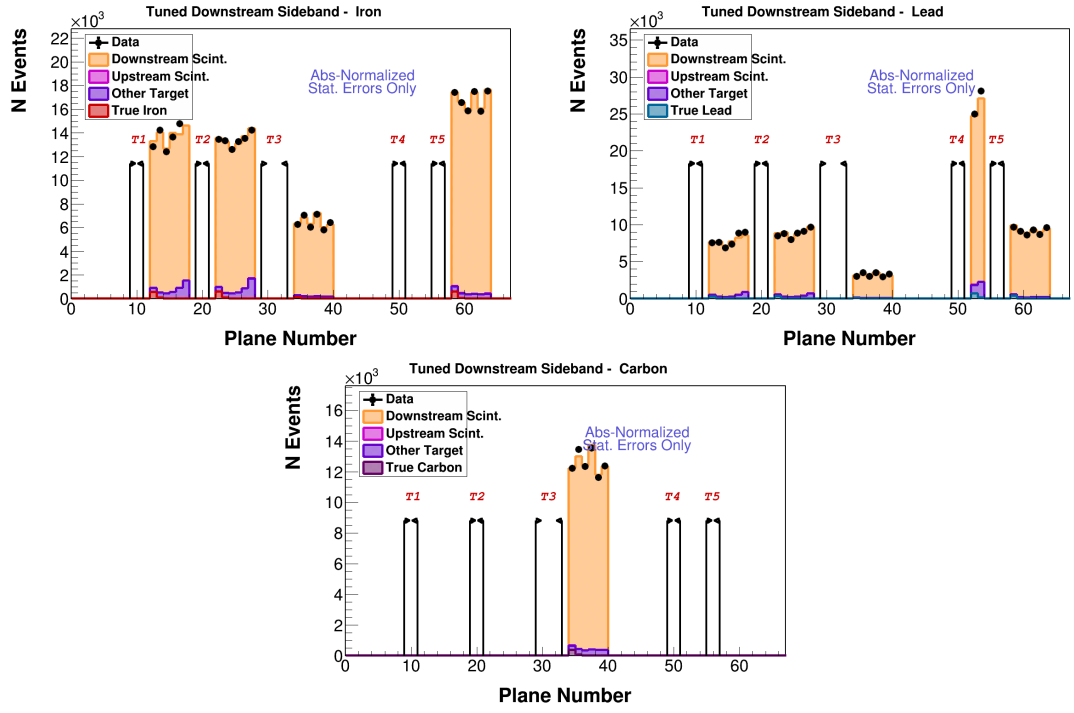
FIG. 7.7: The downstream scintillator sidebands after the tuning was applied for all of the iron targets, all of the lead, and the carbon from left to right.

7.4.2 Physics Sidebands

The physics sideband regions select events with either a Q^2 or W slightly below the threshold for the selected region. These regions are optimized to have a large portion of events that have true kinematic quantities similar to the background events entering the selected selected region, while attempting to minimize the contributions of true DIS events within the reconstructed sideband. Studies had been done with varying sideband definitions before determining that these definitions were optimal [12]. The sideband regions are shown in W–Q^2 space in Fig. 7.8, where the black rectangles are the regions for the selected sidebands and are based on reconstructed quantities. Also shown are three different color regions which are used to classify the true kinematics of the event and are based on the true W and Q^2. The degree to which events truly belonging in each kinematic region smear into different Q^2 and W regions can be seen in the Fig.7.9. This figure shows a scatter plot of the reconstructed W and Q^2 of events truly lying in the DIS and sideband regions for iron. Events with both true low W and true low Q^2 smear into both sideband samples, but are classified as true transition events, resulting in a larger fraction of true transition contamination in the low Q^2 sideband than vice versa.

The physics scale factors are found using a joint fit of both the transition and continuum sidebands in E_μ. The scale factors are applied based on the true kinematic regions, not the reconstructed ones. So the true continuum in the low Q^2 sideband region and the true continuum in the low W sideband region are scaled by the same amount, with the same thing holding for all of the true transition events in each sideband. The true DIS events which are reconstructed into the sideband regions do not have any scale factors applied to them.

Before fits to the physics sidebands are performed, we first subtract wrong target backgrounds. The upstream and downstream scintillator background in the transition
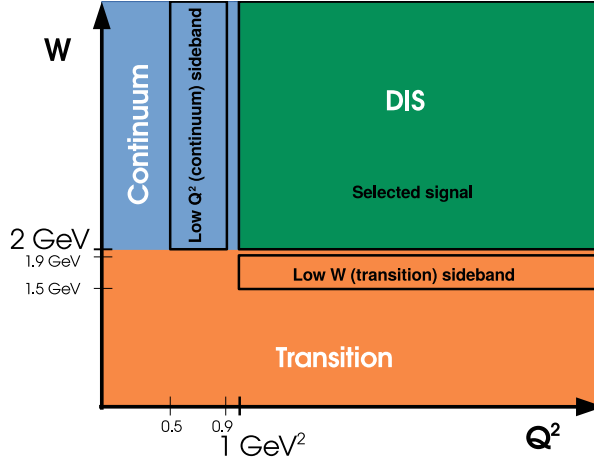
FIG. 7.8: Diagram of the signal and physics sideband regions. The sidebands in black are defined based on reconstructed kinematic definitions, while the colored regions which are used to classify the simulation in other figures are based on the true event kinematics.

Material	Upstream CH	Downstream CH	Transition	Continuum
Lead	1.12	1.10	1.33	0.88
Iron	1.12	1.11	1.35	0.92
Carbon	1.08	1.09	1.42	0.97
Scintillator	-	-	1.23	1.05

TABLE 7.1: The scale factors for the upstream and downstream scintillator background, and transition and continuum physics backgrounds for each material.

and continuum sidebands are each tuned using the scale factors determined in the previous analysis step, and subtracted from the data of each physics sideband. The untuned wrong target backgrounds are similarly removed from the MC distributions.

Fig. 7.10 shows the events selected in the reconstructed low Q^2 sideband region. The simulation is divided into three different categories based on the true W and Q^2 of the event, using the definitions shown in Fig. 7.8. The untuned low W sideband for each target material is shown in Fig. 7.11.

The summed distributions after the tuning is applied in each of the sidebands are shown in Fig. 7.12 for iron, and Fig. 7.13 for the tracker region along with their error summaries. The uncertainty coming from the sidebands will be discussed in Sec. 7.4.3. Additional plots of the lead and carbon, as well as other variable distributions are included

142
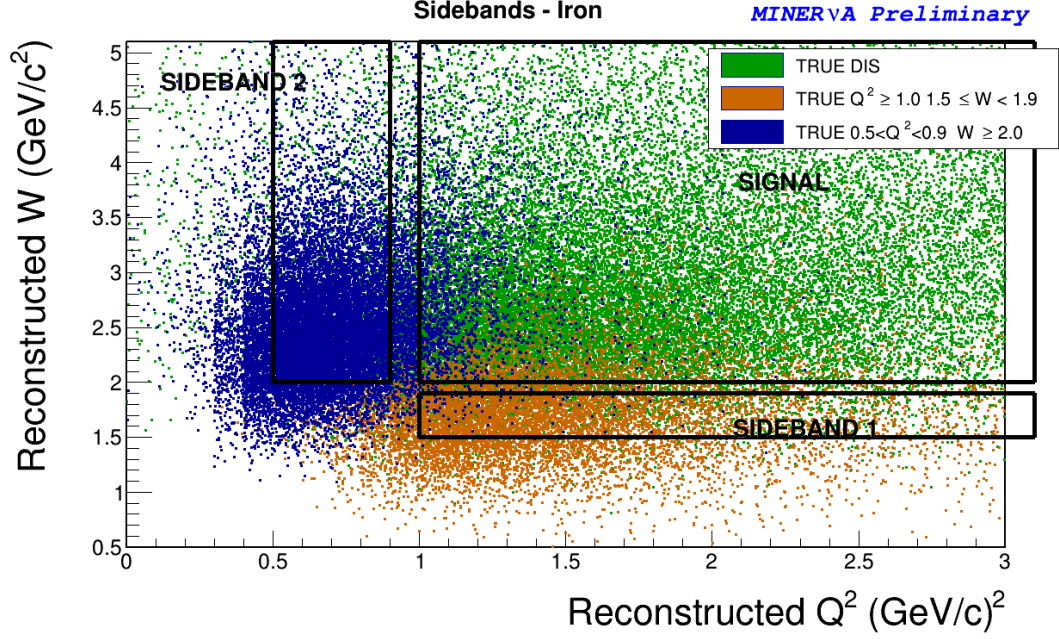
FIG. 7.9: Scatter plot of true DIS (green), true low W (orange), and true low Q^2(blue) events as a function of reconstructed kinematics.

in Appendix B.

7.4.3 Uncertainties on sideband Data/MC agreement

After performing the sideband fit and tuning the MC, there were still $> 1\sigma$ discrepancies between the data and MC in the sideband due to shape differences that cannot be accounted for with uniform scale factors. The purpose of doing a sideband fit is to ensure that we can accurately understand and predict the data backgrounds, however this discrepancy indicates that we are do not fully understand our sideband regions to the precision that is indicated by the uncertainties. Therefore we add an additional uncertainty to the scale factors after the fits in order to account for any remaining discrepancies.

An uncorrelated bin by bin uncertainty is added as a function of muon energy for each of the sidebands, where the uncertainty is calculated so that the total uncertainty after its addition has the data within less then or equal to $1\ \sigma$ away from the MC in all
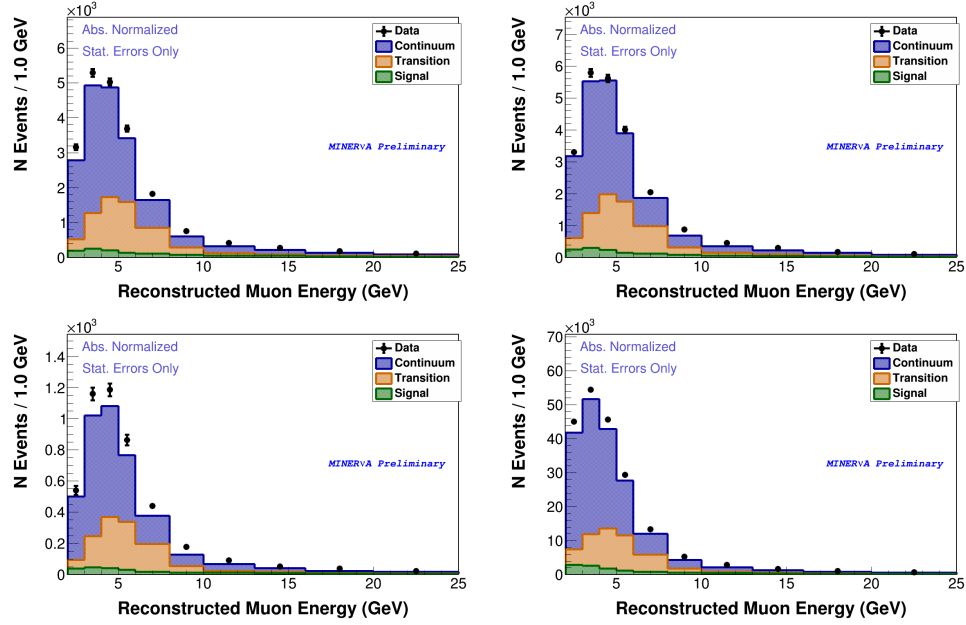
FIG. 7.10: The continuum sideband before tuning in E_μ for all of the iron (top left), lead (top right), carbon(bottom left) and tracker (bottom right). The simulation is broken down into different true kinematic regions, which are shown stacked on top of each other.

bins of muon energy. The additional uncertainties in E_ν and x_{bj} are a function of the E_μ uncertainties for the muon energy corresponding to events in each bin. An example showing the tuned transition sideband data/MC ratio with systematic uncertainties on the MC with and without the added uncertainty for the iron targets are shown in Fig. 7.15.

The backgrounds in turn then also have this additional uncertainty associated with it, as the scale factor uncertainty gets propagated to the backgrounds when the tuning is applied.

The uncertainty summary on each of the scale factors for iron are shown in Figs. 7.16 and 7.17. The scale factor error summaries on the remaining materials can be found in Appendix B.4. Since a single constraint is applied throughout the entire phase space, there is no variable dependence in the standard uncertainties. The only variable dependence comes from the added sideband uncertainties.
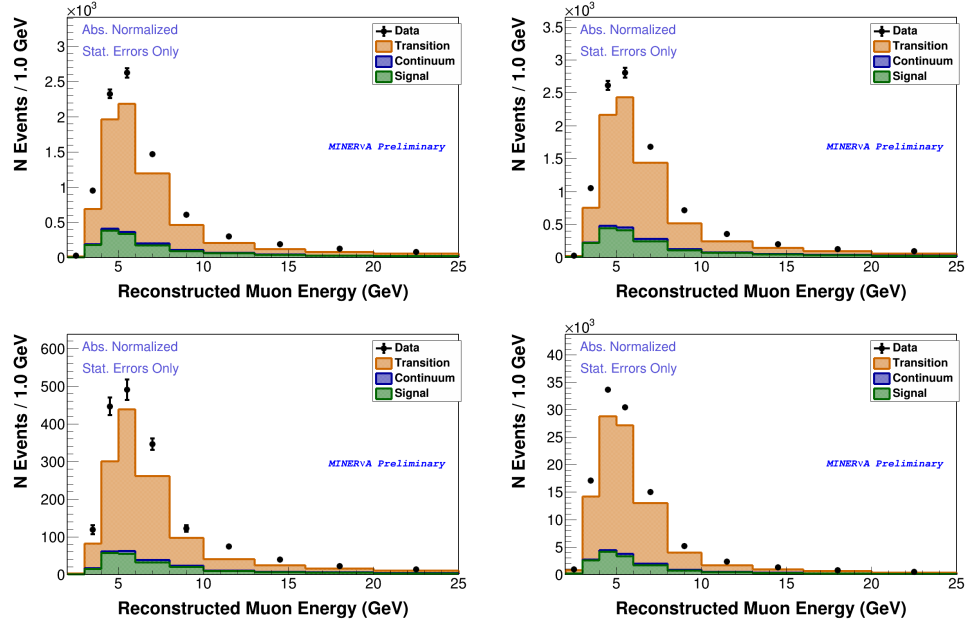
FIG. 7.11: The transition sideband before tuning in E_μ for all of the iron (top left), lead (top right), carbon(bottom left) and tracker (bottom right). The simulation is broken down into different true kinematic regions, which are shown stacked on top of each other.

7.4.4 Background subtraction

In the nuclear targets the predicted MC backgrounds from upstream and downstream scintillator contamination have their associated scale factors applied to them, and are summed together along with the backgrounds from interactions taking place in other target materials (i.e., an iron interaction in the lead event selection) and events with a true vertex outside of the defined fiducial volume (either outside of the 850 mm apothem, or too close to the other target materials). The latter two of these backgrounds do not have a data driven constraint applied to them, as they are make up a much smaller fraction of backgrounds than the scintillator backgrounds. These tuned (untuned) backgrounds are the subtracted from the data (simulation) distribution of selected events. In the tracker, a small number of events with true vertices outside of the apothem fiducial volume are subtracted. After wrong material and fiducial volume backgrounds have been taken care of, the same procedure is applied with the low Q^2 and low W background events in all

145
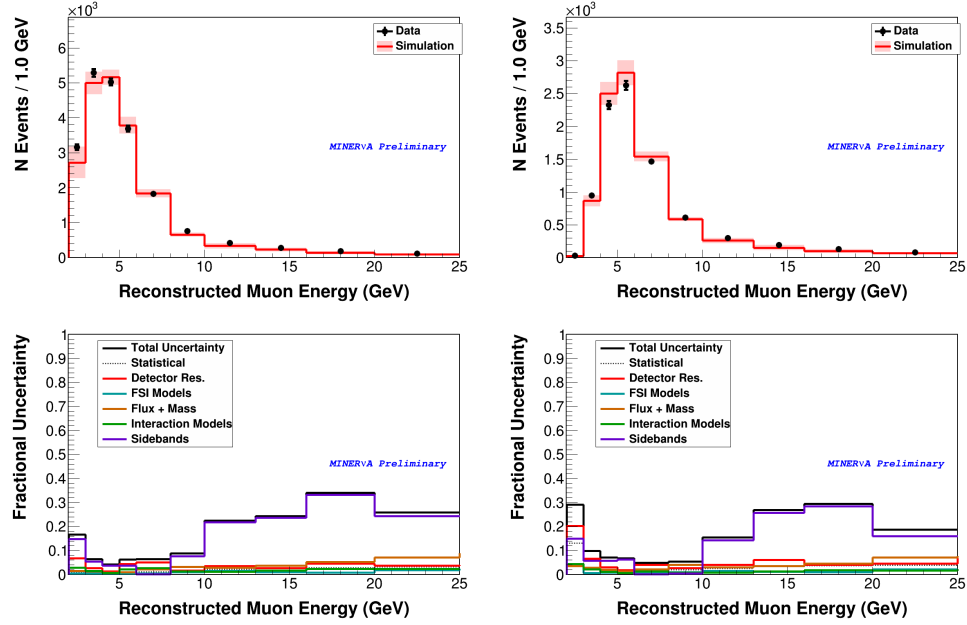
FIG. 7.12: The continuum (left) and transition (right) sidebands after tuning has been applied in iron (top) and their associated data error summaries (bottom).

materials. The scale factors determined for each material and sideband region are shown in Table 7.1.

A breakdown of the background contributions in one target of each material are shown in Figs. 7.18, 7.19 for E_ν and x_{bj}, respectively. The summed backgrounds are shown along with the selected signal region distributions in Figs. 7.1 and 7.2.

A subdominant portion of the background events originate from neutral current and $\bar{\nu}_\mu$ CC events. These are not explicitly handled at the background subtraction stage if the events have true W and Q^2 within the true DIS region, as they do not contribute significant background. Instead they are accounted for at the efficiency correction stage by including them in the efficiency numerator, but not the efficiency denominator.

The background subtracted distributions for a target of each material are shown as Fig. 7.20 and 7.21 with a full set of the targets in Appendix B.

146
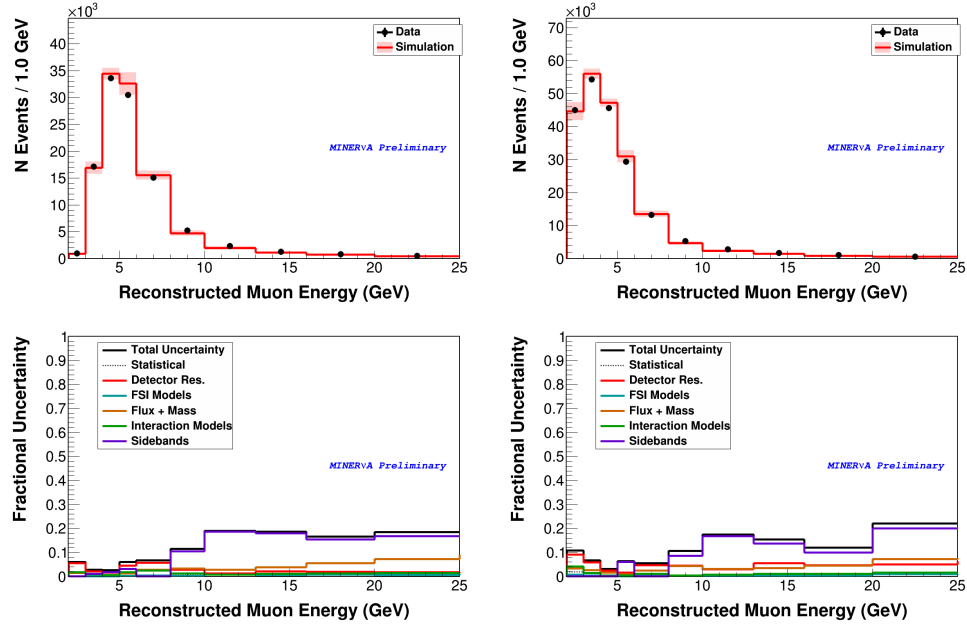
FIG. 7.13: The continuum (left) and transition (right) sidebands after tuning has been applied in tracker (top) and their associated data error summaries (bottom).
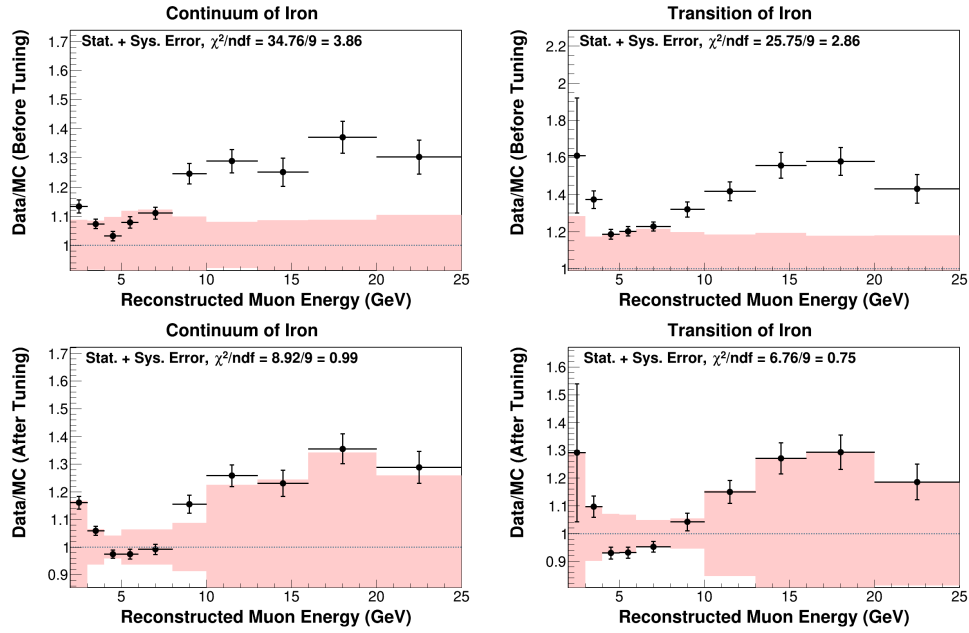
FIG. 7.14: Data/MC ratios for the physics sidebands in iron. Before tuning (top), and after tuning (bottom) for continuum (left) and transition (right) sidebands.
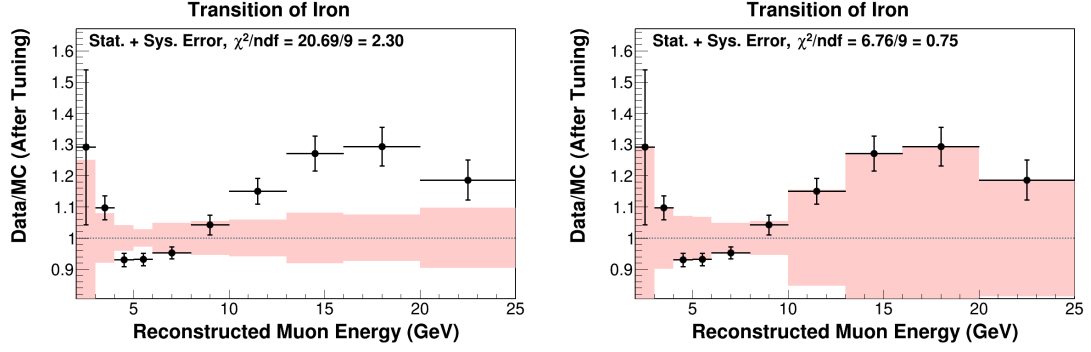
FIG. 7.15: The tuned iron transition sideband ratio of data to MC before (left) and after (right) adding an additional uncertainty which covers any tuned data/MC sideband discrepancies. The pink band represents the total statistical+systematic uncertainties on the tuned simulation.
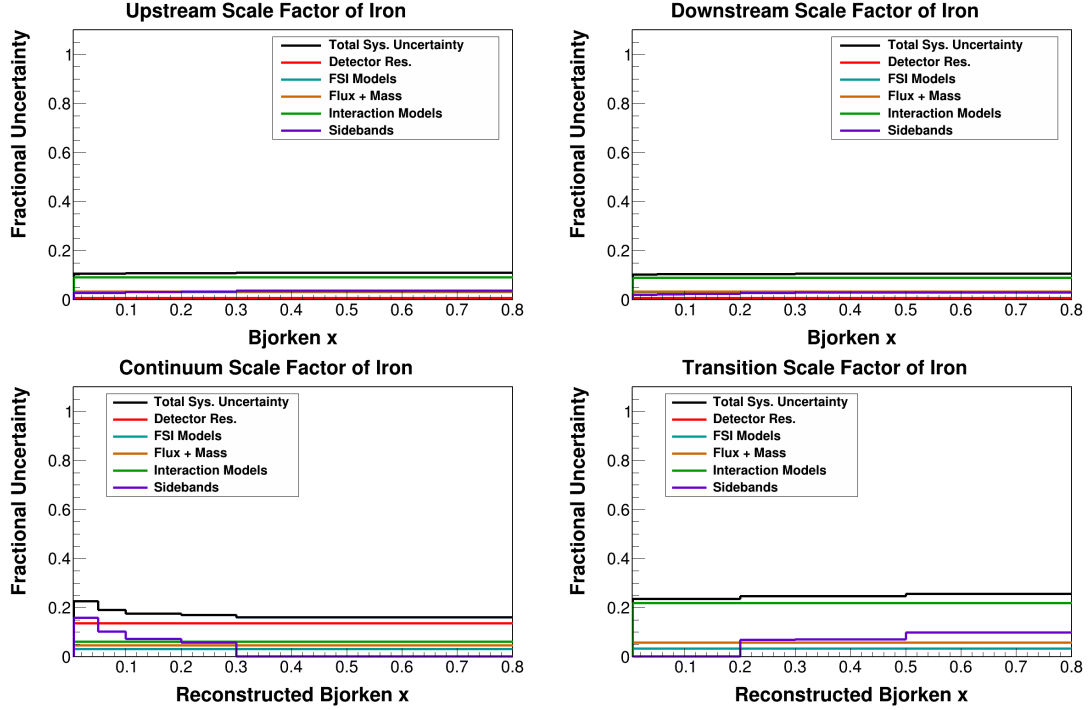
FIG. 7.16: Error summaries for the upstream (top left), downstream (top right), continuum (bottom left) and transition (bottom right) x_{bj} scale factors in iron.

148
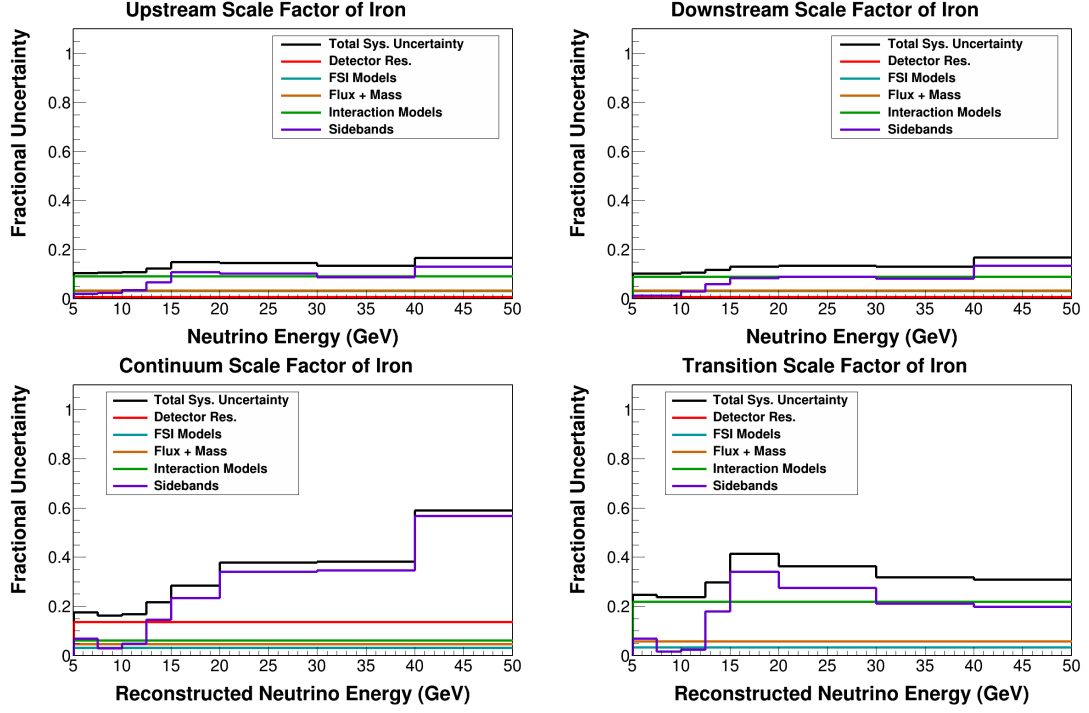
FIG. 7.17: Error summaries for the upstream (top left), downstream (top right), continuum (bottom left) and transition (bottom right) E_ν scale factors in iron.
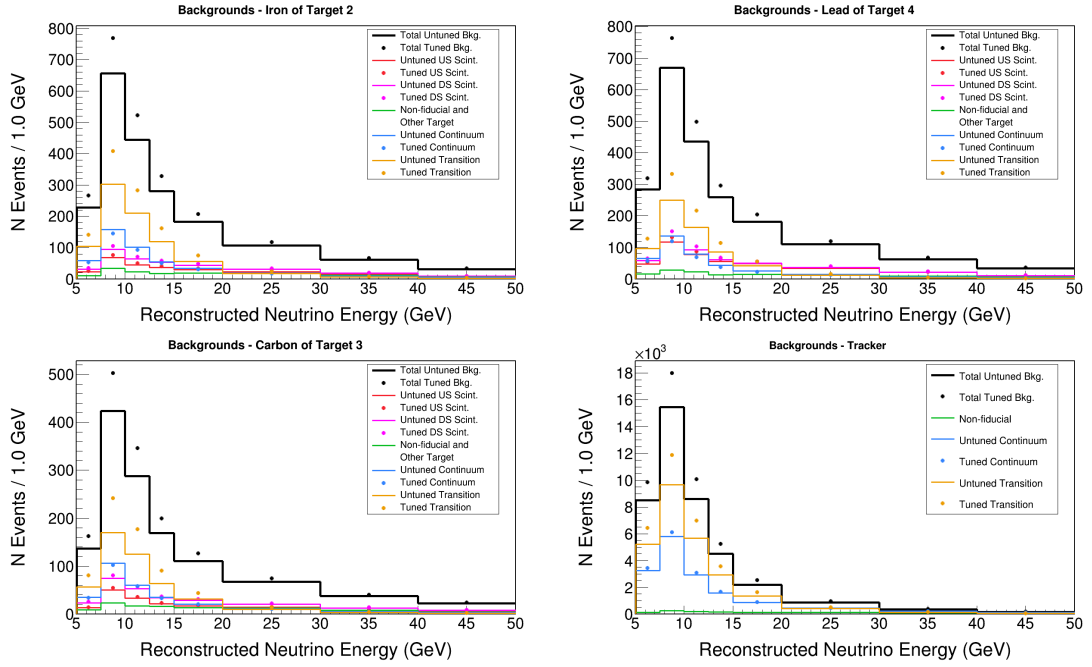
FIG. 7.18: The untuned and tuned E_ν background event contributions to the selected regions in the iron of target 2 (top left), lead of target 4 (top right), carbon target (bottom left), and tracker (bottom right).
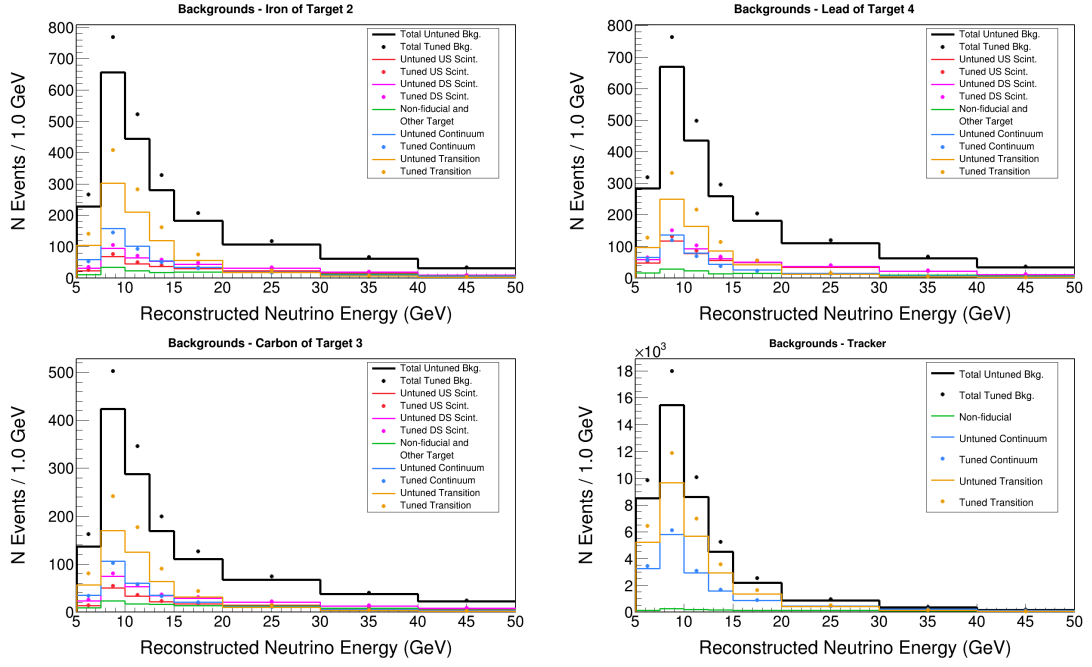
FIG. 7.19: The untuned and tuned x_{bj} background event contributions to the selected regions in the iron of target 2 (top left), lead of target 4 (top right), carbon target (bottom left), and tracker (bottom right).
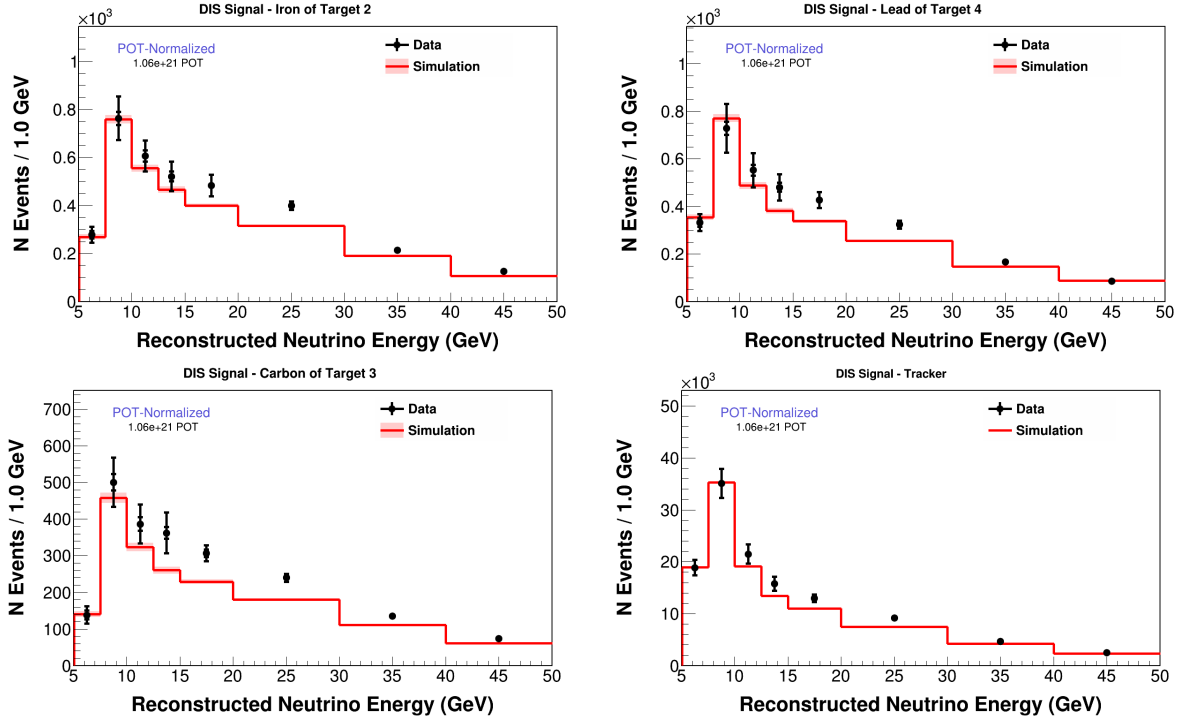
FIG. 7.20: Data (black) and MC (red) background subtracted event distributions in E_ν for iron of target 2 (top left), lead of target 4 (top right), carbon of target 3 (bottom left), and tracker (bottom right). Data has systematic+statistical error bars, and MC shows statistical uncertainties.
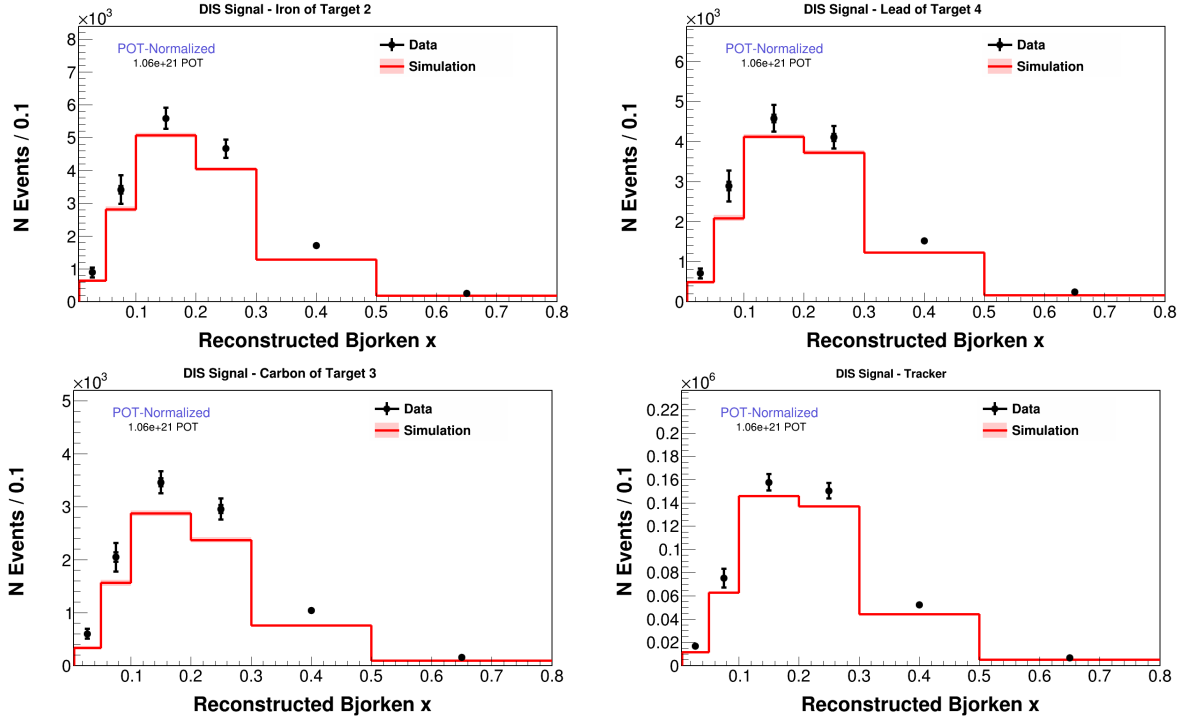
FIG. 7.21: Data (black) and MC (red) background subtracted event distributions in x_{bj} for iron of target 2 (top left), lead of target 4 (top right), carbon of target 3 (bottom left), and tracker (bottom right). Data has systematic+statistical error bars, and MC shows statistical uncertainties.

7.5 Migration matrices and unfolding

7.5.1 Migration matrices

The migration matrices derived from the simulation showing the true E_ν vs the reconstructed E_ν are shown in Fig. 7.22 for iron of target 1. The migration matrices for the remaining targets can be found in Appendix B.5.1. The equivalent migration matrices for x_{bj} are shown in Fig. 7.23 and Appendix B.5.2. The events included in these migration matrices pass all of our event selection criteria, and only true DIS events in the true material are included, however the true muon angle and energy restrictions are not applied as those events can be smeared into the background subtracted sample. As with the wrong sign events, events with which fail true angle and energy cuts are accounted for at the efficiency correction stage. The background subtracted MC will contain the same exact events in it as the migration matrix. The background subtracted event distributions are separately unfolded in each target and material, using the migration matrix for that specific target.

The distributions in E_ν and x_{bj} after unfolding are shown in Fig. 7.24 and 7.25. The migration matrices are mostly diagonal indicating that we are largely able to reconstruct the correct values within the precision of the bin widths, however, the neutrino energy distribution is better reconstructed than the Bjorken-x distribution. In neutrino energy, the majority of bins have more than 60% of the events reconstructed in the bin of their true quantity. There are also very few events in which the neutrino energy is drastically misreconstructed (more than a couple bins away from their true value). In Bjorken-x there is slightly more smearing, with most bins more than 50% diagonal, because the bins were defined with greater interest in preserving regions of distinct nuclear effects than producing a highly diagonal migration matrix. Bjorken-x is also a more challenging

Migration - Iron of Target 1

Percent of Events in Each Neutrino Energy (GeV) Bin - Iron of Target 1
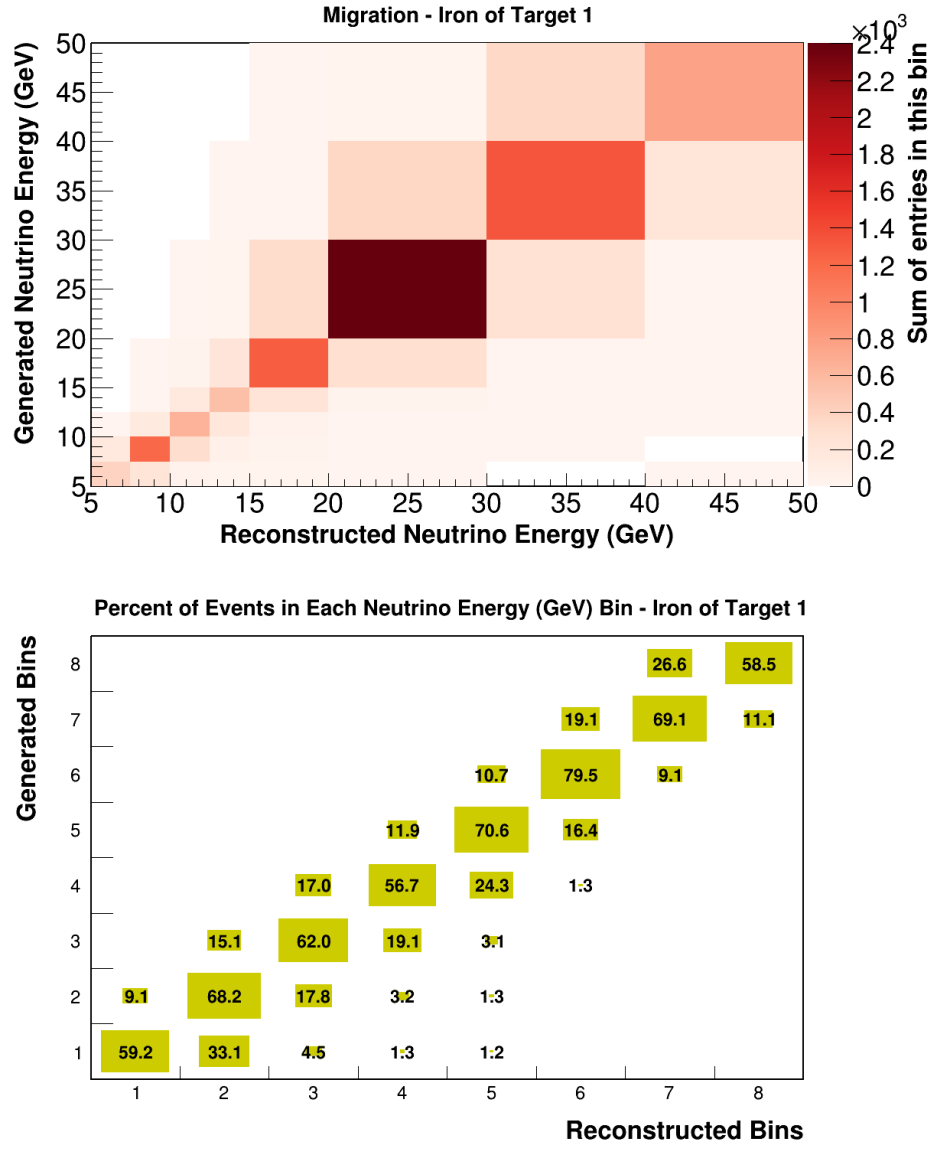
FIG. 7.22: The population of events in migration matrix (top), and the row normalized percentage of events by bin number (bottom) for the iron of target 1 in E_ν.
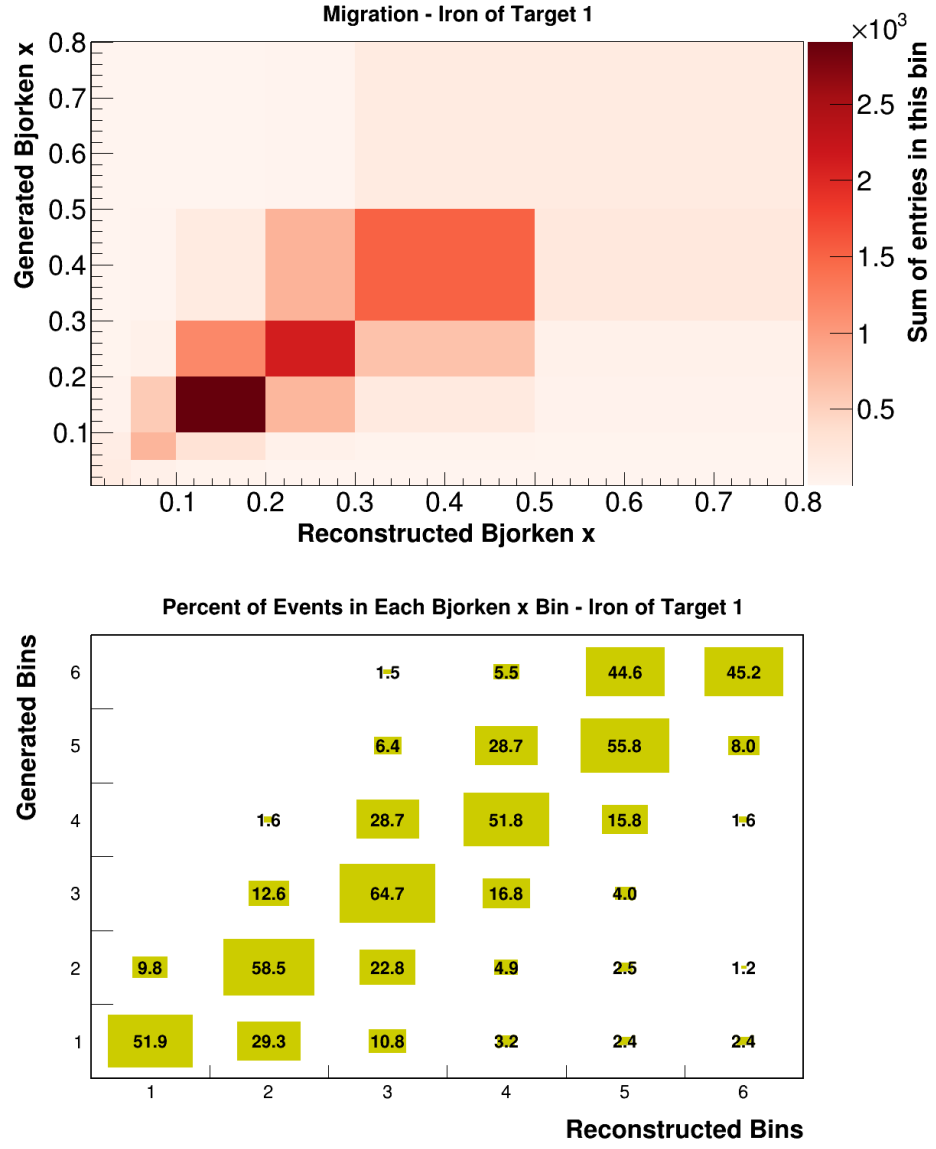
FIG. 7.23: The population of events in migration matrix (top), and the row normalized percentage of events by bin number (bottom) for the iron of target 1 in x_{bj}.
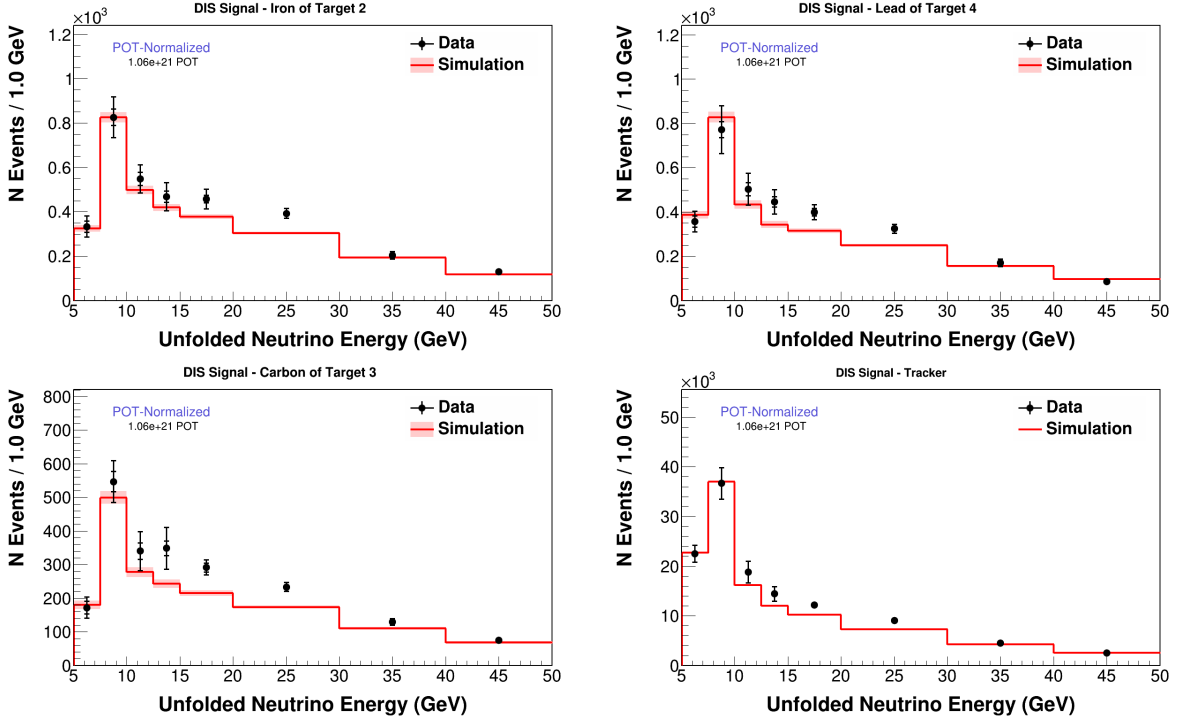
FIG. 7.24: The selected event sample in E_ν after background subtraction and unfolding.

variable to reconstruct than E_ν. The lowest and highest bins in x_{bj} have the lowest fraction of events which were reconstructed in the correct bin, with only 40-50% of true events reconstructed in the correct bin (exact numbers vary by target).

7.5.2 Unfolding studies

As was described in Ch. 5.1.3, we perform a series of studies to test that we are accurately able to unfold all of the reconstructed variable distributions to their corresponding true variable values. In this analysis we are unfolding two sets of variables over many different target materials, so many tests need to be performed to be sure both the target and tracker regions are able to accurately unfold both variables. Unfolding is done independently in each variable.

The tracker is divided into 12 separate radially sliced petals, described in Ch. 3.6.2,
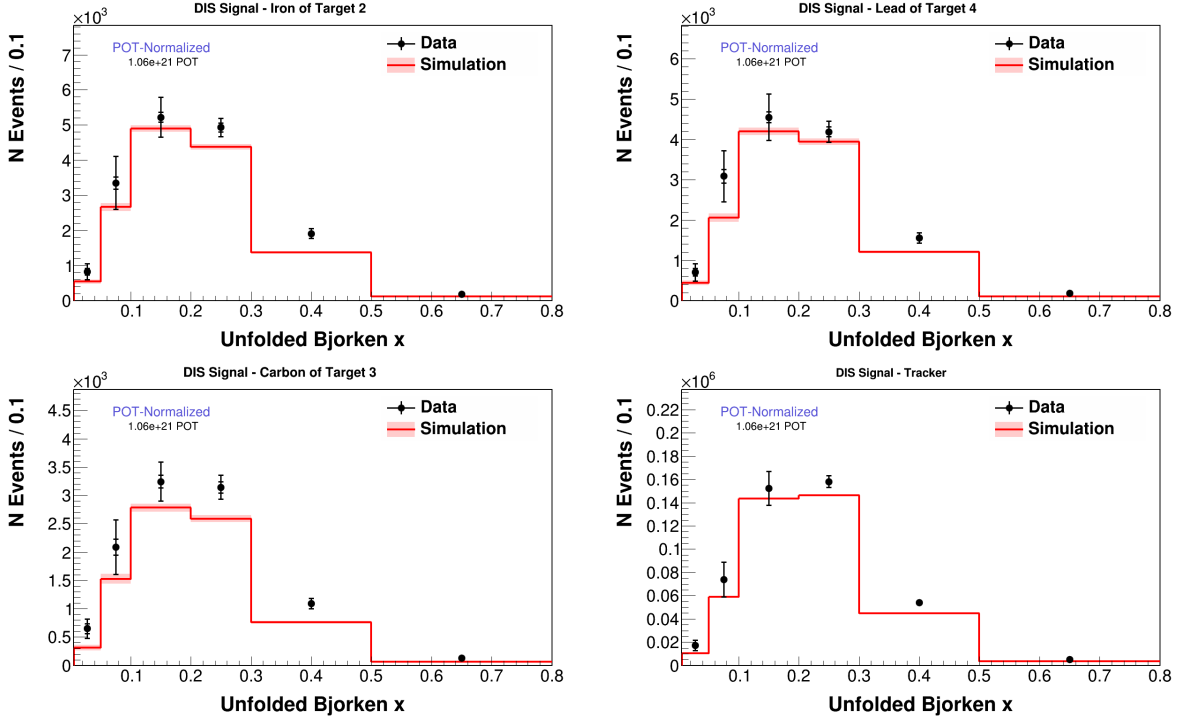
FIG. 7.25: The selected event sample in x_{bj} after background subtraction and unfolding.

for the purpose of accounting for flux differences between the target and tracker regions when taking cross section ratios. In order to be able to perform the weights to the daisy petals to both the data and the MC, we must perform all of the analysis steps through efficiency correction separately for each daisy petal. Thus the daisy petals are each unfolded individually in the tracker, so the unfolding studies are likewise done for each daisy bin separately. All tests were done on a nuclear target of every material, as well as every daisy bin in the tracker region.

The first test, in which we unfold the MINERvA tune v1 distribution using the MINERvA tune v1 migration matrix, reached a χ^2/degree of freedom of 1 within a single iteration in both variables and the tracker and nuclear target regions. We then moved on to a test where we unfold a differently tuned variation of GENIE while continuing to use the MINERvA tune v1 migration matrix that we use for the cross section measurement.
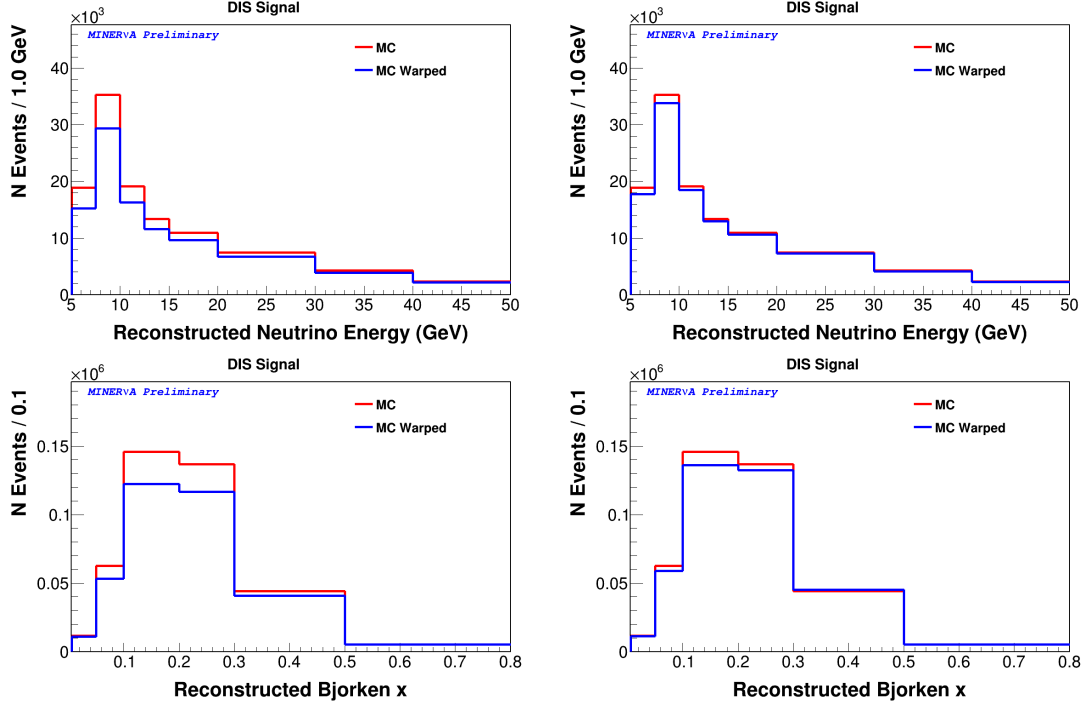
FIG. 7.26: The simulated background subtracted distributions in tracker for the AMU (left) and nCTEQ (right) DIS tunes in E_ν (top) and x_{bj} (bottom). The red "MC" histogram is MINERvA tune v1, while the blue line has the applicable DIS tune additionally applied to it.

For this analysis the tunes which we used had the AMU [52] and nCTEQ [50] DIS model weights applied on top of MINERvA tune v1. The effect that each of these tunes has on the reconstructed signal distributions is shown in Fig. 7.26, compared with MINERvA tune v1, which was used to unfold, in red.

Some selected results of the GENIE tuned unfolding test are shown in Fig. 7.27, where the χ^2 is calculated for each of the 1000 unfolded universes by comparing the unfolded nCTEQ (AMU) distribution to the true nCTEQ (AMU) distribution. We look to find the lowest number of iterations that the unfolding stably converges to approximately the number of degrees of freedom (bins) across each of these tests.

The next study involved finding warping functions which would transform the MC into a distribution more similar to the data distribution. These functions were found by fitting the background subtracted data MC ratios in the tracker with a third degree polynomial
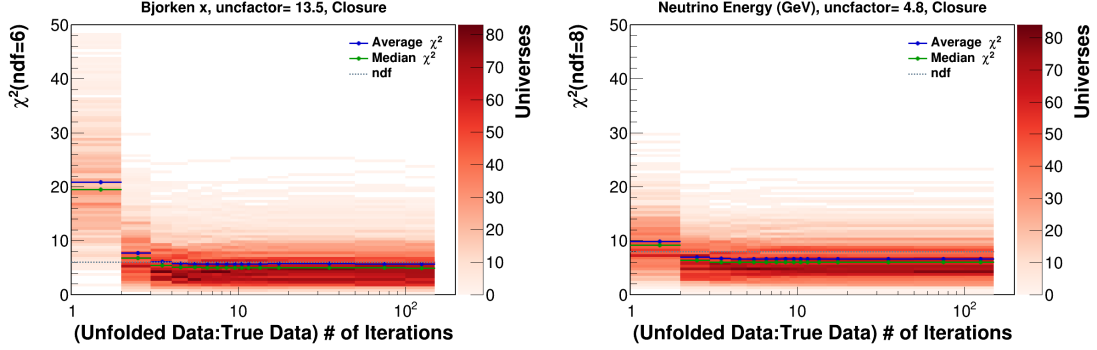
FIG. 7.27: The χ^2 for the unfolded distribution of the nCTEQ tune in x_{bj} of the lead of target 1 (left), and the AMU tune in E_ν for a single daisy bin of the tracker.
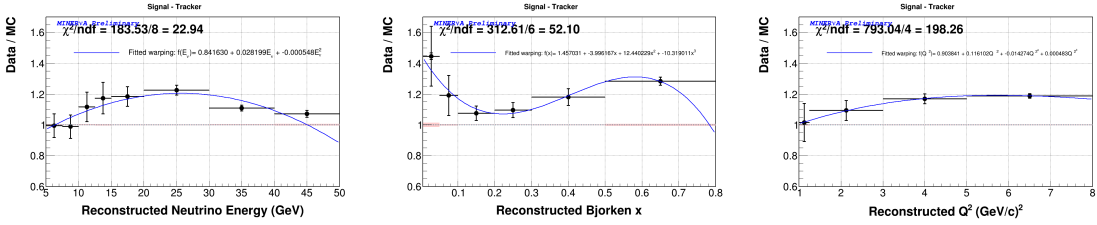
FIG. 7.28: The warping functions derived from the data/mc ratio of the background subtracted distributions in E_ν, x_{bj}, and Q^2 from left to right.

in three different variables which we used to warp the simulation. We performed warpings in E_ν, x_{bj}, and Q^2, the functional forms of which can be found in Fig. 7.28. The E_ν distribution was shaped such that only a second order polynomial fit was required. Each of the warping functions is truncated at the last bin of the fitted region, at which point it becomes a flat warping which maintains the same weight as highest bin. For example, for the warping $w_{E\nu}$ which is a function of neutrino energy, $w_{E\nu}(E_\nu = 60GeV) = w_{E\nu}(50GeV)$, as the fitted region ends at 50 GeV. This is done to prevent drastic warps from being applied to events with values outside the fitted range. The warping functions (derived from the reconstructed variable distributions) are then applied as weights as a function of the corresponding truth variable on an event by event basis to produce a warped MC in both x_{bj} and E_ν for each warping.

The χ^2s after unfolding the E_ν warped simulations for different target materials are
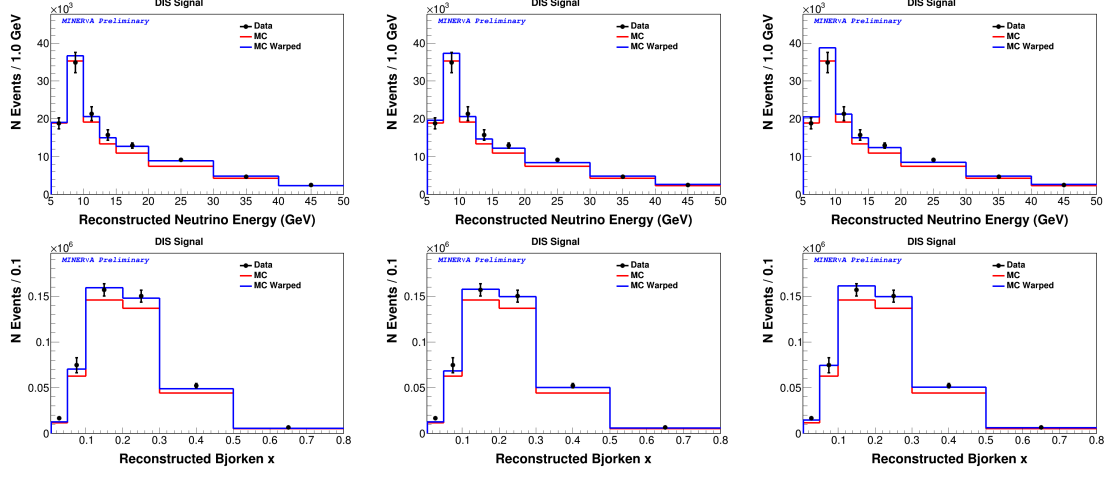
FIG. 7.29: MC signal with (blue) and without (red) warping functions applied to them, shown alongside the background subtracted data. The warping is done as a function of E_ν, Q^2, and x_{bj} from left to right. The top row shows the warped distributions in E_ν, and the bottom shows the warped simulated signal for x_{bj} in tracker.

shown in Fig. 7.30 when unfolding neutrino energy. The largest number of iterations needed to reach a minimum χ^2 out of all of the distributions was 3. The results of unfolding neutrino energy after using an x_{bj} or Q^2 based warp were consistent with this, unfolding with even fewer iterations as they were less severe warps, and are shown in Appendix B.7.

Bjorken-x is a slightly harder variable to unfold than neutrino energy. However, the unfolding studies all showed that a minimum was reached by 5 iterations. The unfolding studies done in x_{bj} using the x_{bj} derived warping was the most stringent unfolding test, and is shown in Fig. 7.31 for select targets. There is a slight increase in the χ^2 in some cases for larger numbers of iterations, however this behavior does not have a steep slope and levels off at at less than $2 \times ndf$ at very high iterations. By performing the unfolding procedure using 5 iterations we avoid this somewhat undesirable behavior.

The result of all of these unfolding studies is that we are able to accurately unfold the reconstructed distributions of various models and data-driven warps, and that this analysis uses 3 iterations to unfold E_ν and 5 iterations when unfolding x_{bj}.
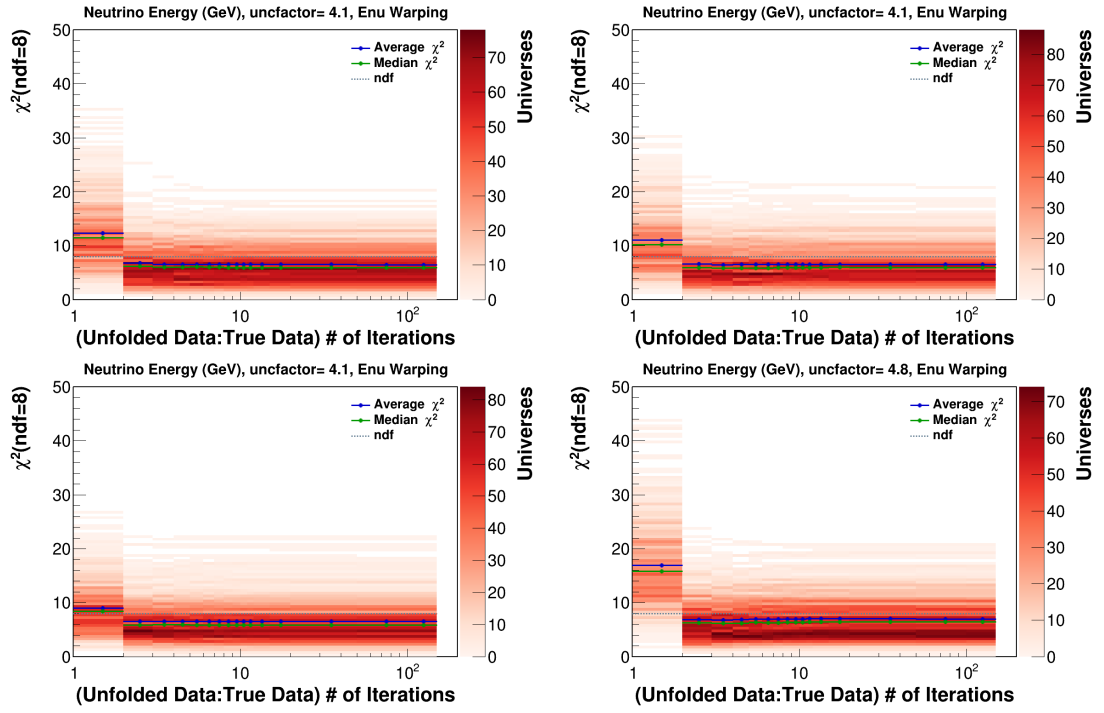
FIG. 7.30: The χ^2 between the unfolded and true warped distributions when unfolding neutrino energy which has had a warping based on E_ν applied to it. The top left is in the iron of target 1, the lead of target 4 is on the top right, the carbon target is on the bottom left, and the bottom right is for a daisy petal of the tracker.
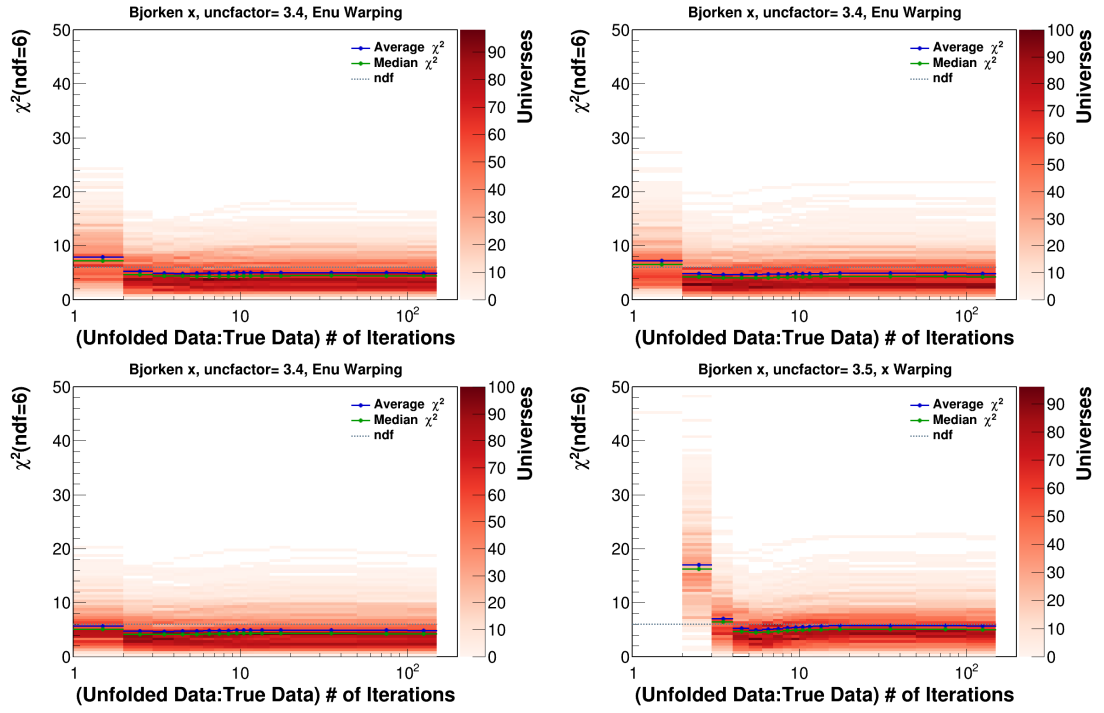
FIG. 7.31: The χ^2 between the unfolded and true warped distributions when unfolding Bjorken-x which has had a warping based on x_{bj} applied to it. The top left is in the iron of target 1, the lead of target 4 is on the top right, the carbon target is on the bottom left, and the bottom right is for a daisy petal of the tracker.
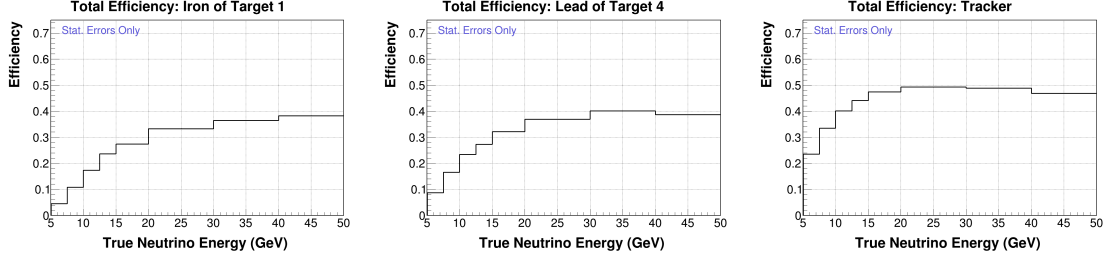
FIG. 7.32: The efficiencies for iron of target 1, lead of target 4, and the tracker in E_ν.
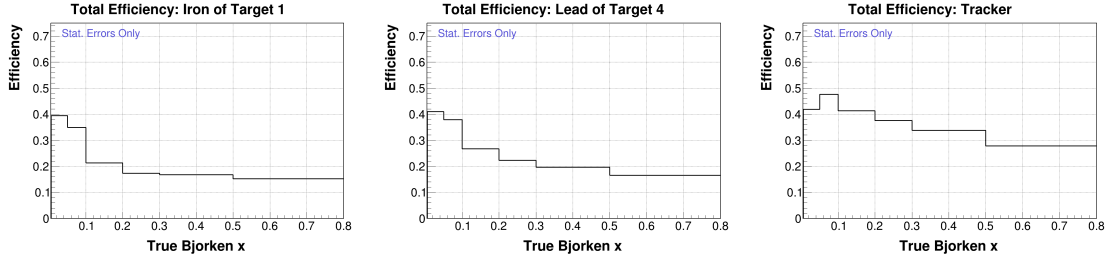
FIG. 7.33: The efficiencies for iron of target 1, lead of target 4, and the tracker in x_{bj}.

7.6 Efficiencies

Efficiencies for selected targets are shown in Figs. 7.32 and 7.33 for E_ν and x_{bj}, respectively. The efficiency increases the further downstream the target is in the detector, due to the rate of acceptance of muons reaching MINOS. The lowest efficiencies occur at low neutrino energy, as low energy muons are less likely to reach the MINOS ND. There is also a decrease in efficiency at the highest neutrino energies originating from challenges reconstructing the muon charge in MINOS due to the small curvature associated with energetic muons. In Bjorken-x the efficiencies are highest at low x_{bj} because the muons have smaller scattering angles and are thus more likely to reach MINOS. A complete set of the efficiencies in each target can be found in Appendix B.6.

Each target has its unfolded signal corrected by the efficiency in that target, the event samples after efficiency correction are shown in Figs. 7.34 and 7.35.
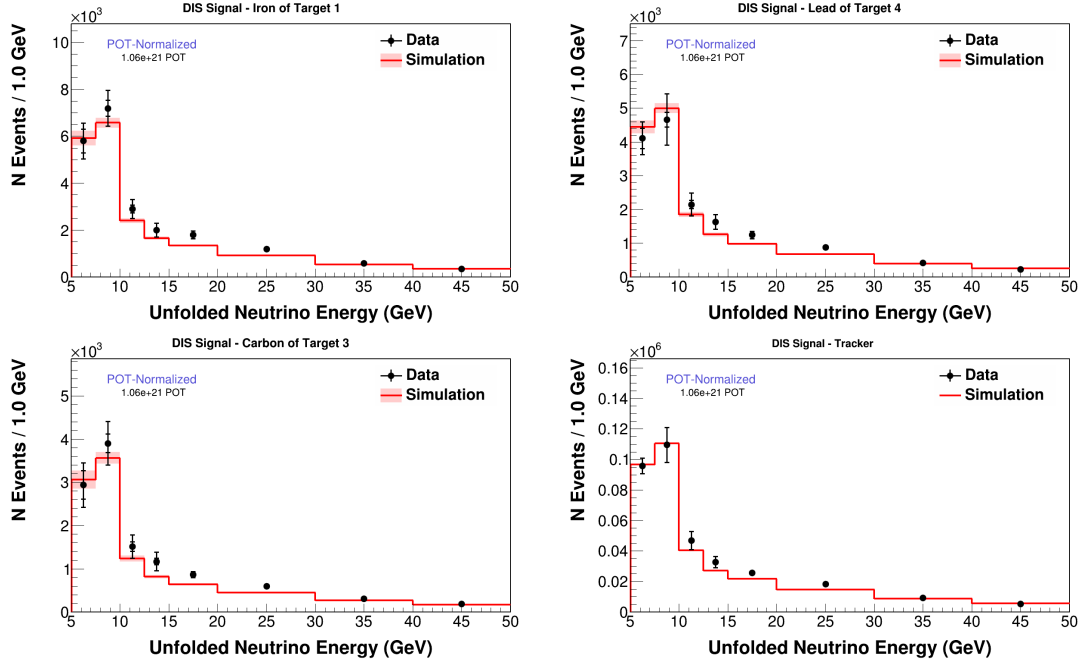
FIG. 7.34: The efficiency corrected signal in iron of target 1 (top left), lead of target 4 (top right), the carbon target (bottom left) and the tracker (bottom right) in E_ν.
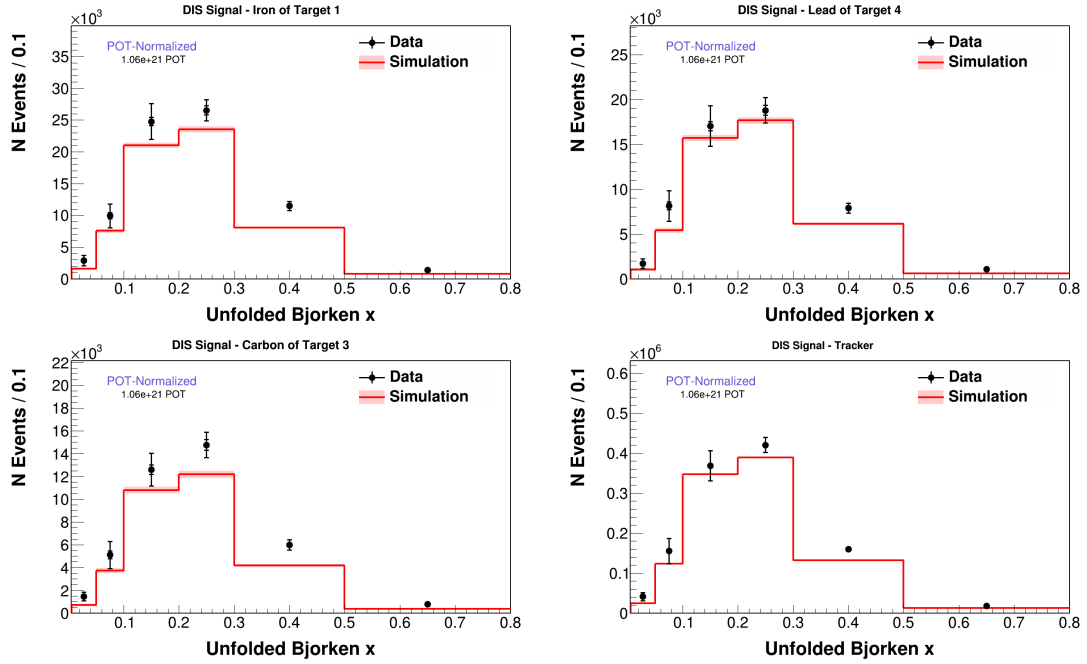
FIG. 7.35: The efficiency corrected signal in iron of target 1 (top left), lead of target 4 (top right), the carbon target (bottom left) and the tracker (bottom right) in x_{bj}.

7.7 Flux and normalization

The final step to producing the cross sections is to sum all of the different targets of the same material together, divide by the number of nucleons in the target, the number of protons on target and the flux. The summed cross sections are shown in Fig. 7.36.
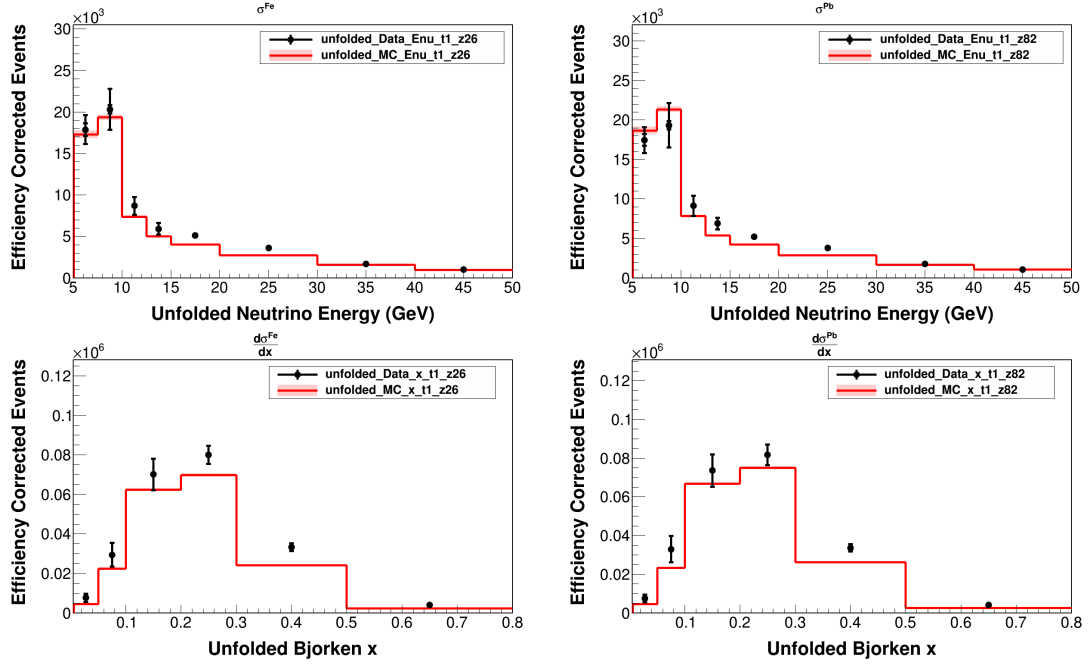
FIG. 7.36: The signal after efficiency correction summed across all of the iron targets (left), and all of the lead targets (right), in neutrino energy (top row), and Bjorken-x (bottom row).

7.7.1 Tracker flux differences

Both data and MC events in the tracker are given weights as a function of the position of the interaction vertices, discussed in further detail in Ch. 3. The events are reweighted in order to simulate the differences between the flux in the tracker and the nuclear target regions which we wish to compare to. A different set of these weights is used for each of the carbon, iron, and lead cross section ratios due to their different target geometries.

Ratios of the daisy-reweighted tracker to the tracker without the daisy weights applied

are shown in Fig. 7.37. The daisy reweighted data is taken as as ratio to the unweighted data, and the reweighted MC is a ratio of the unweighted tracker MC. The same weights are applied to both the data and the MC tracker distributions so any shape differences come from differences in the simulated flux, and the flux which the detector was actually exposed to.
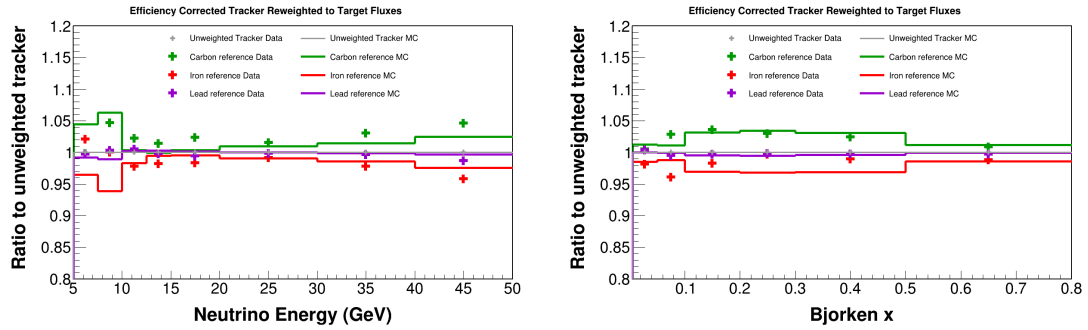
FIG. 7.37: The efficiency corrected tracker in data and MC, with the daisy-flux reweights for each of the nuclear target materials applied. Each reweighted data point is taken as a ratio to the data in the tracker without any weights applied. Similarly the weighted MC is divided by the unweighted tracker MC.

7.8   Systematic uncertainties

The grouping used to display the DIS uncertainties is slightly different than that used in the inclusive analysis because the uncertainties of import differ, but the included systematics are largely the same. Uncertainties on the hadronic energy, muon energy and angle, and vertex reconstruction are all grouped into the "Detector Resolution" uncertainty. The GENIE reweighted uncertainties discussed in Ch. 5.2.1, are separated into two categories of those associated with the final-state interaction model and those based on the interaction model. The FSI model uncertainties with the largest contributions to that group are FrAbs_pi, and MFP_pi, with all others consistently contributing less than 2% of the cross section uncertainties. The interaction model uncertainties that have the

largest effects are MaRES, MvRES, and RvN2pi, though all have very small contributions on the $\mathcal{O} \sim 1\%$. The flux and mass uncertainty is dominated by the flux uncertainty but also includes uncertainties associated with the target masses. The uncertainties added based on the background constraints for the wrong target and physics sidebands are all grouped together into the "Sidebands" uncertainty category.

The error summaries on the data after background subtraction, unfolding, and efficiency correction are shown in Fig. 7.38 for E_ν, and Fig. 7.39 for x_{bj} in the iron of target 1. At the event selection stage the only uncertainty on the data is the statistical uncertainty, so there an error summary is not included here. Full sets of uncertainties on the data and MC in all of the targets can be found in Appendix B. The hadronic energy uncertainties are larger in the Bjorken-x distribution than they are in neutrino energy because the x_{bj} distribution is more challenging to unfold, as shown with the migration matrices in Figs. 7.22 & 7.23.

The tracker error summaries are shown in Figs. 7.40 and 7.41. The systematic uncertainty which originates from the background subtraction is a bit smaller in the tracker since there is no contribution from the scintillator contamination as there is in the target region.

A feature of a measurement of cross section ratios is that most of these systematic uncertainties are correlated between the different material measurements. This means that when the ratios are taken the uncertainties largely cancel each other out, resulting in a much smaller uncertainty on a final cross section ratio measurement.
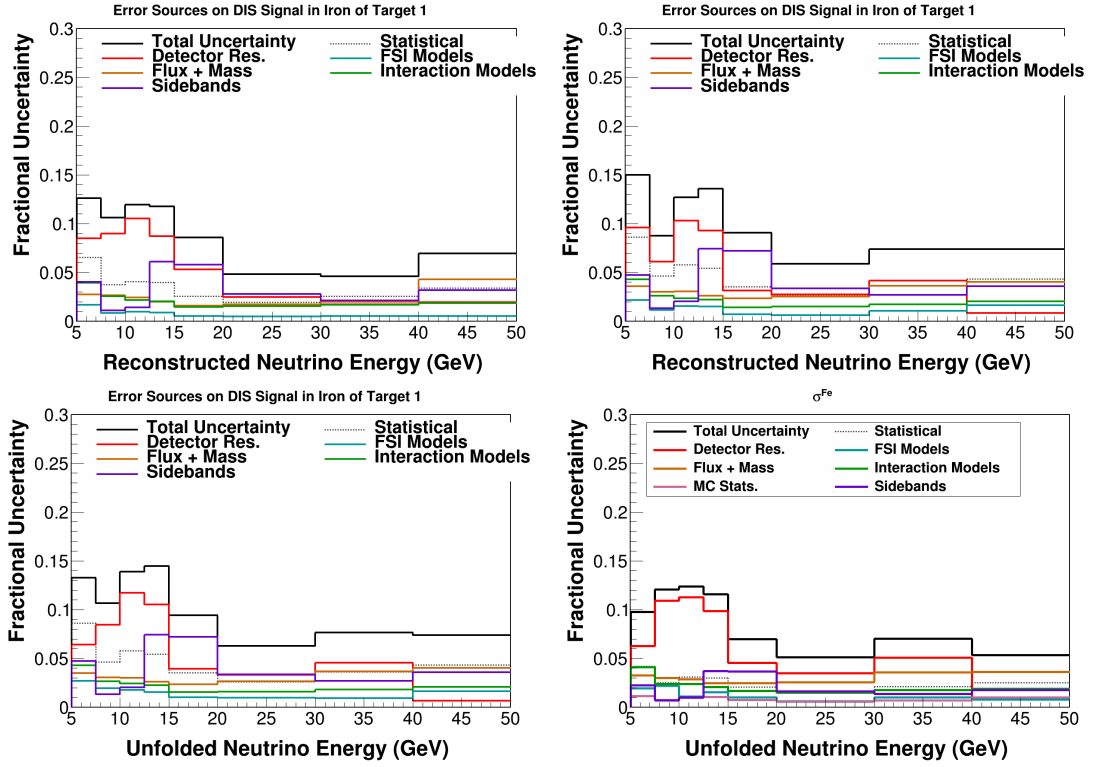
FIG. 7.38: Neutrino energy data error summary in the iron of target 1 after background subtraction (top right), unfolding (top left) and efficiency correction (bottom left). The bottom right shows the uncertainty on the efficiency corrected iron after summing across all iron targets.
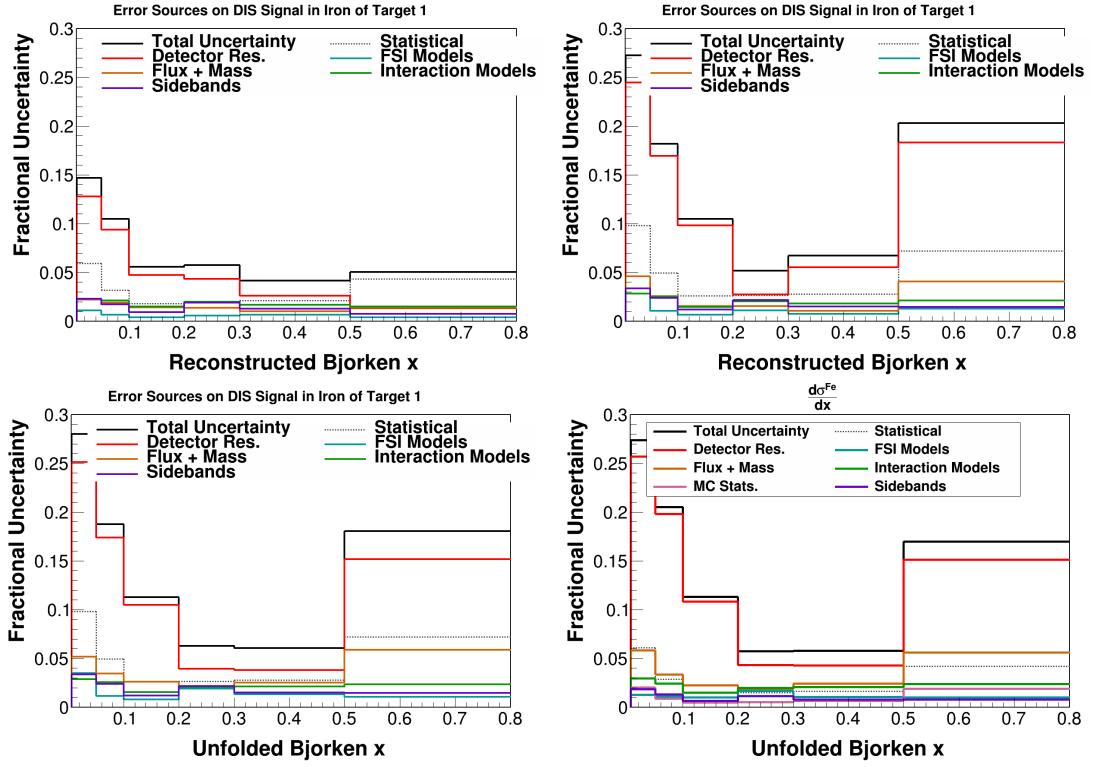
FIG. 7.39: Bjorken-x data error summary in the iron of target 1 after background subtraction (top right), unfolding (top left) and efficiency correction (bottom). The bottom right shows the uncertainty on the efficiency corrected iron after summing across all iron targets.
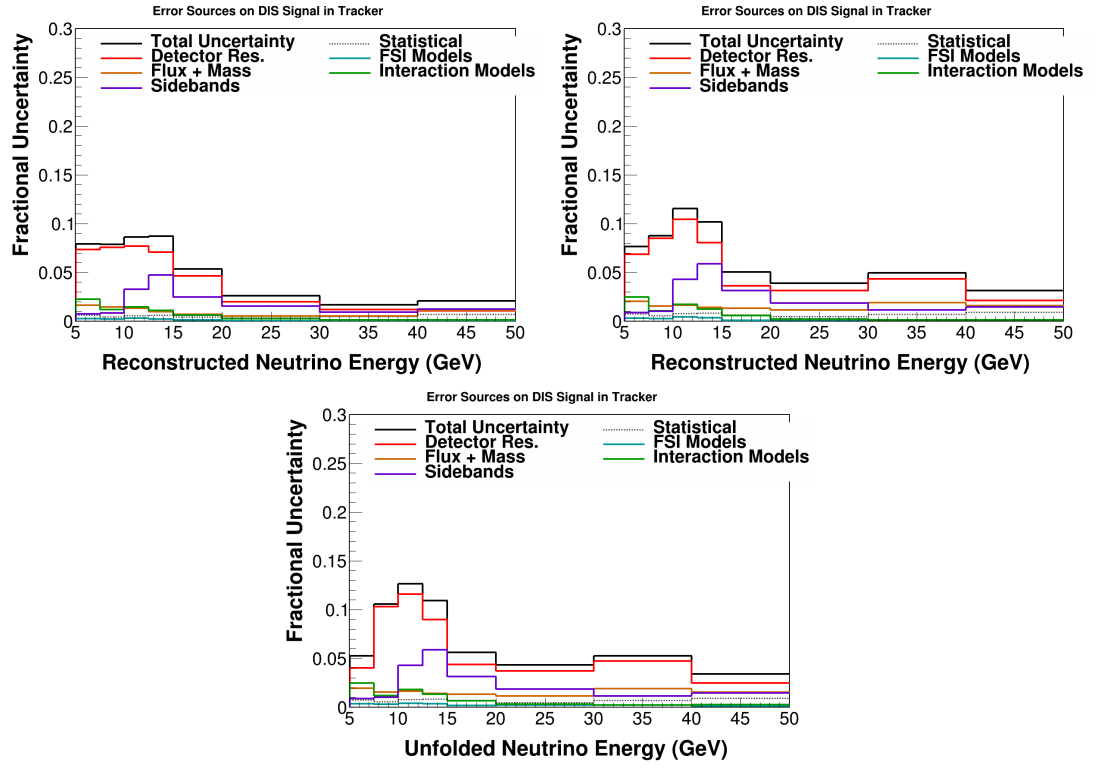
FIG. 7.40: Neutrino energy data error summary in the tracker after background subtraction (top right), unfolding (top left) and efficiency correction (bottom).
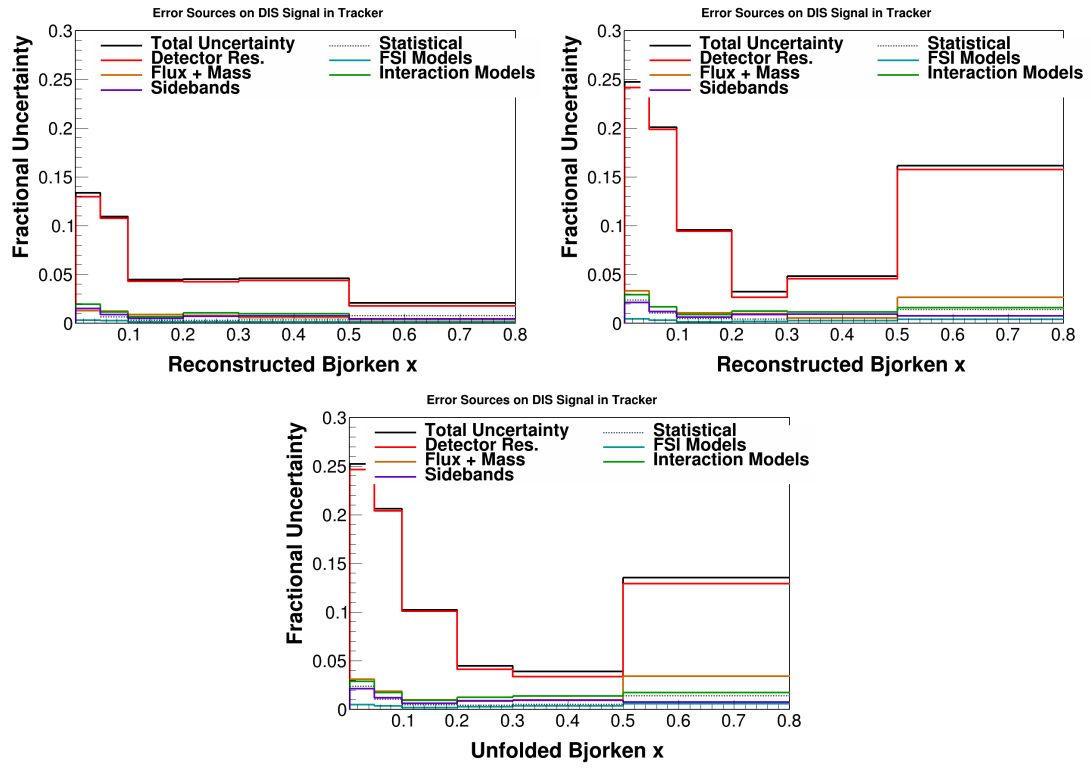
FIG. 7.41: Bjorken-x data error summary in the tracker after background subtraction (top right), unfolding (top left) and efficiency correction (bottom).

7.9   Cross Sections

7.9.1   Absolute and differential cross sections

The absolute cross sections for each of the summed target materials and the tracker are shown in Fig. 7.42 as a function of neutrino energy. All of the materials show a similar pattern in which the data agrees well with the MC prediction at low neutrino energy, then in the range from about 15 to 30 GeV MINERvA tune v1 underpredicts the cross section, with better agreement in the highest energy bin. The flux could be contributing to the data/MC differences seen in the 15-30 GeV range. This pattern can be seen more clearly in data/MC ratios shown in Fig. 7.43. The uncertainty on the cross section measurements are shown in Fig. 7.44, with the largest contributions coming from detector resolution, primarily hadronic energy resolution. In the bin with the lowest uncertainty, $20 < E_\nu < 30$ GeV, the total uncertainties in iron, lead and hydrocarbon are approximately 5%.

The differential cross sections in Bjoken-x for each of the summed target materials and the tracker are shown in Fig. 7.45. The data MC agreement is the best in the region between 0.1 and 0.2, with underpredictions occurring at both low and high x_{bj}. The data MC ratios are shown in Fig. 7.46. The detector resolution again dominates the uncertainties in this measurement, the error summary for which is shown in Fig. 7.44.
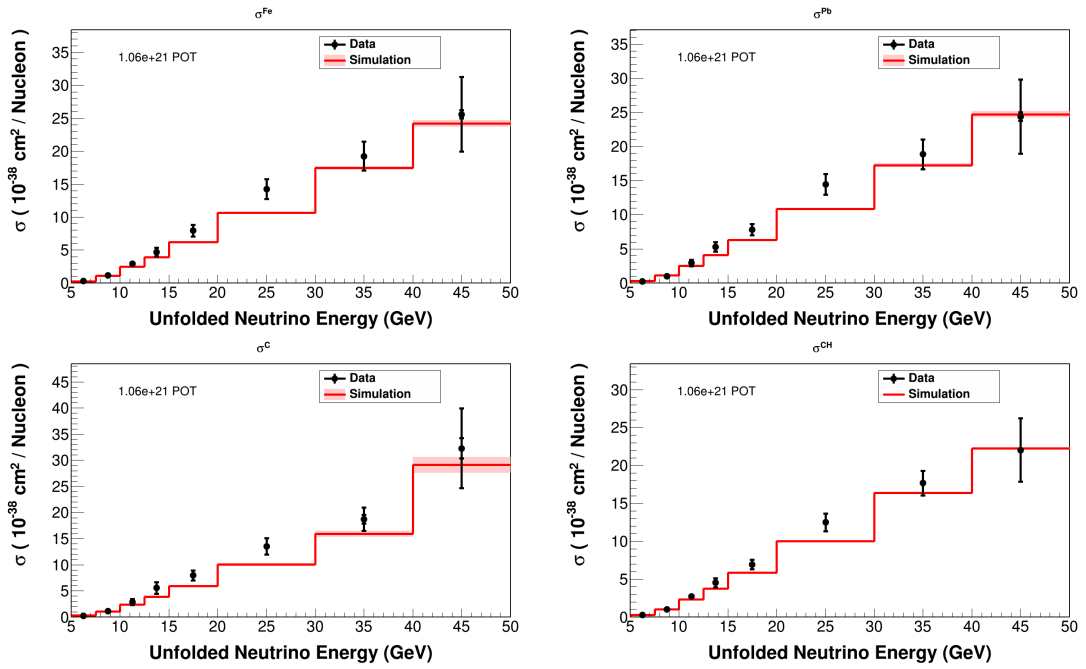
FIG. 7.42: Summed absolute cross sections as a function of neutrino energy for iron (top left), lead (top right), carbon (bottom left), and scintillator (bottom right), shown alongside MINERvA tune v1. The data has statistical (inner) and statistical+systematic (outer) error bars. The error band on the simulation is statistical uncertainty only.
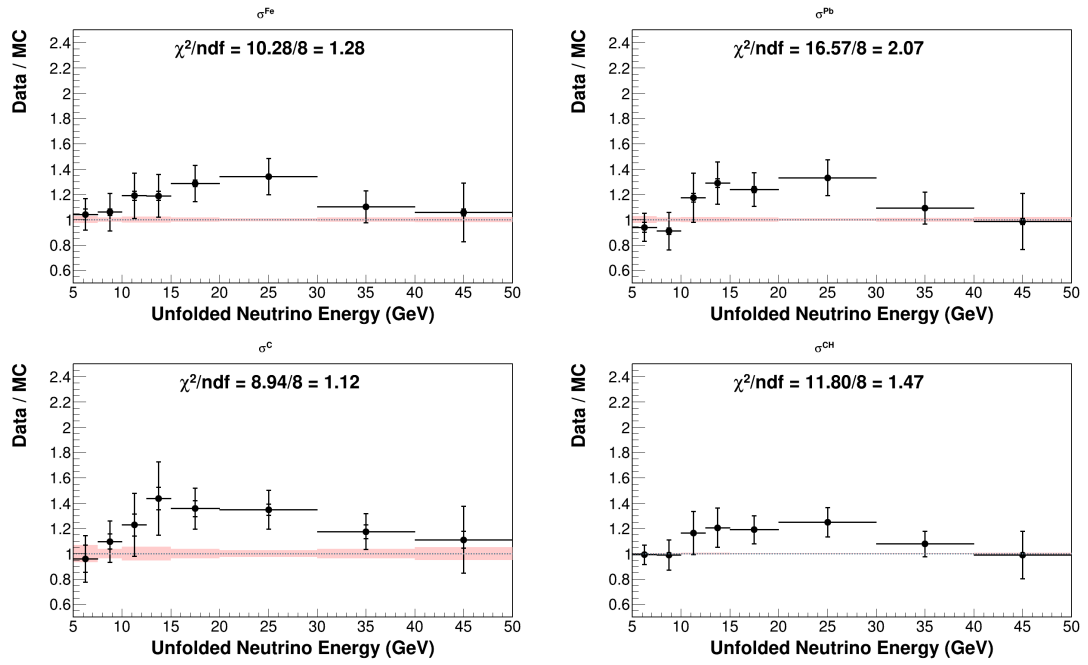
FIG. 7.43: Data/MC ratios of the absolute cross sections as a function of neutrino energy for iron(top left), lead (top right), carbon (bottom left), and scintillator(bottom right). The data has statistical (inner) and statistical+systematic (outer) error bars. The error band on the simulation is statistical uncertainty only.
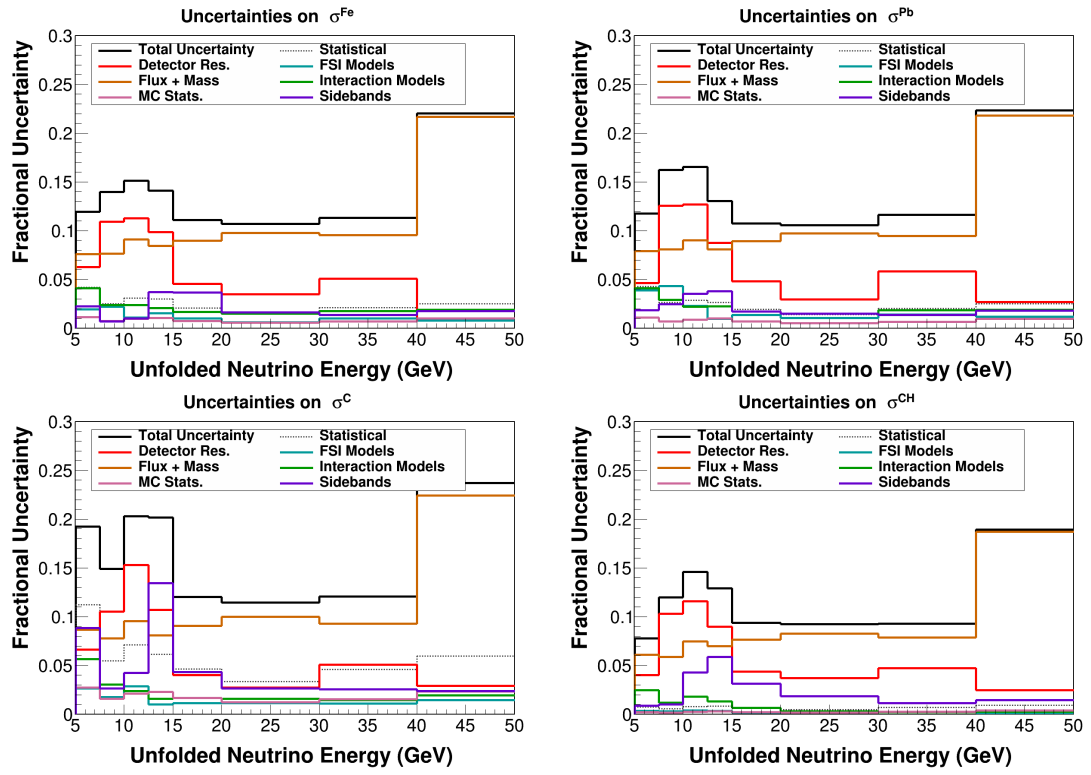
FIG. 7.44: Error summaries for the measured absolute cross sections as a function of neutrino energy for iron (top left), lead (top right), carbon (bottom left), and scintillator (bottom right).
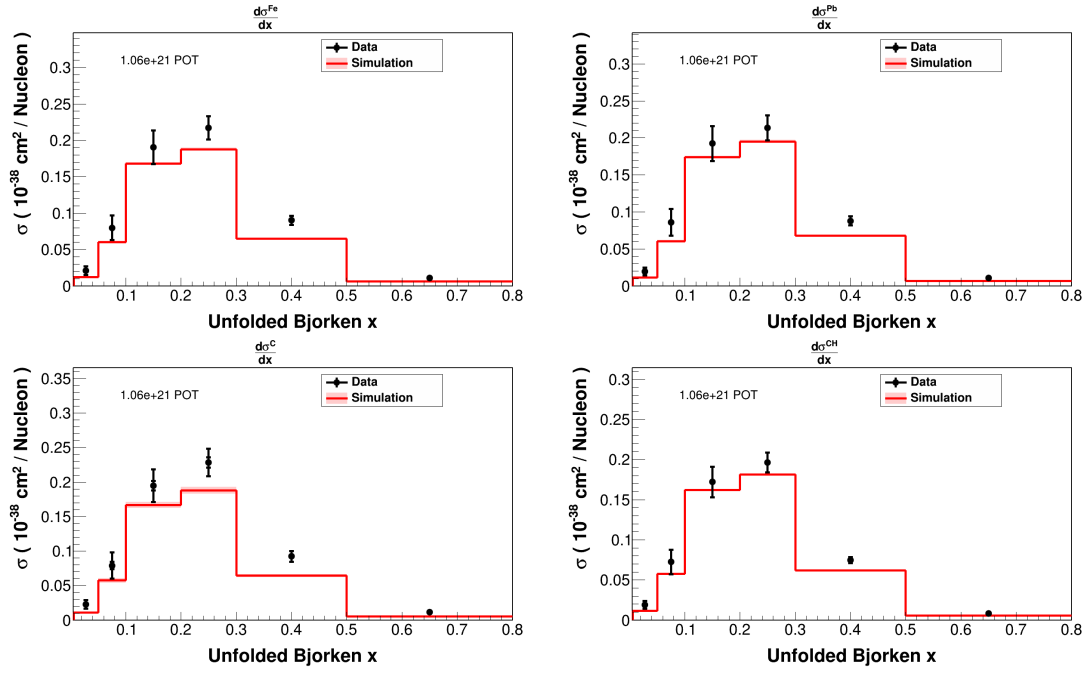
FIG. 7.45: Differential cross sections as a function of Bjorken-x for iron (top left), lead (top right), carbon (bottom left), and scintillator (bottom right) summed across all materials. The simulation shown alongside the data is MINERvA tune v1. The data has statistical (inner) and statistical+systematic (outer) error bars. The error band on the simulation is statistical uncertainty only.
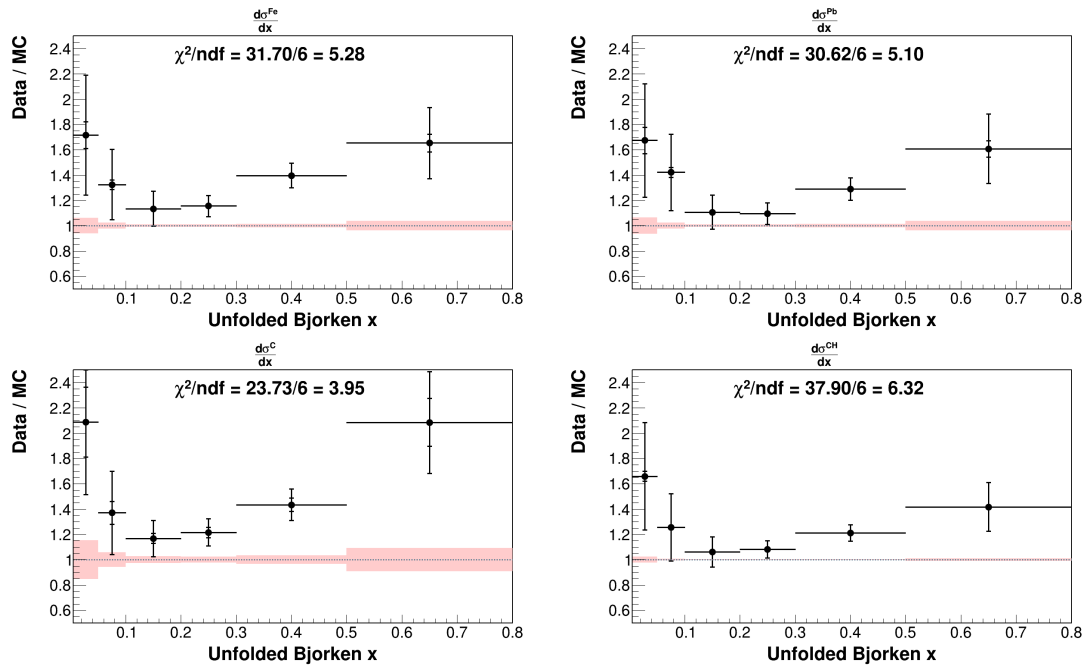
FIG. 7.46: Data/MC ratios of the differential cross sections as a function of Bjorken-x for iron (top left), lead (top right), carbon (bottom left), and scintillator(bottom right) summed across all materials. The data has statistical (inner) and statistical+systematic (outer) error bars. The error band on the simulation is statistical uncertainty only.
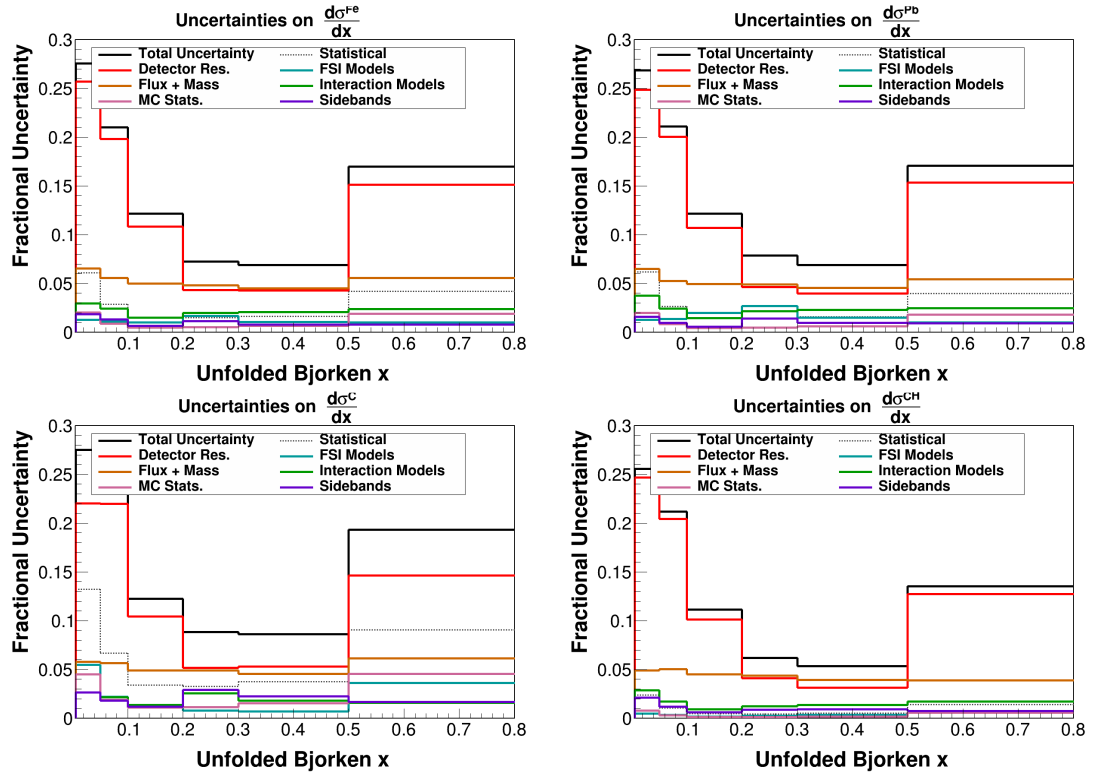
FIG. 7.47: Error summaries for the measured absolute cross sections as a function of Bjorken-x for iron (top left), lead (top right), carbon (bottom left), and scintillator(bottom right).

7.10   Cross section ratios

The ratios of the absolute neutrino energy cross sections and differential Bjorken-x cross sections between each nuclear target material and the corresponding daisy-flux reweighted tracker region are shown in Fig. 7.48. The pink band around the red MC is the statistical uncertainty on the MC only, while the data points have inner statistical and outer statistical+systematic uncertainty error bars on them. The ratios in neutrino energy are all relatively flat. The carbon to scintillator ratio has a slight normalization difference, but agrees with the MC within uncertainties. Some shape differences exist at low neutrino energy in the lead to tracker ratio.

The Bjorken-x distribution has far more shape differences, both between the measured target and scintillator cross sections, and the predicted ratios. All of the nuclear targets (including carbon) have much larger cross sections at high x_{bj} than the scintillator does.

These measurements are able to achieve exceptionally small uncertainties for neutrino cross section measurements. Uncertainties for the neutrino energy cross section ratios are at or below 5% for all neutrino energies greater than 15 GeV in Fe/CH and Pb/CH. The minimum uncertainty is from $20 < E_\nu < 30$ GeV at 3.2% for both iron and lead. Measurements in Bjorken-x have uncertainties below 4% for three bins from $0.1 < x_{bj} < 0.5$ in the iron and lead to hydrocarbon cross section ratios. The minimum uncertainty is in the third x_{bj} bin of 3.1% for Fe/CH, and 3.4% in Pb/CH.

7.11   Conclusion

Measurements of the DIS cross sections on carbon, iron, lead, and hydrocarbon have been made as a function of neutrino energy. Differential cross sections as a function of x_{bj} were also measured, allowing for the x_{bj} dependent nuclear effects to be studied.

The cross sections in all materials are under-predicted by MINERvA tune v1 in the range of neutrino energies from 12 to 40 GeV. At the lowest measured neutrino energies from 5 to 10 GeV, and the highest neutrino energies from 40 to 50 GeV the cross section is in agreement with predictions across all materials.

The flux-integrated cross sections as a function of the Bjorken-x scaling variable show model underpredictions across materials. The best agreement is seen in the region from 0.1 to 0.2.

Cross section ratios between the graphite, iron, and lead, and hydrocarbon were also measured in neutrino energy and Bjorken-x. The neutrino energy cross section ratios show fairly good agreement with simulation across materials. There are overpredictions of the lead:hydrocarbon cross section ratio for $5 < E_\nu < 10$ GeV.

The Bjorken-x cross section ratios generally have worse agreement than the neutrino energy cross section ratios. Fig. 7.48 shows the best agreement in the shadowing region, anti-shadowing and EMC effect regions both have model underpredictions, and we are not sensitive to the Fermi motion region. At high x_{bj}, where EMC effect deficits have been seen, the ratio is consistently underpredicted across materials. The best agreement is seen in the lowest x_{bj} bin and for $0.005 < x_{bj} < 0.05$ in iron and lead, which falls into the nuclear shadowing region. There appears to be an underpredicted anti-shadowing effect in the $0.05 < x_{bj} < 0.1$ bin, which is the most pronounced in lead. In the region from $0.2 < x_{bj} < 0.5$, around which there is the transition from the anti-shadowing region to the EMC effect region, there is better model agreement the heavier the nucleus, with general underpredictions.

Additional DIS models will be added to compare with these results prior to publication. The rich statistics from the $\langle E_\nu \rangle \sim 6$ GeV beam, allows for the possibility of MINERvA to perform double differential cross section measurements of DIS on nuclear targets which would allow for further separation of nuclear effects and, possibly, nuclear

dependent structure function fits with particular interest in studying F_3.
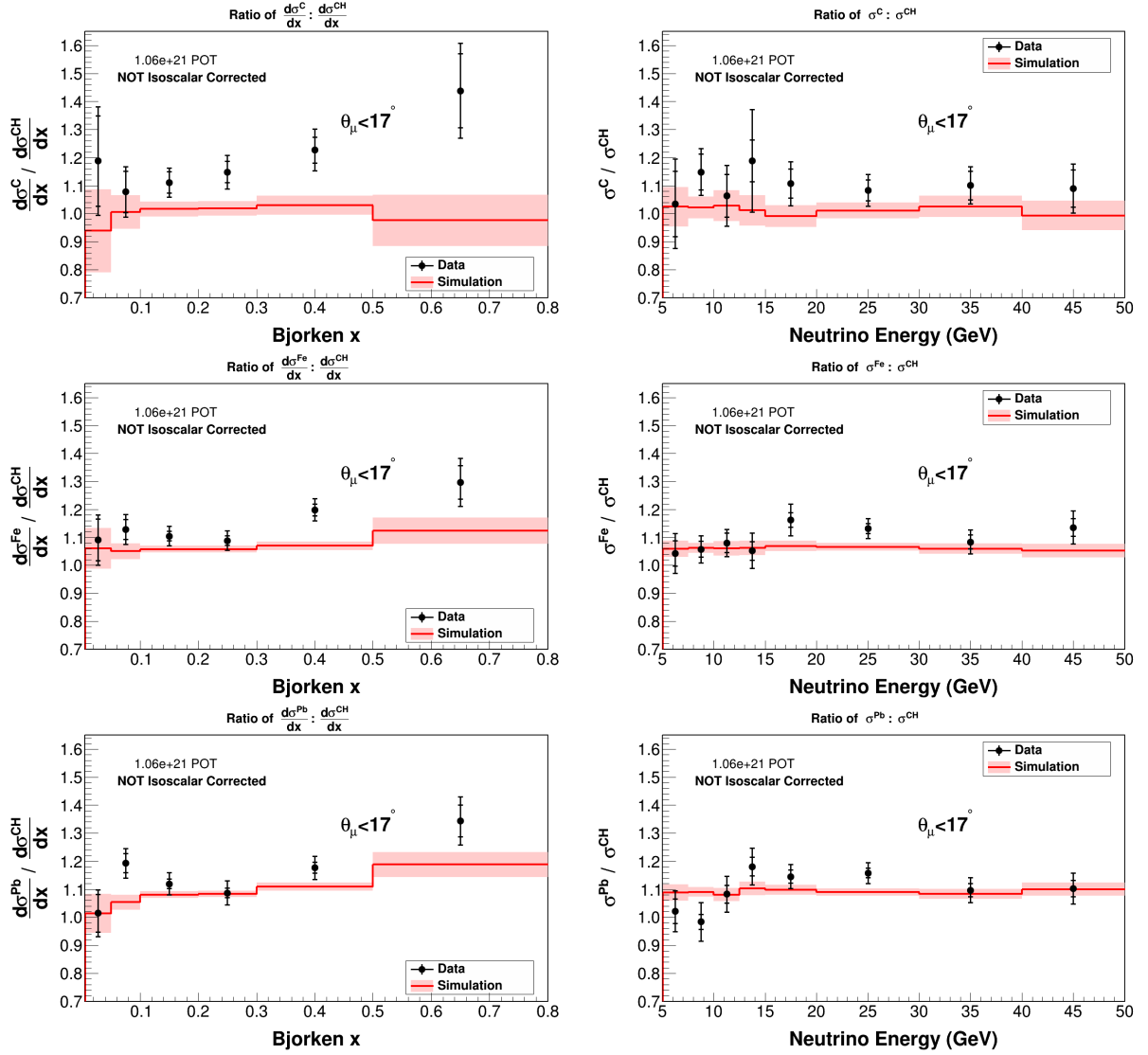
FIG. 7.48: Ratios of the measured and simulated cross sections between the nuclear targets and active tracking scintillator. From top to bottom: carbon/scintillator, and iron/scintillator, lead/scintillator in Bjorken-x on the left, and neutrino energy on the right. Data has statistical (inner) and total (outer) uncertainties. The band around the MC represents the MC statistical uncertainty.
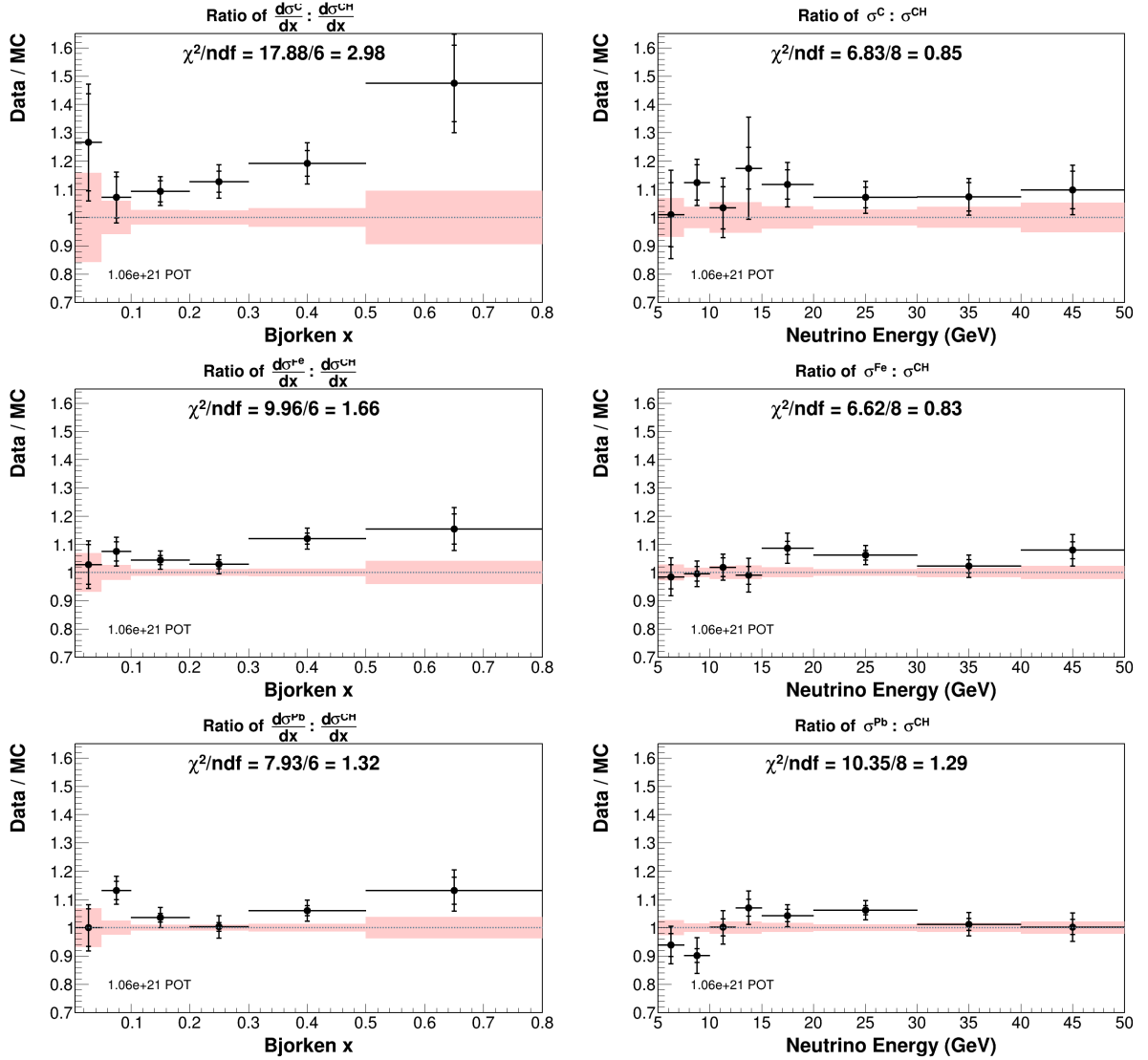
FIG. 7.49: Target to scintillator cross section ratios, as ratios of the data to MC (data/data)/(MC/MC) for carbon/scintillator, iron/scintillator, and lead/scintillator from top to bottom, in Bjorken-x on the left, and neutrino energy on the right. Data has statistical (inner) and total (outer) uncertainties. The band around the MC represents the MC statistical uncertainty.
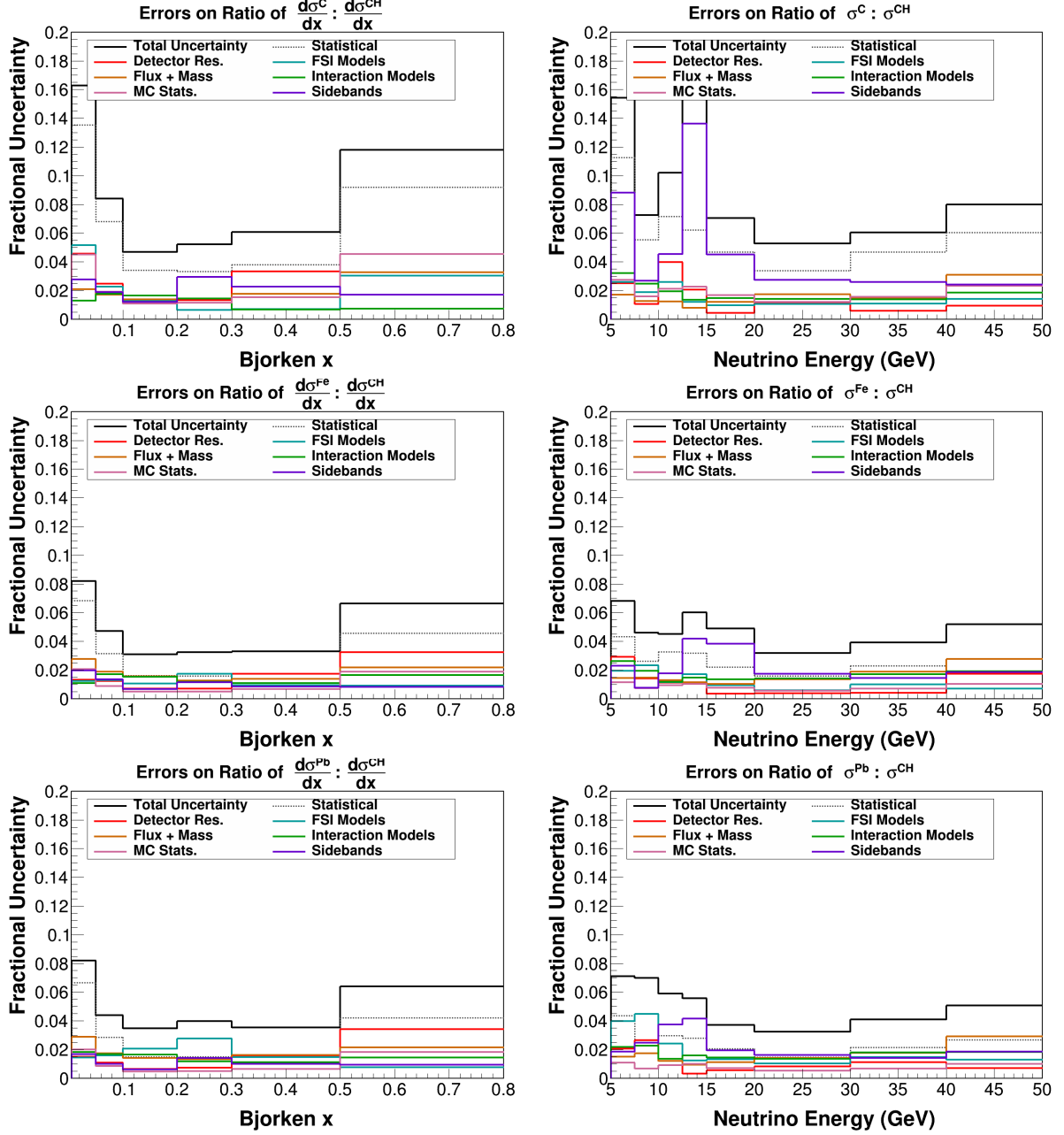
FIG. 7.50: Cross section ratio data error summaries for carbon/CH, iron/CH and lead/CH from top to bottom, in x_{bj} (left) and E_ν (right).

CHAPTER 8

Conclusion

The MINERvA experiment at Fermilab is dedicated to the purpose of studying neutrino interactions on heavy nuclei. We took neutrino interaction data in $\langle E_\nu \rangle \sim 3.5$ GeV and $\langle E_\nu \rangle \sim 6$ GeV accelerator based neutrino beams. I have measured two sets of cross sections in these two different beam energies for inclusive and DIS charged-current muon-neutrino interactions.

Measurements of charged-current inclusive ν_μ double differential cross sections were performed at a peak neutrino energy of 3.5 GeV. These hydrocarbon cross sections, measured as a function of the longitudinal and transverse muon momentum, provide a minimally model-dependent look at the few GeV region. Comparisons to a suite of models of neutrino interactions showed that none of these models were able to accurately predict the cross section throughout the entire kinematic phase space when studied inclusively. In particular regions of low four-momentum transfer and the shallow inelastic scattering transition regions are not being well modeled. These regions in which model builders should focus their attention in order to establish a complete picture of neutrino interactions at a energies of a few GeV.

A parallel analysis to the low-energy inclusive measurement has already been performed using our medium energy data. This additional data supported the conclusions of the low energy data set. Additional analogous measurements could be made looking at antineutrino CC interactions. With the superb available statistics in the medium energy era, a similar analysis in the nuclear target regions could also be possible on MINERvA. These results can also be used in conjunction with analyses in exclusive channels, to allow model builders to alter their generators in order to create better agreement with the measured cross sections. These results indicate that attention should be paid to the low Q^2 resonant behavior and the shallow ineleastic scattering to deep inelastic scattering regions.

Deep inelastic scattering cross sections on carbon, iron, lead and hydrocarbon were measured using MINERvA's $\langle E_\nu \rangle$ ~6.0 GeV data set. Both measurements of absolute cross sections as a function of neutrino energy and differential cross sections as a function of the Bjorken-x scaling variable were performed across all of these materials. Cross section ratios were also taken between each of the nuclear target materials and hydrocarbon in both neutrino energy and Bjorken-x, allowing for comparisons of the dependency of nuclear effects on a wide range of heavy nuclei. These measurements indicate that the cross section shape as a function of x_{bj} is not being modeled by MINERvA tune v1. Future plans for this analysis are to compare these results to different models of DIS. MINERvA plans to further study deep inelastic scattering by measuring double differential cross sections, which will allow for increased separation of kinematic regimes. A measurement such as this will be additionally helpful to model builders, too.

The kinematic regimes probed with both of these measurements share similarities with those the future DUNE will encounter in. Increased understanding of the underlying nuclear physics intrinsic to neutrino-nucleus interaction will allow for a decrease in systematic uncertainties and improved predictions of neutrino energy, an important element of the global neutrino oscillation program.

APPENDIX A

Appendix A − Double-differential Inclusive Analysis

A.1   Migration matrices

Included in Fig. A.1-A.13 are sections of the two dimensional bin by bin migration matrices by bin number, with each figure representing a different bin of p_T. These show zoomed sections of the diagonal and off diagonals of Fig. 6.7. Bin numbers 14-28 represent all of the bins in $p_{\parallel}$ for the first bin of p_T, and so on.
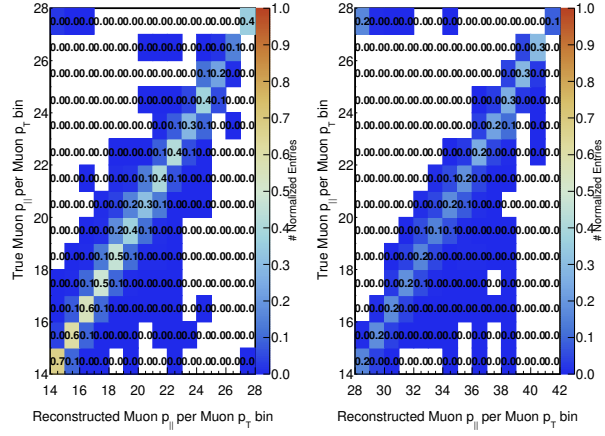
FIG. A.1: Row normalized migration matrix cells by bin number. Both plots show events truly in p_T bin 1, with events reconstructed in p_T bin 1 on the left and bin 2 on the right for the full range of $p_{||}$.
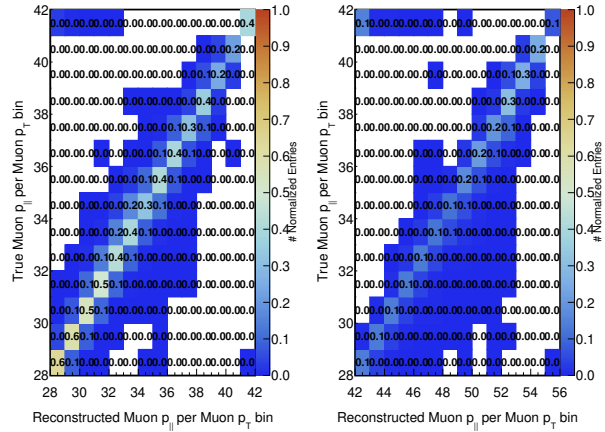
FIG. A.2: Row normalized migration matrix cells by bin number. Both plots show events truly in p_T bin 2, with events reconstructed in p_T bin 2 on the left and bin 3 on the right for the full range of $p_{||}$.
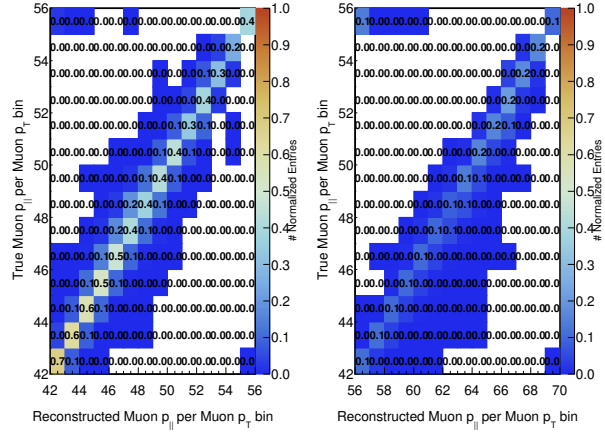
FIG. A.3: Row normalized migration matrix cells by bin number. Both plots show events truly in p_T bin 3, with events reconstructed in p_T bin 3 on the left and bin 4 on the right for the full range of $p_{||}$.
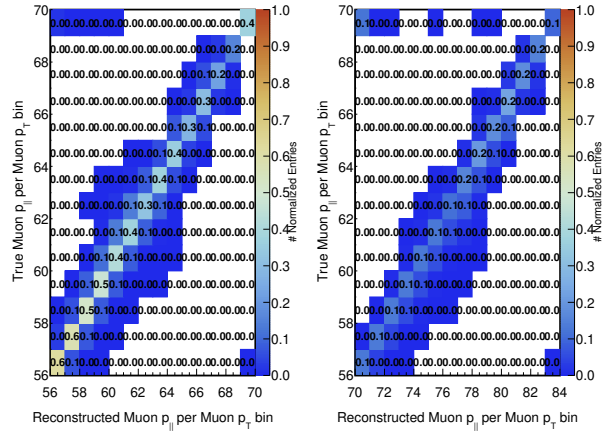
FIG. A.4: Row normalized migration matrix cells by bin number. Both plots show events truly in p_T bin 4, with events reconstructed in p_T bin 4 on the left and bin 5 on the right for the full range of $p_{||}$.
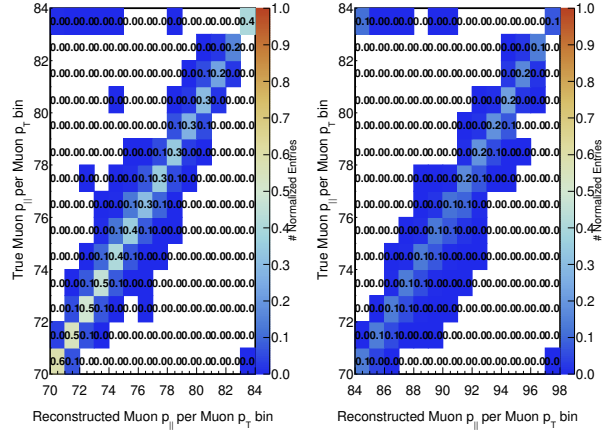
FIG. A.5: Row normalized migration matrix cells by bin number. Both plots show events truly in p_T bin 5, with events reconstructed in p_T bin 5 on the left and bin 6 on the right for the full range of $p_{||}$.
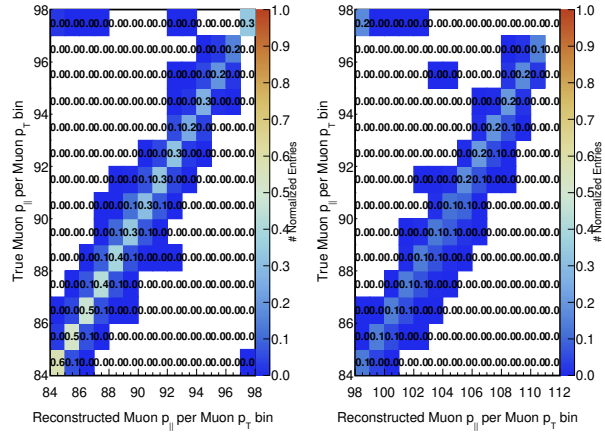
FIG. A.6: Row normalized migration matrix cells by bin number. Both plots show events truly in p_T bin 6, with events reconstructed in p_T bin 6 on the left and bin 7 on the right for the full range of $p_{||}$.
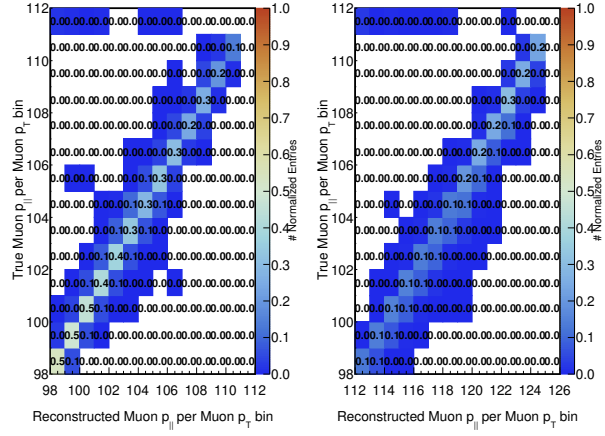
FIG. A.7: Row normalized migration matrix cells by bin number. Both plots show events truly in p_T bin 7, with events reconstructed in p_T bin 7 on the left and bin 8 on the right for the full range of $p_{||}$.
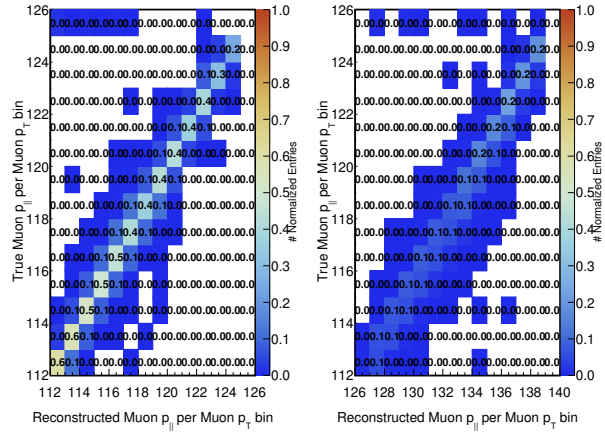
FIG. A.8: Row normalized migration matrix cells by bin number. Both plots show events truly in p_T bin 8, with events reconstructed in p_T bin 8 on the left and bin 9 on the right for the full range of $p_{||}$.
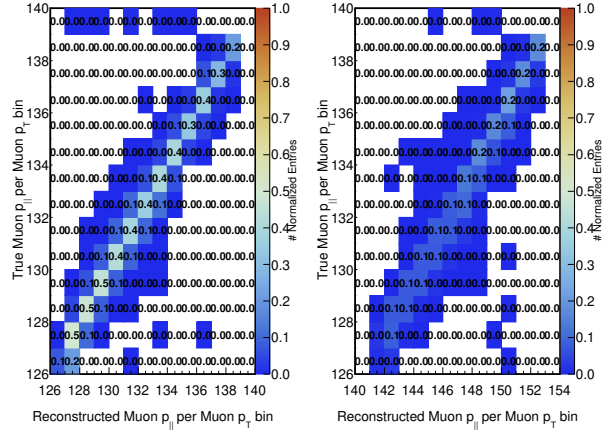
FIG. A.9: Row normalized migration matrix cells by bin number. Both plots show events truly in p_T bin 9, with events reconstructed in p_T bin 9 on the left and bin 10 on the right for the full range of $p_{||}$.
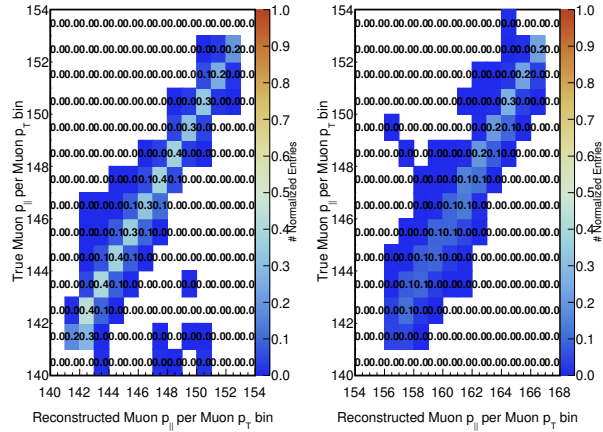
FIG. A.10: Row normalized migration matrix cells by bin number. Both plots show events truly in p_T bin 10, with events reconstructed in p_T bin 10 on the left and bin 11 on the right for the full range of $p_{||}$.
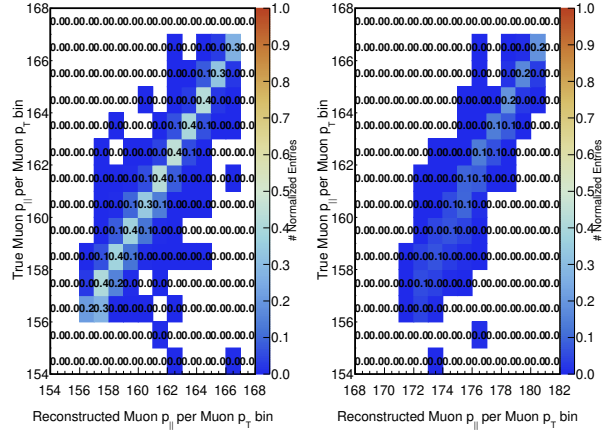
FIG. A.11: Row normalized migration matrix cells by bin number. Both plots show events truly in p_T bin 11, with events reconstructed in p_T bin 11 on the left and bin 12 on the right for the full range of $p_{||}$.
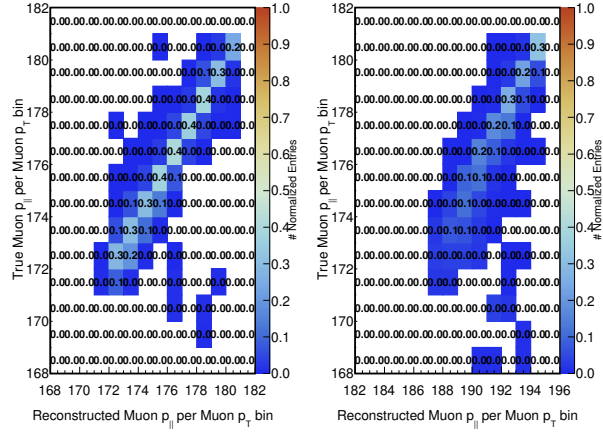
FIG. A.12: Row normalized migration matrix cells by bin number. Both plots show events truly in p_T bin 12, with events reconstructed in p_T bin 12 on the left and bin 13 on the right for the full range of $p_{||}$.
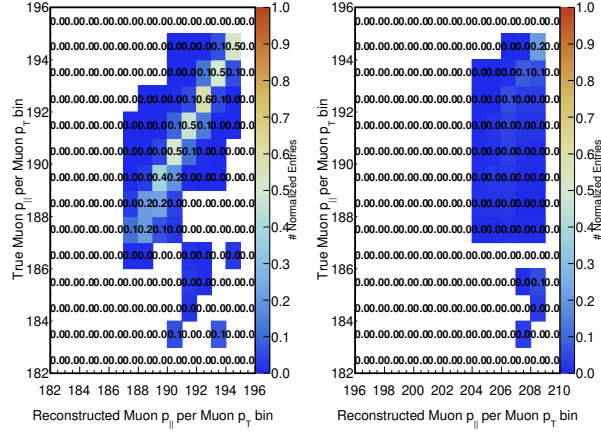
FIG. A.13: Row normalized migration matrix cells by bin number. Both plots show events truly in p_T bin 13, with events reconstructed in p_T bin 13 on the left and bin 14 on the right for the full range of $p_{||}$.

A.2 Average W and Q^2 distributions

The average true W and Q^2 as defined in **Ch. 1** in each double-differential bin for the inclusive analysis are show in Fig.A.14 and Fig.A.15, respectively.
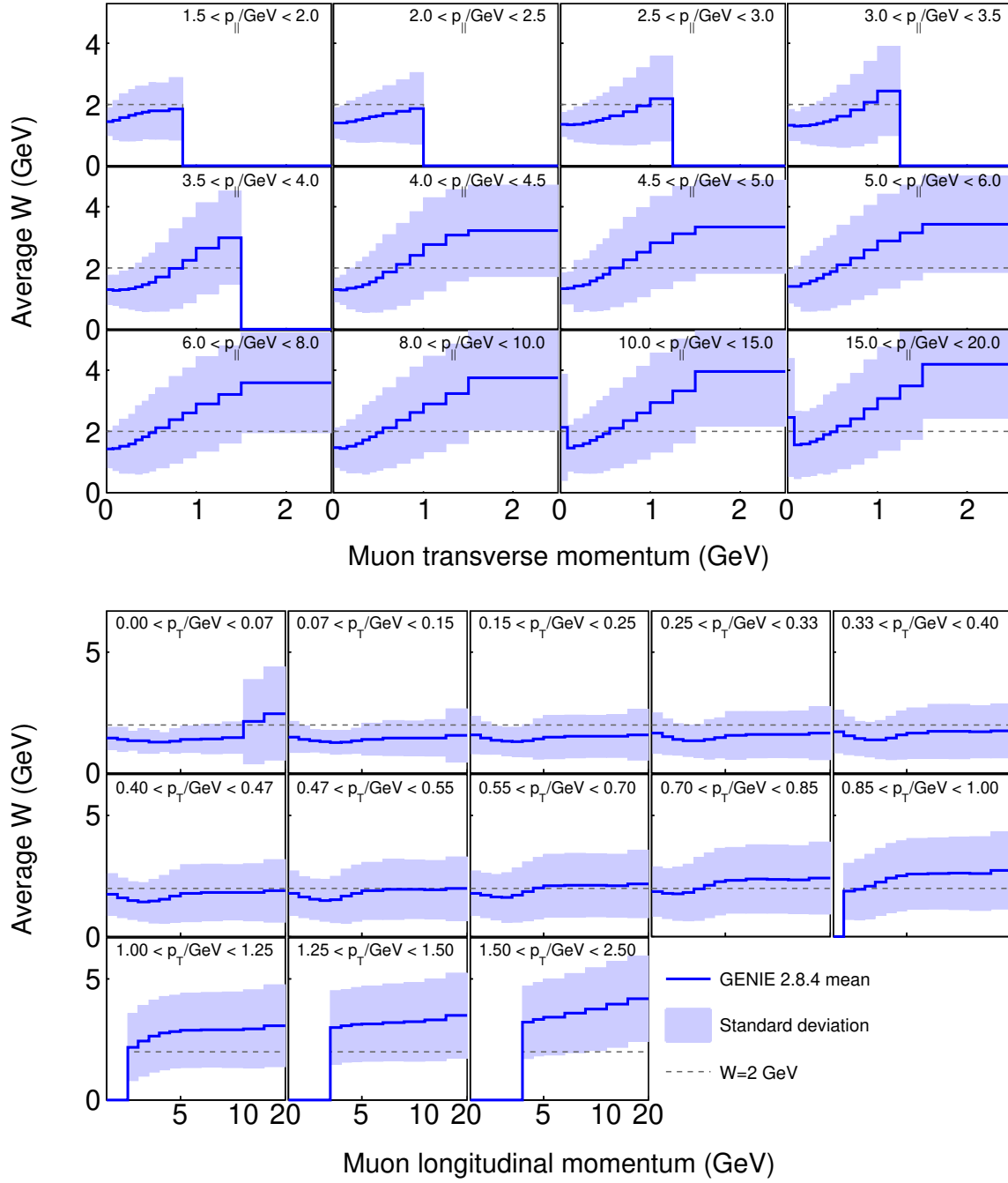
FIG. A.14: Average W distribution for the double differential inclusive cross section in bins of p_T and $p_{||}$.

195
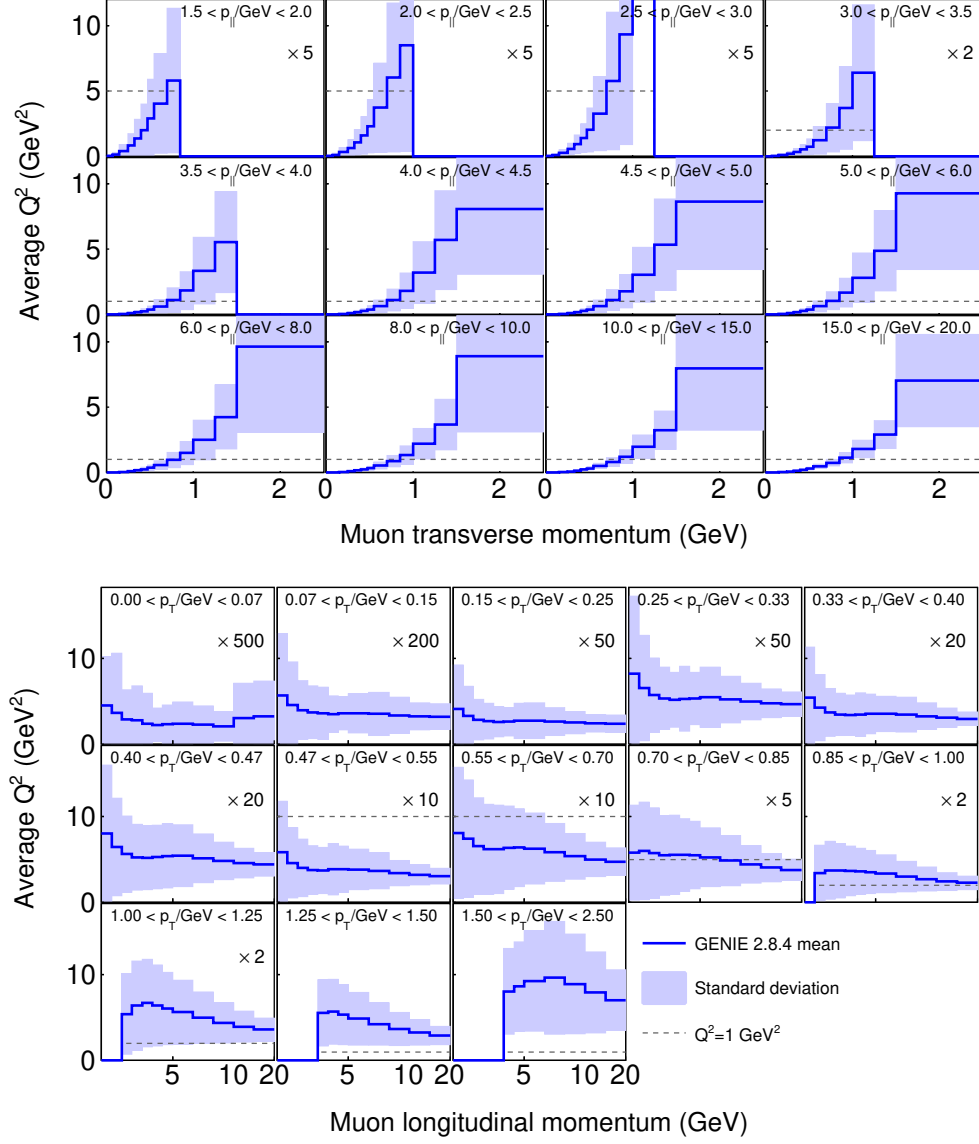
FIG. A.15: Average Q^2 distribution for the double differential inclusive cross section in bins of p_T and $p_{||}$.

A.3 Additional cross section model and tune comparisons

Included are a series of comparisons between MINERvA tune v1, GENIE 2.8.4, and various tunes to GENIE or alternate event generators. The tunes are shown in the form of *Base model + any tunes* The non-resonant pion suppression is referred to as "pion tuned" and the quasielastic low four momentum transfer as "RPA". The tunes which have an additional 2p2h sample included are labeled with "2p2h". All tunes labeled with MINERvA tune v1+*tune* include the non-resonant suppression, the 2p2h sample with enhancement based on the low recoil analysis, and the QE RPA suppression. The three DIS models discussed in the main text of the thesis are shown as AMU DIS, nCTEQ15 DIS, and nCTEQν DIS. The final set of modifications in these plots are suppressions to the low Q^2 resonance production: one based on MINOS data (MINOS RPA Res), one which applies the Nieves RPA based on the QE channel to resonant events (Nieves RPA Res), and one based on MINERvA data (MINERvA tune v2), all of which are applied in addition to all of the modifications in MINERvA tune v1. Also shown are GIBUU and the NuWro spectral function and local Fermi gas models.
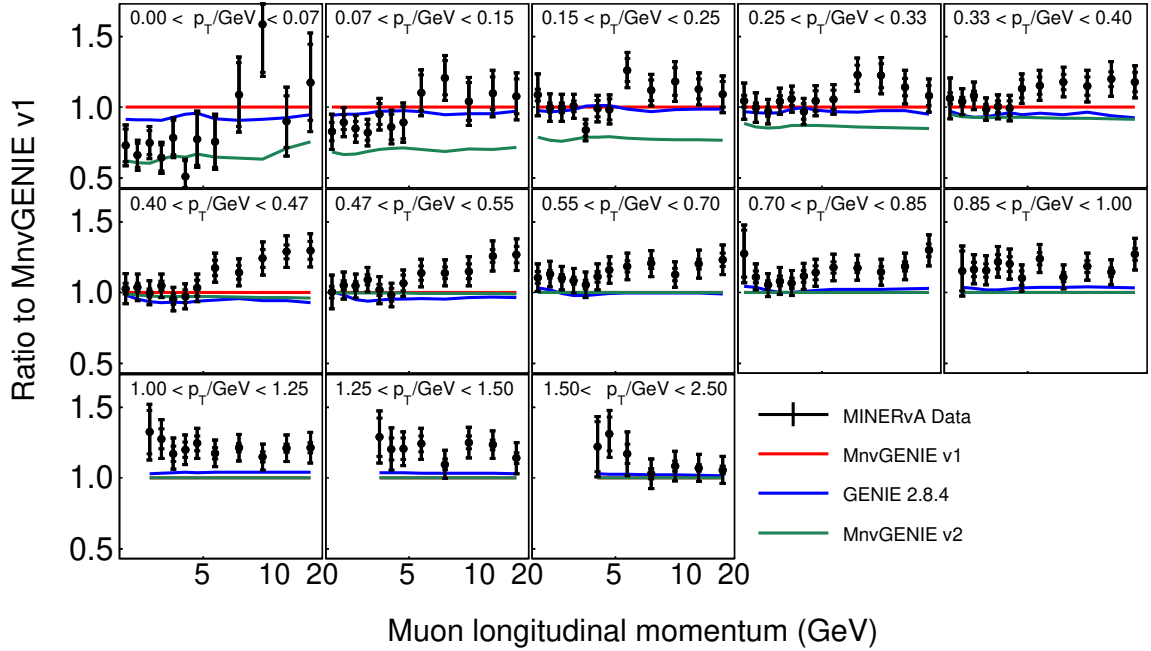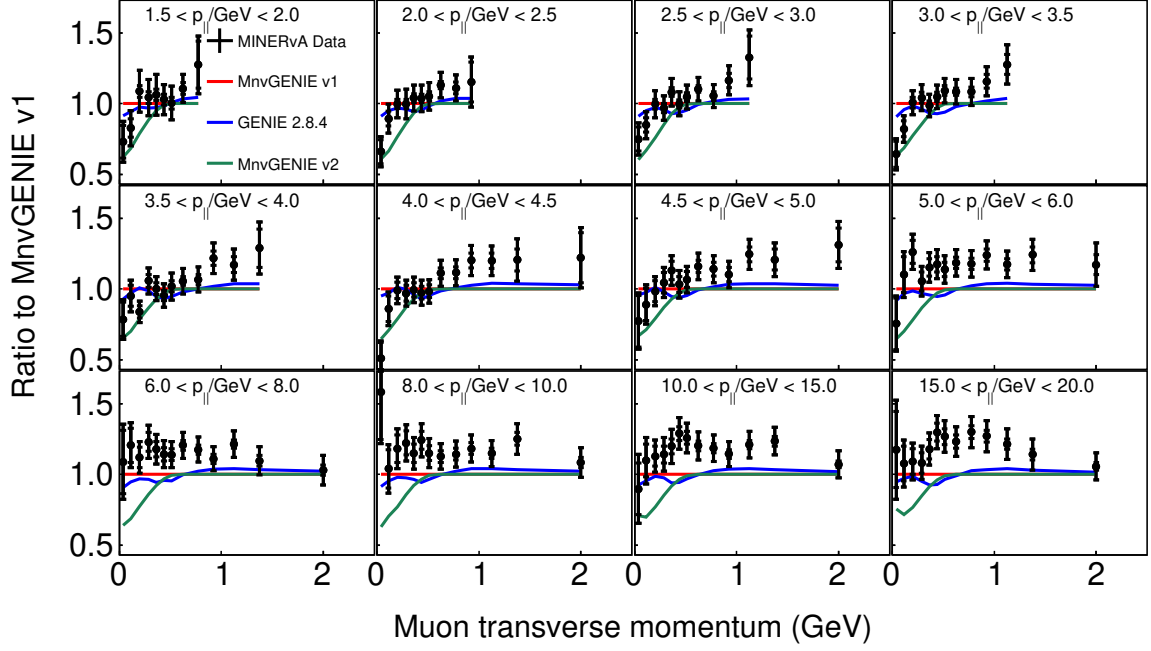
FIG. A.16: Comparisons of MINERvA tune v1, GENIE 2.8.4 and alternate tunes and models with the absolute normalization (1/13).

FIG. A.17: Comparisons of MINERvA tune v1, GENIE 2.8.4 and alternate tunes and models with the absolute normalization (2/13).

199
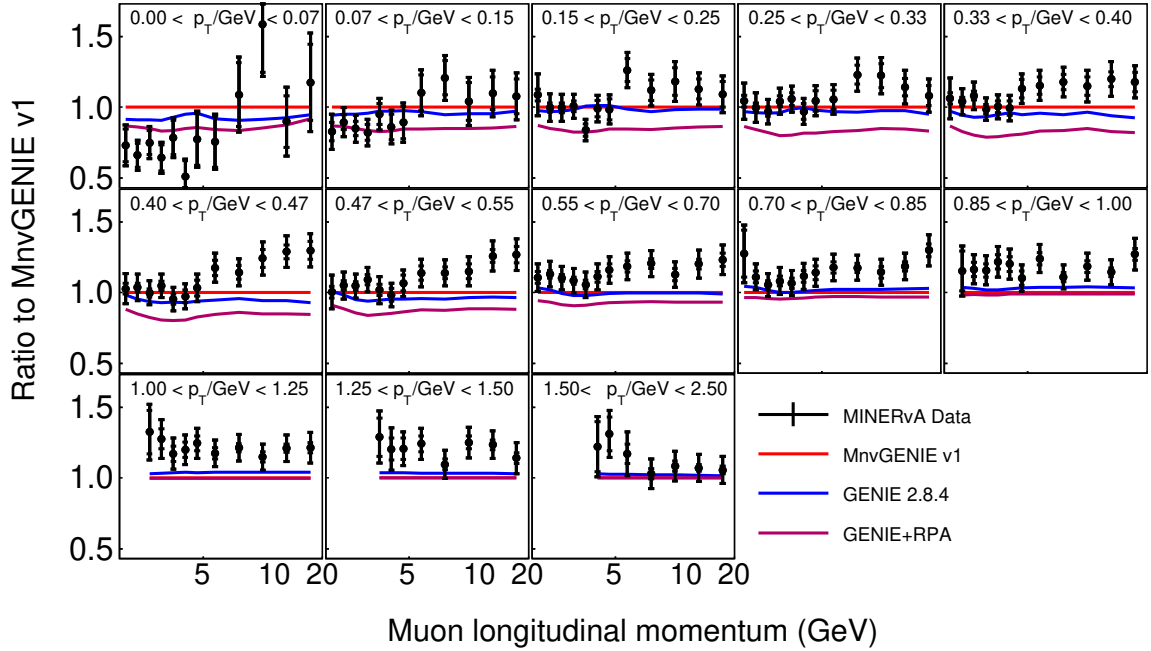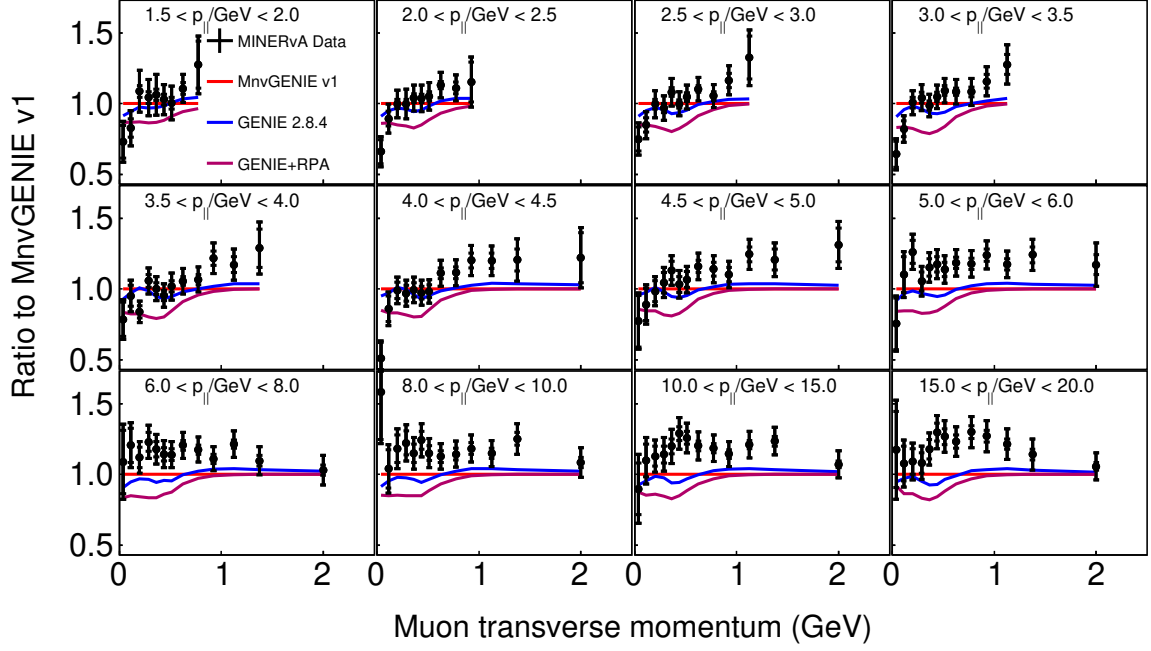
FIG. A.18: Comparisons of MINERvA tune v1, GENIE 2.8.4 and alternate tunes and models with the absolute normalization (3/13).
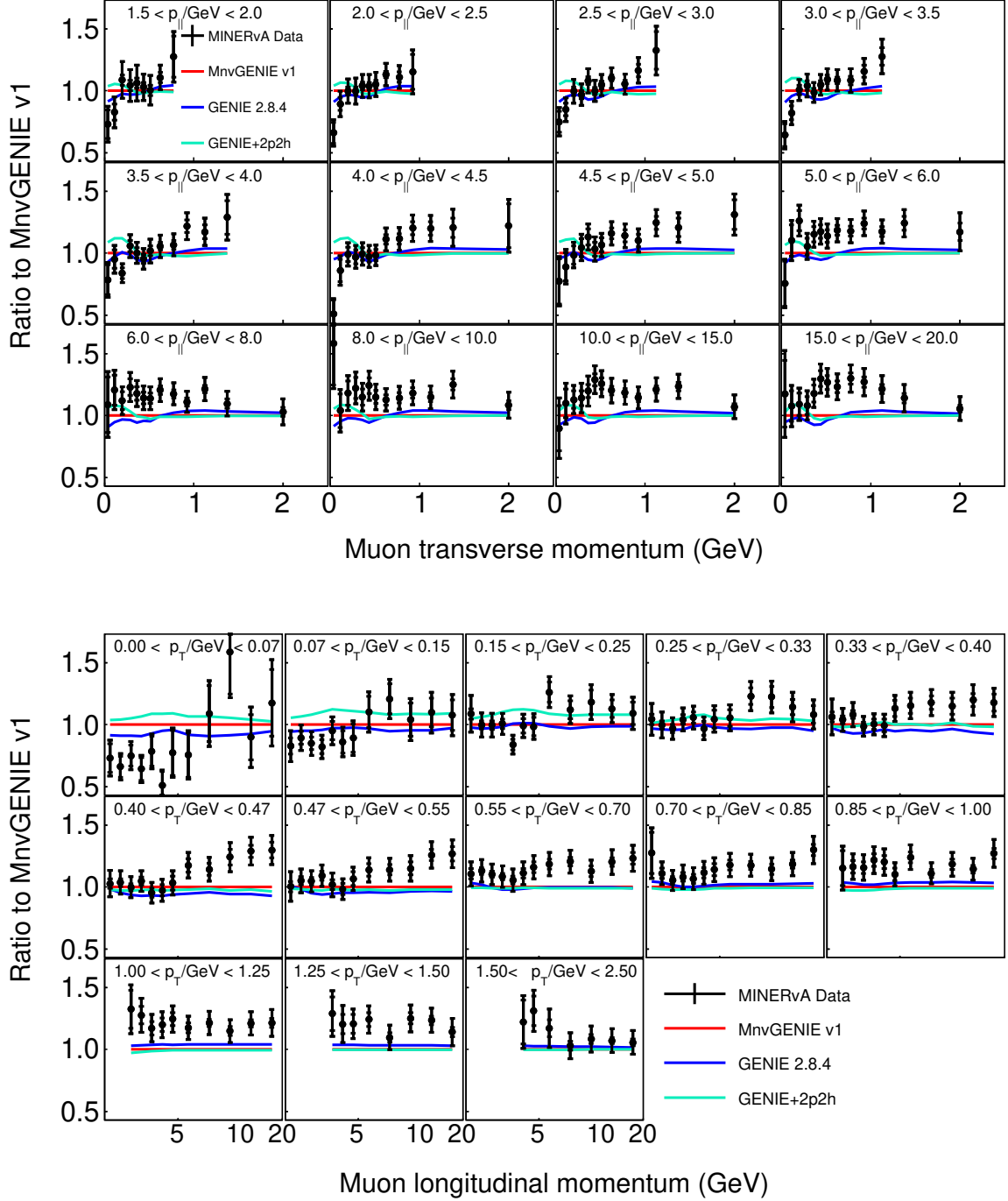
FIG. A.19: Comparisons of MINERvA tune v1, GENIE 2.8.4 and alternate tunes and models with the absolute normalization (4/13).
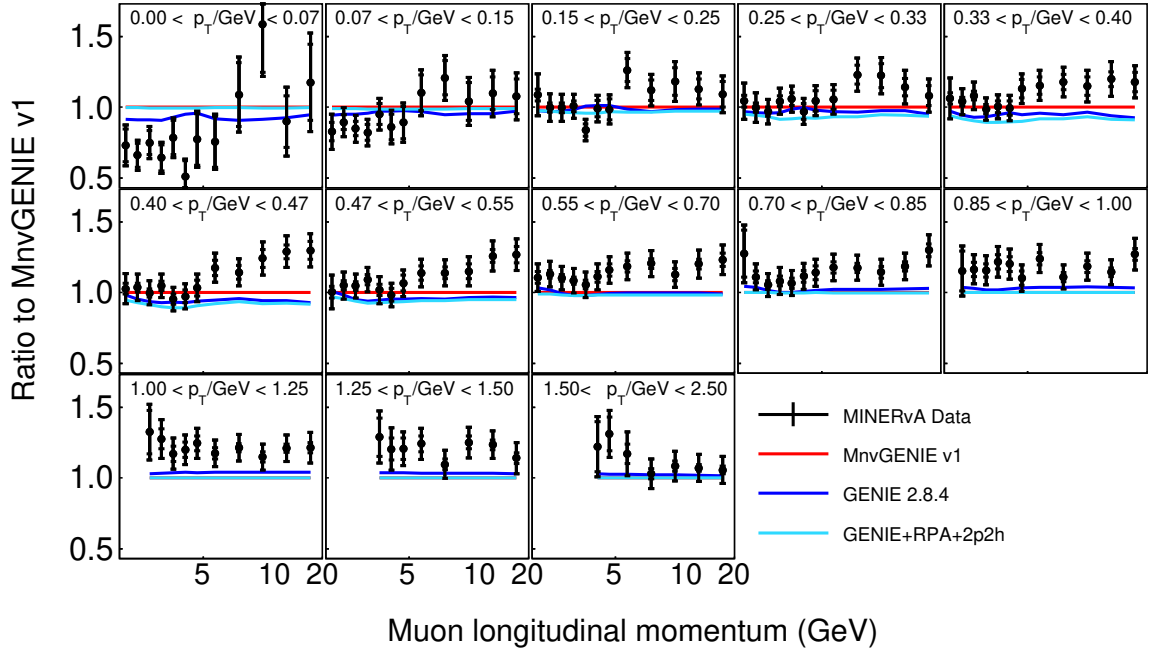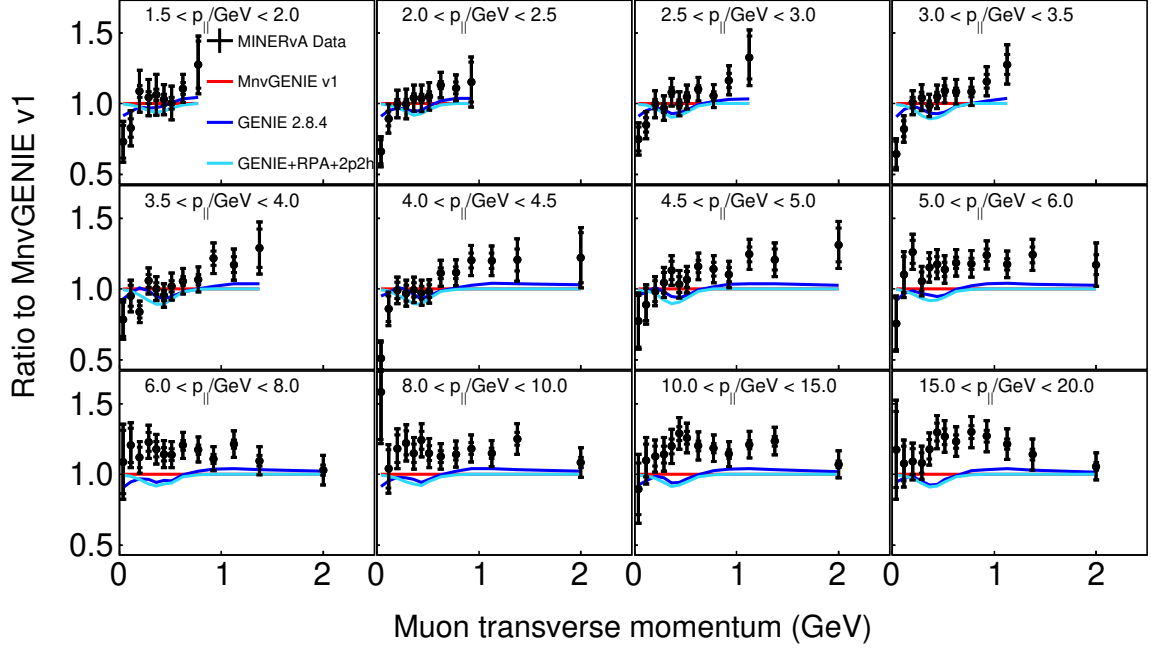
FIG. A.20: Comparisons of MINERvA tune v1, GENIE 2.8.4 and alternate tunes and models with the absolute normalization (5/13).

202
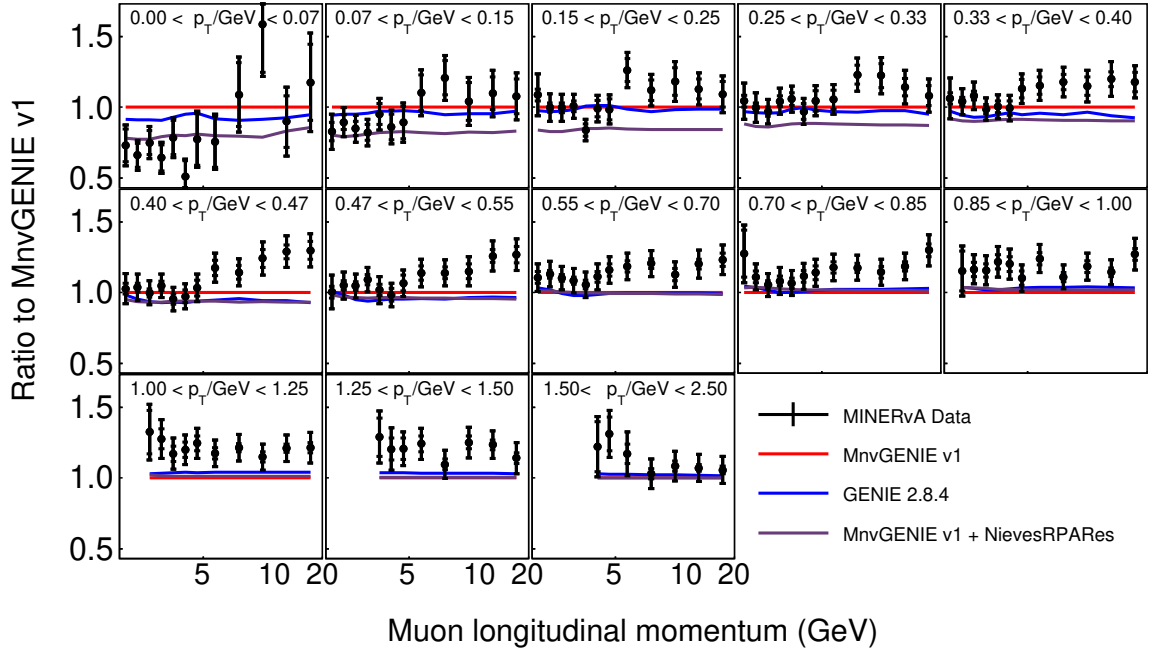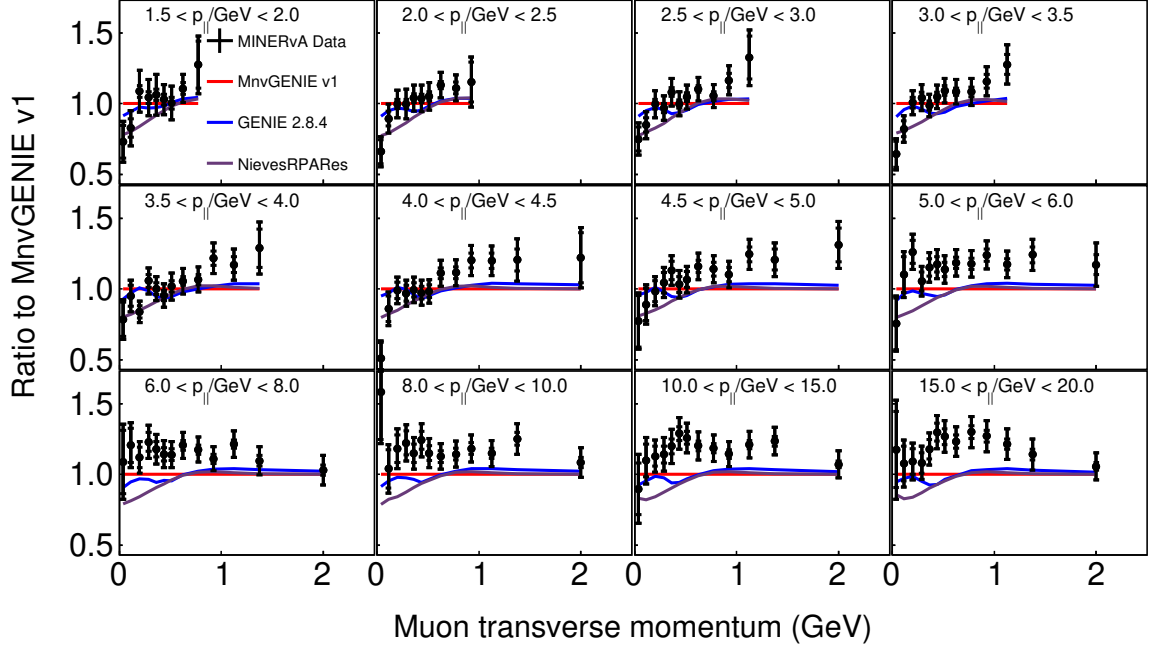
FIG. A.21: Comparisons of MINERvA tune v1, GENIE 2.8.4 and alternate tunes and models with the absolute normalization (6/13).
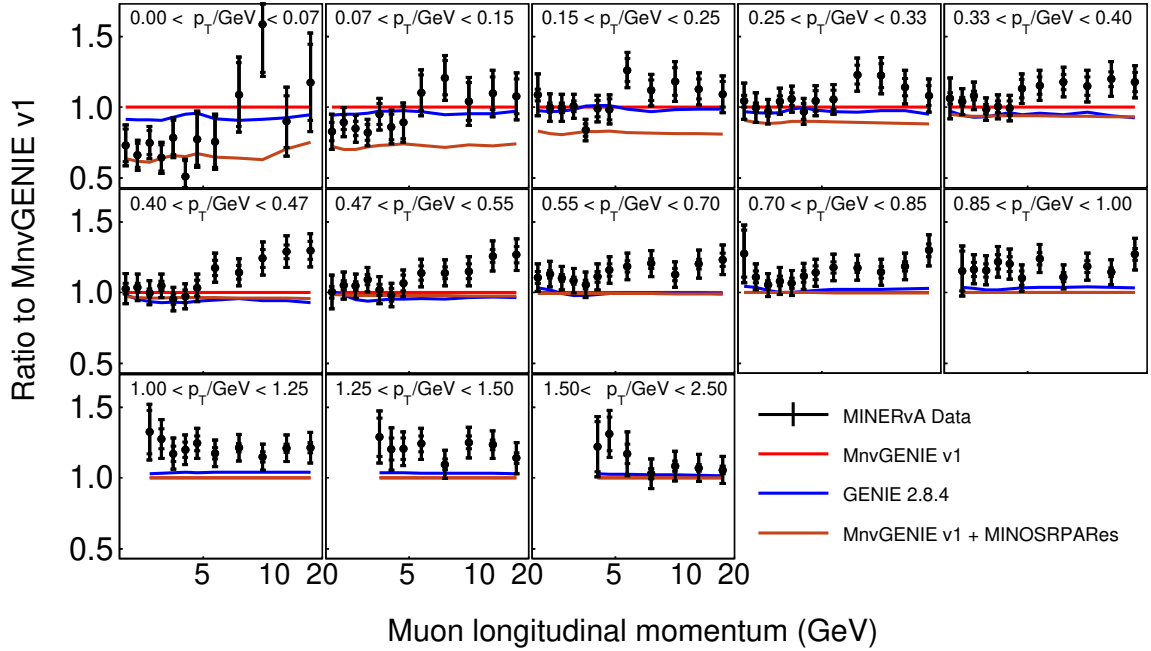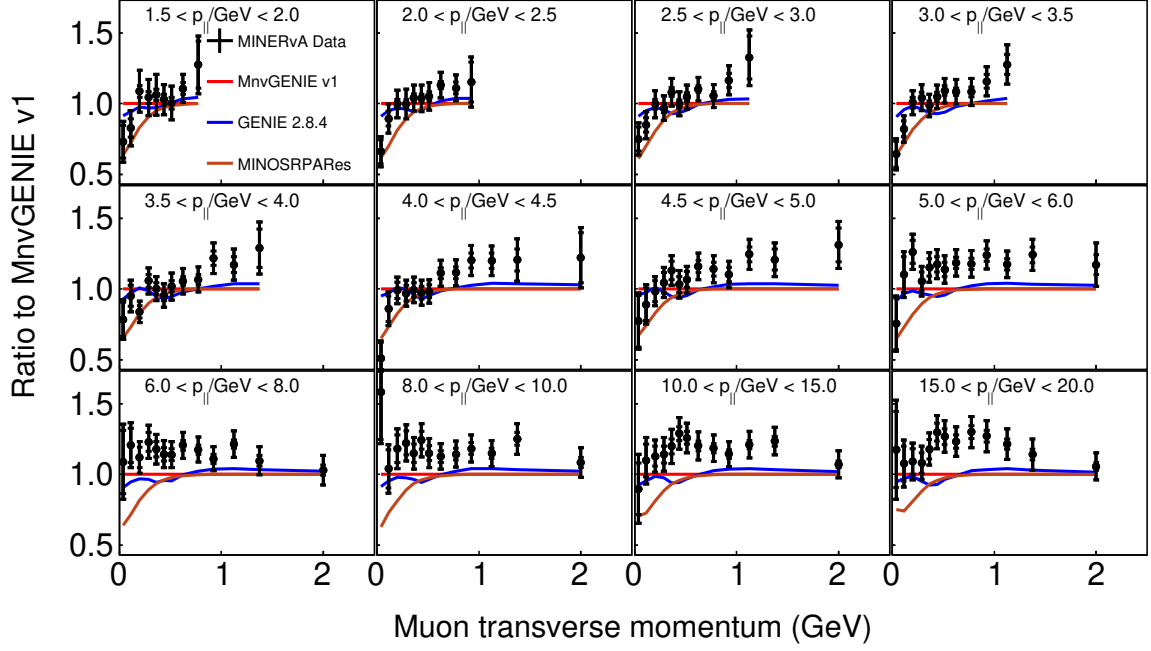
FIG. A.22: Comparisons of MINERvA tune v1, GENIE 2.8.4 and alternate tunes and models with the absolute normalization (7/13).
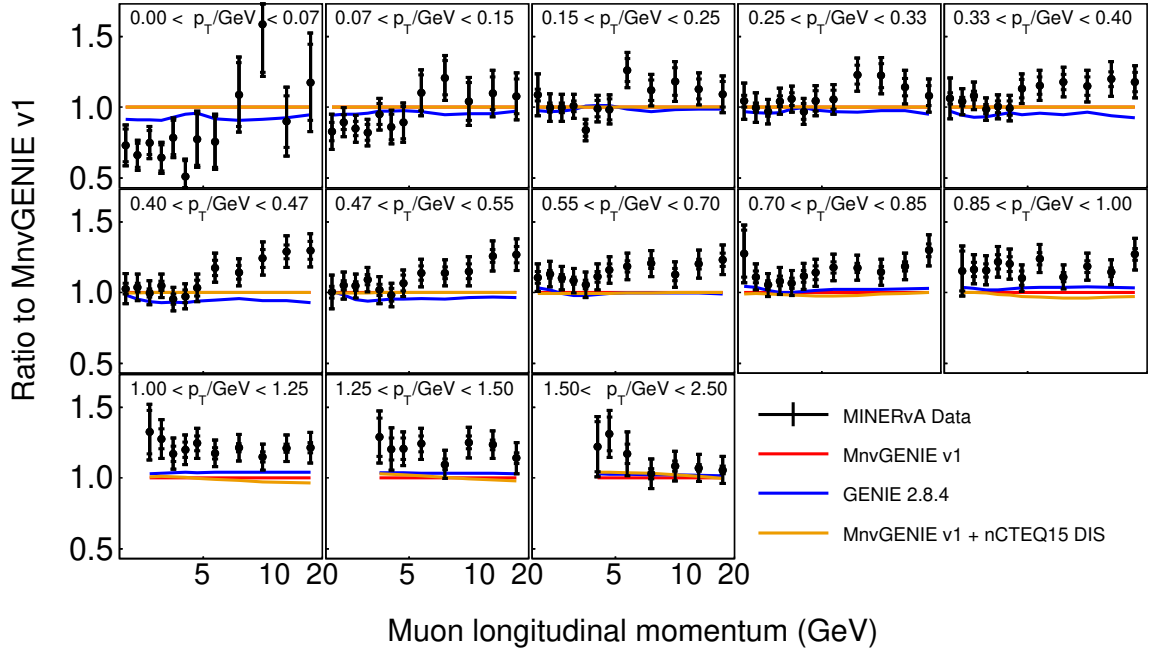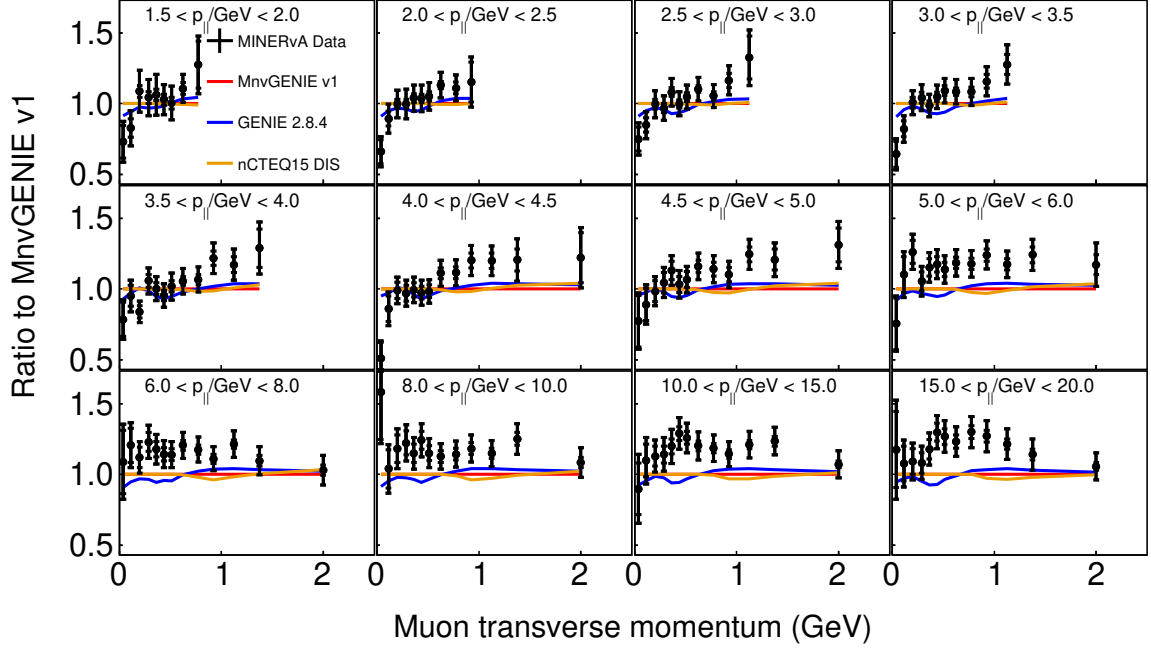
FIG. A.23: Comparisons of MINERvA tune v1, GENIE 2.8.4 and alternate tunes and models with the absolute normalization (8/13).
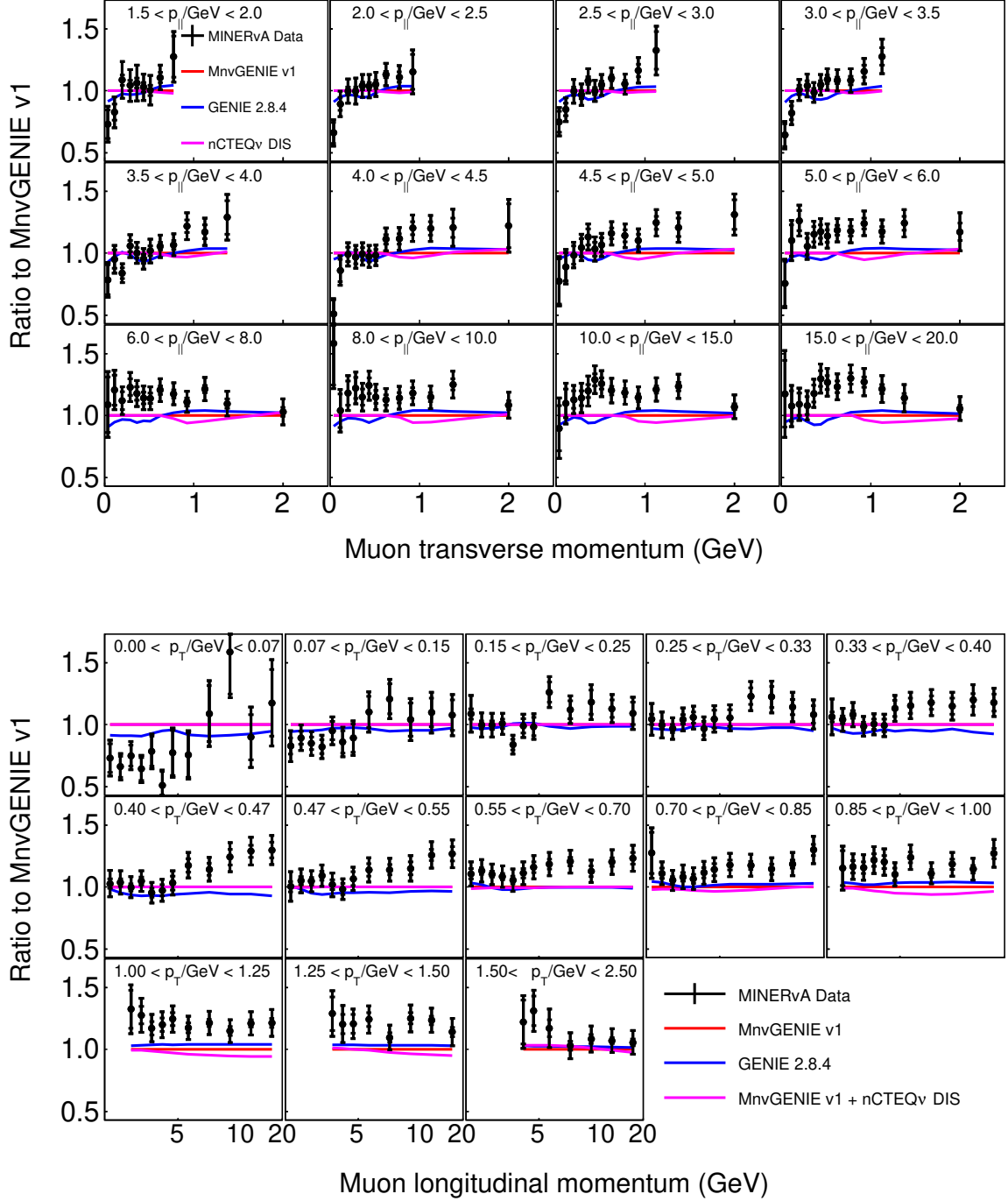
FIG. A.24: Comparisons of MINERvA tune v1, GENIE 2.8.4 and alternate tunes and models with the absolute normalization (9/13).
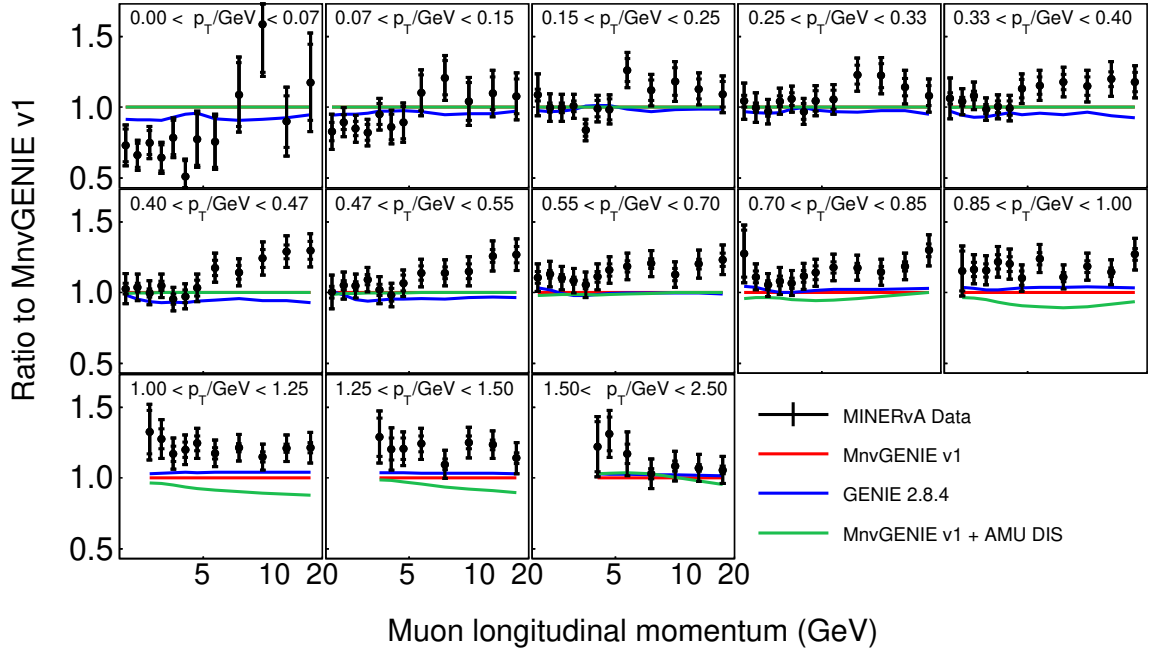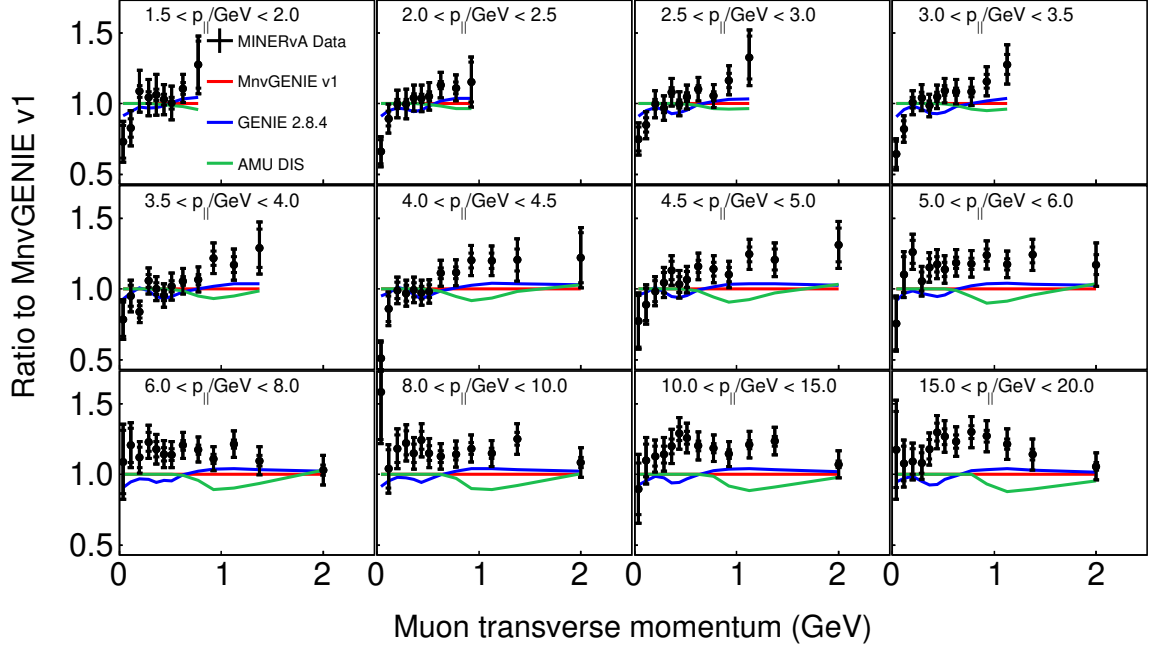
FIG. A.25: Comparisons of MINERvA tune v1, GENIE 2.8.4 and alternate tunes and models with the absolute normalization (10/13).
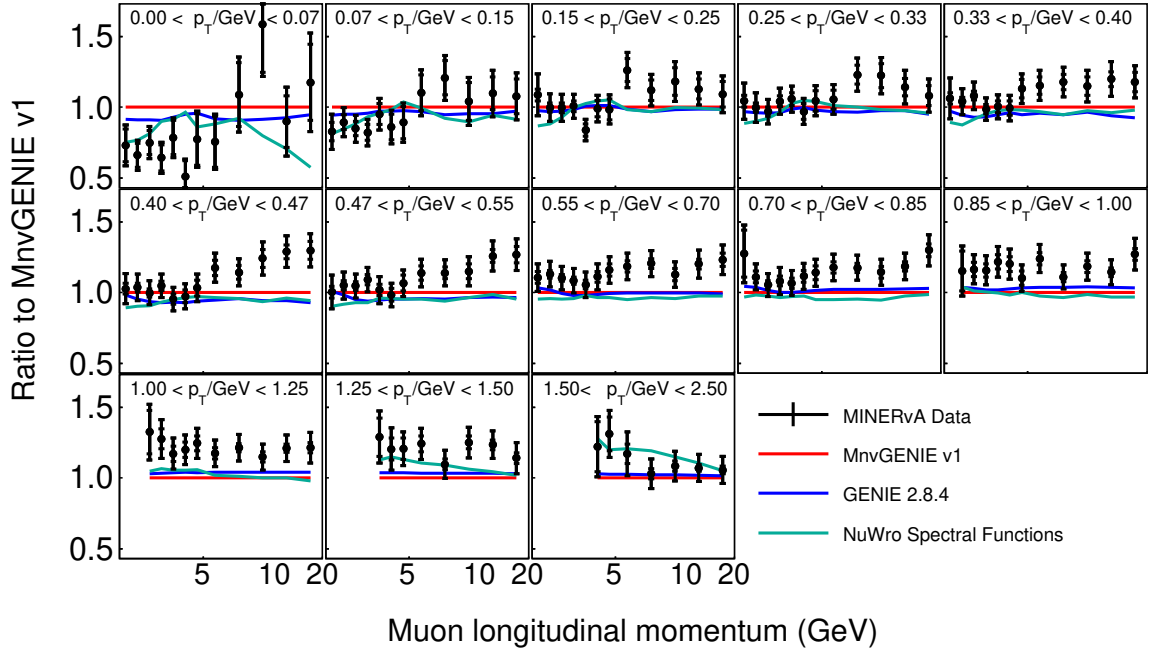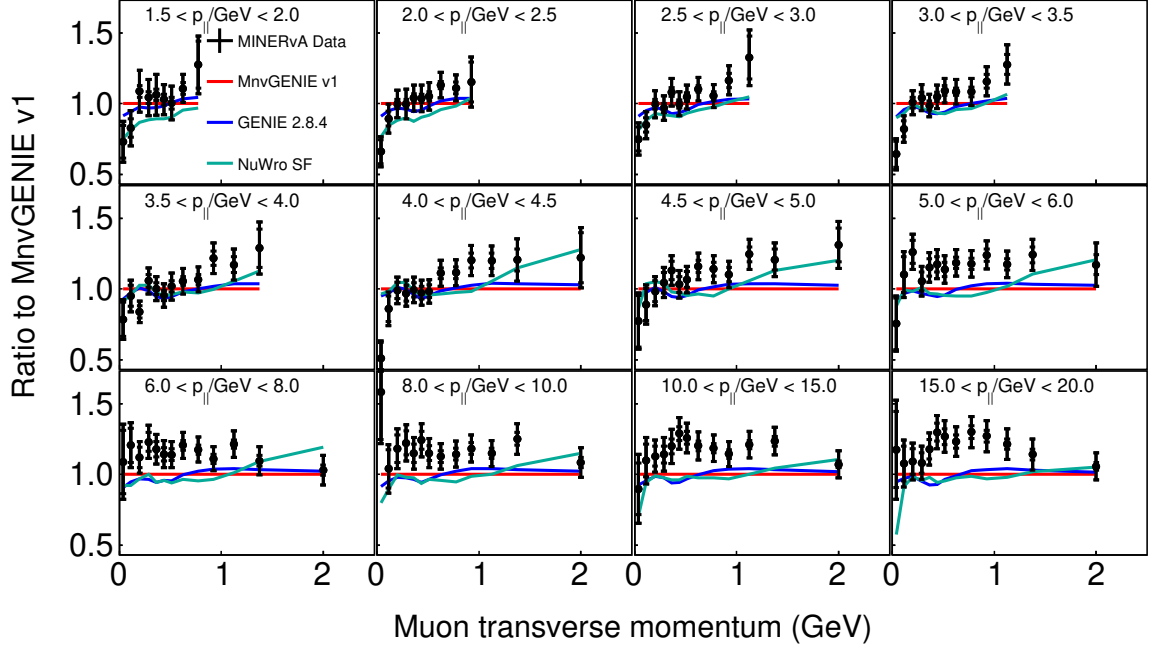
FIG. A.26: Comparisons of MINERvA tune v1, GENIE 2.8.4 and alternate tunes and models with the absolute normalization (11/13).

208
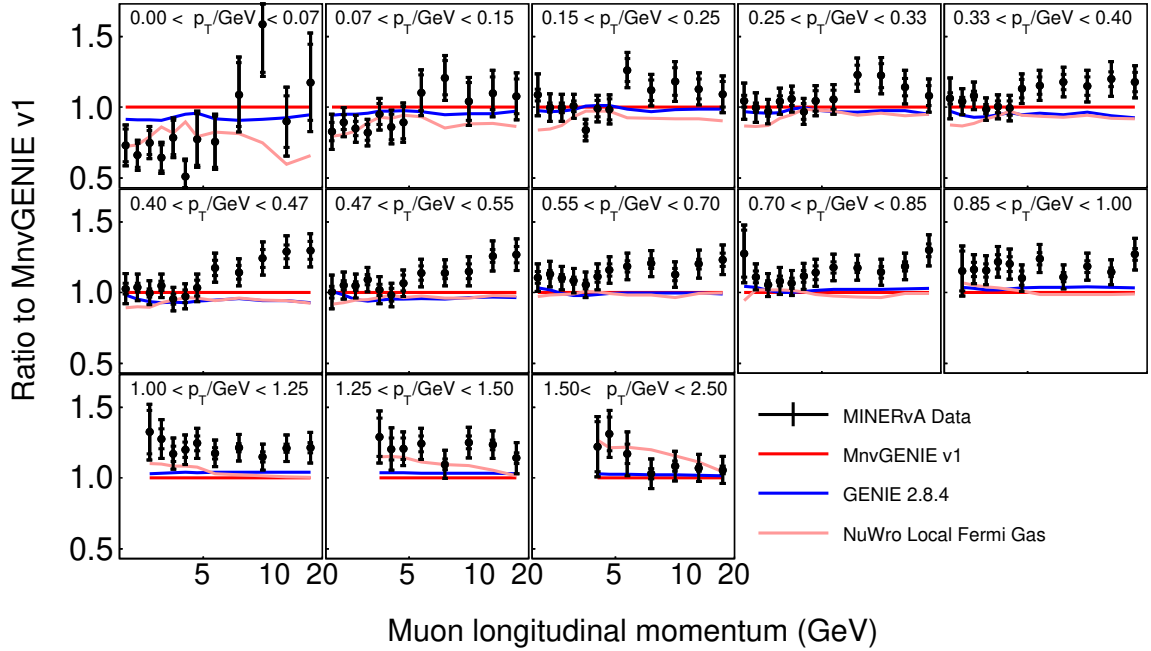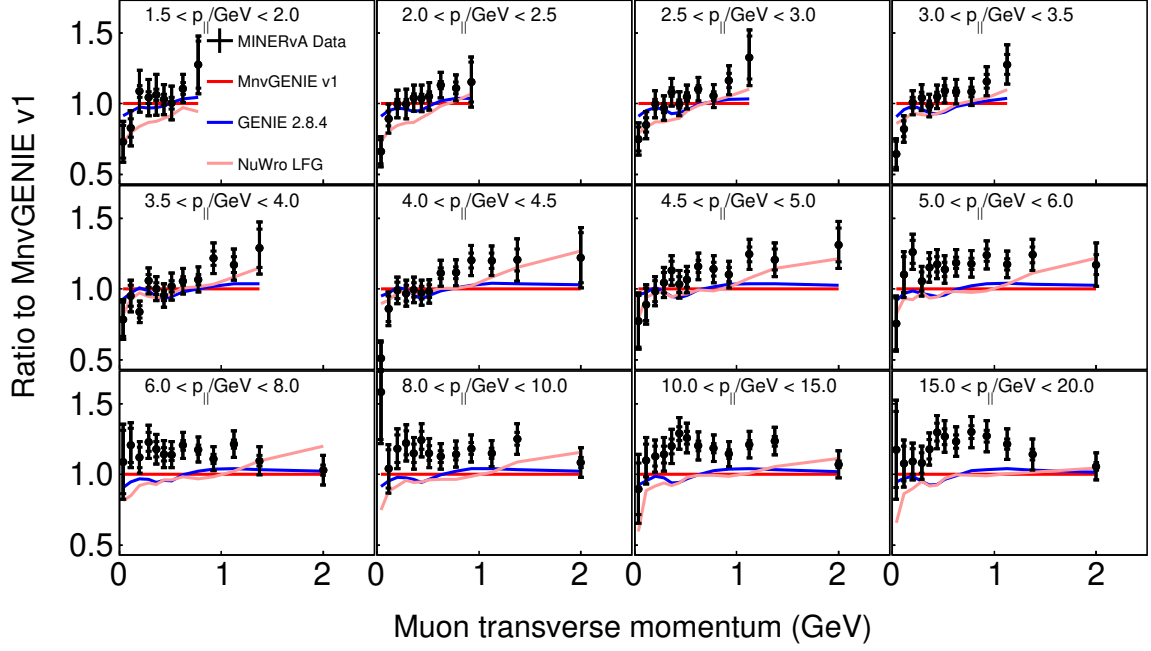
FIG. A.27: Comparisons of MINERvA tune v1, GENIE 2.8.4 and alternate tunes and models with the absolute normalization (12/13).

209
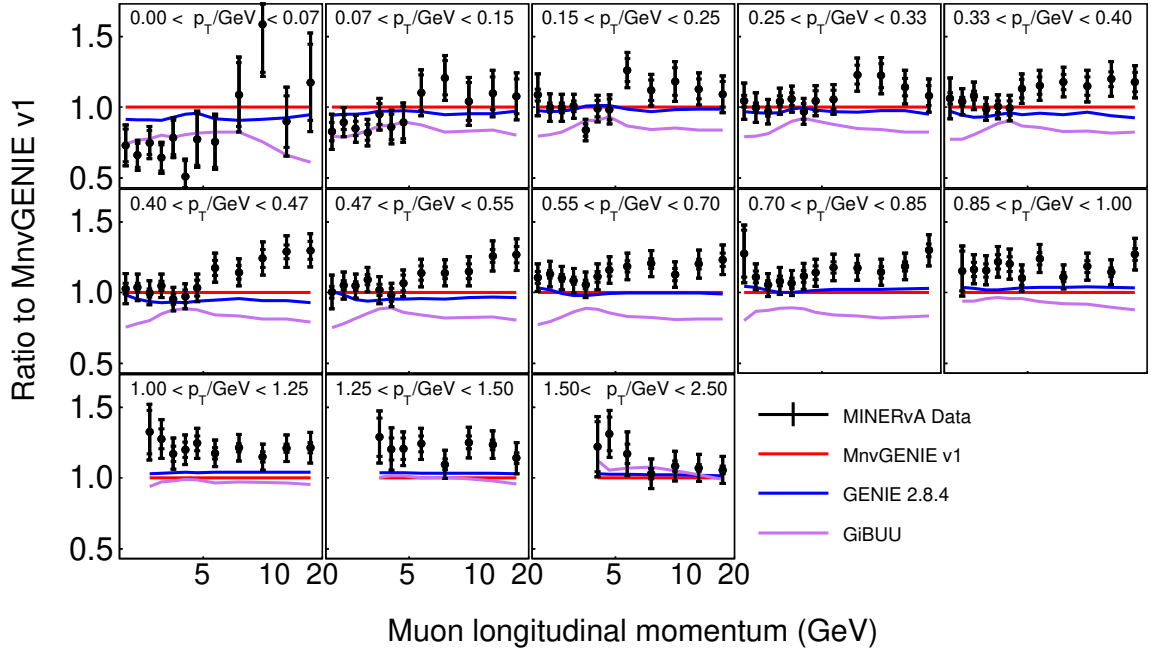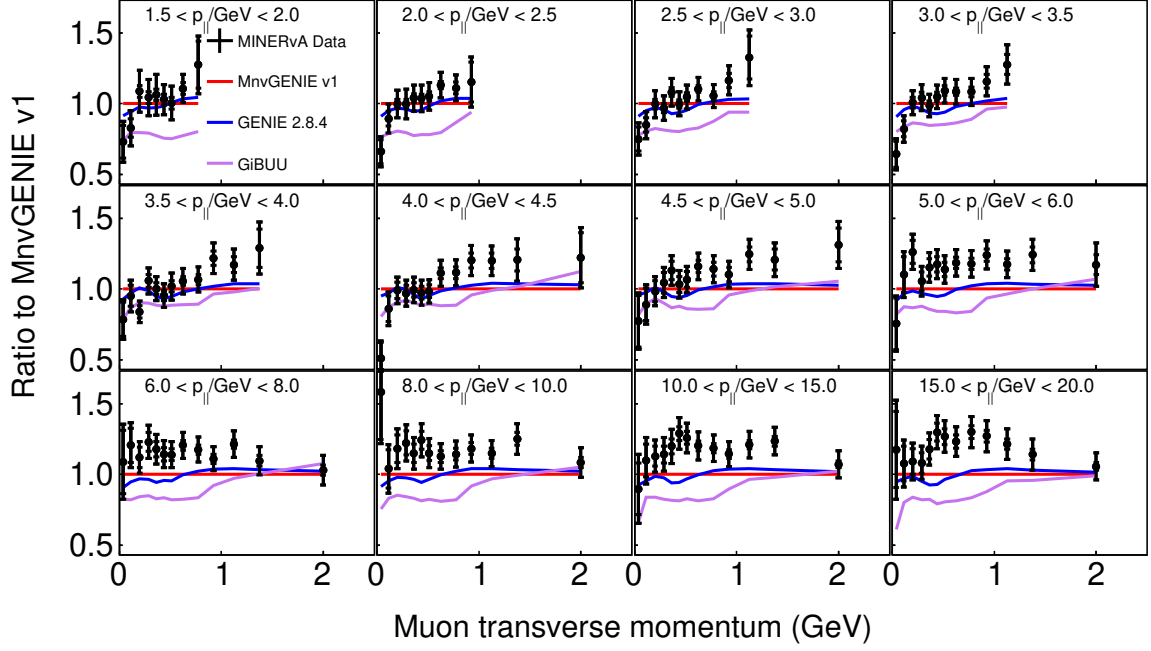
FIG. A.28: Comparisons of MINERvA tune v1, GENIE 2.8.4 and alternate tunes and models with the absolute normalization (13/13).
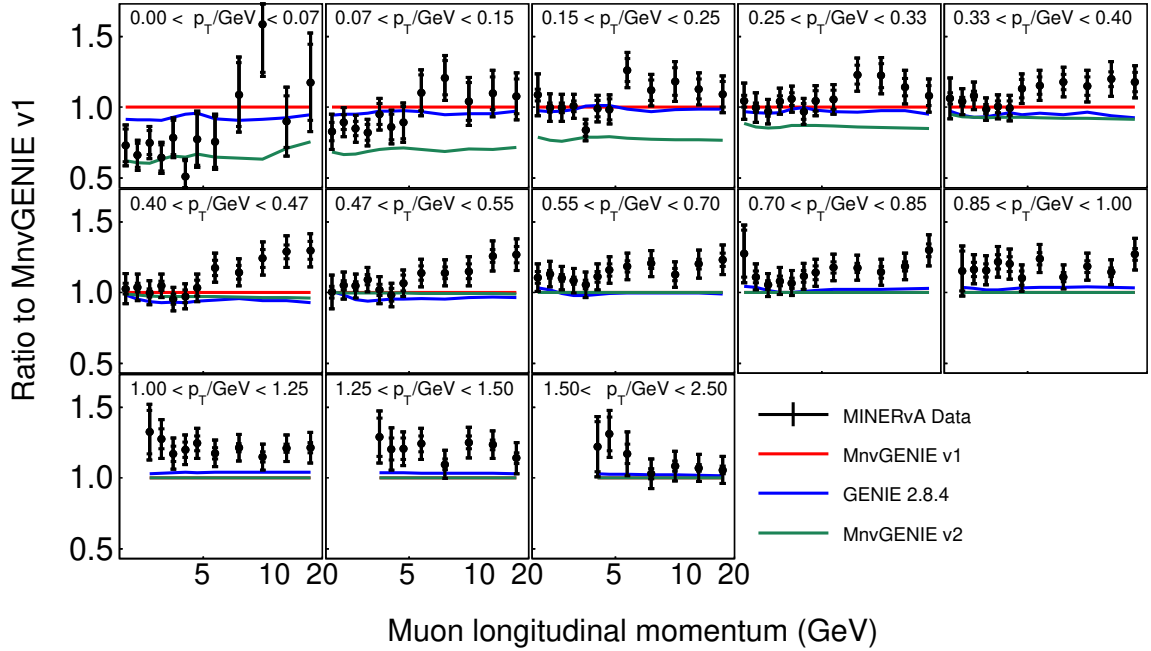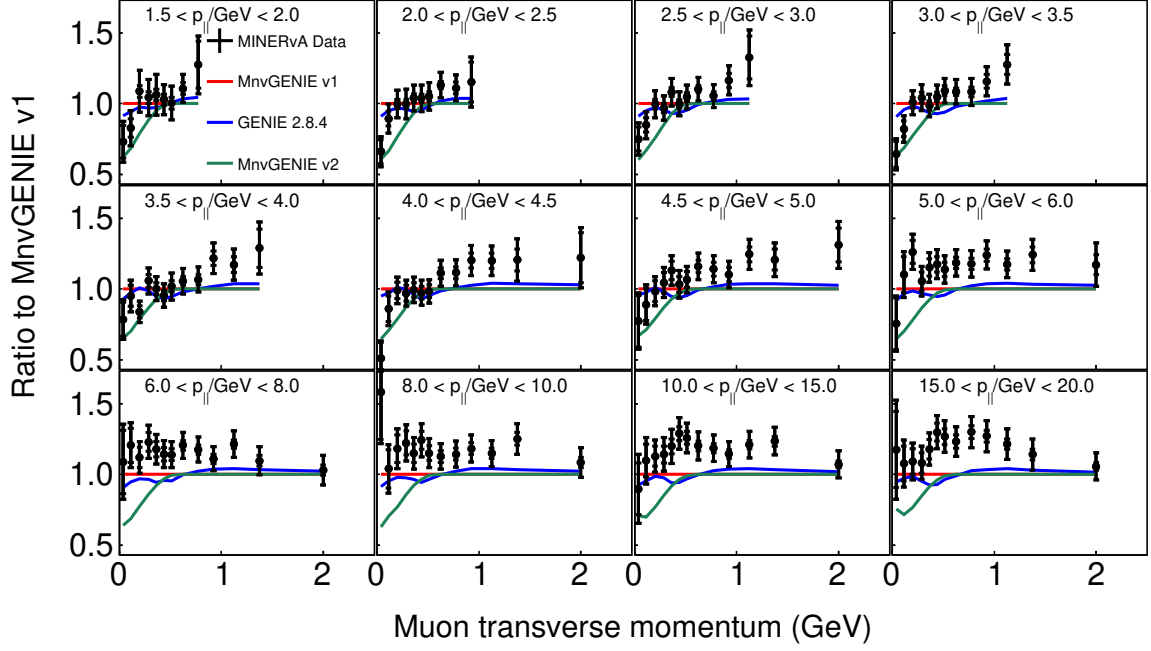
FIG. A.29: Area normalized comparisons of MINERvA tune v1, GENIE 2.8.4 and alternate tunes and models (1/13).
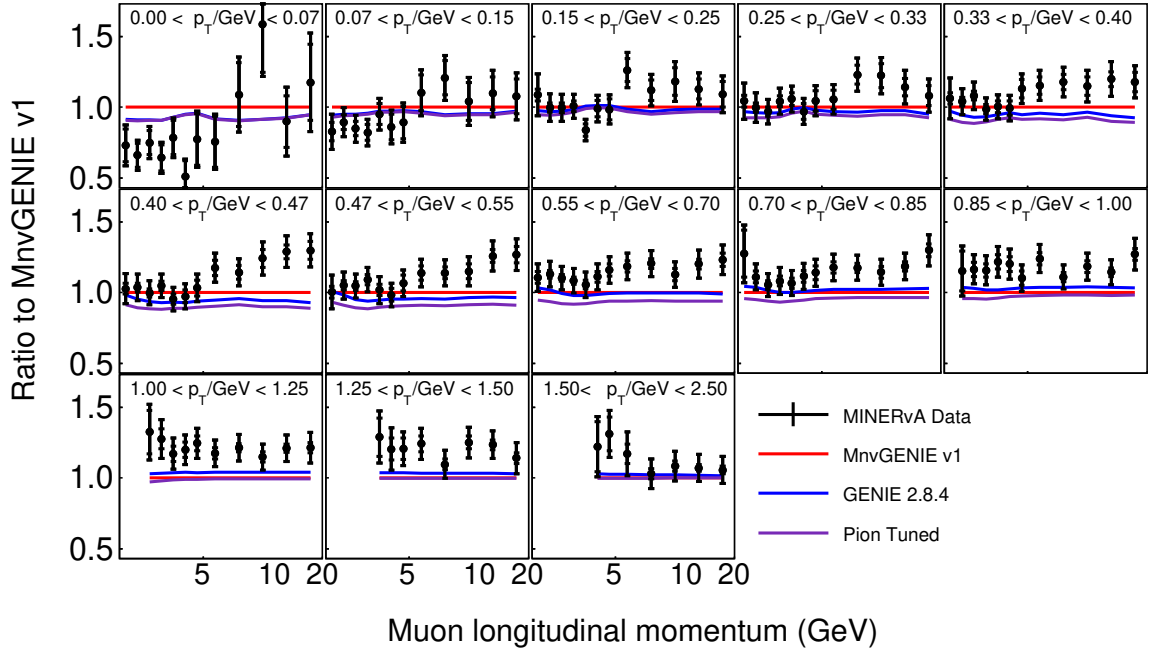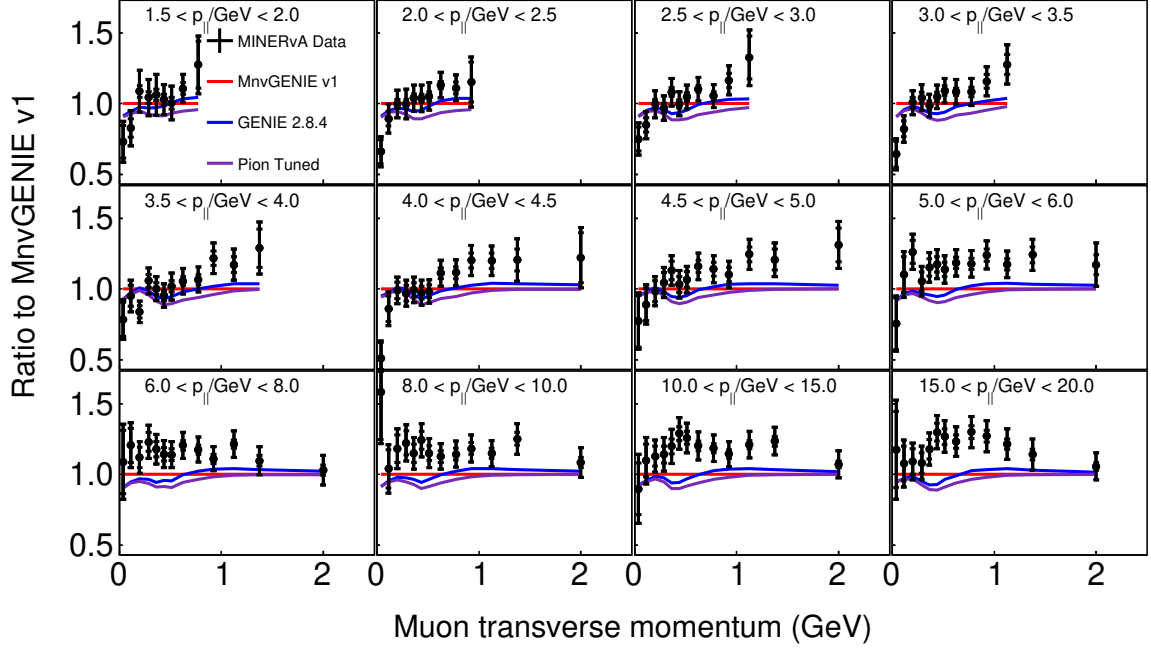
FIG. A.30: Area normalized comparisons of MINERvA tune v1, GENIE 2.8.4 and alternate tunes and models (2/13).
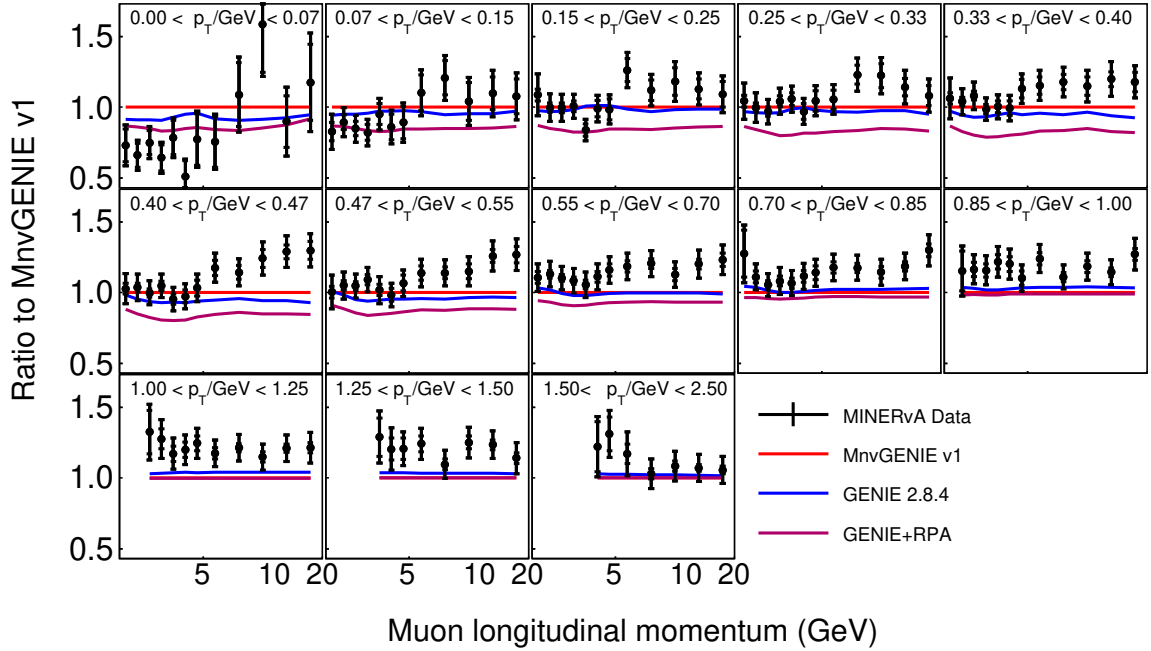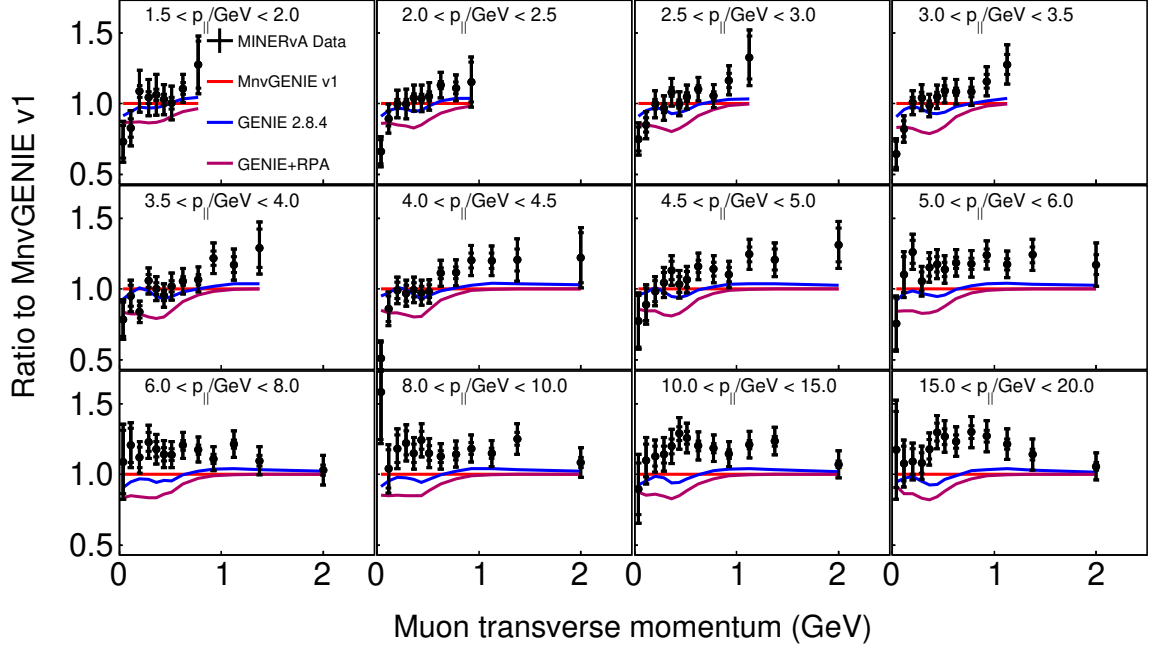
FIG. A.31: Area normalized comparisons of MINERvA tune v1, GENIE 2.8.4 and alternate tunes and models (3/13).
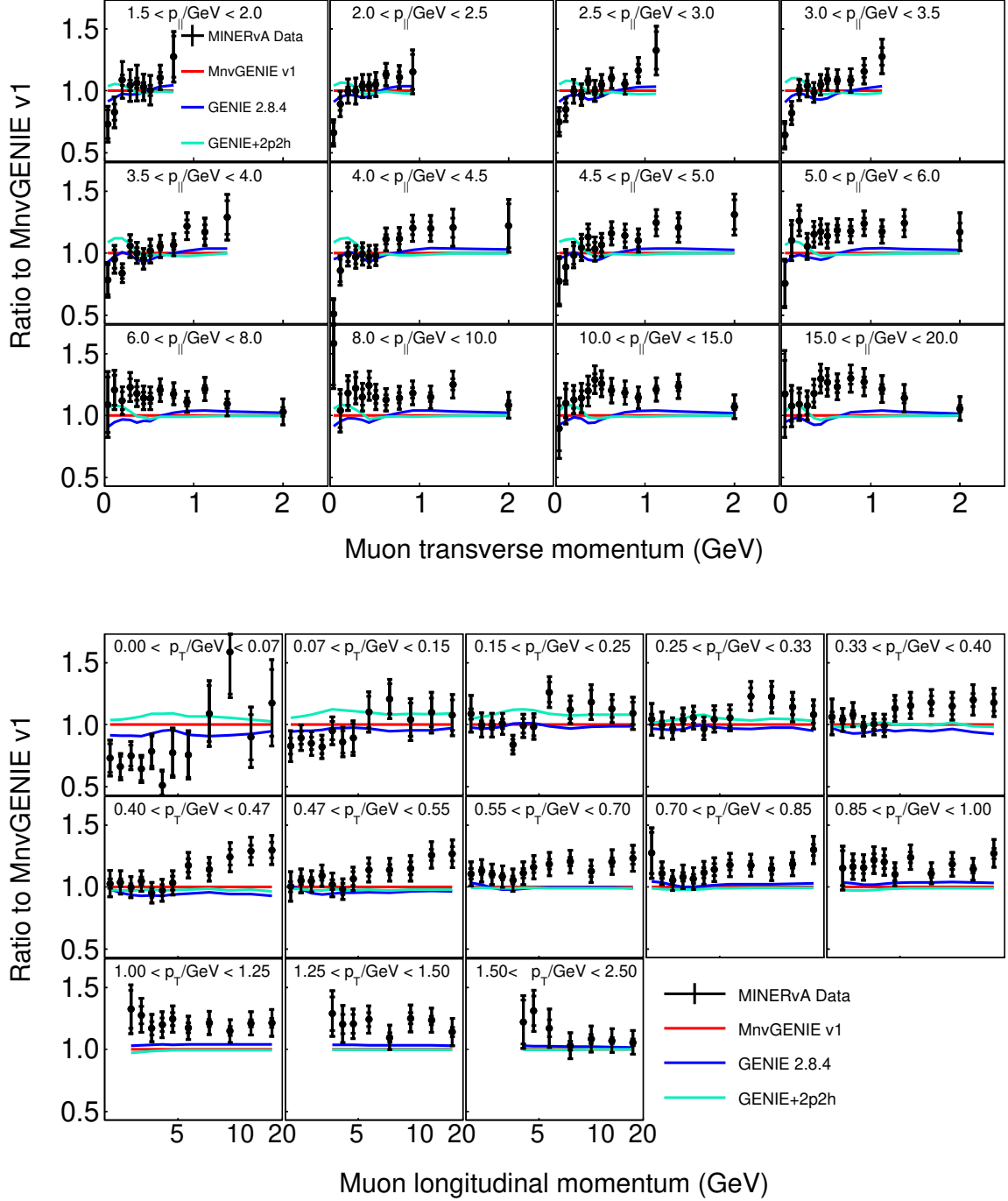
FIG. A.32: Area normalized comparisons of MINERvA tune v1, GENIE 2.8.4 and alternate tunes and models (4/13).
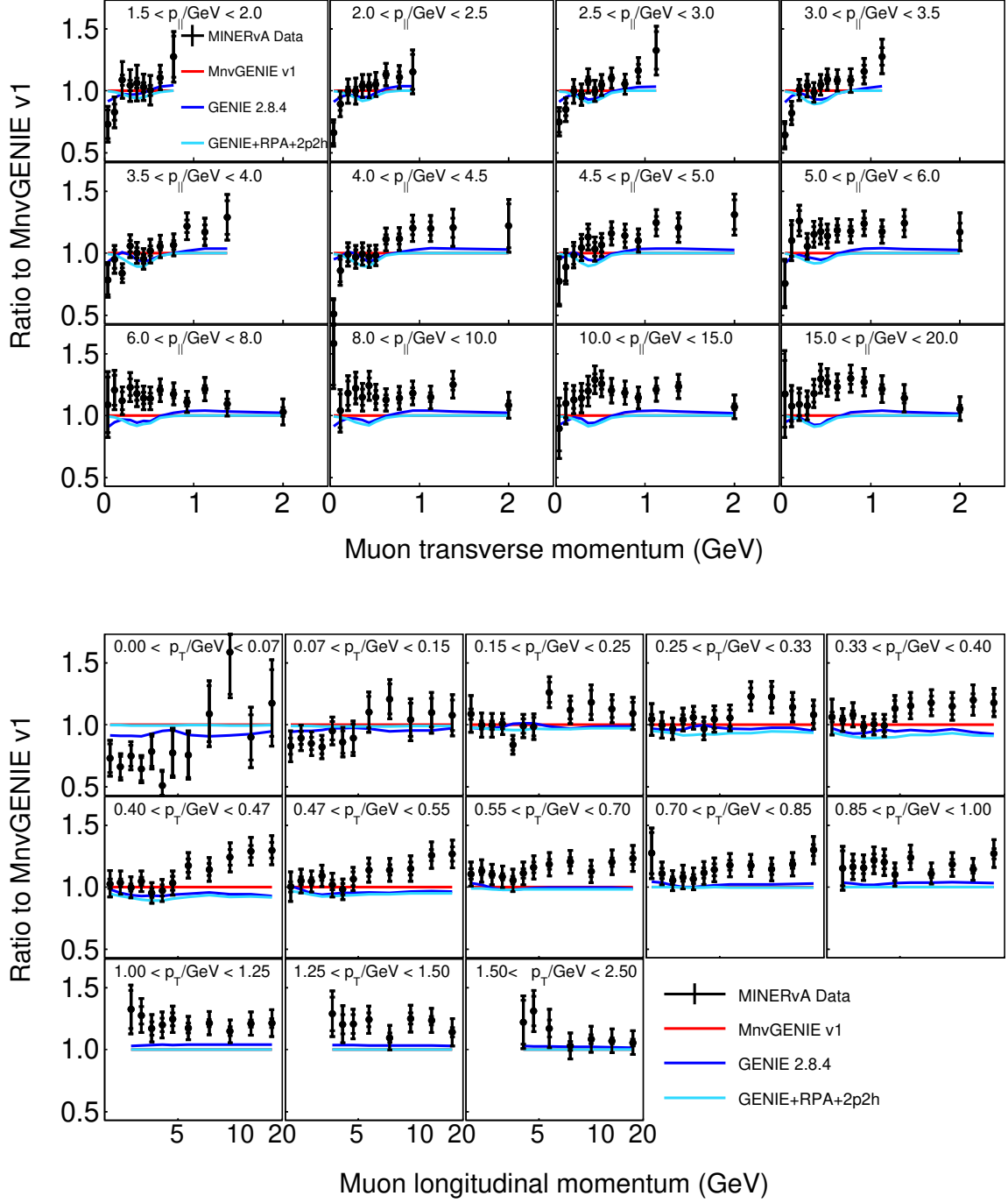
FIG. A.33: Area normalized comparisons of MINERvA tune v1, GENIE 2.8.4 and alternate tunes and models (5/13).
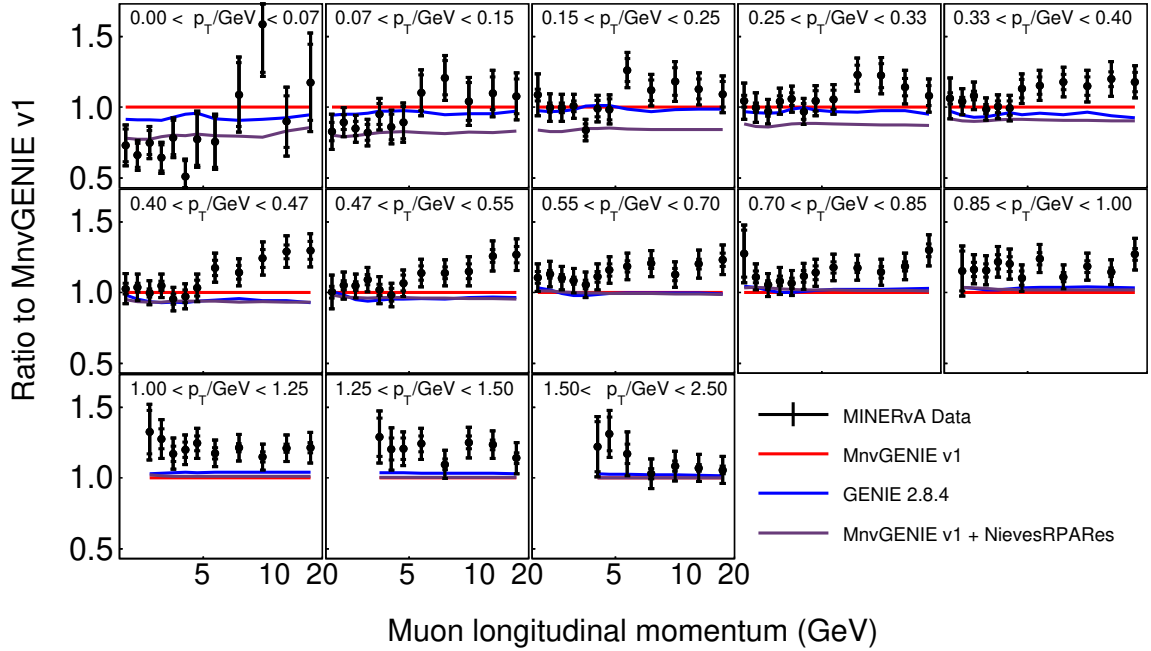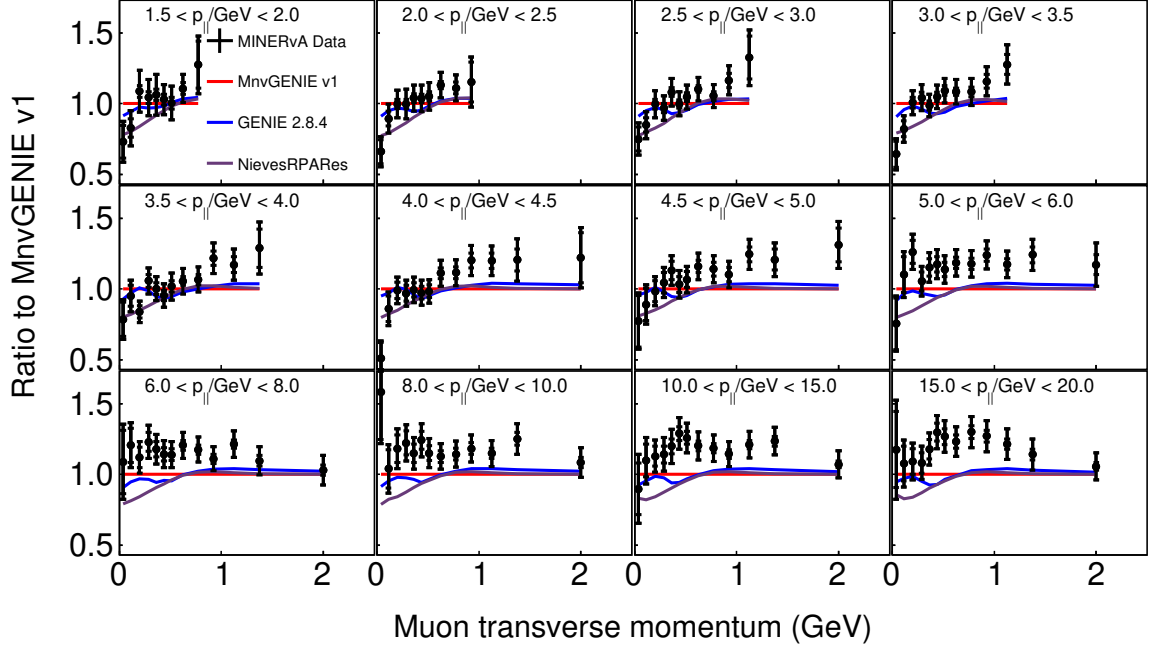
FIG. A.34: Area normalized comparisons of MINERvA tune v1, GENIE 2.8.4 and alternate tunes and models (6/13).
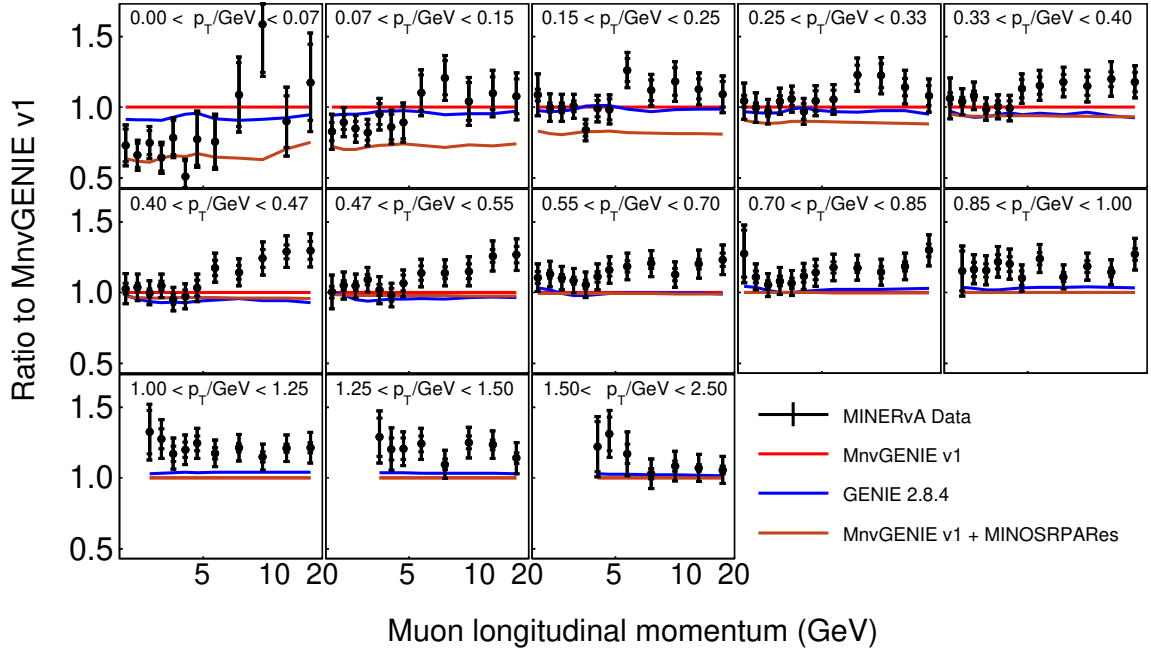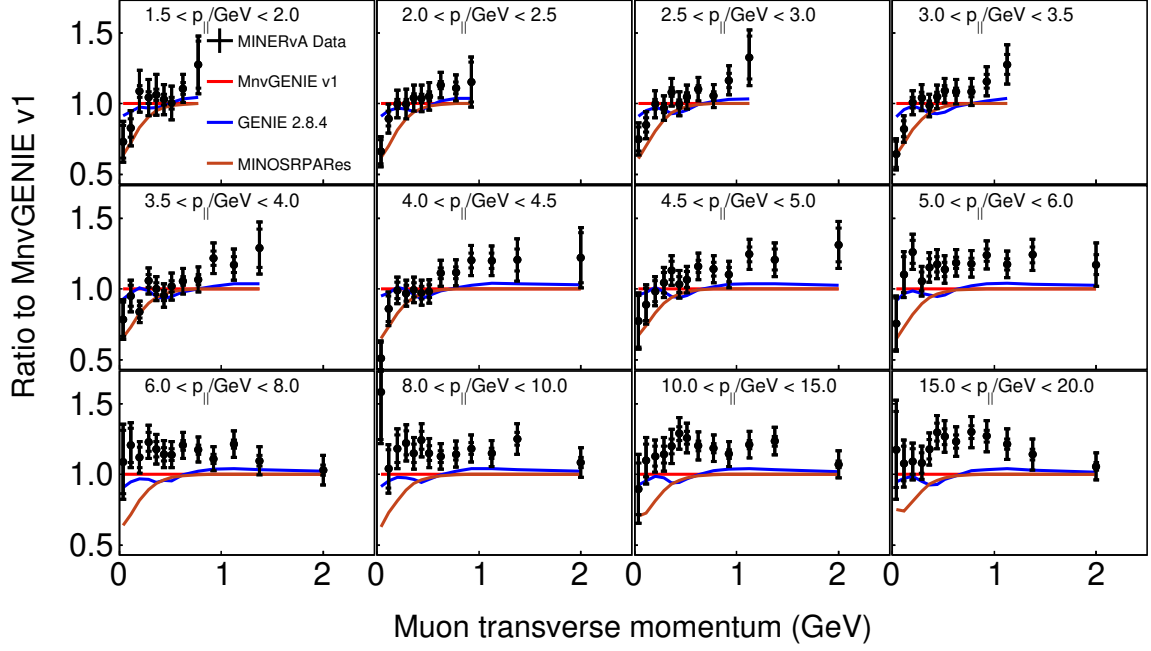
FIG. A.35: Area normalized comparisons of MINERvA tune v1, GENIE 2.8.4 and alternate tunes and models (7/13).

217
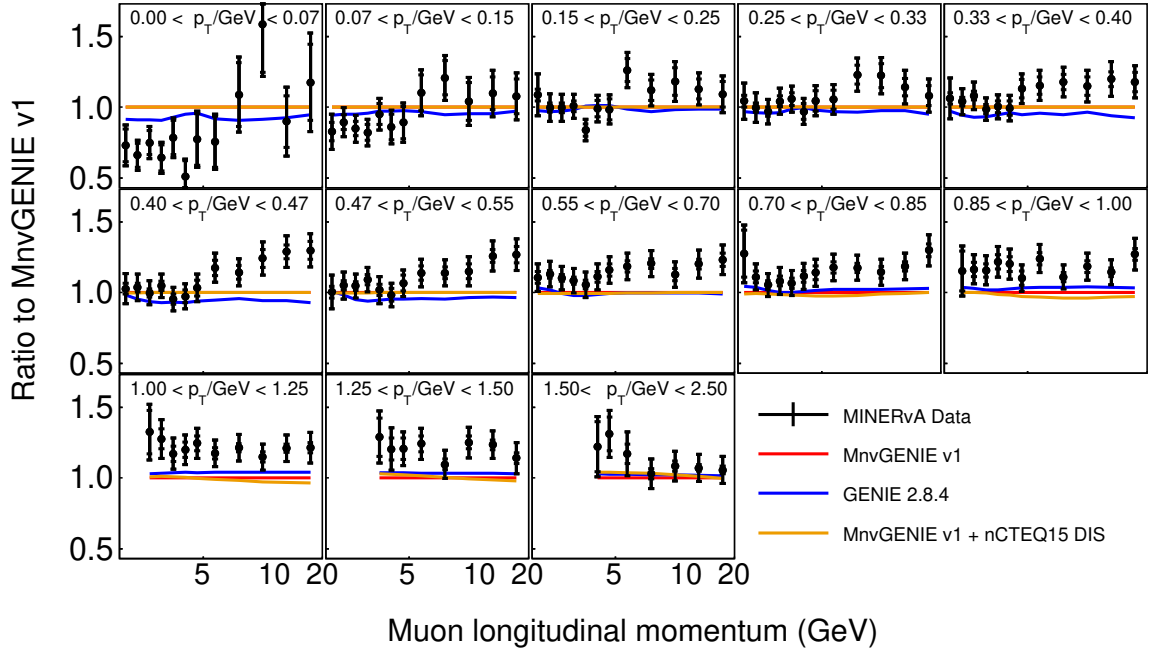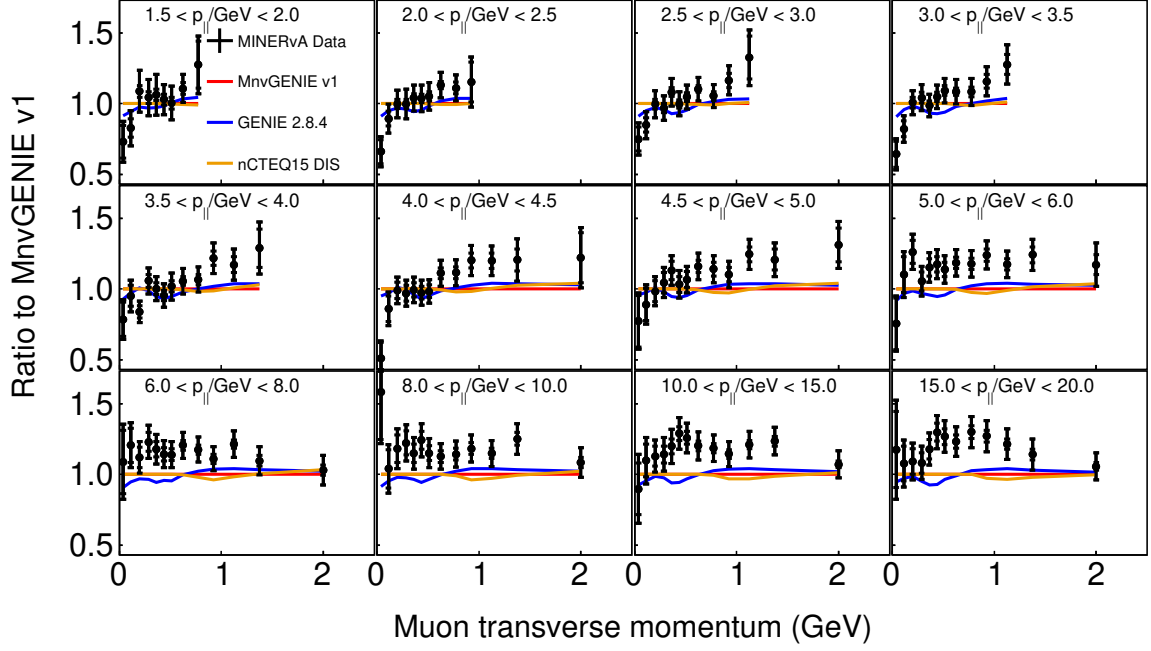
FIG. A.36: Area normalized comparisons of MINERvA tune v1, GENIE 2.8.4 and alternate tunes and models (8/13).
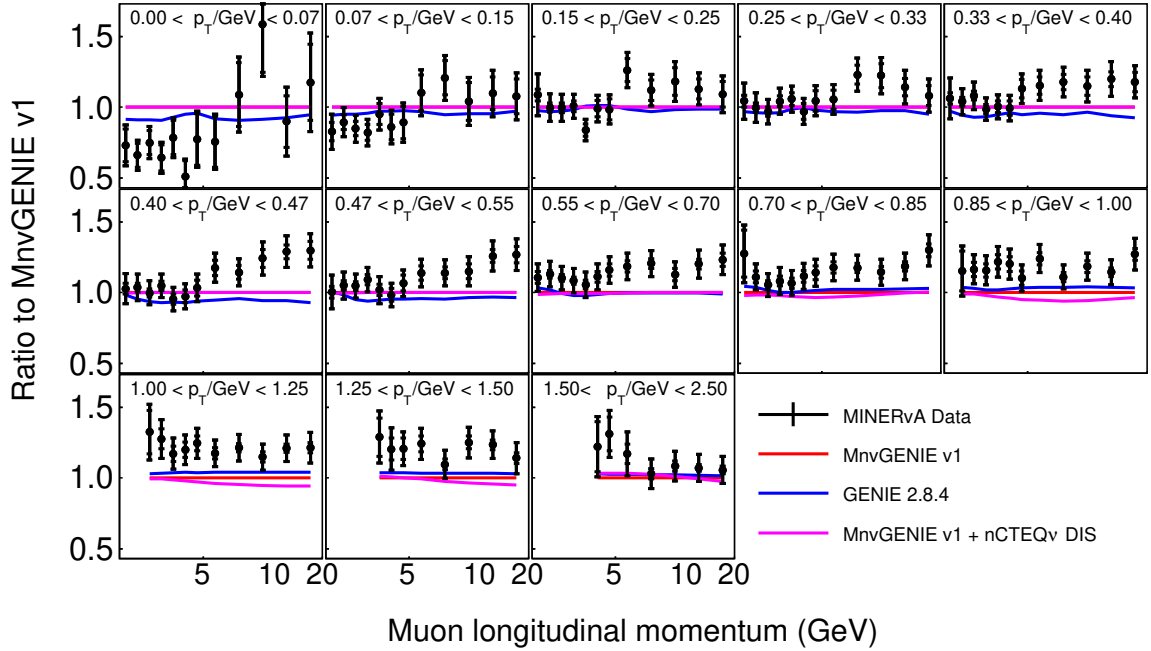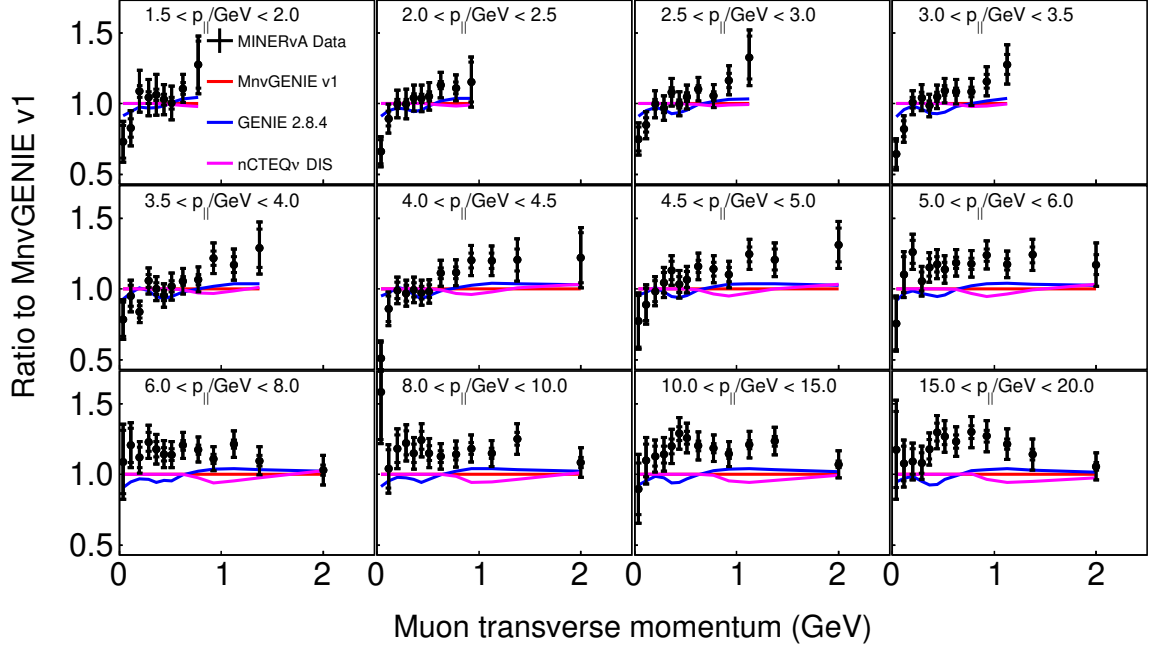
FIG. A.37: Area normalized comparisons of MINERvA tune v1, GENIE 2.8.4 and alternate tunes and models (9/13).

219
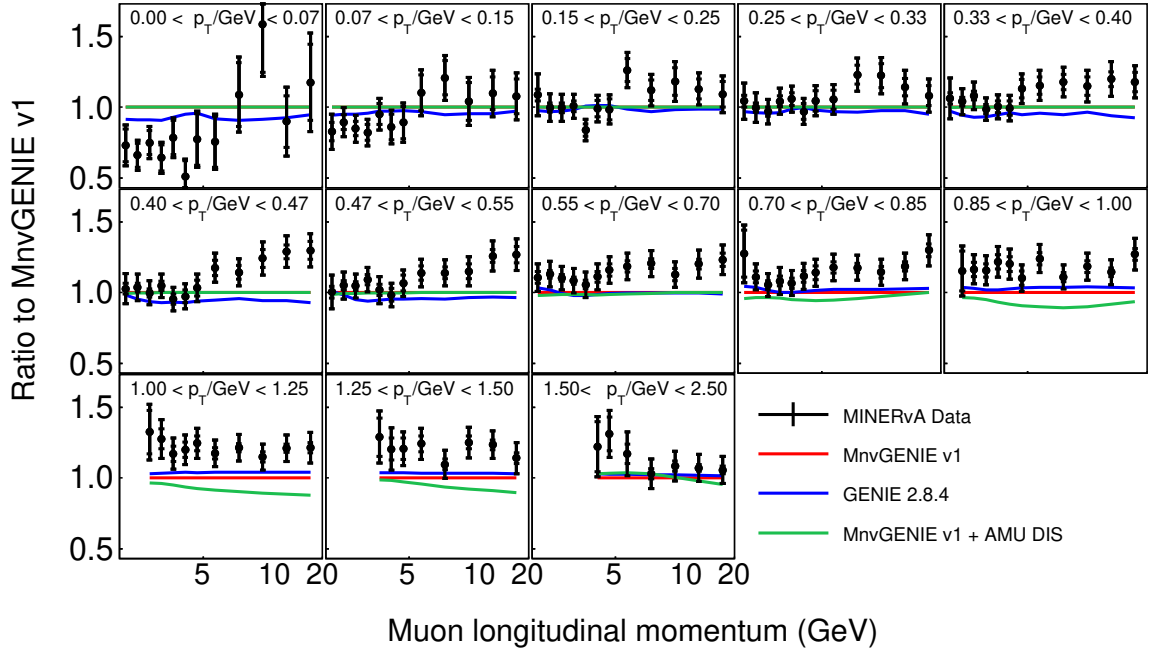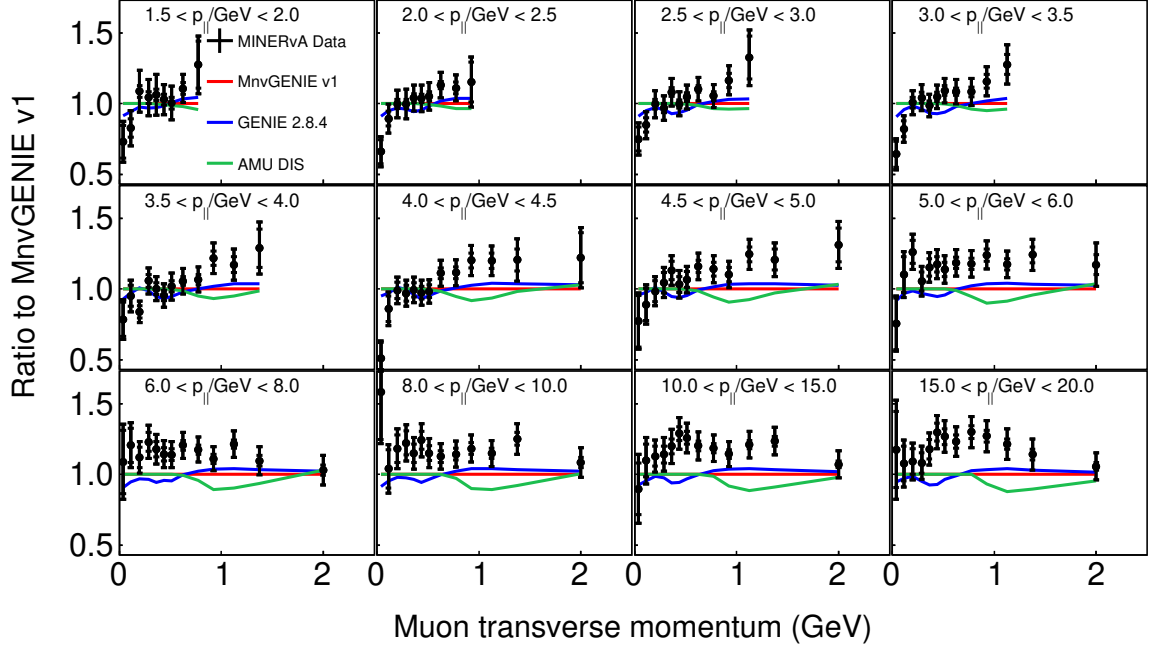
FIG. A.38: Area normalized comparisons of MINERvA tune v1, GENIE 2.8.4 and alternate tunes and models (10/13).
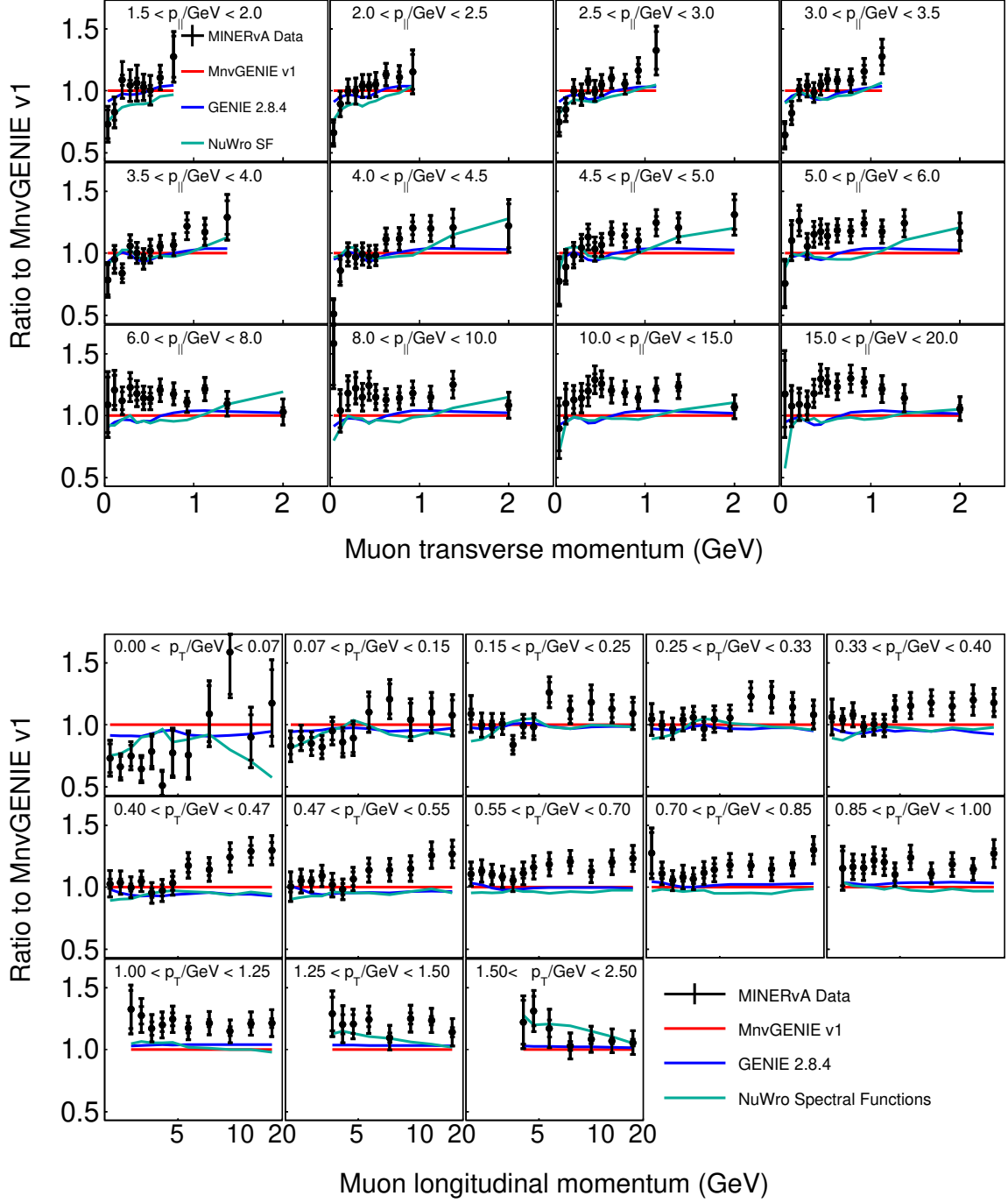
FIG. A.39: Area normalized comparisons of MINERvA tune v1, GENIE 2.8.4 and alternate tunes and models (11/13).
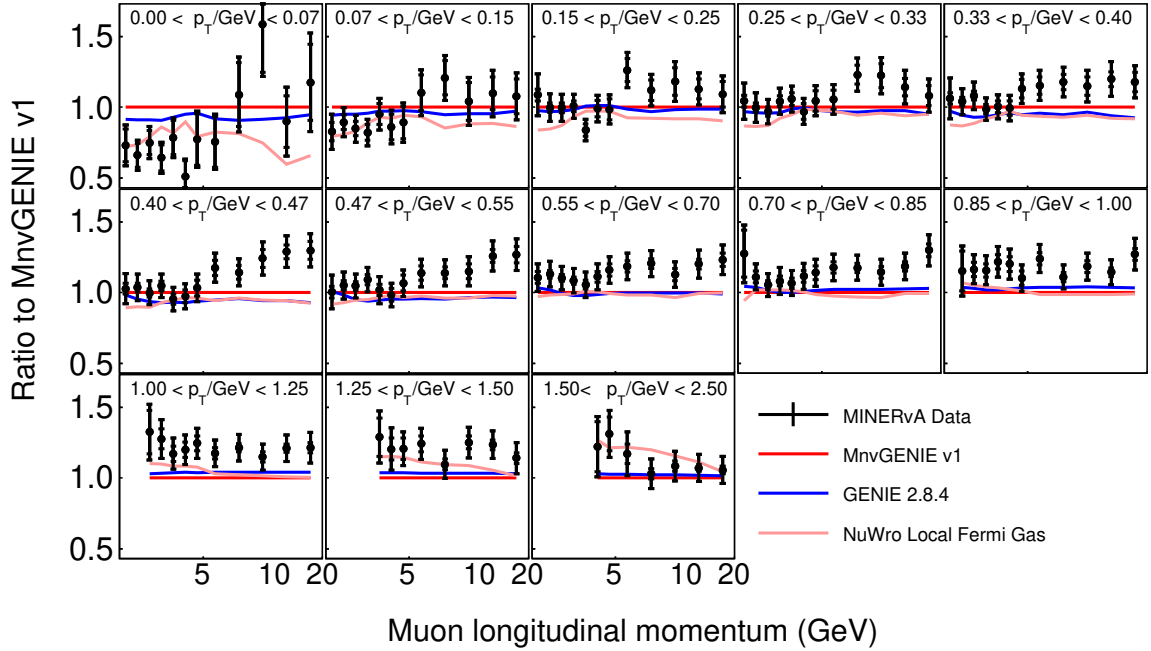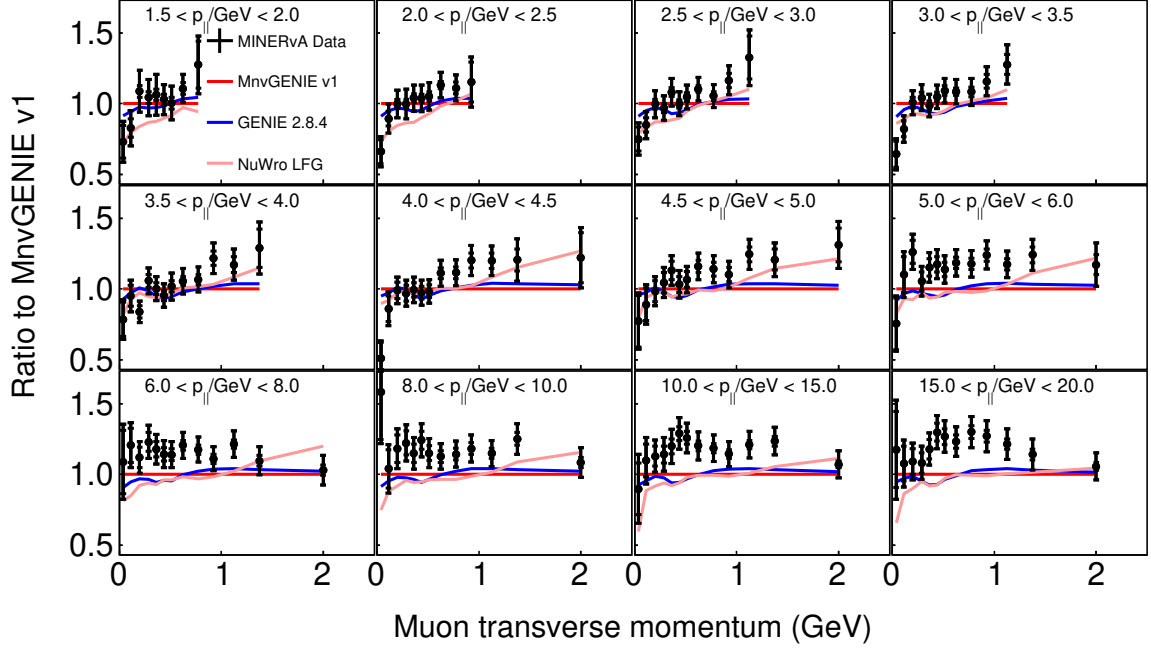
FIG. A.40: Area normalized comparisons of MINERvA tune v1, GENIE 2.8.4 and alternate tunes and models (12/13).

222
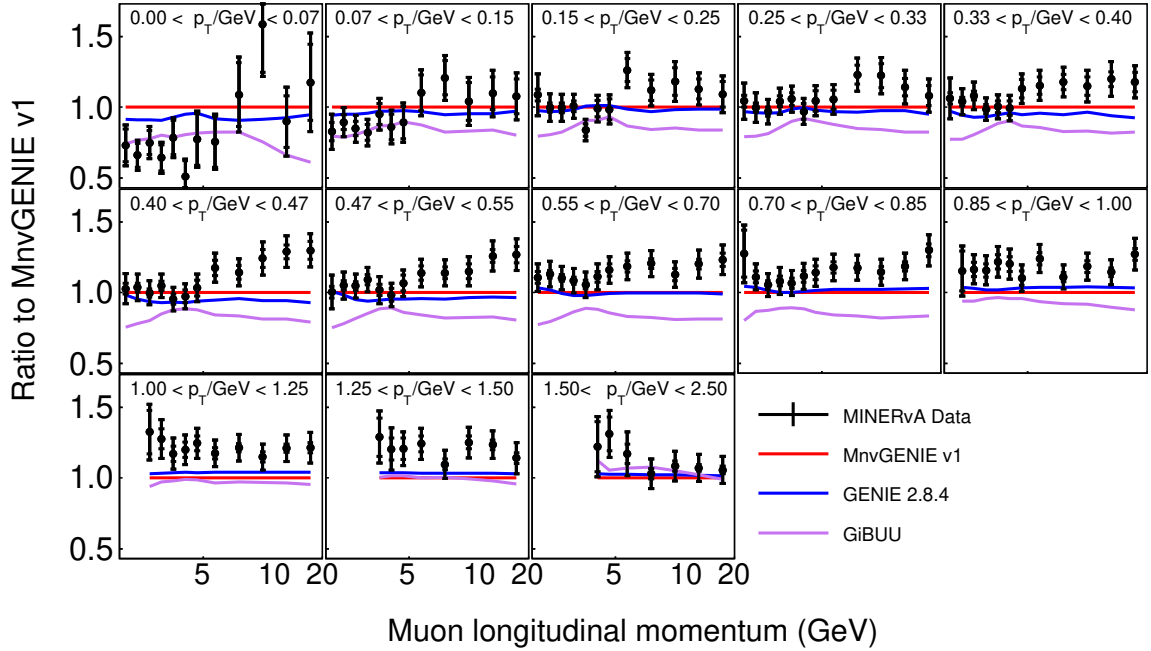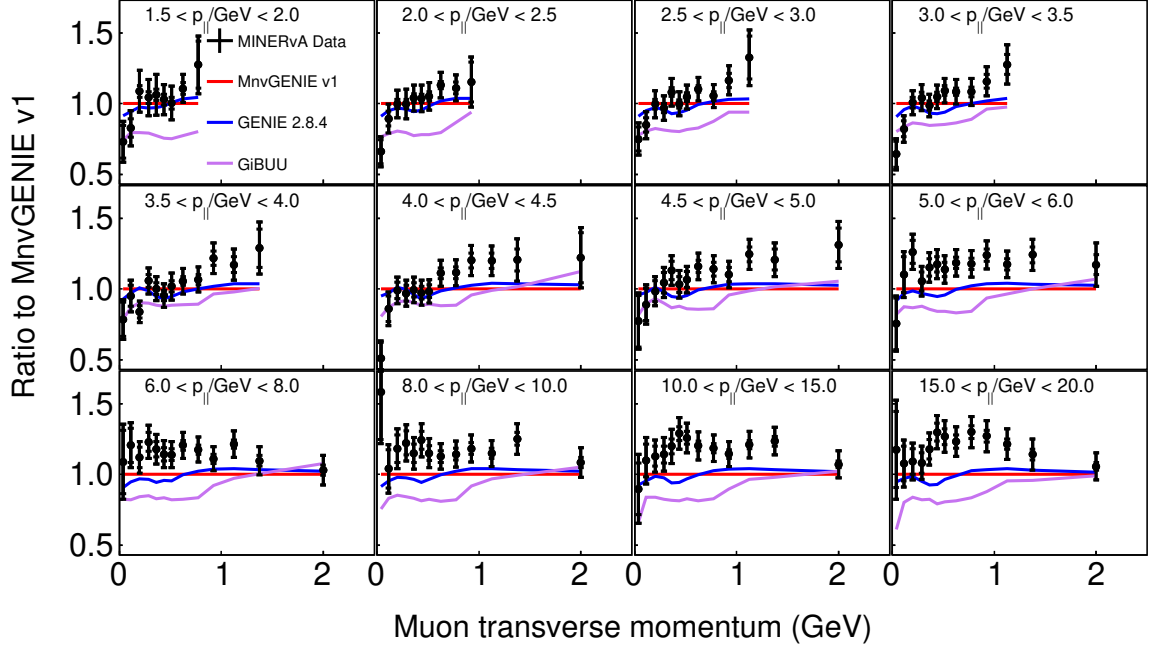
FIG. A.41: Area normalized comparisons of MINERvA tune v1, GENIE 2.8.4 and alternate tunes and models (13/13).

APPENDIX B

Appendix - DIS

Supporting plots for the deep inelastic scattering analysis discussed in Ch. 7.

B.1   Event Selection, Background subtracted, Unfolded and Efficiency Corrected Distributions

B.1.1   Enu

Iron of target 1
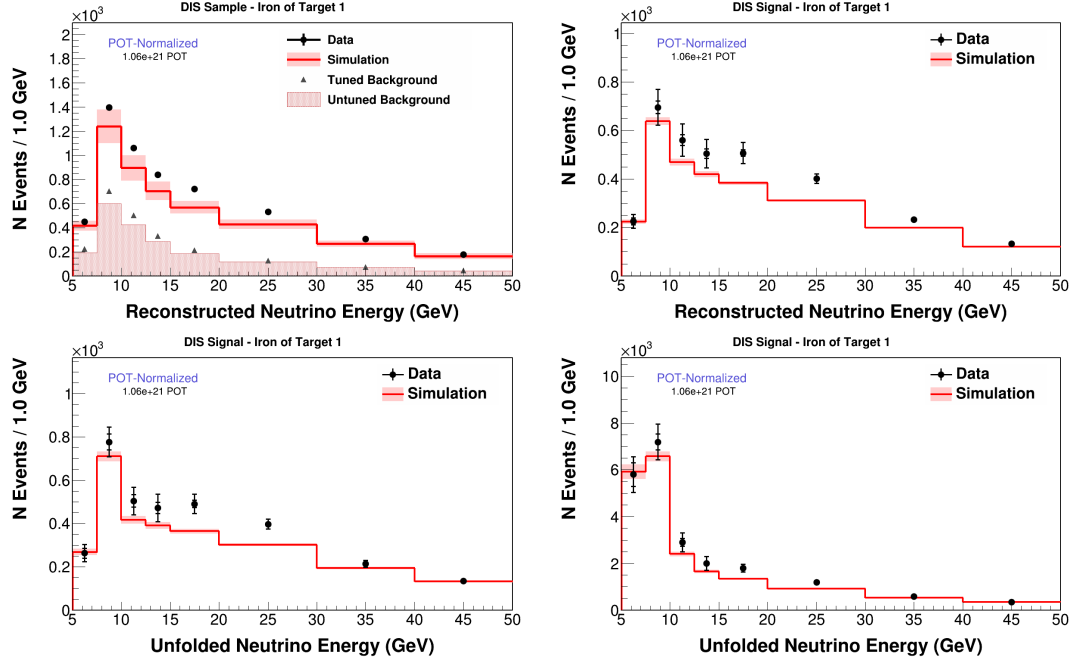
FIG. B.1: Iron of target 1 in E_ν after event selection (top right), background subtraction (top left), unfolding (bottom right) and efficiency correction (bottom left).
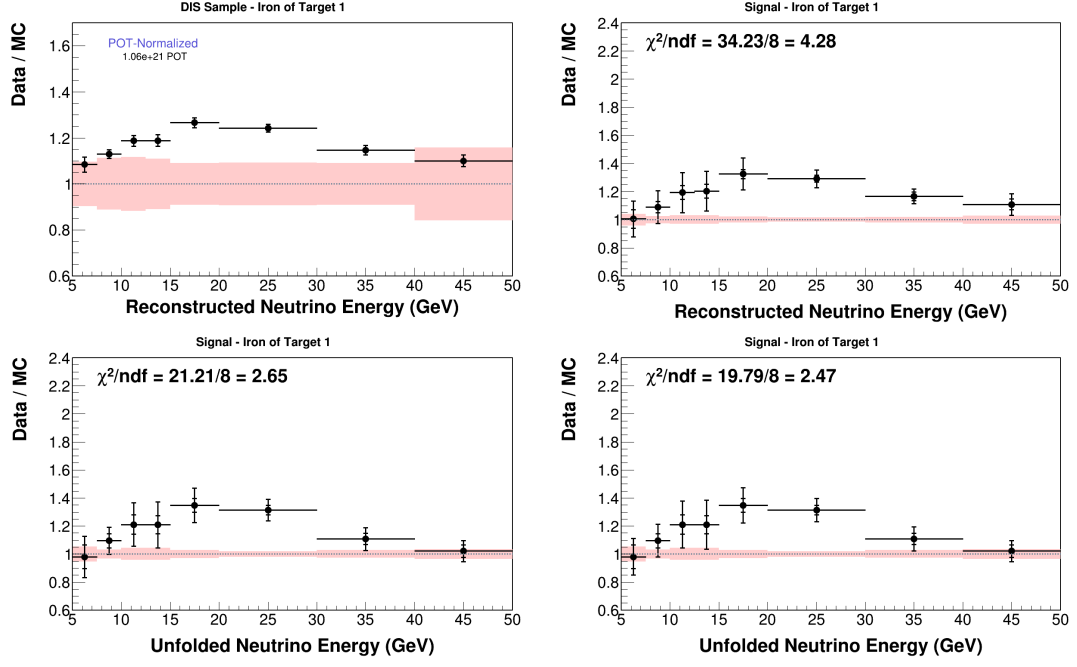
FIG. B.2: Iron of target 1 in E_ν data MC ratios after event selection (top right), background subtraction (top left), unfolding (bottom right) and efficiency correction (bottom left).
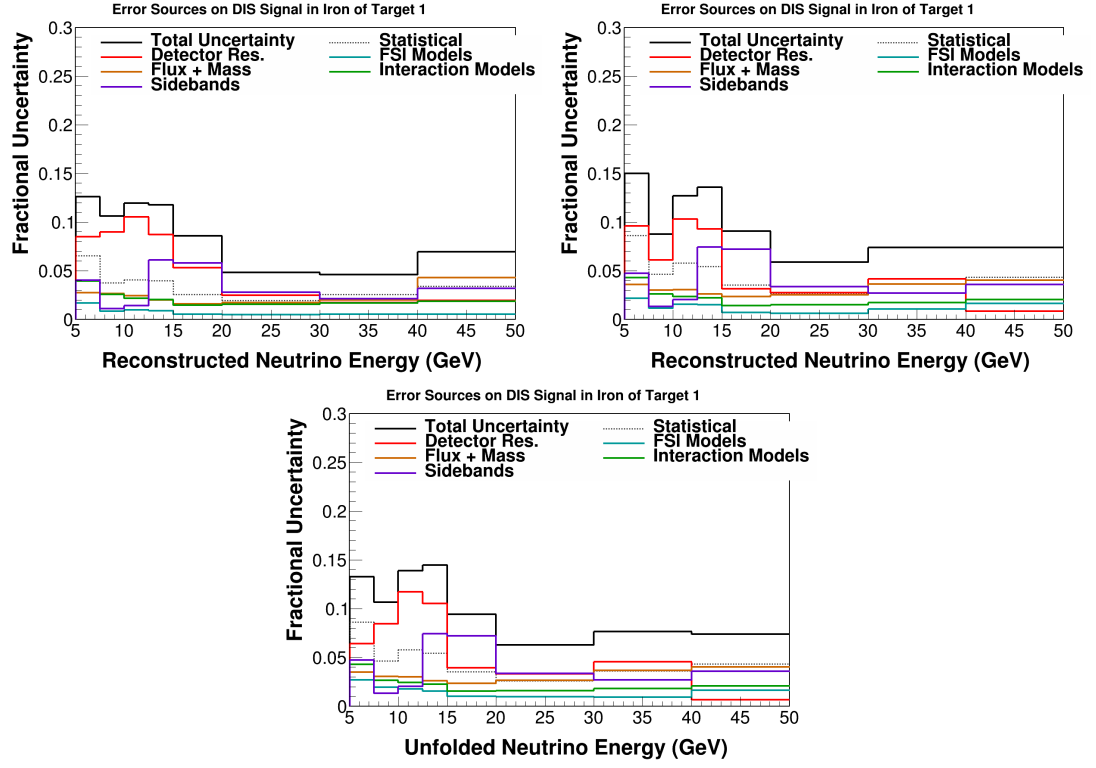
Iron of target 2
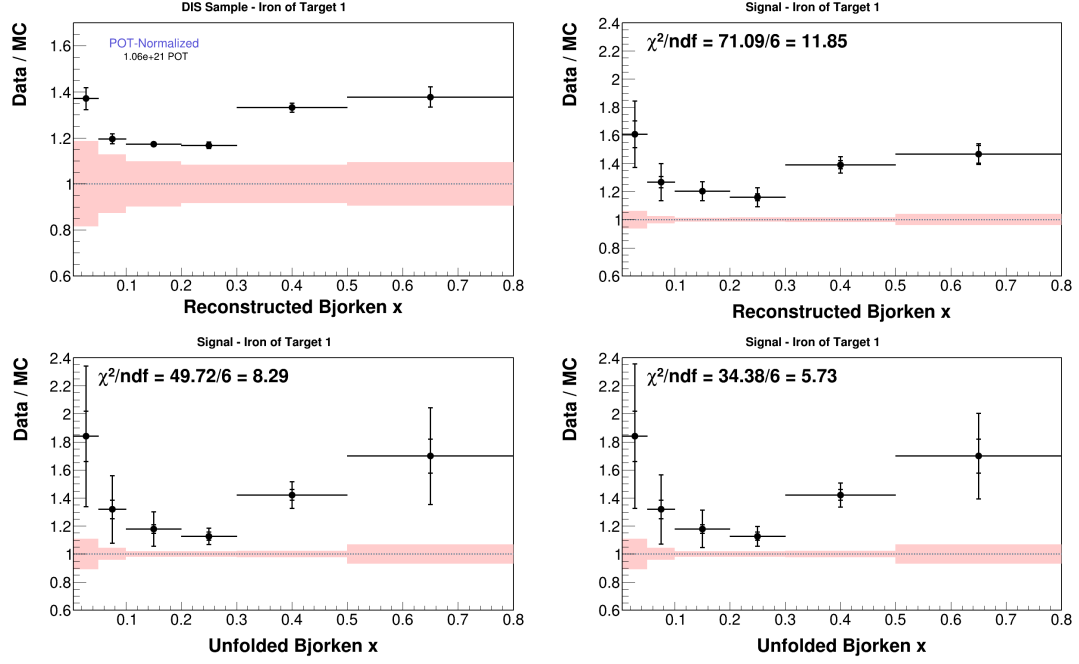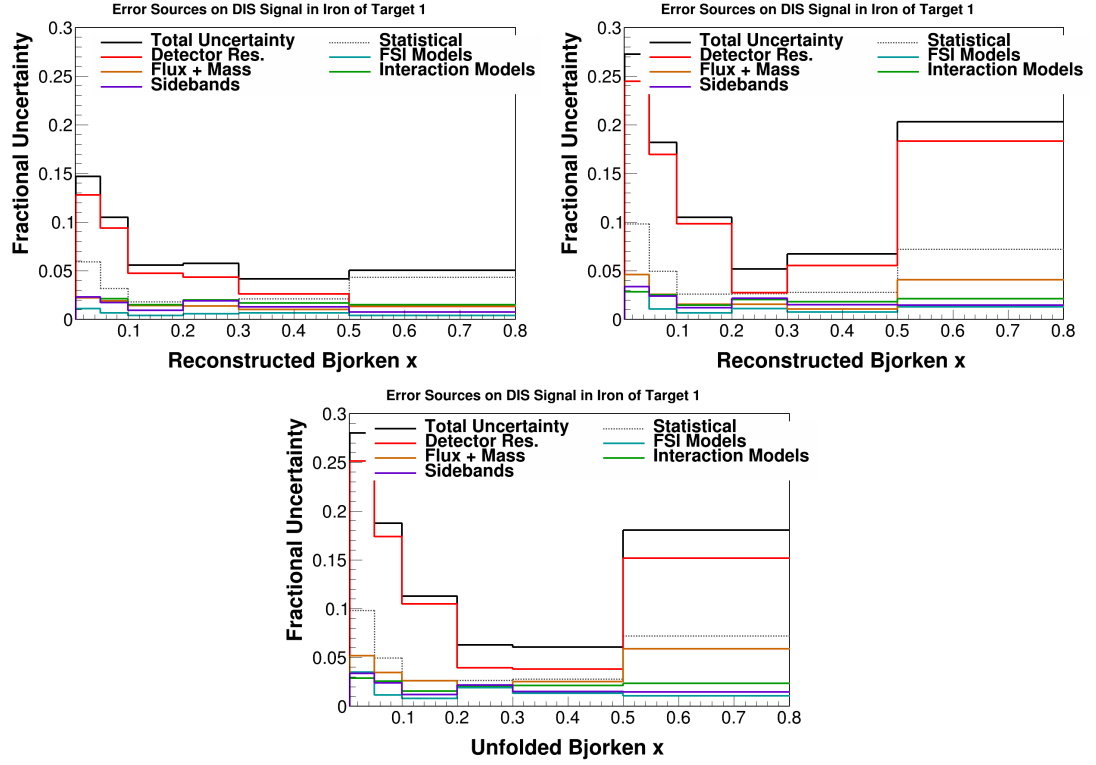
FIG. B.3: Iron of target 1 in E_ν data error summary after background subtraction (top right), unfolding (top left) and efficiency correction (bottom). At the event selection stage there are only statistical errors on the data distributions, so a systematic error summary is not included here.
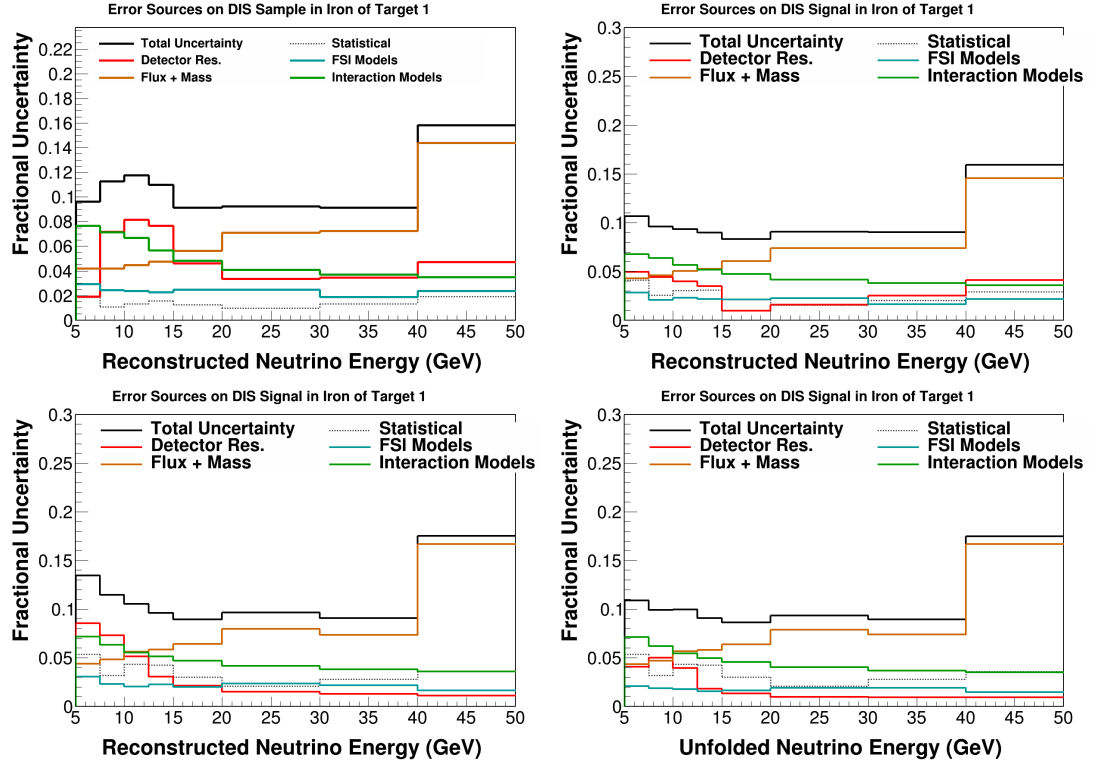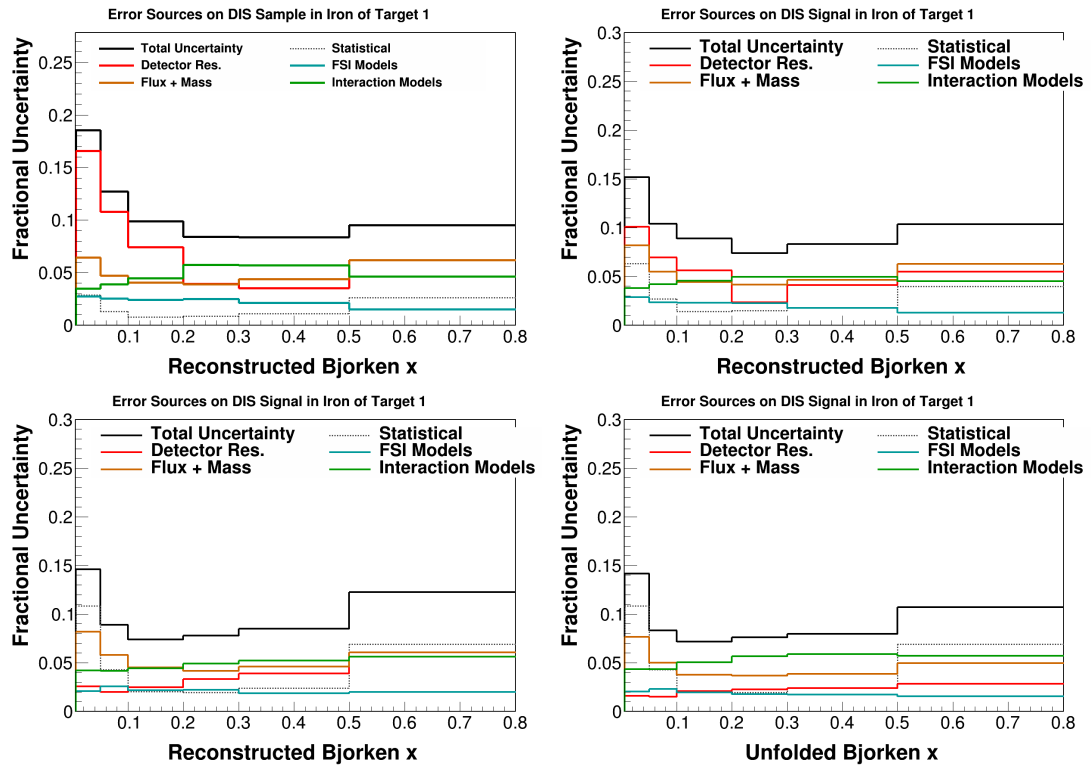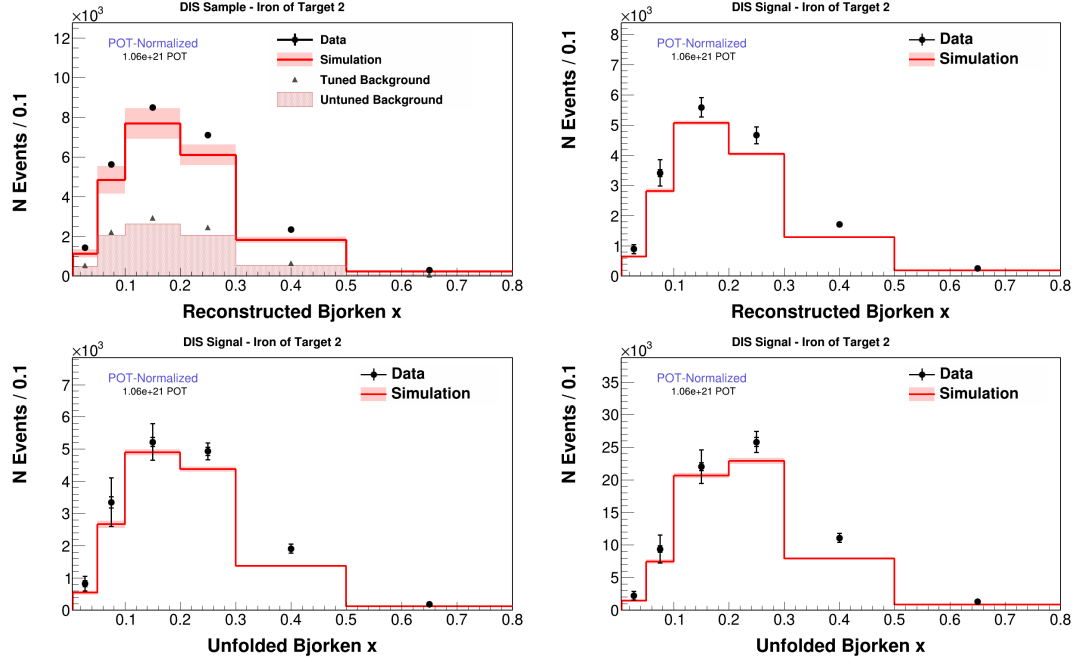
FIG. B.4: Iron of target 1 in E_ν MC error summary after event selection (top right), background subtraction (top left), unfolding (bottom right) and efficiency correction (bottom left).
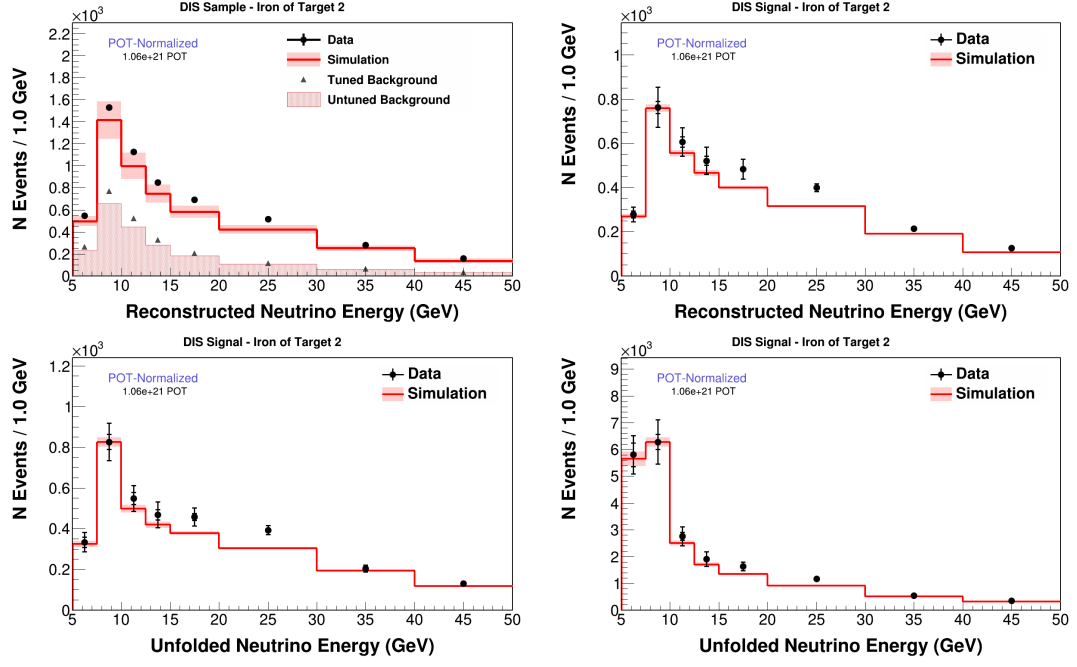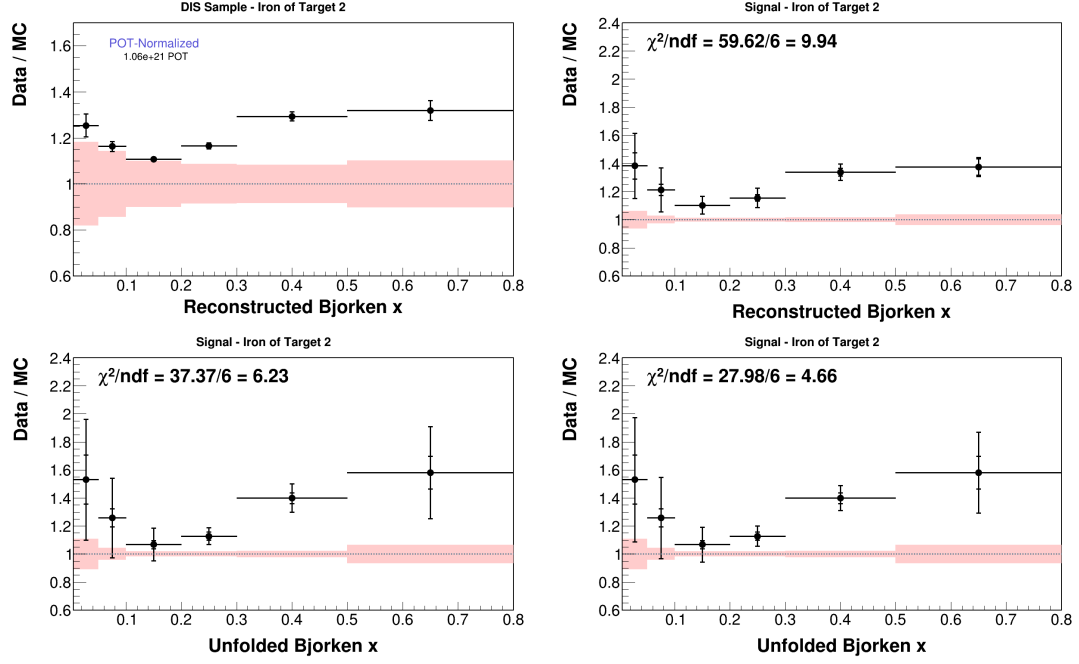
FIG. B.5: Iron of target 2 in E_ν after event selection (top right), background subtraction (top left), unfolding (bottom right) and efficiency correction (bottom left).
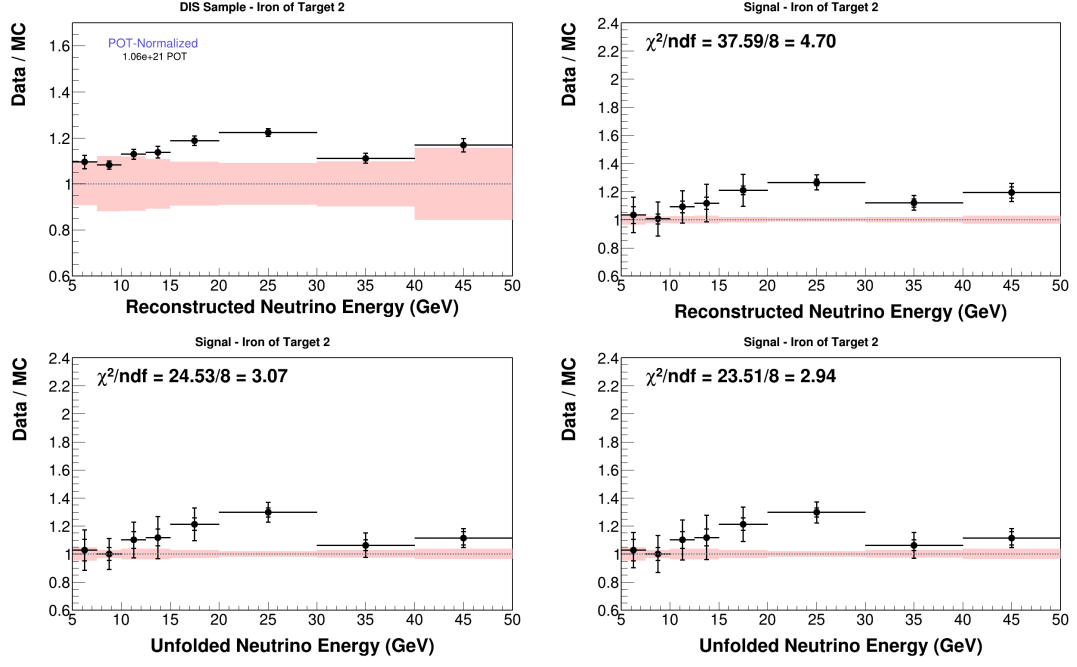
FIG. B.6: Iron of target 2 in E_ν data MC ratios after event selection (top right), background subtraction (top left), unfolding (bottom right) and efficiency correction (bottom left).
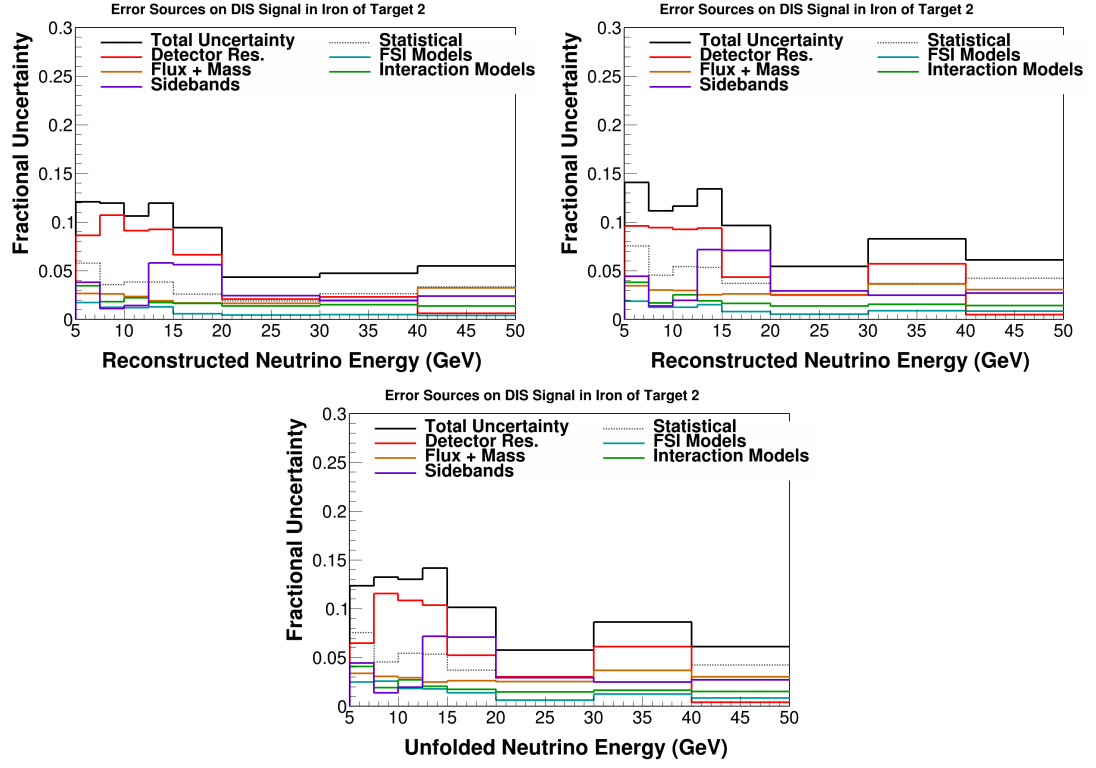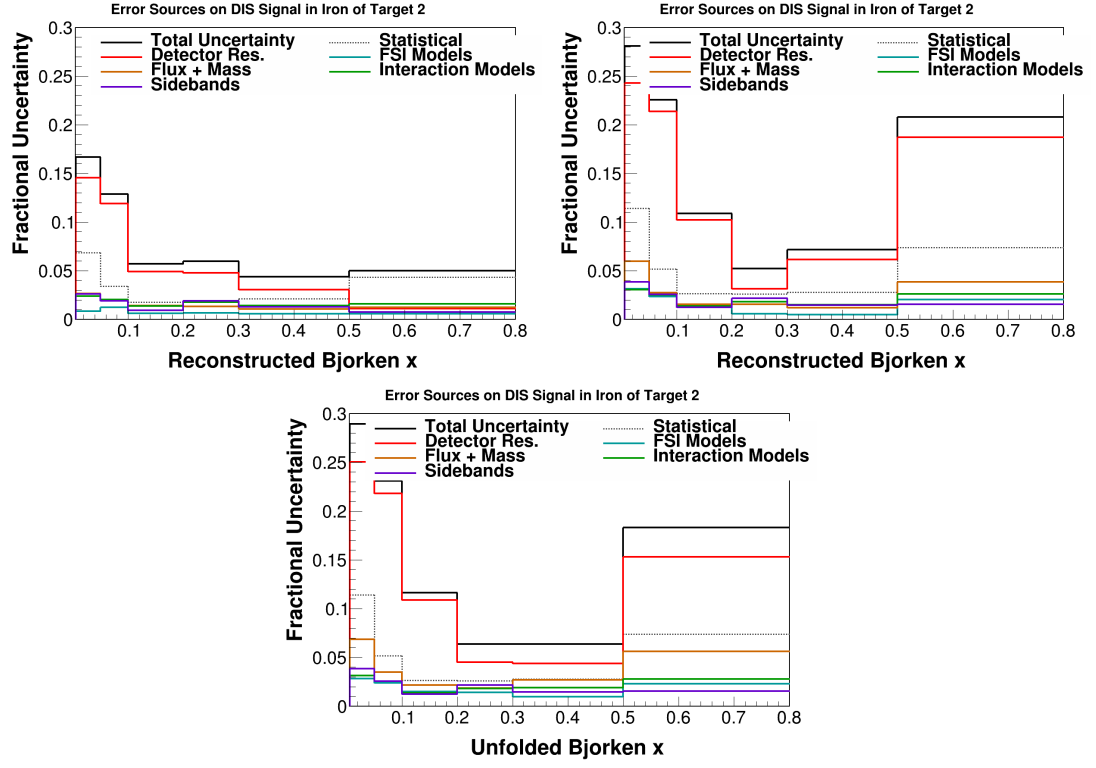
Iron of target 3

FIG. B.7: Iron of target 2 in E_ν data error summary after background subtraction (top right), unfolding (top left) and efficiency correction (bottom). At the event selection stage there are only statistical errors on the data distributions, so a systematic error summary is not included here.
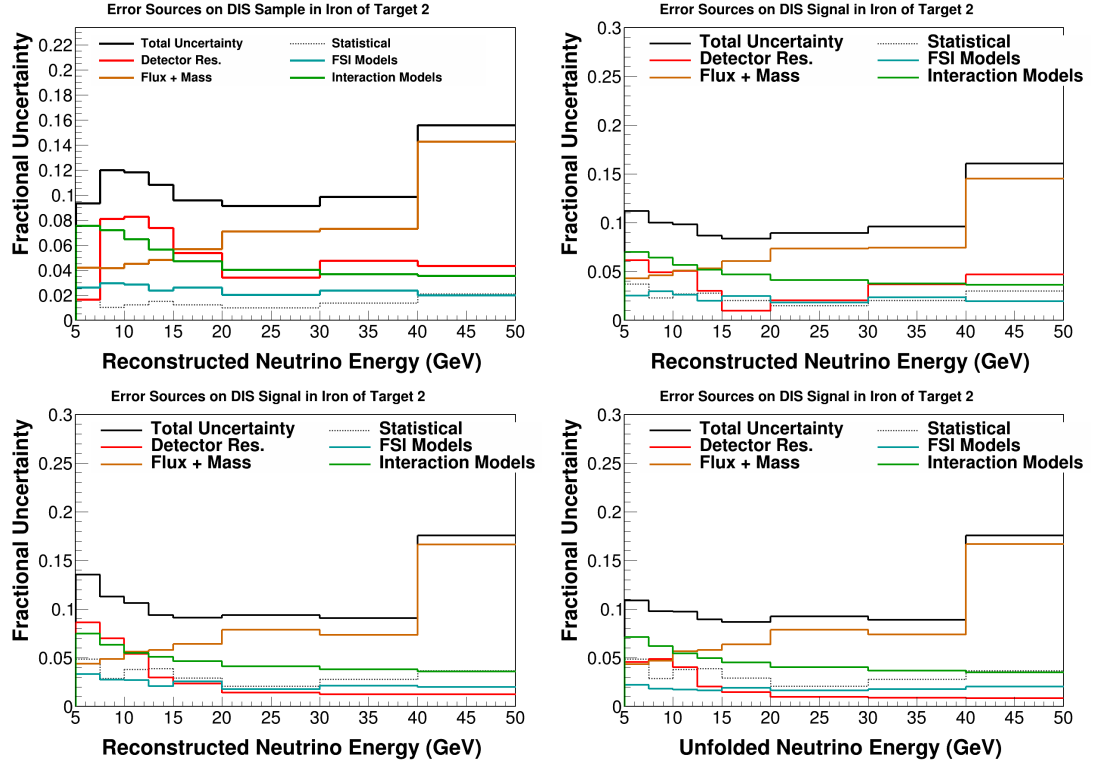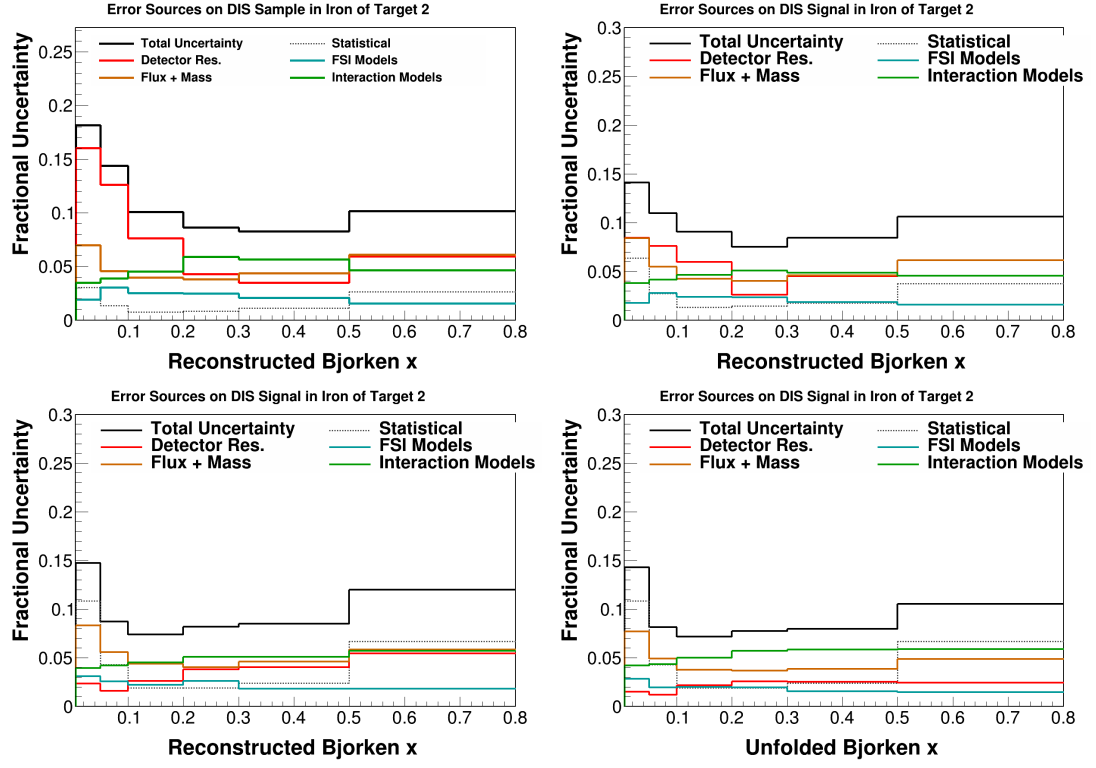
FIG. B.8: Iron of target 2 in E_ν MC error summary after event selection (top right), background subtraction (top left), unfolding (bottom right) and efficiency correction (bottom left).
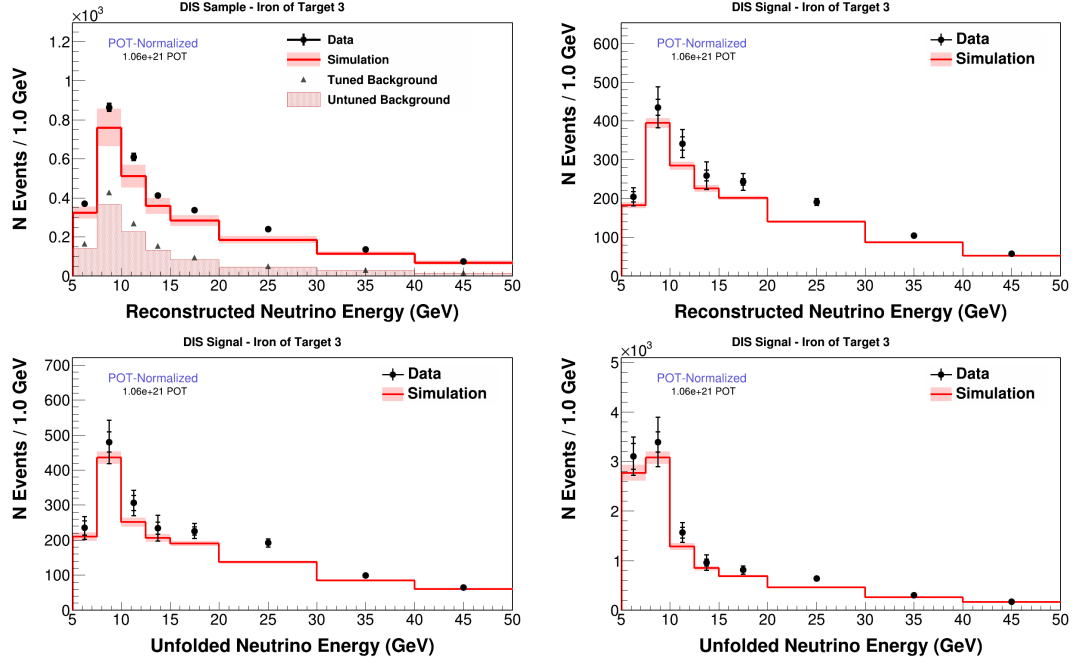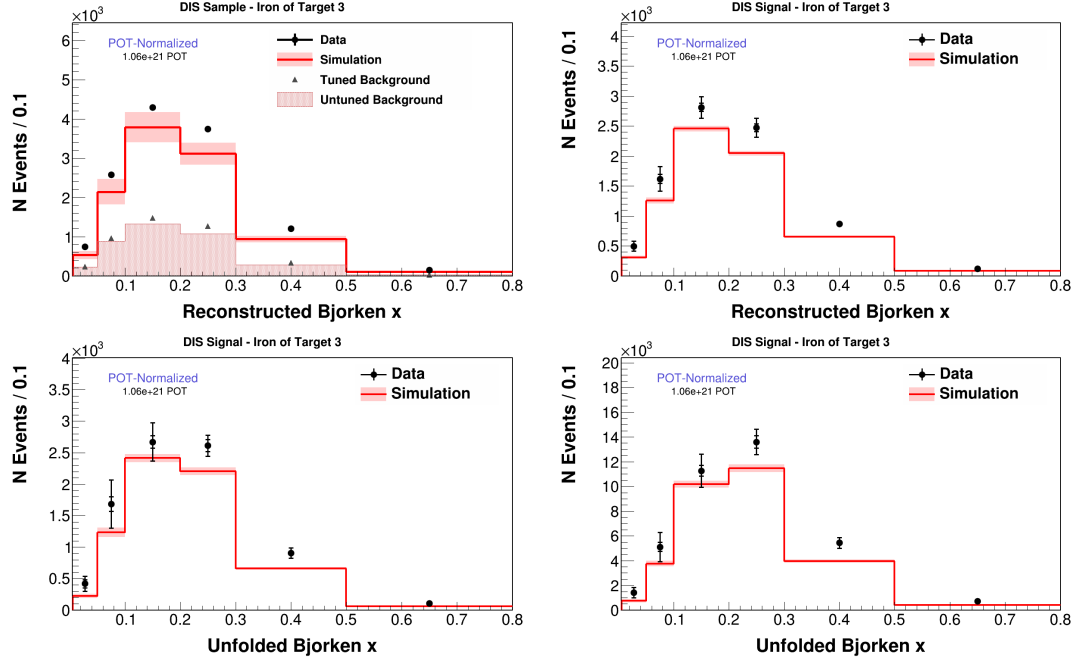
FIG. B.9: Iron of target 3 in E_ν after event selection (top right), background subtraction (top left), unfolding (bottom right) and efficiency correction (bottom left).
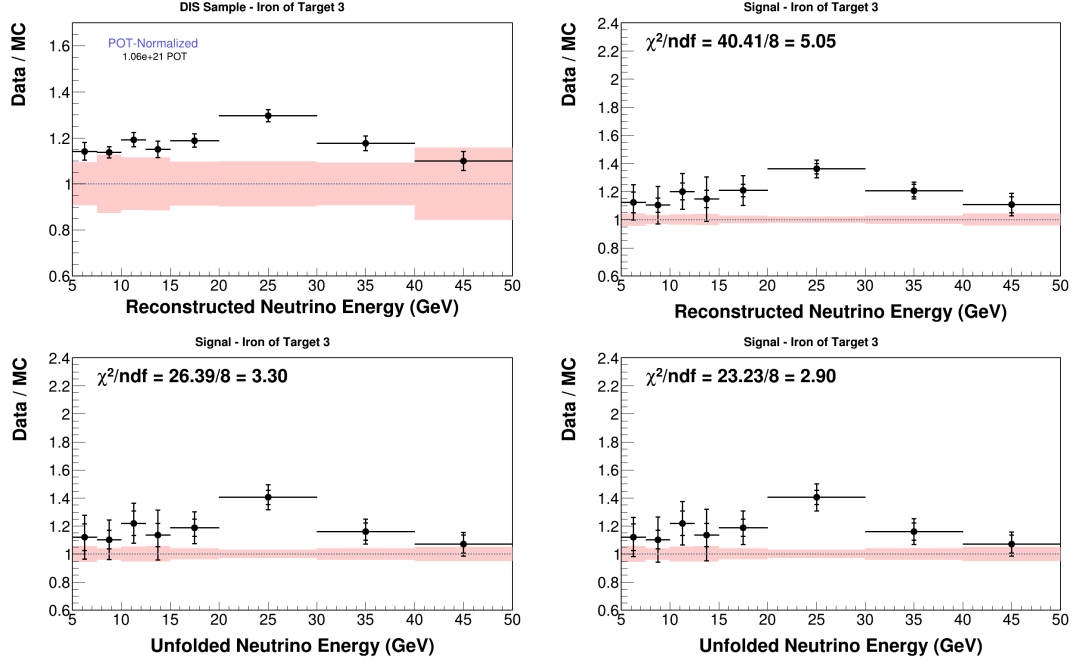
FIG. B.10: Iron of target 3 in E_ν data MC ratios after event selection (top right), background subtraction (top left), unfolding (bottom right) and efficiency correction (bottom left).
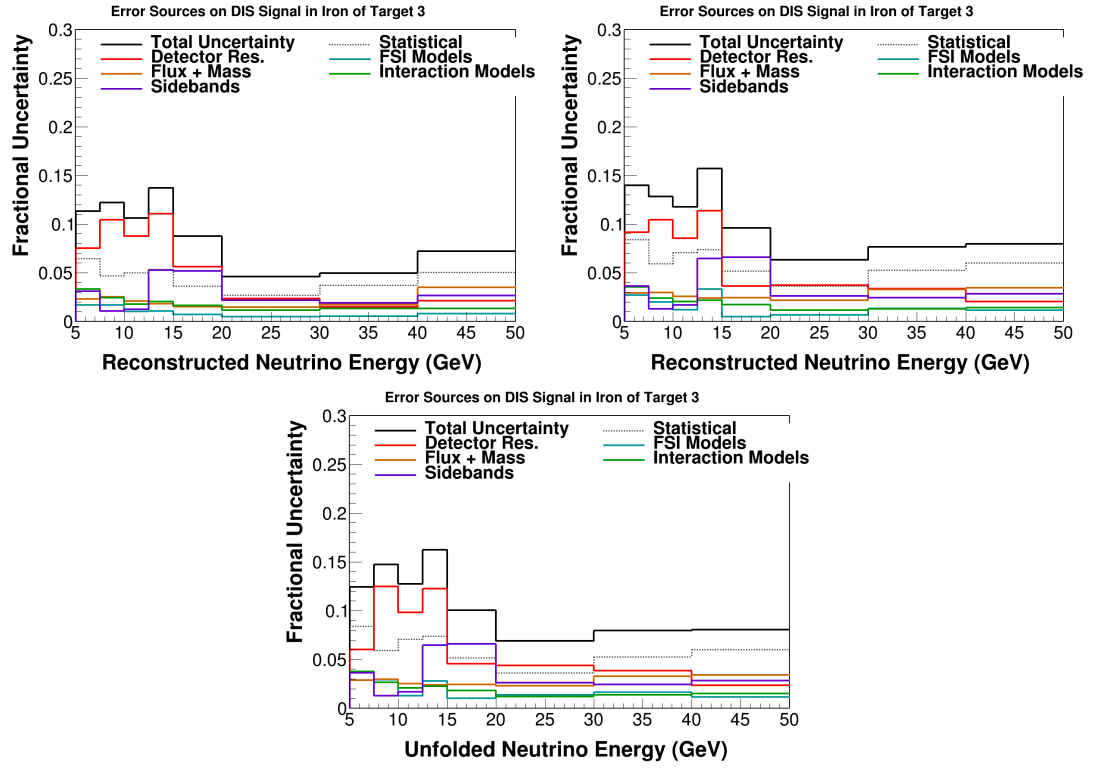
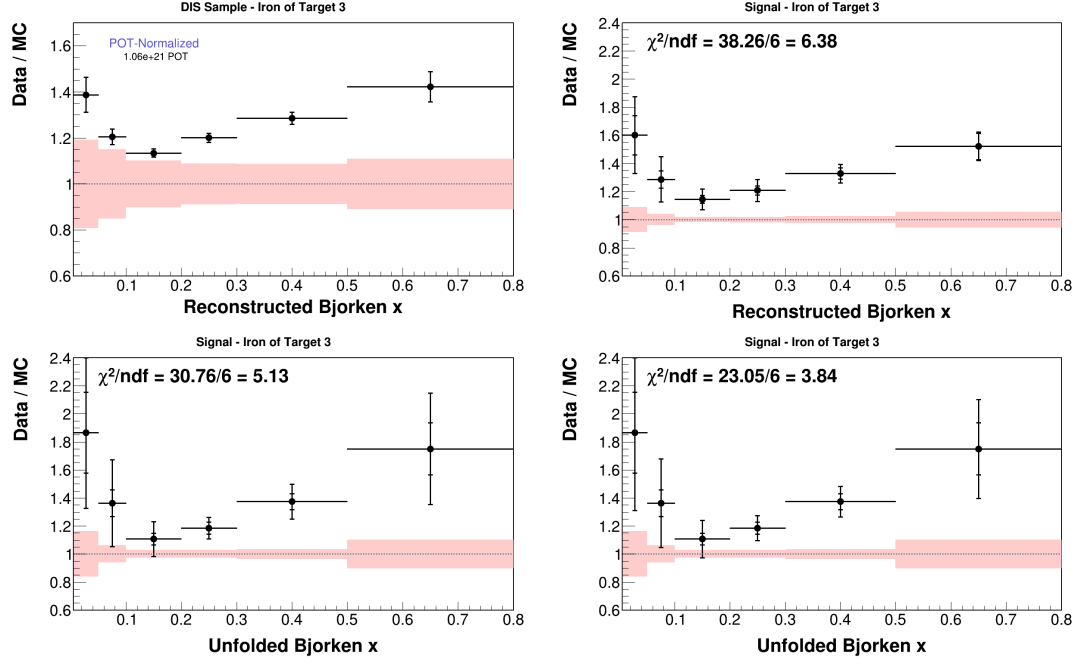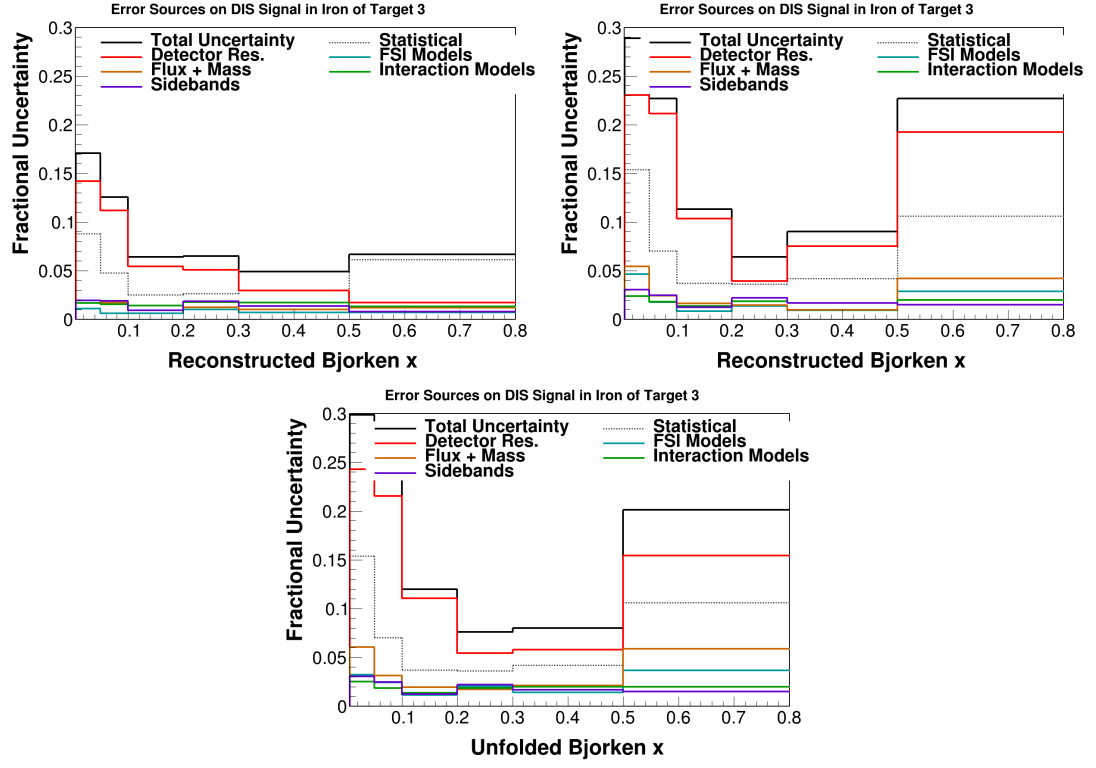**Iron of target 5**

FIG. B.11: Iron of target 3 in E_ν data error summary after background subtraction (top right), unfolding (top left) and efficiency correction (bottom). At the event selection stage there are only statistical errors on the data distributions, so a systematic error summary is not included here.
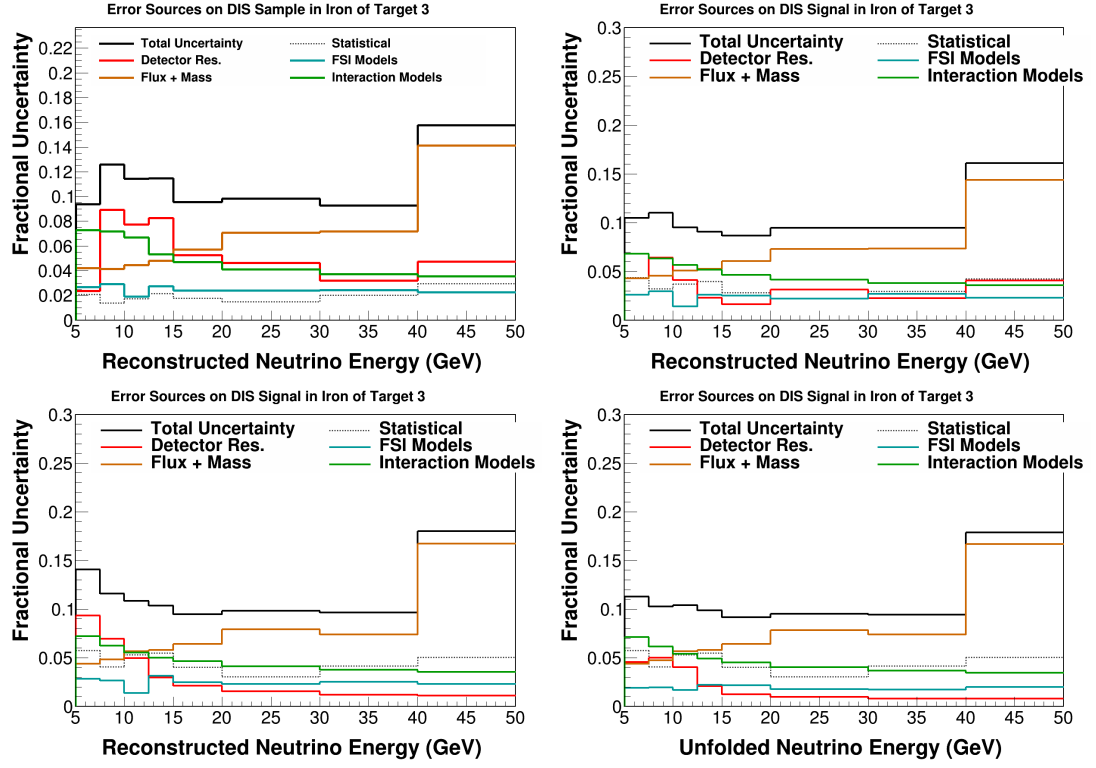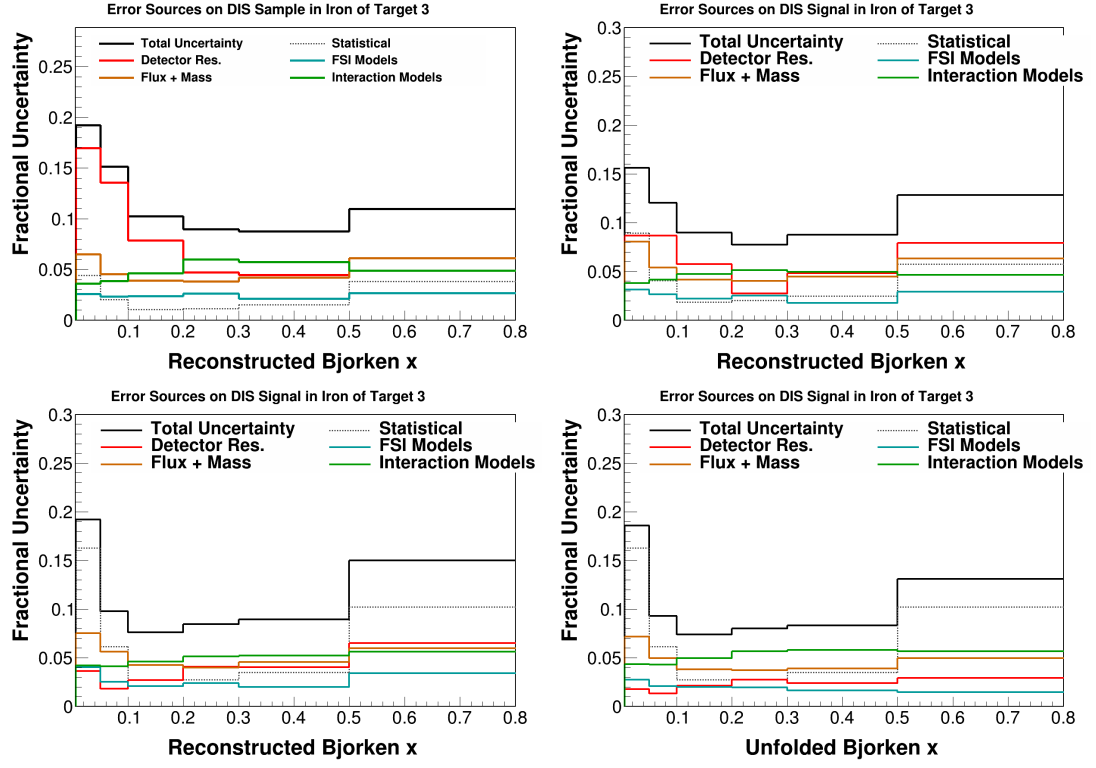
FIG. B.12: Iron of target 3 in E_ν MC error summary after event selection (top right), background subtraction (top left), unfolding (bottom right) and efficiency correction (bottom left).
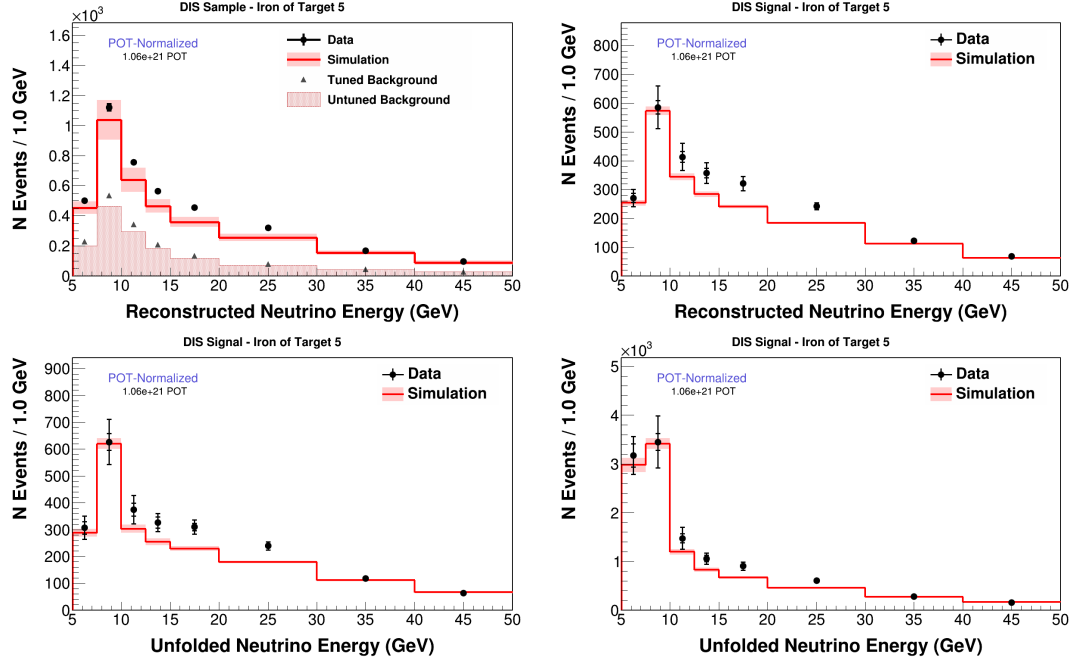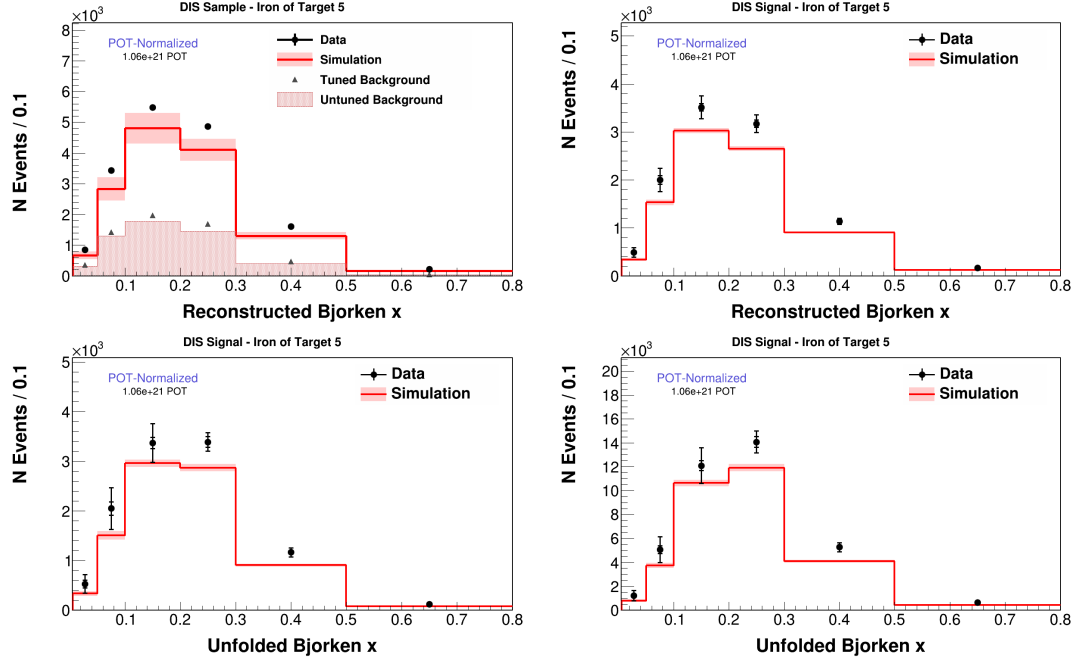
FIG. B.13: Iron of target 5 in E_ν after event selection (top right), background subtraction (top left), unfolding (bottom right) and efficiency correction (bottom left).

FIG. B.14: Iron of target 5 in E_ν data MC ratios after event selection (top right), background subtraction (top left), unfolding (bottom right) and efficiency correction (bottom left).
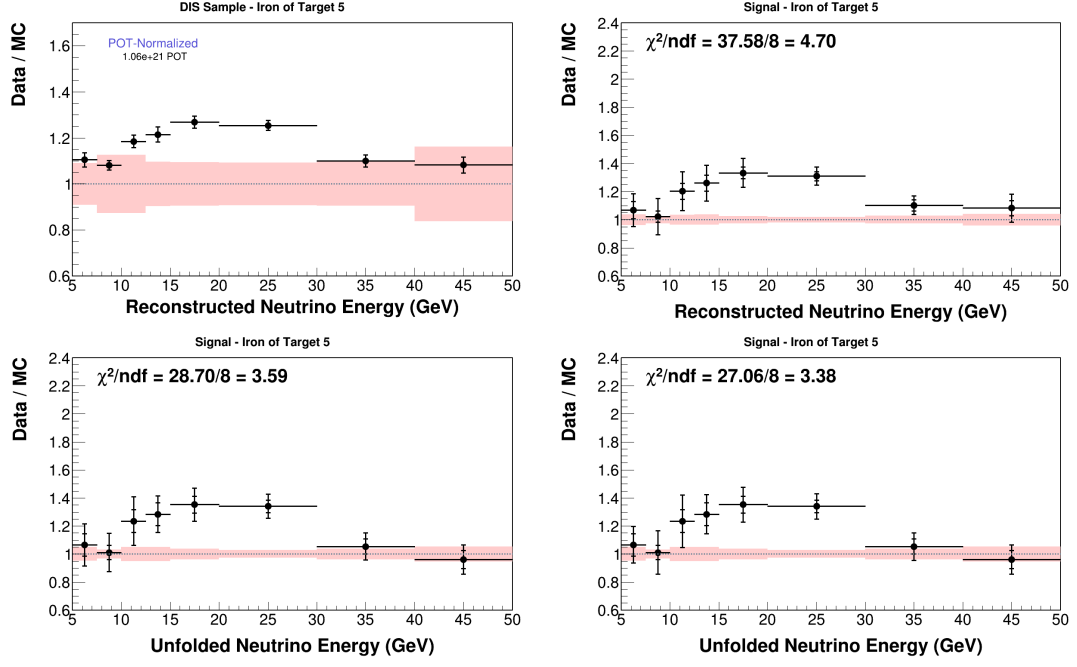
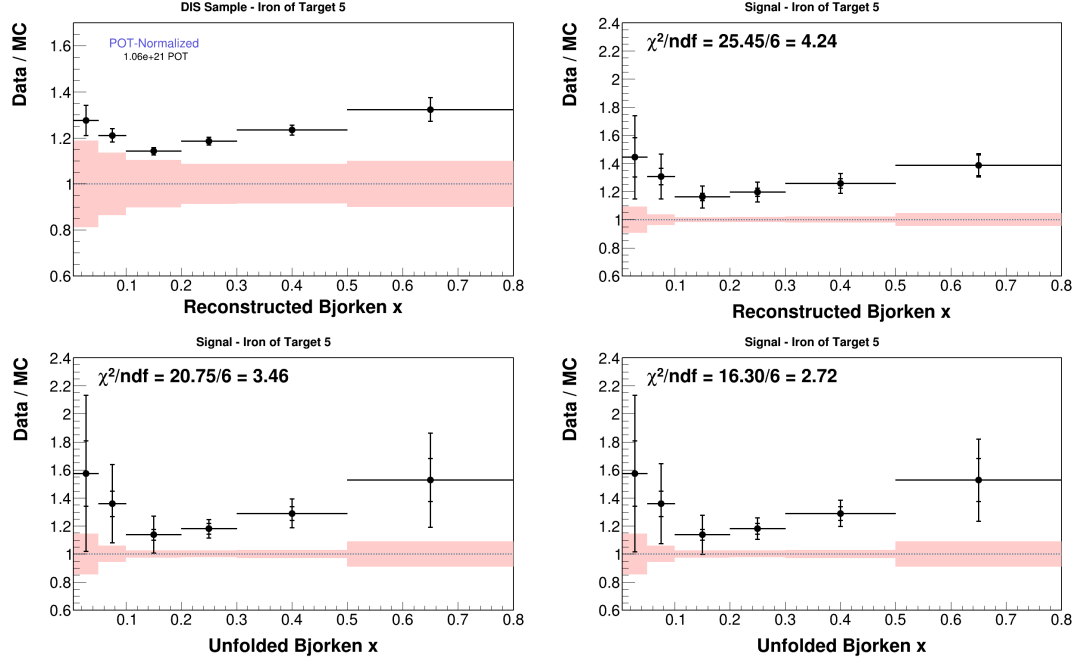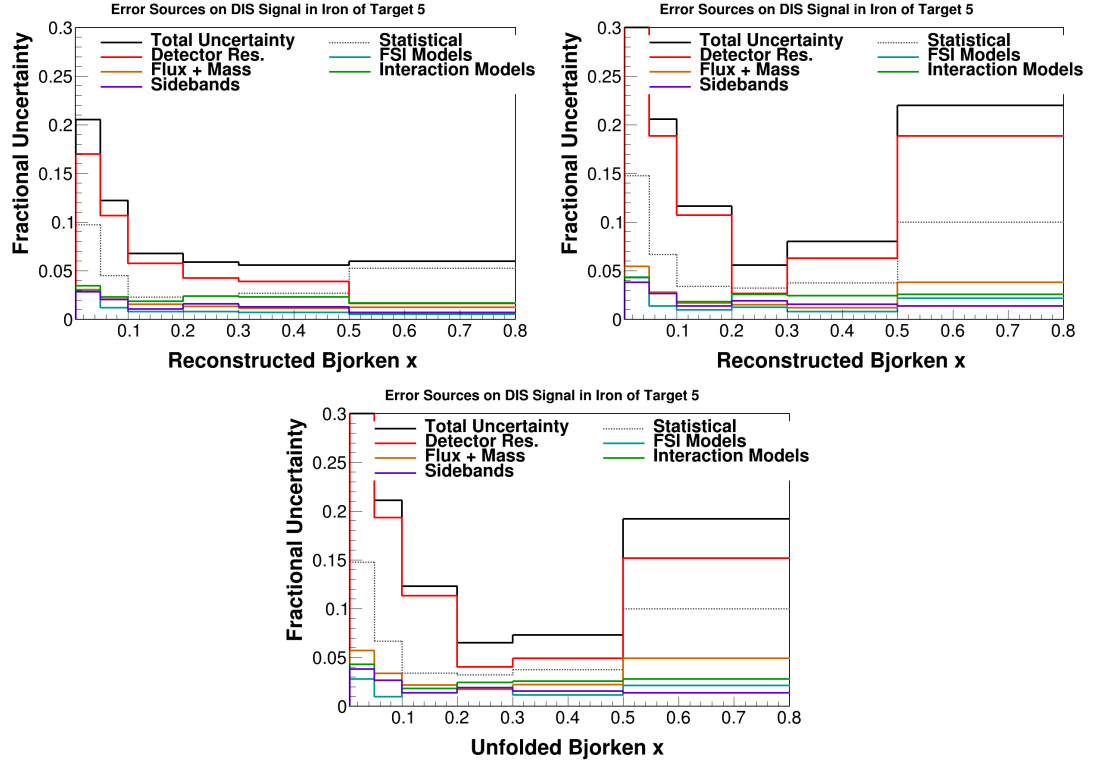**Lead of target 1**
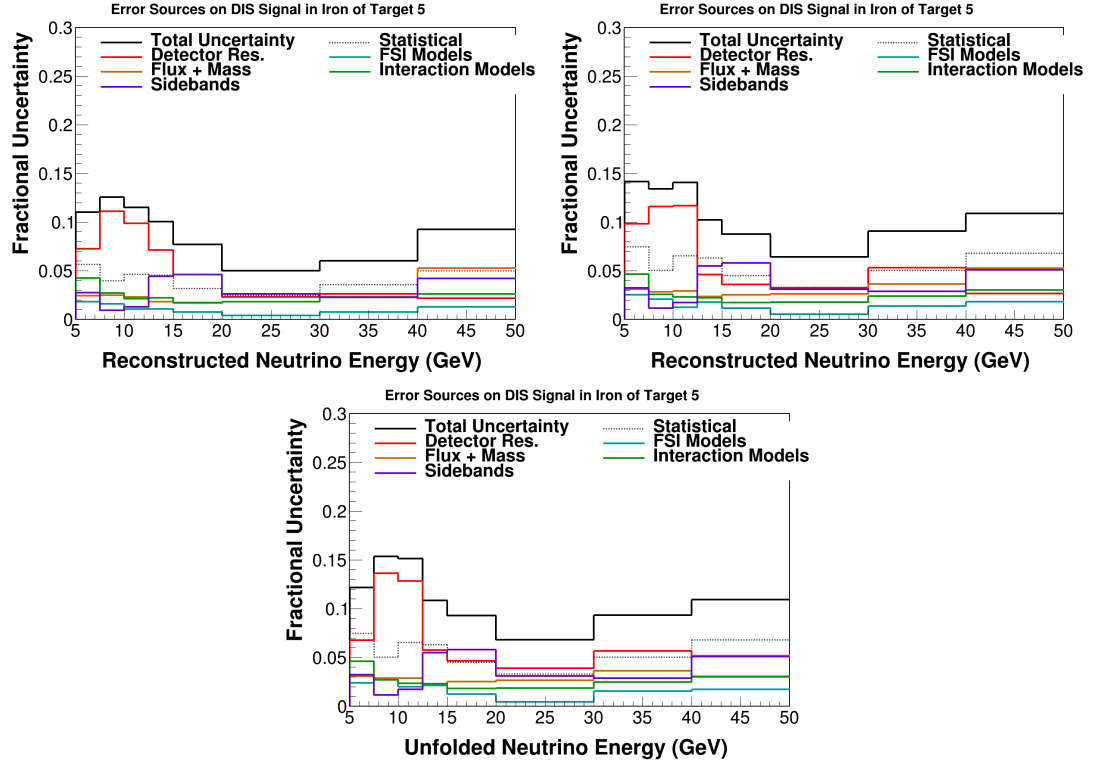
FIG. B.15: Iron of target 5 in E_ν data error summary after background subtraction (top right), unfolding (top left) and efficiency correction (bottom). At the event selection stage there are only statistical errors on the data distributions, so a systematic error summary is not included here.
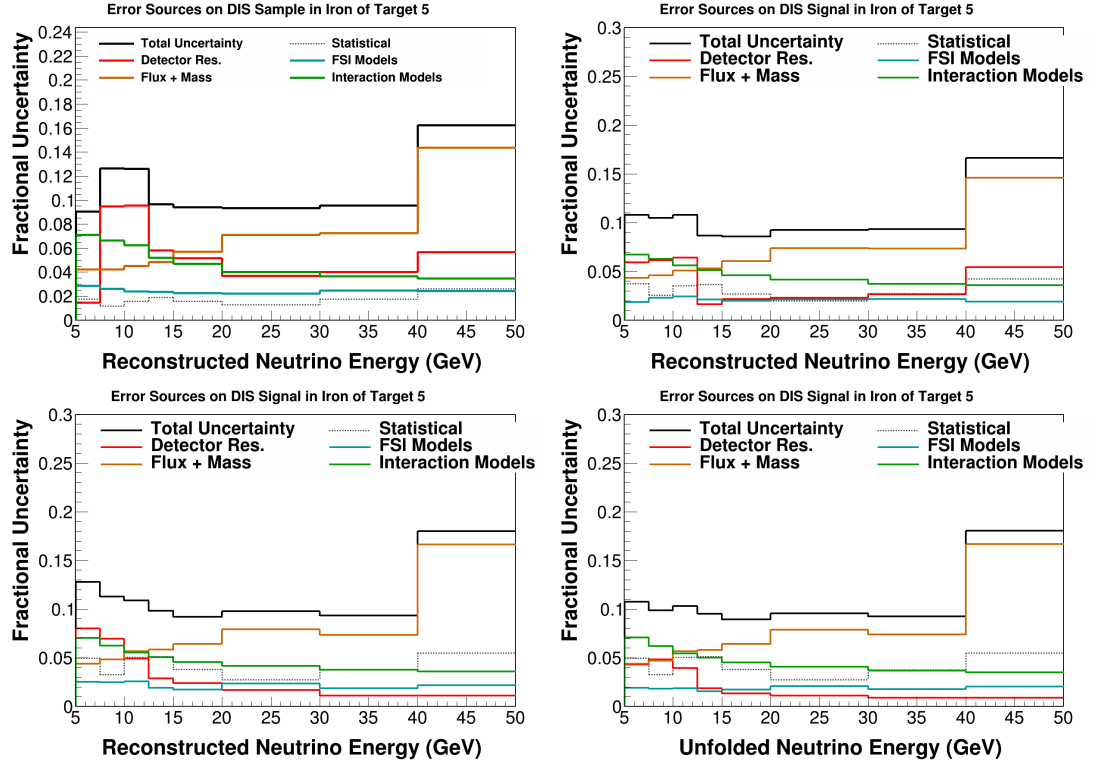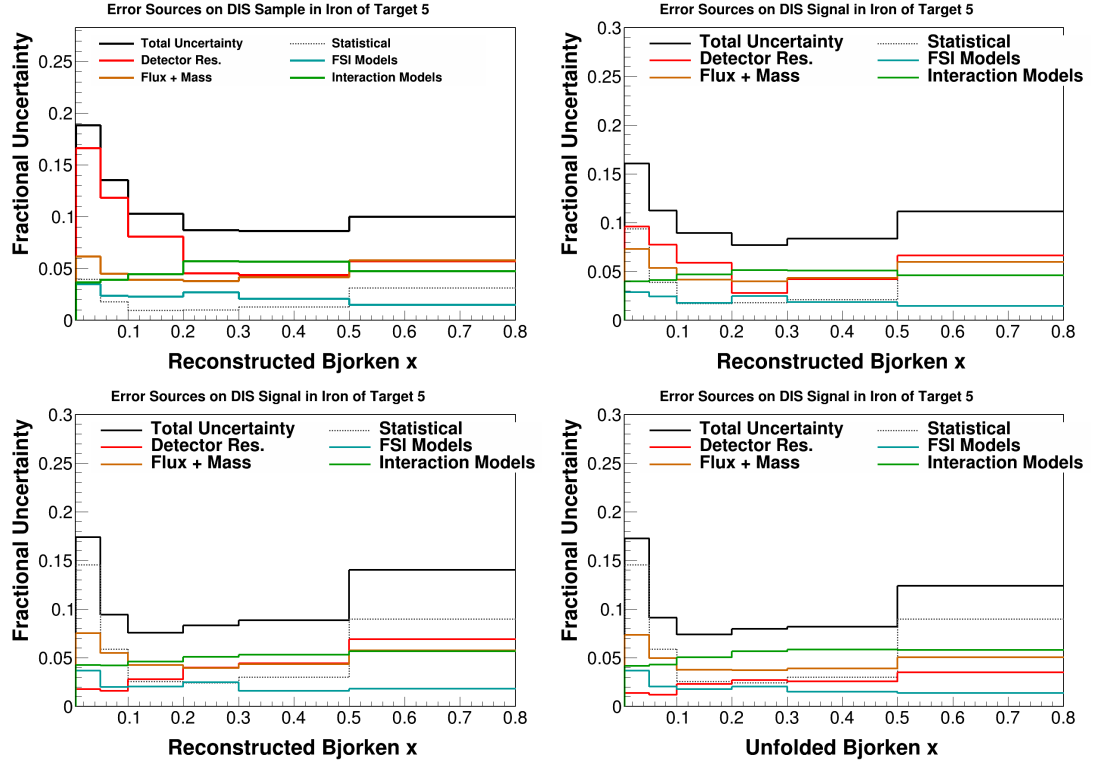
FIG. B.16: Iron of target 5 in E_ν MC error summary after event selection (top right), background subtraction (top left), unfolding (bottom right) and efficiency correction (bottom left).
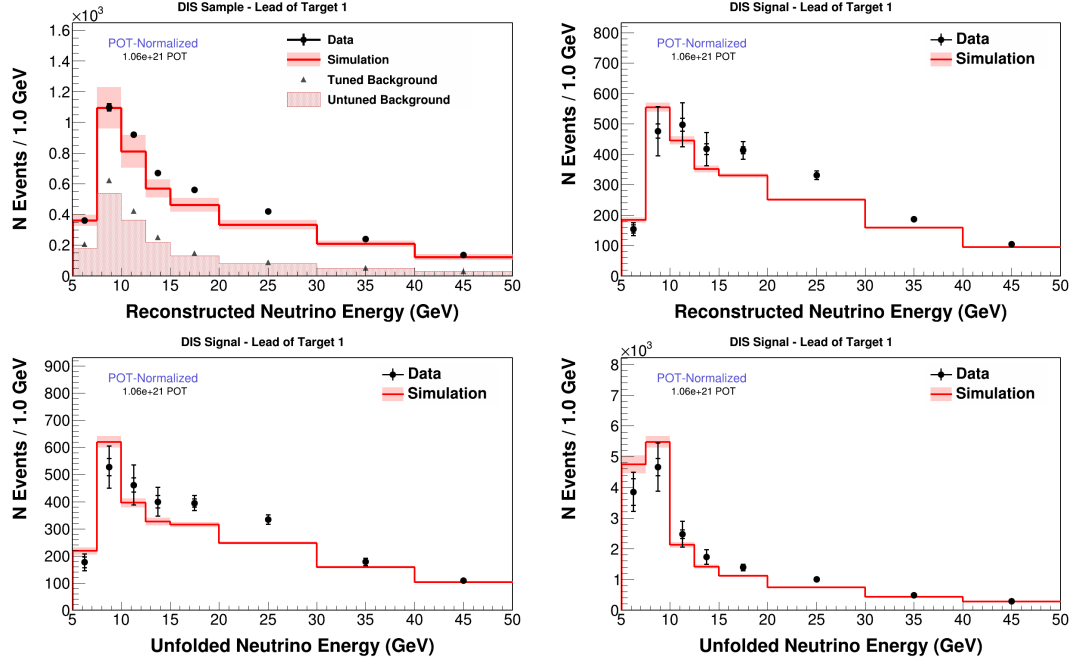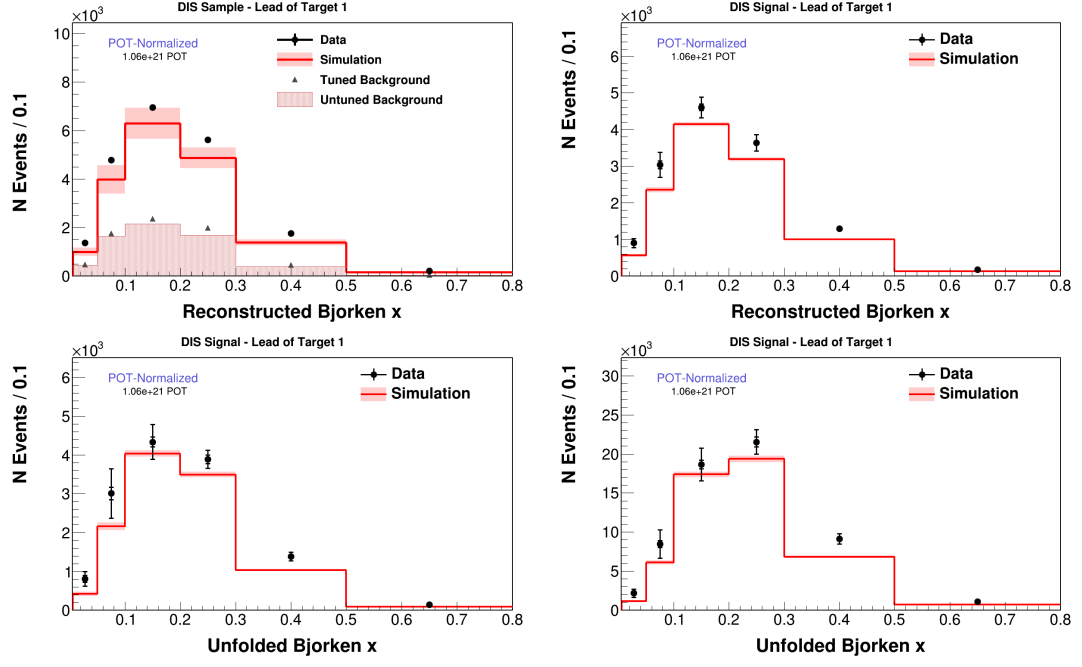
FIG. B.17: Lead of target 1 in E_ν after event selection (top right), background subtraction (top left), unfolding (bottom right) and efficiency correction (bottom left).
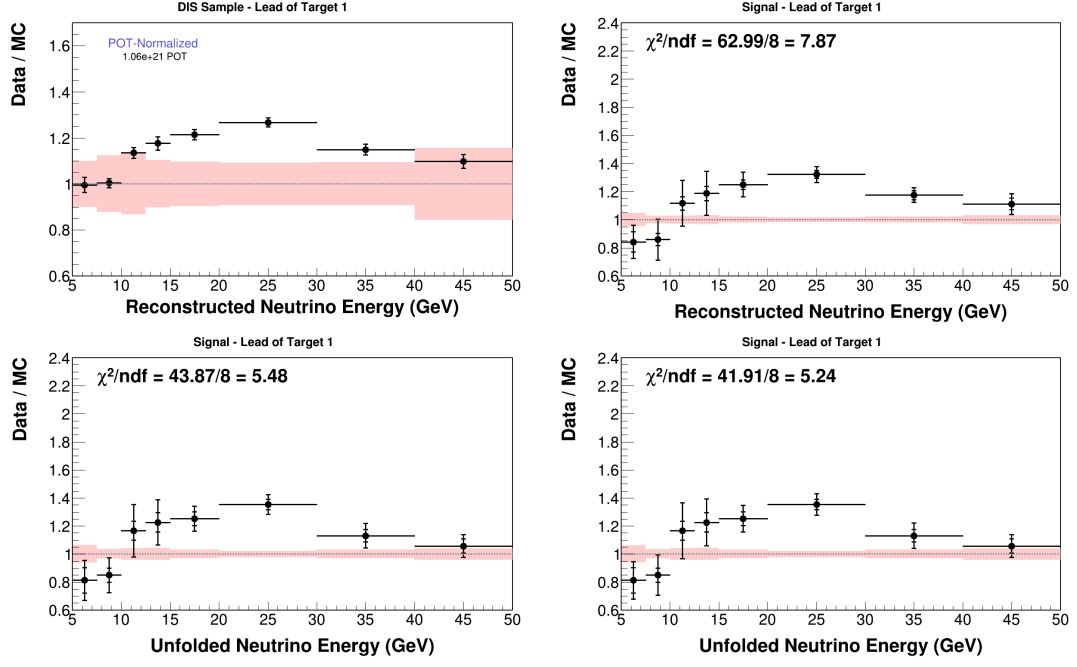
FIG. B.18: Lead of target 1 in E_ν data MC ratios after event selection (top right), background subtraction (top left), unfolding (bottom right) and efficiency correction (bottom left).
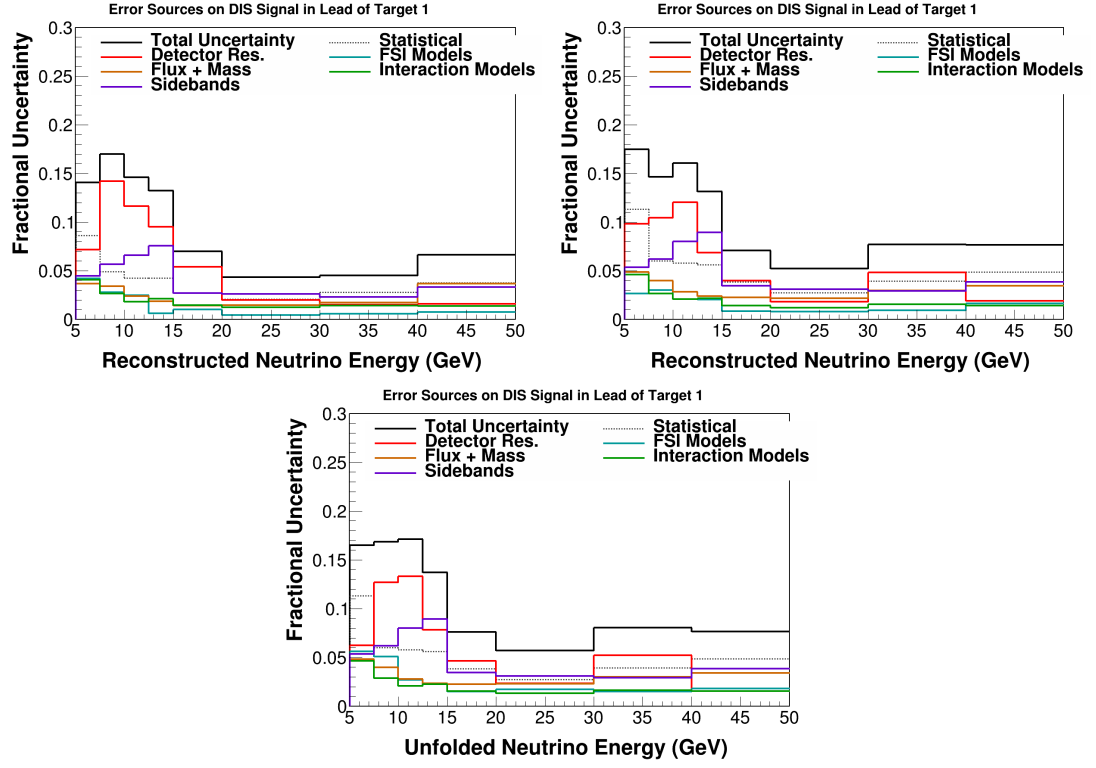
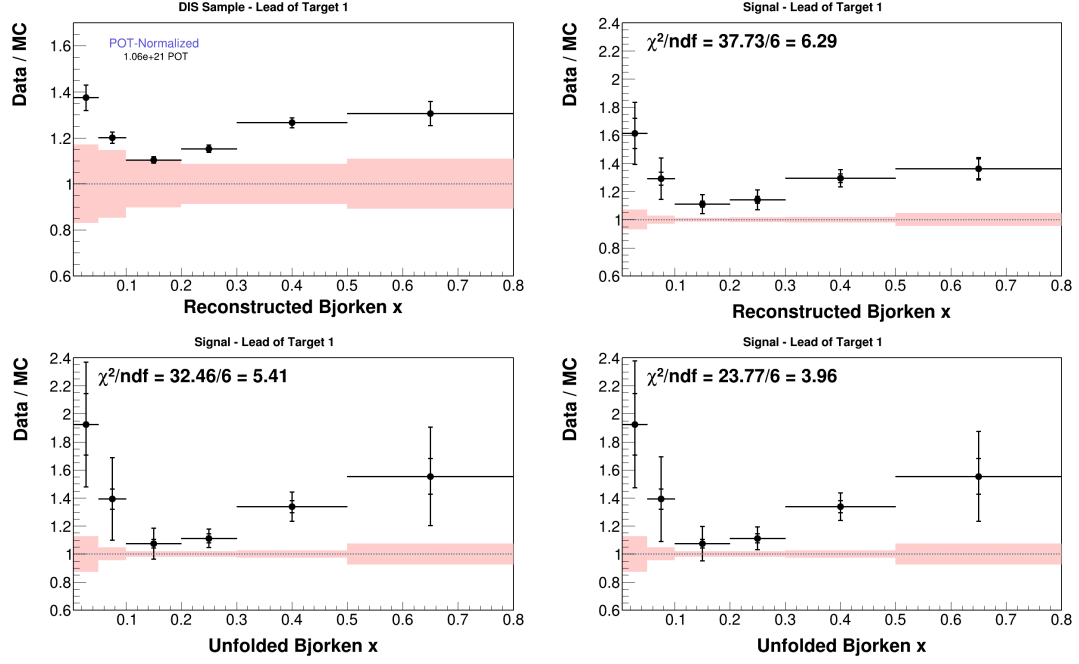## Lead of target 2

FIG. B.19: Lead of target 1 in E_ν data error summary after background subtraction (top right), unfolding (top left) and efficiency correction (bottom). At the event selection stage there are only statistical errors on the data distributions, so a systematic error summary is not included here.
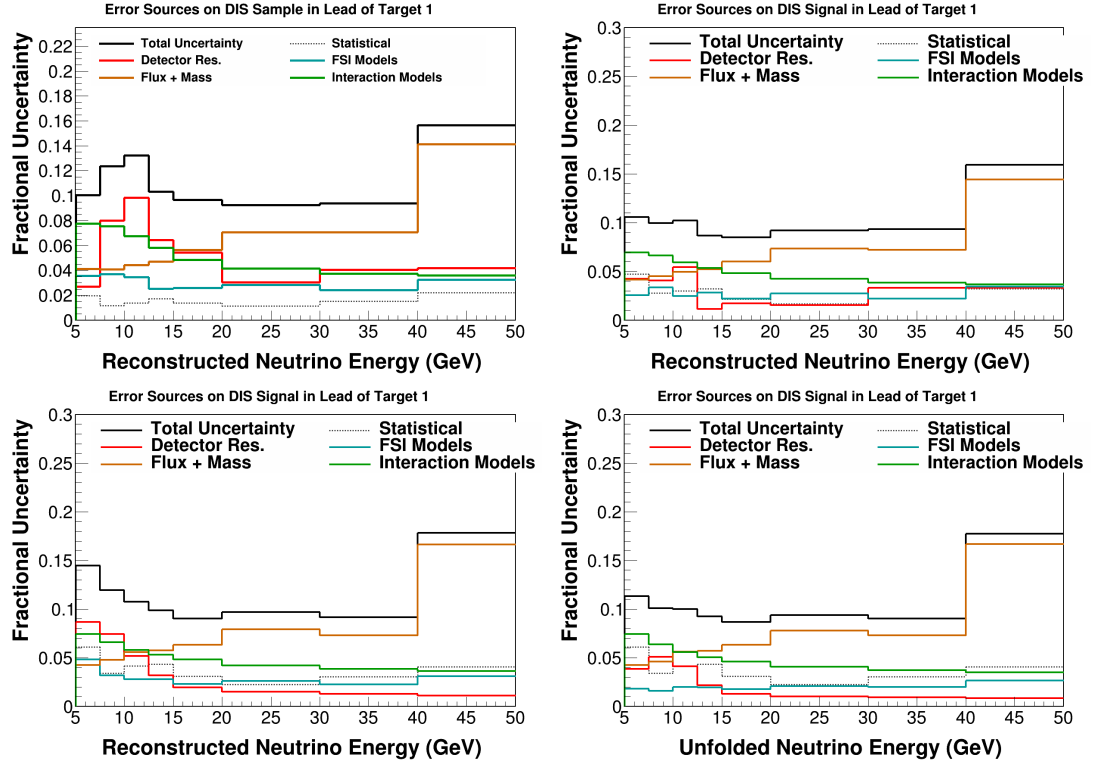
FIG. B.20: Lead of target 1 in E_ν MC error summary after event selection (top right), background subtraction (top left), unfolding (bottom right) and efficiency correction (bottom left).
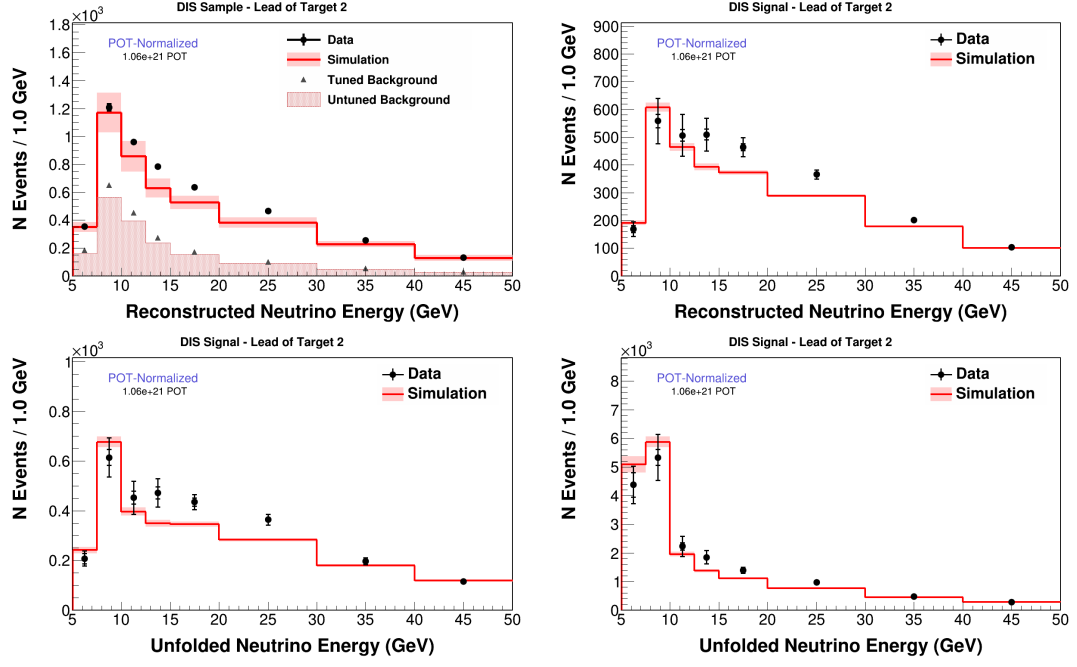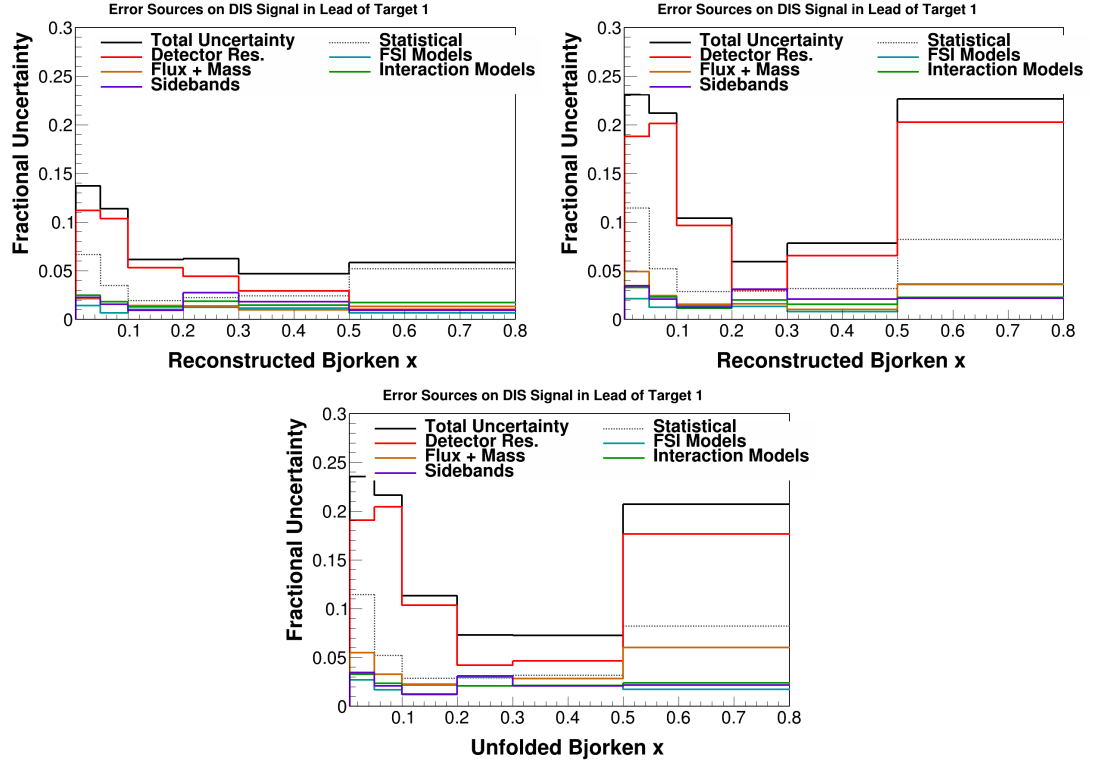
FIG. B.21: Lead of target 2 in E_ν after event selection (top right), background subtraction (top left), unfolding (bottom right) and efficiency correction (bottom left).

FIG. B.22: Lead of target 2 in E_ν data MC ratios after event selection (top right), background subtraction (top left), unfolding (bottom right) and efficiency correction (bottom left).
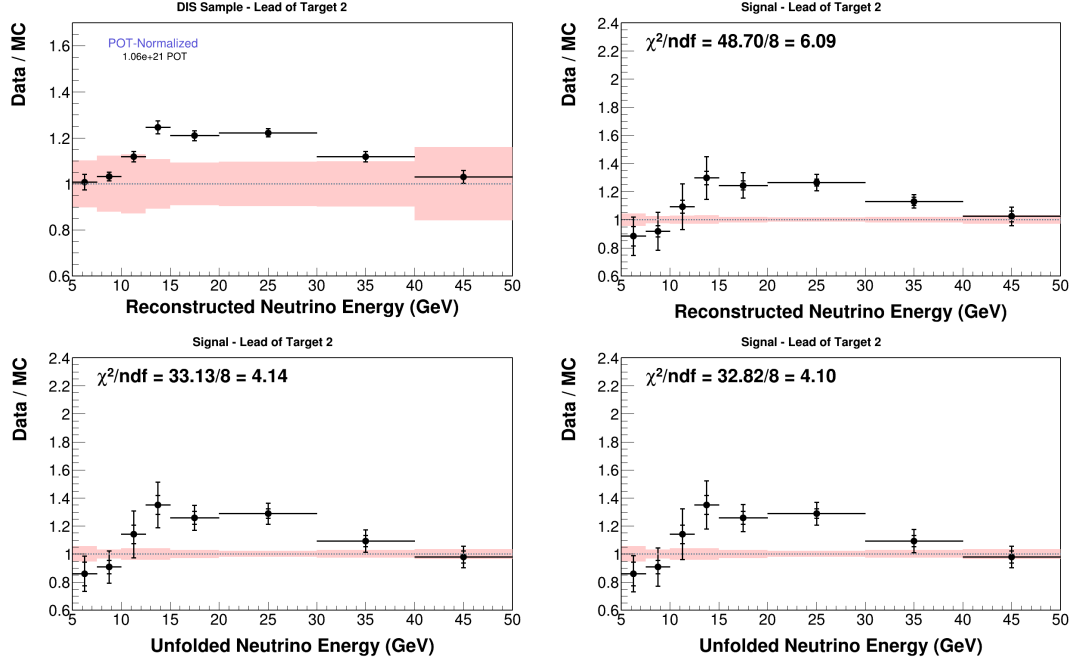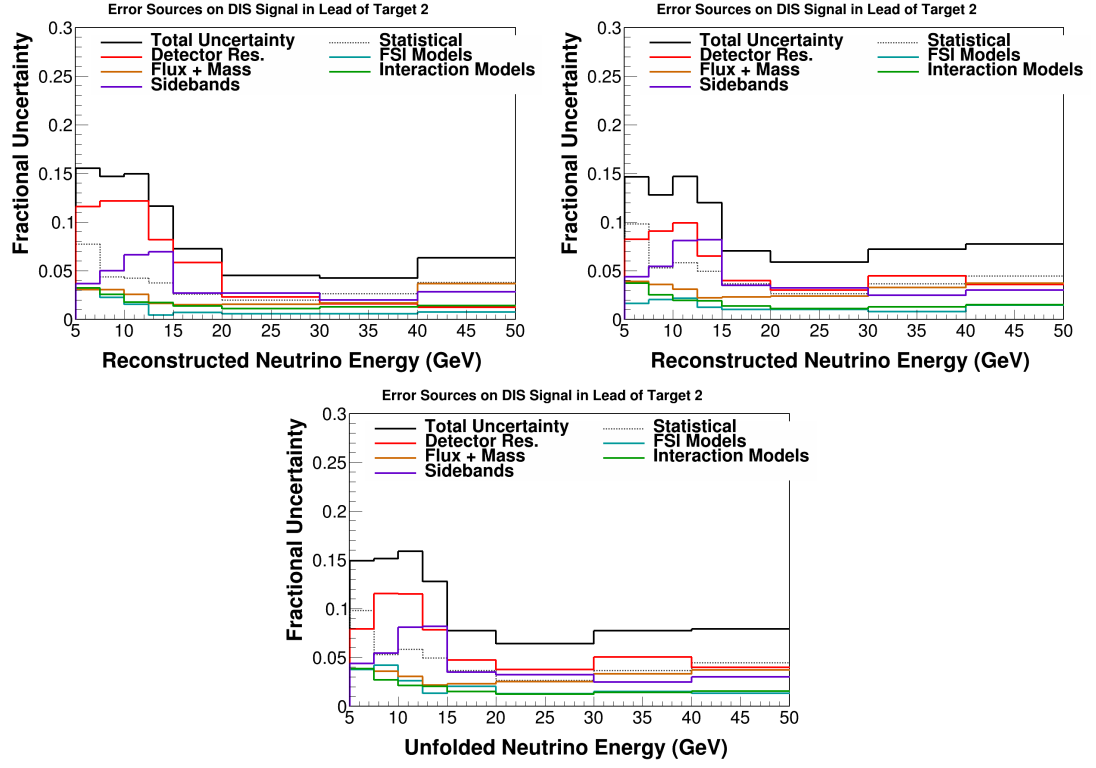
Lead of target 3

FIG. B.23: Lead of target 2 in E_ν data error summary after background subtraction (top right), unfolding (top left) and efficiency correction (bottom). At the event selection stage there are only statistical errors on the data distributions, so a systematic error summary is not included here.
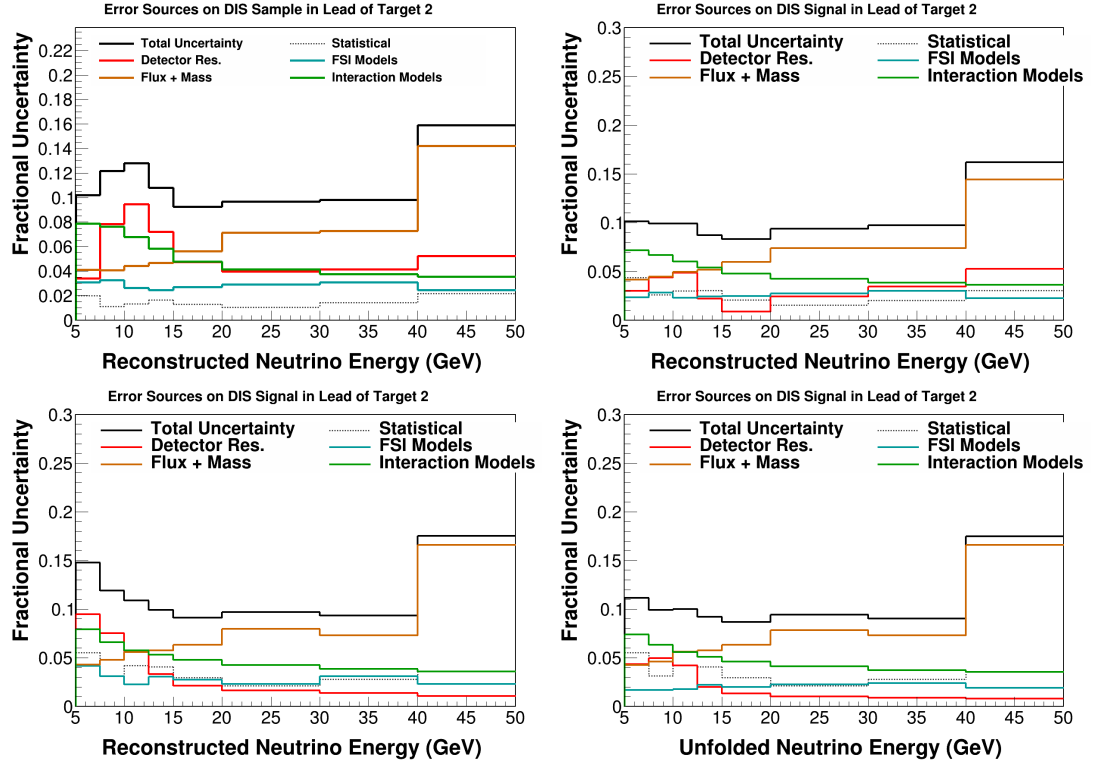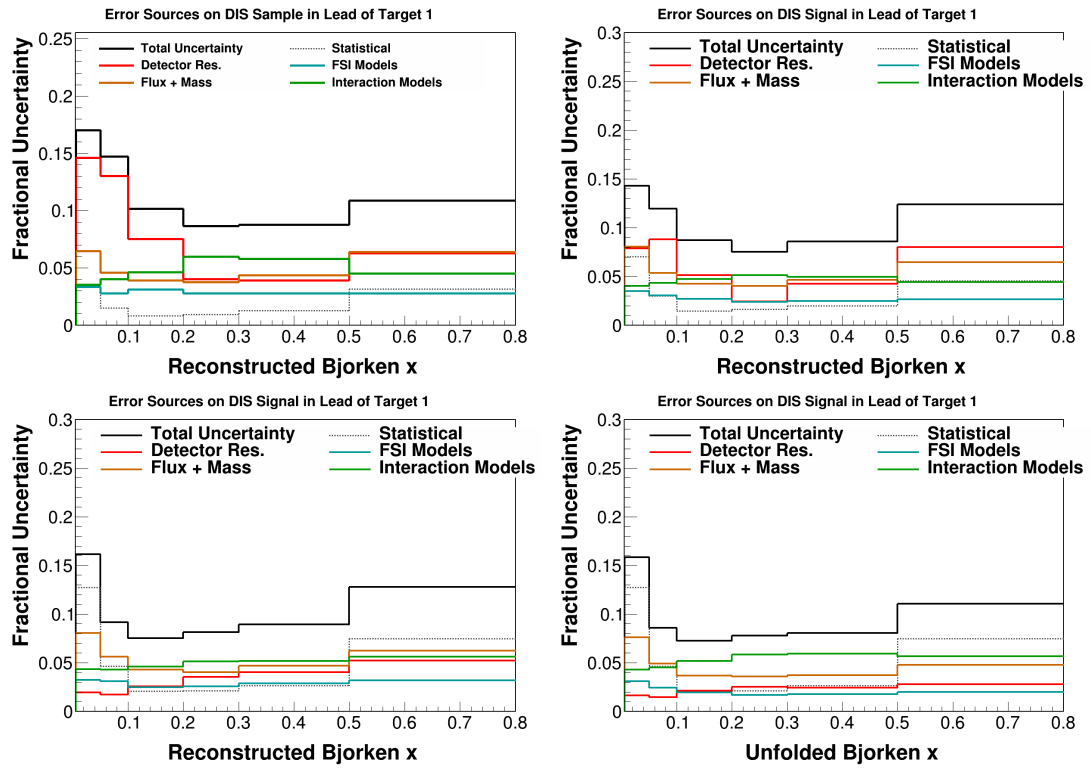
FIG. B.24: Lead of target 2 in E_ν MC error summary after event selection (top right), background subtraction (top left), unfolding (bottom right) and efficiency correction (bottom left).
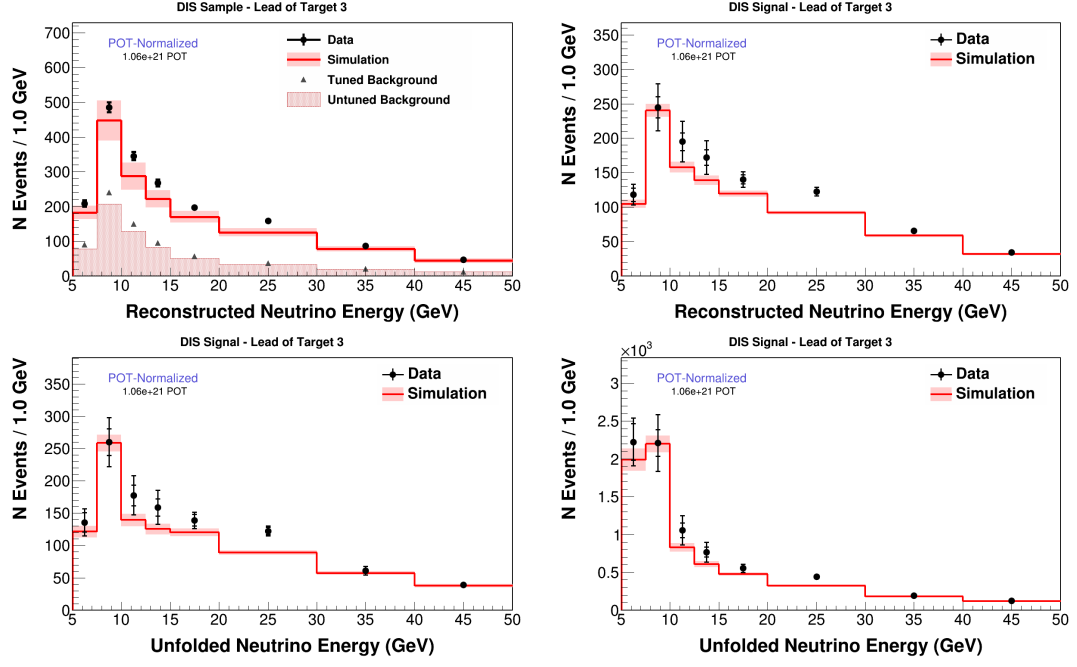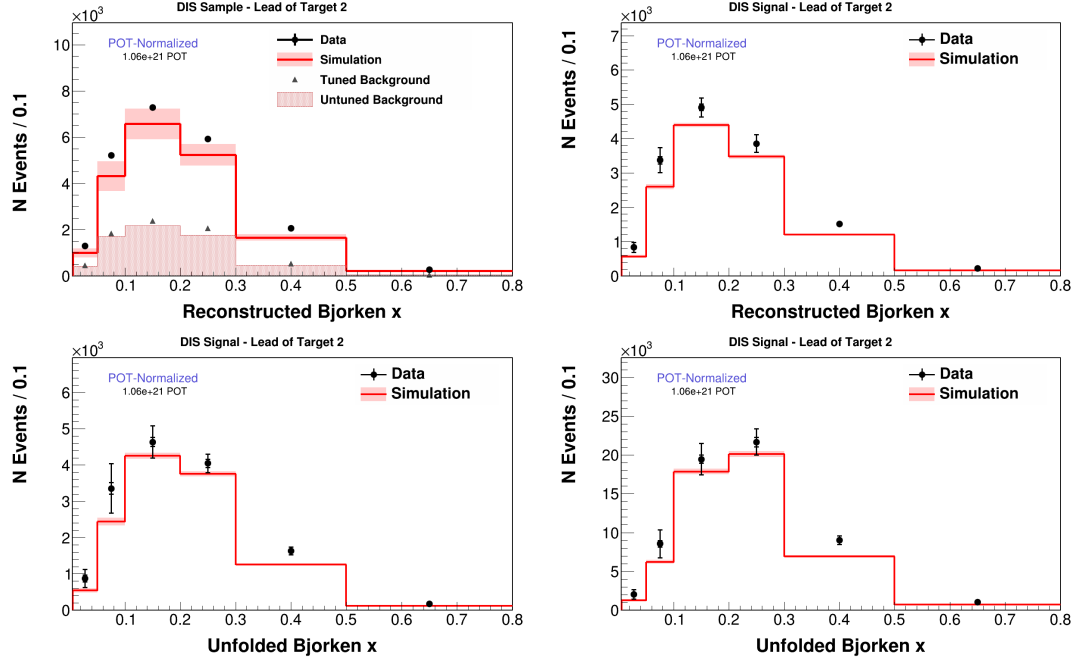
FIG. B.25: Lead of target 3 in E_ν after event selection (top right), background subtraction (top left), unfolding (bottom right) and efficiency correction (bottom left).
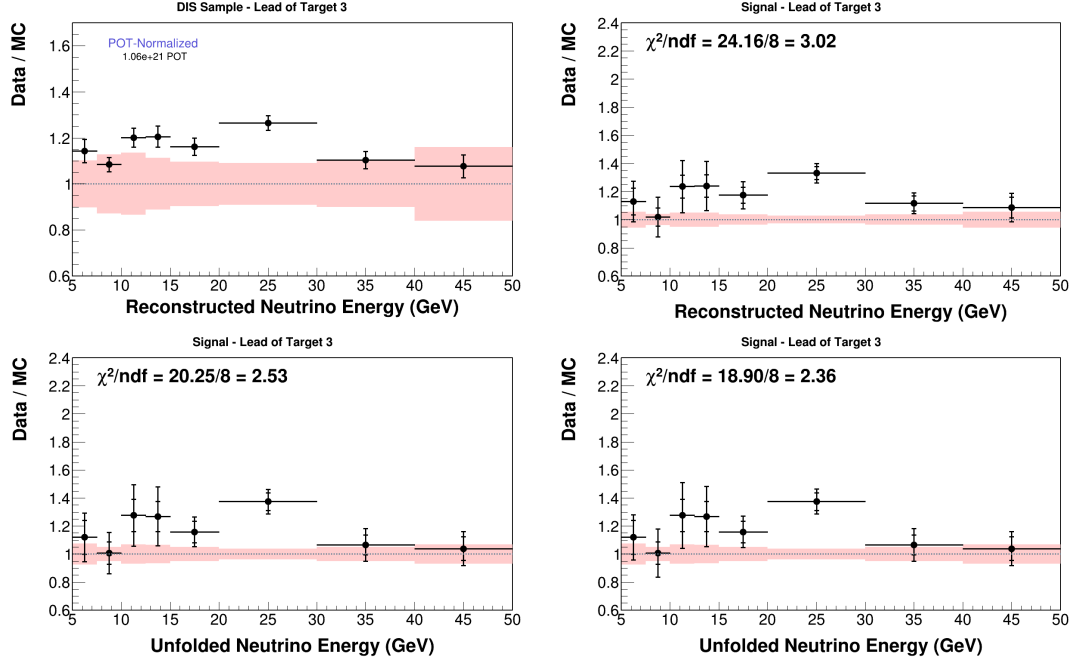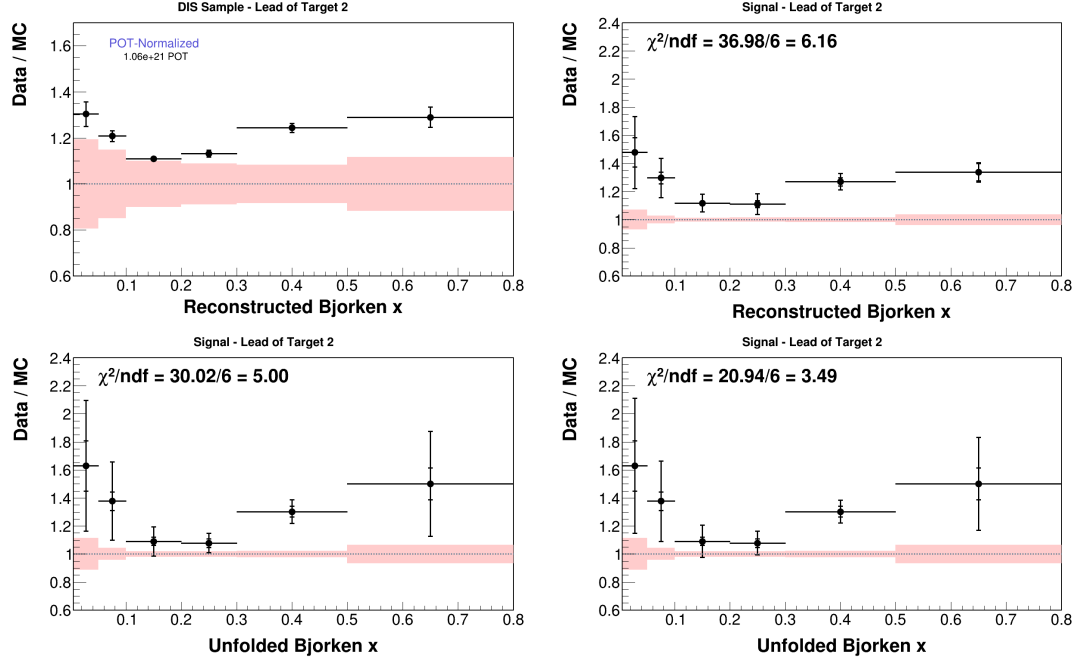
FIG. B.26: Lead of target 3 in E_ν data MC ratios after event selection (top right), background subtraction (top left), unfolding (bottom right) and efficiency correction (bottom left).
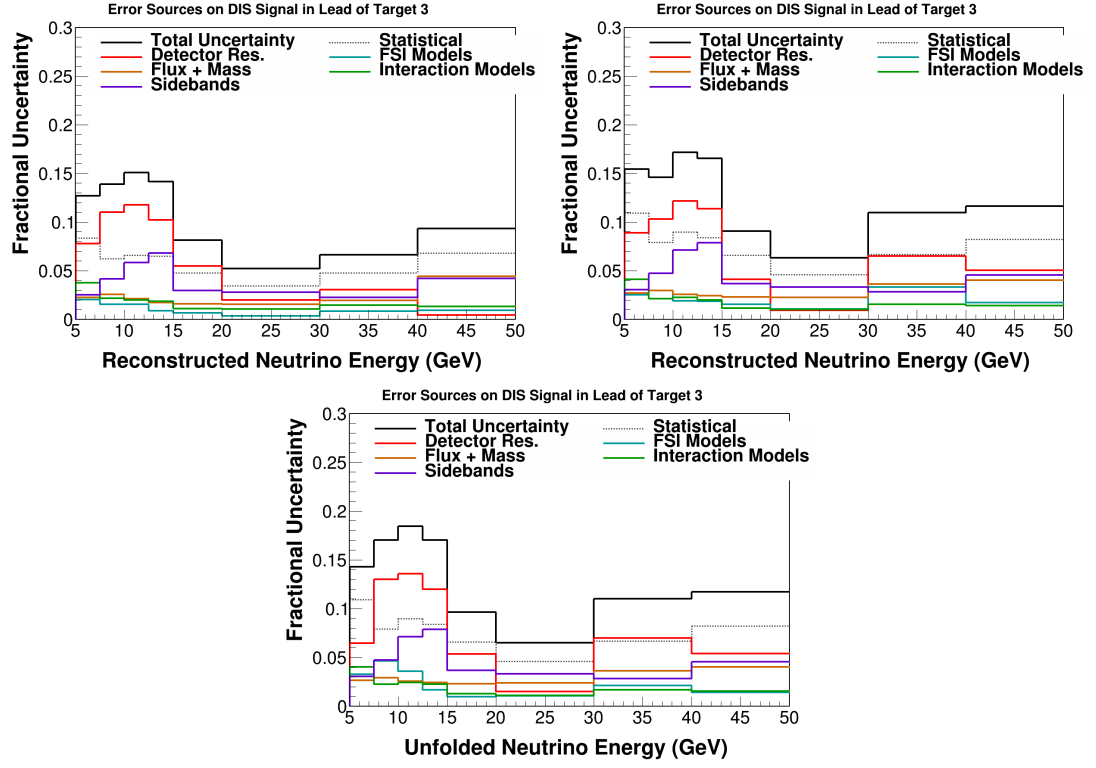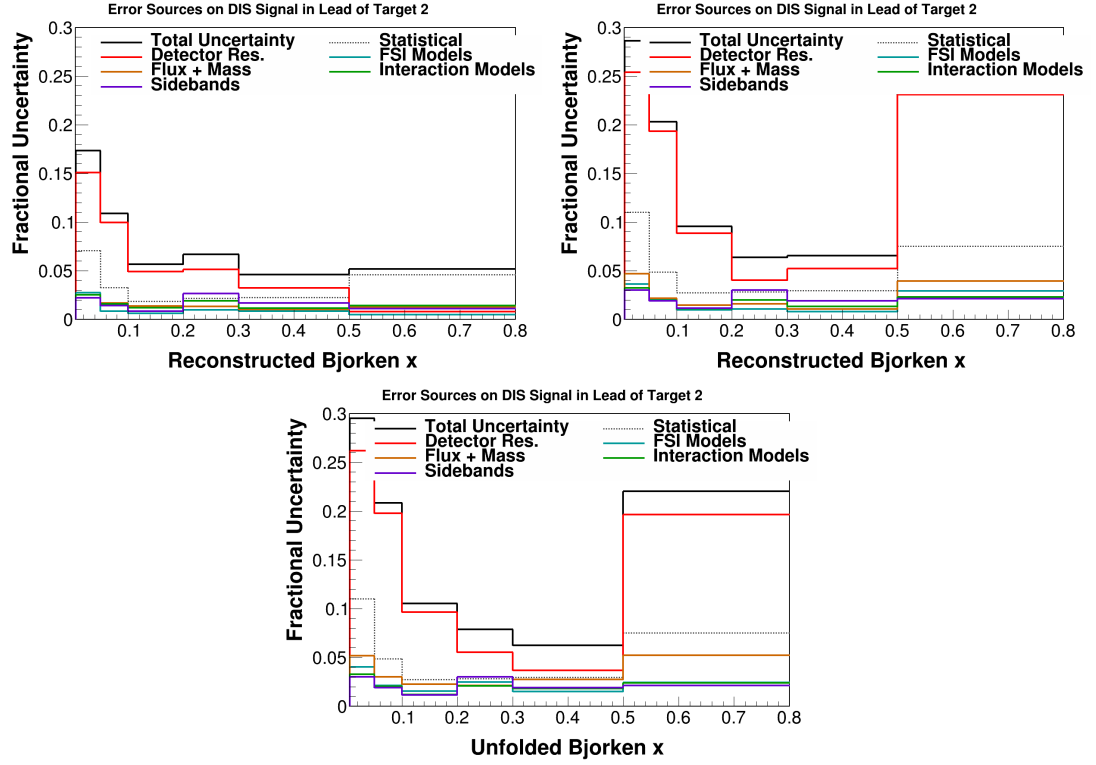
Lead of target 4

FIG. B.27: Lead of target 3 in E_ν data error summary after background subtraction (top right), unfolding (top left) and efficiency correction (bottom). At the event selection stage there are only statistical errors on the data distributions, so a systematic error summary is not included here.
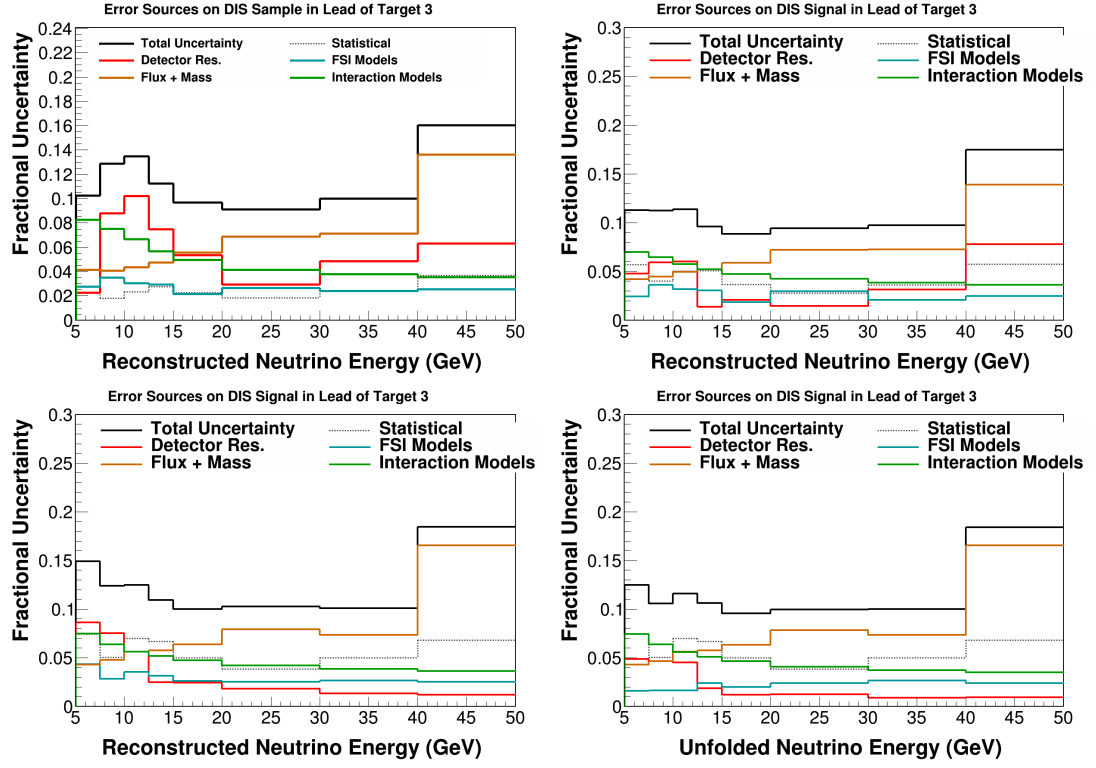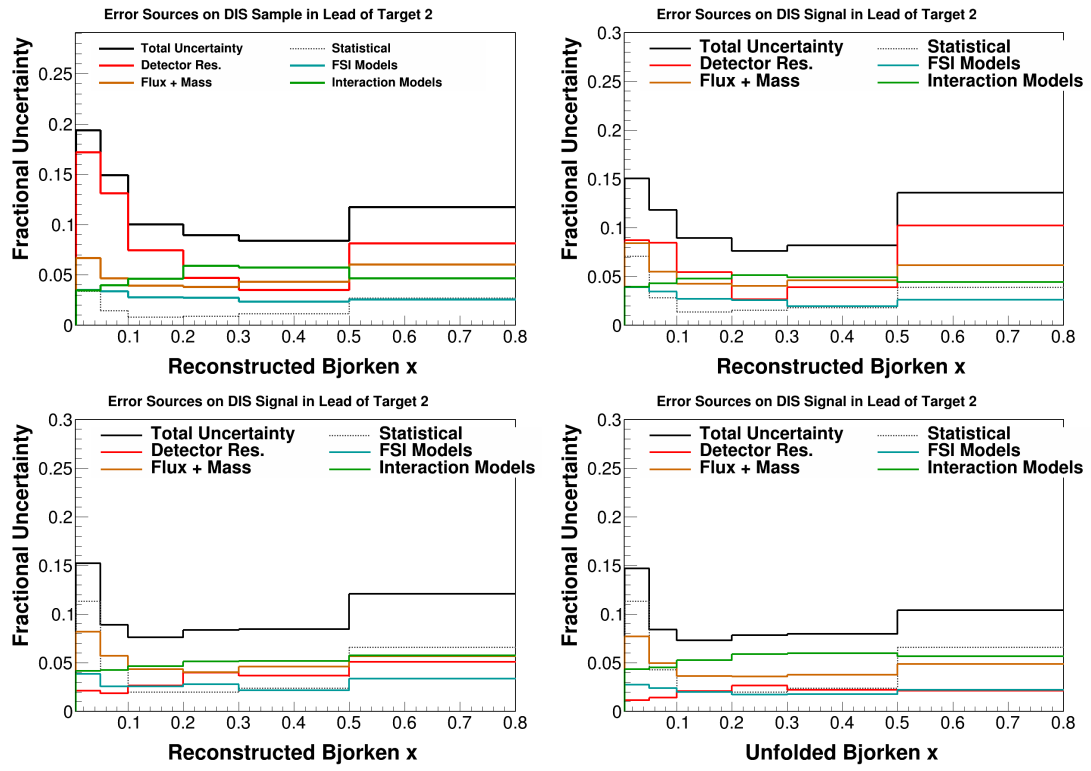
FIG. B.28: Lead of target 3 in E_ν MC error summary after event selection (top right), background subtraction (top left), unfolding (bottom right) and efficiency correction (bottom left).
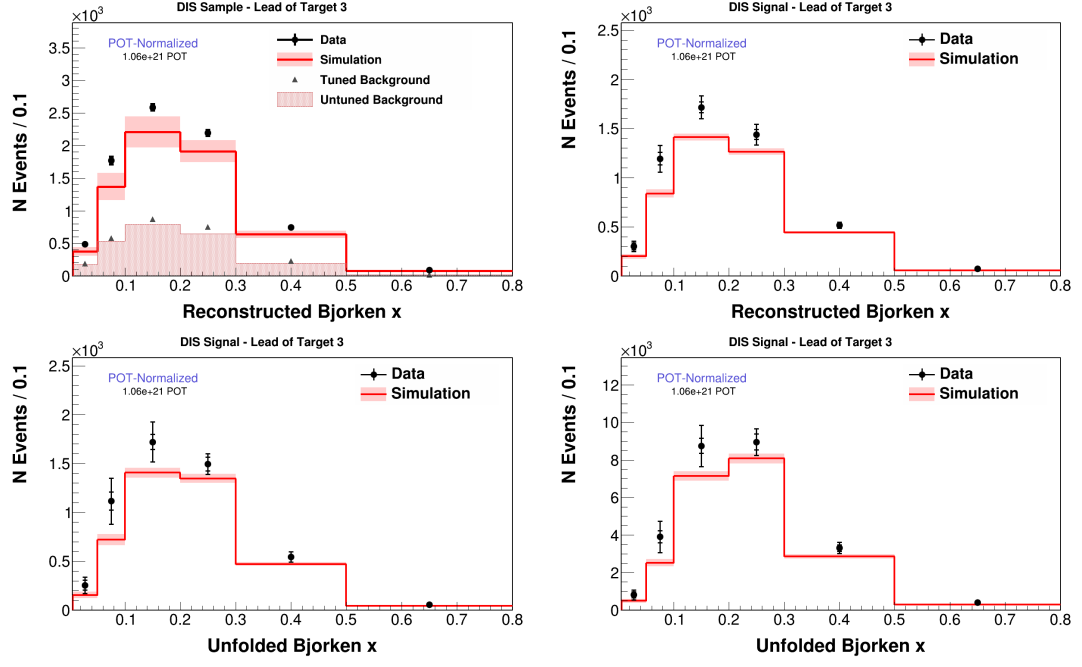
FIG. B.29: Lead of target 4 in E_ν after event selection (top right), background subtraction (top left), unfolding (bottom right) and efficiency correction (bottom left).
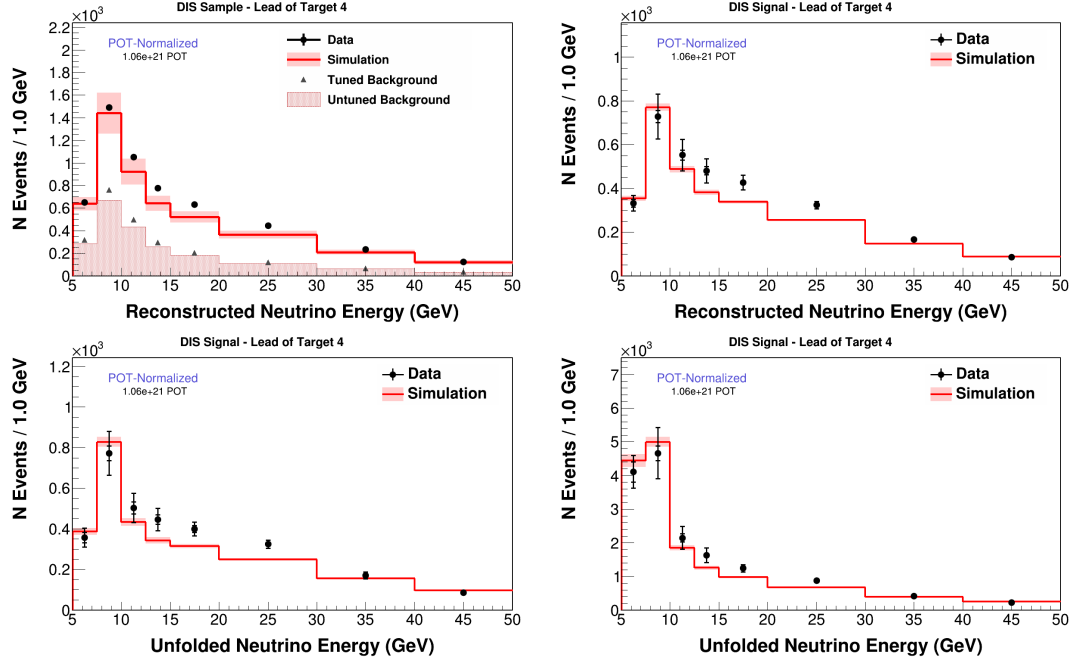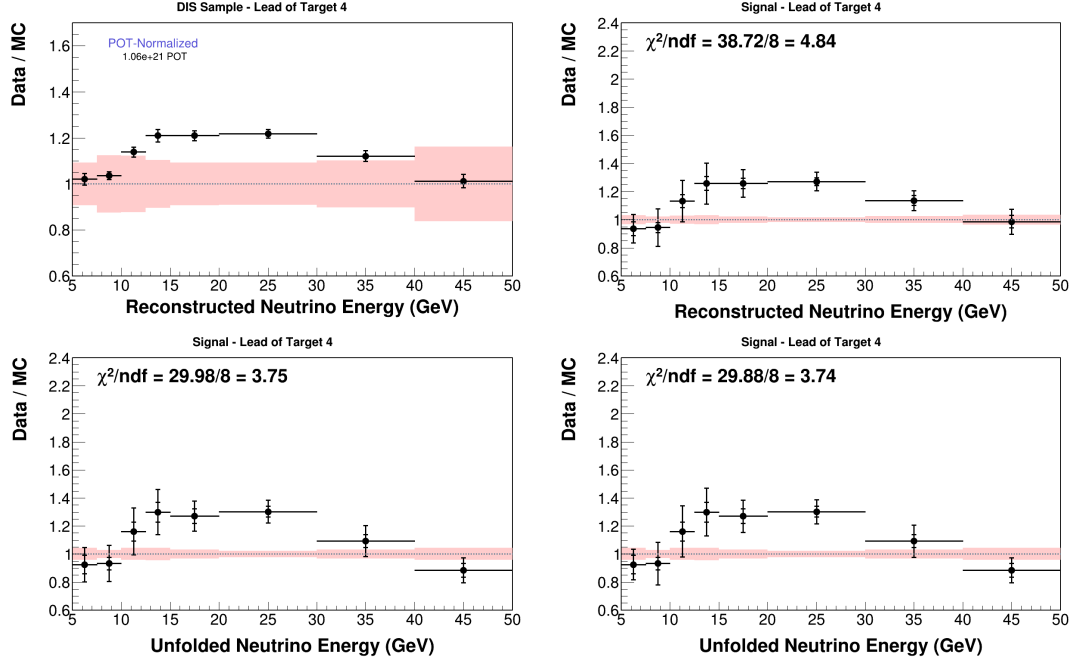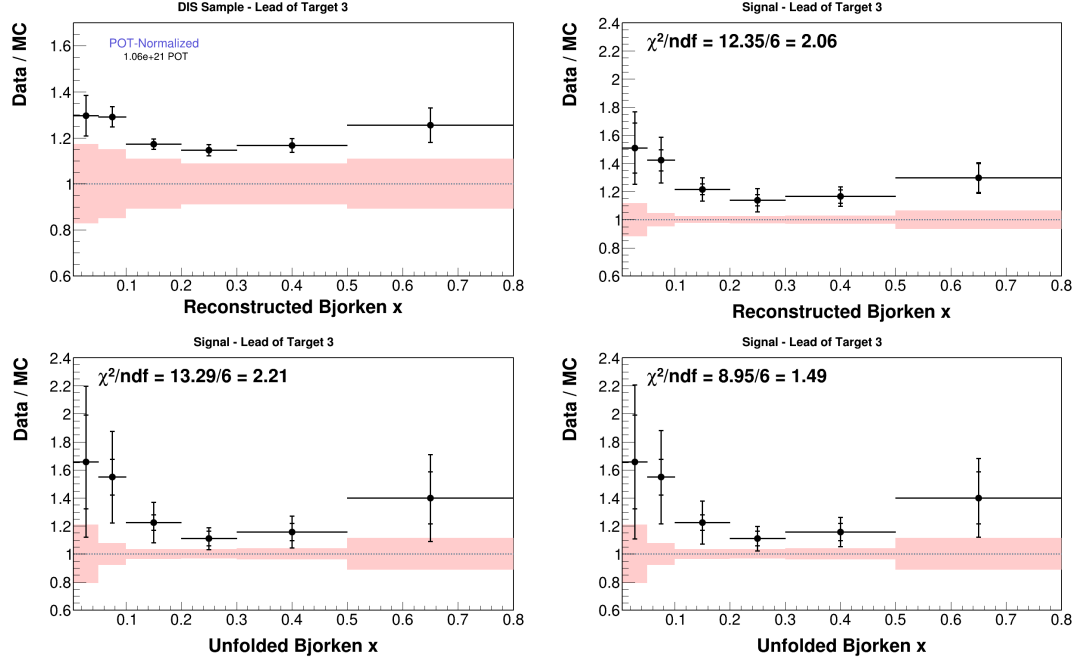
FIG. B.30: Lead of target 4 in E_ν data MC ratios after event selection (top right), background subtraction (top left), unfolding (bottom right) and efficiency correction (bottom left).
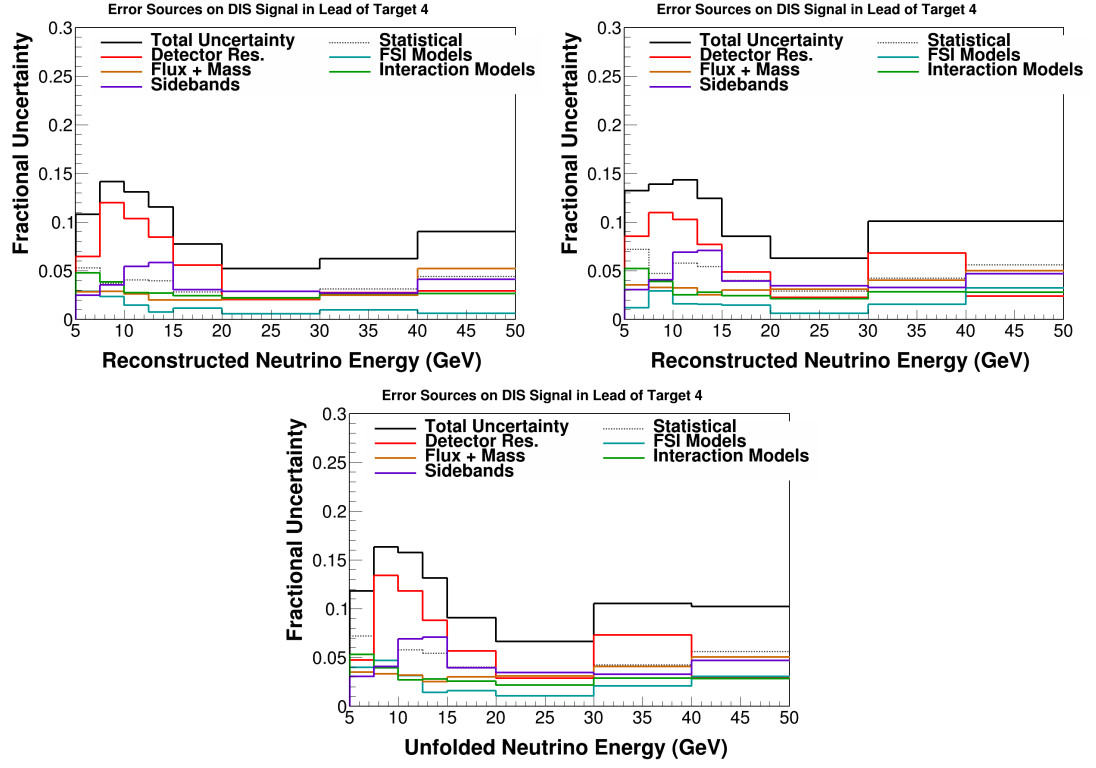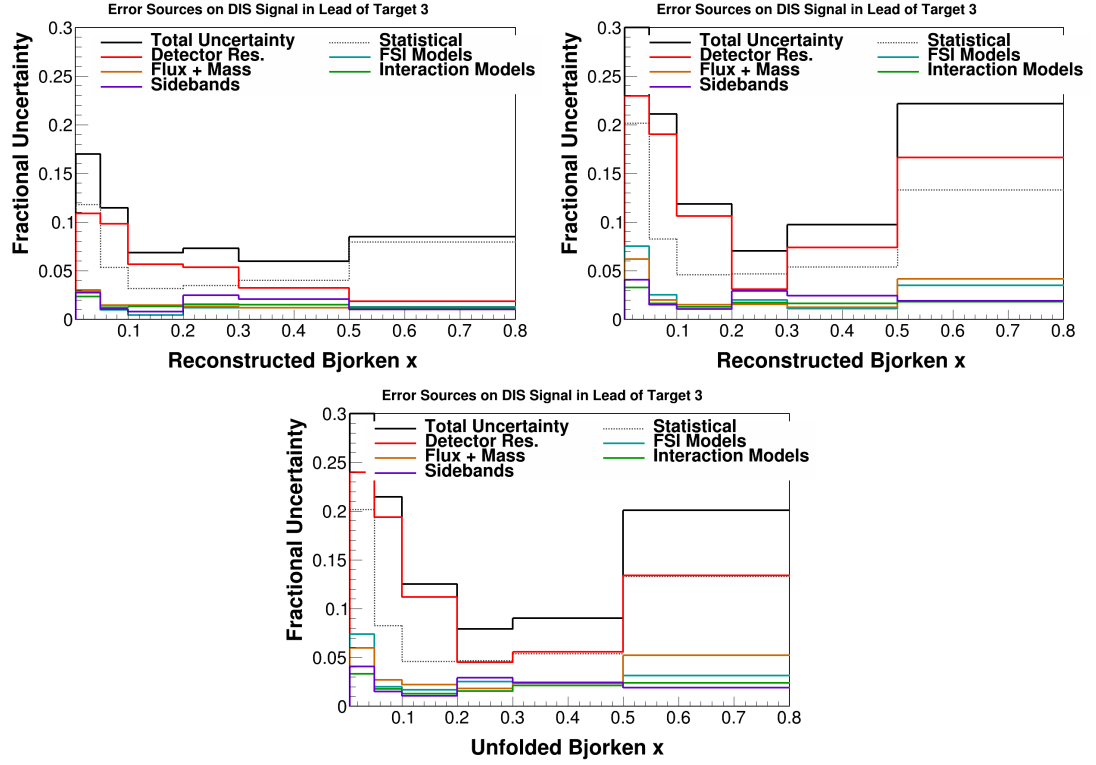
Lead of target 5

FIG. B.31: Lead of target 4 in E_ν data error summary after background subtraction (top right), unfolding (top left) and efficiency correction (bottom). At the event selection stage there are only statistical errors on the data distributions, so a systematic error summary is not included here.
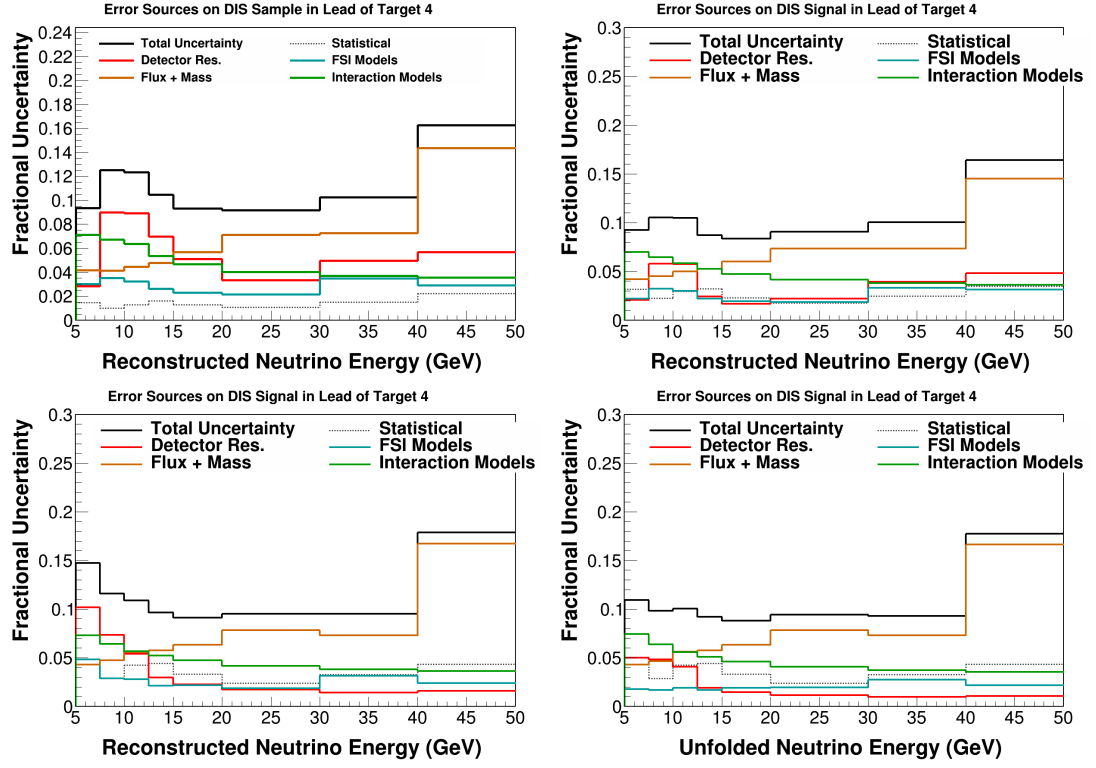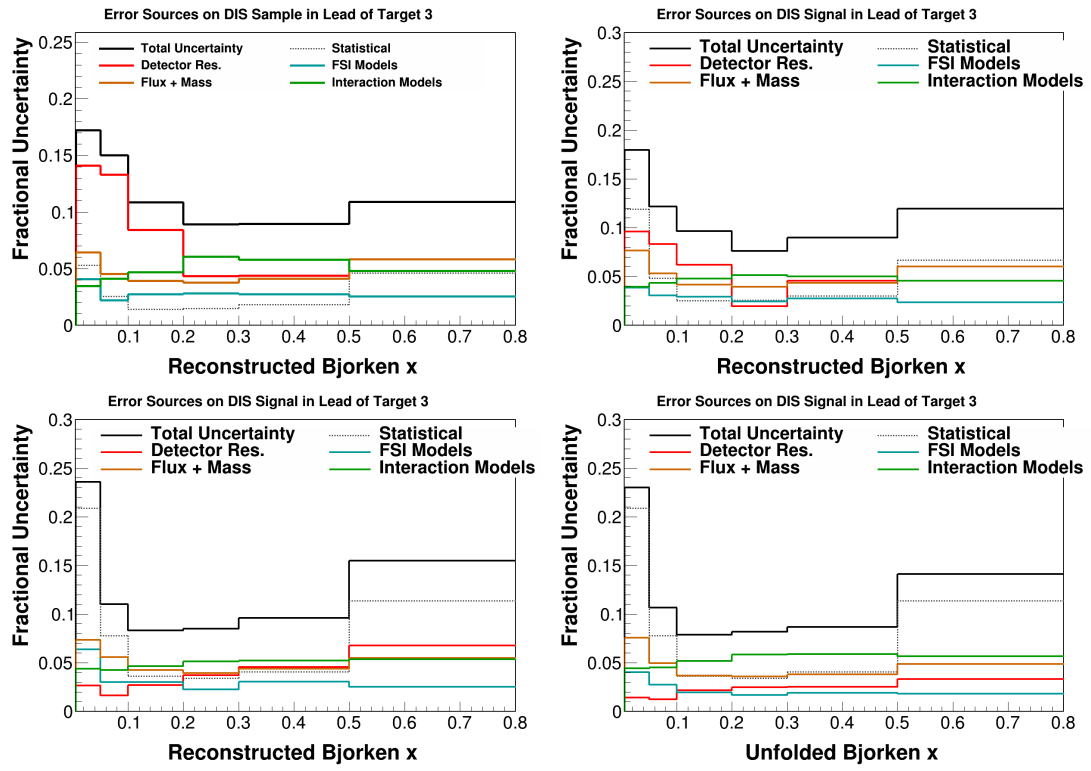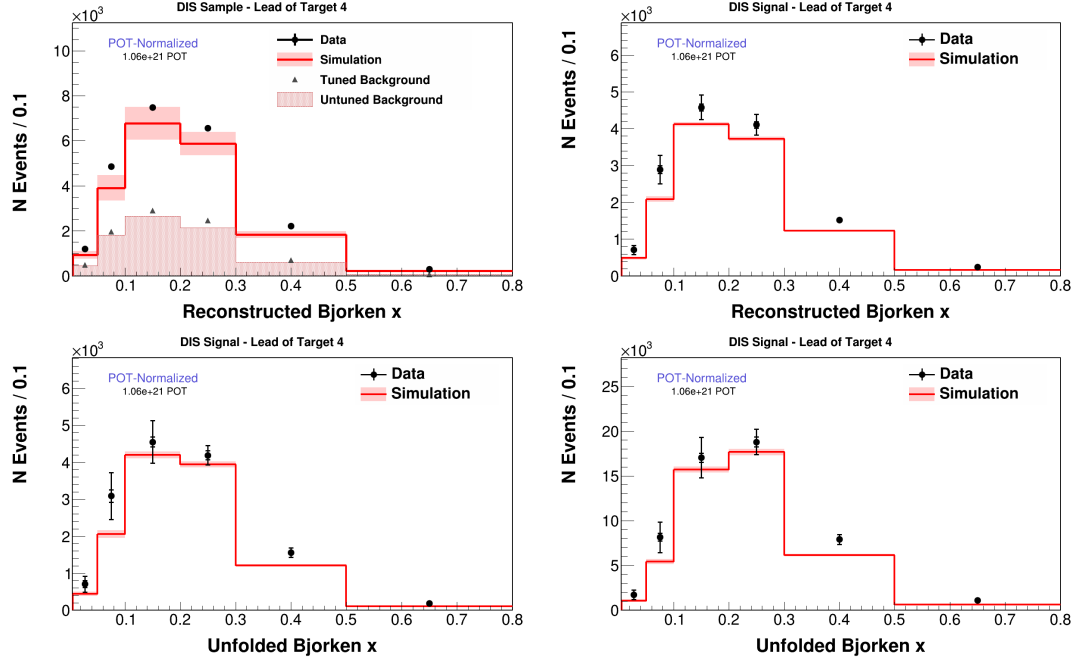
FIG. B.32: Lead of target 4 in E_ν MC error summary after event selection (top right), background subtraction (top left), unfolding (bottom right) and efficiency correction (bottom left).
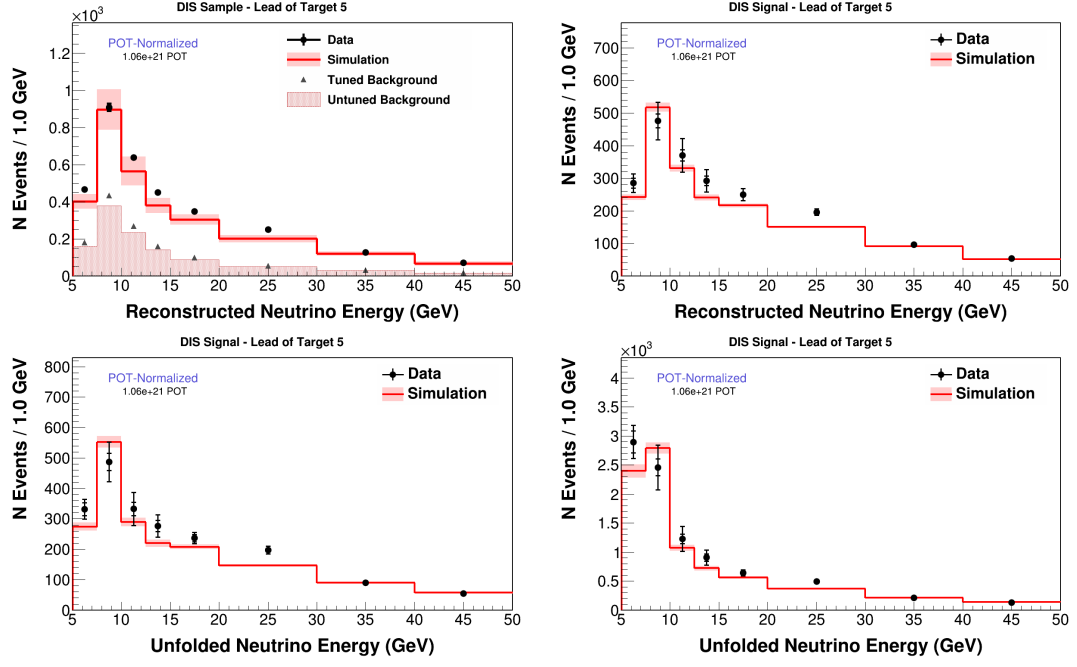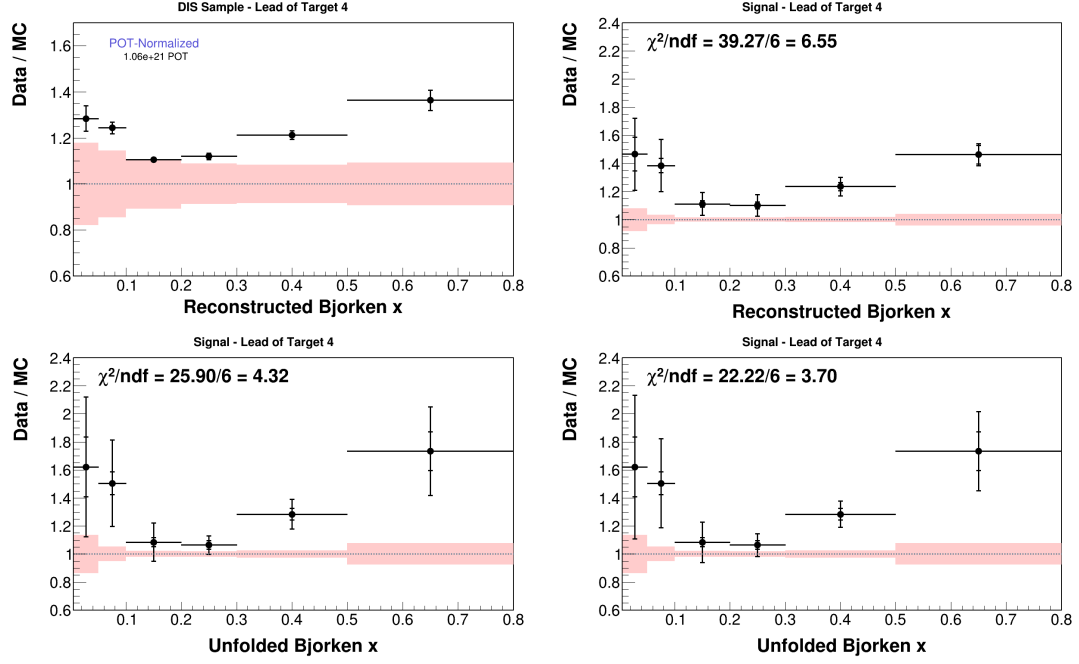
FIG. B.33: Lead of target 5 in E_ν after event selection (top right), background subtraction (top left), unfolding (bottom right) and efficiency correction (bottom left).
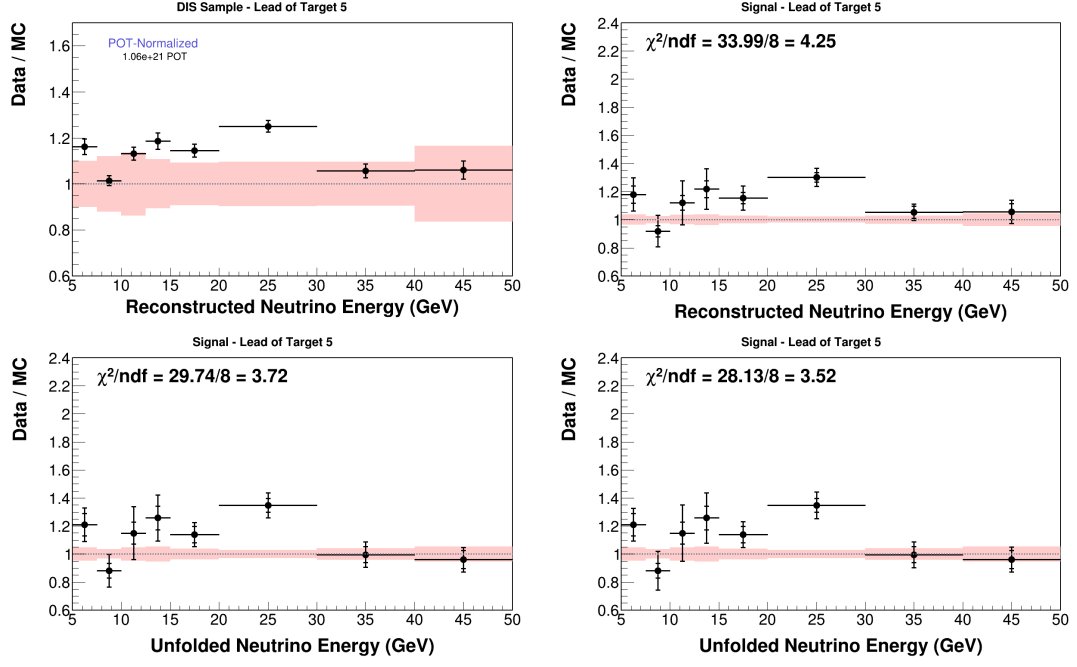
FIG. B.34: Lead of target 5 in E_ν data MC ratios after event selection (top right), background subtraction (top left), unfolding (bottom right) and efficiency correction (bottom left).
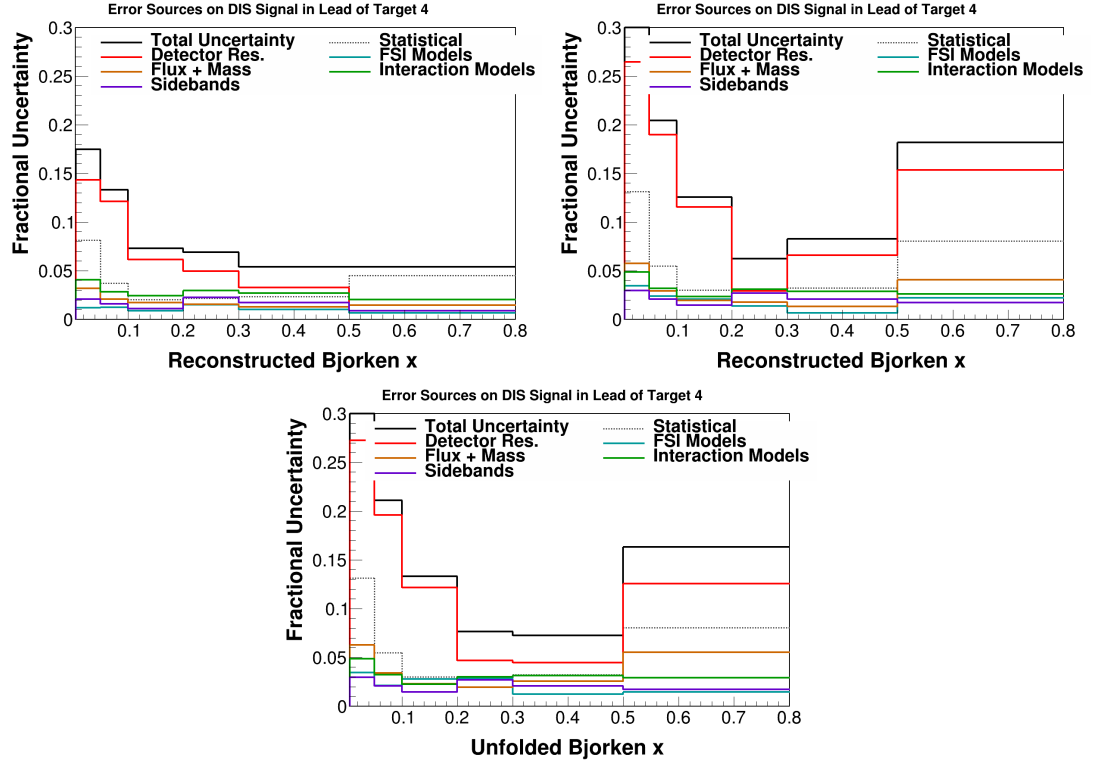
Carbon of target 3
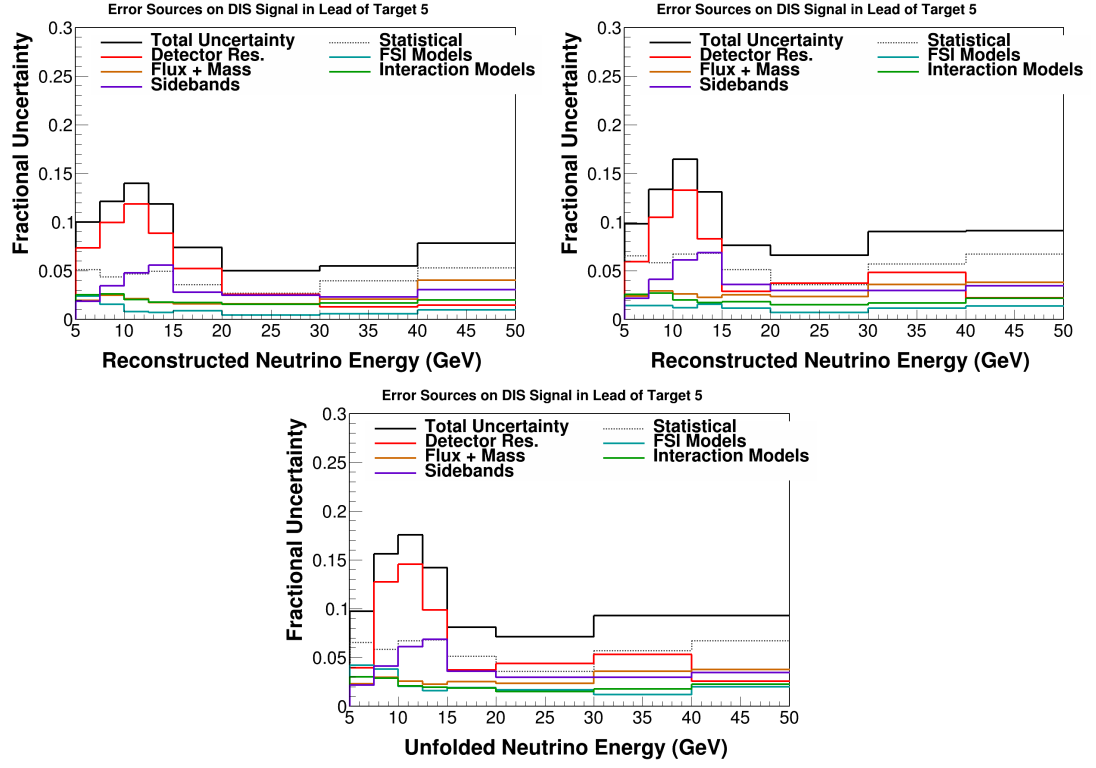
FIG. B.35: Lead of target 5 in E_ν data error summary after background subtraction (top right), unfolding (top left) and efficiency correction (bottom). At the event selection stage there are only statistical errors on the data distributions, so a systematic error summary is not included here.
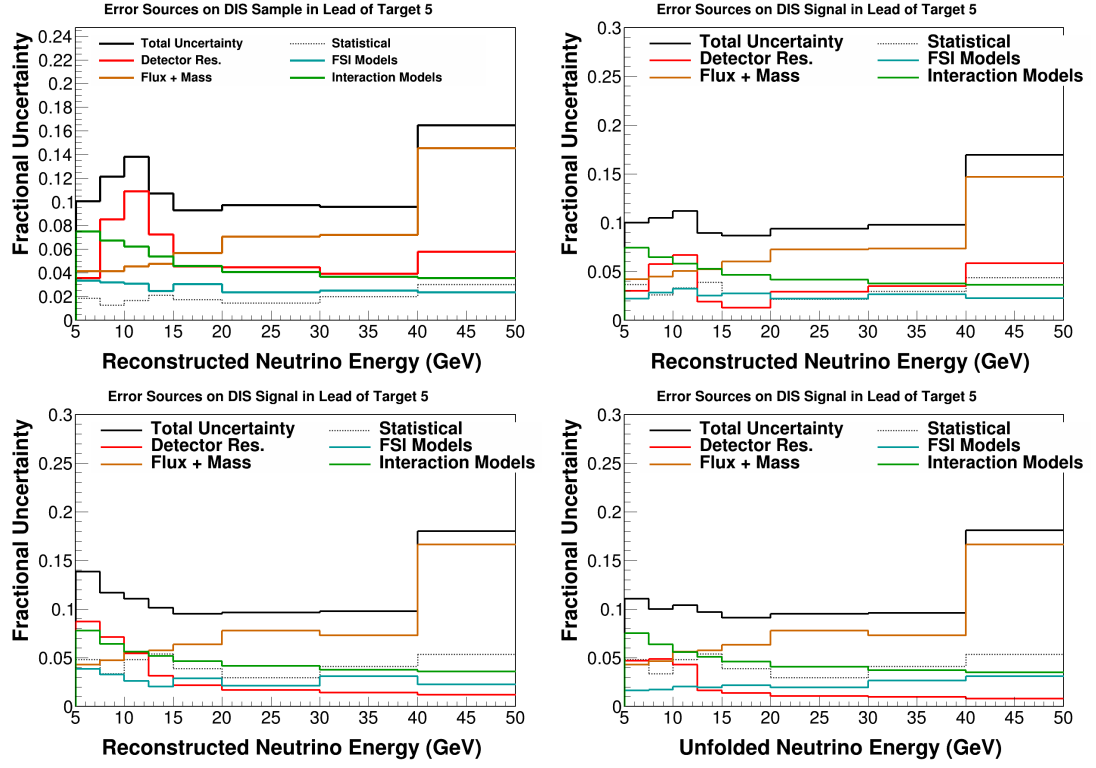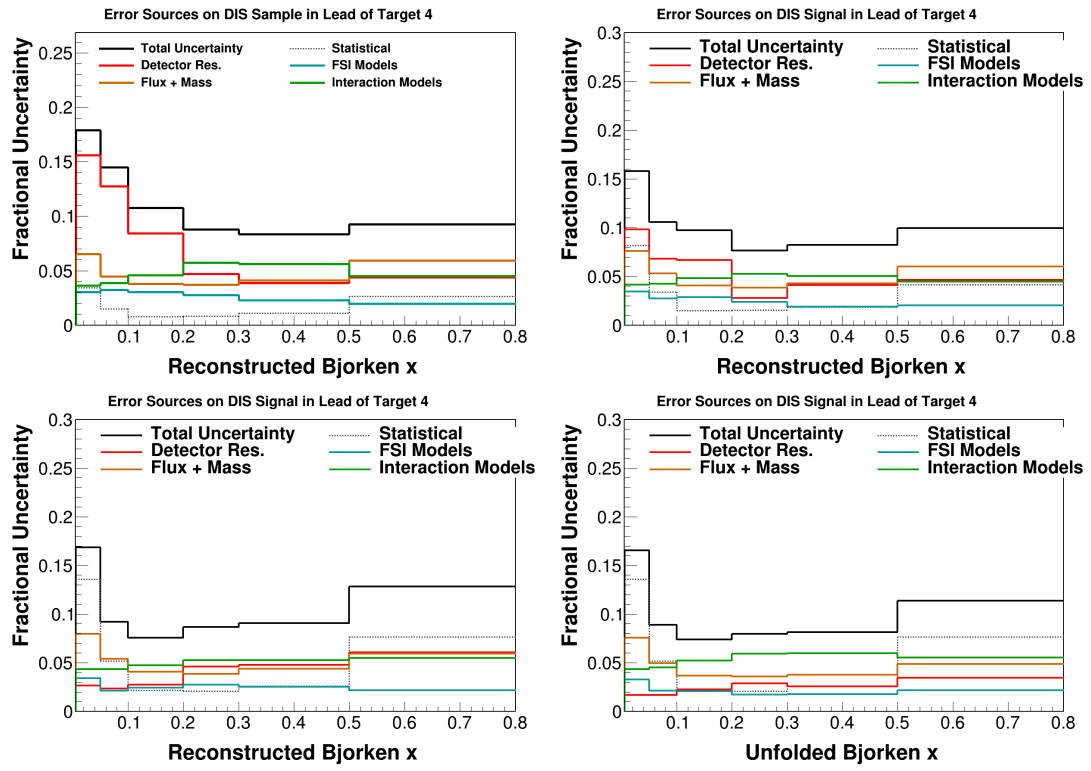
FIG. B.36: Lead of target 5 in E_ν MC error summary after event selection (top right), background subtraction (top left), unfolding (bottom right) and efficiency correction (bottom left).
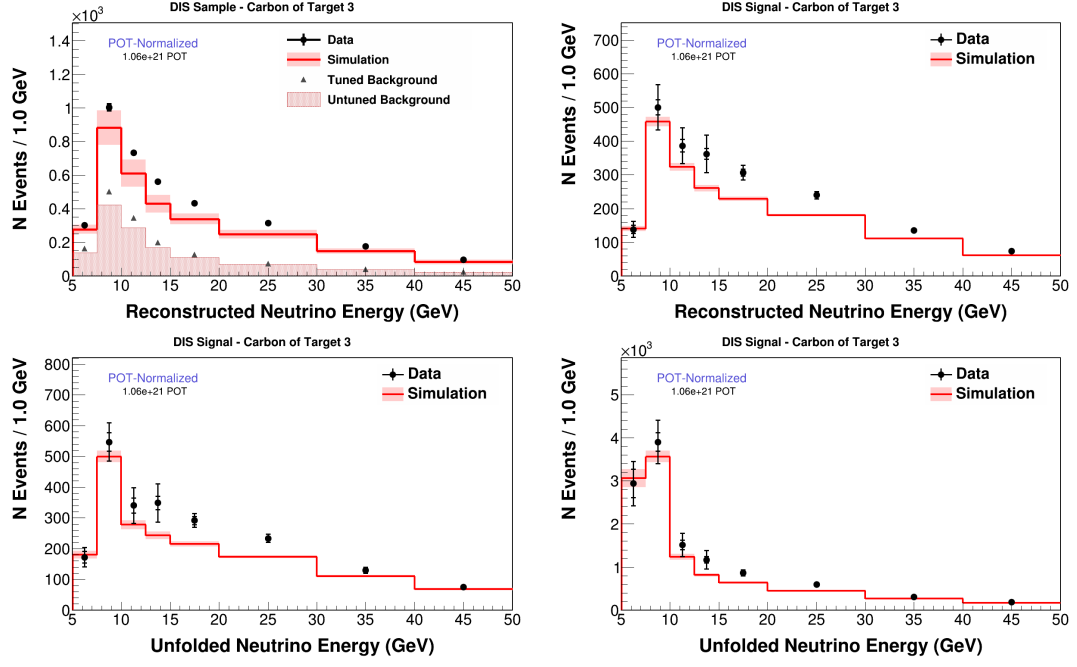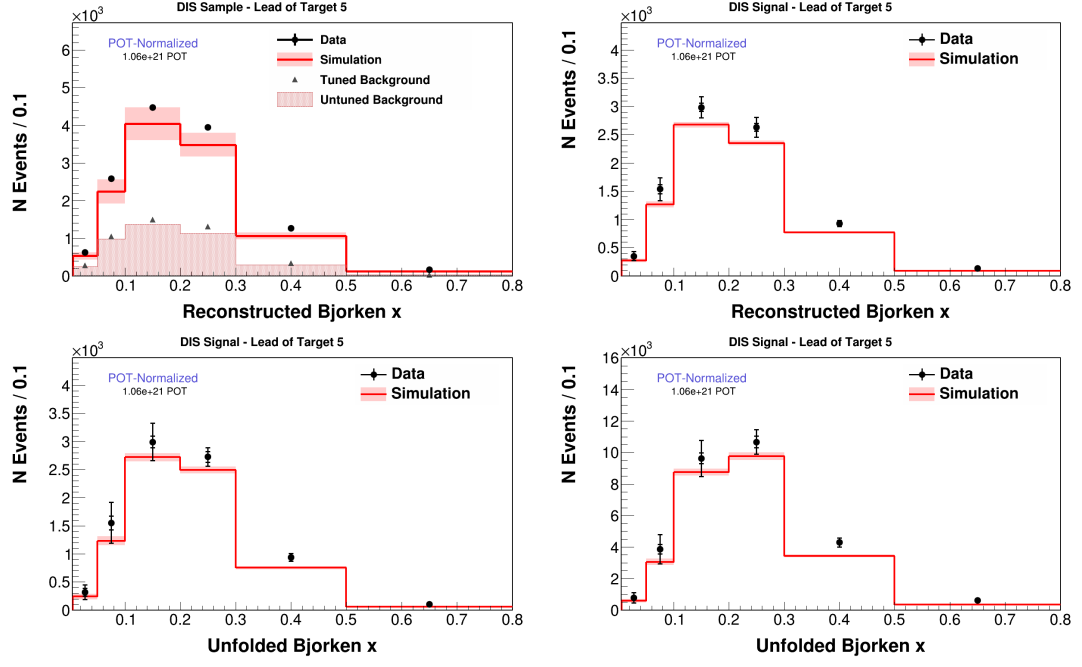
FIG. B.37: Carbon of target 3 in E_ν after event selection (top right), background subtraction (top left), unfolding (bottom right) and efficiency correction (bottom left).
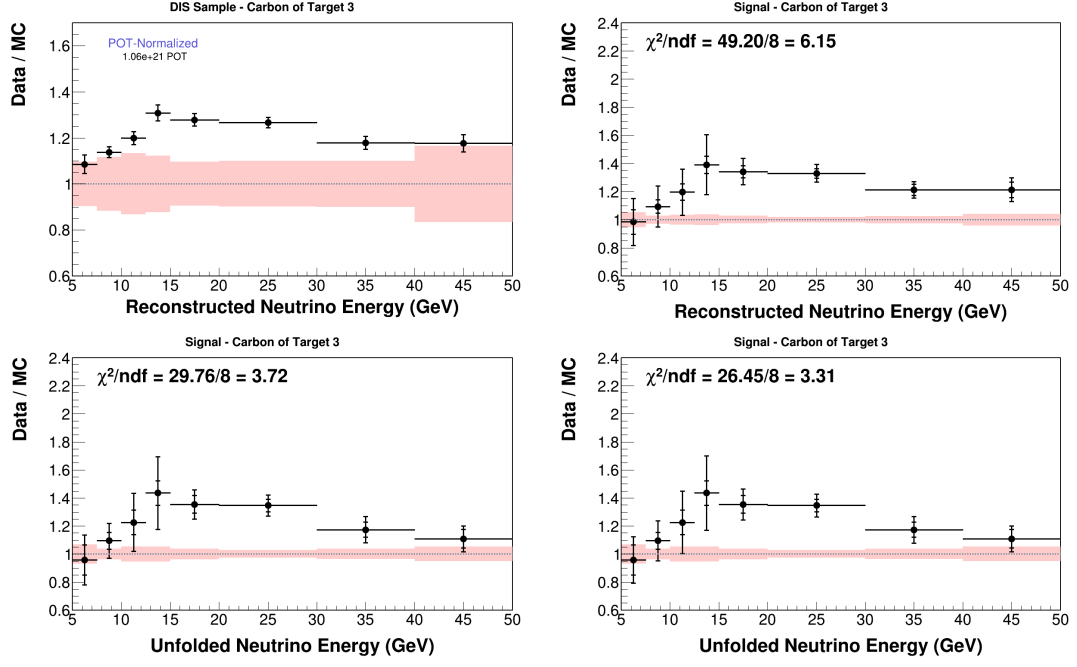
FIG. B.38: Carbon of target 3 in E_ν data MC ratios after event selection (top right), background subtraction (top left), unfolding (bottom right) and efficiency correction (bottom left).

All tracker
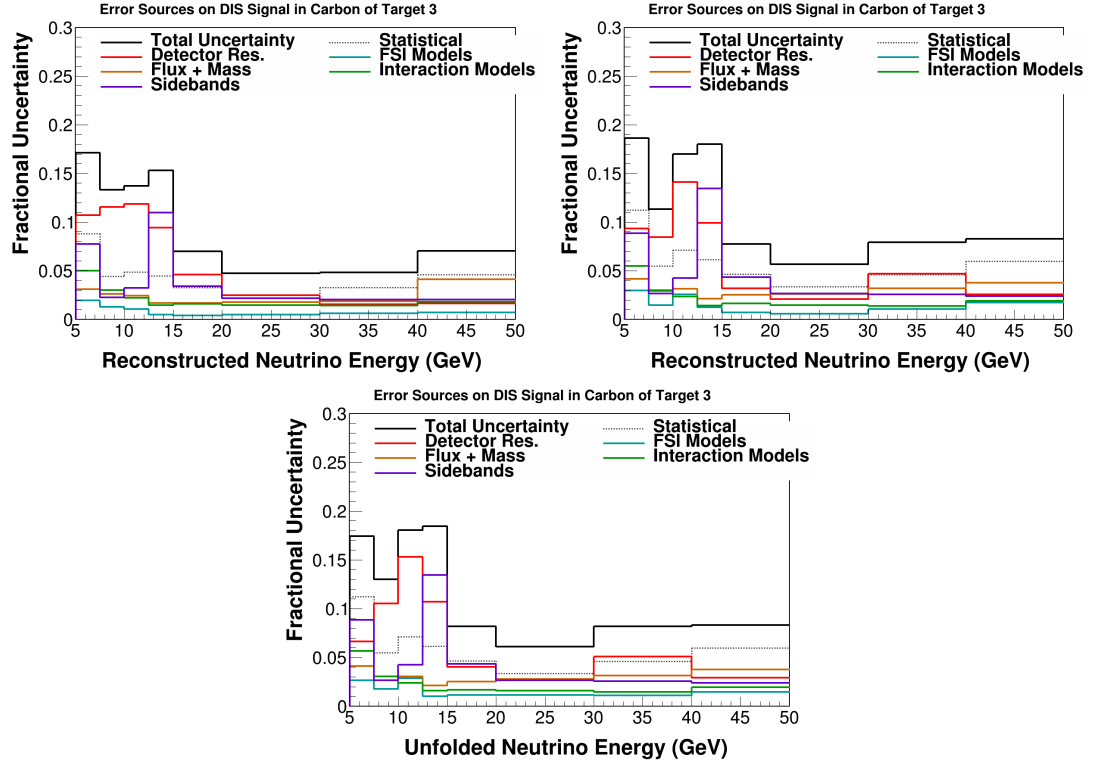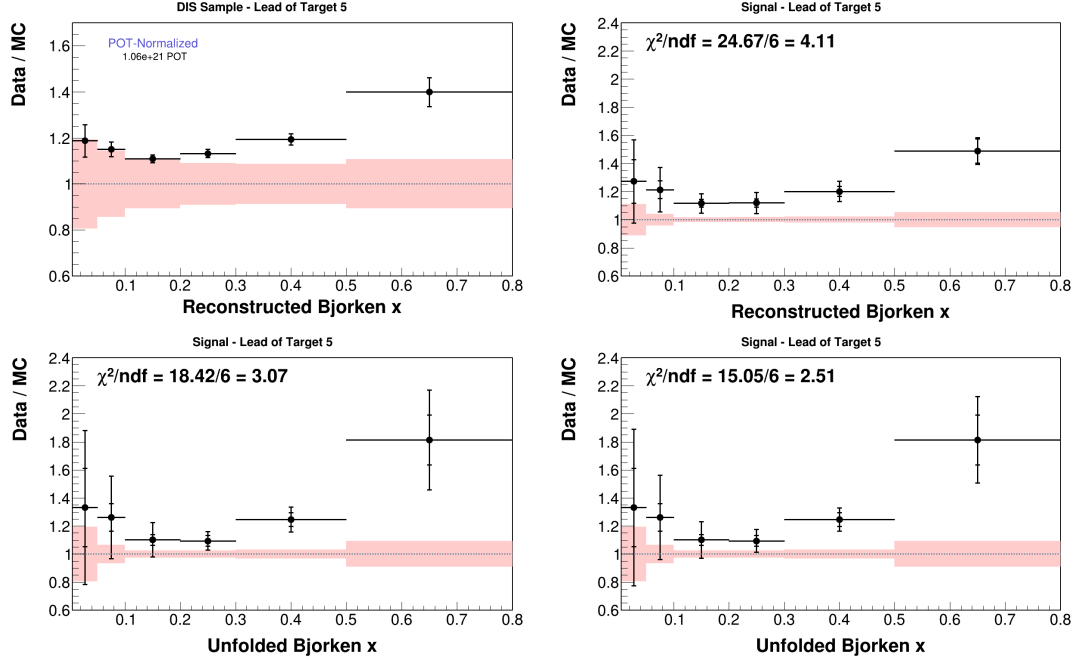
FIG. B.39: Carbon of target 3 in E_ν data error summary after background subtraction (top right), unfolding (top left) and efficiency correction (bottom). At the event selection stage there are only statistical errors on the data distributions, so a systematic error summary is not included here.
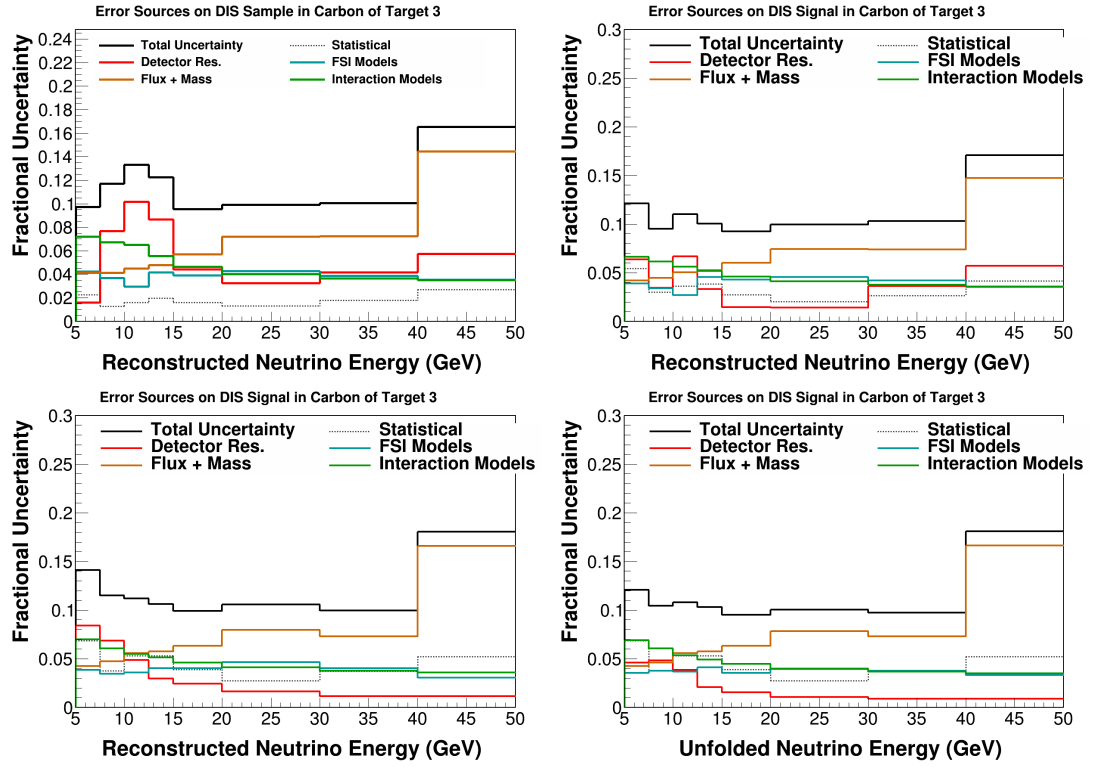
FIG. B.40: Carbon of target 3 in E_ν MC error summary after event selection (top right), background subtraction (top left), unfolding (bottom right) and efficiency correction (bottom left).
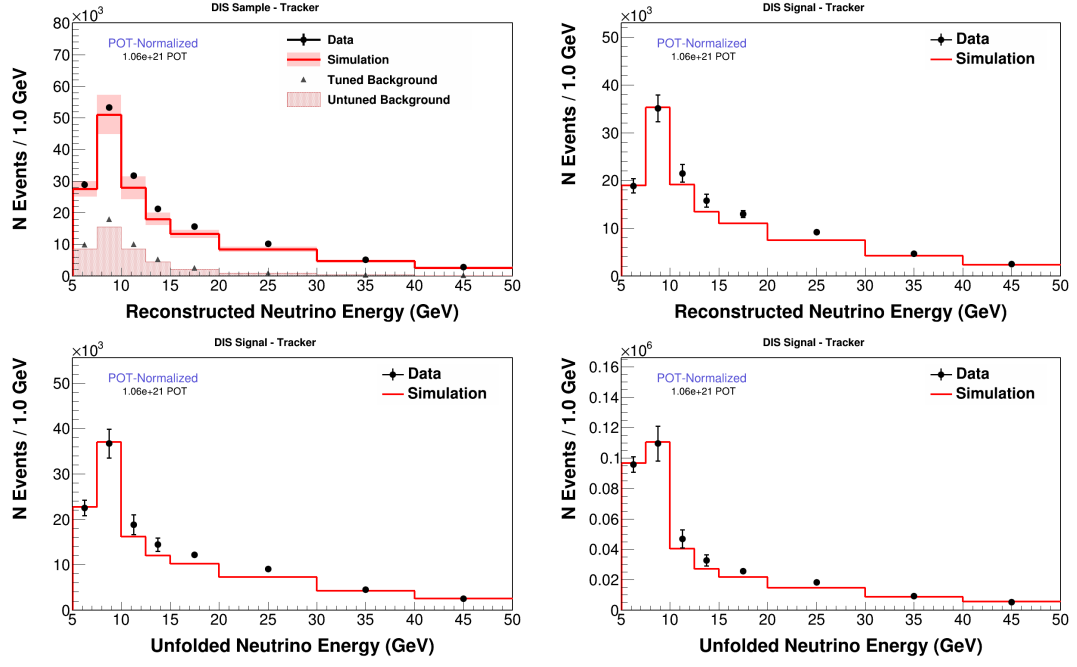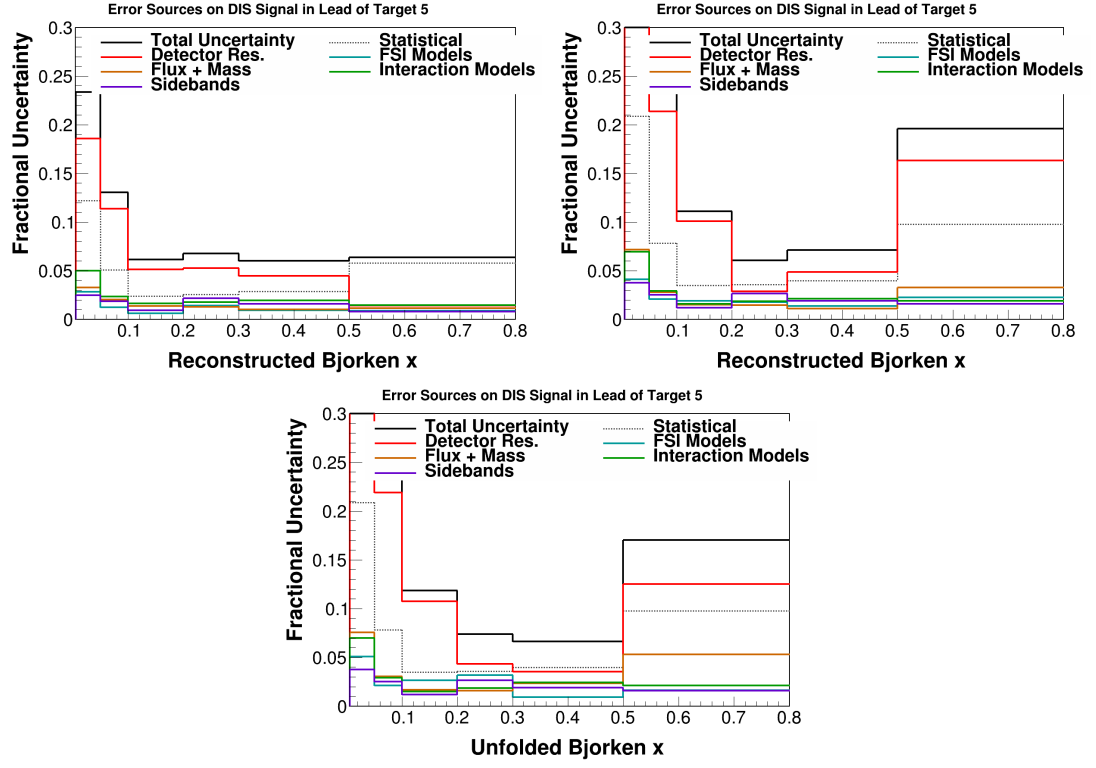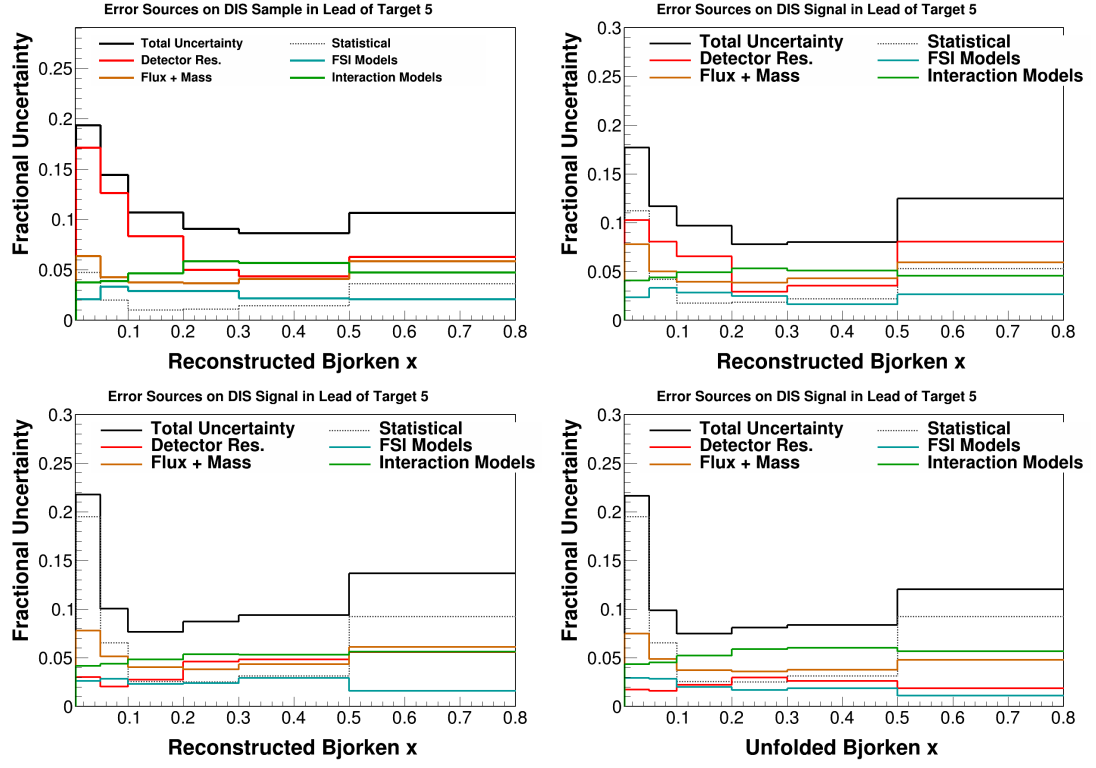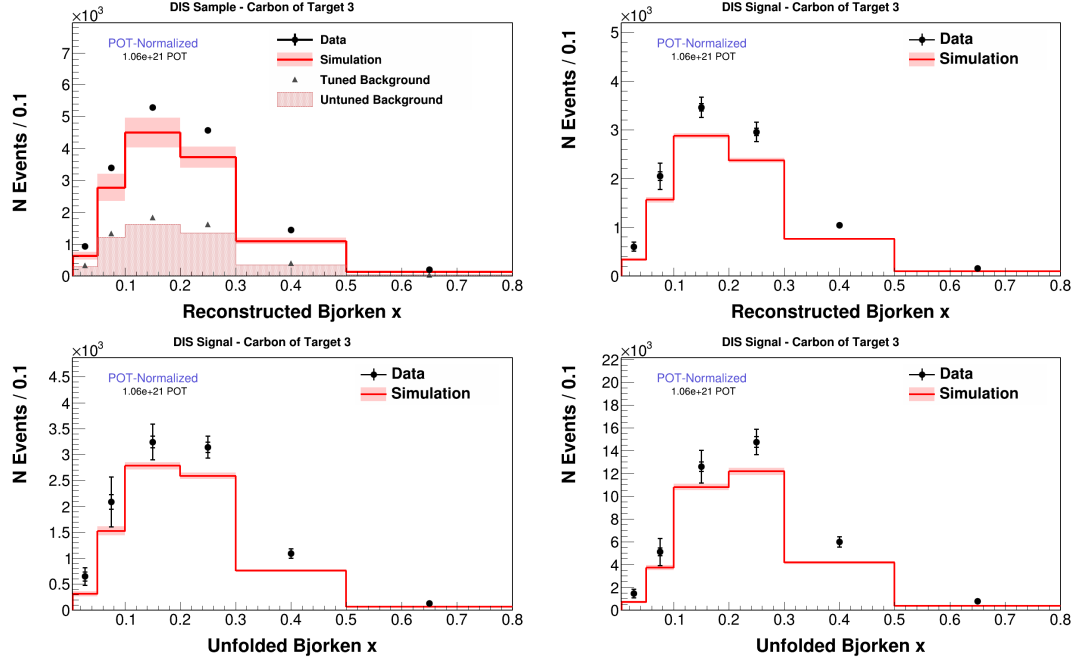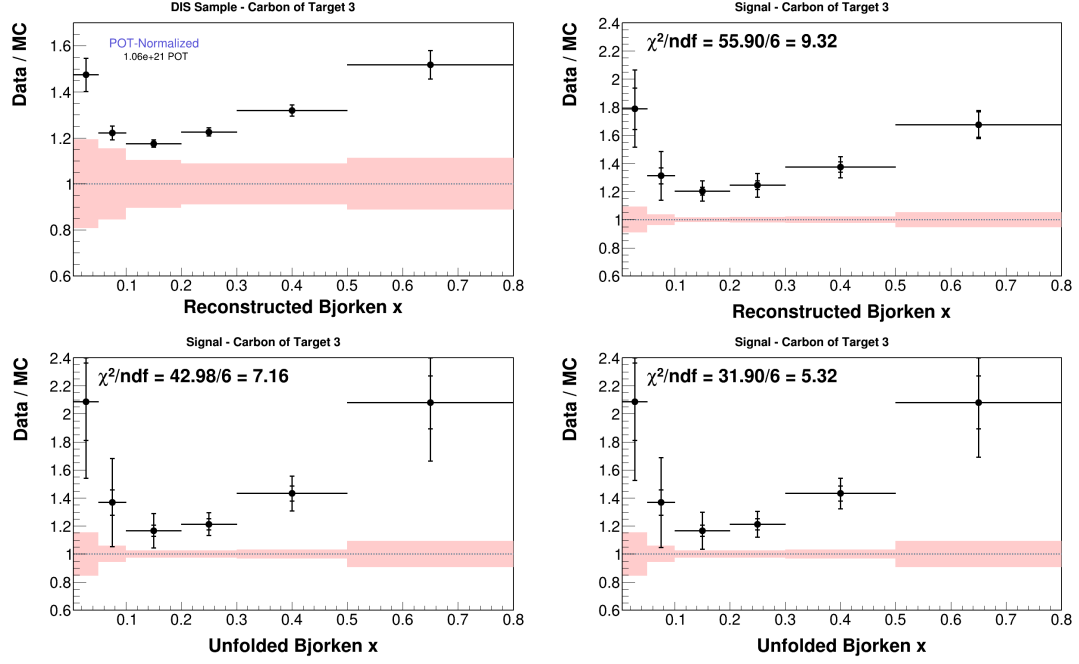
FIG. B.41: All tracker in E_ν after event selection (top right), background subtraction (top left), unfolding (bottom right) and efficiency correction (bottom left).
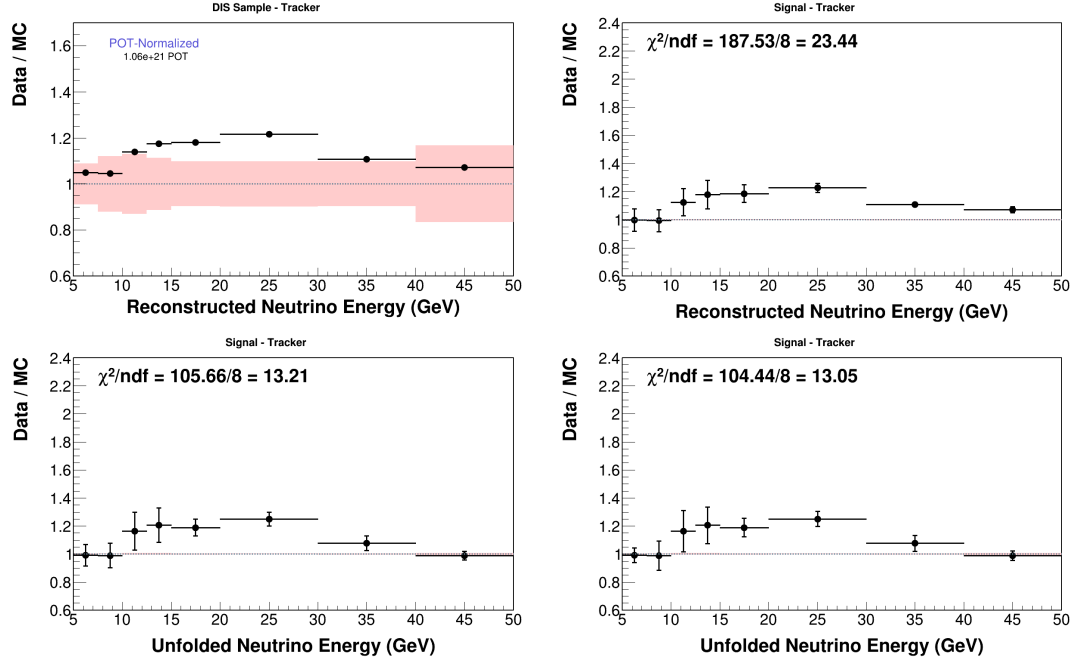
FIG. B.42: All tracker in E_ν data MC ratios after event selection (top right), background subtraction (top left), unfolding (bottom right) and efficiency correction (bottom left).

B.1.2   x

Iron of target 1
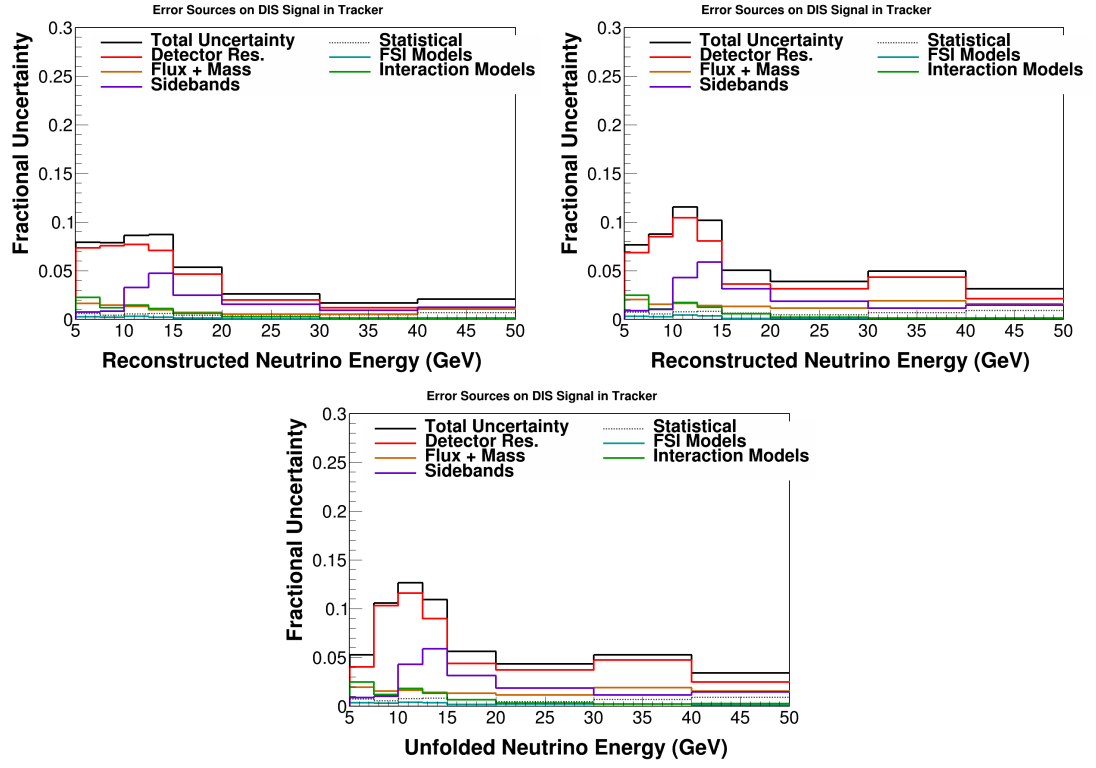
FIG. B.43: All tracker in E_ν data error summary after background subtraction (top right), unfolding (top left) and efficiency correction (bottom). At the event selection stage there are only statistical errors on the data distributions, so a systematic error summary is not included here.

FIG. B.44: All tracker in E_ν MC error summary after event selection (top right), background subtraction (top left), unfolding (bottom right) and efficiency correction (bottom left).
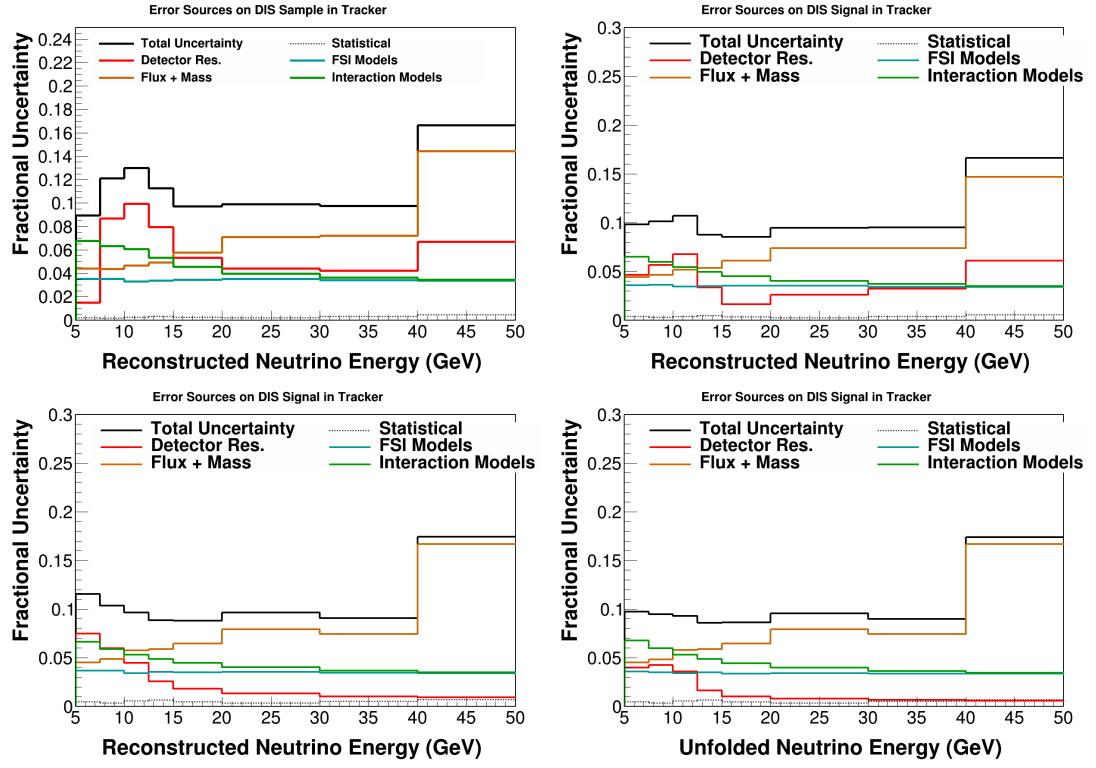
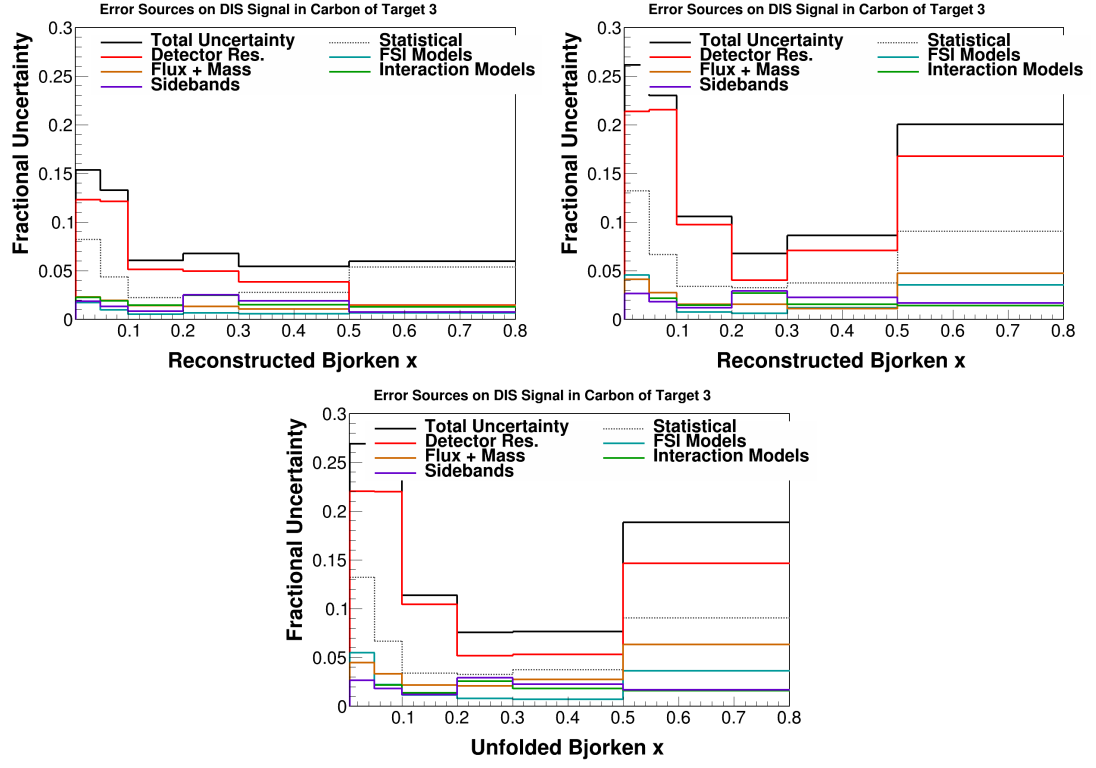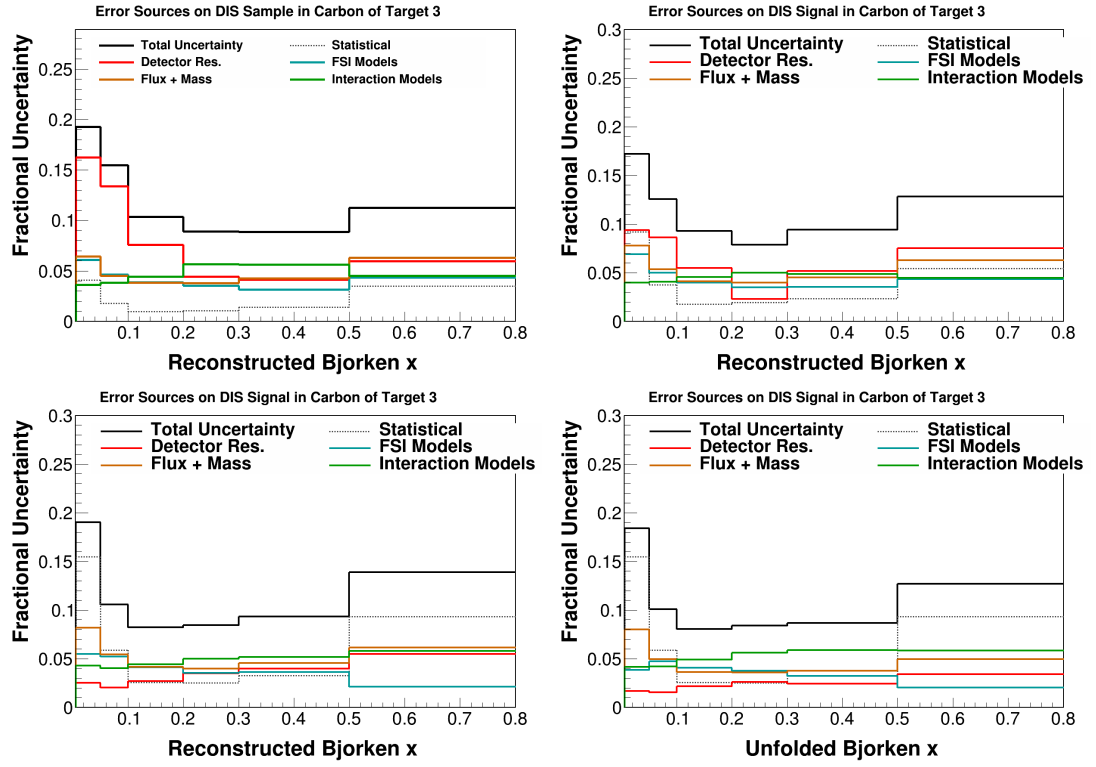FIG. B.45: Iron of target 1 in x_{bj} after event selection (top right), background subtraction (top left), unfolding (bottom right) and efficiency correction (bottom left).
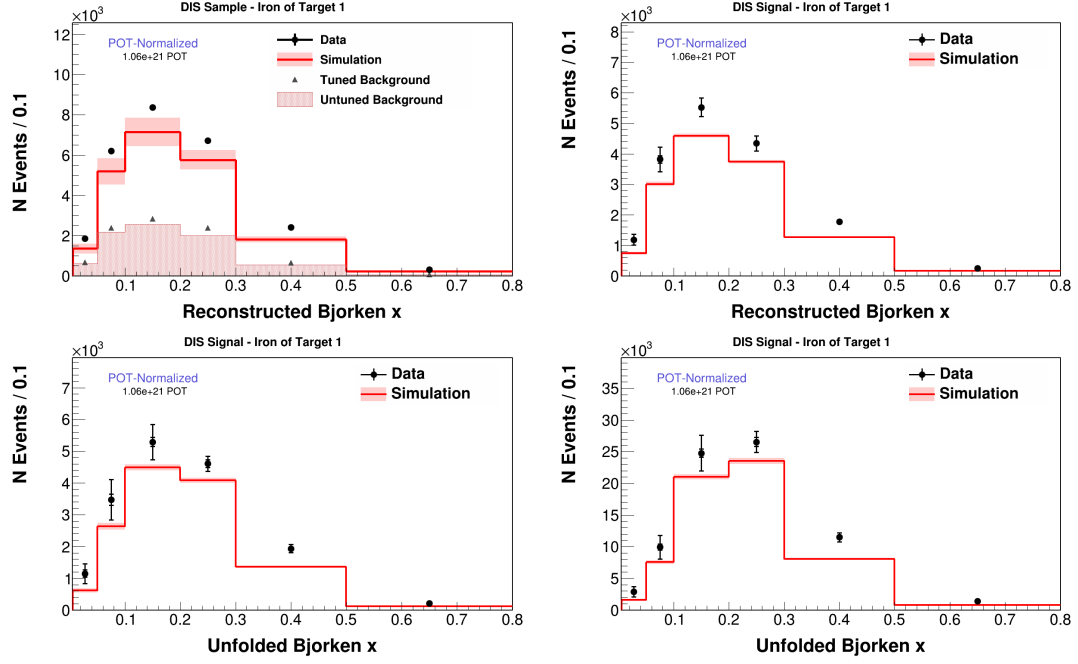
FIG. B.46: Iron of target 1 in x_{bj} data MC ratios after event selection (top right), background subtraction (top left), unfolding (bottom right) and efficiency correction (bottom left).

Iron of target 2

FIG. B.47: Iron of target 1 in x_{bj} data error summary after background subtraction (top right), unfolding (top left) and efficiency correction (bottom). At the event selection stage there are only statistical errors on the data distributions, so a systematic error summary is not included here.
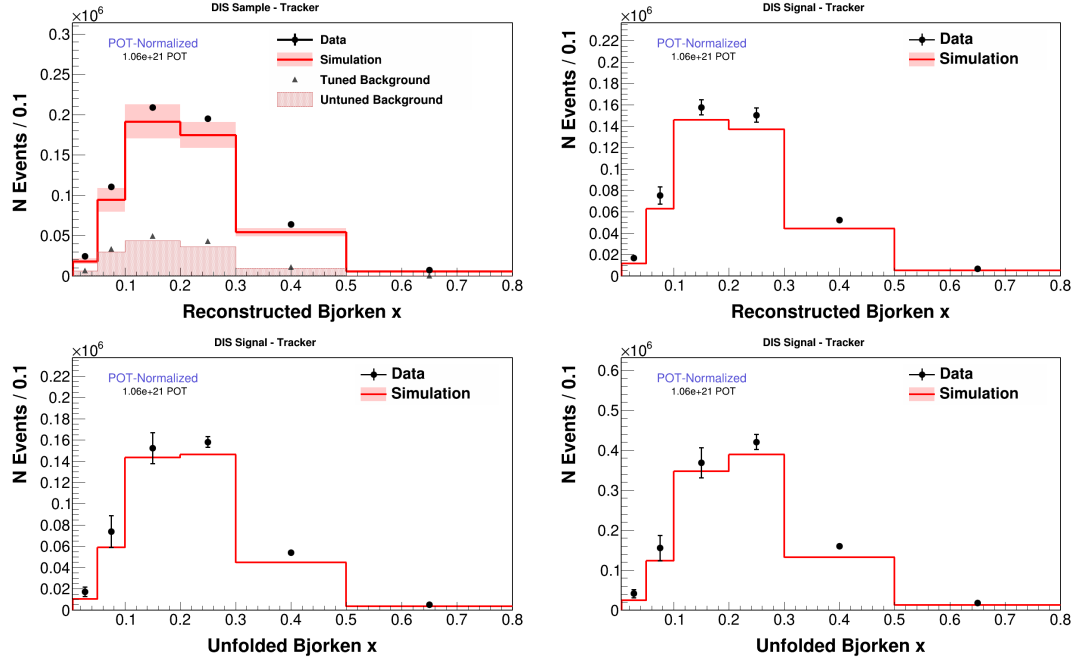
FIG. B.48: Iron of target 1 in x_{bj} MC error summary after event selection (top right), background subtraction (top left), unfolding (bottom right) and efficiency correction (bottom left).
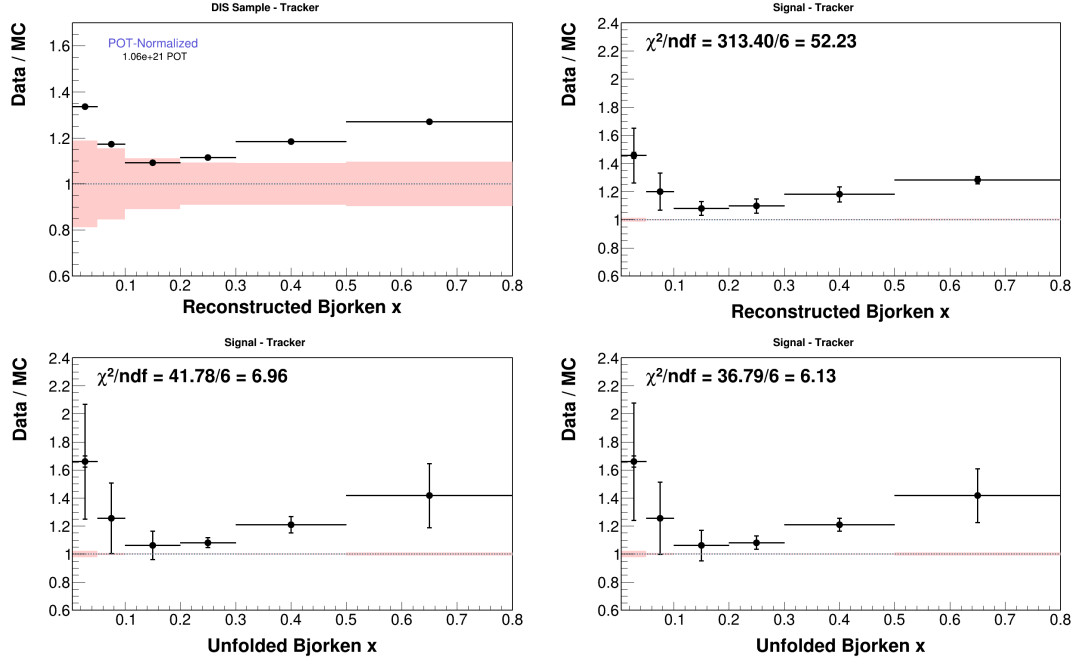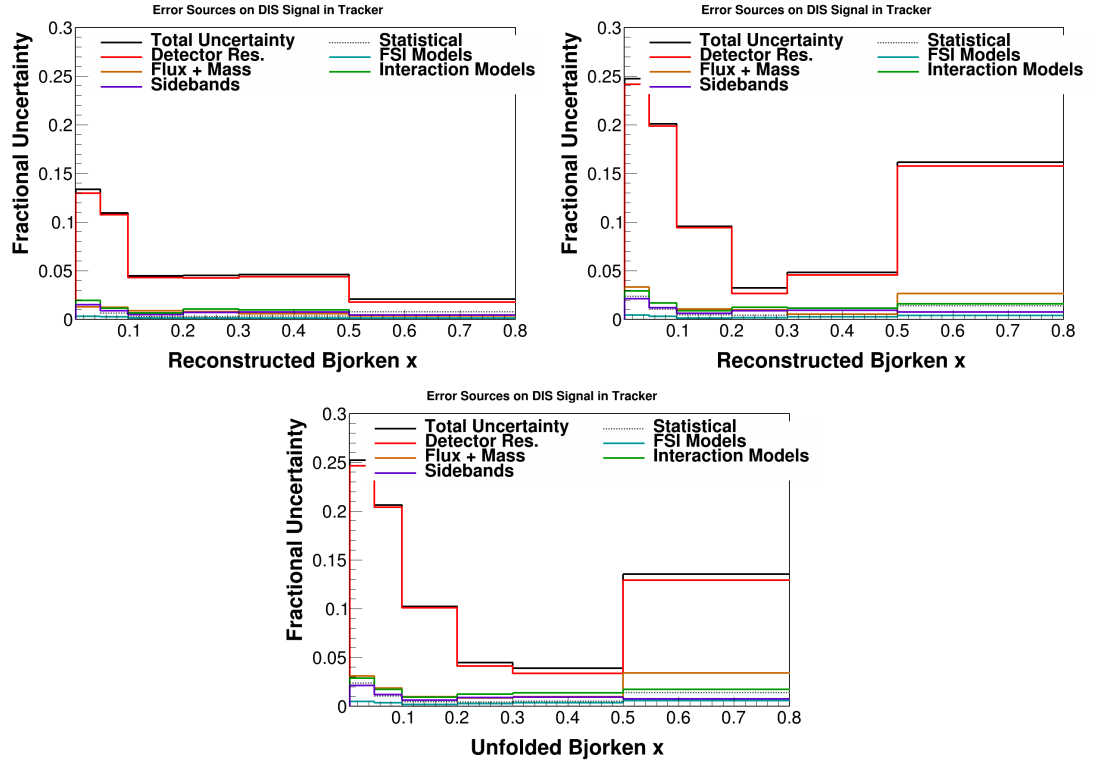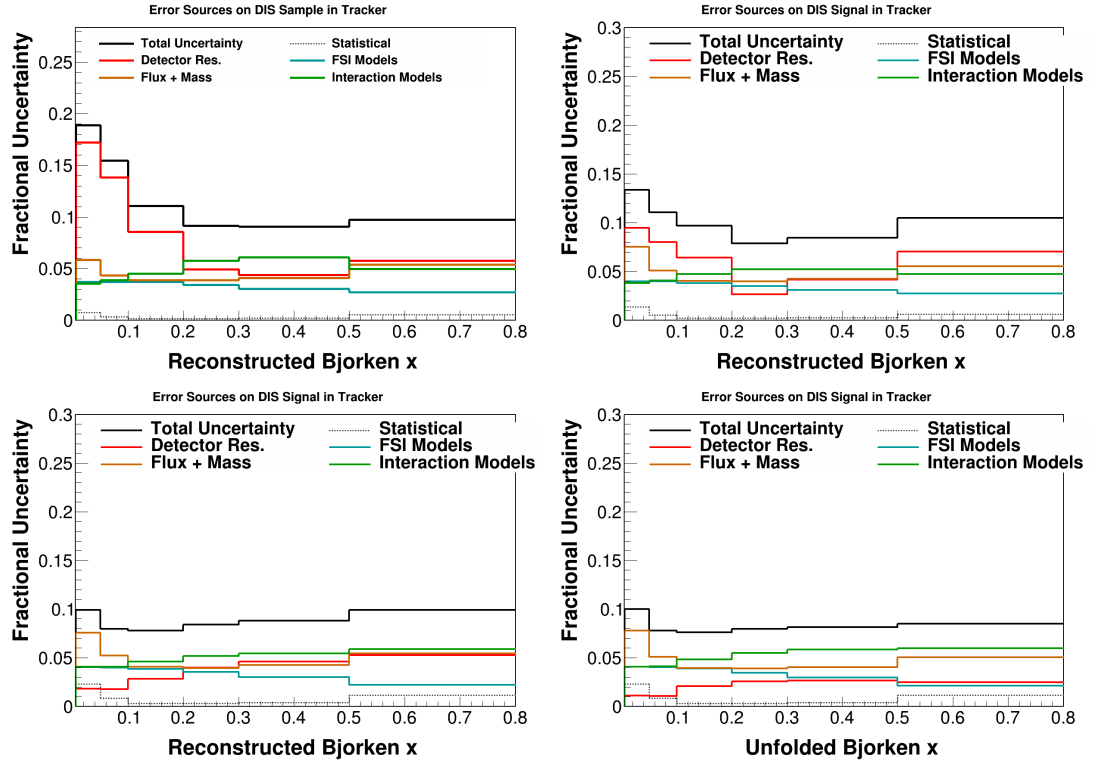
FIG. B.49: Iron of target 2 in x_{bj} after event selection (top right), background subtraction (top left), unfolding (bottom right) and efficiency correction (bottom left).

FIG. B.50: Iron of target 2 in x_{bj} data MC ratios after event selection (top right), background subtraction (top left), unfolding (bottom right) and efficiency correction (bottom left).

Iron of target 3

FIG. B.51: Iron of target 2 in x_{bj} data error summary after background subtraction (top right), unfolding (top left) and efficiency correction (bottom). At the event selection stage there are only statistical errors on the data distributions, so a systematic error summary is not included here.

FIG. B.52: Iron of target 2 in x_{bj} MC error summary after event selection (top right), background subtraction (top left), unfolding (bottom right) and efficiency correction (bottom left).

276

FIG. B.53: Iron of target 3 in x_{bj} after event selection (top right), background subtraction (top left), unfolding (bottom right) and efficiency correction (bottom left).

FIG. B.54: Iron of target 3 in x_{bj} data MC ratios after event selection (top right), background subtraction (top left), unfolding (bottom right) and efficiency correction (bottom left).

Iron of target 5

FIG. B.55: Iron of target 3 in x_{bj} data error summary after background subtraction (top right), unfolding (top left) and efficiency correction (bottom). At the event selection stage there are only statistical errors on the data distributions, so a systematic error summary is not included here.

FIG. B.56: Iron of target 3 in x_{bj} MC error summary after event selection (top right), background subtraction (top left), unfolding (bottom right) and efficiency correction (bottom left).

FIG. B.57: Iron of target 5 in x_{bj} after event selection (top right), background subtraction (top left), unfolding (bottom right) and efficiency correction (bottom left).

FIG. B.58: Iron of target 5 in x_{bj} data MC ratios after event selection (top right), background subtraction (top left), unfolding (bottom right) and efficiency correction (bottom left).

Lead of target 1

FIG. B.59: Iron of target 5 in x_{bj} data error summary after background subtraction (top right), unfolding (top left) and efficiency correction (bottom). At the event selection stage there are only statistical errors on the data distributions, so a systematic error summary is not included here.

FIG. B.60: Iron of target 5 in x_{bj} MC error summary after event selection (top right), background subtraction (top left), unfolding (bottom right) and efficiency correction (bottom left).

FIG. B.61: Lead of target 1 in x_{bj} after event selection (top right), background subtraction (top left), unfolding (bottom right) and efficiency correction (bottom left).

FIG. B.62: Lead of target 1 in x_{bj} data MC ratios after event selection (top right), background subtraction (top left), unfolding (bottom right) and efficiency correction (bottom left).

Lead of target 2

FIG. B.63: Lead of target 1 in x_{bj} data error summary after background subtraction (top right), unfolding (top left) and efficiency correction (bottom). At the event selection stage there are only statistical errors on the data distributions, so a systematic error summary is not included here.

FIG. B.64: Lead of target 1 in x_{bj} MC error summary after event selection (top right), background subtraction (top left), unfolding (bottom right) and efficiency correction (bottom left).

FIG. B.65: Lead of target 2 in x_{bj} after event selection (top right), background subtraction (top left), unfolding (bottom right) and efficiency correction (bottom left).

FIG. B.66: Lead of target 2 in x_{bj} data MC ratios after event selection (top right), background subtraction (top left), unfolding (bottom right) and efficiency correction (bottom left).

Lead of target 3

FIG. B.67: Lead of target 2 in x_{bj} data error summary after background subtraction (top right), unfolding (top left) and efficiency correction (bottom). At the event selection stage there are only statistical errors on the data distributions, so a systematic error summary is not included here.

FIG. B.68: Lead of target 2 in x_{bj} MC error summary after event selection (top right), background subtraction (top left), unfolding (bottom right) and efficiency correction (bottom left).

FIG. B.69: Lead of target 3 in x_{bj} after event selection (top right), background subtraction (top left), unfolding (bottom right) and efficiency correction (bottom left).

FIG. B.70: Lead of target 3 in x_{bj} data MC ratios after event selection (top right), background subtraction (top left), unfolding (bottom right) and efficiency correction (bottom left).

Lead of target 4

FIG. B.71: Lead of target 3 in x_{bj} data error summary after background subtraction (top right), unfolding (top left) and efficiency correction (bottom). At the event selection stage there are only statistical errors on the data distributions, so a systematic error summary is not included here.

FIG. B.72: Lead of target 3 in x_{bj} MC error summary after event selection (top right), background subtraction (top left), unfolding (bottom right) and efficiency correction (bottom left).

FIG. B.73: Lead of target 4 in x_{bj} after event selection (top right), background subtraction (top left), unfolding (bottom right) and efficiency correction (bottom left).

FIG. B.74: Lead of target 4 in x_{bj} data MC ratios after event selection (top right), background subtraction (top left), unfolding (bottom right) and efficiency correction (bottom left).

Lead of target 5

FIG. B.75: Lead of target 4 in x_{bj} data error summary after background subtraction (top right), unfolding (top left) and efficiency correction (bottom). At the event selection stage there are only statistical errors on the data distributions, so a systematic error summary is not included here.

FIG. B.76: Lead of target 4 in x_{bj} MC error summary after event selection (top right), background subtraction (top left), unfolding (bottom right) and efficiency correction (bottom left).

300

FIG. B.77: Lead of target 5 in x_{bj} after event selection (top right), background subtraction (top left), unfolding (bottom right) and efficiency correction (bottom left).

FIG. B.78: Lead of target 5 in x_{bj} data MC ratios after event selection (top right), background subtraction (top left), unfolding (bottom right) and efficiency correction (bottom left).

Carbon of target 3

FIG. B.79: Lead of target 5 in x_{bj} data error summary after background subtraction (top right), unfolding (top left) and efficiency correction (bottom). At the event selection stage there are only statistical errors on the data distributions, so a systematic error summary is not included here.

FIG. B.80: Lead of target 5 in x_{bj} MC error summary after event selection (top right), background subtraction (top left), unfolding (bottom right) and efficiency correction (bottom left).

FIG. B.81: Carbon of target 3 in x_{bj} after event selection (top right), background subtraction (top left), unfolding (bottom right) and efficiency correction (bottom left).

FIG. B.82: Carbon of target 3 in x_{bj} data MC ratios after event selection (top right), background subtraction (top left), unfolding (bottom right) and efficiency correction (bottom left).

All tracker

FIG. B.83: Carbon of target 3 in x_{bj} data error summary after background subtraction (top right), unfolding (top left) and efficiency correction (bottom). At the event selection stage there are only statistical errors on the data distributions, so a systematic error summary is not included here.

FIG. B.84: Carbon of target 3 in x_{bj} MC error summary after event selection (top right), background subtraction (top left), unfolding (bottom right) and efficiency correction (bottom left).

FIG. B.85: All tracker in x_{bj} after event selection (top right), background subtraction (top left), unfolding (bottom right) and efficiency correction (bottom left).

FIG. B.86: All tracker in x_{bj} data MC ratios after event selection (top right), background subtraction (top left), unfolding (bottom right) and efficiency correction (bottom left).

B.2 Plastic sidebands

FIG. B.87: All tracker in x_{bj} data error summary after background subtraction (top right), unfolding (top left) and efficiency correction (bottom). At the event selection stage there are only statistical errors on the data distributions, so a systematic error summary is not included here.

FIG. B.88: All tracker in x_{bj} MC error summary after event selection (top right), background subtraction (top left), unfolding (bottom right) and efficiency correction (bottom left).

B.2.1   Plane Number

All iron
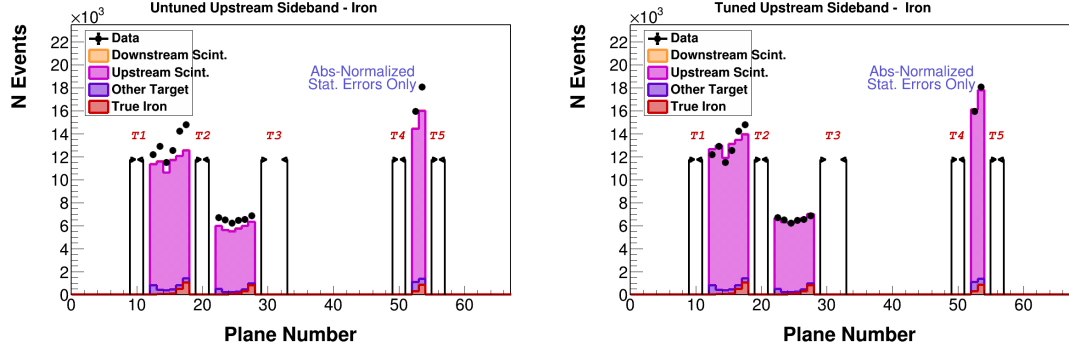
FIG. B.89: All iron upstream scintillator sideband stack plot before (left) and after (right) tuning for plane number.
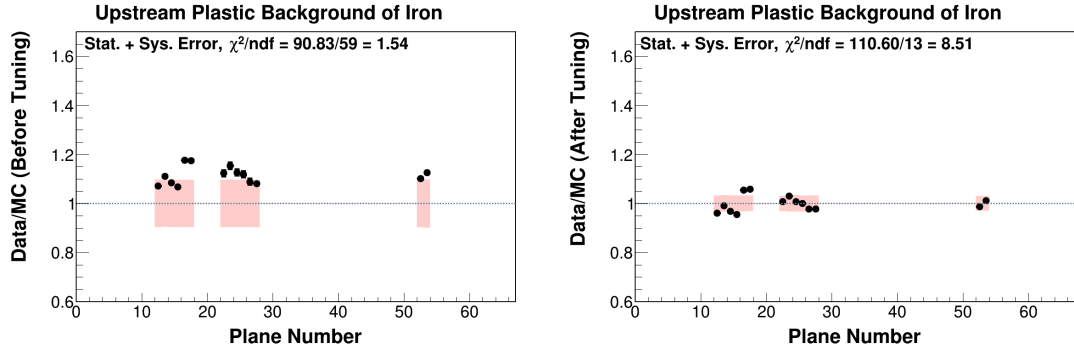
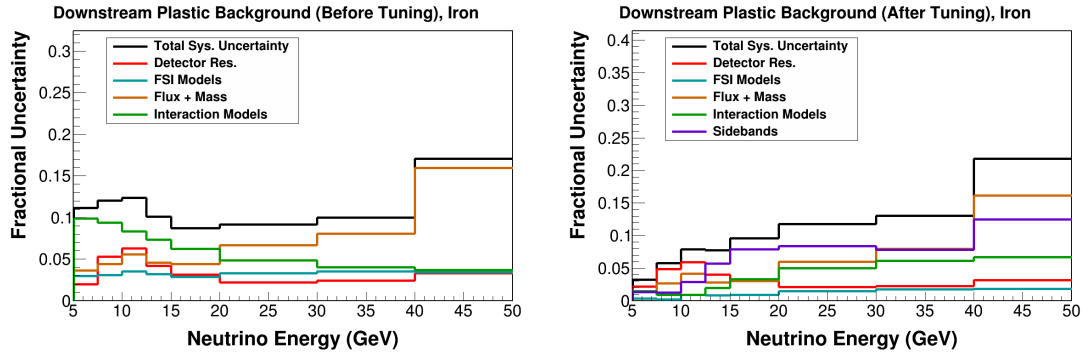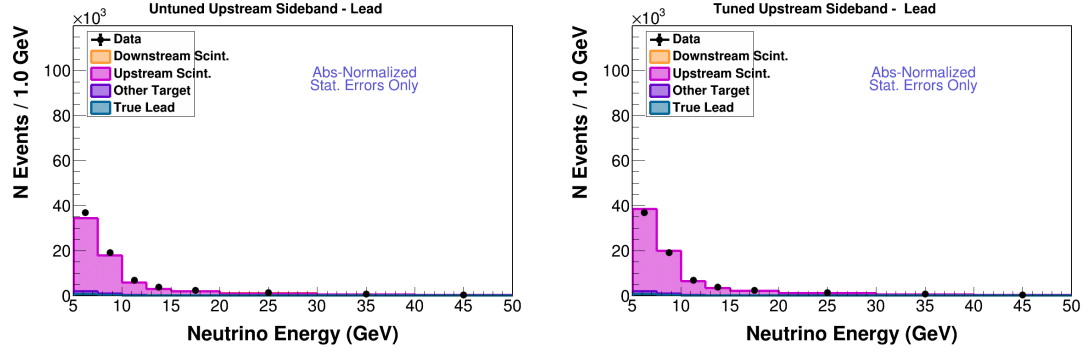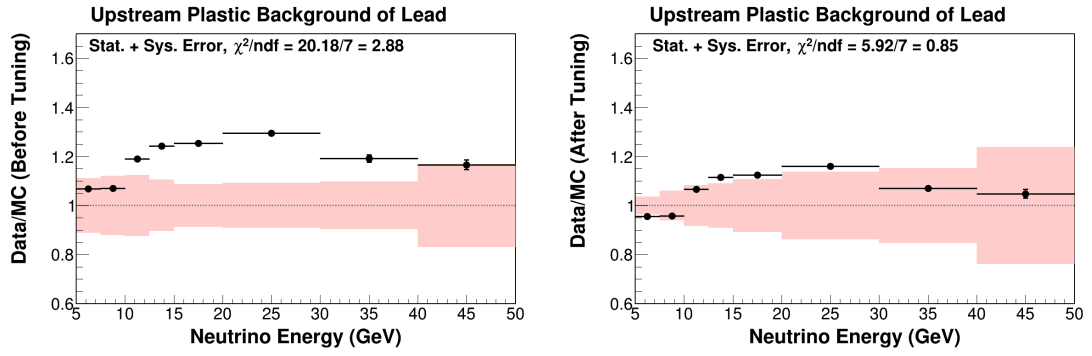FIG. B.90: All iron upstream scintillator sideband data MC ratio before (left) and after (right) tuning for plane number.
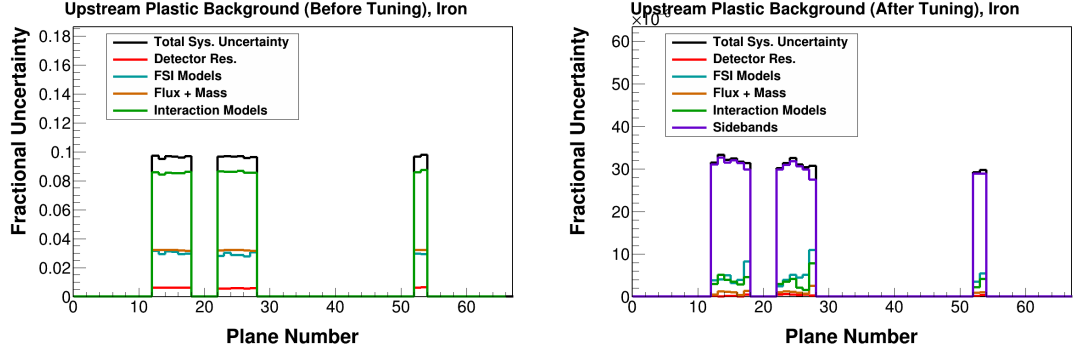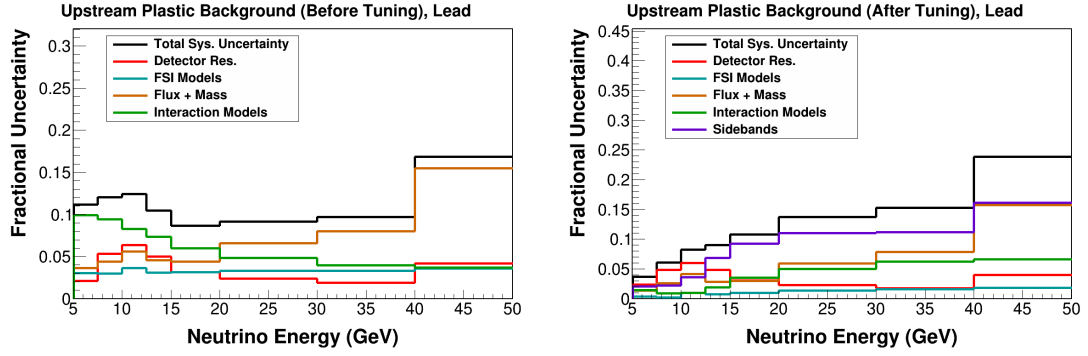
FIG. B.91: All iron upstream scintillator sideband data error summary before (left) and after (right) tuning for plane number.
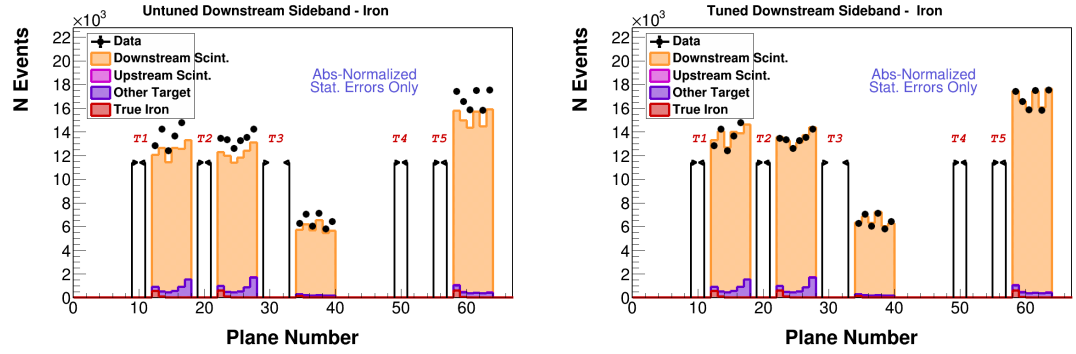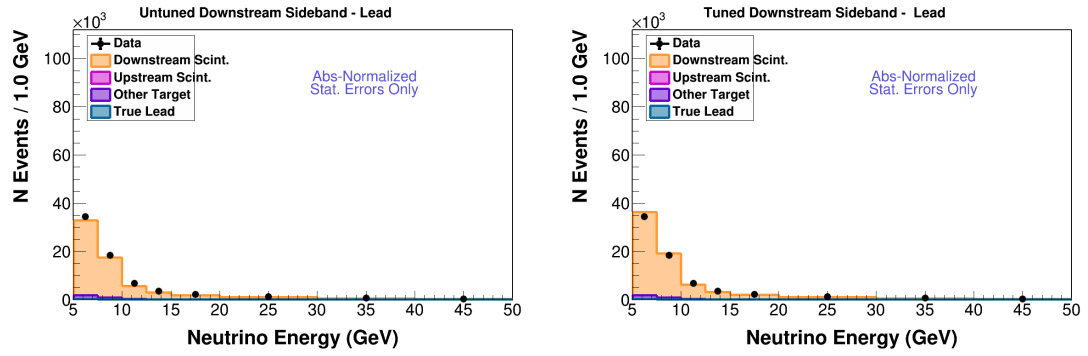

FIG. B.92: All iron downstream scintillator sideband stack plot before (left) and after (right) tuning for plane number.
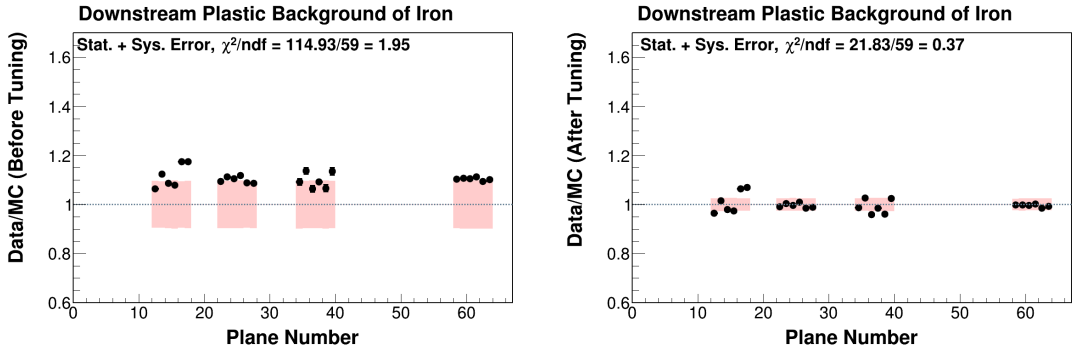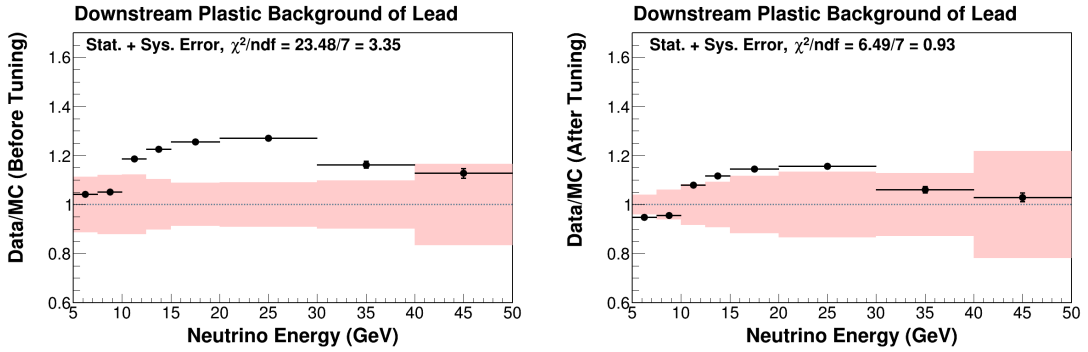

FIG. B.93: All iron downstream scintillator sideband data MC ratio before (left) and after (right) tuning for plane number.
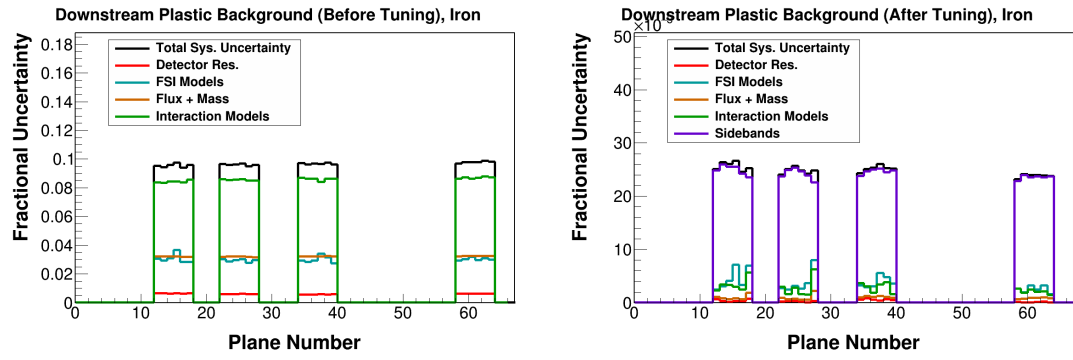
FIG. B.94: All iron downstream scintillator sideband data error summary before (left) and after (right) tuning for plane number.

All lead
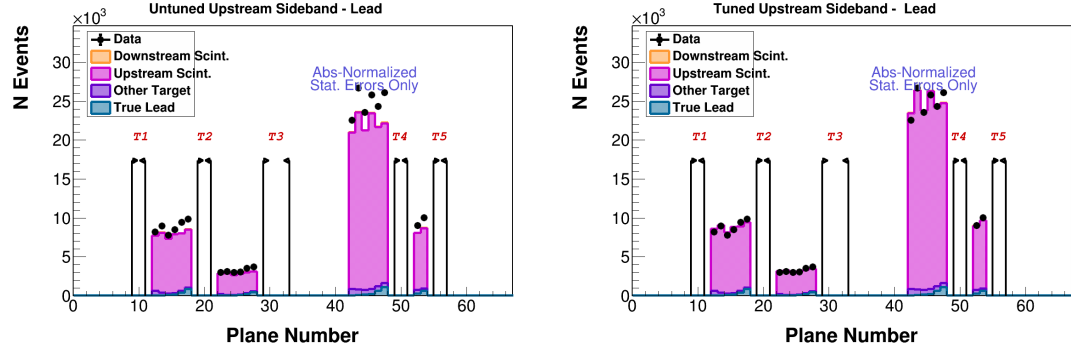
FIG. B.95: All lead upstream scintillator sideband stack plot before (left) and after (right) tuning for plane number.
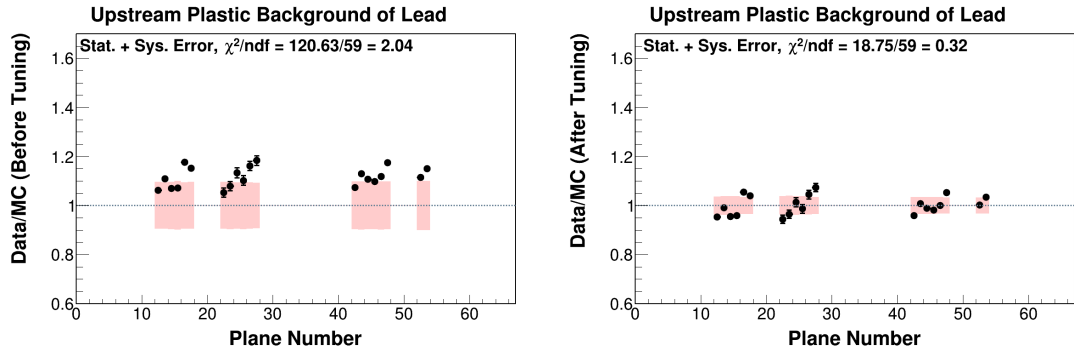
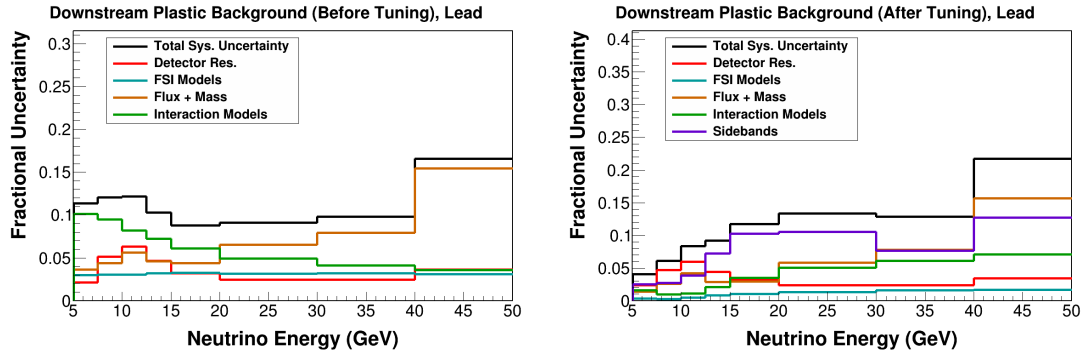FIG. B.96: All lead upstream scintillator sideband data MC ratio before (left) and after (right) tuning for plane number.
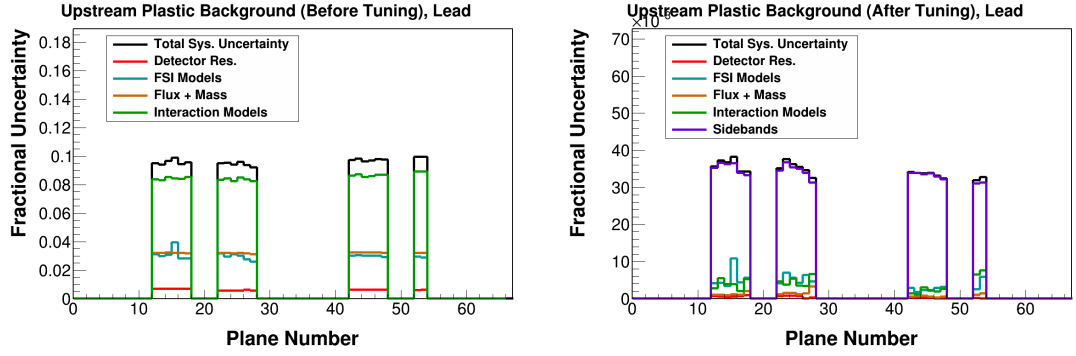
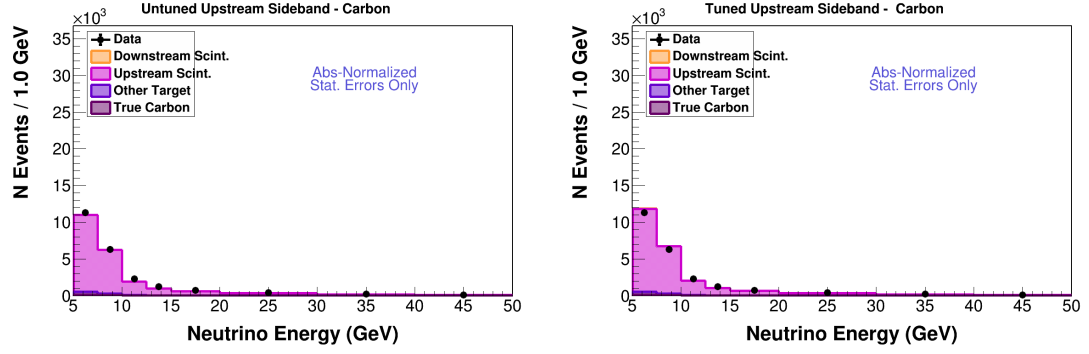FIG. B.97: All lead upstream scintillator sideband data error summary before (left) and after (right) tuning for plane number.
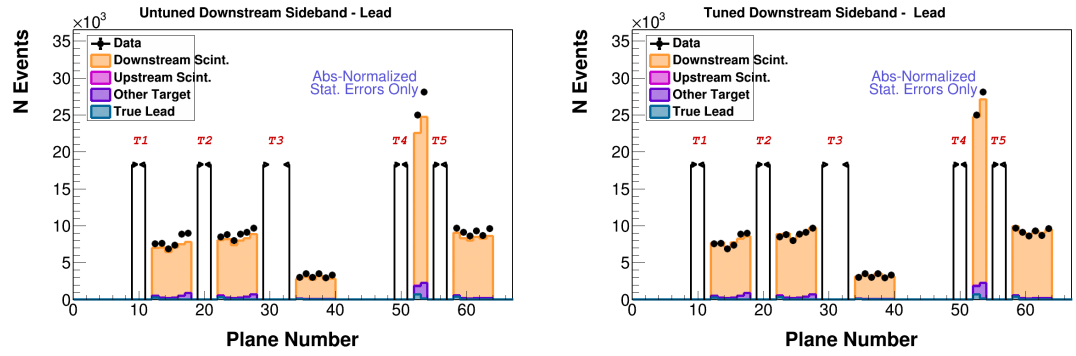
FIG. B.98: All lead downstream scintillator sideband stack plot before (left) and after (right) tuning for plane number.
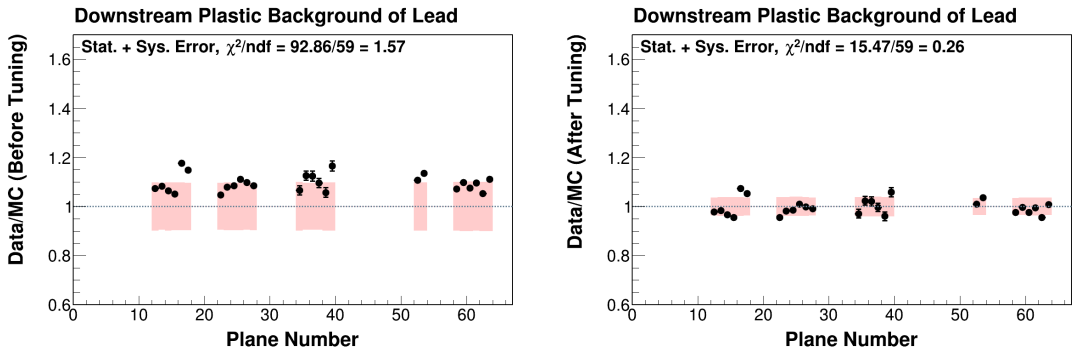
FIG. B.99: All lead downstream scintillator sideband data MC ratio before (left) and after (right) tuning for plane number.
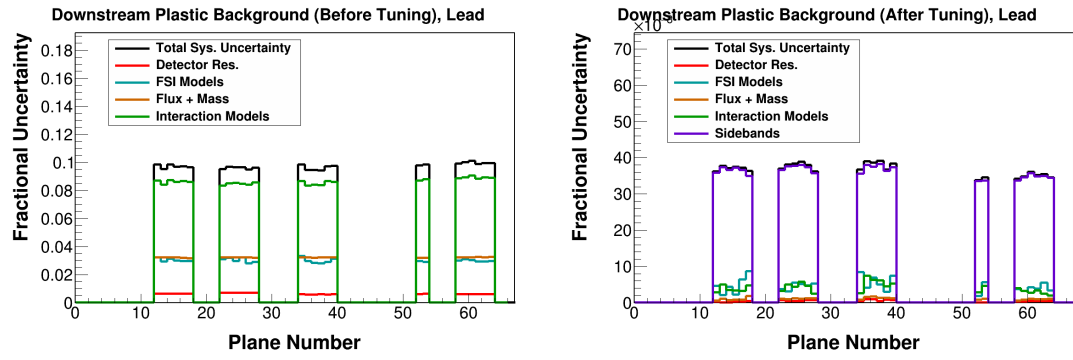
FIG. B.100: All lead downstream scintillator sideband data error summary before (left) and after (right) tuning for plane number.

318
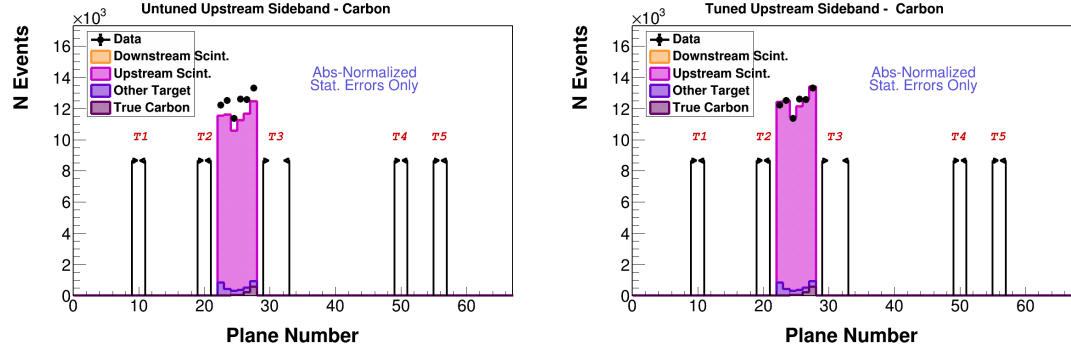
Carbon

FIG. B.101: Carbon upstream scintillator sideband stack plot before (left) and after (right) tuning for plane number.
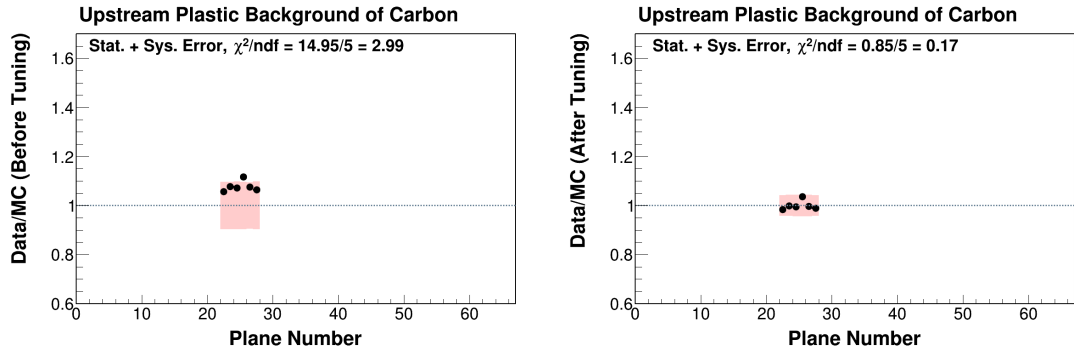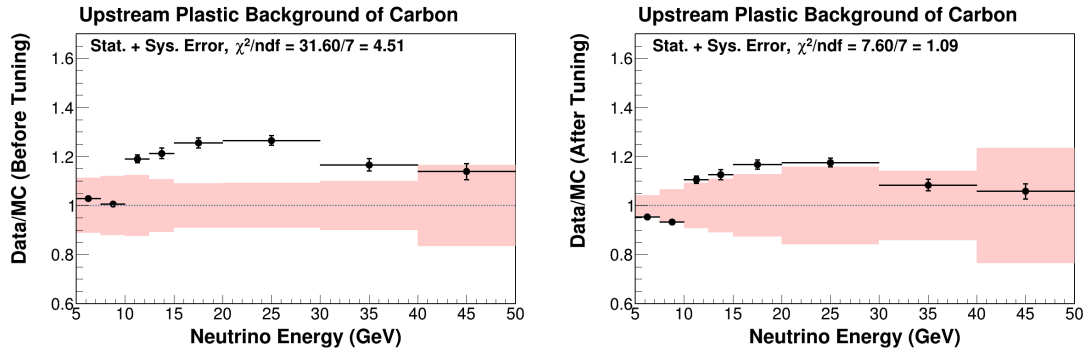

FIG. B.102: Carbon upstream scintillator sideband data MC ratio before (left) and after (right) tuning for plane number.
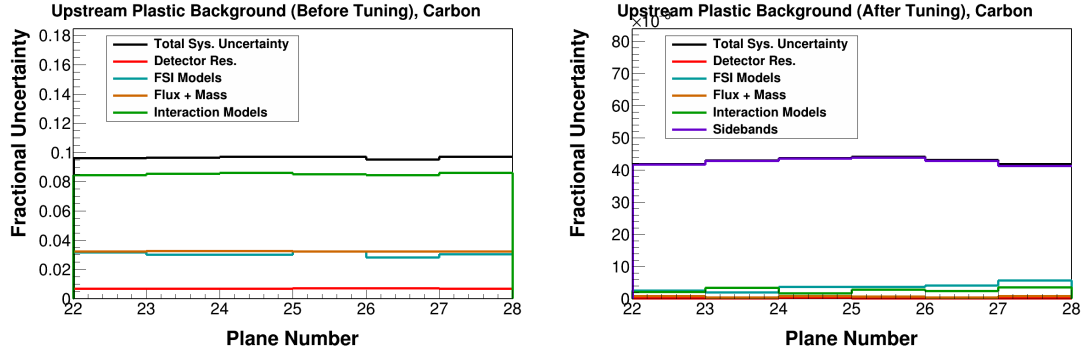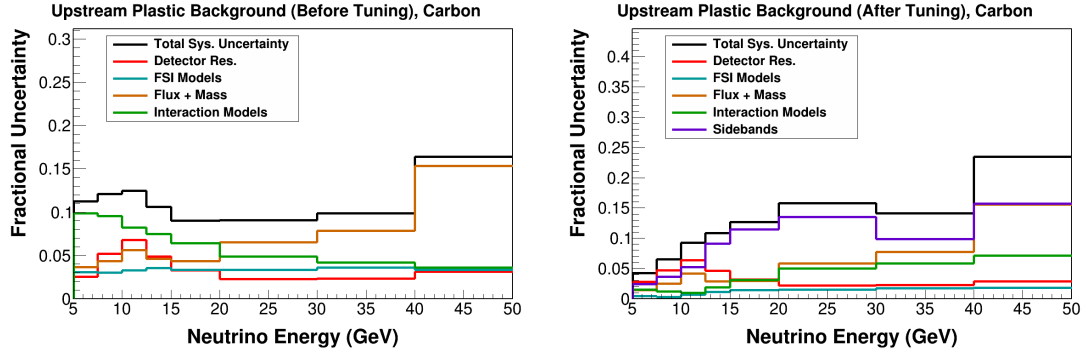
FIG. B.103: Carbon upstream scintillator sideband data error summary before (left) and after (right) tuning for plane number.
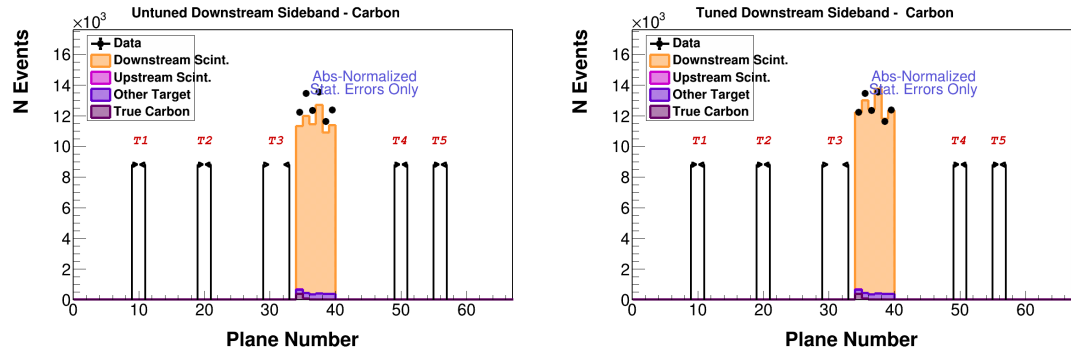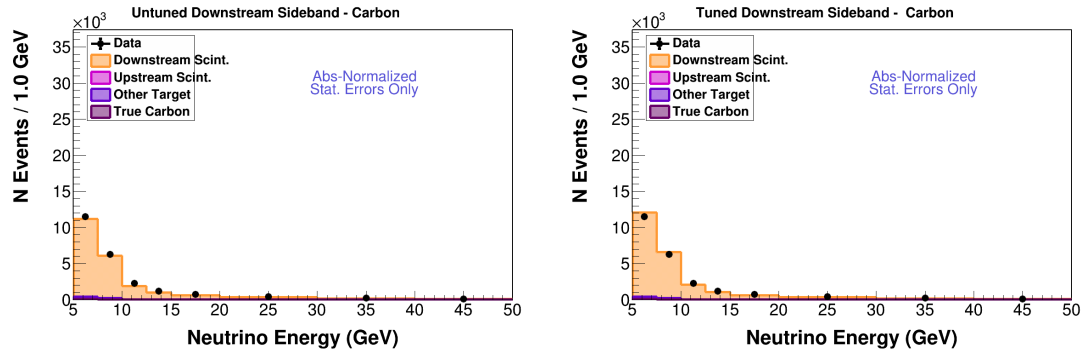

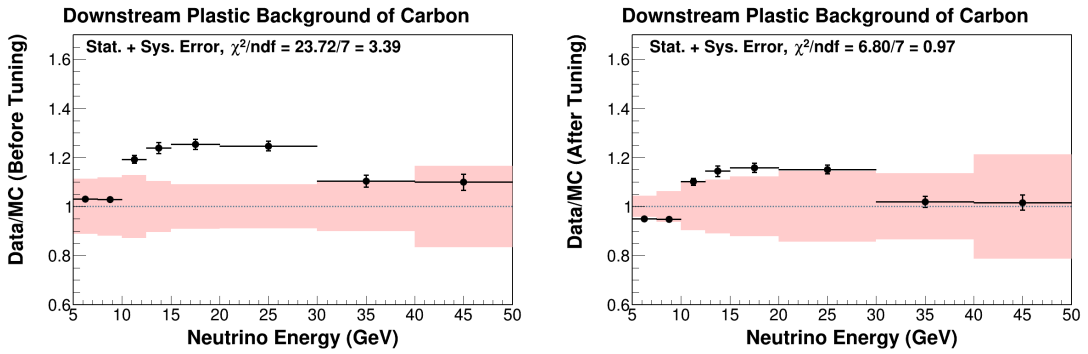FIG. B.104: Carbon downstream scintillator sideband stack plot before (left) and after (right) tuning for plane number.
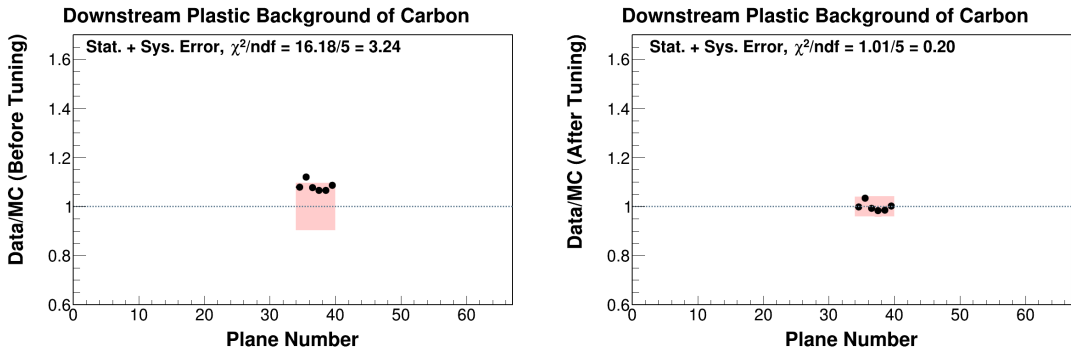
FIG. B.105: Carbon downstream scintillator sideband data MC ratio before (left) and after (right) tuning for plane number.
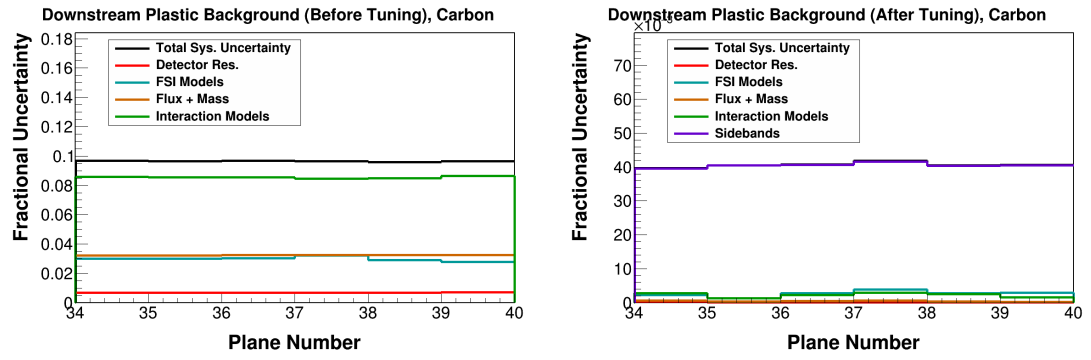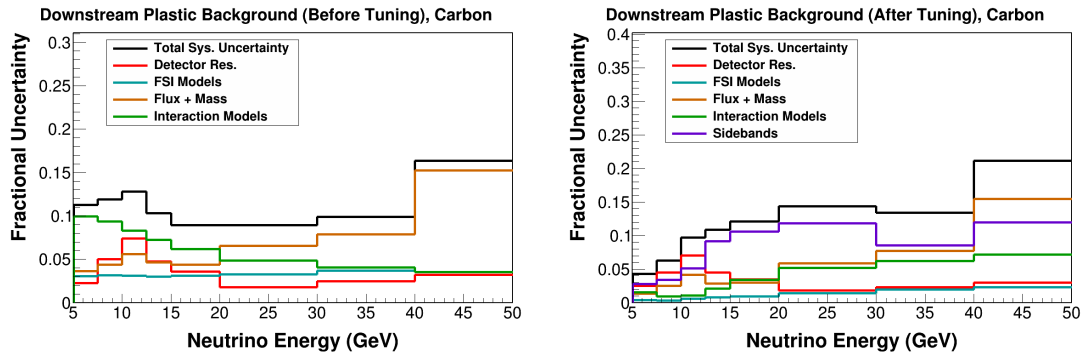
FIG. B.106: Carbon downstream scintillator sideband data error summary before (left) and after (right) tuning for plane number.
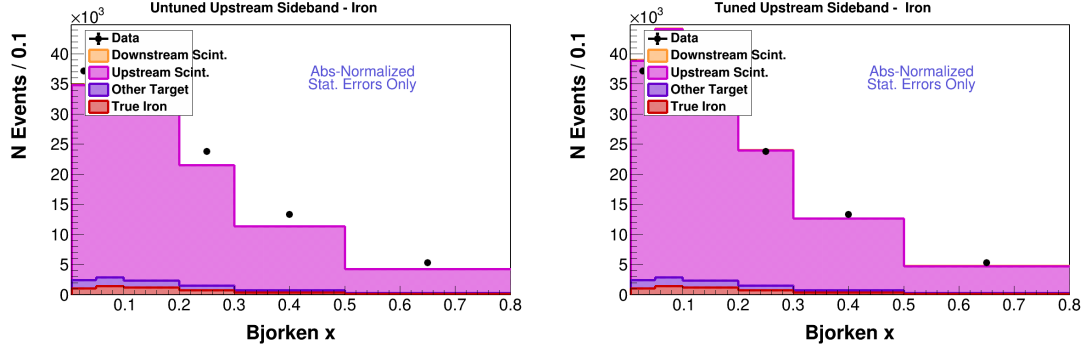
B.2.2 Muon Energy

All iron
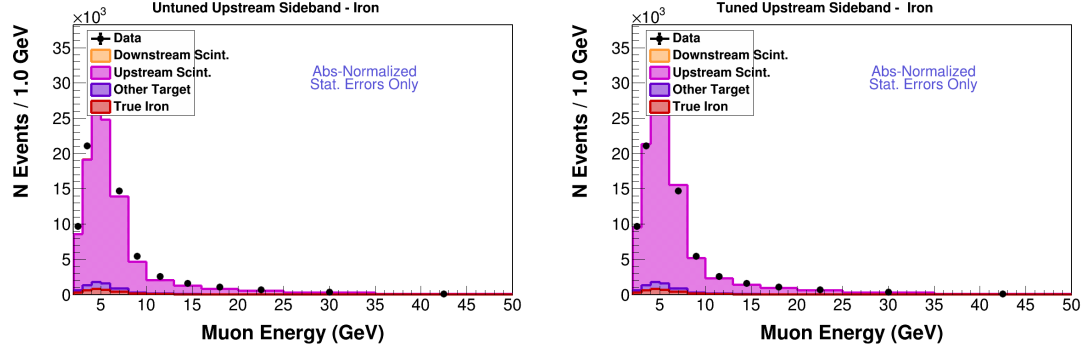
FIG. B.107: All iron upstream scintillator sideband stack plot before (left) and after (right) tuning for E_μ.
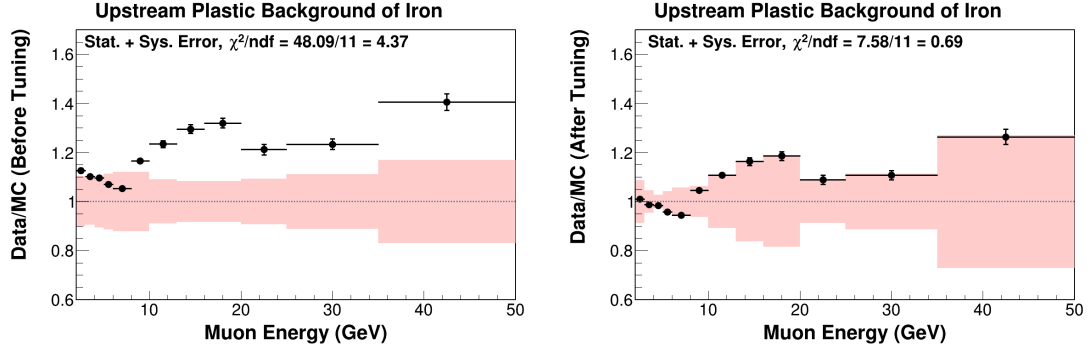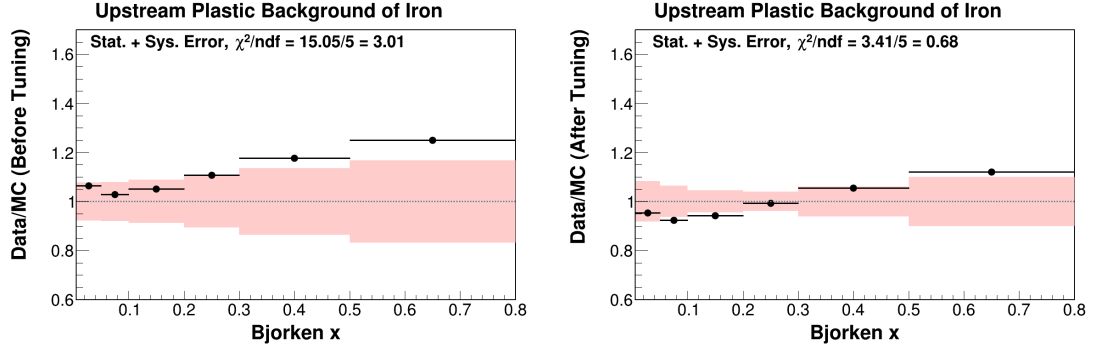

FIG. B.108: All iron upstream scintillator sideband data MC ratio before (left) and after (right) tuning for E_μ.
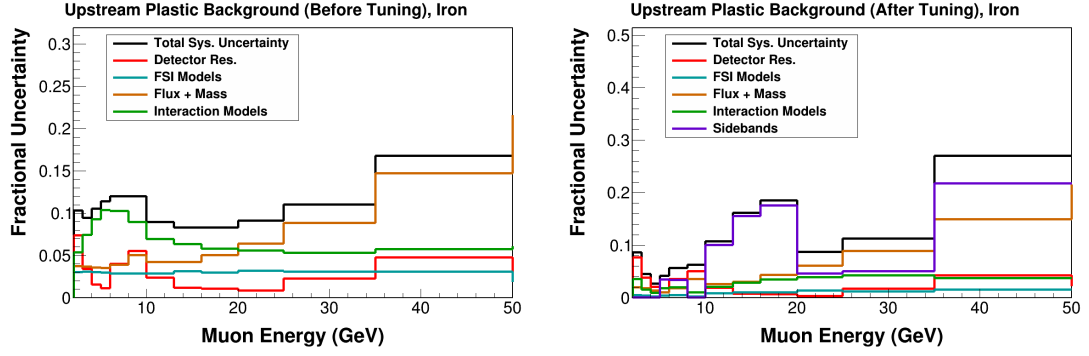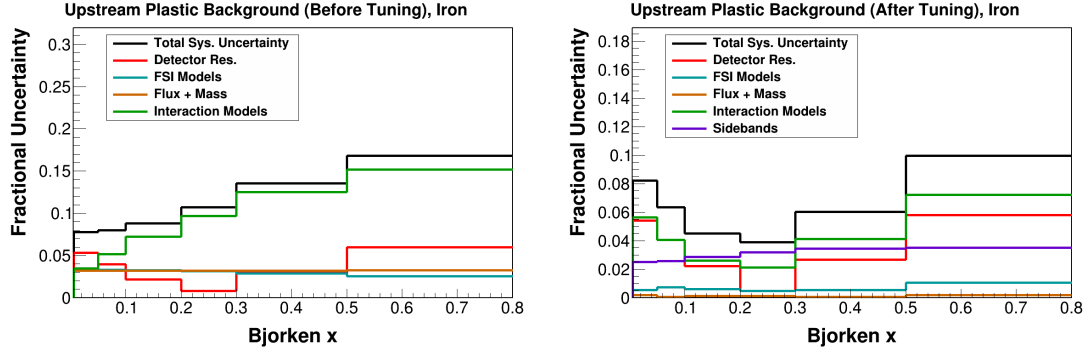
FIG. B.109: All iron upstream scintillator sideband data error summary before (left) and after (right) tuning for E_μ.
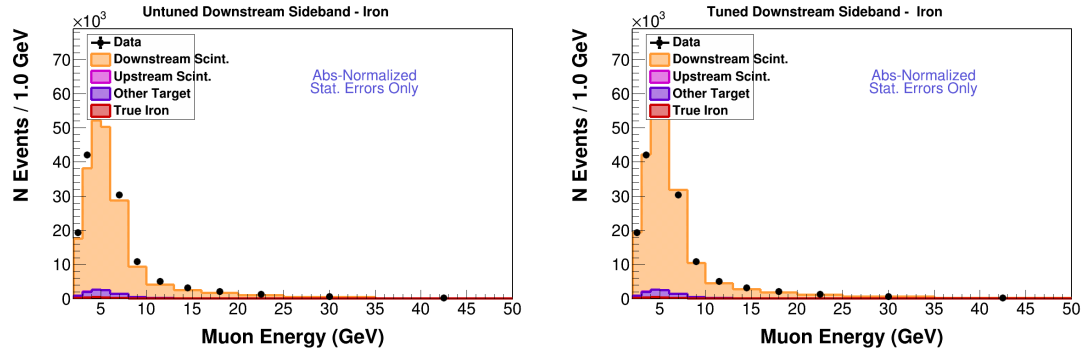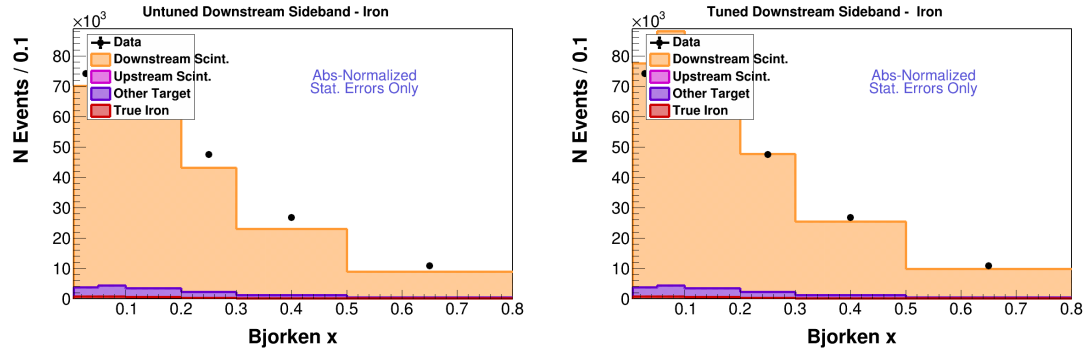

FIG. B.110: All iron downstream scintillator sideband stack plot before (left) and after (right) tuning for E_μ.
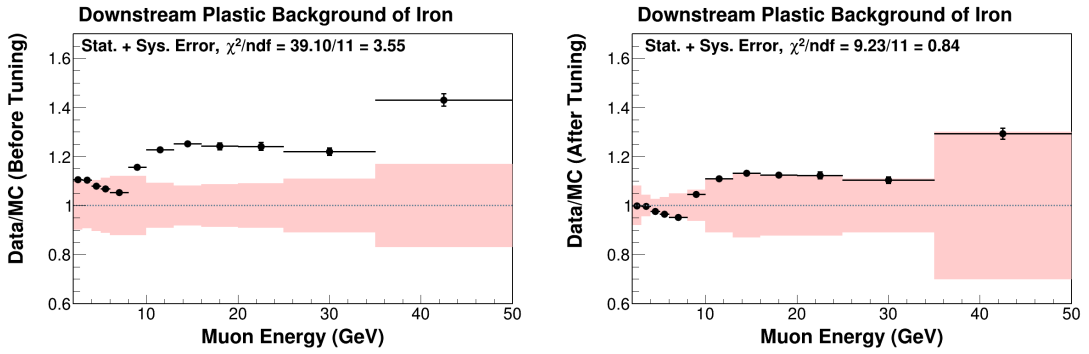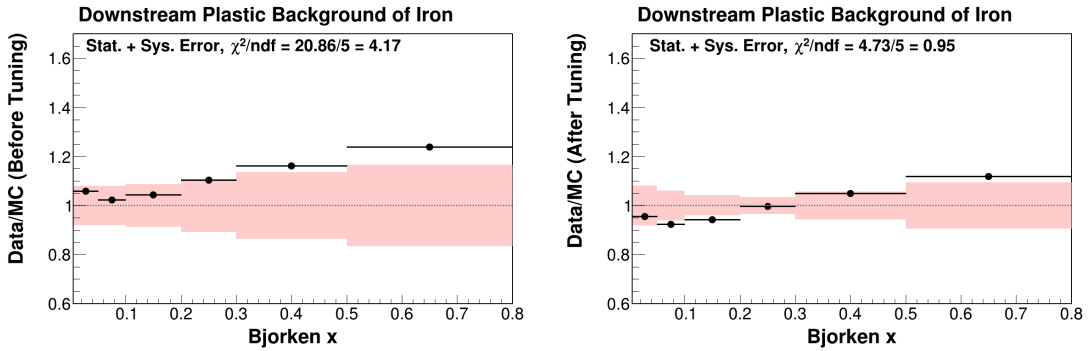

FIG. B.111: All iron downstream scintillator sideband data MC ratio before (left) and after (right) tuning for E_μ.
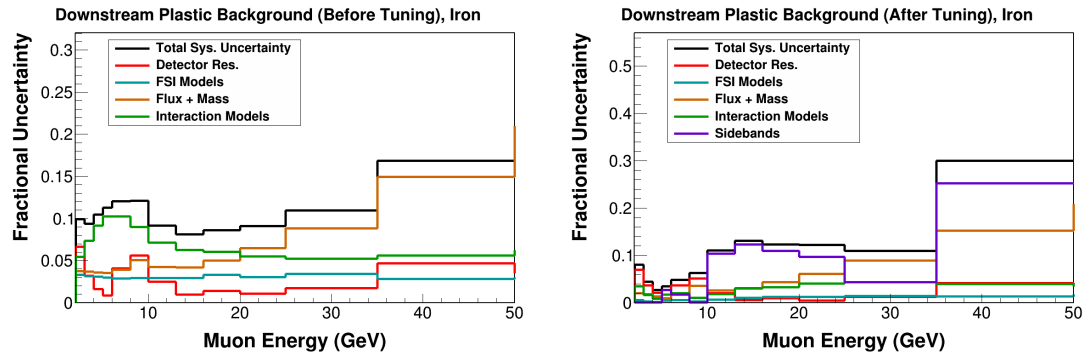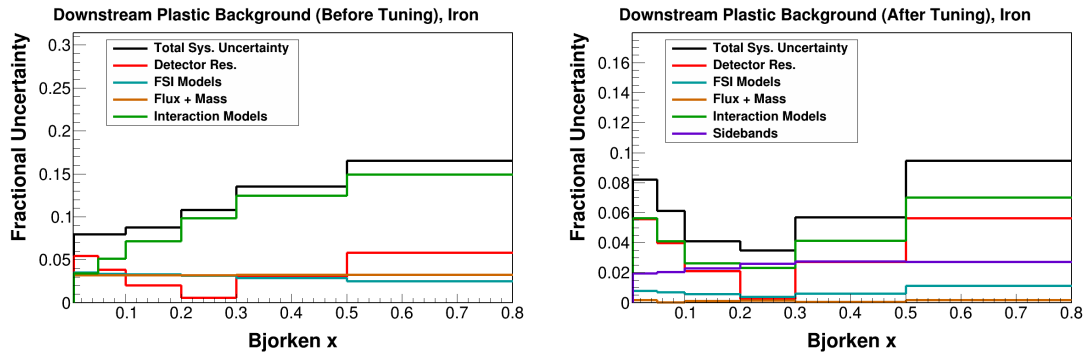
FIG. B.112: All iron downstream scintillator sideband data error summary before (left) and after (right) tuning for E_μ.
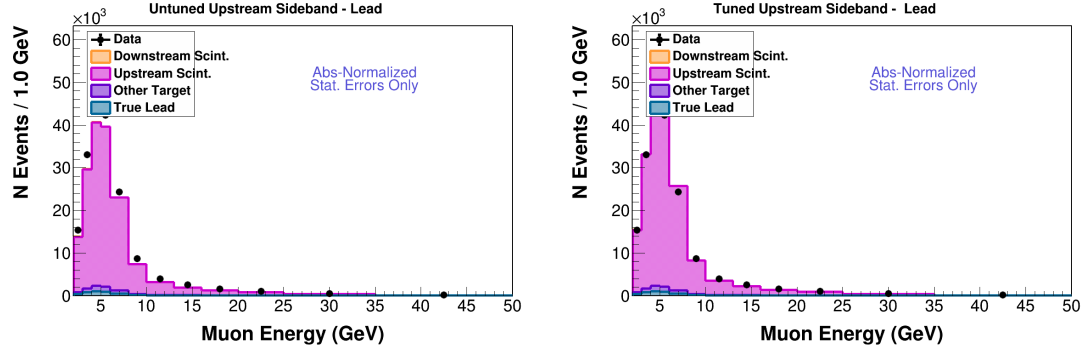
All lead

FIG. B.113: All lead upstream scintillator sideband stack plot before (left) and after (right) tuning for E_μ.
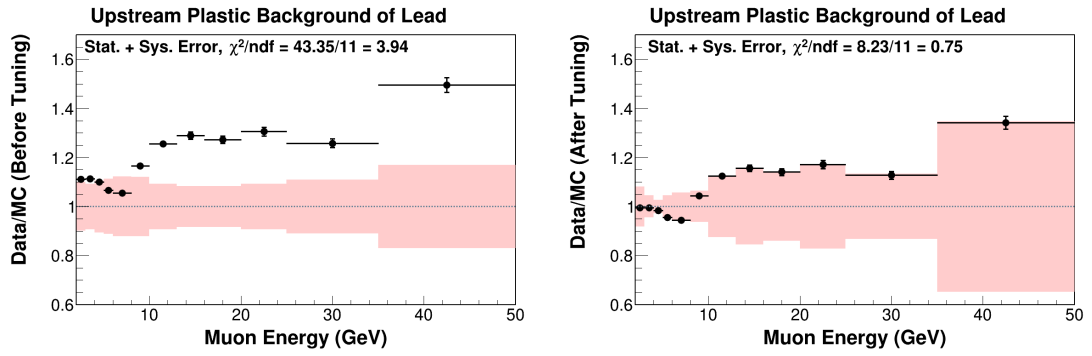
FIG. B.114: All lead upstream scintillator sideband data MC ratio before (left) and after (right) tuning for E_μ.

FIG. B.115: All lead upstream scintillator sideband data error summary before (left) and after (right) tuning for E_μ.
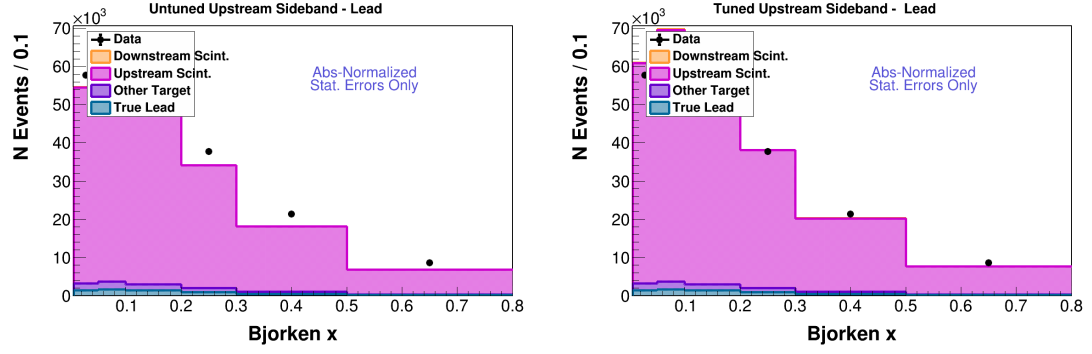

FIG. B.116: All lead downstream scintillator sideband stack plot before (left) and after (right) tuning for E_μ.
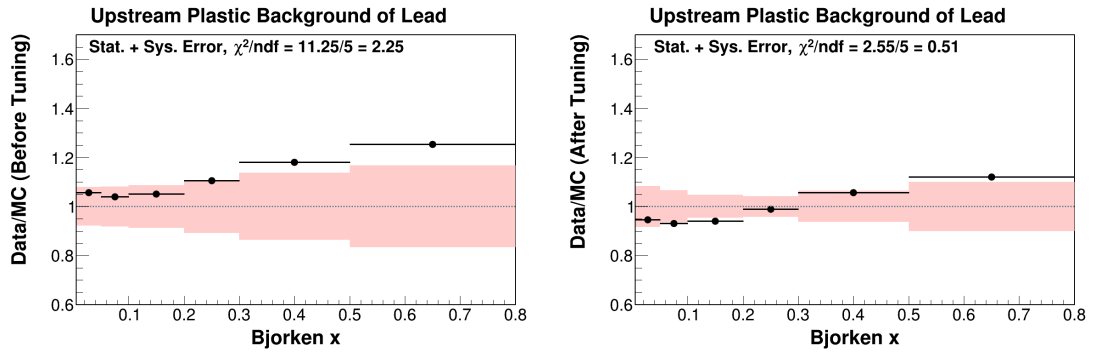

FIG. B.117: All lead downstream scintillator sideband data MC ratio before (left) and after (right) tuning for E_μ.
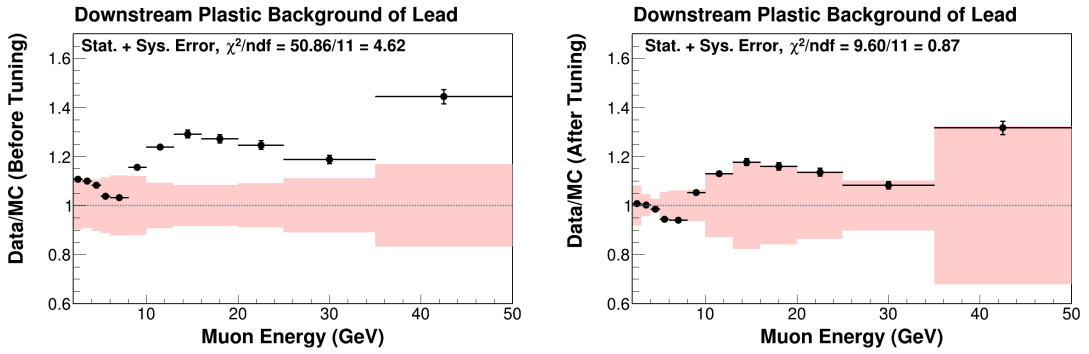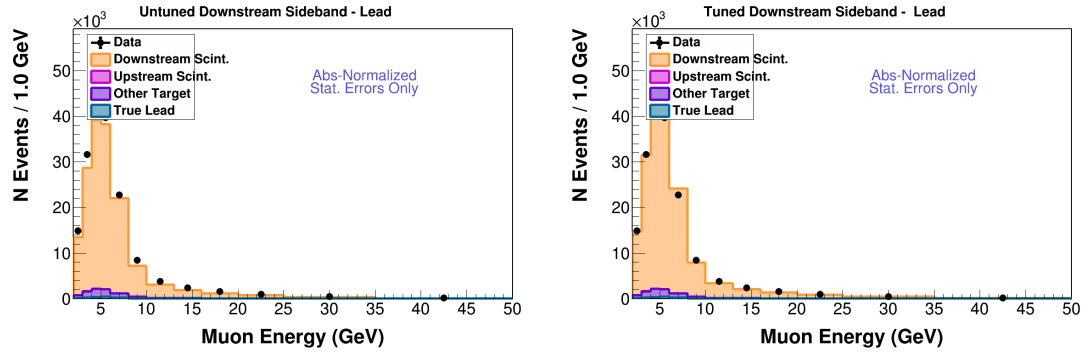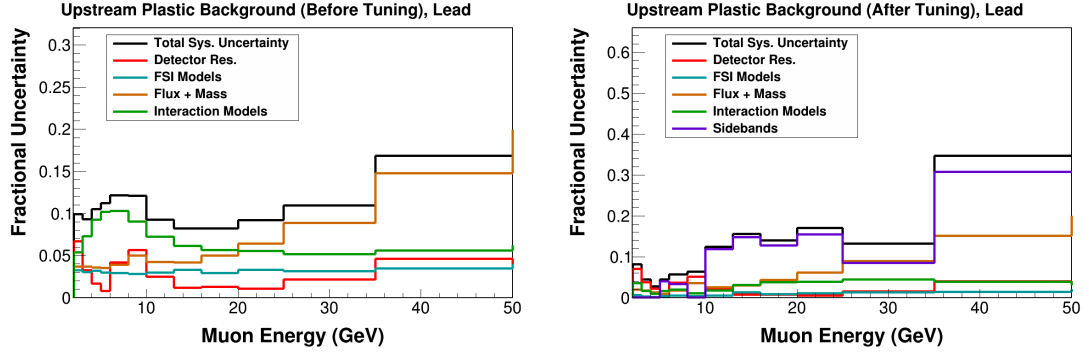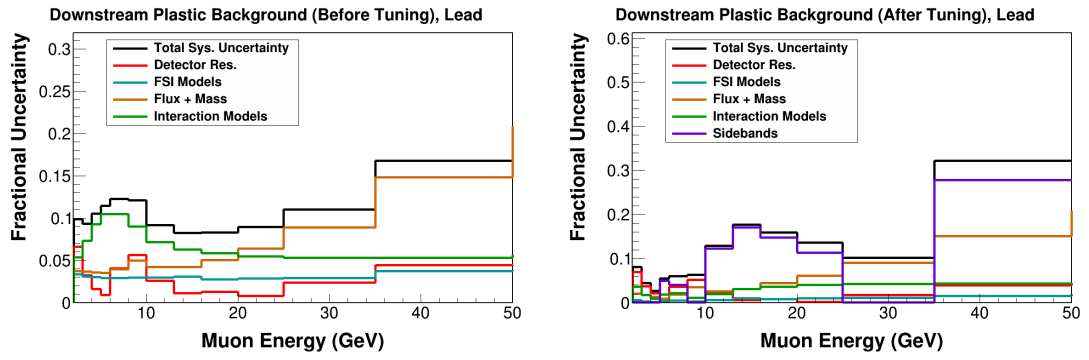
FIG. B.118: All lead downstream scintillator sideband data error summary before (left) and after (right) tuning for E_μ.
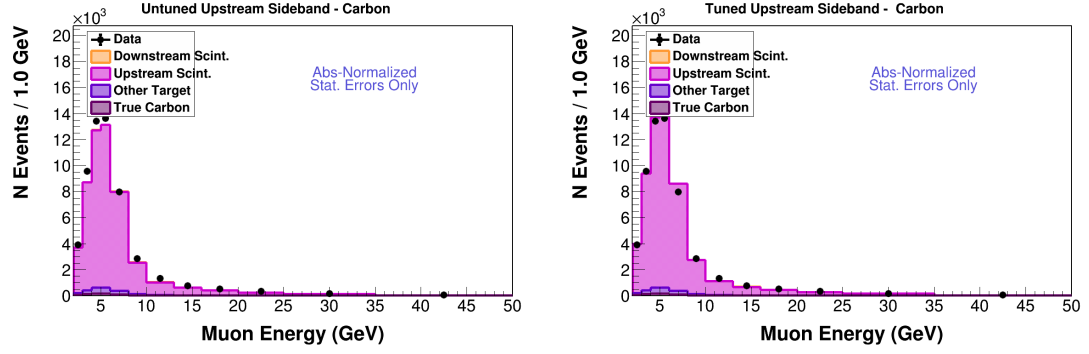
Carbon

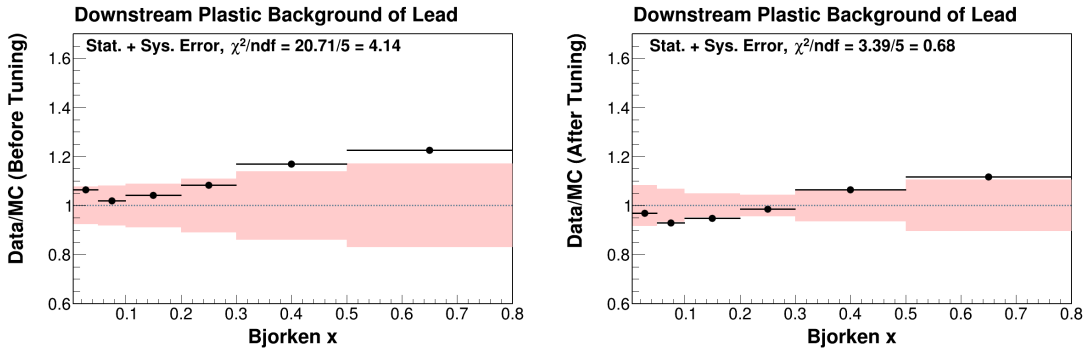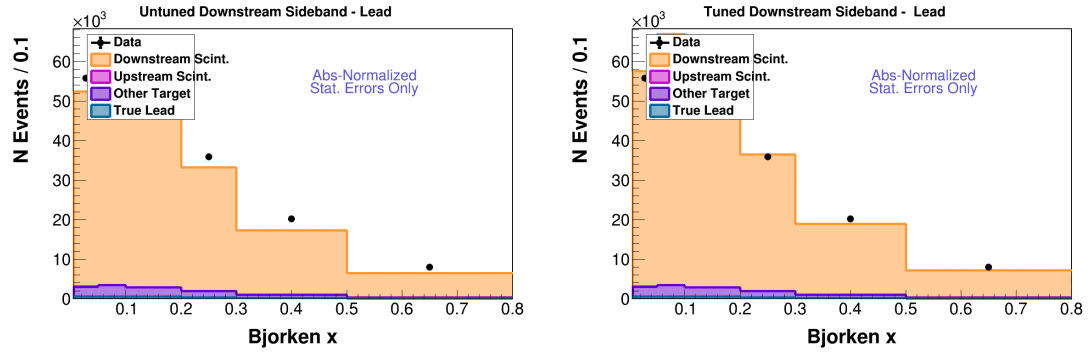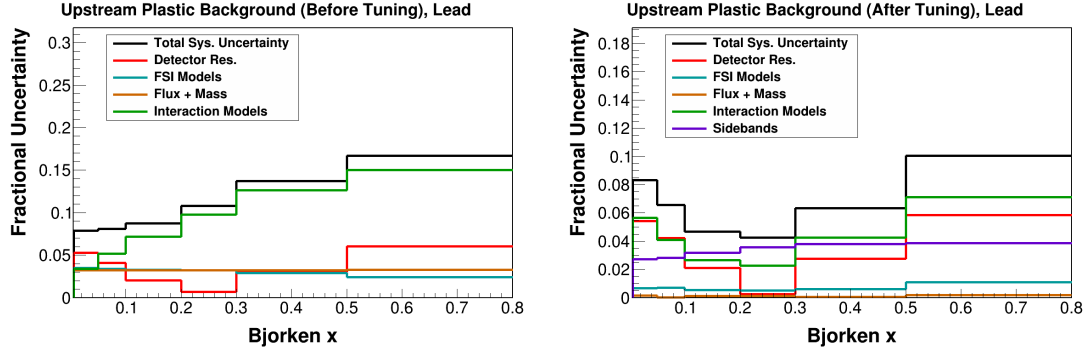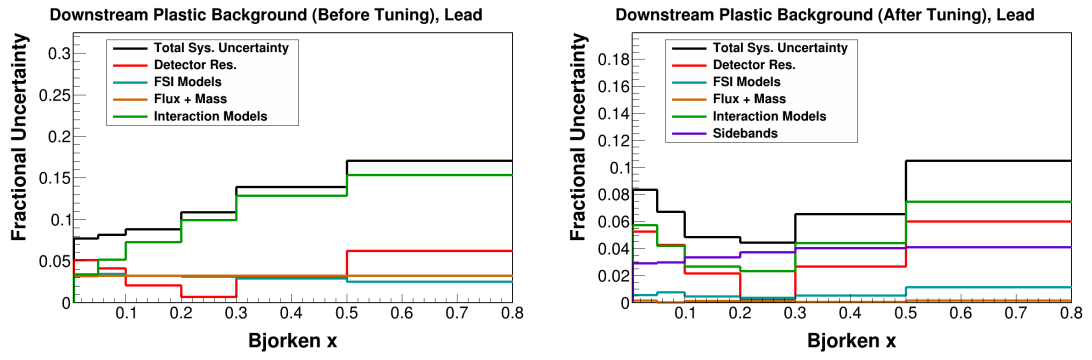FIG. B.119: Carbon upstream scintillator sideband stack plot before (left) and after (right) tuning for E_μ.
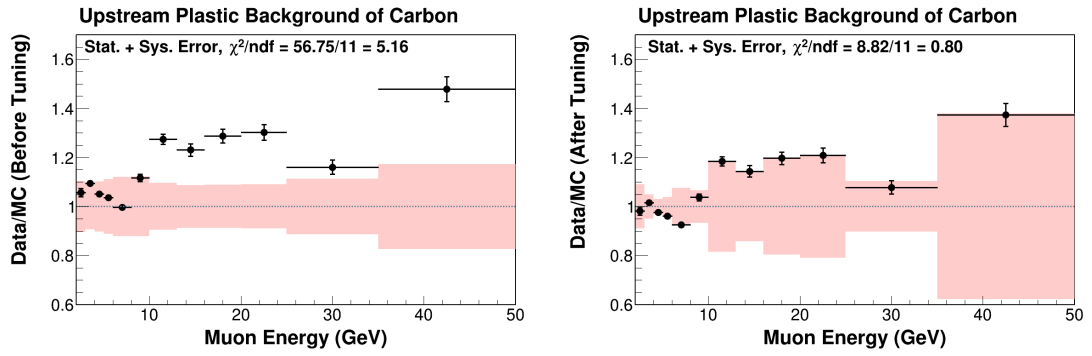
FIG. B.120: Carbon upstream scintillator sideband data MC ratio before (left) and after (right) tuning for E_μ.
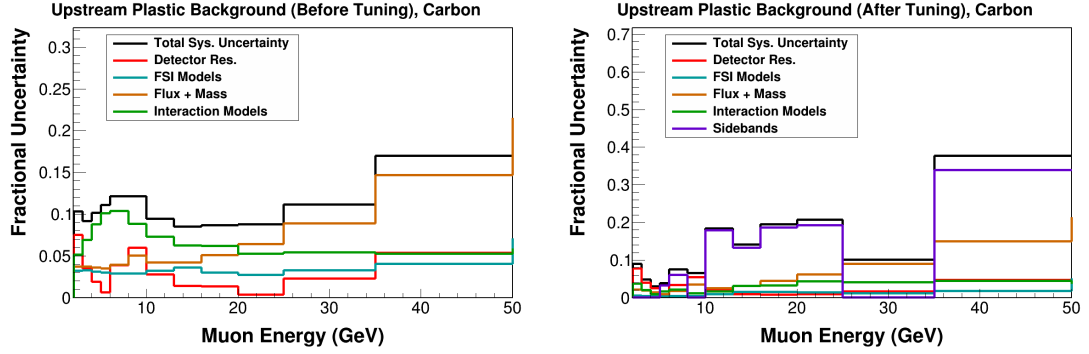
FIG. B.121: Carbon upstream scintillator sideband data error summary before (left) and after (right) tuning for E_μ.
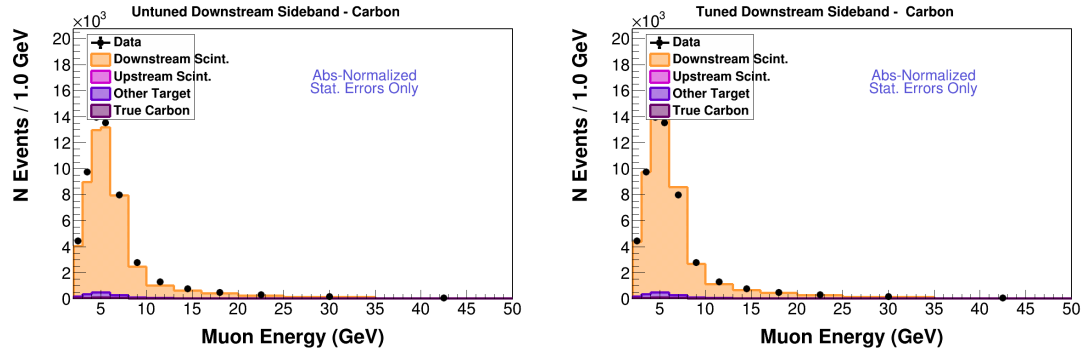
FIG. B.122: Carbon downstream scintillator sideband stack plot before (left) and after (right) tuning for E_μ.
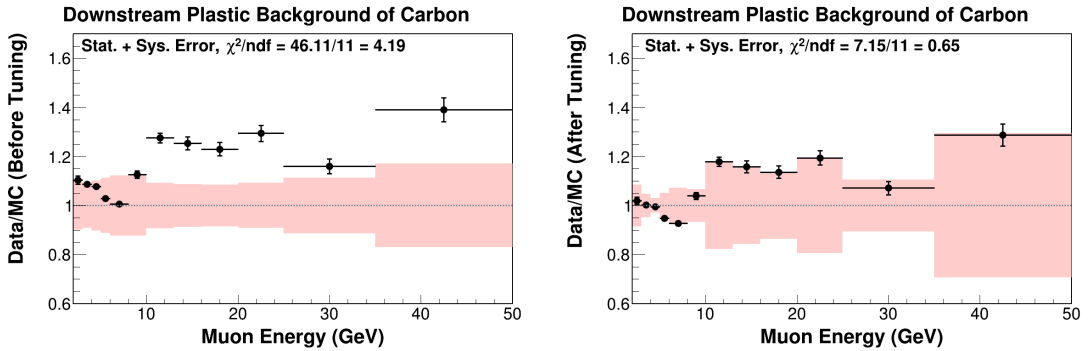
FIG. B.123: Carbon downstream scintillator sideband data MC ratio before (left) and after (right) tuning for E_μ.
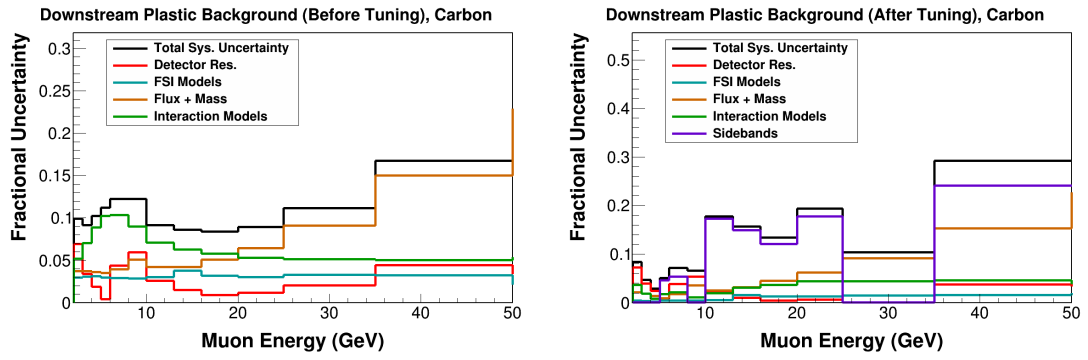
FIG. B.124: Carbon downstream scintillator sideband data error summary before (left) and after (right) tuning for E_μ.

B.2.3   Neutrino Energy
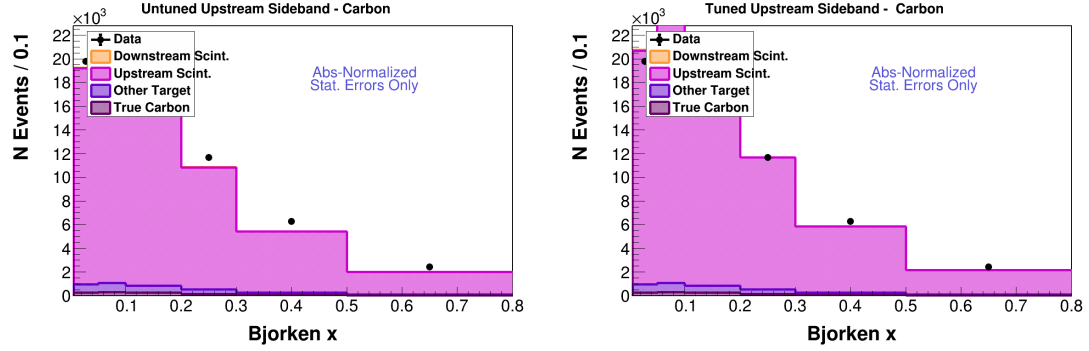
All iron
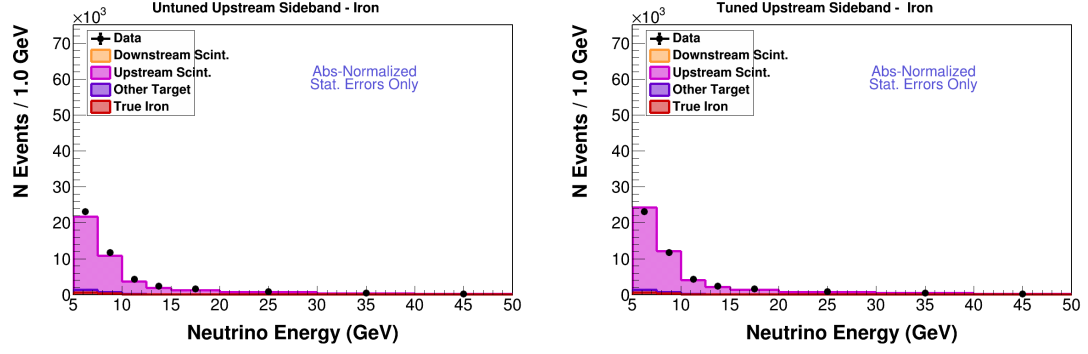
FIG. B.125: All iron upstream scintillator sideband stack plot before (left) and after (right) tuning for E_ν.
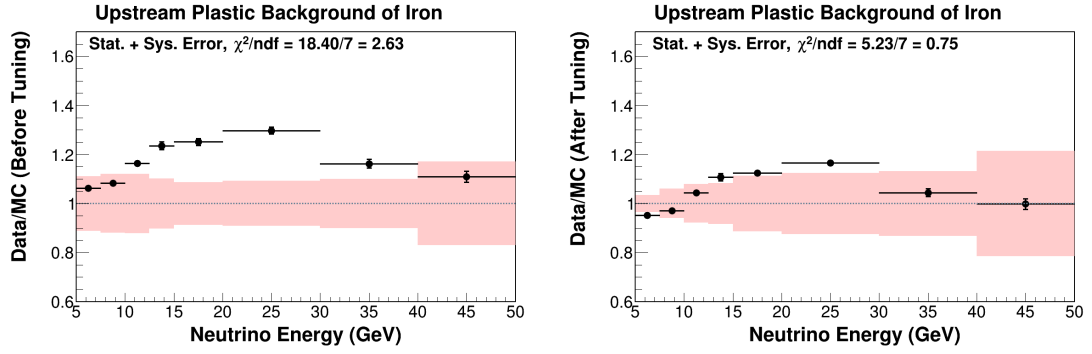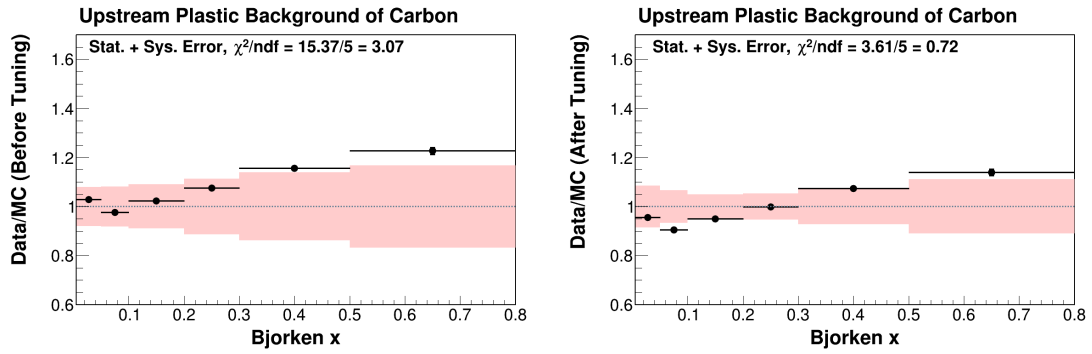

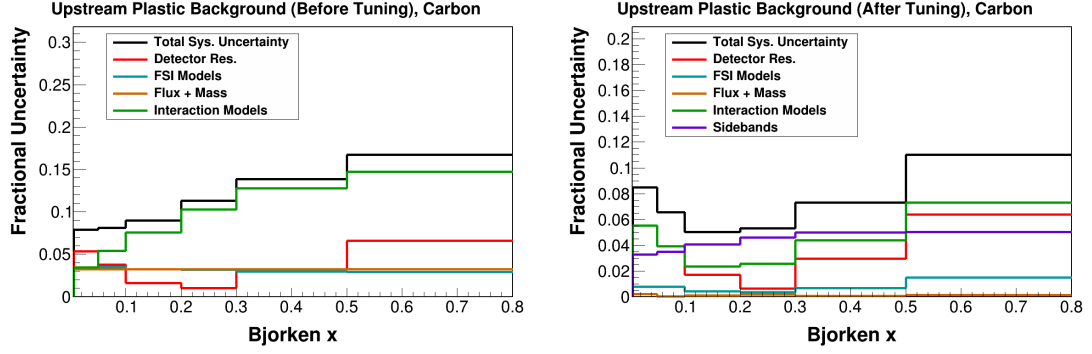FIG. B.126: All iron upstream scintillator sideband data MC ratio before (left) and after (right) tuning for E_ν.
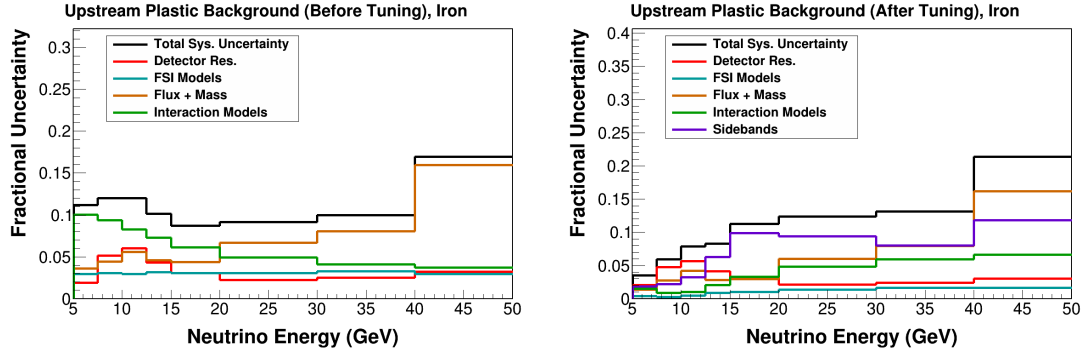
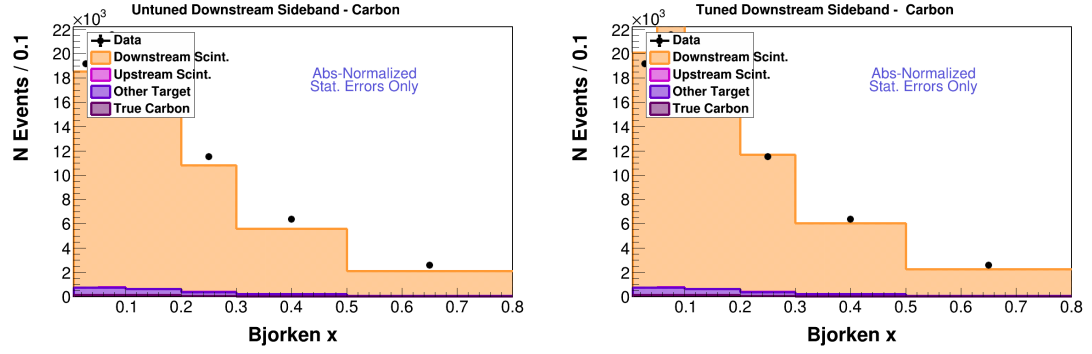FIG. B.127: All iron upstream scintillator sideband data error summary before (left) and after (right) tuning for E_ν.
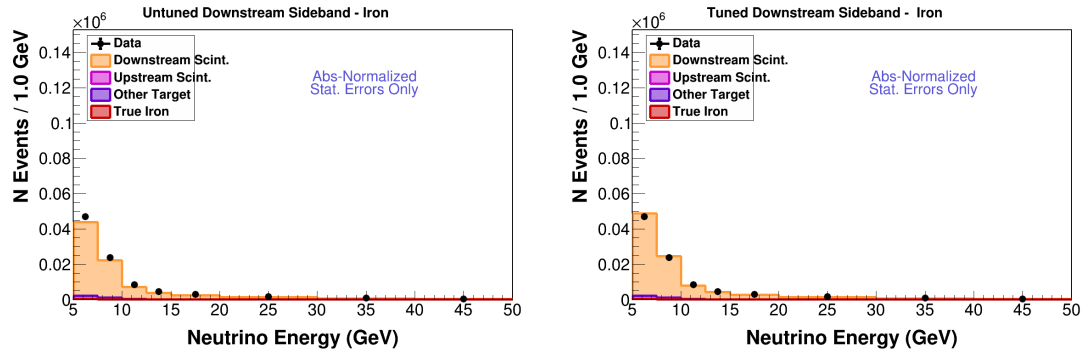
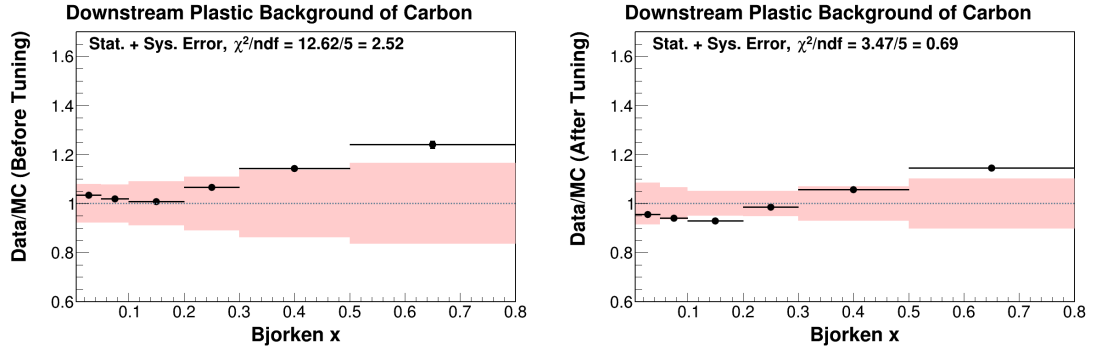FIG. B.128: All iron downstream scintillator sideband stack plot before (left) and after (right) tuning for E_ν.
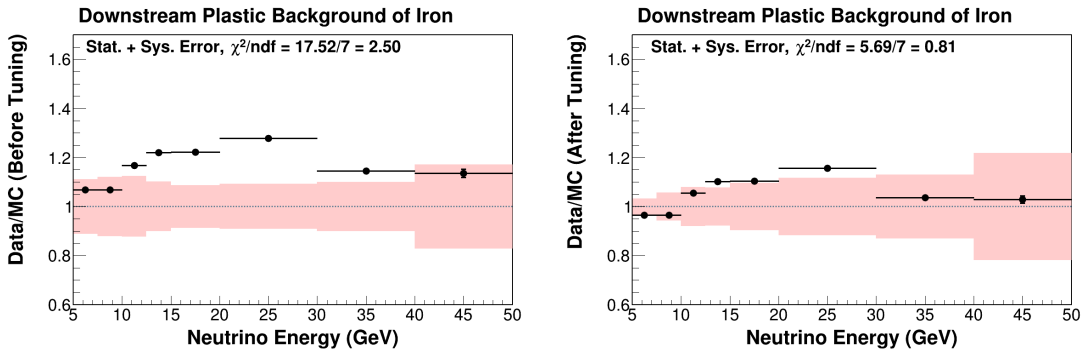
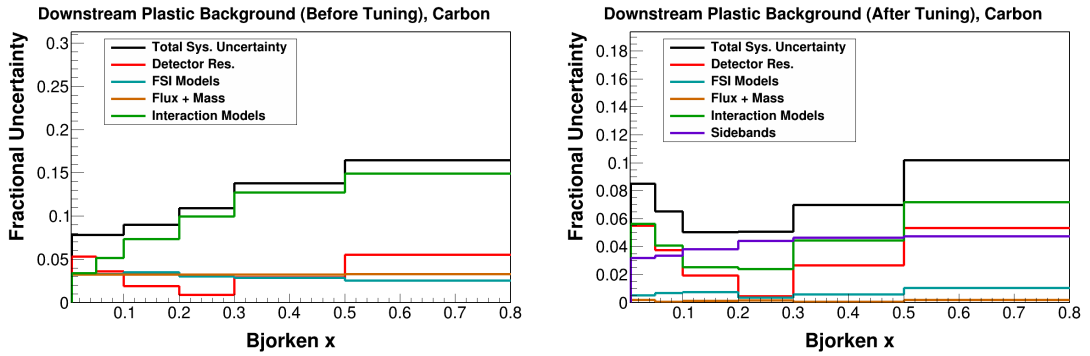FIG. B.129: All iron downstream scintillator sideband data MC ratio before (left) and after (right) tuning for E_ν.

FIG. B.130: All iron downstream scintillator sideband data error summary before (left) and after (right) tuning for E_ν.

All lead

FIG. B.131: All lead upstream scintillator sideband stack plot before (left) and after (right) tuning for E_ν.

FIG. B.132: All lead upstream scintillator sideband data MC ratio before (left) and after (right) tuning for E_ν.

Upstream Plastic Background (Before Tuning), Lead

Upstream Plastic Background (After Tuning), Lead

FIG. B.133: All lead upstream scintillator sideband data error summary before (left) and after (right) tuning for E_ν.

Untuned Downstream Sideband - Lead

Tuned Downstream Sideband - Lead

Abs-Normalized
Stat. Errors Only

FIG. B.134: All lead downstream scintillator sideband stack plot before (left) and after (right) tuning for E_ν.

Downstream Plastic Background of Lead

Stat. + Sys. Error, χ^2/ndf = 23.48/7 = 3.35

Downstream Plastic Background of Lead

Stat. + Sys. Error, χ^2/ndf = 6.49/7 = 0.93

FIG. B.135: All lead downstream scintillator sideband data MC ratio before (left) and after (right) tuning for E_ν.

FIG. B.136: All lead downstream scintillator sideband data error summary before (left) and after (right) tuning for E_ν.

Carbon

FIG. B.137: Carbon upstream scintillator sideband stack plot before (left) and after (right) tuning for E_ν.

FIG. B.138: Carbon upstream scintillator sideband data MC ratio before (left) and after (right) tuning for E_ν.

FIG. B.139: Carbon upstream scintillator sideband data error summary before (left) and after (right) tuning for E_ν.

FIG. B.140: Carbon downstream scintillator sideband stack plot before (left) and after (right) tuning for E_ν.

FIG. B.141: Carbon downstream scintillator sideband data MC ratio before (left) and after (right) tuning for E_ν.

FIG. B.142: Carbon downstream scintillator sideband data error summary before (left) and after (right) tuning for E_ν.

B.2.4 Bjorken-x

All iron

FIG. B.143: All iron upstream scintillator sideband stack plot before (left) and after (right) tuning for x_{bj}.

FIG. B.144: All iron upstream scintillator sideband data MC ratio before (left) and after (right) tuning for x_{bj}.

FIG. B.145: All iron upstream scintillator sideband data error summary before (left) and after (right) tuning for x_{bj}.

FIG. B.146: All iron downstream scintillator sideband stack plot before (left) and after (right) tuning for x_{bj}.

FIG. B.147: All iron downstream scintillator sideband data MC ratio before (left) and after (right) tuning for x_{bj}.

FIG. B.148: All iron downstream scintillator sideband data error summary before (left) and after (right) tuning for x_{bj}.

All lead

FIG. B.149: All lead upstream scintillator sideband stack plot before (left) and after (right) tuning for x_{bj}.

FIG. B.150: All lead upstream scintillator sideband data MC ratio before (left) and after (right) tuning for x_{bj}.

FIG. B.151: All lead upstream scintillator sideband data error summary before (left) and after (right) tuning for x_{bj}.

FIG. B.152: All lead downstream scintillator sideband stack plot before (left) and after (right) tuning for x_{bj}.

FIG. B.153: All lead downstream scintillator sideband data MC ratio before (left) and after (right) tuning for x_{bj}.

FIG. B.154: All lead downstream scintillator sideband data error summary before (left) and after (right) tuning for x_{bj}.

Carbon

FIG. B.155: Carbon upstream scintillator sideband stack plot before (left) and after (right) tuning for x_{bj}.

FIG. B.156: Carbon upstream scintillator sideband data MC ratio before (left) and after (right) tuning for x_{bj}.

FIG. B.157: Carbon upstream scintillator sideband data error summary before (left) and after (right) tuning for x_{bj}.

FIG. B.158: Carbon downstream scintillator sideband stack plot before (left) and after (right) tuning for x_{bj}.

B.3 Physics sidebands

B.3.1 Before tuning

FIG. B.159: Carbon downstream scintillator sideband data MC ratio before (left) and after (right) tuning for x_{bj}.

FIG. B.160: Carbon downstream scintillator sideband data error summary before (left) and after (right) tuning for x_{bj}.

FIG. B.161: Continuum sideband before tuning in E_ν for all of the iron (top left), lead (top right), carbon(bottom left) and tracker (bottom right). The simulation is broken down into different true kinematic regions, which are shown stacked on top of each other.

FIG. B.162: Transition sideband before tuning in E_ν for all of the iron (top left), lead (top right), carbon(bottom left) and tracker (bottom right). The simulation is broken down into different true kinematic regions, which are shown stacked on top of each other.

FIG. B.163: Continuum sideband before tuning in x_{bj} for all of the iron (top left), lead (top right), carbon(bottom left) and tracker (bottom right). The simulation is broken down into different true kinematic regions, which are shown stacked on top of each other.
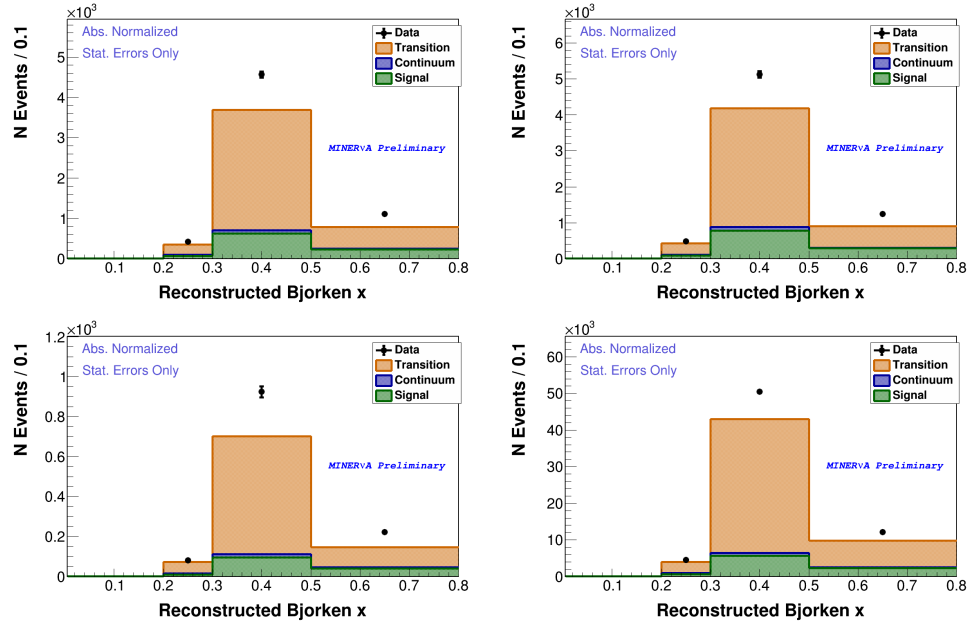
FIG. B.164: Transition sideband before tuning in x_{bj} for all of the iron (top left), lead (top right), carbon(bottom left) and tracker (bottom right). The simulation is broken down into different true kinematic regions, which are shown stacked on top of each other.
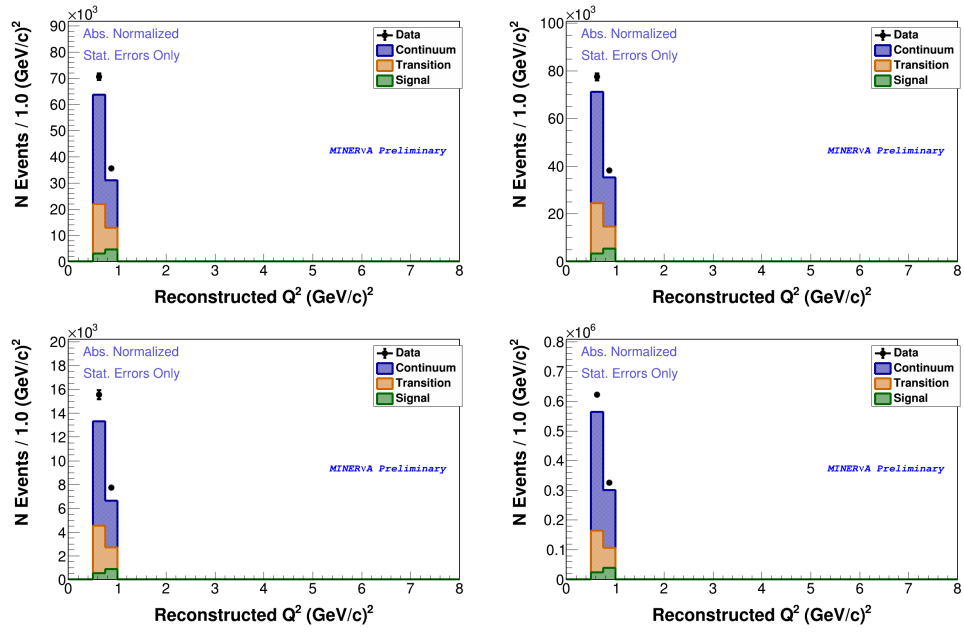
FIG. B.165: Continuum sideband before tuning in Q^2 for all of the iron (top left), lead (top right), carbon(bottom left) and tracker (bottom right). The simulation is broken down into different true kinematic regions, which are shown stacked on top of each other.
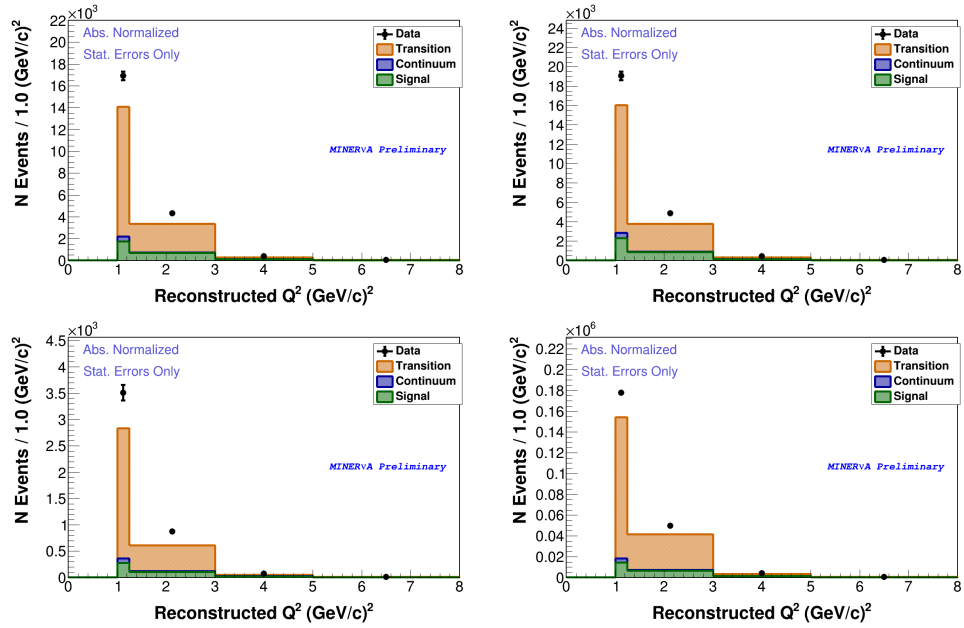
FIG. B.166: Transition sideband before tuning in Q^2 for all of the iron (top left), lead (top right), carbon(bottom left) and tracker (bottom right). The simulation is broken down into different true kinematic regions, which are shown stacked on top of each other.

FIG. B.167: Continuum sideband before tuning in W for all of the iron (top left), lead (top right), carbon(bottom left) and tracker (bottom right). The simulation is broken down into different true kinematic regions, which are shown stacked on top of each other.

FIG. B.168: Transition sideband before tuning in W for all of the iron (top left), lead (top right), carbon(bottom left) and tracker (bottom right). The simulation is broken down into different true kinematic regions, which are shown stacked on top of each other.
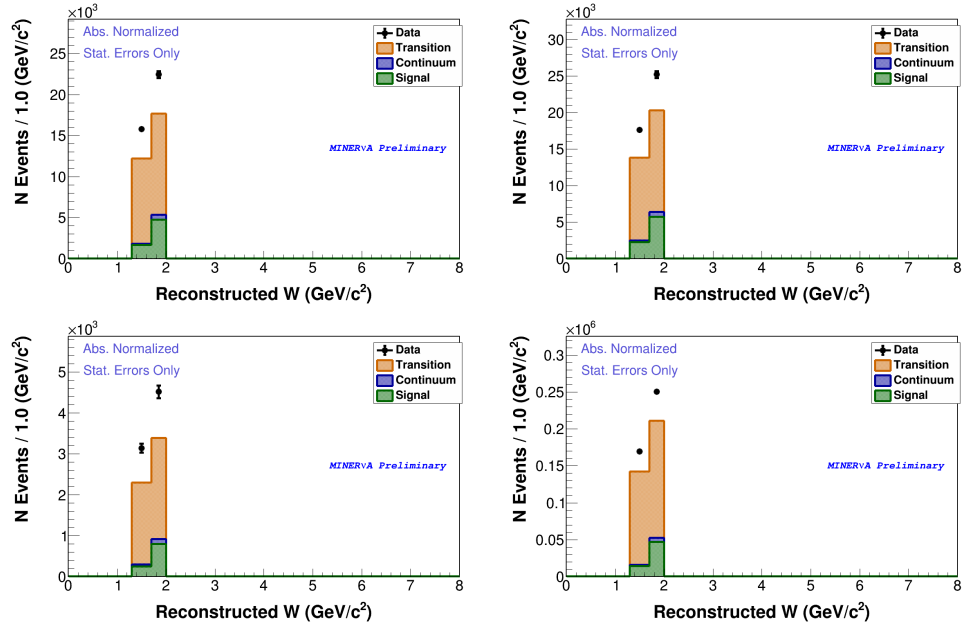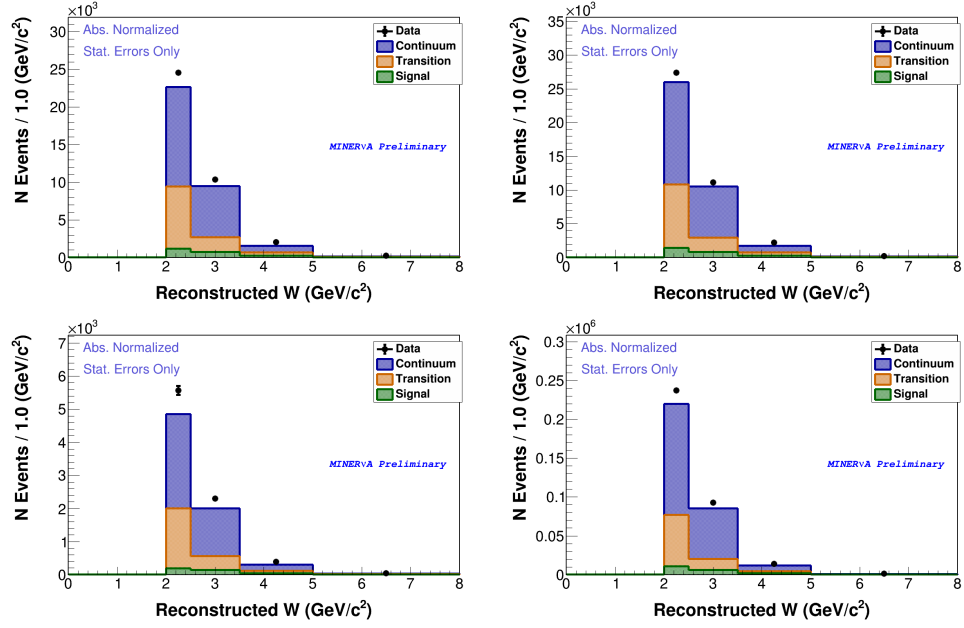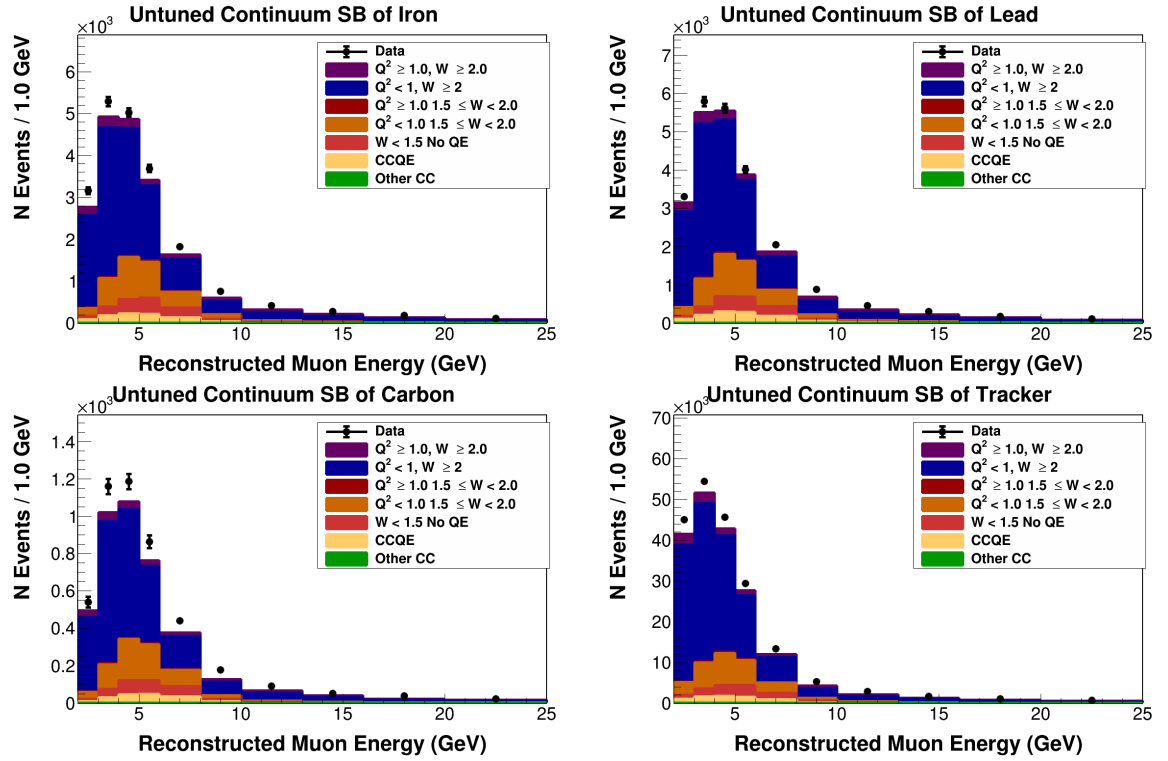
FIG. B.169: Continuum sideband before tuning in E_μ for all of the iron (top left), lead (top right), carbon(bottom left) and tracker (bottom right). The simulation is broken down into different true kinematic regions, which are shown stacked on top of each other.
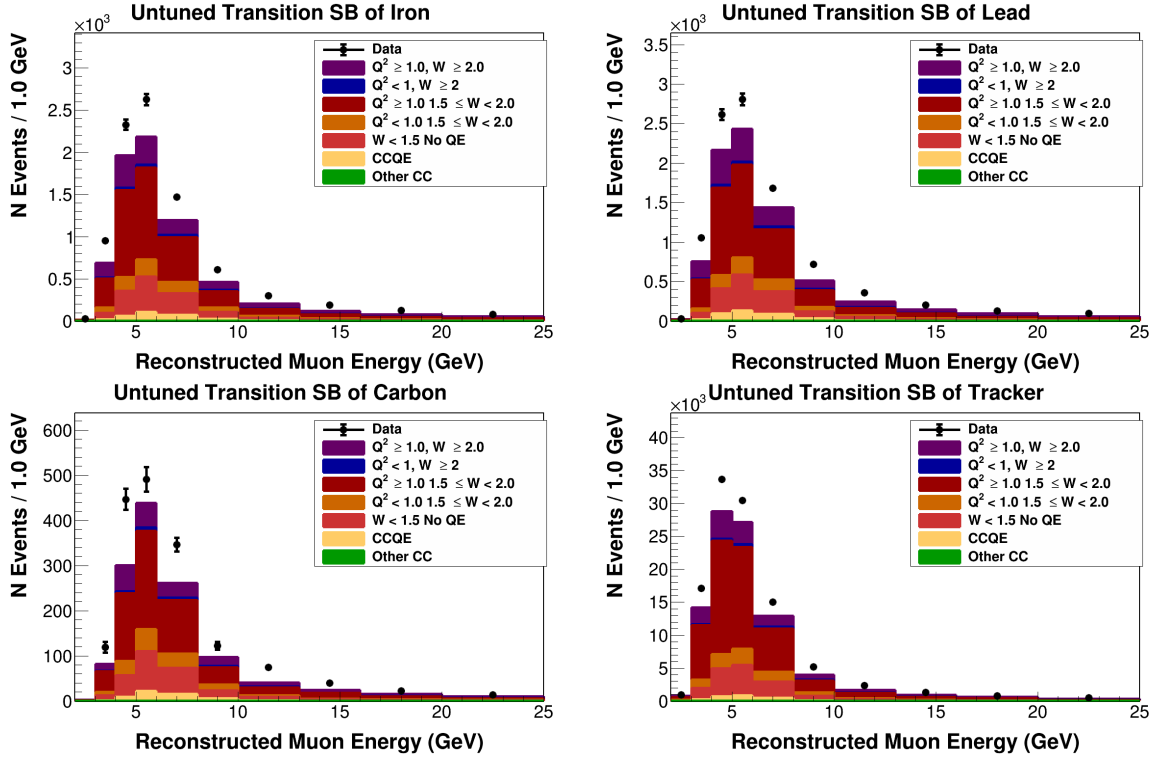
FIG. B.170: Transition sideband before tuning in E_μ for all of the iron (top left), lead (top right), carbon(bottom left) and tracker (bottom right). The simulation is broken down into different true kinematic regions, which are shown stacked on top of each other.

B.3.2 After tuning
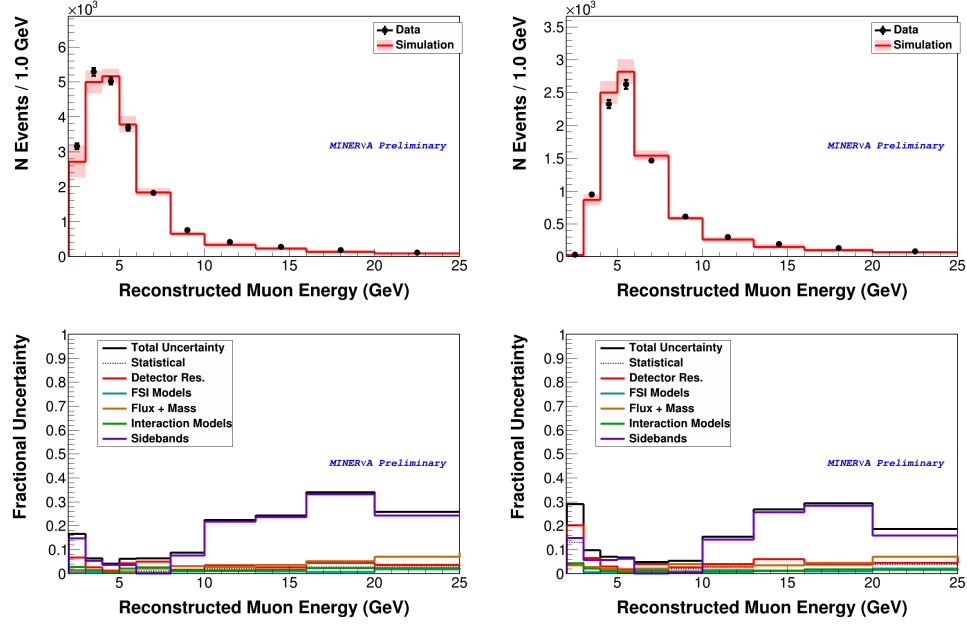
FIG. B.171: The continuum (left) and transition (right) sidebands in E_μ after tuning has been applied in iron (top) and their associated data error summaries (bottom).
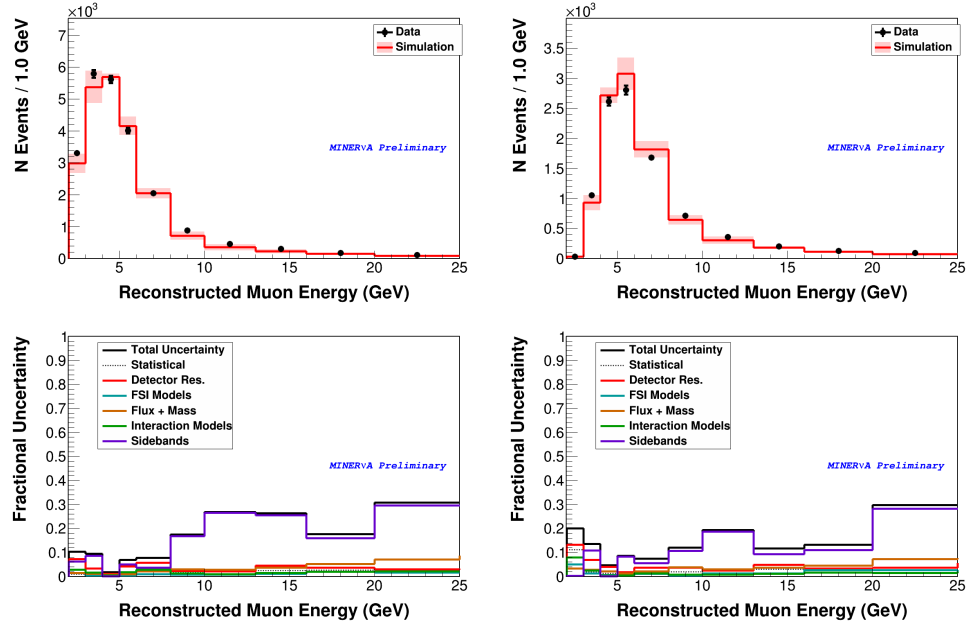
FIG. B.172: The continuum (left) and transition (right) sidebands in E_μ after tuning has been applied in lead (top) and their associated data error summaries (bottom).
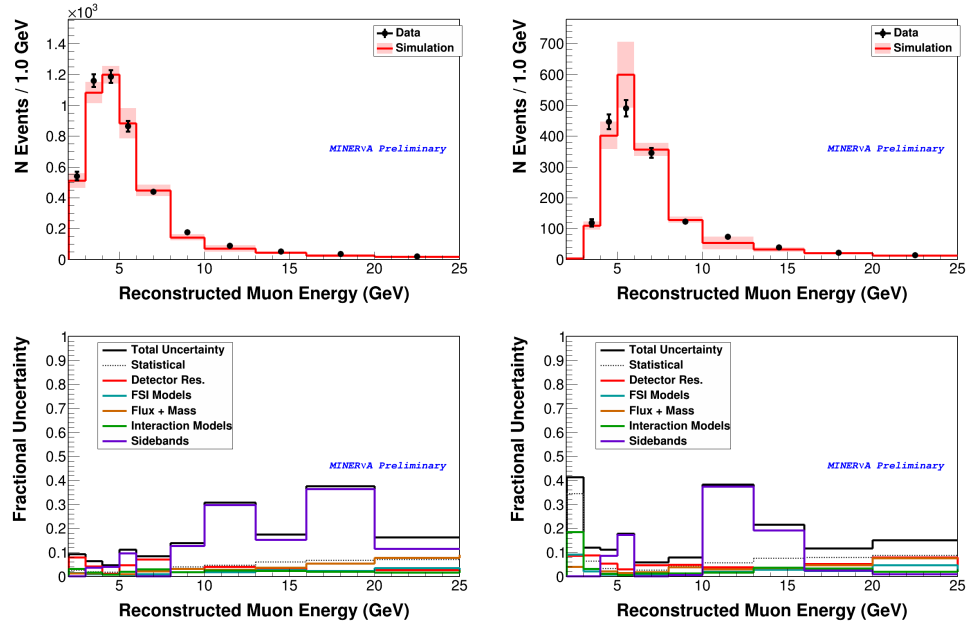
FIG. B.173: The continuum (left) and transition (right) sidebands in E_μ after tuning has been applied in carbon (top) and their associated data error summaries (bottom).
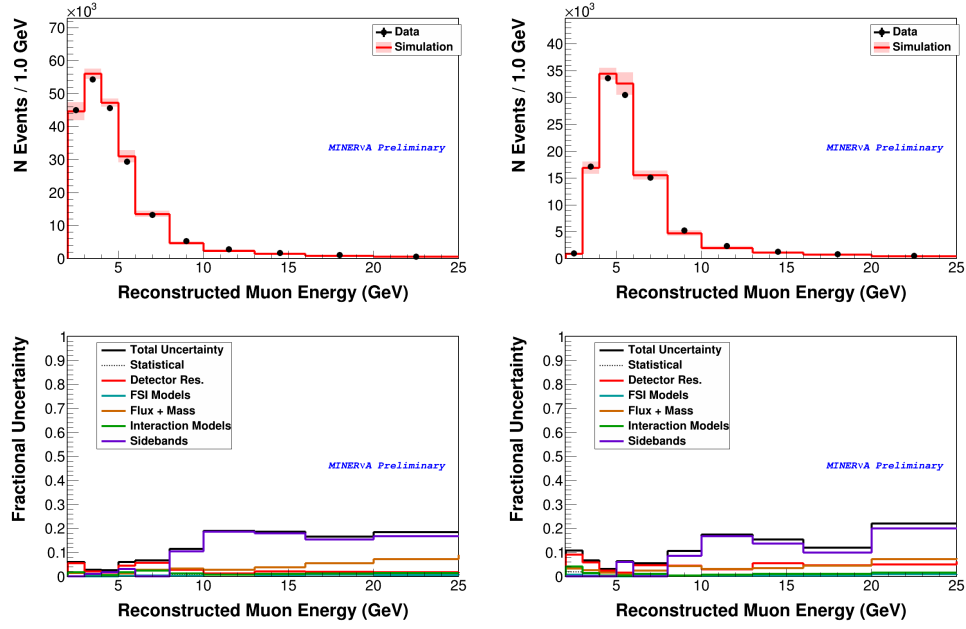
FIG. B.174: The continuum (left) and transition (right) sidebands in E_μ after tuning has been applied in tracker (top) and their associated data error summaries (bottom).
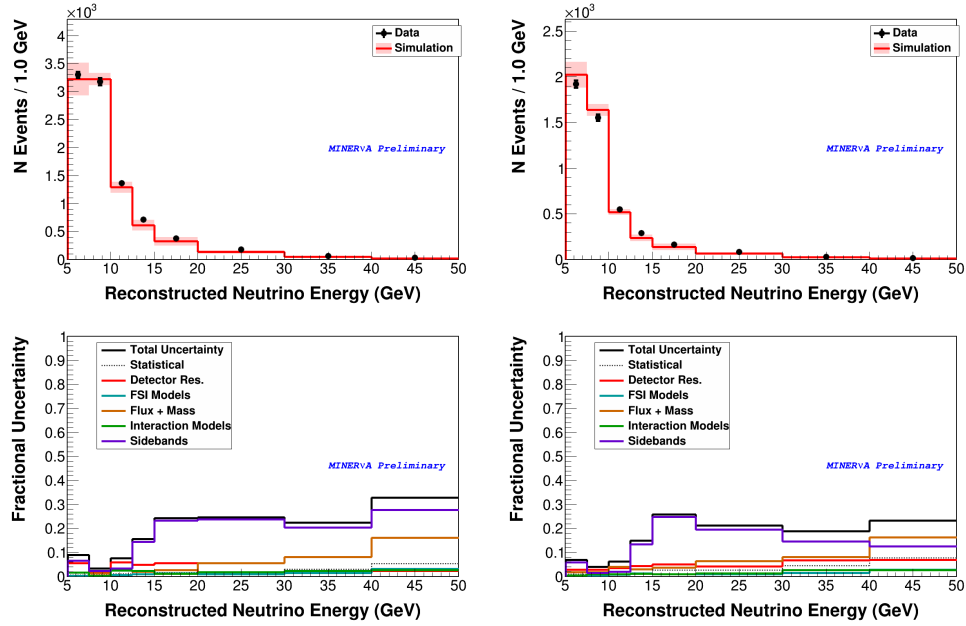
FIG. B.175: The continuum (left) and transition (right) sidebands in E_ν after tuning has been applied in iron (top) and their associated data error summaries (bottom).

357
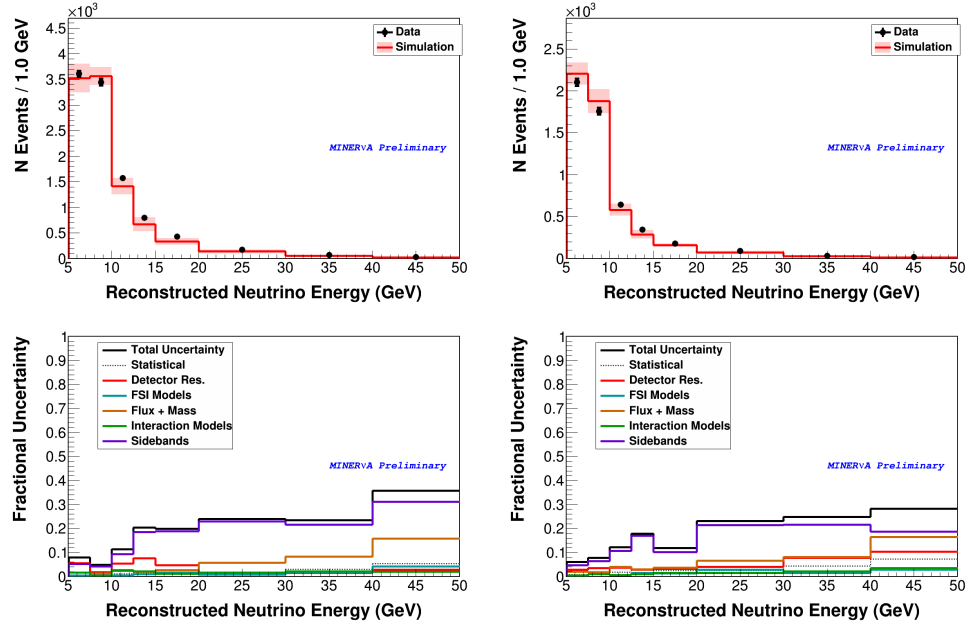
FIG. B.176: The continuum (left) and transition (right) sidebands in E_ν after tuning has been applied in lead (top) and their associated data error summaries (bottom).
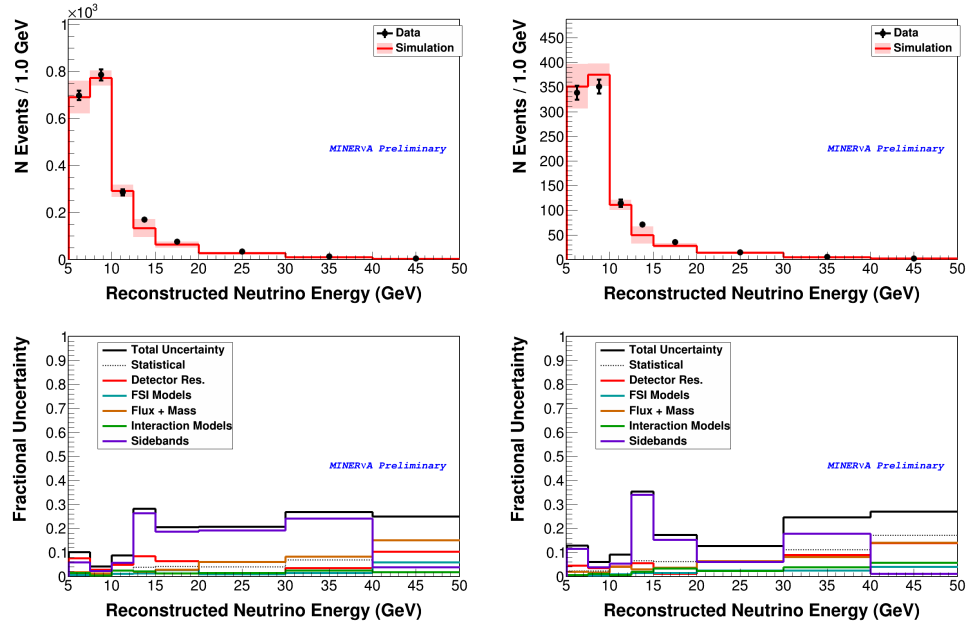
FIG. B.177: The continuum (left) and transition (right) sidebands in E_ν after tuning has been applied in carbon (top) and their associated data error summaries (bottom).
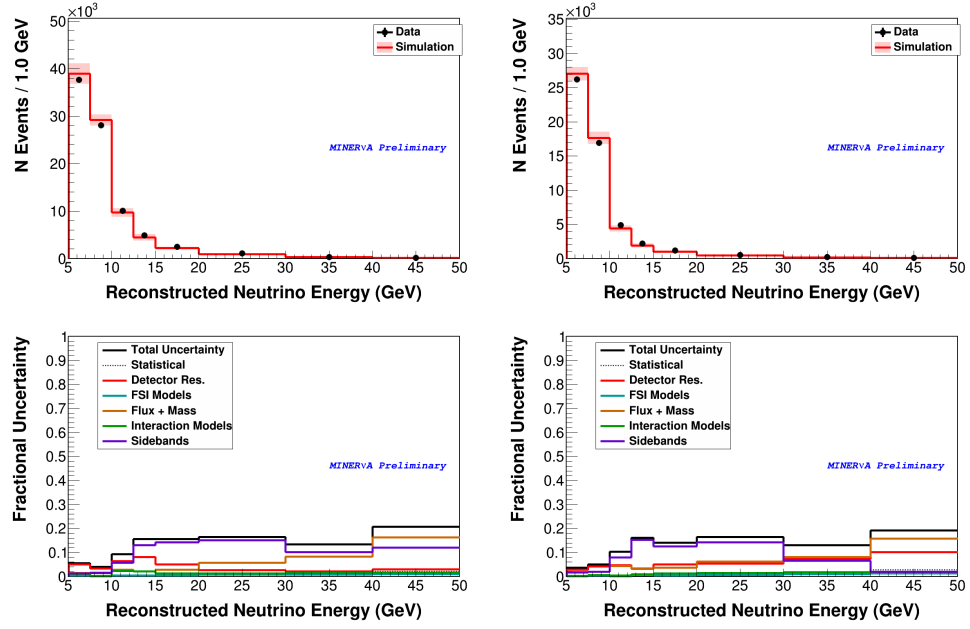
FIG. B.178: The continuum (left) and transition (right) sidebands in E_ν after tuning has been applied in tracker (top) and their associated data error summaries (bottom).
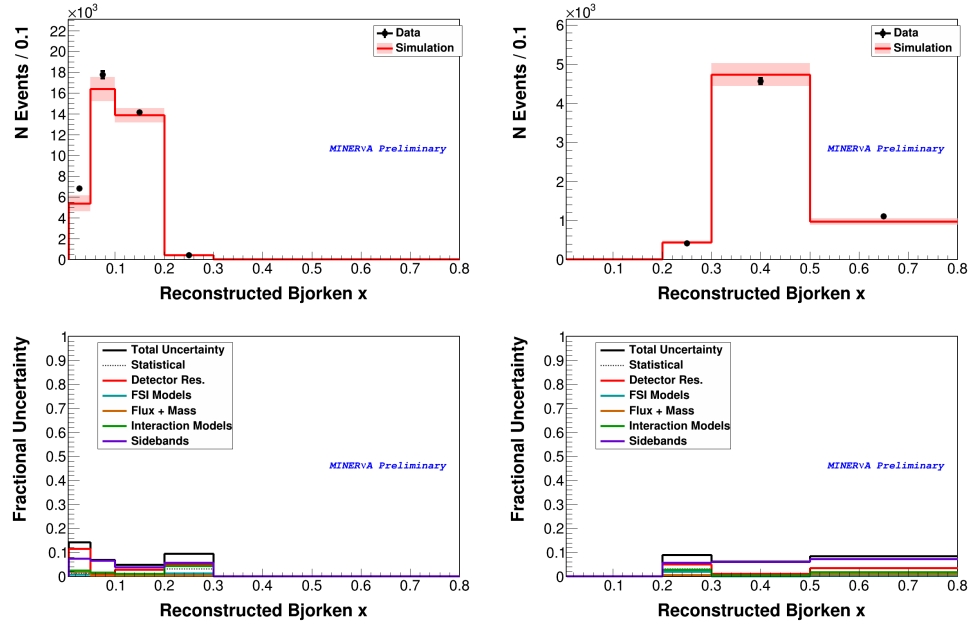
FIG. B.179: The continuum (left) and transition (right) sidebands in x_{bj} after tuning has been applied in iron (top) and their associated data error summaries (bottom).
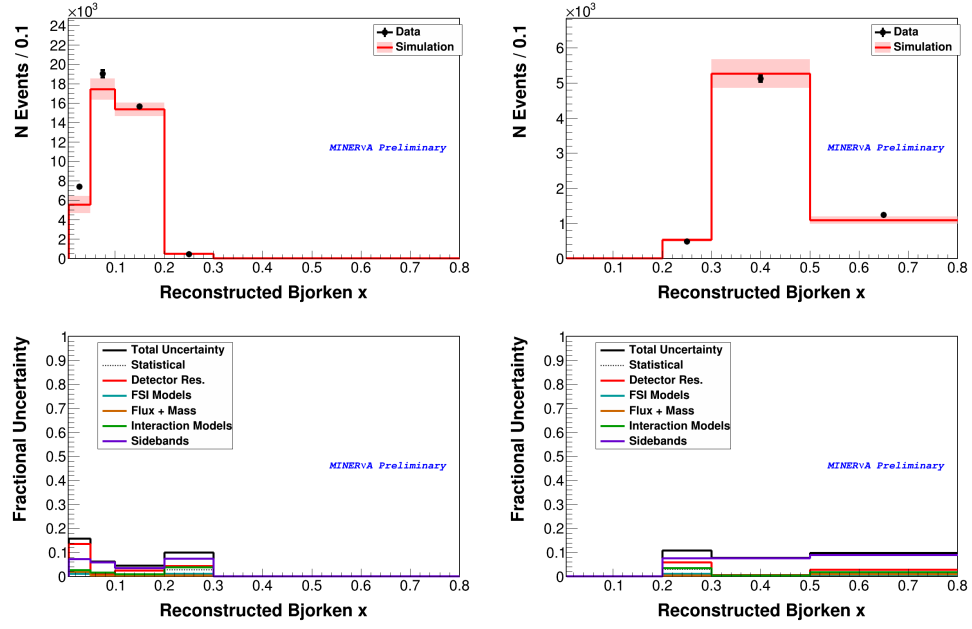
FIG. B.180: The continuum (left) and transition (right) sidebands in x_{bj} after tuning has been applied in lead (top) and their associated data error summaries (bottom).
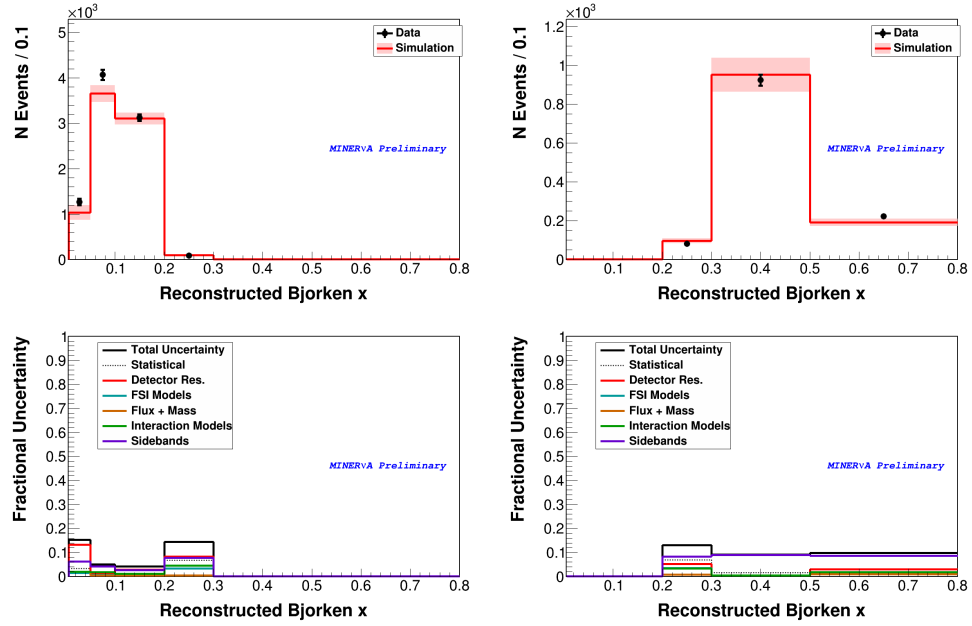
FIG. B.181: The continuum (left) and transition (right) sidebands in x_{bj} after tuning has been applied in carbon (top) and their associated data error summaries (bottom).
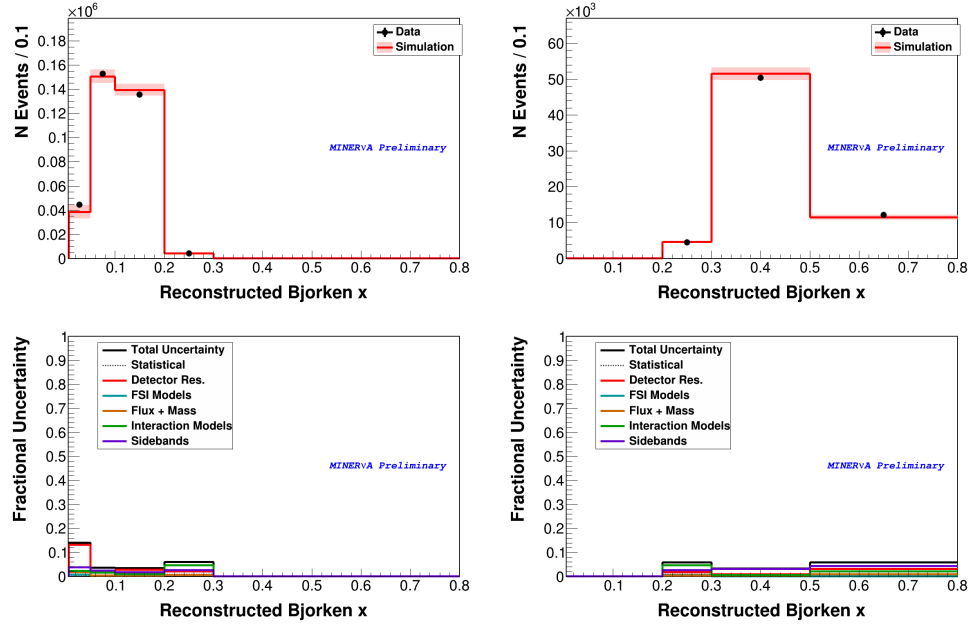
FIG. B.182: The continuum (left) and transition (right) sidebands in x_{bj} after tuning has been applied in tracker (top) and their associated data error summaries (bottom).

FIG. B.183: Data/MC E_μ ratios for the physics sidebands in iron. Before tuning (top), and after tuning (bottom) for continuum (left) and transition (right) sidebands.

361
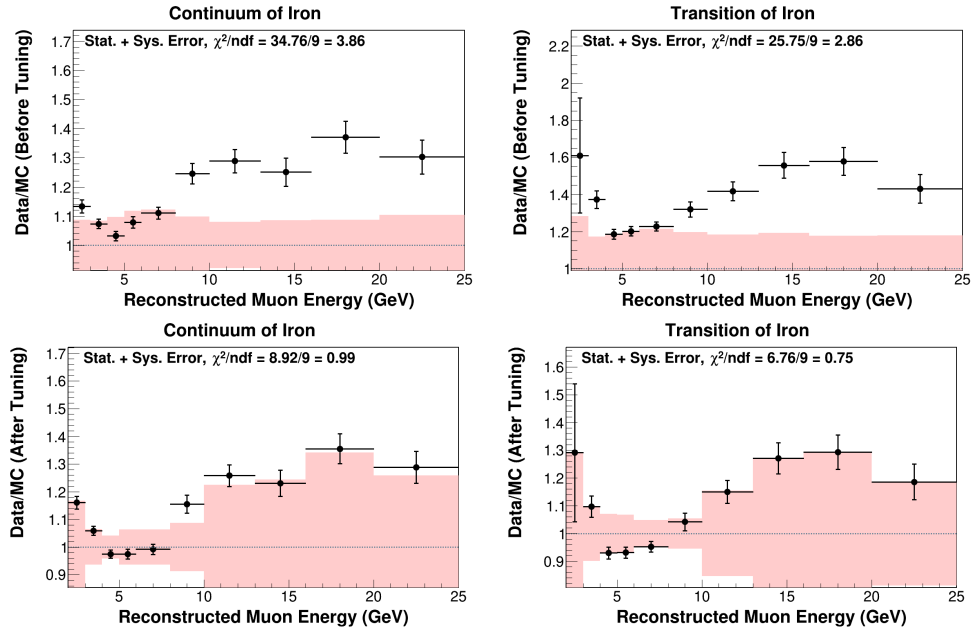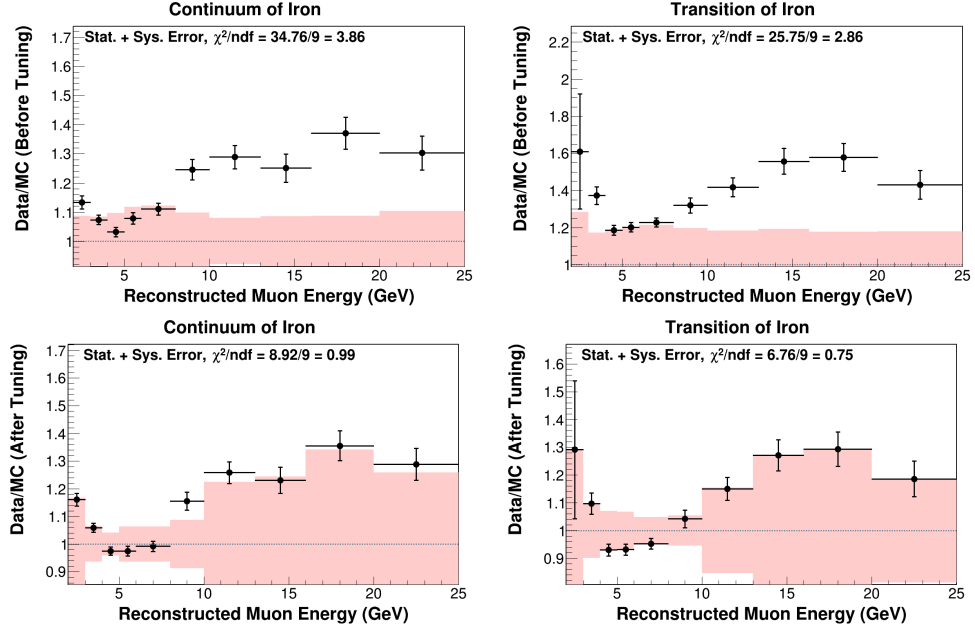
FIG. B.184: Data/MC E_μ ratios for the physics sidebands in lead. Before tuning (top), and after tuning (bottom) for continuum (left) and transition (right) sidebands.
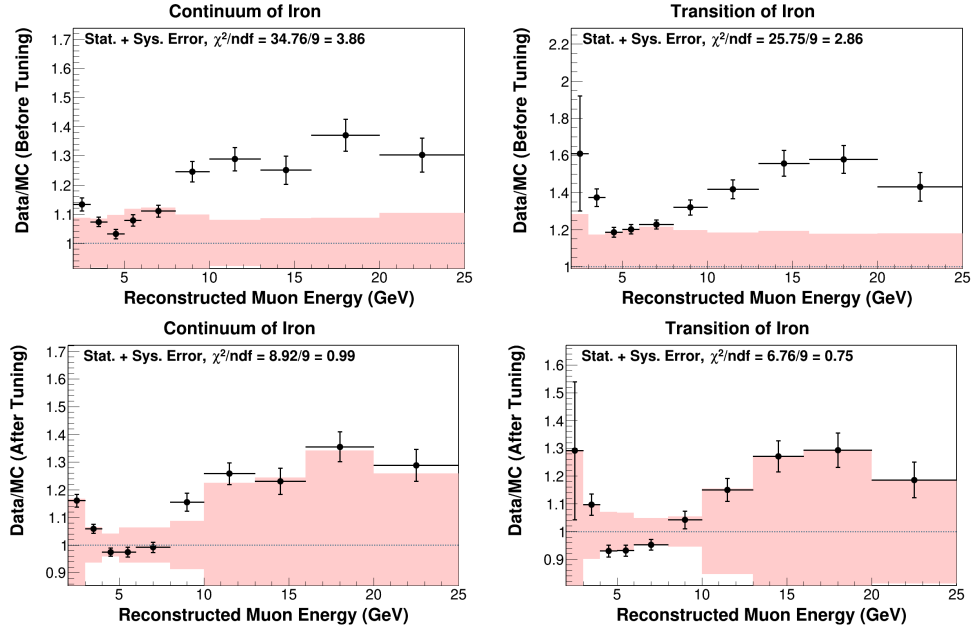
FIG. B.185: Data/MC E_μ ratios for the physics sidebands in carbon. Before tuning (top), and after tuning (bottom) for continuum (left) and transition (right) sidebands.
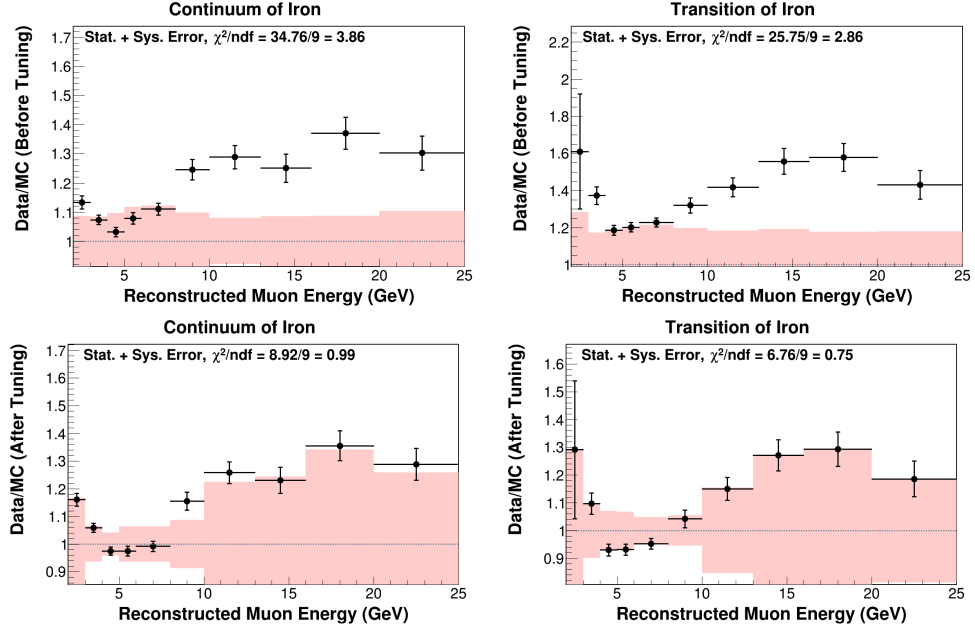
FIG. B.186: Data/MC E_μ ratios for the physics sidebands in tracker. Before tuning (top), and after tuning (bottom) for continuum (left) and transition (right) sidebands.
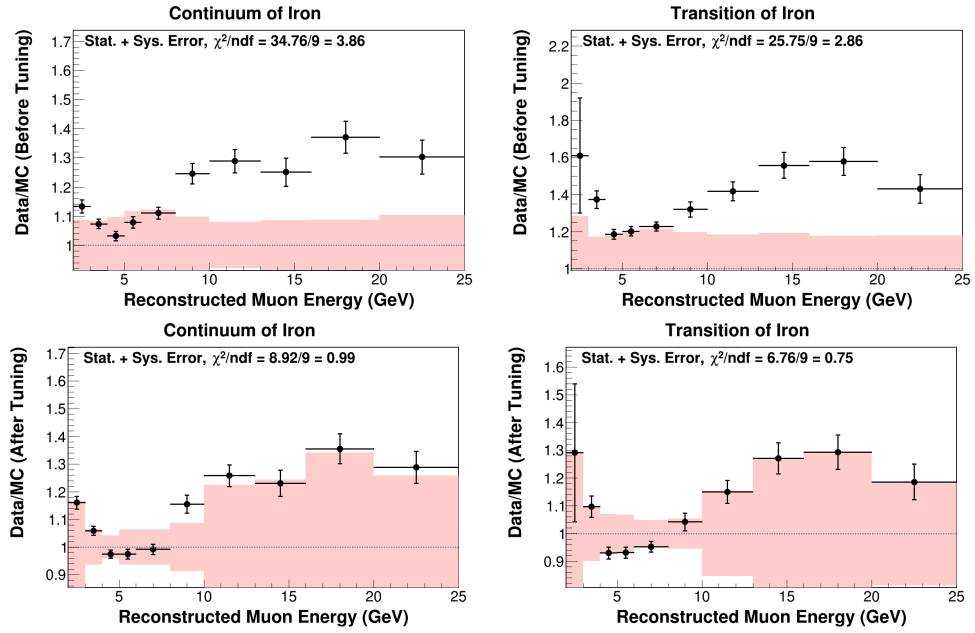
FIG. B.187: Data/MC E_ν ratios for the physics sidebands in iron. Before tuning (top), and after tuning (bottom) for continuum (left) and transition (right) sidebands.
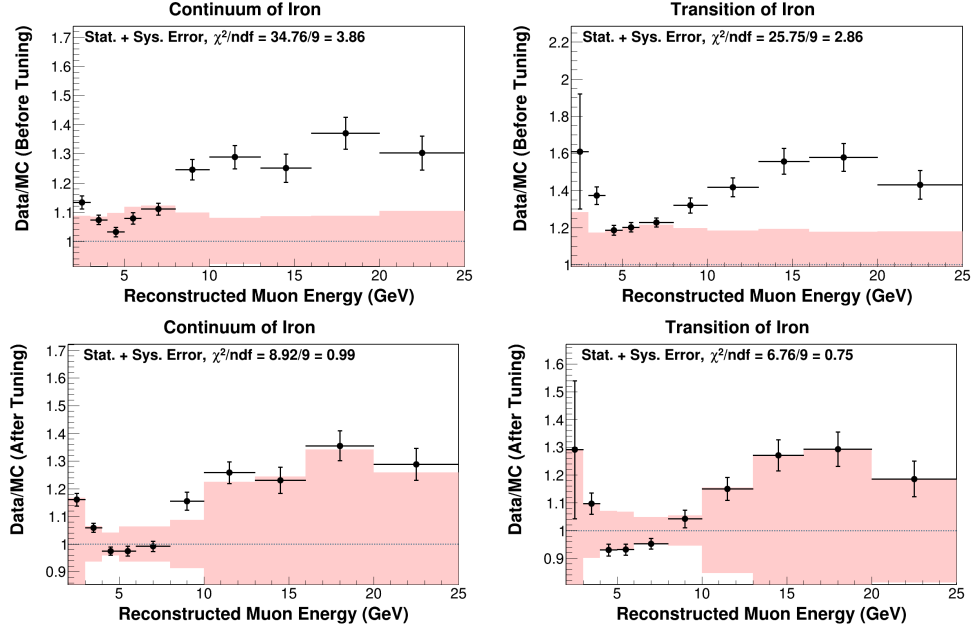
FIG. B.188: Data/MC E_ν ratios for the physics sidebands in lead. Before tuning (top), and after tuning (bottom) for continuum (left) and transition (right) sidebands.
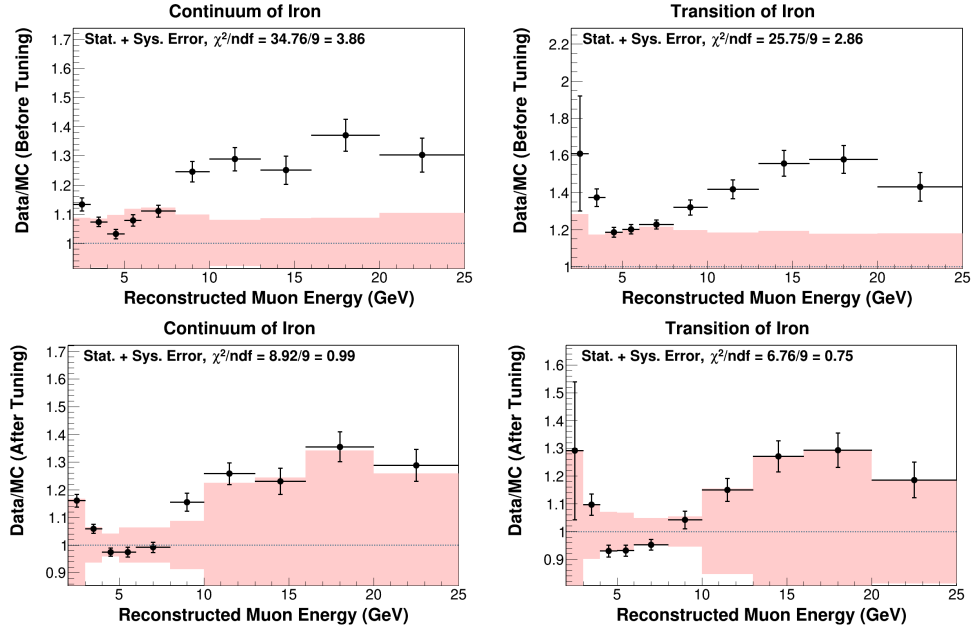
FIG. B.189: Data/MC E_ν ratios for the physics sidebands in carbon. Before tuning (top), and after tuning (bottom) for continuum (left) and transition (right) sidebands.
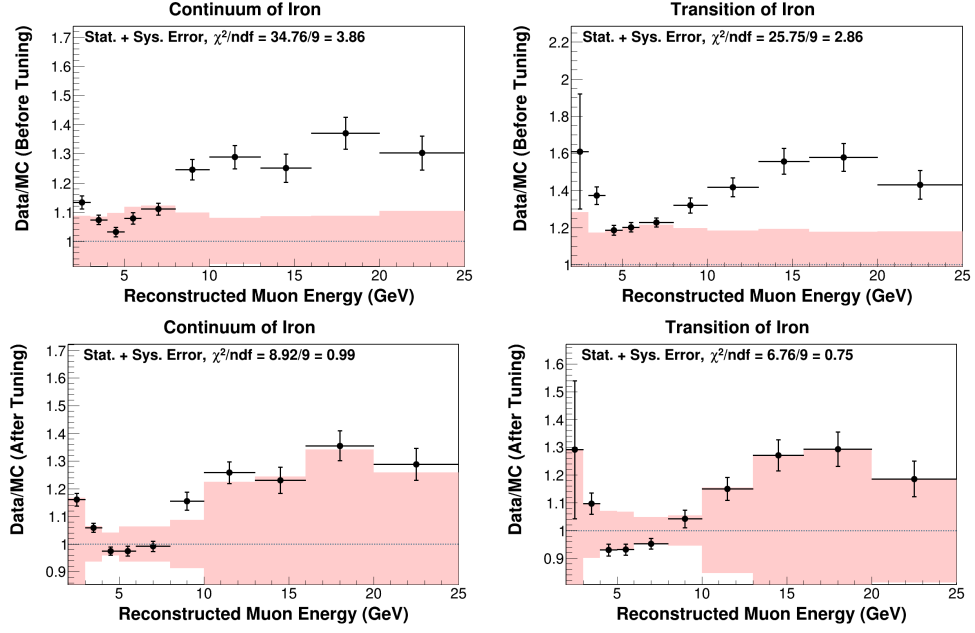
FIG. B.190: Data/MC E_ν ratios for the physics sidebands in tracker. Before tuning (top), and after tuning (bottom) for continuum (left) and transition (right) sidebands.
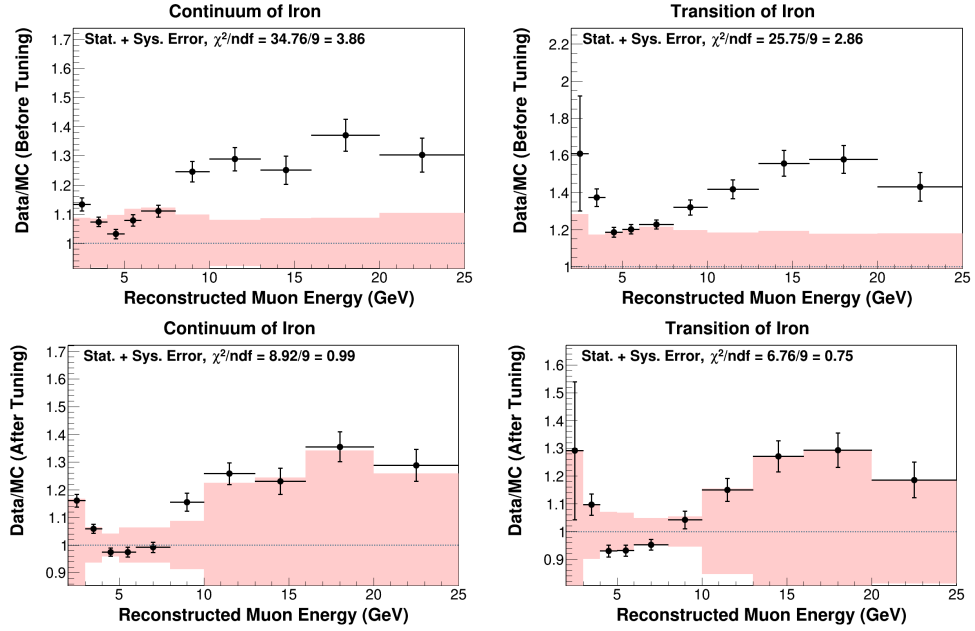
FIG. B.191: Data/MC x_{bj} ratios for the physics sidebands in iron. Before tuning (top), and after tuning (bottom) for continuum (left) and transition (right) sidebands.
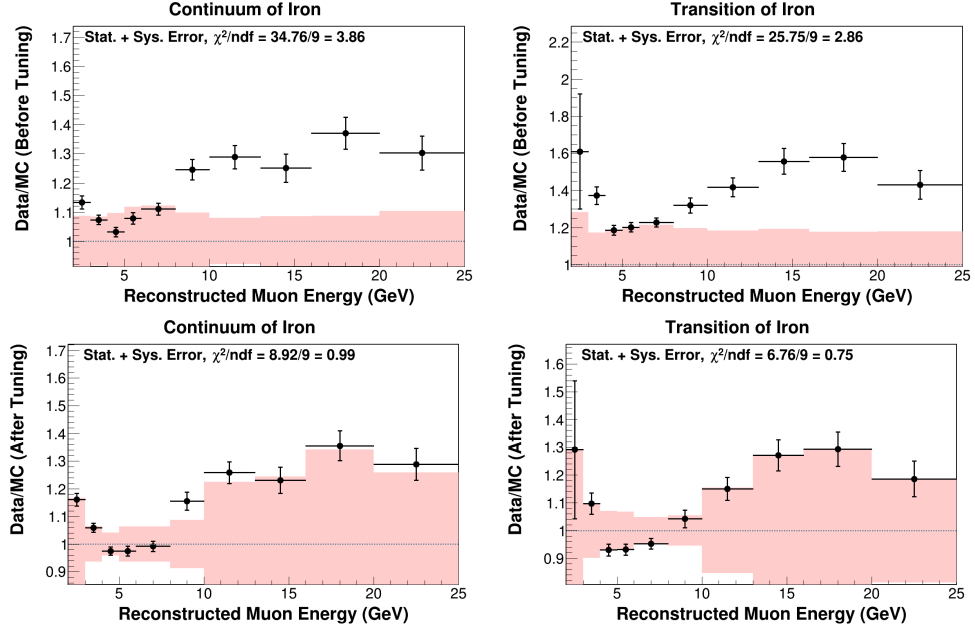
FIG. B.192: Data/MC x_{bj} ratios for the physics sidebands in lead. Before tuning (top), and after tuning (bottom) for continuum (left) and transition (right) sidebands.
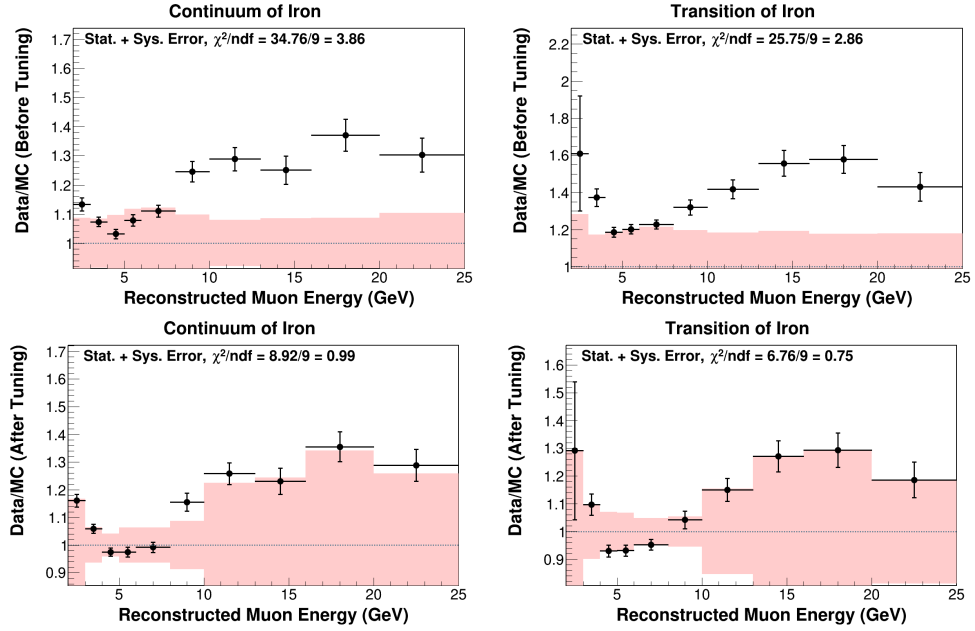
FIG. B.193: Data/MC x_{bj} ratios for the physics sidebands in carbon. Before tuning (top), and after tuning (bottom) for continuum (left) and transition (right) sidebands.
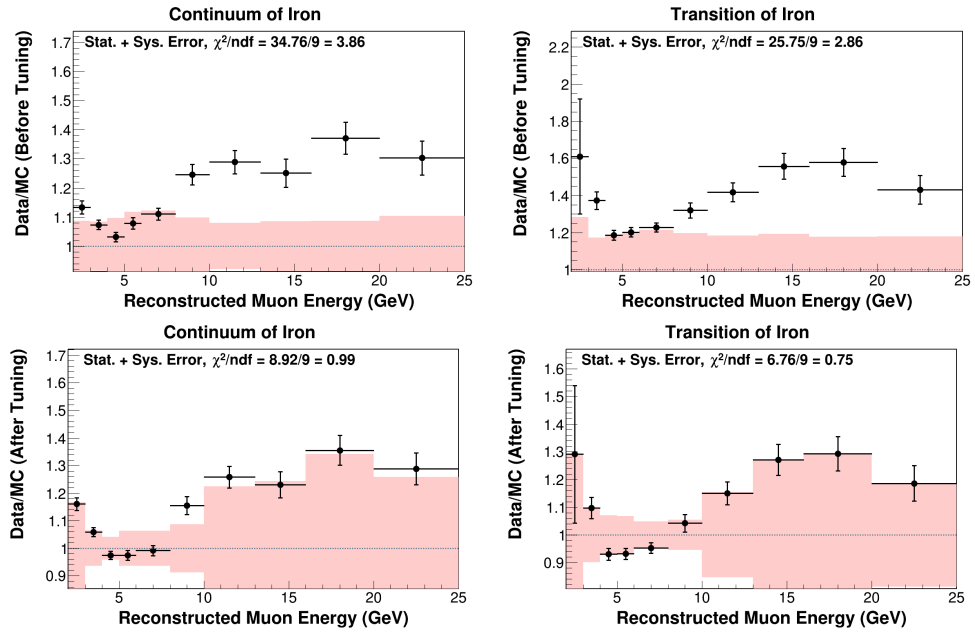
FIG. B.194: Data/MC x_{bj} ratios for the physics sidebands in tracker. Before tuning (top), and after tuning (bottom) for continuum (left) and transition (right) sidebands.

B.4   Scale factor error summaries

B.4.1   Enu
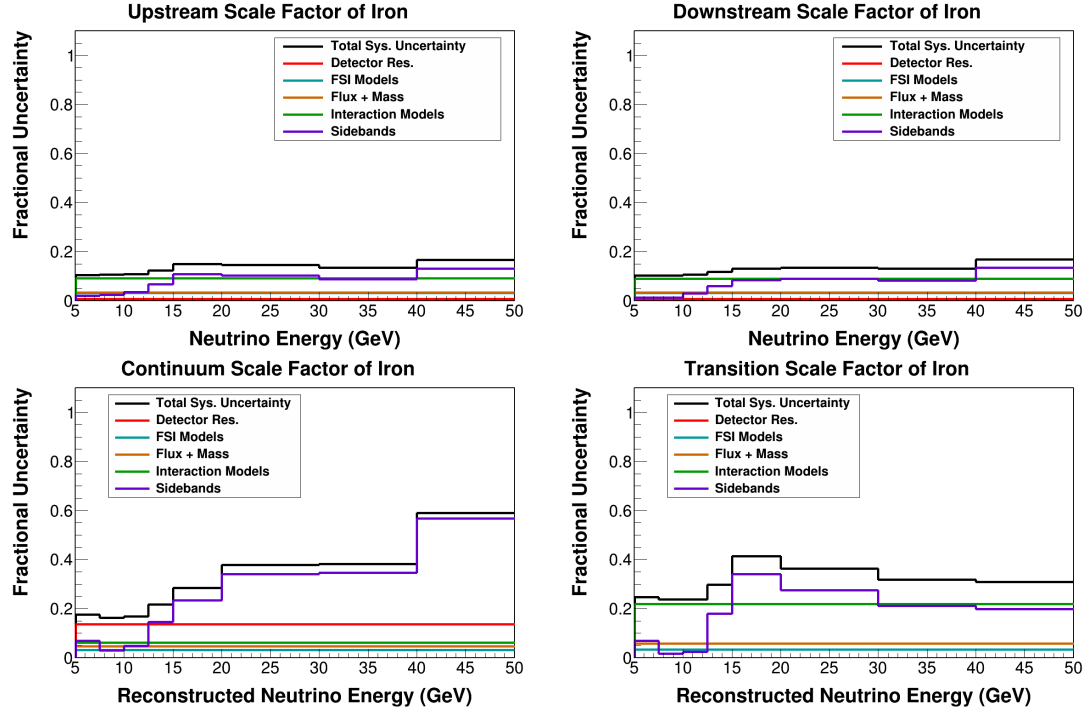
FIG. B.195: Error summaries for the upstream (top left), downstream (top right), continuum (bottom left) and transition (bottom right) E_ν scale factors in iron.
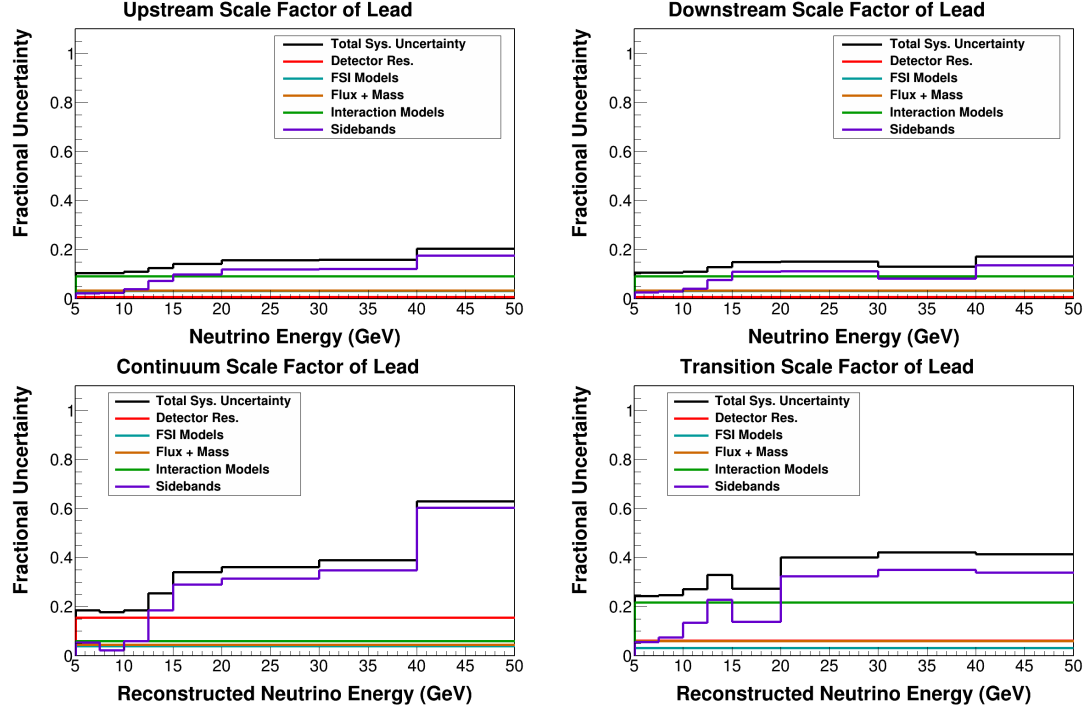
FIG. B.196: Error summaries for the upstream (top left), downstream (top right), continuum (bottom left) and transition (bottom right) E_ν scale factors in lead.
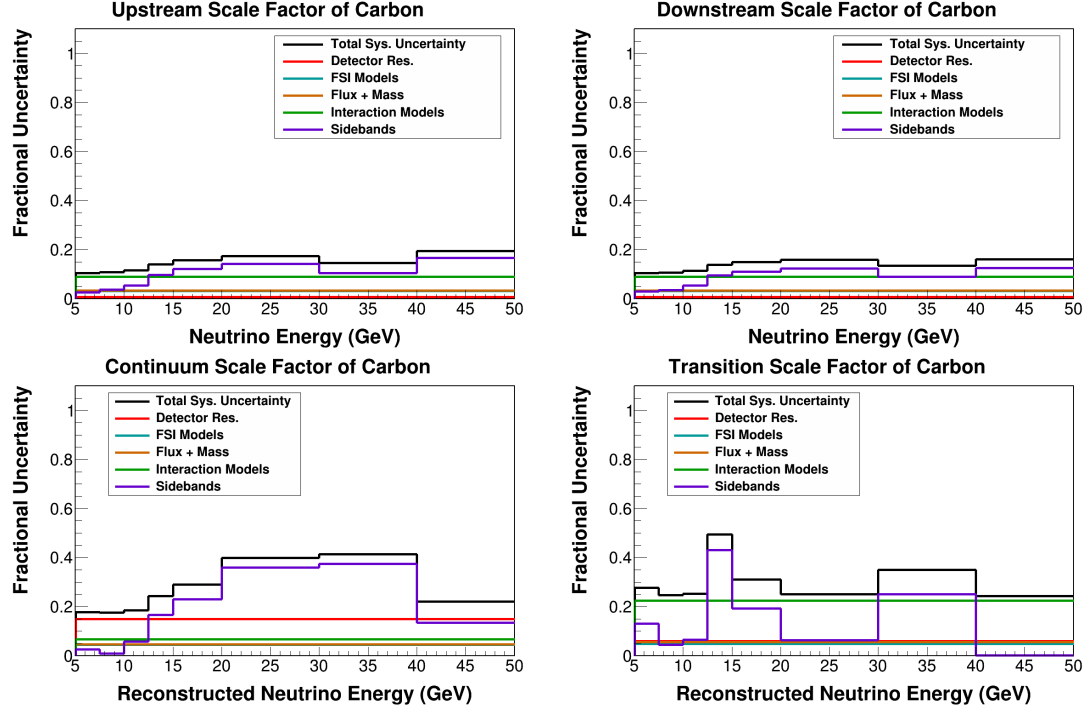
FIG. B.197: Error summaries for the upstream (top left), downstream (top right), continuum (bottom left) and transition (bottom right) E_ν scale factors in carbon.
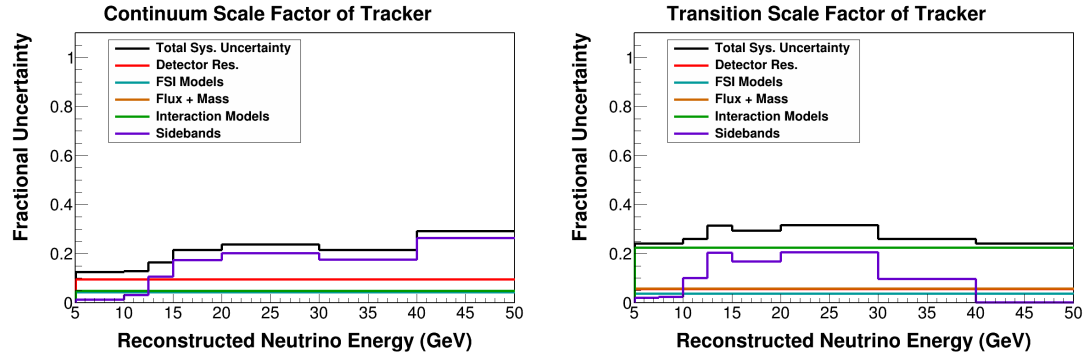
FIG. B.198: Error summaries for continuum (left) and transition (right) E_ν scale factors in tracker.

B.4.2 x
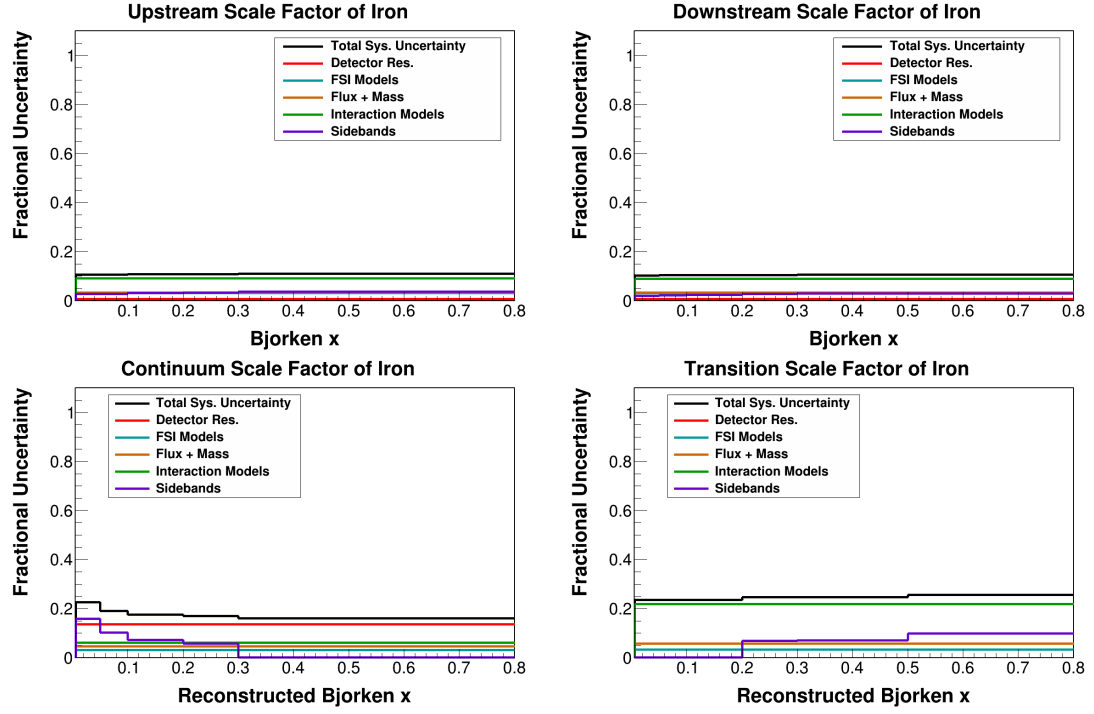
FIG. B.199: Error summaries for the upstream (top left), downstream (top right), continuum (bottom left) and transition (bottom right) x_{bj} scale factors in iron.
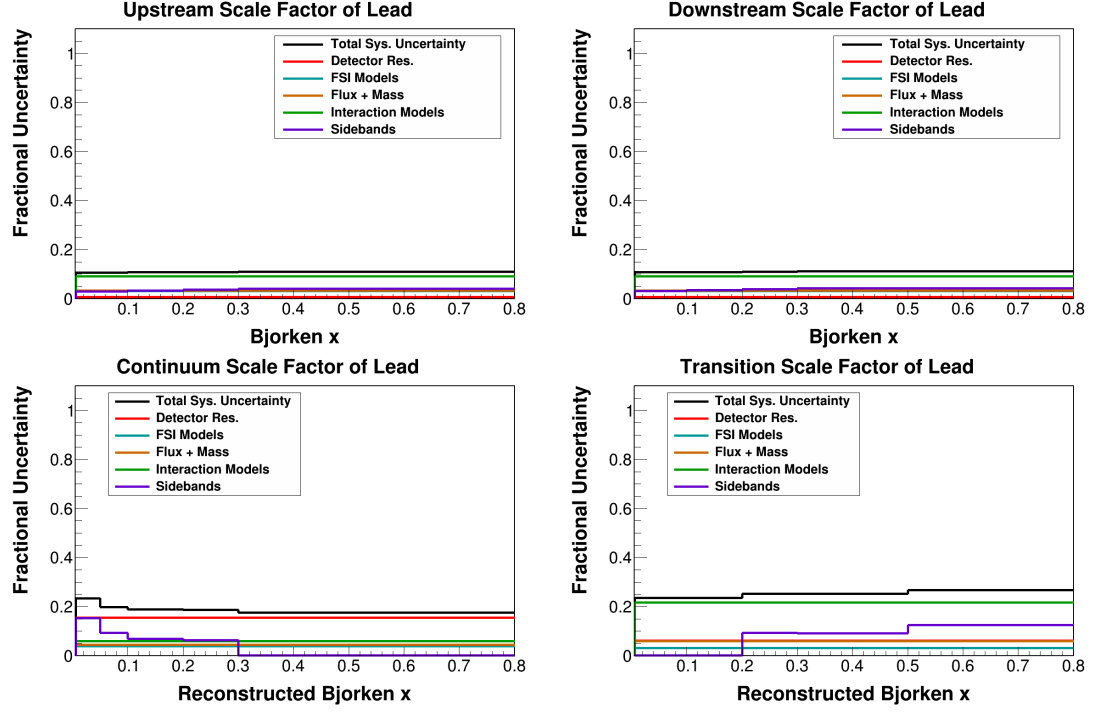
FIG. B.200: Error summaries for the upstream (top left), downstream (top right), continuum (bottom left) and transition (bottom right) x_{bj} scale factors in lead.
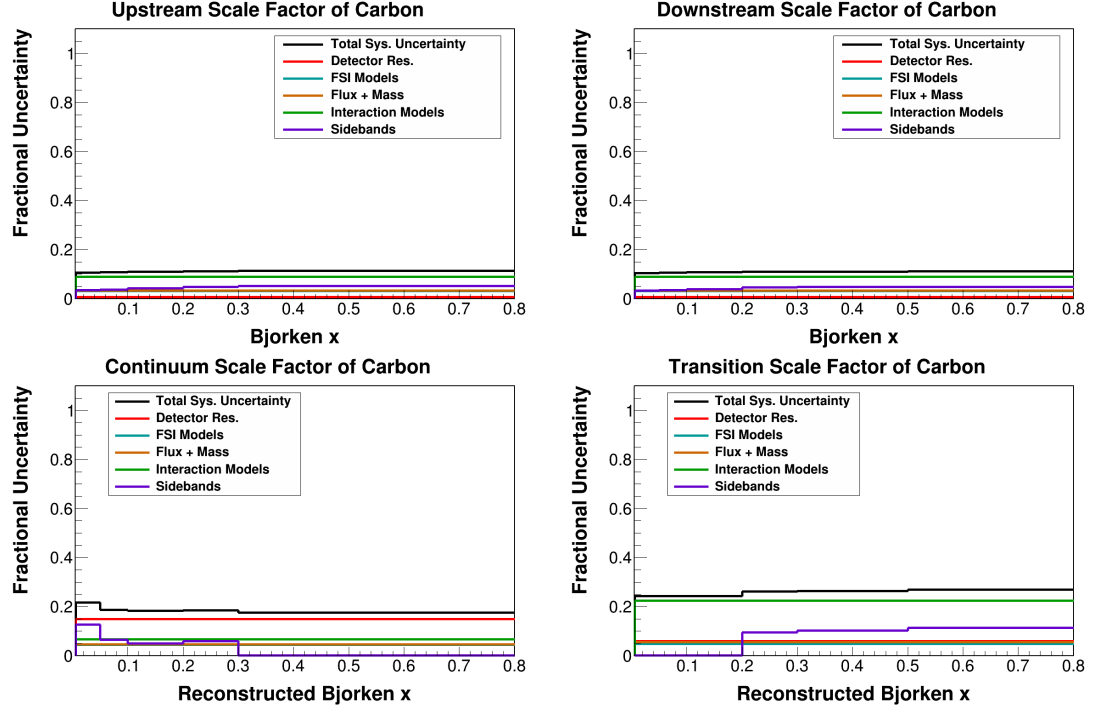
FIG. B.201: Error summaries for the upstream (top left), downstream (top right), continuum (bottom left) and transition (bottom right) x_{bj} scale factors in carbon.
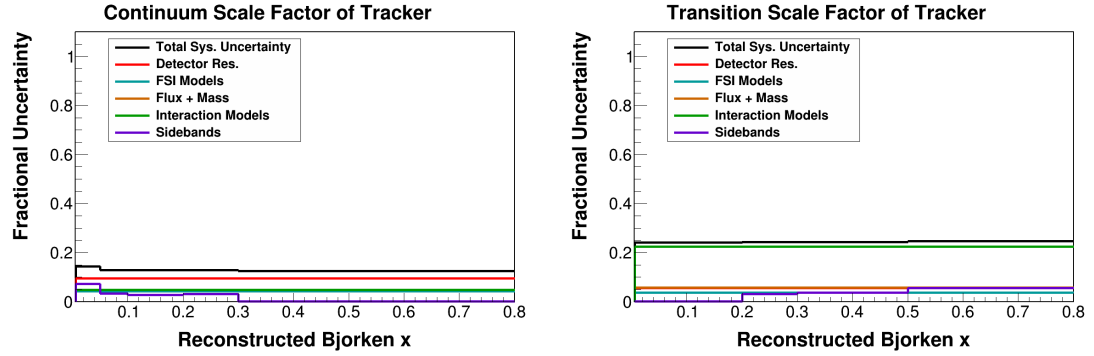
FIG. B.202: Error summaries for continuum (left) and transition (right) x_{bj} scale factors in tracker.

B.4.3 Emu
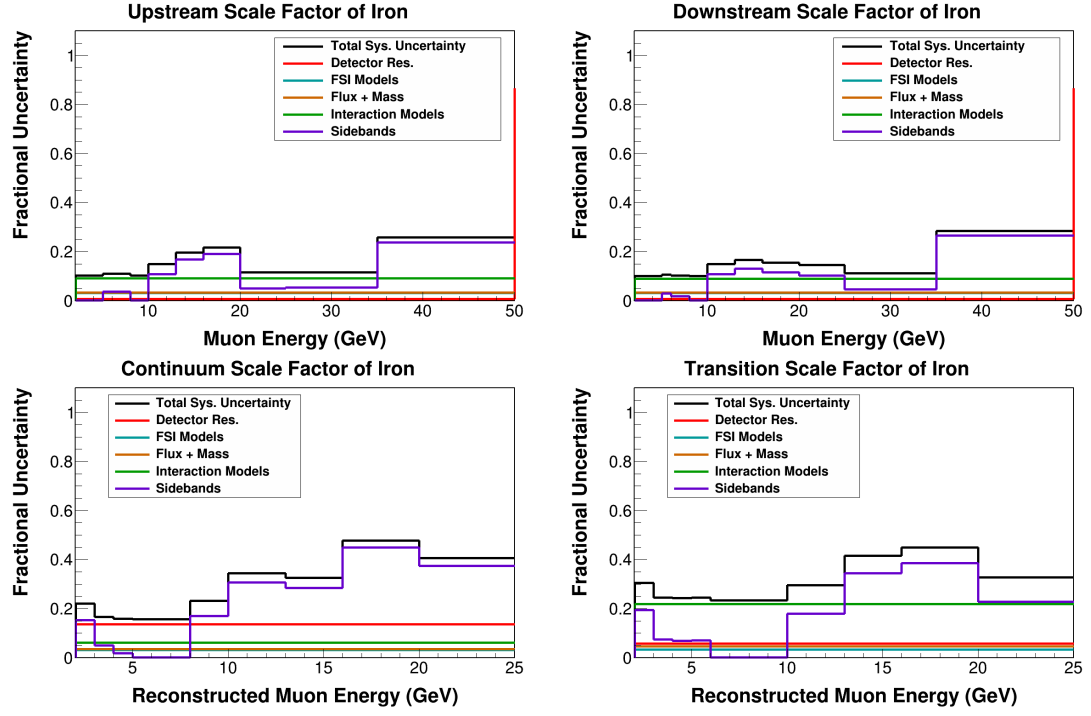
FIG. B.203: Error summaries for the upstream (top left), downstream (top right), continuum (bottom left) and transition (bottom right) E_μ scale factors in iron.
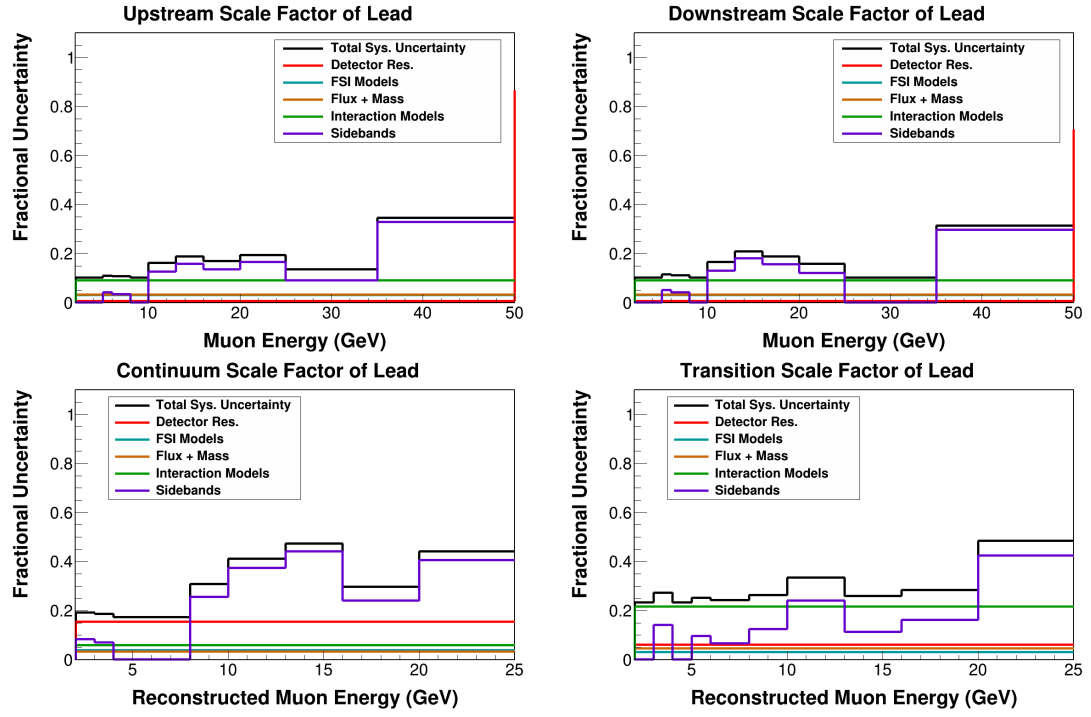
FIG. B.204: Error summaries for the upstream (top left), downstream (top right), continuum (bottom left) and transition (bottom right) E_μ scale factors in lead.
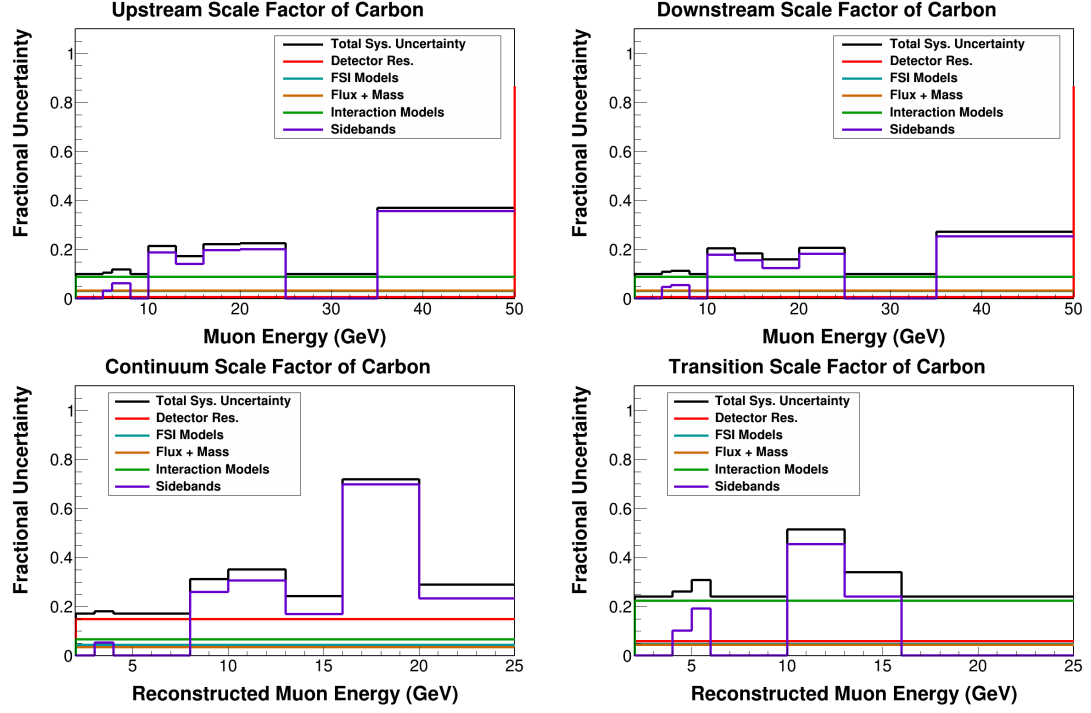
FIG. B.205: Error summaries for the upstream (top left), downstream (top right), continuum (bottom left) and transition (bottom right) E_μ scale factors in carbon.
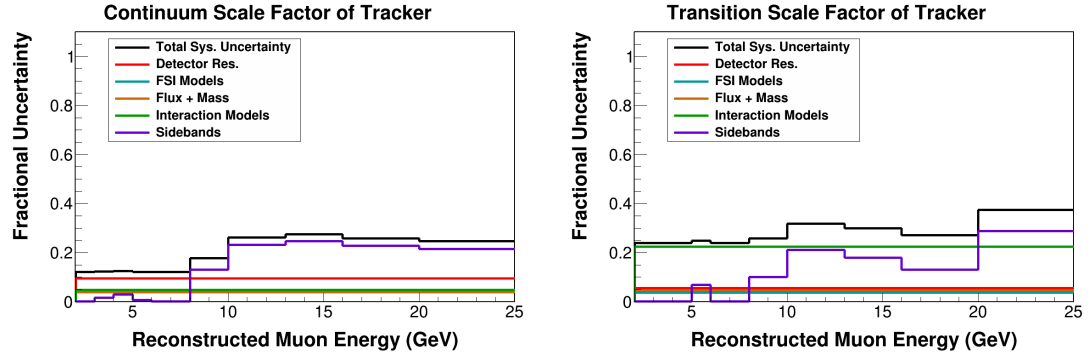
FIG. B.206: Error summaries for continuum (left) and transition (right) E_μ scale factors in tracker.
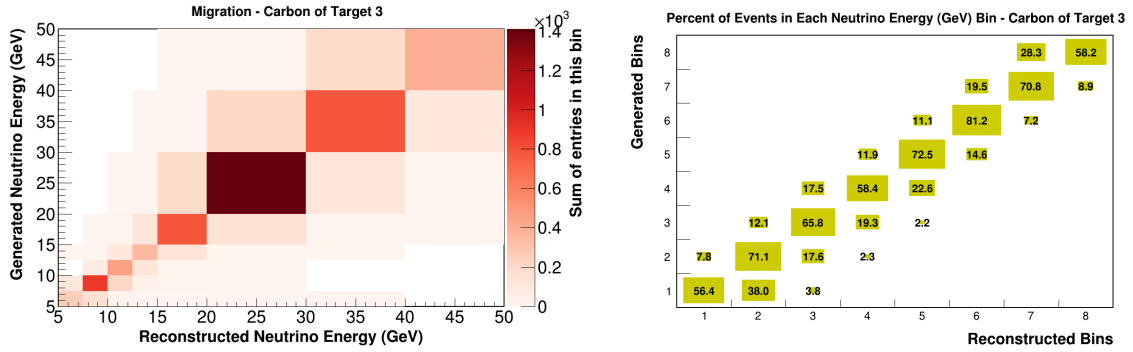
B.5 Migration matrices

B.5.1 Neutrino Energy
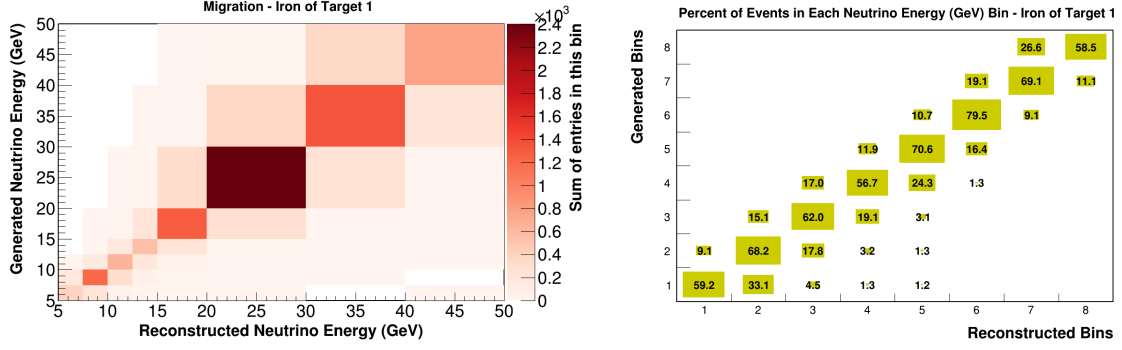
FIG. B.207: Iron of target 1 E_ν migration matrix by population (left), and row normalized percentage of events (right).
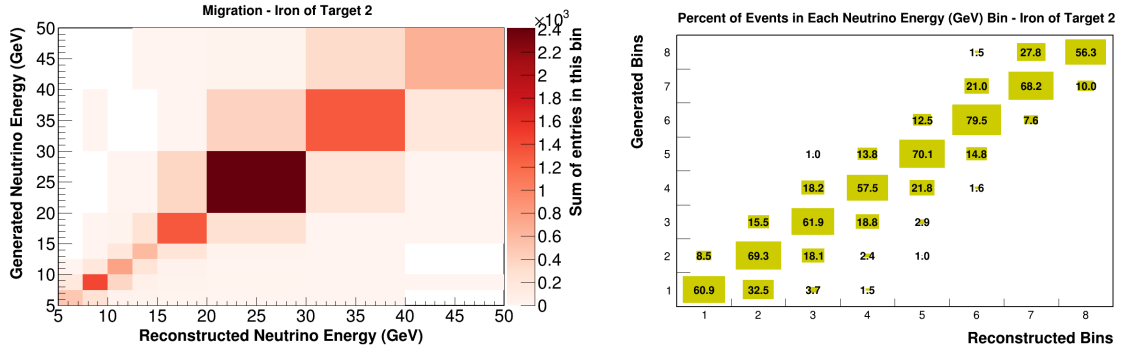
FIG. B.208: Iron of target 2 E_ν migration matrix by population (left), and row normalized percentage of events (right).
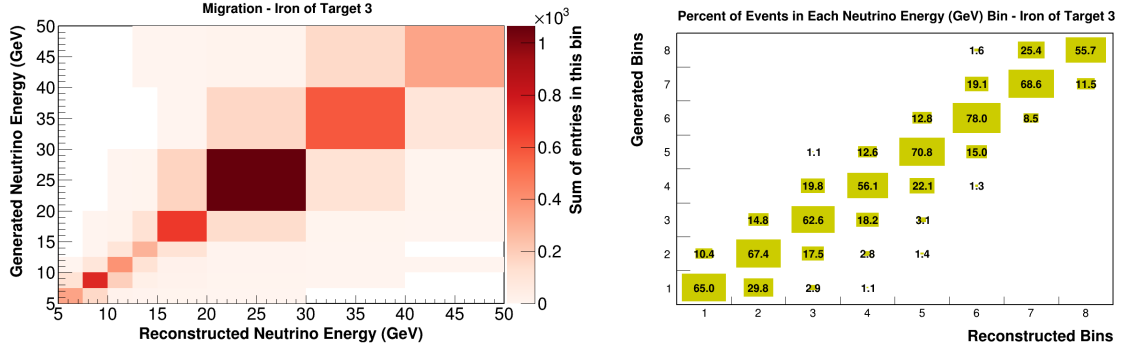
FIG. B.209: Iron of target 3 E_ν migration matrix by population (left), and row normalized percentage of events (right).
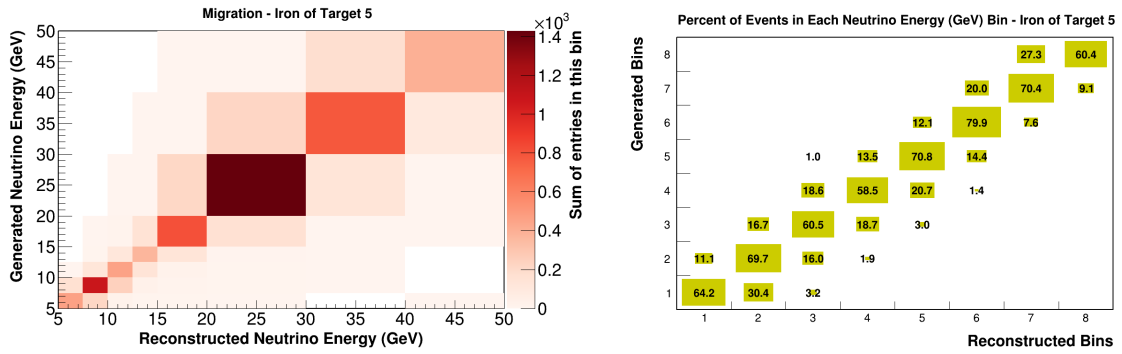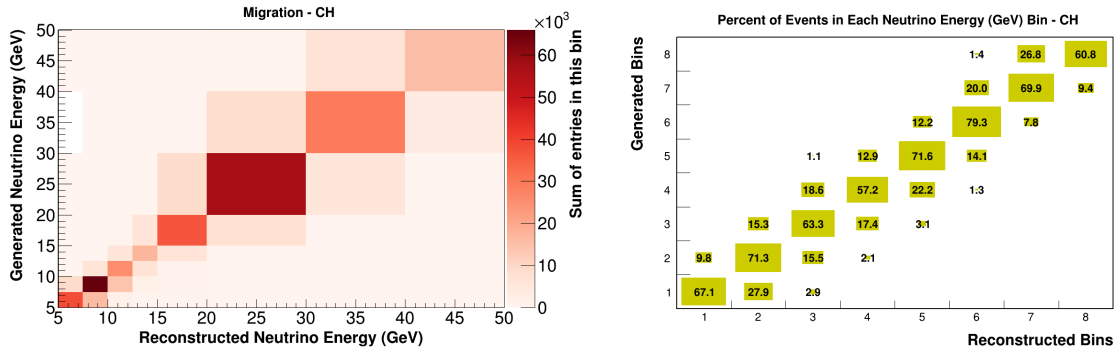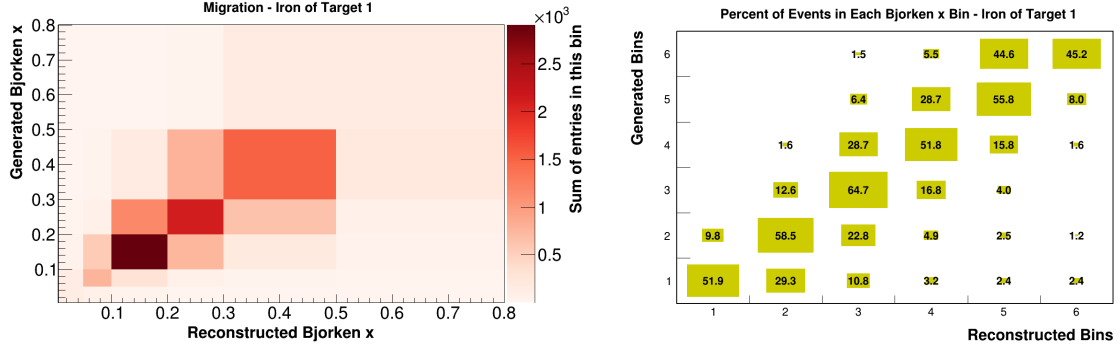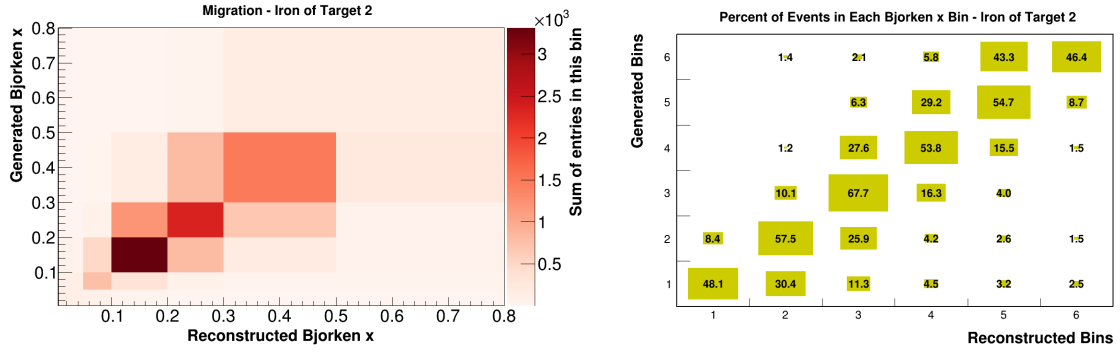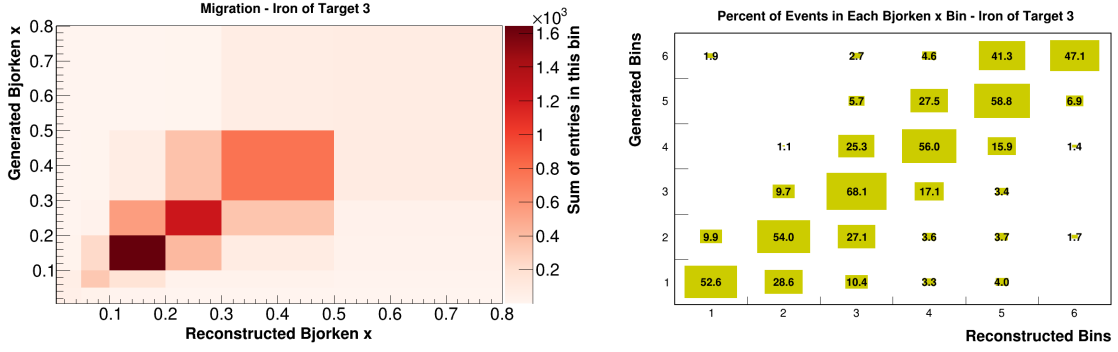

FIG. B.210: Iron of target 5 E_ν migration matrix by population (left), and row normalized percentage of events (right).
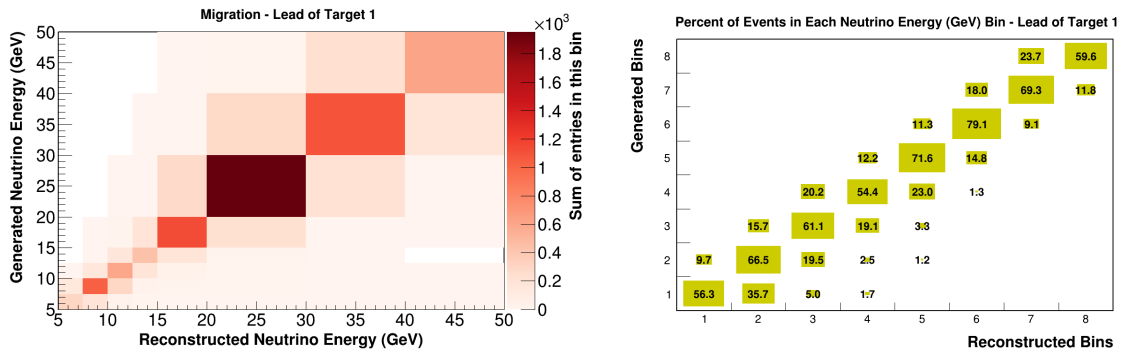
FIG. B.211: Lead of target 1 E_ν migration matrix by population (left), and row normalized percentage of events (right).
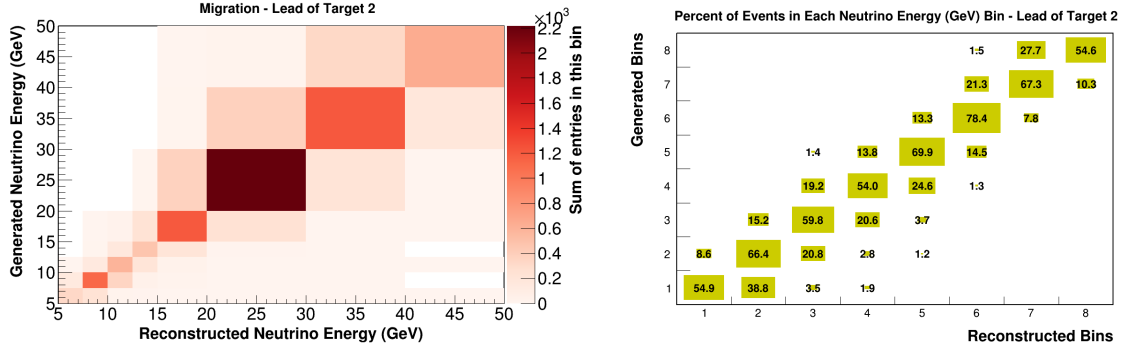
FIG. B.212: Lead of target 2 E_ν migration matrix by population (left), and row normalized percentage of events (right).
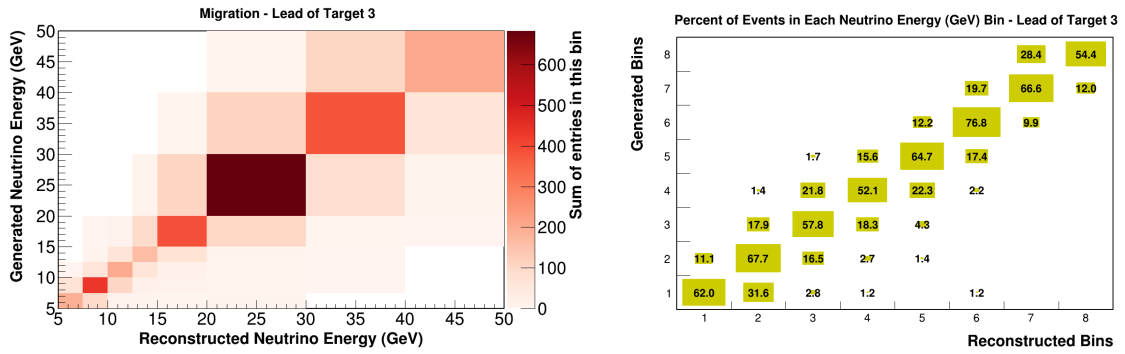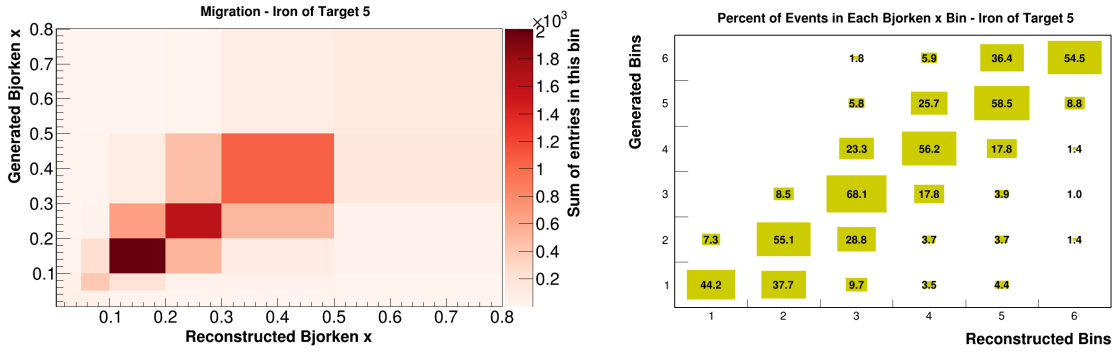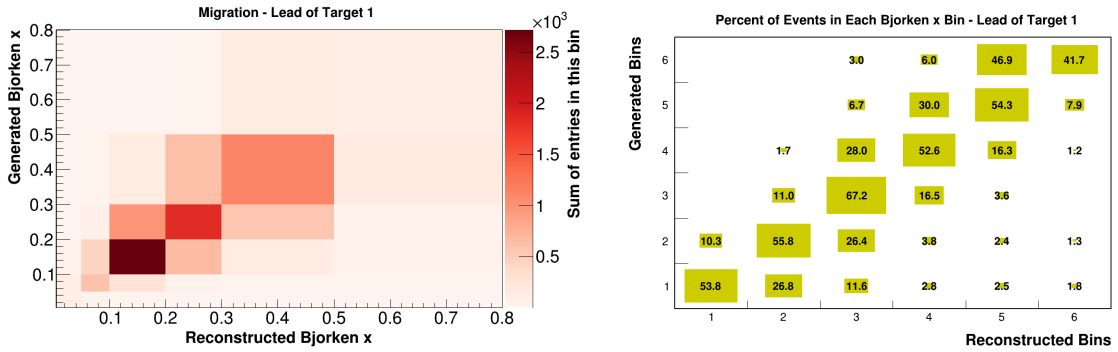

FIG. B.213: Lead of target 3 E_ν migration matrix by population (left), and row normalized percentage of events (right).
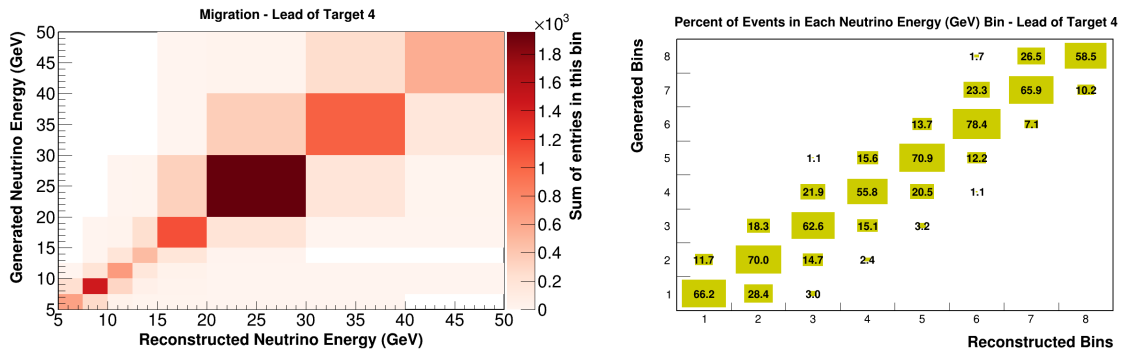
FIG. B.214: Lead of target 4 E_ν migration matrix by population (left), and row normalized percentage of events (right).
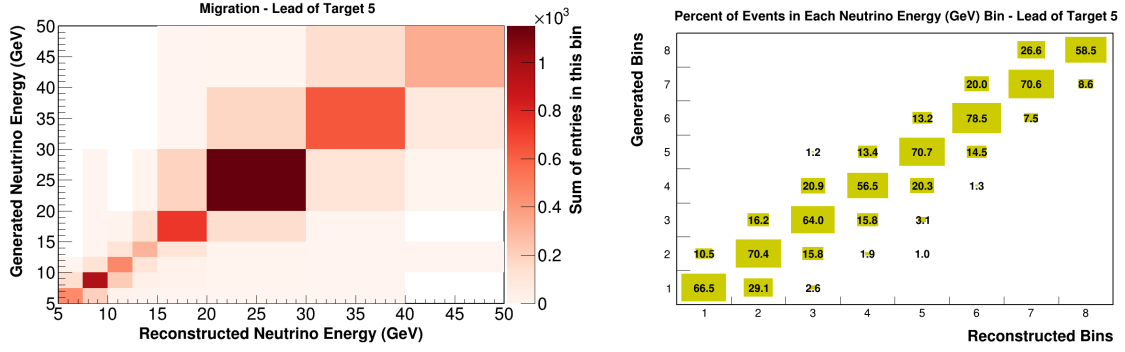
FIG. B.215: Lead of target 5 E_ν migration matrix by population (left), and row normalized percentage of events (right).
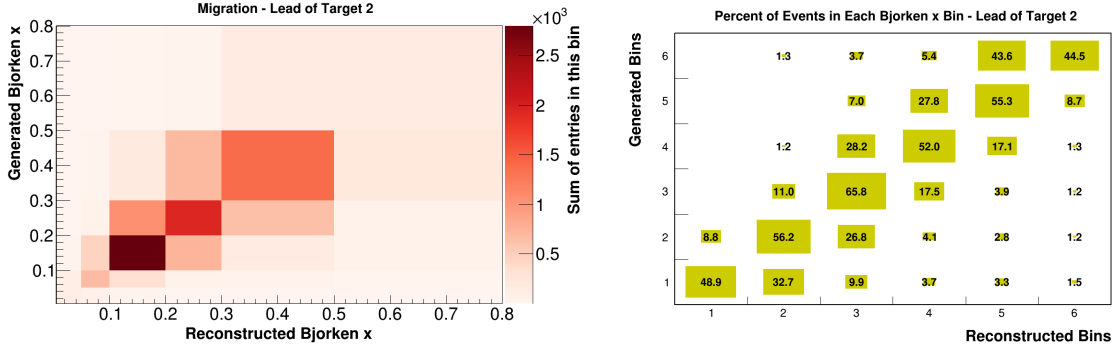

FIG. B.216: Carbon of target 3 E_ν migration matrix by population (left), and row normalized percentage of events (right).

FIG. B.217: All tracker E_ν migration matrix by population (left), and row normalized percentage of events (right).

B.5.2 Bjorken-x

FIG. B.218: Iron of target 1 x_{bj} migration matrix by population (left), and row normalized percentage of events (right).

FIG. B.219: Iron of target 2 x_{bj} migration matrix by population (left), and row normalized percentage of events (right).
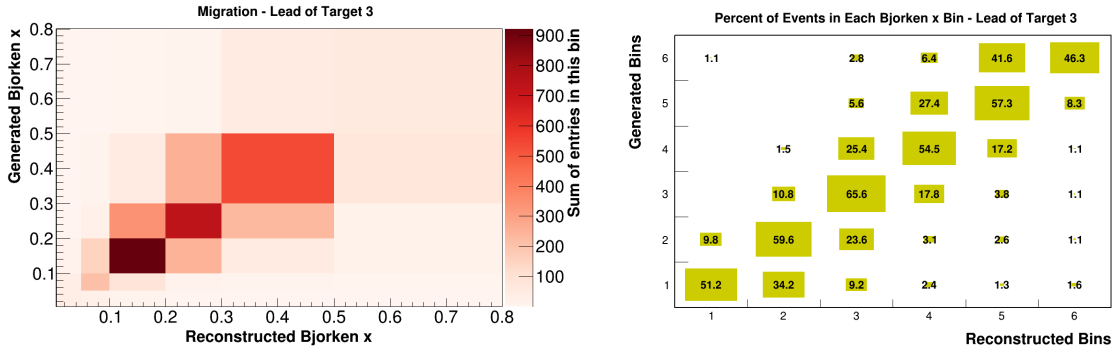
FIG. B.220: Iron of target 3 x_{bj} migration matrix by population (left), and row normalized percentage of events (right).

FIG. B.221: Iron of target 5 x_{bj} migration matrix by population (left), and row normalized percentage of events (right).
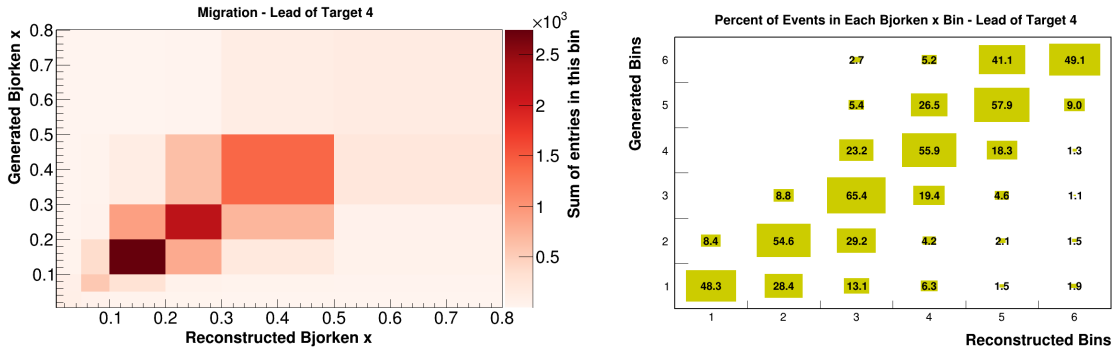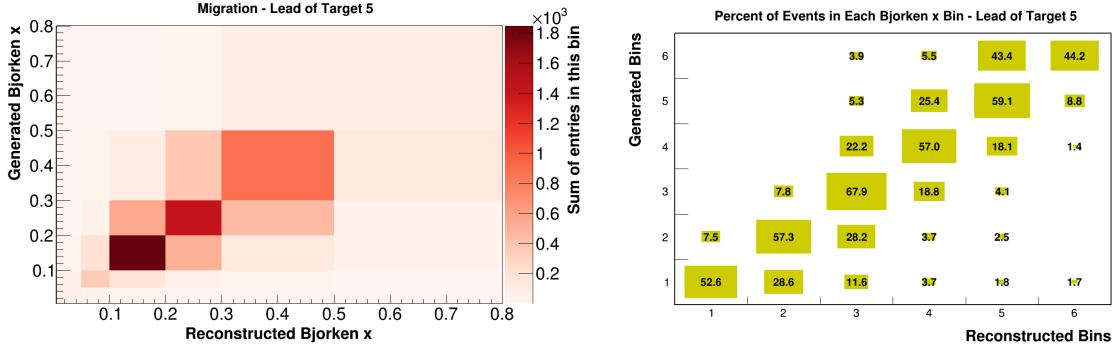

FIG. B.222: Lead of target 1 x_{bj} migration matrix by population (left), and row normalized percentage of events (right).
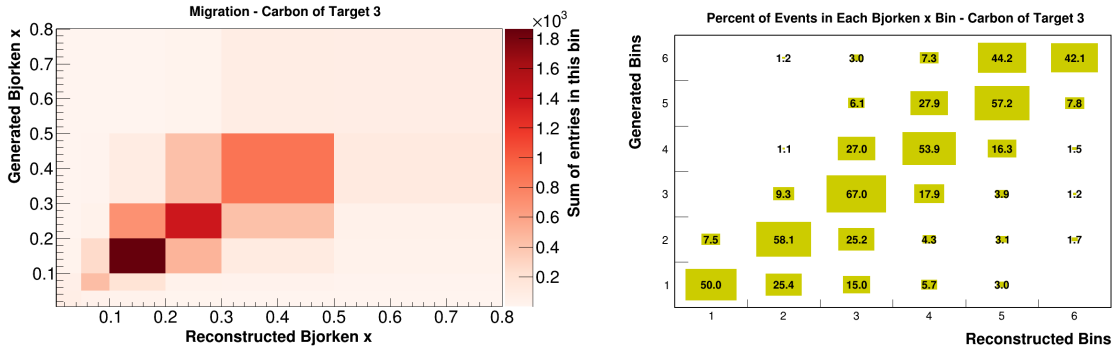
FIG. B.223: Lead of target 2 x_{bj} migration matrix by population (left), and row normalized percentage of events (right).

FIG. B.224: Lead of target 3 x_{bj} migration matrix by population (left), and row normalized percentage of events (right).
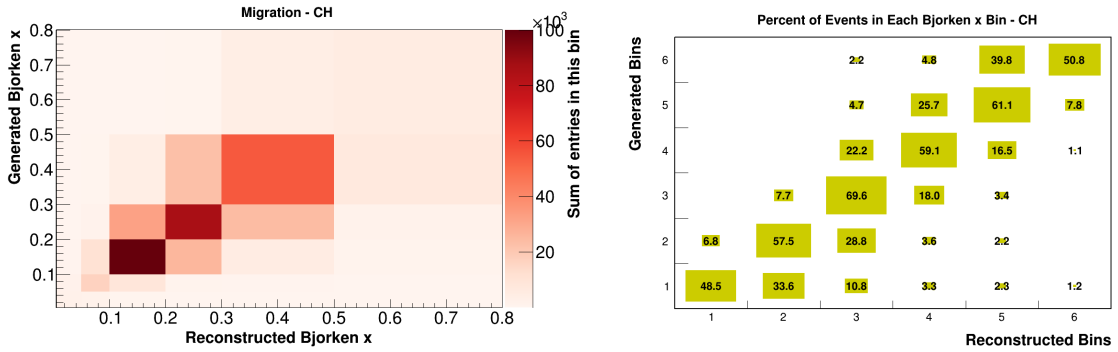

FIG. B.225: Lead of target 4 x_{bj} migration matrix by population (left), and row normalized percentage of events (right).

FIG. B.226: Lead of target 5 x_{bj} migration matrix by population (left), and row normalized percentage of events (right).

FIG. B.227: Carbon of target 3 x_{bj} migration matrix by population (left), and row normalized percentage of events (right).

FIG. B.228: All tracker x_{bj} migration matrix by population (left), and row normalized percentage of events (right).

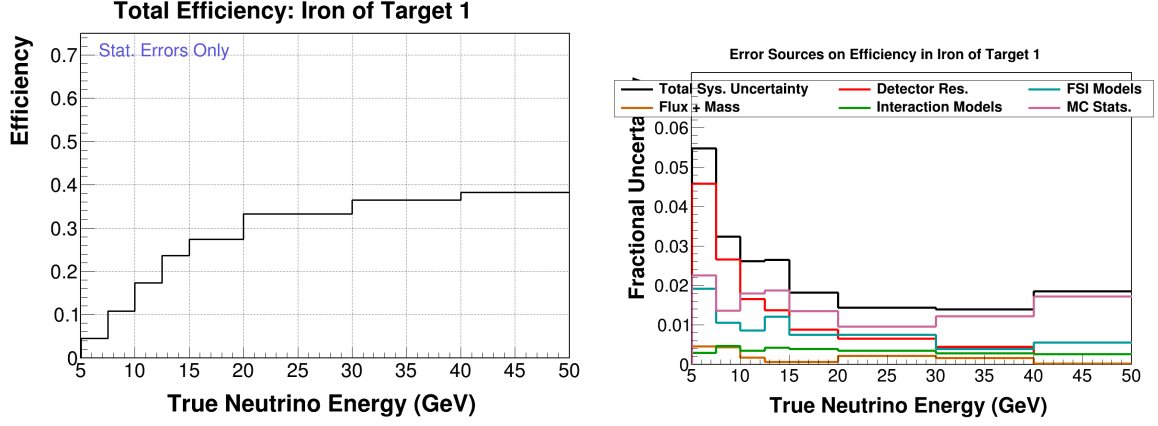# B.6 Efficiency

B.6.1 Neutrino Energy

FIG. B.229: Iron of target 1 E_ν efficiency (left), and MC uncertainty (right).
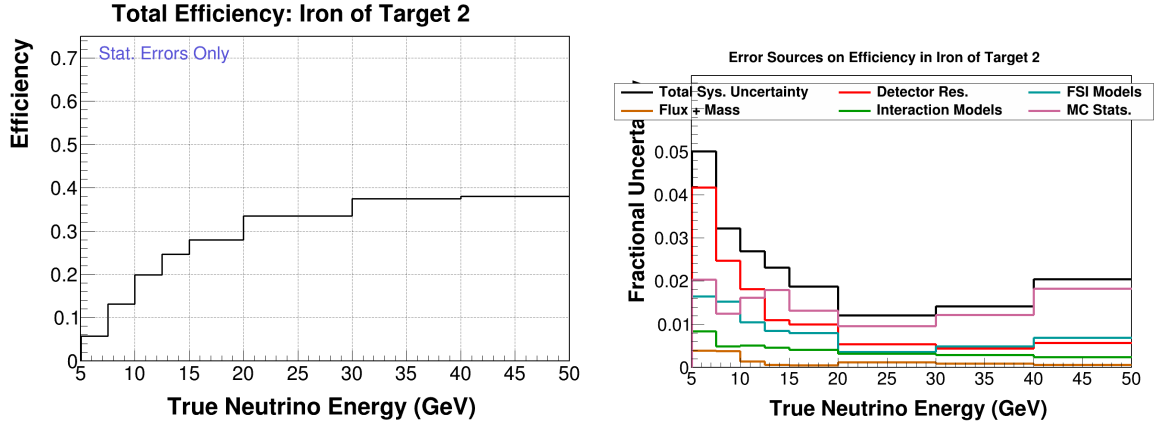

FIG. B.230: Iron of target 2 E_ν efficiency (left), and MC uncertainty (right).
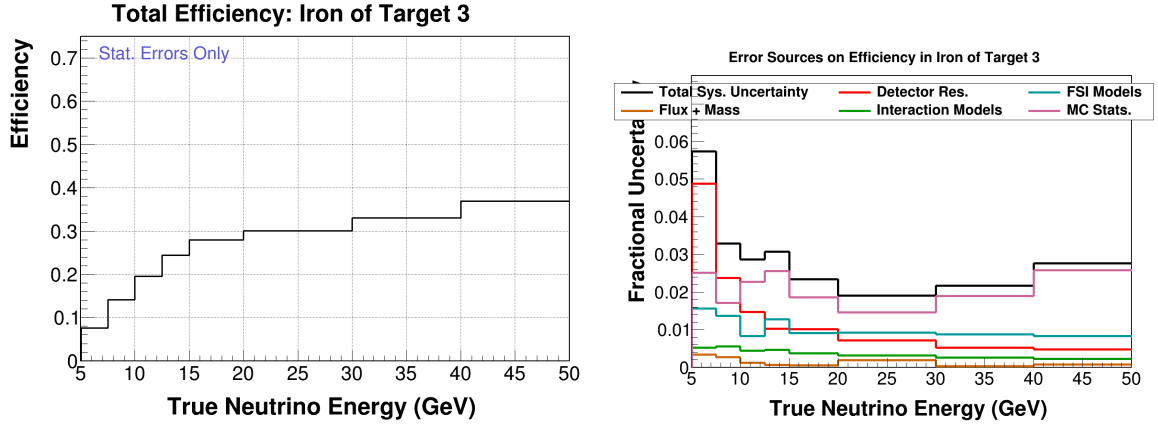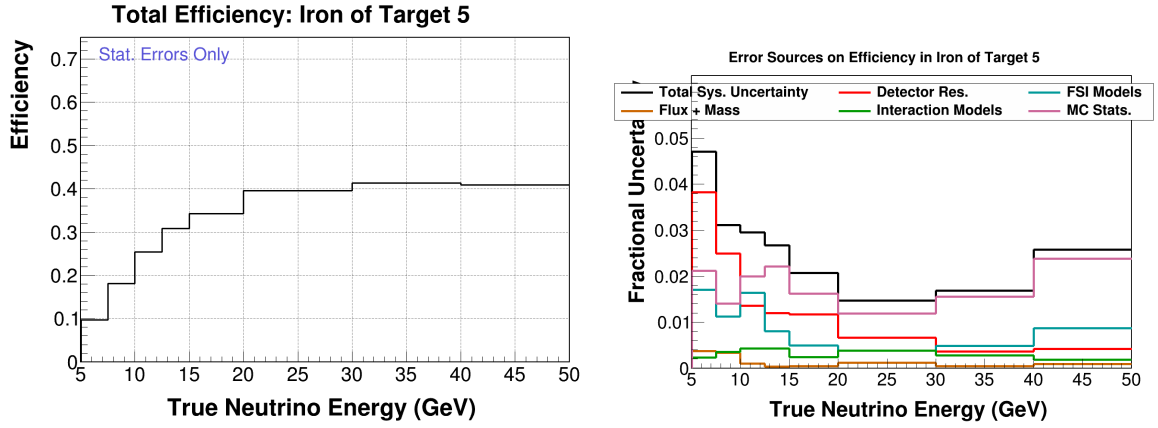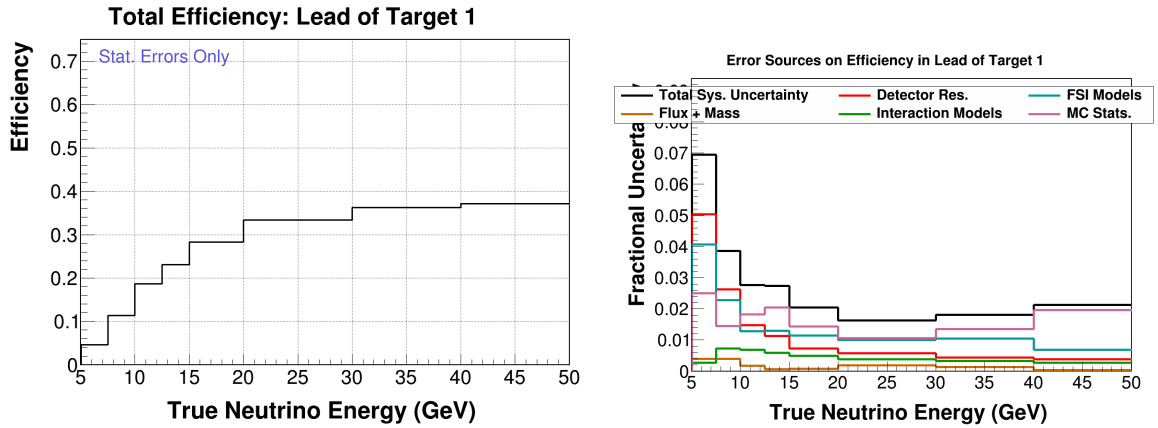
Total Efficiency: Iron of Target 3

FIG. B.231: Iron of target 3 E_ν efficiency (left), and MC uncertainty (right).

Total Efficiency: Iron of Target 5

FIG. B.232: Iron of target 5 E_ν efficiency (left), and MC uncertainty (right).

Total Efficiency: Lead of Target 1

FIG. B.233: Lead of target 1 E_ν efficiency (left), and MC uncertainty (right).
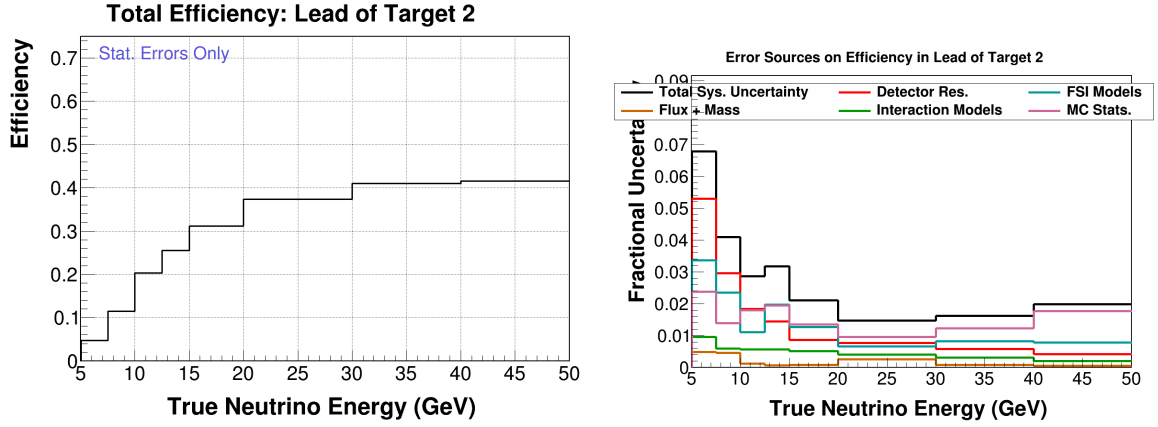
FIG. B.234: Lead of target 2 E_ν efficiency (left), and MC uncertainty (right).
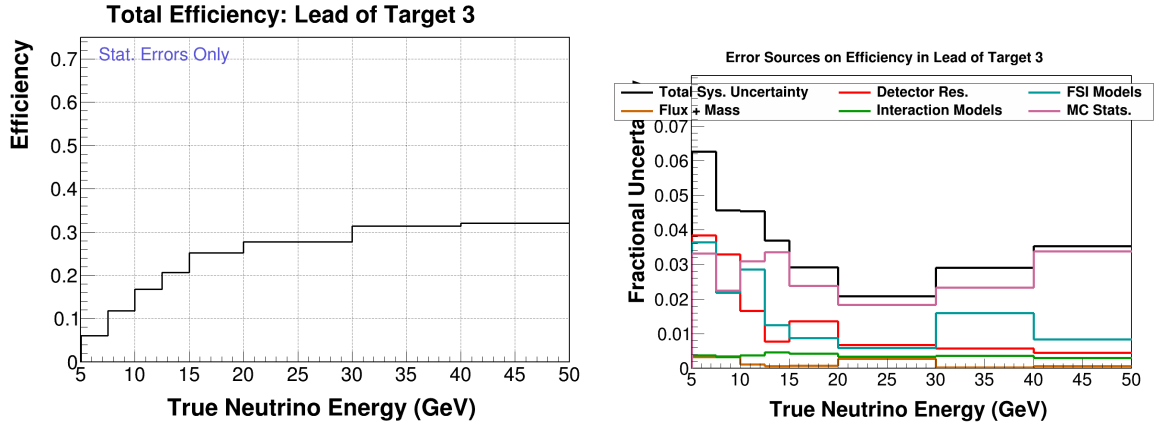

FIG. B.235: Lead of target 3 E_ν efficiency (left), and MC uncertainty (right).
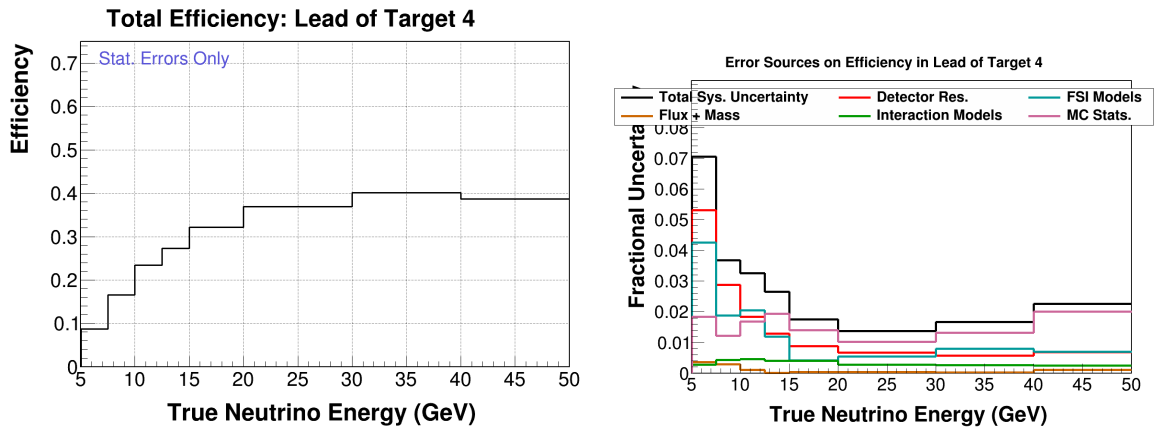

FIG. B.236: Lead of target 4 E_ν efficiency (left), and MC uncertainty (right).
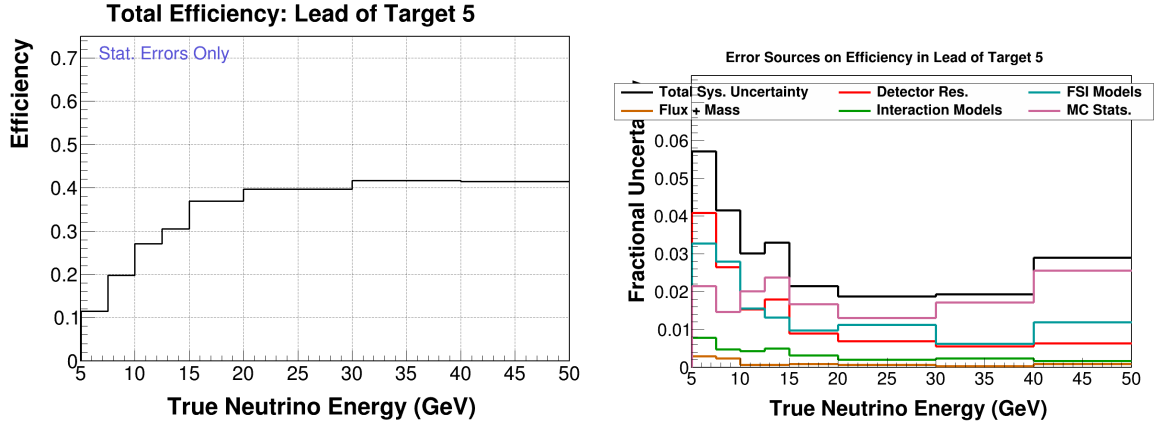
FIG. B.237: Lead of target 5 E_ν efficiency (left), and MC uncertainty (right).
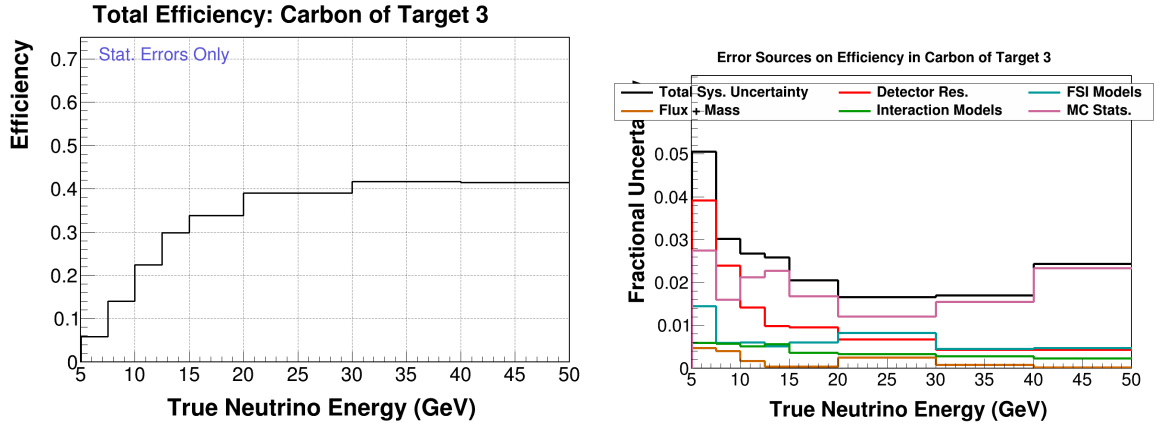

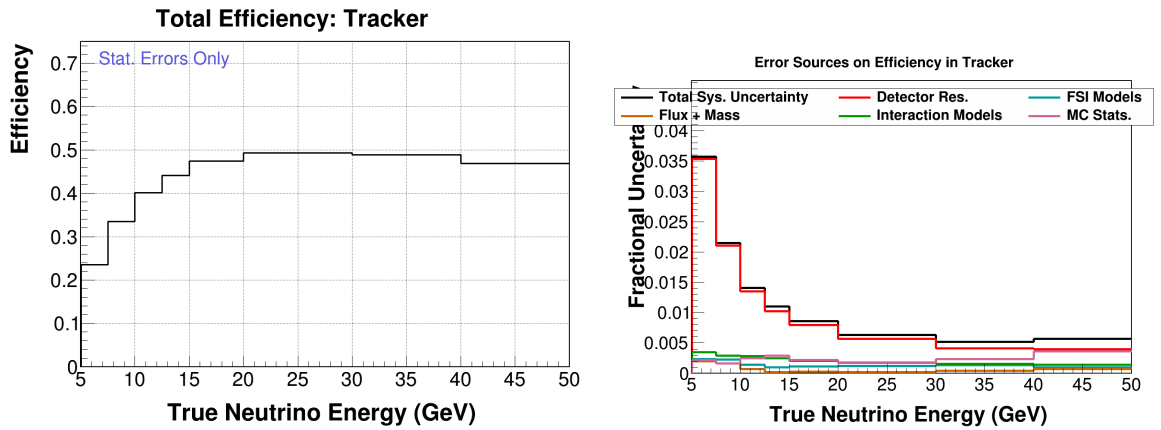FIG. B.238: Carbon of target 3 E_ν efficiency (left), and MC uncertainty (right).

FIG. B.239: All tracker E_ν efficiency (left), and MC uncertainty (right).

B.6.2 Bjorken-x

FIG. B.240: Iron of target 1 x_{bj} efficiency (left), and MC uncertainty (right).

FIG. B.241: Iron of target 2 x_{bj} efficiency (left), and MC uncertainty (right).
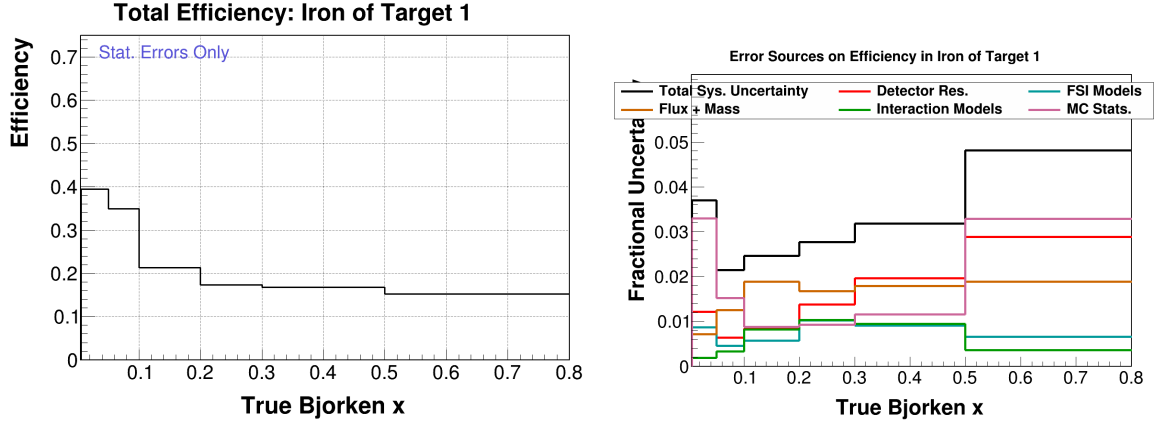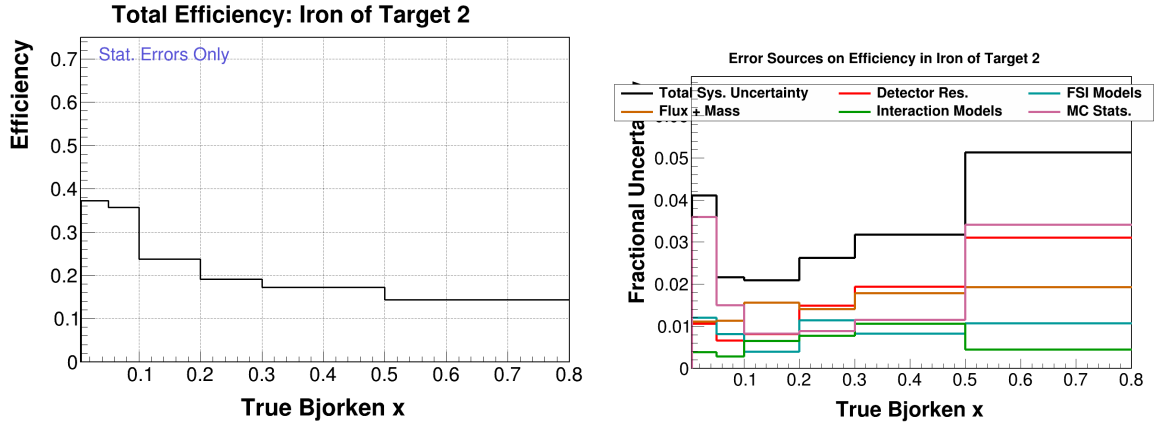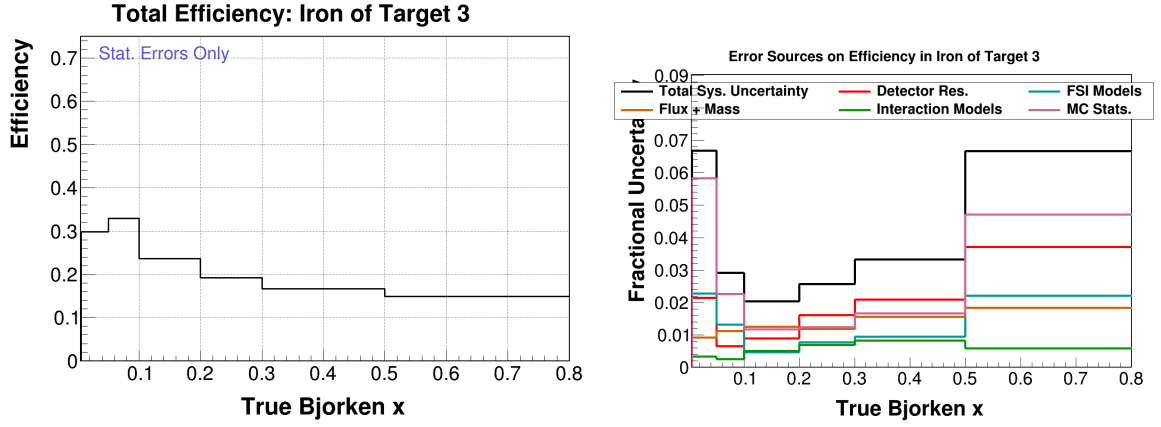
FIG. B.242: Iron of target 3 x_{bj} efficiency (left), and MC uncertainty (right).

FIG. B.243: Iron of target 5 x_{bj} efficiency (left), and MC uncertainty (right).

FIG. B.244: Lead of target 1 x_{bj} efficiency (left), and MC uncertainty (right).

FIG. B.245: Lead of target 2 x_{bj} efficiency (left), and MC uncertainty (right).
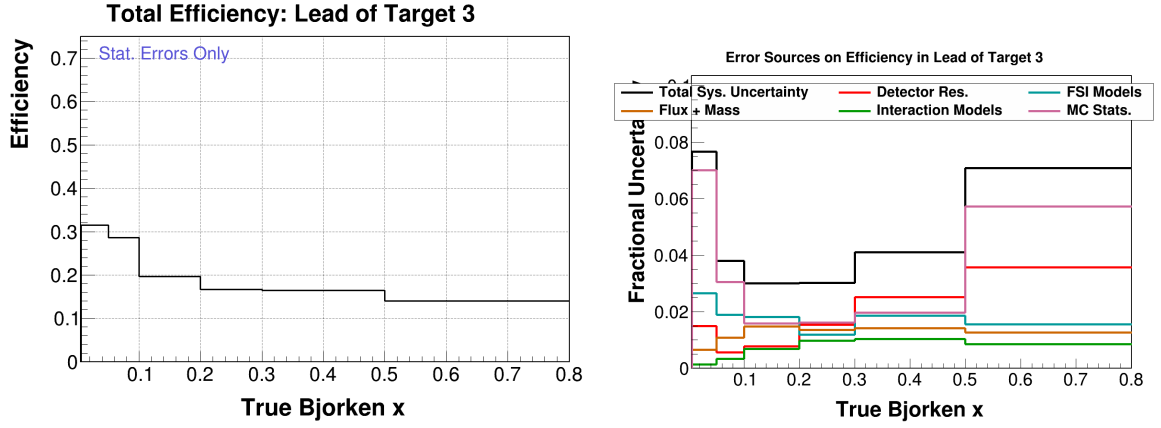
FIG. B.246: Lead of target 3 x_{bj} efficiency (left), and MC uncertainty (right).
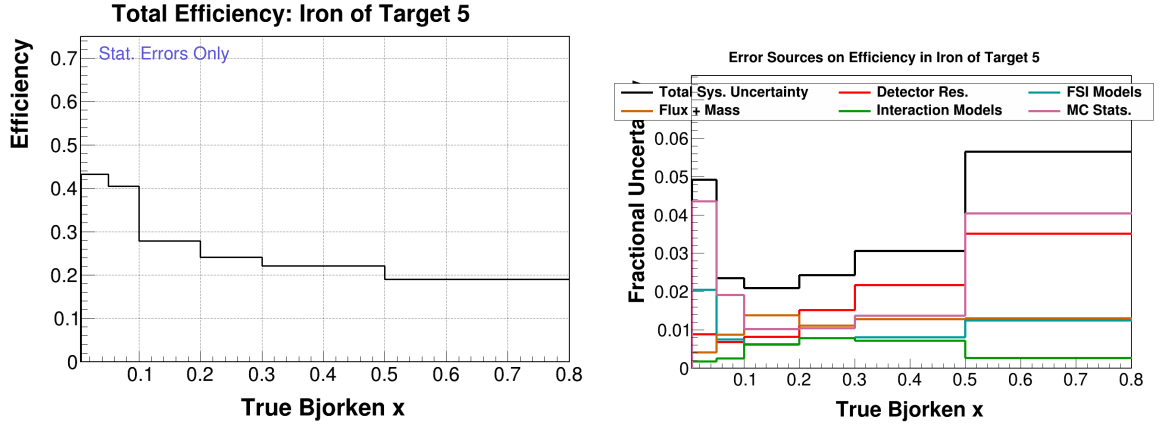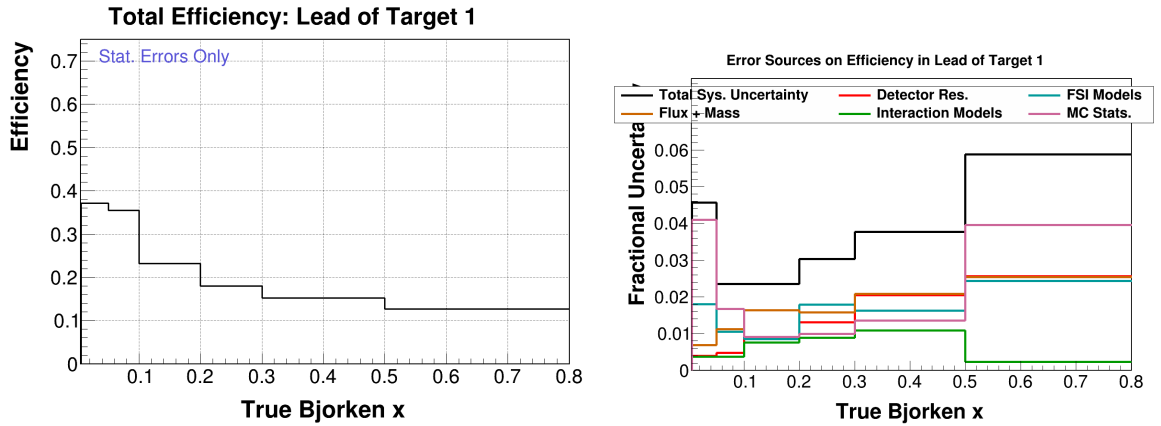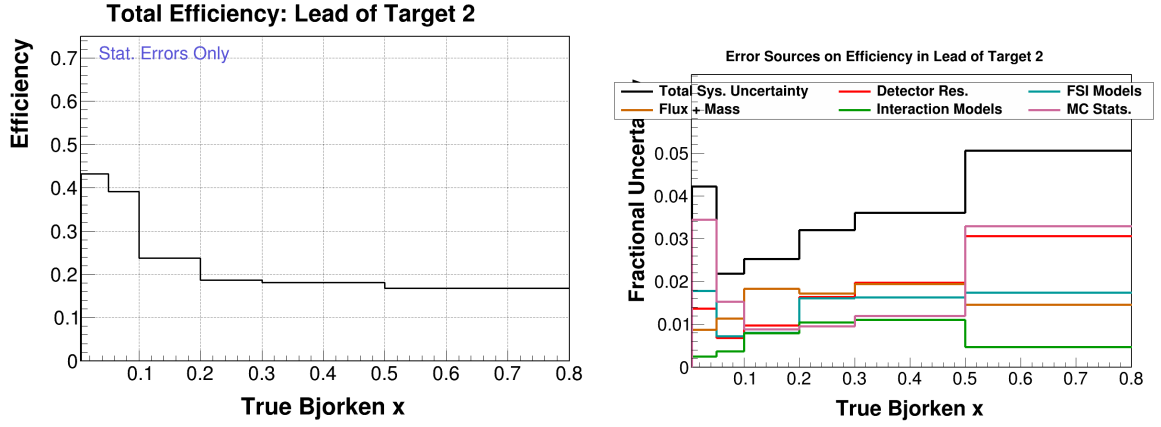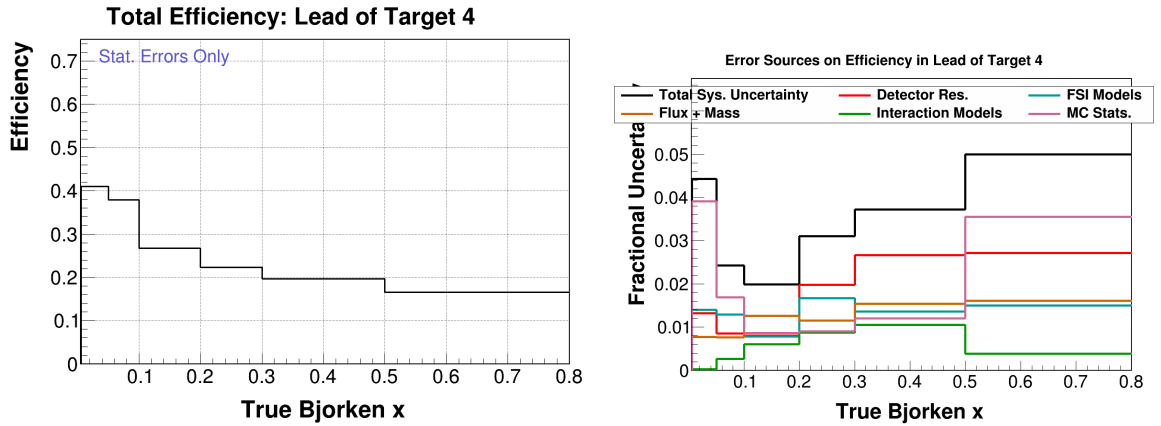

FIG. B.247: Lead of target 4 x_{bj} efficiency (left), and MC uncertainty (right).

Total Efficiency: Lead of Target 5

Error Sources on Efficiency in Lead of Target 5
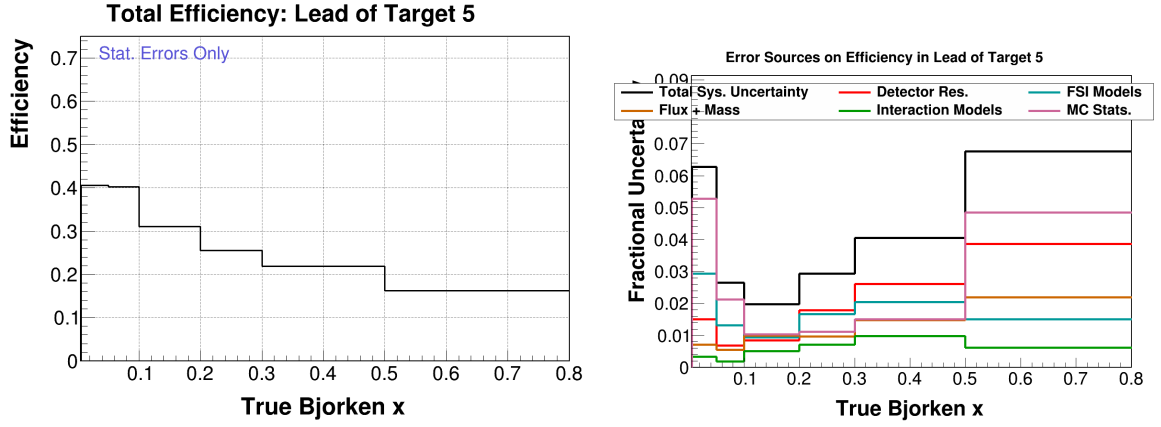
FIG. B.248: Lead of target 5 x_{bj} efficiency (left), and MC uncertainty (right).

Total Efficiency: Carbon of Target 3

Error Sources on Efficiency in Carbon of Target 3
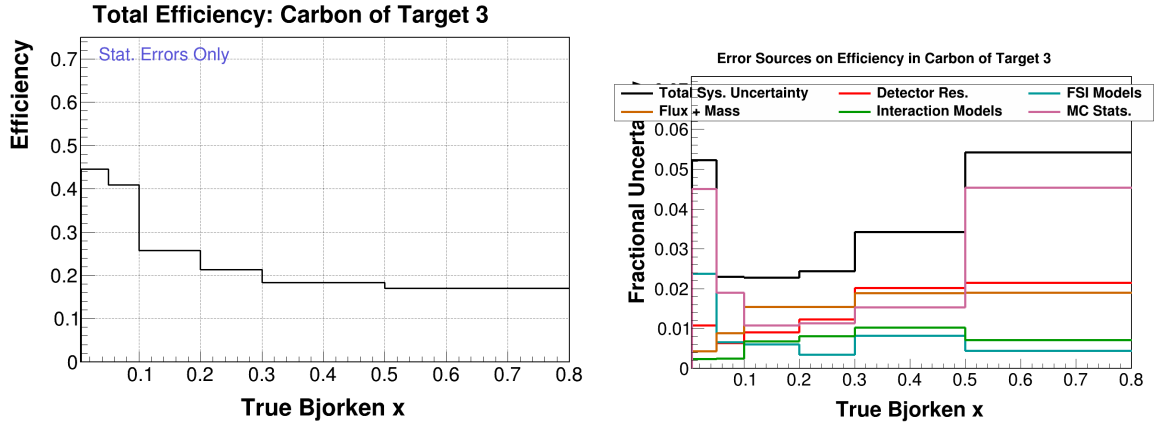
FIG. B.249: Carbon of target 3 x_{bj} efficiency (left), and MC uncertainty (right).

Total Efficiency: Tracker

Error Sources on Efficiency in Tracker
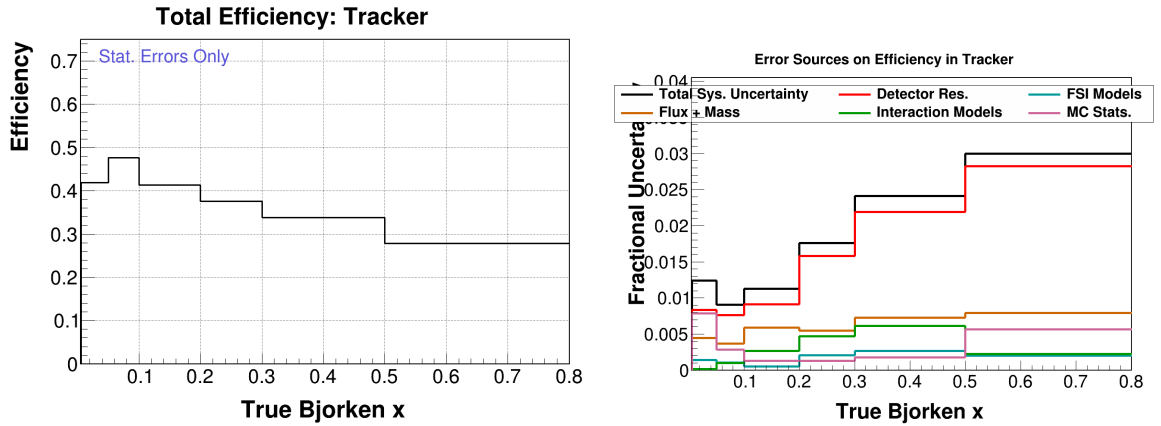
FIG. B.250: All tracker x_{bj} efficiency (left), and MC uncertainty (right).

392

B.7 Unfolding study

B.7.1 Neutrino Energy unfolding studies

FIG. B.251: The unfolding studies using a warping in E_ν, Q^2, and x_{bj} when unfolding neutrino energy in iron of target 1.

FIG. B.252: The unfolding studies using a warping in E_ν, Q^2, and x_{bj} when unfolding neutrino energy in lead of target 1.

FIG. B.253: The unfolding studies using a warping in E_ν, Q^2, and x_{bj} when unfolding neutrino energy in carbon of target 3.

FIG. B.254: The unfolding studies using a warping in E_ν, Q^2, and x_{bj} when unfolding neutrino energy in lead of target 4.

FIG. B.255: The χ^2 for the unfolding studies in tracker in each daisy petal from 0 (top left) to 11 (bottom right) in neutrino energy with the E_ν warping applied.
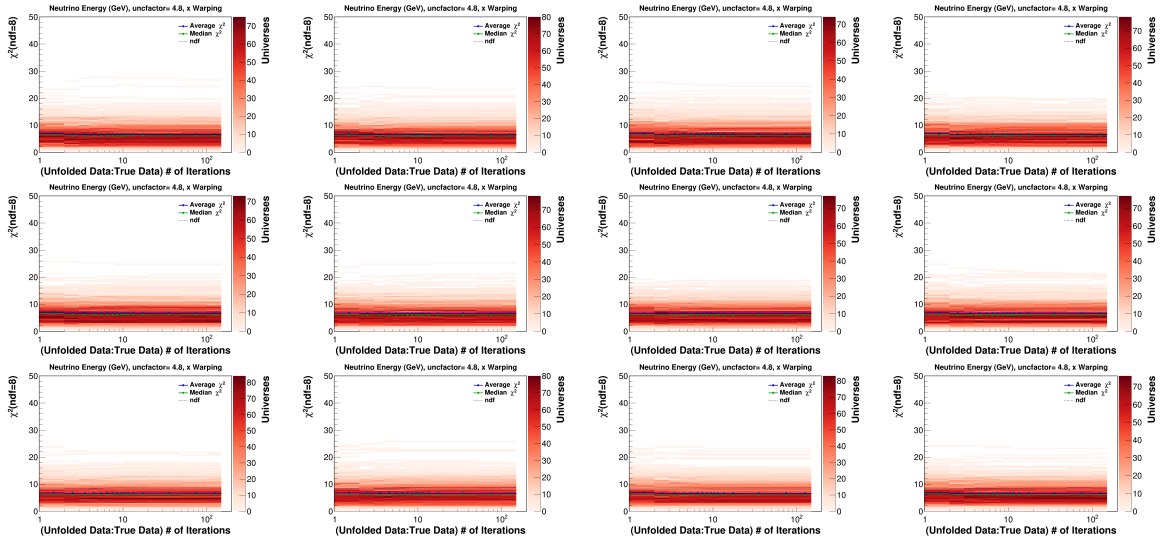
FIG. B.256: The χ^2 for the unfolding studies in tracker in each daisy petal from 0 (top left) to 11 (bottom right) in neutrino energy with the x_{bj} warping applied.
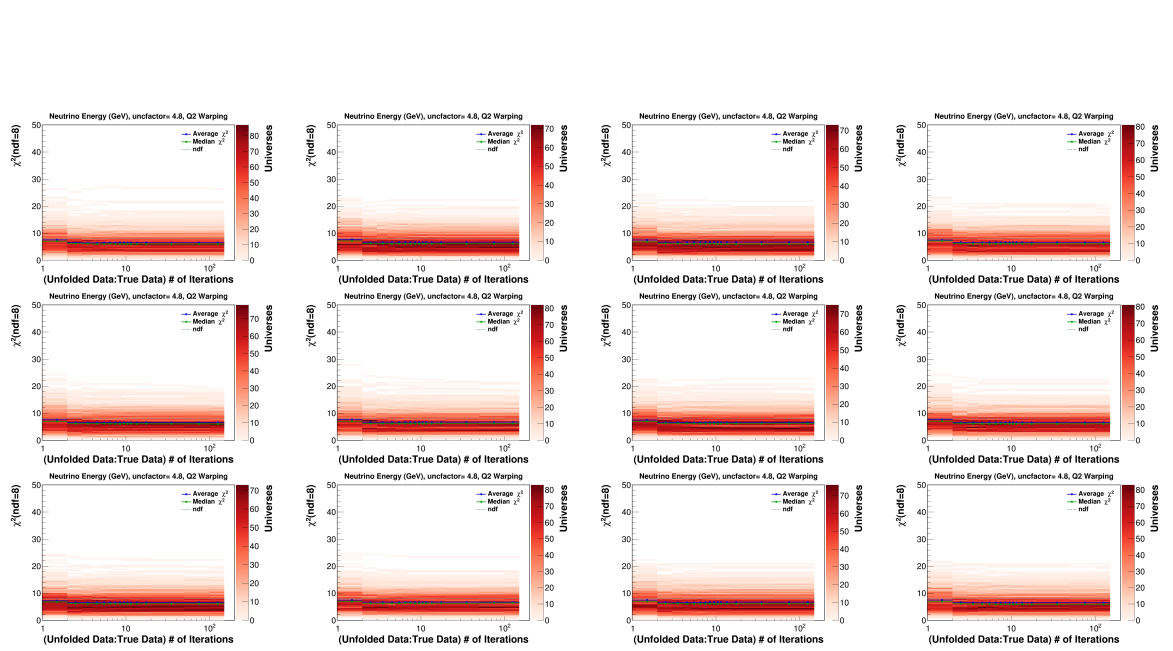
FIG. B.257: The χ^2 for the unfolding studies in tracker in each daisy petal from 0 (top left) to 11 (bottom right) in neutrino energy with the Q^2 warping applied.
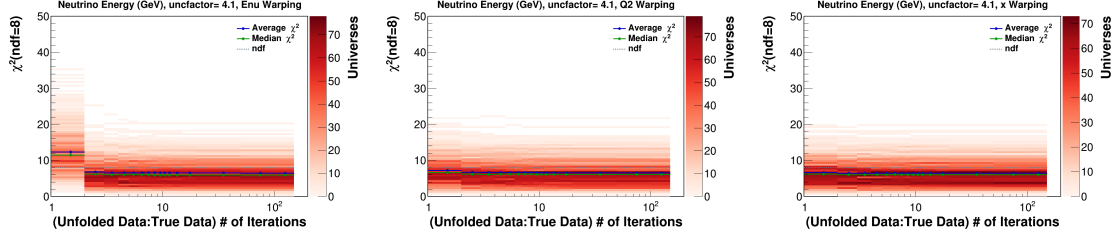
B.7.2 Bjorken-x unfolding studies
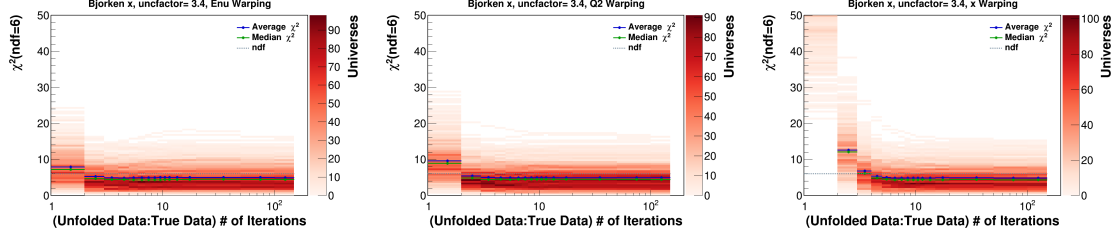
FIG. B.258: The unfolding studies using a warping in E_ν, Q^2, and x_{bj} when unfolding neutrino energy in iron of target 1.
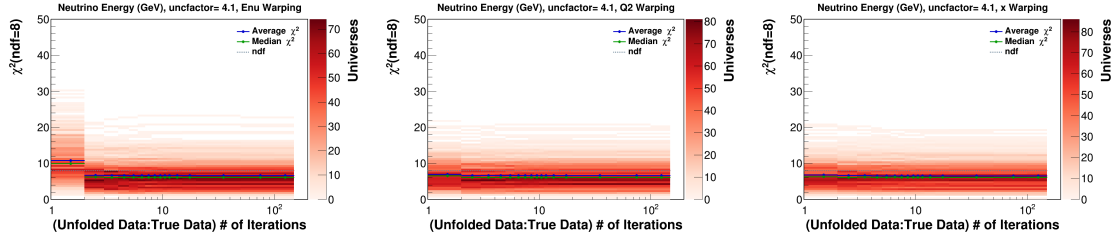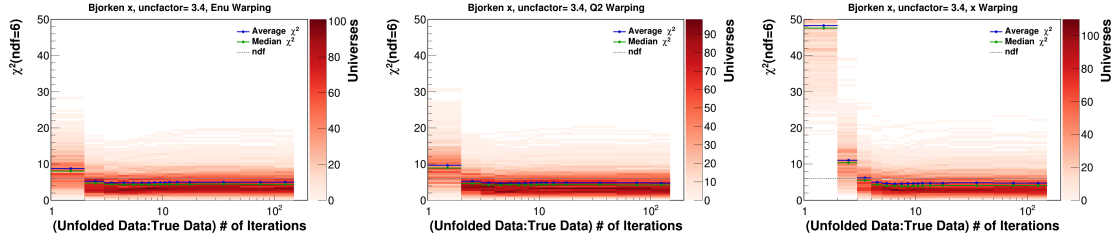

FIG. B.259: The unfolding studies using a warping in E_ν, Q^2, and x_{bj} when unfolding neutrino energy in lead of target 1.
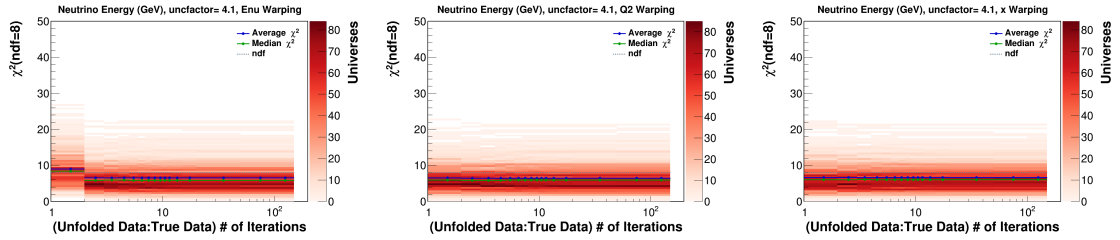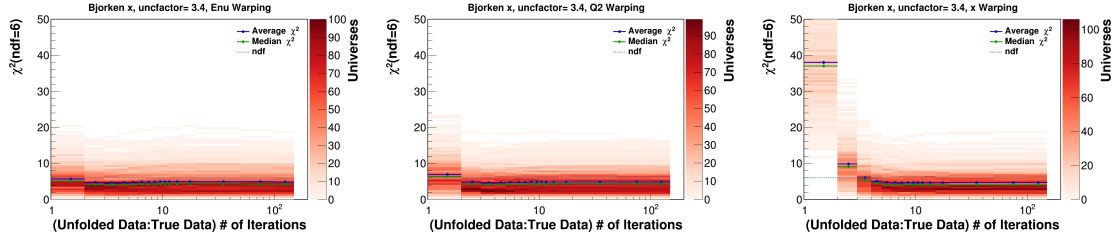

FIG. B.260: The unfolding studies using a warping in E_ν, Q^2, and x_{bj} when unfolding neutrino energy in carbon of target 3.
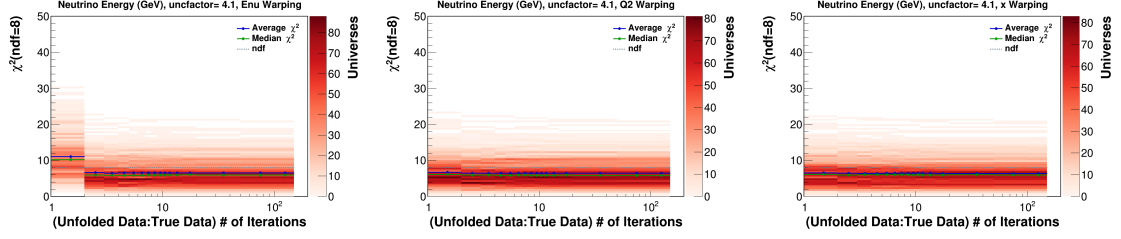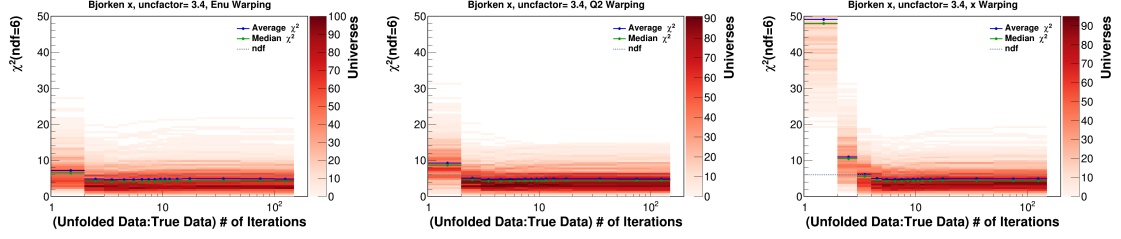
FIG. B.261: The unfolding studies using a warping in E_ν, Q^2, and x_{bj} when unfolding neutrino energy in lead of target 4.
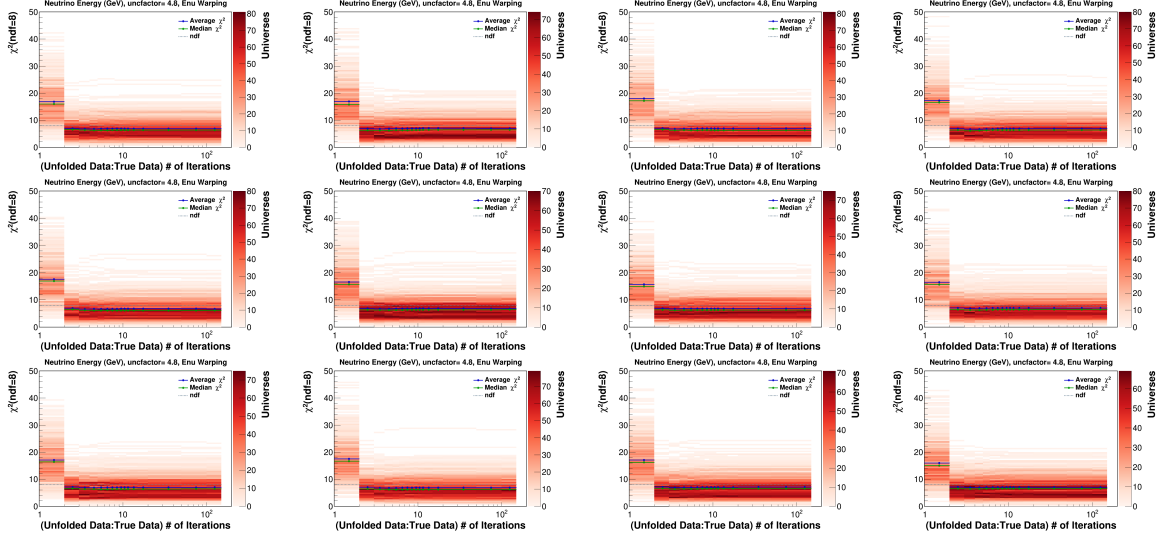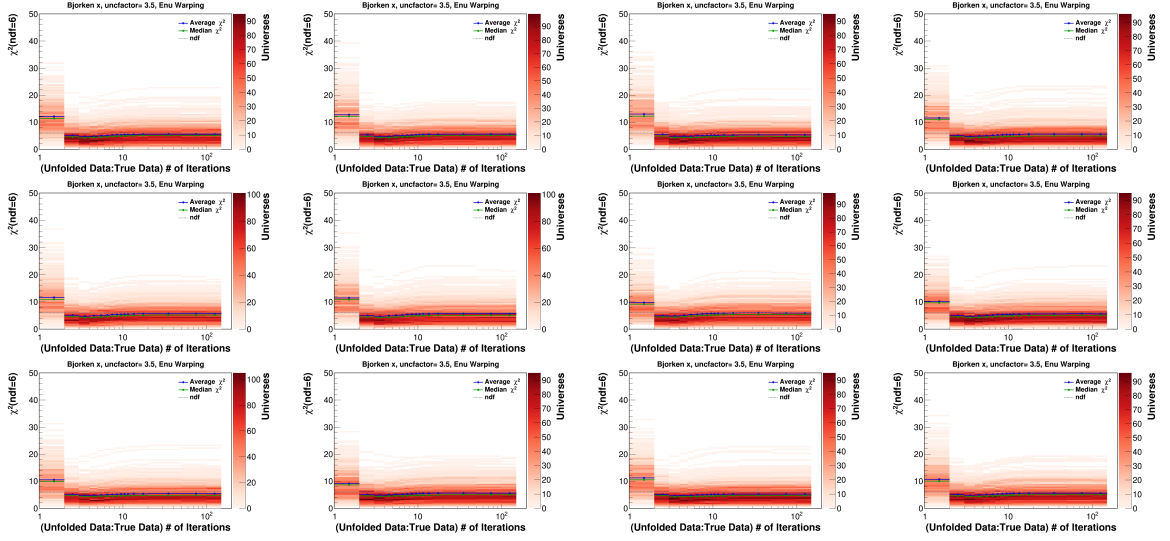

FIG. B.262: The χ^2 for the unfolding studies in tracker in each daisy petal from 0 (top left) to 11 (bottom right) in bjorken-x with the E_ν warping applied.
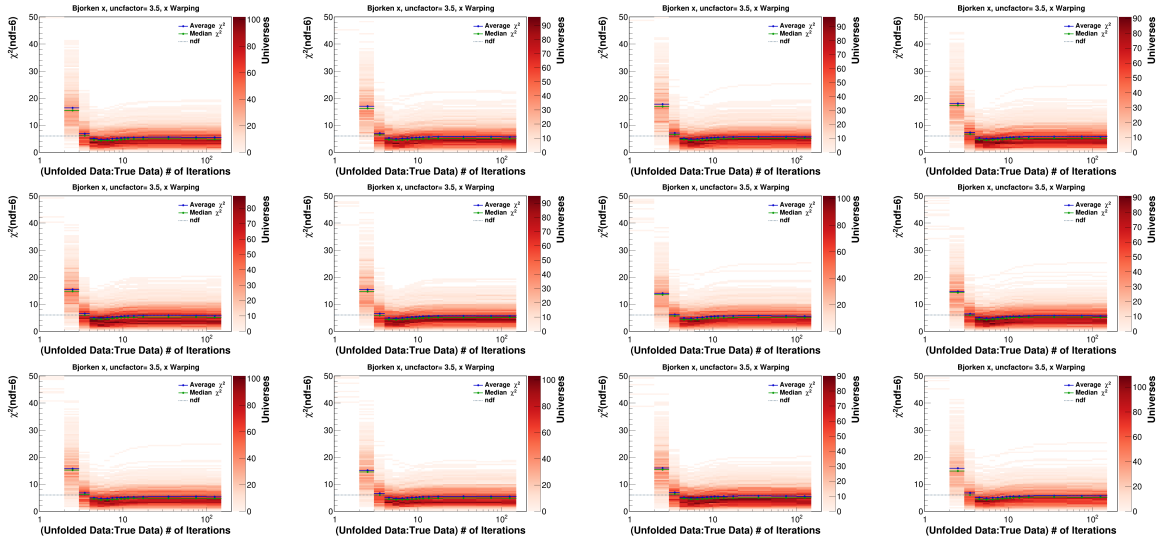
FIG. B.263: The χ^2 for the unfolding studies in tracker in each daisy petal from 0 (top left) to 11 (bottom right) in bjorken-x with the x_{bj} warping applied.
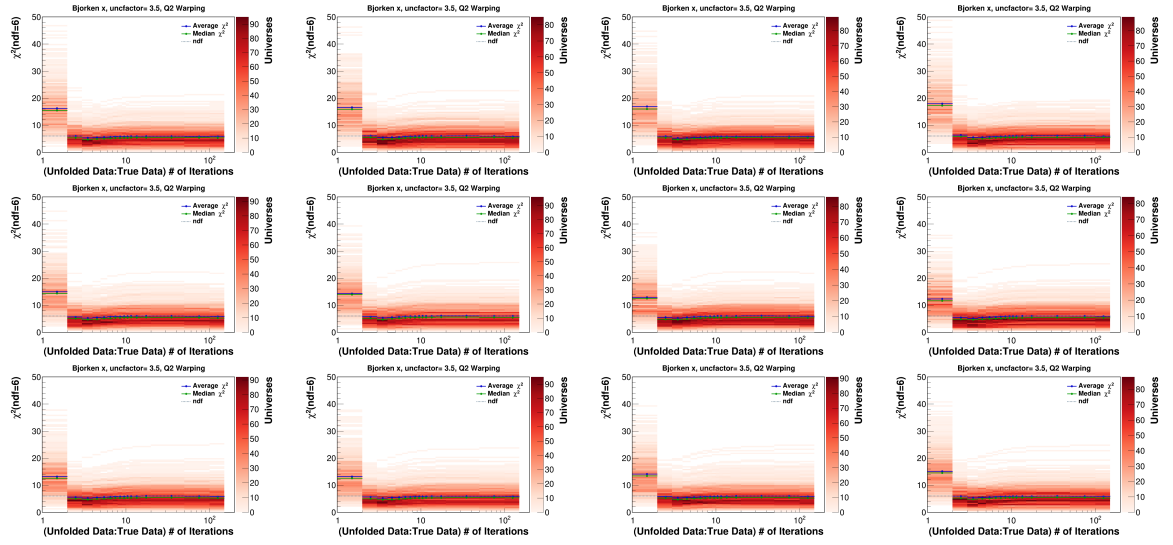
FIG. B.264: The χ^2 for the unfolding studies in tracker in each daisy petal from 0 (top left) to 11 (bottom right) in bjorken-x with the Q^2 warping applied.

# B.8 Cross Section Uncertainties

B.8.1 Absolute and differential error summaries

MC Error Summaries
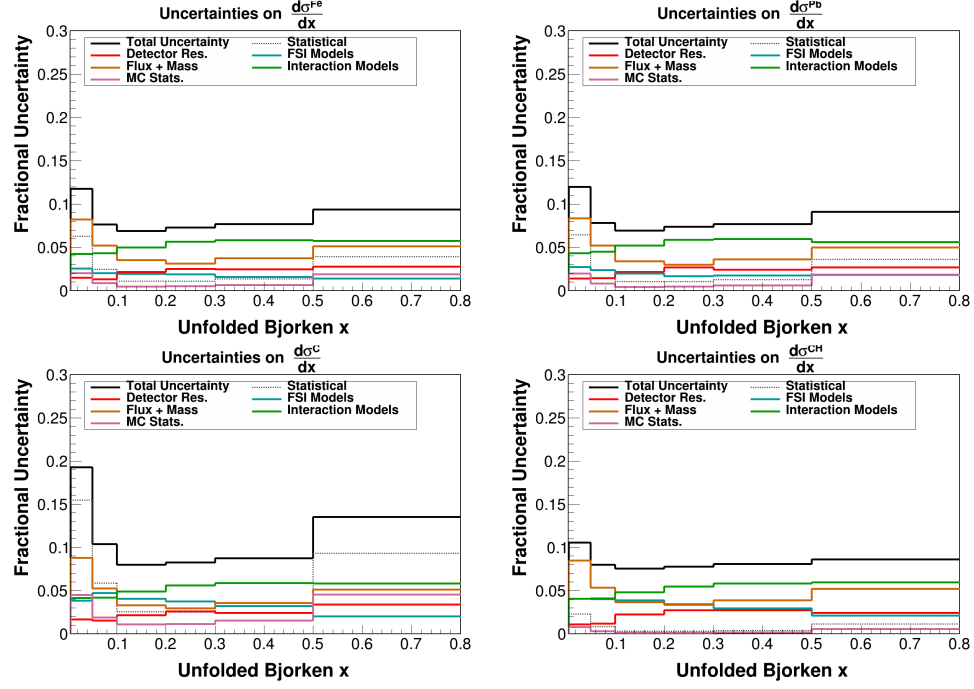
FIG. B.265: Summed cross sections MC error summary for iron, lead, carbon, and tracker in x_{bj}.
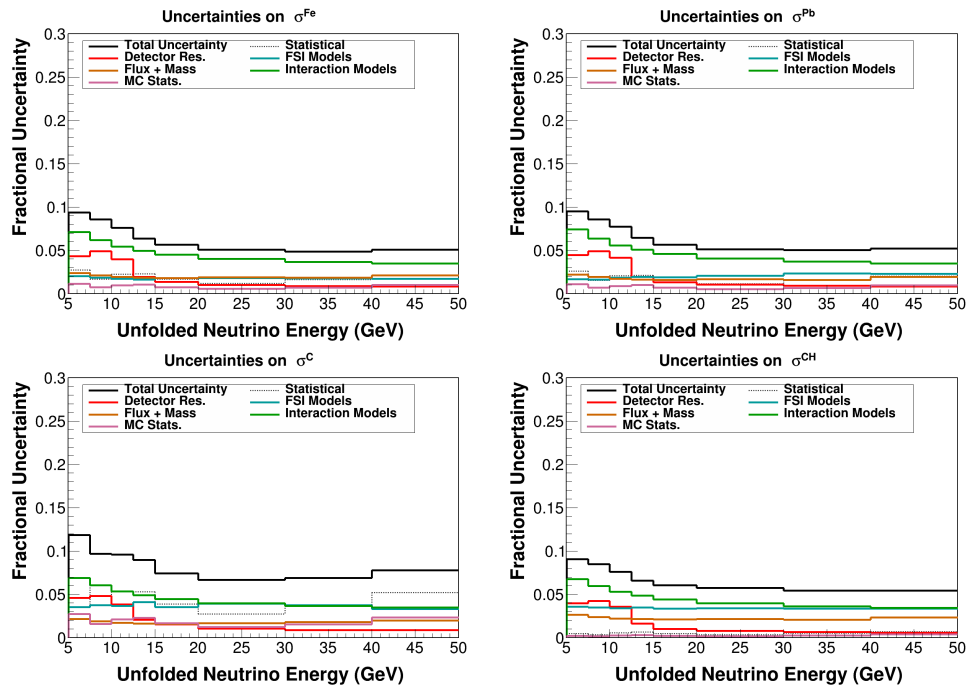
FIG. B.266: Summed cross sections MC error summary for iron, lead, carbon, and tracker in E_ν.

Data Error Group Breakdowns
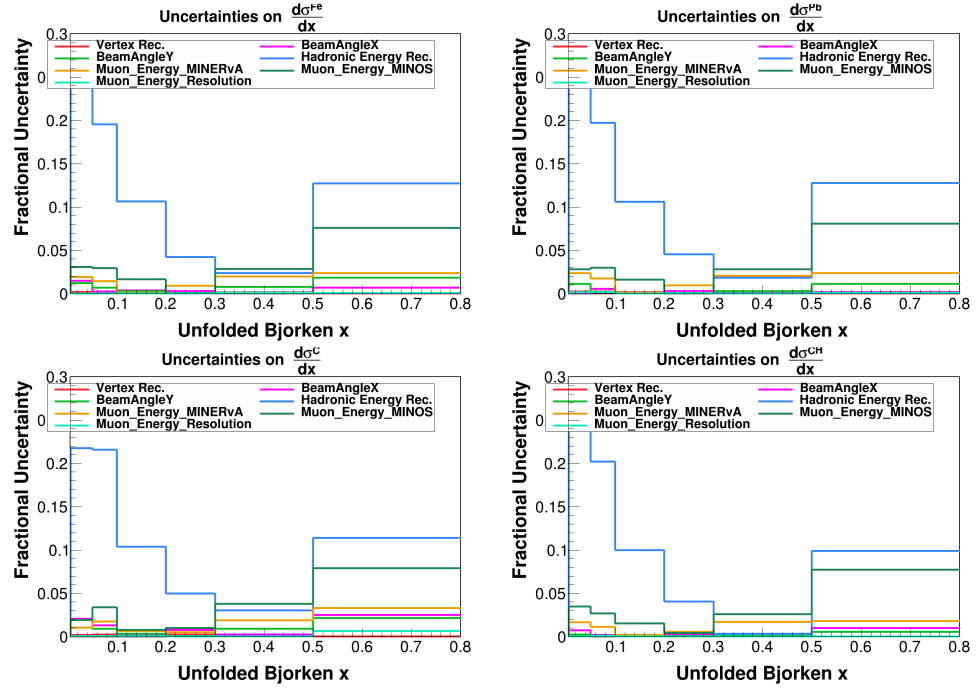
FIG. B.267: Data error summary for error group DetRes for iron(top left), lead (top right), carbon (bottom left), and tracker (bottom right) in x_{bj}
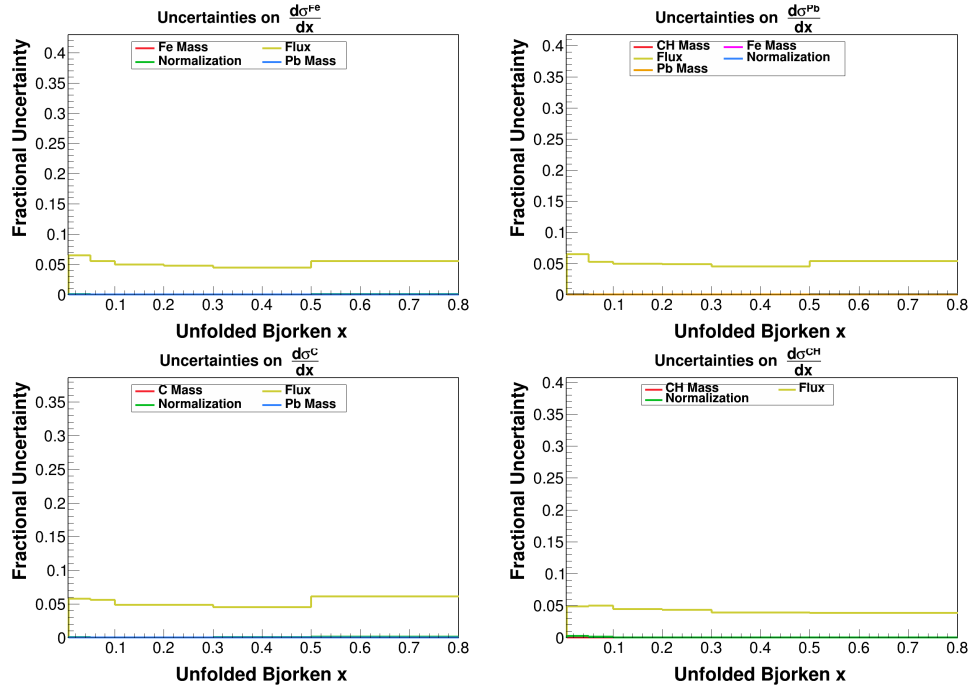
FIG. B.268: Data error summary for error group FluxMass for iron(top left), lead (top right), carbon (bottom left), and tracker (bottom right) in x_{bj}
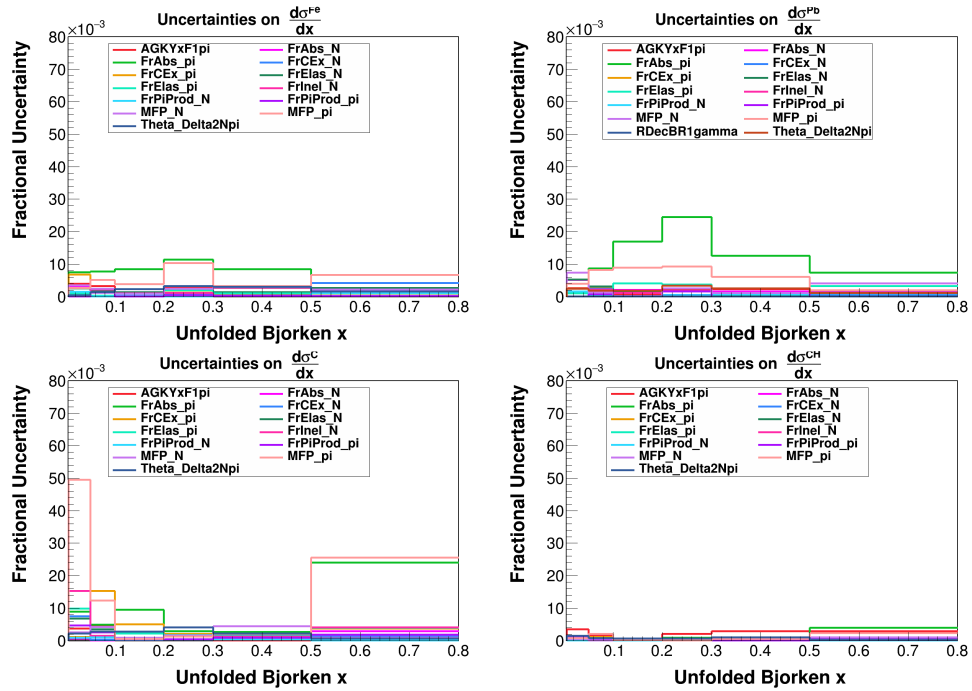
FIG. B.269: Data error summary for error group FSIModels for iron(top left), lead (top right), carbon (bottom left), and tracker (bottom right) in x_{bj}
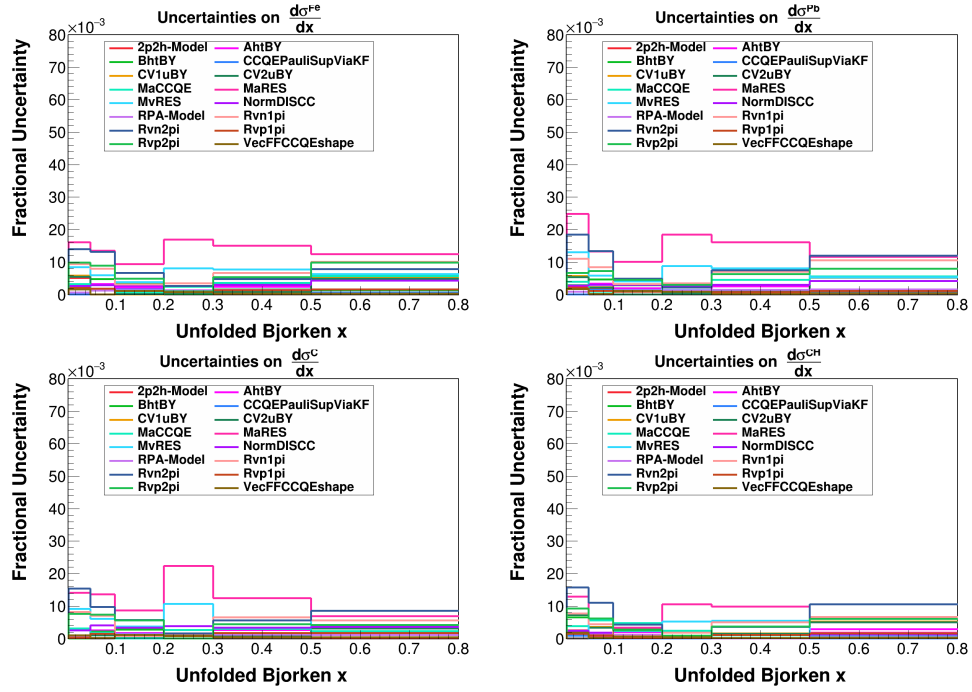
FIG. B.270: Data error summary for error group IntModels for iron(top left), lead (top right), carbon (bottom left), and tracker (bottom right) in x_{bj}
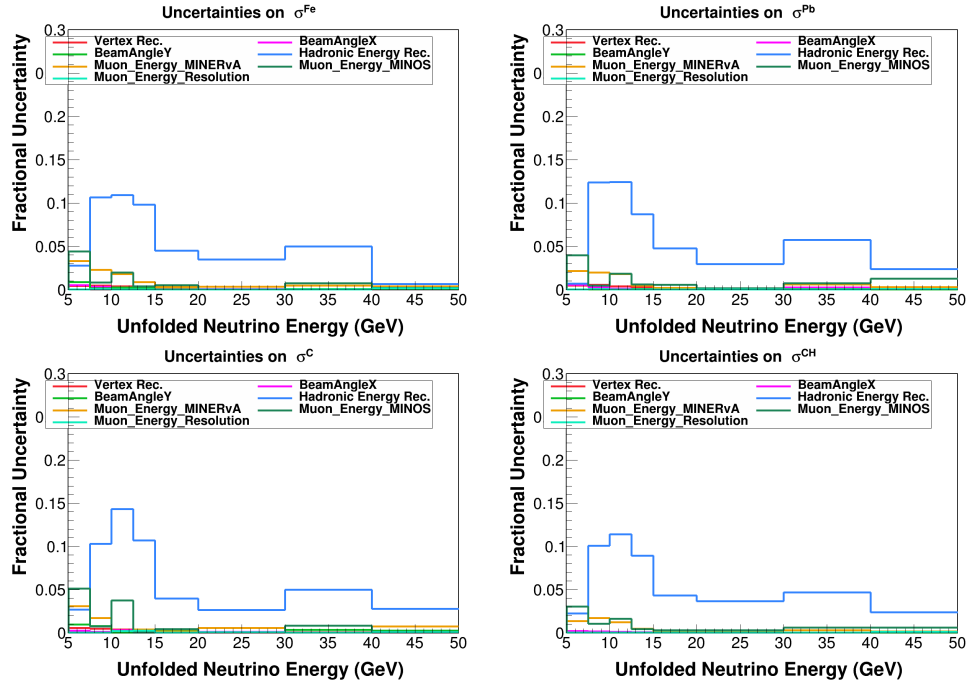
FIG. B.271: Data error summary for error group DetRes for iron(top left), lead (top right), carbon (bottom left), and tracker (bottom right) in E_ν

FIG. B.272: Data error summary for error group FluxMass for iron(top left), lead (top right), carbon (bottom left), and tracker (bottom right) in E_ν

FIG. B.273: Data error summary for error group FSIModels for iron(top left), lead (top right), carbon (bottom left), and tracker (bottom right) in E_ν
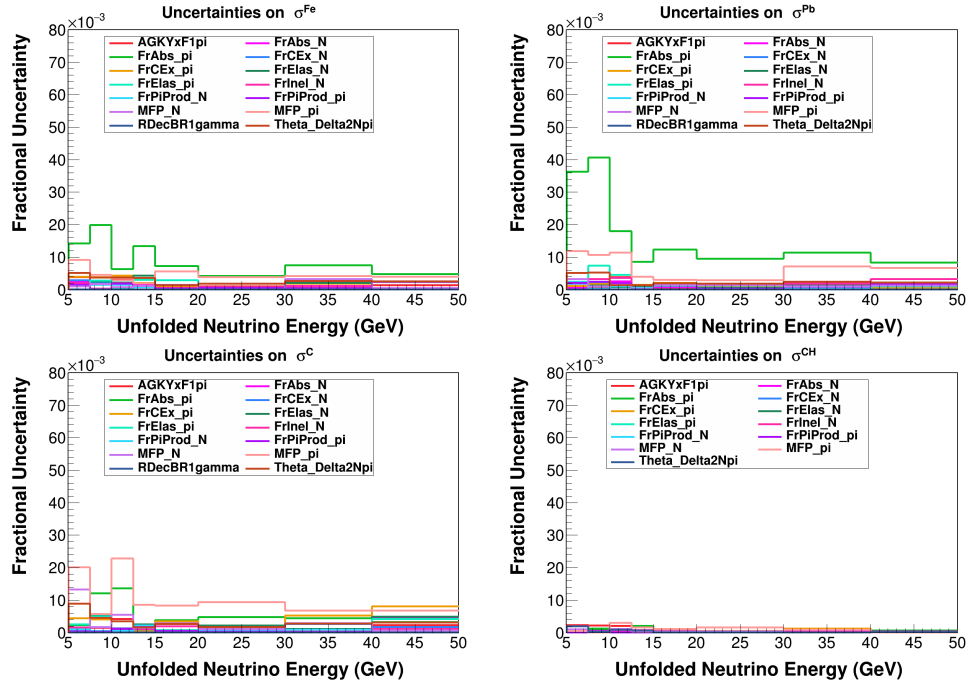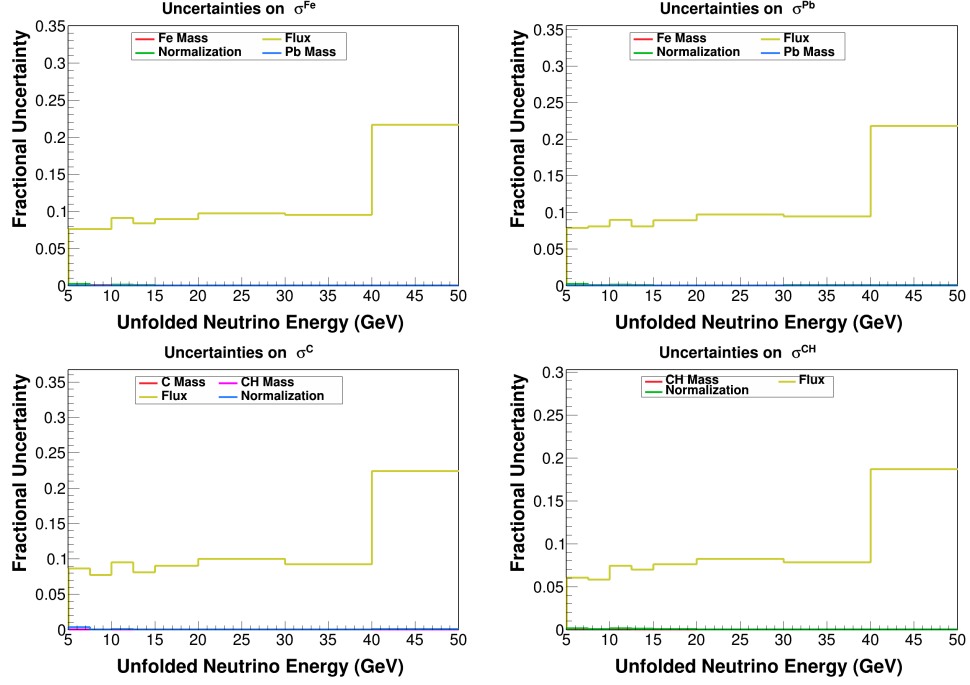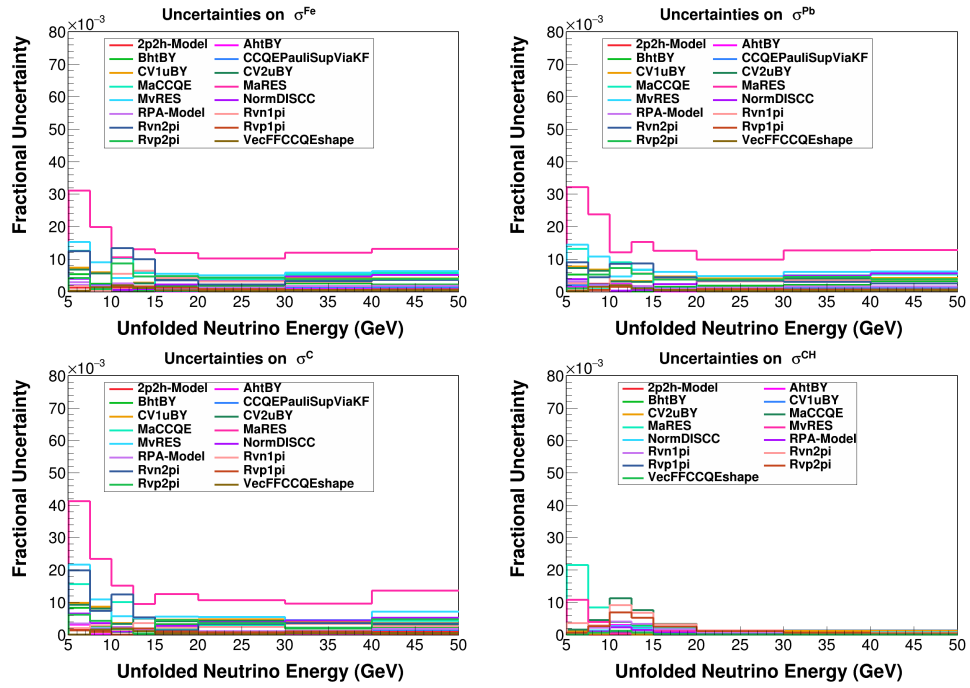
FIG. B.274: Data error summary for error group IntModels for iron(top left), lead (top right), carbon (bottom left), and tracker (bottom right) in E_ν

BIBLIOGRAPHY

[1] "Standard model of elementary particles," `https://commons.wikimedia.org/wiki/File:Standard_Model_of_Elementary_Particles.svg`.

[2] M. A. Acero *et al.* (NOvA), (2021), arXiv:2108.08219 [hep-ex] .

[3] K. Abe *et al.* (T2K), Phys. Rev. D **103**, 112008 (2021), arXiv:2101.03779 [hep-ex] .

[4] J. A. Formaggio and G. P. Zeller, Rev. Mod. Phys. **84**, 1307 (2012), arXiv:1305.7513 [hep-ex] .

[5] D. Casper, Nucl. Phys. Proc. Suppl. **112**, 161 (2002), arXiv:hep-ph/0208030 [hep-ph] .

[6] K. Rith, Subnucl. Ser. **51**, 431 (2015), arXiv:1402.5000 [hep-ex] .

[7] B. Abi *et al.* (DUNE), (2020), arXiv:2002.03005 [hep-ex] .

[8] M. Sajjad Athar and J. G. Morfín, J. Phys. G **48**, 034001 (2021), arXiv:2006.08603 [hep-ph] .

[9] J. Kleykamp, *A-scaling of CCQE-like cross sections at MINERvA*, Ph.D. thesis, Rochester U., Rochester U. (2021).

[10] L. Aliaga *et al.* (MINERvA Collaboration), Nucl. Instrum. Meth. A **743**, 130 (2014), arXiv:1305.5199 [physics.ins-det] .

[11] A. E. Norrick, *A Measurement of Nuclear Effects in Deep Inelastic Scattering in Neutrino-Nucleus Interactions*, Ph.D. thesis, William-Mary Coll. (2018).

[12] M. O. Wospakrik, *Measurement of Neutrino Absolute Deep Inelastic Scattering Cross Section in Iron, Lead, Carbon, and Plastic Using MINERvA Detector at $E_\nu = 6$ GeV*, Ph.D. thesis, Florida U. (2018).

[13] L. Aliaga Soplin, *Neutrino Flux Prediction for the NuMI Beamline*, Ph.D. thesis, William-Mary Coll. (2016).

[14] C. L. Cowan, F. Reines, F. B. Harrison, H. W. Kruse, and A. D. McGuire, Science **124**, 103 (1956).

[15] B. T. Cleveland, T. Daily, R. Davis, Jr., J. R. Distel, K. Lande, C. K. Lee, P. S. Wildenhain, and J. Ullman, Astrophys. J. **496**, 505 (1998).

[16] M. C. Gonzalez-Garcia and M. Maltoni, Phys. Rept. **460**, 1 (2008), arXiv:0704.1800 [hep-ph] .

[17] I. Esteban *et al.*, "Nufit 5.1," www.nu-fit.org (2021).

[18] I. Esteban, M. C. Gonzalez-Garcia, M. Maltoni, T. Schwetz, and A. Zhou, JHEP **09**, 178 (2020), arXiv:2007.14792 [hep-ph] .

[19] X. Qian and P. Vogel, Prog. Part. Nucl. Phys. **83**, 1 (2015), arXiv:1505.01891 [hep-ex] .

[20] K. J. Kelly, P. A. N. Machado, S. J. Parke, Y. F. Perez-Gonzalez, and R. Z. Funchal, Phys. Rev. D **103**, 013004 (2021), arXiv:2007.08526 [hep-ph] .

[21] C. Andreopoulos *et al.*, Nucl. Instrum. Meth. A **614**, 87 (2010), arXiv:0905.2517 [hep-ph] .

[22] Y. Hayato, Acta Phys. Polon. B **40**, 2477 (2009).

[23] T. Golan, C. Juszczak, and J. T. Sobczyk, Phys. Rev. C **86**, 015505 (2012), arXiv:1202.4197 [nucl-th] .

[24] O. Buss, T. Gaitanos, K. Gallmeister, H. van Hees, M. Kaskulov, *et al.*, Phys. Rept. **512**, 1 (2012), arXiv:1106.1344 [hep-ph] .

[25] S. Agostinelli *et al.*, Nucl. Instrum. Meth. A **506**, 250 (2003).

[26] R. A. Smith and E. J. Moniz, Nucl. Phys. B **43**, 605 (1972).

[27] A. Bodek and J. L. Ritchie, Phys. Rev. D **24**, 1400 (1981).

[28] C. H. Llewellyn Smith, Phys. Rept. **3**, 261 (1972).

[29] R. Bradford, A. Bodek, H. S. Budd, and J. Arrington, Nucl. Phys. Proc. Suppl. **159**, 127 (2006), arXiv:hep-ex/0602017 [hep-ex] .

[30] D. Rein and L. M. Sehgal, Annals Phys. **133**, 79 (1981).

[31] A. Bodek, I. Park, and U.-K. Yang, Nucl. Phys. Proc. Suppl. **139**, 113 (2005), arXiv:hep-ph/0411202 [hep-ph] .

[32] S. Dytman, *Proceedings, Hadronic Shower Simulation Workshop: Batavia, ILL, September 6-8, 2006*, AIP Conf. Proc. **896**, 178 (2007), [,178(2007)].

[33] S. Dytman and A. Meyer, AIP Conf. Proc. **1405**, 213 (2011).

[34] C. Wilkinson, P. Rodrigues, S. Cartwright, L. Thompson, and K. McFarland, Phys. Rev. D **90**, 112017 (2014), arXiv:1411.4482 [hep-ex] .

[35] P. Rodrigues, C. Wilkinson, and K. McFarland, Eur. Phys. J. **C76**, 474 (2016), arXiv:1601.01888 [hep-ex] .

[36] J. Nieves, J. E. Amaro, and M. Valverde, Phys. Rev. C **70**, 055503 (2004), arXiv:nucl-th/0408005 [nucl-th] .

[37] R. Gran, (2017), arXiv:1705.02932 [hep-ex] .

[38] J. Nieves, I. Ruiz Simo, and M. J. Vicente Vacas, Phys. Rev. C **83**, 045501 (2011), arXiv:1102.2777 [hep-ph] .

[39] R. Gran, J. Nieves, F. Sanchez, and M. J. Vicente Vacas, Phys. Rev. D **88**, 113007 (2013), arXiv:1307.8105 [hep-ph] .

[40] J. Schwehr, D. Cherdack, and R. Gran, (2016), arXiv:1601.02038 [hep-ph] .

[41] P. A. Rodrigues *et al.* (MINERvA Collaboration), Phys. Rev. Lett. **116**, 071802 (2016), arXiv:1511.05944 [hep-ex] .

[42] R. Gran *et al.* (MINERvA Collaboration), Phys. Rev. Lett. **120**, 221805 (2018), arXiv:1803.09377 [hep-ex] .

[43] D. Ruterbories *et al.* (MINERvA Collaboration), Phys. Rev. D **99**, 012004 (2019), arXiv:1811.02774 [hep-ex] .

[44] C. E. Patrick *et al.* (MINERvA Collaboration), Phys. Rev. D **97**, 052002 (2018), arXiv:1801.01197 [hep-ex] .

[45] B. Eberly *et al.* (MINERvA Collaboration), Phys. Rev. D **92**, 092008 (2015), arXiv:1406.6415 [hep-ex] .

[46] C. L. McGivern *et al.* (MINERvA Collaboration), Phys. Rev. D **94**, 052005 (2016), arXiv:1606.07127 [hep-ex] .

[47] O. Altinok *et al.* (MINERvA Collaboration), Phys. Rev. D **96**, 072003 (2017), arXiv:1708.03723 [hep-ex] .

[48] P. Stowell *et al.* (MINERvA Collaboration), Phys. Rev. **D100**, 072005 (2019), arXiv:1903.01558 [hep-ex] .

[49] P. Adamson *et al.* (MINOS Collaboration), Phys. Rev. D **91**, 012005 (2015), arXiv:1410.8613 [hep-ex] .

[50] K. Kovarik *et al.*, Phys. Rev. D **93**, 085037 (2016), arXiv:1509.00792 [hep-ph] .

[51] I. Schienbein, J. Y. Yu, C. Keppel, J. G. Morfin, F. Olness, and J. F. Owens, Phys. Rev. D **77**, 054013 (2008), arXiv:0710.4897 [hep-ph] .

[52] H. Haider, F. Zaidi, M. Sajjad Athar, S. K. Singh, and I. Ruiz Simo, Nucl. Phys. **A955**, 58 (2016), arXiv:1603.00164 [nucl-th] .

[53] Z. Koba, H. B. Nielsen, and P. Olesen, Nucl. Phys. B **40**, 317 (1972).

[54] T. Sjostrand, S. Mrenna, and P. Z. Skands, JHEP **05**, 026 (2006), arXiv:hep-ph/0603175 .

[55] T. Yang, C. Andreopoulos, H. Gallagher, K. Hoffmann, and P. Kehayias, Eur. Phys. J. C **63**, 1 (2009), arXiv:0904.4043 [hep-ph] .

[56] J. Estrada, C. Garcia, B. Hoeneisen, and P. Rubinov, (2003), 10.2172/820406.

[57] G. N. Perdue *et al.* (MINERvA Collaboration), Nucl. Instrum. Meth. A **694**, 179 (2012), arXiv:1209.1120 [physics.ins-det] .

[58] J. B. Birks, Proc. Phys. Soc. A **64**, 874 (1951).

[59] P. Adamson *et al.*, Nucl. Instrum. Meth. A **806**, 279 (2016), arXiv:1507.06690 [physics.acc-ph] .

[60] Fermilab, "Fermilab's accelerator complex," .

[61] B. Andersson, G. Gustafson, and B. Nilsson-Almqvist, Nucl. Phys. B **281**, 289 (1987).

[62] M. P. Guthrie, R. G. Alsmiller, and H. W. Bertini, Nucl. Instrum. Meth. **66**, 29 (1968).

[63] B. Nilsson-Almqvist and E. Stenlund, Computer Physics Communications **43**, 387 (1987).

[64] C. Alt *et al.* (NA49), Eur. Phys. J. C **49**, 897 (2007), arXiv:hep-ex/0606028 .

[65] J. M. Paley *et al.* (MIPP), Phys. Rev. D **90**, 032001 (2014), arXiv:1404.5882 [hep-ex] .

[66] C. Birattari, E. De Ponti, A. Esposito, A. Ferrari, M. Pelliccioni, and M. Silari, Nucl. Instrum. Meth. A **338**, 534 (1994).

[67] L. Aliaga *et al.* (MINERvA Collaboration), Phys. Rev. D **94**, 092005 (2016), [Addendum: Phys. Rev.D95,no.3,039903(2017)], arXiv:1607.00704 [hep-ex] .

[68] D. Ruterbories *et al.* (MINERvA), Phys. Rev. D **104**, 092010 (2021), arXiv:2107.01059 [hep-ex] .

[69] J. Park *et al.* (MINERvA Collaboration), Phys. Rev. D **93**, 112007 (2016), arXiv:1512.07699 [physics.ins-det] .

[70] L. Zazueta *et al.* (MINERvA), "Improved Constraint on the MINERvA Medium Energy Neutrino Flux using $\bar{\nu}e^- \to \bar{\nu}e^-$ data," In preperation.

[71] G. A. Diaz Bautista, *Determinacion del error sistematico del momentum de muones producidos por interacciones neutrino-nucleon en el detector MINERνA*, Master's thesis, Lima, Pont. U. Catolica (2015).

[72] L. Aliaga *et al.* (MINERvA Collaboration), Nucl. Instrum. Meth. A **789**, 28 (2015), arXiv:1501.06431 [physics.ins-det] .

[73] G. N. Perdue *et al.* (MINERvA), JINST **13**, P11020 (2018), arXiv:1808.08332 [physics.data-an] .

[74] C. Patrick, "Minerva 101 – extracting cross-sections," `https://minerva-docdb.fnal.gov/cgi-bin/sso/ShowDocument?docid=9992` (2014), [Internal document].

[75] G. D'Agostini, Nucl. Instrum. Meth. **A362**, 487 (1995).

[76] G. D'Agostini, in *Alliance Workshop on Unfolding and Data Correction Hamburg, Germany, May 27-28, 2010* (2010) arXiv:1010.0632 [physics.data-an] .

[77] R. Brun and F. Rademakers, Nuclear Instruments and Methods in Physics Research Section A: Accelerators, Spectrometers, Detectors and Associated Equipment **389**, 81 (1997), new Computing Techniques in Physics Research V.

[78] T. Adye, in *PHYSTAT 2011* (CERN, Geneva, 2011) pp. 313–318, arXiv:1105.1160 [physics.data-an] .

[79] A. Filkins *et al.* (MINERvA), Phys. Rev. D **101**, 112007 (2020), arXiv:2002.12496 [hep-ex] .

[80] K. Abe *et al.* (T2K Collaboration), Phys. Rev. D **98**, 012004 (2018), arXiv:1801.05148 [hep-ex] .

[81] P. Abratenko *et al.* (MicroBooNE Collaboration), Phys. Rev. Lett. **123**, 131801 (2019), arXiv:1905.09694 [hep-ex] .

[82] M. A. Acero *et al.* (NOvA), (2021), arXiv:2109.12220 [hep-ex] .

[83] X. G. Lu *et al.* (MINERvA Collaboration), Phys. Rev. Lett. **121**, 022504 (2018), arXiv:1805.05486 [hep-ex] .

[84] T. Cai *et al.* (MINERvA Collaboration), Phys. Rev. D **101**, 092001 (2020), arXiv:1910.08658 [hep-ex] .

[85] T. Le *et al.* (MINERvA Collaboration), Phys. Rev. **D100**, 052008 (2019), arXiv:1906.08300 [hep-ex] .

[86] D. Ruterbories *et al.* (MINERvA), Phys. Rev. D **104**, 092007 (2021), arXiv:2106.16210 [hep-ex] .

VITA

Amy Filkins

Amy Filkins was born in Albany, New York and attended Shenendehowa Central Schools for elementary through high school, graduating in 2012. She received her BA in physics from the State University of New York at Geneseo in 2016. Following graduation from SUNY Geneseo, Amy entered in the PhD program at William & Mary where she has been working on the MINERvA experiment. She has since studied neutrino-nucleus interactions under the supervision of Professor Jeffrey Nelson.